THÈSE DE DOCTORAT

UPEC
Connaissance - Action
UNIVERSITÉ
PARIS-EST CRÉTEIL
VAL DE MARNE

PARIS
EST
SUP

Porphyrines photoactives : synthèse et utilisation en photochimie dans l'élaboration de revêtements biosourcés pour des applications biomédicales et environnementales

Thèse de doctorat de l'Université Paris-Est Créteil

École doctorale n° 531, Sciences, Ingénierie et Environnement – SIE
Chimie des Matériaux

Thèse préparée à l'Institut de Chimie et des Matériaux Paris-Est (ICMPE)
sous la co-direction de **Davy-Louis VERSACE**, Professeur des Universités,
la co-direction de **Yamin LEPRINCE-WANG**, Professeure des Universités,
la co-direction de **Isabelle NAVIZET**, Professeure des Universités,
le co-encadrement de **Marc PRESSET**, Maître de conférences,

Thèse soutenue à l'ICMPE, le 5 février 2024, par

Fanny SCHNETZ

Composition du jury

Membres du jury avec voix délibérative :

Jean-Pierre MALVAL, Professeur des Universités, IS2M	Rapporteur
Zacharias AMARA, Maître de conférences, CNAM	Rapporteur
Rachel MEALLET, Professeure des Universités, ISMO	Examinatrice
Nathalie JARROUX, Professeure des Universités, LAMBE	Examinatrice
Sébastien RICHETER, Maître de conférences, ICGM	Invité

Remerciements

Je tiens tout d'abord à remercier particulièrement les membres du jury, pour avoir accepté d'évaluer mes travaux de thèse, Monsieur Jean-Pierre Malval et Monsieur Zacharias Amara en tant que rapporteurs ainsi que Madame Rachel Meallet et Madame Nathalie Jarroux en tant qu'examinatrices. Je remercie également Monsieur Sébastien Richeter d'avoir participé à ma soutenance en tant qu'invité.

Mes travaux de thèse ont été menés dans différents laboratoires. Deux parties de ces travaux ont été réalisés au sein des l'équipes Biomacromolécules et matériaux durables (BioM&Ms) et Electrosynthèse catalyse et chimie organique (ECCO) du département Chimie Moléculaire et Matériaux Macromoléculaire (C3M) de l'Institut de Chimie et des Matériaux Paris-Est (ICMPE), et deux autres parties ont été réalisés dans le groupe de recherche Nanomatériaux du laboratoire Électronique, Systèmes de Communication et Microsystèmes (ESYCOM) et dans l'équipe de Chimie Théorique (CT) du laboratoire de Modélisation Simulation Multi-Echelle (MSME) de l'Université Gustave Eiffel (UGE). Mes séjours dans ces laboratoires ont toujours été extraordinaires, et je souhaite donc remercier les personnes de ces différents laboratoires.

Je tiens donc à remercier en premier lieu Monsieur Daniel Grande, directeur de l'ICMPE, Monsieur Jean-Marc Laheurte, directeur du laboratoire ESYCOM, ainsi que Madame Céline Leonard, directrice du laboratoire MSME pour leur accueil dans leur laboratoire. Je remercie également le LabEx MMCD pour le financement de ma thèse, ainsi que pour la gestion de mes différents projets.

Durant ces trois années de thèse, j'ai eu la chance d'être suivie par une équipe de quatre encadrants. Je tiens donc à remercier mes directeurs de thèse, le Pr. Davy-Louis Versace, la Pr. Yamin Leprince-Wang, la Pr. Isabelle Navizet, ainsi que mon encadrant, le Dr. Marc Presset pour m'avoir donné l'opportunité de réaliser cette thèse. Merci pour votre confiance au cours de ces trois ans, et pour toutes les discussions scientifiques (et surtout celles non scientifiques) que nous avons pu avoir. Vous avez su m'enseigner vos connaissances, dont dans des domaines que je connaissais à peine avant de venir, avec beaucoup de patience et de prévenance. Merci pour votre disponibilité à toute épreuve et vos conseils. Je vous remercie également pour toutes les opportunités que vous m'avez offertes, que ce soit des conférences ou des collaborations, qui m'ont permis de développer des compétences transverses.

Un grand merci également aux membres de l'ICMPE, sans qui ses travaux de recherche auraient été impossibles : Tina Modjinou, Séna Hamadi et Laurent Michely pour la plateforme analytique et Patrice Renevret et Isabelle Lachaise pour la plateforme chromatographie. Merci également à Stéphane Segmany pour avoir passé autant de temps avec moi en voltamétrie. Je tenais à remercier aussi toute l'équipe administrative des différents laboratoires, ça n'a pas toujours été facile de trouver les bons correspondants, mais merci de m'avoir toujours soutenu. En particulier je souhaite remercier Dominique Alain, pour toute la paperasse accumulée en trois ans, et sans qui mon départ en Australie n'aurait sans doute pas été possible.

Je tiens également à remercier les collaborateurs hors ICMPE, d'avoir accepté de m'accueillir dans vos laboratoires : merci à Samir Abbad-Andaloussi et toute l'équipe du LEESU à l'UPEC de m'avoir fait découvrir la microbiologie, merci à Fabienne Peyrot et Sonia Lajnef pour m'avoir accueillie en RPE, Arnaud Brosseau et Minh-Huong Ha-Thi pour les caractérisations en laser. I am also very grateful to Cyrille Boyer and his team for welcoming me in his research group in Sydney. Thank you for your support. This was a great opportunity for me to discover a new chemistry and a new country.

Je tenais également à remercier toutes les personnes qui ont participé à la superbe vie du labo à l'ICMPE du bâtiment H. Merci Estelle et Valérie pour votre soutien sans faille, vos conseils, les pauses

à la cafet et toutes nos aventures. Merci également à Agustin et Benoit, pour pouvoir oublier efficacement le travail. Merci à la team des désormais docteurs et des doctorants, qui ont su aider à affronter les épreuves d'une thèse : Louise, merci de m'avoir tout appris ; Fannie, pour tous ces cours de sports pas du tout assidus et ta motivation de fer contagieuse ; Julie, pour ton humour à marier et tes références cinématographiques ; Lucie, pour ton énergie et ton courage ; Maeva, pour ta positivité et ta folie ; Hassan pour ton humour décapant ; Tamsir ; Marion et Corentin. Merci aussi aux nouveaux doctorants, qui remettent de l'énergie dans cette équipe : Stéphanie, Laura, Bastien, Balthazar, Ambre, Karim et Fares. Un énorme merci au bureau des High Five et à ses occupants. Ce bureau terrible où il est parfois difficile de se concentrer, mais si agréable grâce à vous. Laura, merci pour ta bonne humeur légendaire, ton rhum, tes danses et nos paris ; Eva, merci pour tes remarques impertinentes et pour rappel : tu as un ordinateur ; Christine, merci pour tous ces regards échangés entre nos écrans, et pour tes notes sur ta liste de l'enfer. Merci pour tous nos délires, nos conversations profondes, les vidéos de catsitting et nos virées à Belle ep' en 206.

Je tenais également à remercier toute l'équipe ECCO. Mes visites reposaient essentiellement pour des blind-tests de musique pop, mais également des barbecues et des raclettes, et un peu de synthèse. Merci à Marine et Baptiste, derrière vos moqueries, je sais que vous m'enviiez mes colonnes noires interminables ; Senabou, nous étions dans la même galère des colorants, dommage que nos séjours respectifs au laboratoire n'étaient pas toujours coordonnés ; Louis-Antoine, nos conversations sur la littérature, les jeux vidéo et nos chats me manque ; Farah, merci pour tes visites lors de toutes tes escapades en RMN et Iryna pour la magie de Noël en octobre. Enfin, Marc, merci pour ton investissement, ton soutien et tes conseils, c'est grâce à toi si j'en suis là aujourd'hui, à avoir obtenu cette noix dorée.

Merci également aux autres laboratoires que j'ai eu la chance d'intégrer : au laboratoire ESYCOM, Marie et Nathan, pour m'avoir appris tout ce qu'il y avait à savoir, vos conseils, et tous les repas partagés ensemble. Au laboratoire CT, merci à Mohammed, Houda, Rolande et Rosa. Les serveurs à distance n'ont pas vraiment permis de vous voir régulièrement, mais c'est bien dommage, mes passages en chimie théorique étaient toujours bien plus agréables avec vous.

Merci également aux stagiaires que j'ai pu encadrer : Sofia, désolée de t'avoir embarqué là-dedans. La biblio disait que ça marchait. Merci pour toutes molécules que tu as pu faire, et merci d'avoir toujours soutenu le projet, même quand tu voyais que les autres stagiaires avaient des projets bien mieux préparés ! Santina, tu étais exceptionnelle, mais pitié ne prends jamais plus 18 mg de porphyrine pour une seule expérience. Je vous souhaite beaucoup de réussite dans la suite de vos parcours. J'ai énormément appris de vous, alors merci de m'avoir supportée. J'espère avoir pu vous apporter la même passion de la chimie que mes anciens encadrants m'ont apporté.

Enfin, merci aux personnes hors du laboratoire qui m'ont permis d'avancer dans ce parcours : Mehdi, merci de m'avoir soutenue pendant ces trois ans (et les huit années avant). On s'est rencontré au début de nos études et on a découvert la chimie ensemble. Merci pour ton amour, ta compréhension et ton aide. Merci aussi pour ton soutien immesuré, tes conseils et tes attentions quand c'était difficile. Je n'y serai pas arrivée sans toi. D'un point de vue logistique surtout.

Merci également à mes parents Brigitte et Bernard, pour leur soutien dans la vie et dans mes études. Merci de m'avoir donné l'opportunité de faire les études que je voulais, même si j'étais loin. Merci pour vos conseils aussi, le fait de diluer m'a beaucoup aidé. Merci à mon frère Nicolas, ma belle-sœur Adeline et mes neveux Valentin et Raphaël pour m'avoir soutenue tout ce temps.

Liste des abréviations

)))	Ultrason
A	Additif
AcOEt	Acetate d'éthyl
ADN	Acide désoxyribonucléique
AIBN	Azobisisobutyronitrile
AOP	Advanced oxidation processes
AR14	Acid red 14
ATRP	Polymérisation radicalaire contrôlée par transfert d'atome
BP	Benzophénone
BTPA	2-(n-Butyltrithiocarbonate)propionic acid
CFU	Colony forming units
CIT	Conversion inter-système
Co	Co amorceur
COV	Composés organiques volatils
CP	Polymérisation cationique
CQ	Camphorquinone
CRP	Polymérisation radicalaire contrôlée
DCM	Dichlorométhane
DDQ	2,3-dichloro-5,6-dicyano-1,4-benzoquinone
DF	Diformazan
DFT	Density Functional Theory
DH	Donneur d'hydrogène
DMA	Dimethylacrylamide
DMF	Dimethylformamide
DMPO	5,5-diméthyl-pyrroline-N-oxyde
DMSO	Dimethylsulfoxyde
DPBF	1,3-Diphenylisobenzofurane
DSSC	Dye-sensitized solar cell
EPOX	3,4-epoxycyclohexylmethyl-3-4'-epoxycyclohexane carboxylate
EPR	Electron paramagnetic resonance

FC	Franck-Condon
FRP	Free radical polymerization
GPC	Gel Permeation Chromatography
HOMO	High occupied Molecular Orbital
HT	Herzberg-Teller
ICT	Intramolecular charge transfer
Iod	Bis(4-methylphenyl)iodonium hexafluorophosphate
IR	Infrared
IUPAC	Union internationale de chimie pure et appliquée
LED	Light emitting diode
LFP	Laser flash photolysis
LRP	Living radical polymerization
LUMO	Low unoccupied Molecular Orbital
M	Monomère
MDEA	N-methyldiéthanolamine
MeOH	Methanol
MF	Monoformazan
MO	Molecular Orbital
NBS	N-bromosuccinimide
NBT	Nitroblue tetrazolium chloride
NIR	Near-infrared
NMP	Polymérisation radicalaire contrôlée par les nitroxydes
NMR	Nuclear Magnetic Resonance
NTO	Natural orbital transition
OEP	Octaethylporphyrine
PA	Photoamorceur
PC	Photocatalyseur
PCM	Polarizable Continuum Model
PDT	Photodynamic therapy
PE	Petroleum ether
PET	Photo-induced Electron/energy Transfer

PI	Photoinitiator
POP	Polymères organiques poreux
PS	Photosensibilisateur
RAFT	Transfert réversible par addition-fragmentation
RhB	Rhodamine B
ROS	Reactive Oxygen Species
ROS	Reactive oxygen species
RT-FTIR	Real Time Fourier transform infrared spectroscopy
SCE	Saturated calomel electrode
SCRF	Self Consistent Reaction Field
Sn	Singlet state n
SOA	Soybean oil acrylate
SOD	Superoxyde dismutase
TD-DFT	Time-Dependent Density Functional Theory
TFA	Trifluoroacetic acid
THF	Tetrahydrofuran
TLC	Thin layer chromatography
TMPTA	Trimethylolpropane triacrylate
Tn	Excited triplet state n
TPB	Tetraphenymbacteriochlorine
TPC	Tetraphenylchlorine
TPCPD	Tetraphenylcyclopentadienone
TPP	Tetraphénylporphyrine
UV	Ultra-violet
ZPE	Point zéro d'énergie

Sommaire

Introduction générale 1

Chapitre I : Étude bibliographique **5**

Contexte 7

Partie A : Photopolymérisation 8

I. Introduction 8
II. Principe 8
III. Système photoamorceur 9
IV. Polymérisation radicalaire 12
V. Polymérisation sous oxygène 19
VI. Références 20

Partie B : Article 1 – Influence of porphyrin functionalization on properties for visible-light photopolymerization. 23

I. Introduction 24
II. Synthesis and modification of porphyrins 25
III. Electronic state of porphyrins 44
IV. Photophysical properties at excited states 50
V. Redox properties of porphyrins 51
VI. Porphyrins as new visible photo-initiating systems 52
VII. Conclusion 60
VIII. References 104

Partie C : Applications pour les matériaux 109

I. Formation des espèces réactives de l'oxygène 109
II. Application antibactérienne 113
III. Dépollution de l'eau 123
IV. Références 132

Partie D : Méthodes de chimie quantique 137

I. Introduction à la chimie théorique 137
II. Description de la méthode de calcul 141
III. Références 142

Conclusion du chapitre I 144

Chapitre II : Utilisation de photosensibilisateurs pour la création de matériaux dépolluants de l'eau 145

Contexte 147

Partie A : Article 2 – New porphyrins for water depollution under UV irradiation 149

I. Introduction 149
II. Materiel & Methods 150
III. Results and discussion 155
IV. Conclusion 166
V. References 166
VI. Supporting informations 169

Transition 184

Partie B : Article 3 – New porphyrins for the depollution of water under visible irradiation 185

I. Introduction 185
II. Experiment part 186
III. Results and discussion 190
IV. Conclusion 201
V. Reference 202
VI. Supporting information 204

Conclusion du chapitre II 208

Chapitre III : Modélisation et synthèse des porphyrines 209

Contexte 211

Partie A : Design of new porphyrins for photopolymerization assisted by modelisation 212

I. Introduction 212
II. Experiment part 213
III. Results and discussion 215
IV. Conclusion 228
V. Reference 228
VI. Supporting information 231

Partie B : Généralisation à d'autres structures 240

I. Push Pull 240
II. Reduced porphyrins 268

Conclusion du chapitre III 271

Chapitre IV : Utilisation des porphyrines pour la réalisation de matériaux antibactériens 273

Contexte 275

Partie A : Article 4 – Porphyrin-based photosensitizers for visible-light photopolymerization and antibacterial applications 276

I. Introduction 276
II. Experimental part 277
III. Results and discussion 282
IV. Conclusion 288
V. Reference 289
VI. Supporting information 291

Partie B : PET RAFT Polymerization for photosynthesis of antibacterial polymer 307

I. Introduction 307
II. Results and discussion 307
III. Conclusion 315
IV. Experimental part 315
V. References 316

Conclusion du chapitre IV 317

Conclusion générale et perspectives 318

Introduction générale

La conception de nouvelles molécules photoactives offre une large gamme d'application, que ce soit dans la synthèse de composés par photochimie [1,2], la thérapie photodynamique pour lutter contre le cancer [3] ou encore la conversion d'énergie [4]. Les porphyrines, par leur efficacité d'absorption de la lumière visible et leur facilité de fonctionnalisation, sont une gamme de composés particulièrement intéressante pour la photochimie, notamment en photopolymérisation.

La photopolymérisation permet d'obtenir des matériaux solides à partir de monomères, par l'utilisation d'un système photoamorceur et en activant la réaction de polymérisation par irradiation lumineuse.[5] Cette méthode permet une réduction de la consommation d'énergie et de solvant en comparaison de la polymérisation thermique.[6] Elle permet également un meilleur contrôle spatio-temporel de la polymérisation, permettant par exemple la réalisation de polymères par impression 3D.[7] Le système photoamorceur est habituellement composé d'un ou de plusieurs composés, capable de former des espèces réactives avec l'énergie lumineuse absorbée. Ces espèces vont ensuite pouvoir amorcer la polymérisation des fonctions réactives des monomères. Cependant, la plupart des systèmes photoamorceurs actuellement disponibles permettent seulement une activation sous irradiation UV, [8–10] entrainant l'utilisation de lampes énergivore et dangereuses pour le manipulateur. [11,12] La recherche de nouveaux systèmes capable d'absorber les longueurs d'onde du visible a conduit à l'essor de l'utilisation de colorants.[13]

Les colorants sont de plus capables de jouer un double rôle, puisqu'ils possèdent la capacité de réagir avec l'oxygène moléculaire pour former des espèces réactives de l'oxygène (ERO ou ROS en anglais). [14–16] Ces espèces sont très oxydantes et ont été mises à profit pour développer des matériaux antibactériens en permettant la destruction de bactéries à la surface de ceux-ci.

Les surfaces antibactériennes photoactives peuvent être utilisées pour la lutte contre les infections bactériennes, et en particulier les infections contractées en milieu hospitalier, appelées maladies nosocomiales. Ces infections touchent en moyenne un patient hospitalisé sur vingt, et sont principalement dues à trois souches bactériennes, *Escherichia coli*, *Staphylococcus aureus* et *Pseudomonas aeruginosa*.[17] Afin de lutter contre ces infections et éviter la prise d'antibiotiques susceptible d'induire l'émergence de résistance bactérienne, la prévention de ces infections est essentielle. Pour cela, la mise en place de surfaces antibactériennes,[18] activables par irradiation, permet de contrôler la formation de colonies bactériennes en milieu hospitalier.

Mais la photoactivité des molécules pourrait également être utilisée pour la photodégradation de polluants, et ainsi permettre des applications en dépollution de l'eau. En 2023, il y a 2 milliards de personnes n'ayant pas accès à un système d'eau potable géré de façon sûre.[19] Cela est dû en partie à la présence de polluants dans l'eau, causée notamment par le rejet par les stations d'épuration d'eaux uniquement partiellement traitées. Une partie de ces polluants est également produite par le rejet des eaux industrielles, comme la présence de colorants azoïques rejetés par les industries textiles ou agroalimentaires. En Europe, ce sont 90% des eaux des rivières qui présentent des traces de polluants résiduels.[20] L'utilisation de surfaces photoactives en sortie de station d'épuration pourrait permettre une photodégradation des polluants sous irradiation lumineuse.

Les porphyrines ont démontré de bonnes efficacités dans ces trois domaines. Que ce soit pour le photoamorçage de polymérisation,[21,22] le développement de surfaces antibactériennes,[23–25] ainsi

que la dépollution de l'eau.[26–29] Cependant, les exemples décrivant la réalisation de matériaux photosynthétisés pour ces applications à base de porphyrines sont très limités, et uniquement axés sur des applications antibactériennes. [30,31]

Ce travail de recherche porte donc sur la conception et la synthèse de nouvelles porphyrines qui vont agir en tant que photoamorceur pour la synthèse de polymères à base de monomères biosourcés et en tant que photosensibilisateur pour une utilisation en surfaces antibactériennes ou dépolluantes. Dans ce but, la modélisation des porphyrines et la simulation de leurs propriétés ont été réalisées au laboratoire MSME et vont donc permettre de sélectionner les meilleurs candidats, qui seront ensuite synthétisés au laboratoire ECCO de l'ICMPE. La détermination des mécanismes d'amorçage de la photopolymérisation impliqués ainsi que la synthèse des matériaux vont être réalisées au laboratoire BioM&Ms de l'ICMPE et, enfin, ces matériaux seront exploités pour la dépollution de l'eau au laboratoire ESYCOM, et pour le développement de surfaces antibactériennes.

Le premier chapitre de ce manuscrit est consacré à une étude bibliographique permettant de placer le projet dans le contexte des recherches actuelles. Les principes de la photopolymérisation seront présentés dans une première partie, puis l'utilisation spécifique des porphyrines va être développée en insistant sur leurs synthèses et l'effet de leurs fonctionnalisations sur leurs propriétés. Cet aspect sera présenté sous la forme d'une revue soumise. Les applications proposées en lutte antibactérienne et de dépollution de l'eau seront ensuite présentées, en insistant sur les utilisations des porphyrines dans ces domaines. Enfin, les méthodes de chimie théorique utilisées seront décrites.

La suite du manuscrit sera présentée sous la forme d'un recueil d'articles. Le deuxième chapitre portera sur la synthèse et l'utilisation de ces matériaux photoactifs permettant la dépollution de l'eau. Un premier article présentera deux nouvelles porphyrines utilisées pour la réalisation de nombreux systèmes photoamorceurs, en combinaison avec un co-amorceur. Les propriétés de ces systèmes seront étudiées pour déterminer leurs interactions sous irradiation. La réalisation de matériaux permettra ensuite leur utilisation en dépollution de l'eau sous irradiation UV. Le deuxième article reprendra le système optimal de la partie précédente pour s'intéresser aux interactions présentes ainsi que la synthèse de deux matériaux photoactifs qui seront exploités pour la dépollution sous irradiation visible.

Le troisième chapitre se concentrera sur la modélisation d'une série de nouvelles porphyrines pour améliorer les propriétés photophysiques des photoamorceurs, ainsi qu'à la comparaison de ces résultats avec les propriétés expérimentales. La première partie sera consacré à l'étude d'un premier type de porphyrines et sera présentée sous la forme d'un article. Deux autres types de porphyrines seront modélisées, pour permettre de comparer leurs propriétés théoriques avec leur capacité de photoamorçage de la polymérisation.

Enfin, le dernier chapitre s'intéressera à l'utilisation des porphyrines pour la réalisation de matériaux antibactériens. Une première partie composée d'un article présentera la synthèse de matériaux photoactifs, tandis que la deuxième partie présentera un autre type de polymérisation, la polymérisation PET-RAFT pour la création de matériaux de structure contrôlée, compatible avec une utilisation en matériaux antibactériens.

Références

1 C. Grundke, R. C. Silva, W. R. Kitzmann, K. Heinze, K. T. de Oliveira and T. Opatz, *J. Org. Chem.*, 2022, **87**, 5630–5642.

2 T. Toyao, N. Ueno, K. Miyahara, Y. Matsui, T.-H. Kim, Y. Horiuchi, H. Ikeda and M. Matsuoka, *Chem. Commun.*, 2015, **51**, 16103–16106.

3 S. A. Mosaddad, R. A. Namanloo, S. S. Aghili, P. Maskani, M. Alam, K. Abbasi, F. Nouri, E. Tahmasebi, M. Yazdanian and H. Tebyaniyan, *Med Oncol*, 2023, **40**, 91.

4 J. Feng, J. Alves, D. M. De Clercq and T. W. Schmidt, *Annu. Rev. Phys. Chem.*, 2023, **74**, 145–168.

5 J.-P. Fouassier and J. Lalevée, *Photoinitiators for Polymer Synthesis: Scope, Reactivity, and Efficiency*, John Wiley & Sons, 2012.

6 M. A. Tehfe, F. Louradour, J. Lalevée and J.-P. Fouassier, *Applied Sciences*, 2013, **3**, 490–514.

7 J. Li, C. Boyer and X. Zhang, *Macromolecular Materials and Engineering*, 2022, **307**, 2200010.

8 M. Chen, M. Zhong and J. A. Johnson, *Chem. Rev.*, 2016, **116**, 10167–10211.

9 C. Mendes-Felipe, J. Oliveira, I. Etxebarria, J. L. Vilas-Vilela and S. Lanceros-Mendez, *Advanced Materials Technologies*, 2019, **4**, 1800618.

10 V. Shukla, M. Bajpai, D. K. Singh, M. Singh and R. Shukla, *Pigment & Resin Technology*, 2004, **33**, 272–279.

11 K. J. Gromkowska-Kępka, A. Puścion-Jakubik, R. Markiewicz-Żukowska and K. Socha, *J of Cosmetic Dermatology*, 2021, **20**, 3427–3431.

12 H. Claus, *Photochemistry and Photobiology*, 2021, **97**, 471–476.

13 J.-P. Fouassier, F. Morlet-Savary, J. Lalevée, X. Allonas and C. Ley, *Materials*, 2010, **3**, 5130–5142.

14 D.-L. Versace, G. Moran, M. Belqat, A. Spangenberg, R. Méallet-Renault, S. Abbad-Andaloussi, V. Brezová and J.-P. Malval, *ACS Appl. Mater. Interfaces*, 2020, **12**, 5050–5057.

15 P. Sautrot-Ba, A. Contreras, S. A. Andaloussi, T. Coradin, C. Hélary, N. Razza, M. Sangermano, P.-E. Mazeran, J.-P. Malval and D.-L. Versace, *J. Mater. Chem. B*, 2017, **5**, 7572–7582.

16 L. Breloy, V. Brezová, A. Blacha-Grzechnik, M. Presset, M. S. Yildirim, I. Yilmaz, Y. Yagci and D.-L. Versace, *Macromolecules*, 2020, **53**, 112–124.

17 Santé Publique France, *Principaux résultats de l'enquête nationale de prévalence 2022 des infections nosocomiales et des traitements anti-infectieux en établissement de santé*, 2023.

18 X. Yang, J. Hou, Y. Tian, J. Zhao, Q. Sun and S. Zhou, *Sci. China Technol. Sci.*, 2022, **65**, 1000–1010.

19 R. Connor and M. Miletto, *UN World Water Development Report 2023*, 2023.

20 R. Loos, B. M. Gawlik, G. Locoro, E. Rimaviciute, S. Contini and G. Bidoglio, *Environmental Pollution*, 2009, **157**, 561–568.

21 G. Noirbent, Y. Xu, A.-H. Bonardi, D. Gigmes, J. Lalevée and F. Dumur, *European Polymer Journal*, 2020, **139**, 110019.

22 A. Bonardi, F. Bonardi, G. Noirbent, F. Dumur, C. Dietlin, D. Gigmes, J.-P. Fouassier and J. Lalevée, *Polym. Chem.*, 2019, **10**, 6505–6514.

23 J. Bozja, J. Sherrill, S. Michielsen and I. Stojiljkovic, *Journal of Polymer Science Part A: Polymer Chemistry*, 2003, **41**, 2297–2303.

24 J. P. C. Tomé, M. G. P. M. S. Neves, A. C. Tomé, J. A. S. Cavaleiro, M. Soncin, M. Magaraggia, S. Ferro and G. Jori, *J. Med. Chem.*, 2004, **47**, 6649–6652.

25 R. Rahimi, F. Fayyaz and M. Rassa, *Materials Science and Engineering: C*, 2016, **59**, 661–668.

26 V. B. Khajone and P. R. Bhagat, *Res Chem Intermed*, 2020, **46**, 783–802.

27 W. Gao, J. Tian, Y. Fang, T. Liu, X. Zhang, X. Xu and X. Zhang, *Chemosphere*, 2020, **243**, 125334.

28 R. Lyubimenko, B. S. Richards, A. I. Schäfer and A. Turshatov, *Journal of Membrane Science*, 2022, **642**, 119981.

29 R. Lyubimenko, D. Busko, B. S. Richards, A. I. Schäfer and A. Turshatov, *ACS Appl. Mater. Interfaces*, 2019, **11**, 31763–31776.

30 H. Marcille, J.-P. Malval, M. Presset, N. Bogliotti, A. Blacha-Grzechnik, V. Brezová, Y. Yagci and D.-L. Versace, *Polym. Chem.*, 2020, **11**, 4237–4249.

31 P. R. Judzewitsch, N. Corrigan, E. H. H. Wong and C. Boyer, *Angewandte Chemie*, 2021, **133**, 24450–24458.

Chapitre I

Étude bibliographique

Contexte

Ce premier chapitre d'étude bibliographique permet de rendre compte des avancées actuelles en matière de matériaux photosynthétisés et photoactifs, et plus principalement sur l'importance des porphyrines dans ce domaine. Il est décomposé en quatre grandes parties.

La **première partie** présente l'état de l'art de la photopolymérisation radicalaire, en mettant en lumière les principaux systèmes photoamorceurs ainsi que les mécanismes de polymérisation. Une attention particulière est portée aux systèmes permettant un amorçage sous irradiation visible.

La **deuxième partie** de ce chapitre se penche plus particulièrement sur l'utilisation des porphyrines pour la photopolymérisation, en présentant les différentes synthèses possibles, l'influence de la structure sur leurs propriétés et enfin leur utilisation en photopolymérisation. Ce chapitre est présenté sous forme d'un article puisqu'il est en cours de soumission.

La **troisième partie** se concentre sur les applications possibles des matériaux photoactifs. Après avoir présenté le principe de la photosensibilisation et la formation des ROS, les deux applications possibles des matériaux seront présentés, à savoir les matériaux antibactériens et les matériaux pour la dépollution de l'eau. Ces deux sujets sont présentés en détail, avec un état de l'art concernant les principaux problèmes rencontrés et les différentes solutions existantes. Les matériaux photoactifs sont plus particulièrement étudiés et la pertinence de développer des matériaux photoactifs à base de porphyrine sera mise en avant.

Enfin, la **quatrième partie** se concentre sur la présentation des méthodes de chimie théorique qui permettent de modéliser les porphyrines afin d'évaluer au mieux les capacités d'absorption de la lumière de celles-ci.

Partie A : Photopolymérisation

I. Introduction

La photopolymérisation consiste à transformer un monomère en un matériau polymère solide grâce à une irradiation lumineuse. Cette méthode présente de nombreux avantages par rapport à la polymérisation dite thermique [1–3]. En effet, la photopolymérisation permet d'effectuer des réactions plus rapides, de l'ordre de quelques secondes à quelques minutes, contre plusieurs heures en polymérisation thermique. L'absence de chauffage présente un intérêt économique et écologique, puisqu'il permet de limiter la consommation d'énergie, mais également en terme de stratégie, puisqu'il permet l'utilisation de composés sensibles à la chaleur. Cette méthode permet également de limiter la formation de composés organiques volatils (COV) en raison de l'absence de solvant. Enfin, un excellent contrôle spatio-temporel peut être obtenu car l'amorçage de la polymérisation se déroule grâce à une activation lumineuse qui peut être à la fois précise et modulée. En effet, la polymérisation peut être activée sur une surface restreinte, en utilisant un laser par exemple, et stoppée par simple arrêt de l'irradiation.

Cette méthode est utilisée dans de nombreuses applications, comme la peinture, les revêtements, la microélectronique, les biomatériaux [4,5], ou encore l'impression 3D [6]. Finalement, la possibilité d'incorporer des agents photoactivables peut permettre d'ajouter des propriétés supplémentaires au polymère, comme dans le cas de polymères photo-stimulables [7].

II. Principe

La photopolymérisation nécessite l'utilisation d'un système photoamorceur pour amorcer la polymérisation des fonctions réactives d'un monomère sous irradiation. Le système photoamorceur va absorber l'énergie lumineuse pour la convertir en espèces réactives comme des radicaux, des espèces à l'états excité ou des cations, par exemple.

La photochimie est basée sur le fait qu'une espèce soit capable d'absorber l'énergie lumineuse pour passer de l'état fondamental à un état excité. Ce phénomène peut être schématisé selon le diagramme de Perrin-Jablonski (**Figure IA-1**). Quand une molécule absorbe un photon après avoir été irradiée, elle passe de son état fondamental S_0 à un état singulet excité S_n. Depuis cet état, plusieurs mécanismes sont possibles pour la désexcitation :

- Une désexcitation non-radiative. Dans ce cas, l'énergie accumulée est émise sous forme de chaleur. Elle peut avoir lieu depuis un état excité vers l'état fondamental ($S_n \rightarrow S_0$), ou vers un autre niveau d'énergie plus bas ($S_n \rightarrow S_{n-x}$). On parle aussi de conversion interne.

- Une désexcitation radiative. Lors du passage de l'électron à son état fondamental, celui-ci va émettre un photon, produisant de la luminescence appelée fluorescence dans le cas d'un état singulet. Ce photon émis possède une énergie plus faible que celle des photons absorbés, entrainant l'émission d'une lumière à une longueur d'onde plus grande que la longueur d'onde d'excitation.

- Un croisement inter-système (CIS). Un électron va subir un changement de spin pour former un état triplet. La molécule peut ensuite se désexciter pour retourner dans l'état fondamental soit par conversion non-radiative, soit par conversion radiative en émettant de la

phosphorescence. Ces processus impliquent à nouveau un changement de spin, ce qui se traduit par des transitions beaucoup plus lentes, allongeant ainsi le temps de vie de l'état triplet.

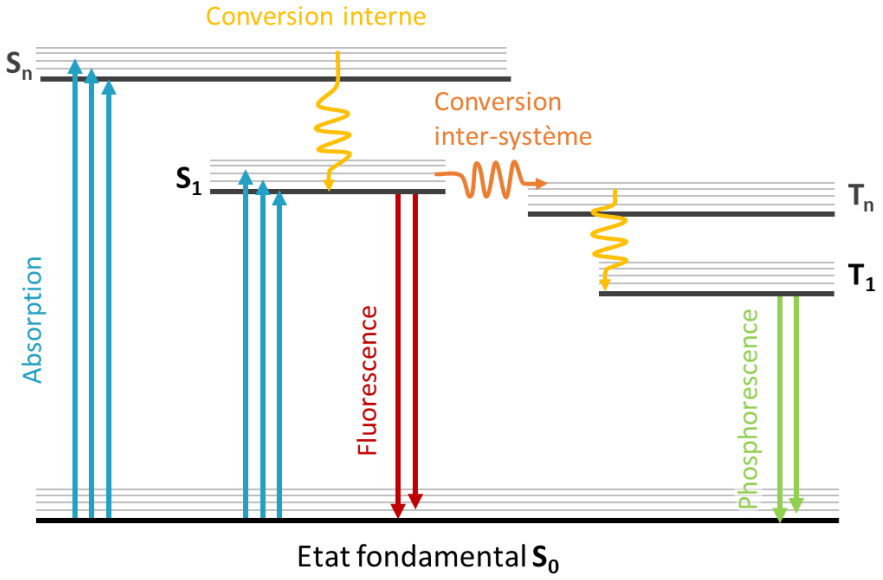

***Figure IA-1**: Diagramme de Perrin-Jablonski.*

Les molécules excitées (dans leurs états S_1 ou T_1) possèdent une orbitale occupée demi-vide, et sont donc capables de capter plus facilement des électrons que dans leur état fondamental. Elles sont donc plus oxydantes dans leurs états excités. De la même manière, elles possèdent un électron dans une orbitale précédemment inoccupée, et sont donc capables de réduire des composés. Les espèces excitées sont ainsi plus réactives vis-à-vis des réactions d'oxydo-réduction que dans leur état fondamental.[8]

III. Système photoamorceur

Le système photoamorceur peut comprendre un ou plusieurs composés. Trois grandes catégories de systèmes photoamorceurs peuvent être distinguées en fonction du type de réaction impliquée.

III. 1. Photoamorceurs de Type I

Les photoamorceurs Norrish Type I réagissent directement sous irradiation pour produire des radicaux par clivage homolytique direct (**Figure IA-2**)[9]. Ces molécules sont souvent des composés cétoniques aromatiques [2]. Le mécanisme implique le clivage de la liaison entre le carbonyle et le carbone en alpha sous irradiation pour former deux radicaux. L'énergie de dissociation de la liaison est généralement assez haute, et requiert l'utilisation de longueur d'onde à haute énergie, comme l'UV. L'énergie de liaison peut être abaissée en utilisant des molécules conjuguées permettant de stabiliser le radical formé, d'où l'intérêt d'utiliser des cétones aromatiques. Cependant, la plupart de ces photoamorceurs ne sont actifs que sous irradiation UV. Pour contourner cette limitation, il est possible d'ajouter un photosensibilisateur au système, qui sera capable d'absorber l'énergie de la lumière visible pour la transférer au photoamorceur afin de permettre le clivage de la liaison. L'intérêt est de

garder l'efficacité du photoamorceur activable sous UV, dont les radicaux générés sont souvent très réactifs, et de pouvoir travailler dans la gamme du visible.

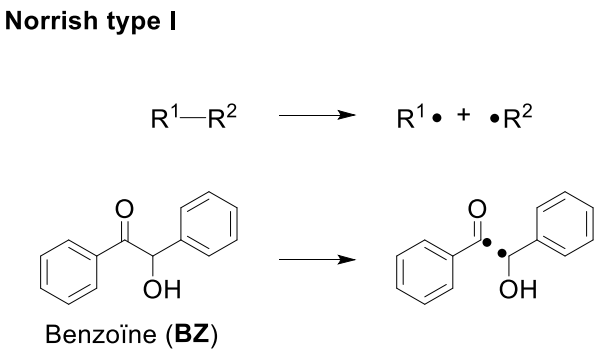

***Figure IA-2** : Exemple d'amorçage par photoamorceur Norrish Type I.*

III. 2. Photoamorceurs de Type II

Les systèmes photoamorceurs Norrish Type II vont produire des radicaux après arrachement d'un atome d'hydrogène (**Figure IA-3**). Les systèmes sont composés d'un photosensibilisateur, souvent associé à une fonction carbonyle [2,10], qui absorbe la lumière et d'un co-amorceur. Après excitation, un hydrogène est arraché par le photosensibilisateur à un co-amorceur possédant un hydrogène labile (DH). Le processus de transfert d'hydrogène peut se faire en une ou deux étapes en fonction du co-amorceur. Pour des co-amorceurs de type amine ou thiol, une fois le PA excité, il formera un complexe avec le co-amorceur pour permettre le transfert de charge, complexe appelé exciplexe. Une fois le transfert électronique effectué, un transfert d'hydrogène a lieu, permettant de générer un radical sur le co-amorceur qui va amorcer la polymérisation. Les co-amorceurs peuvent aussi être des éthers ou des alcools. Dans ce cas, il y a directement un transfert d'hydrogène permettant de former un radical cétyle et un radical issu du donneur d'hydrogène initiant la polymérisation. L'intérêt de ce système photoamorceur est la grande variété de PS compatibles. Cependant, ces systèmes sont en général moins efficaces et plus lents que les systèmes de type I, qui n'impliquent pas de transfert d'hydrogène intermoléculaire.

Norrish type II

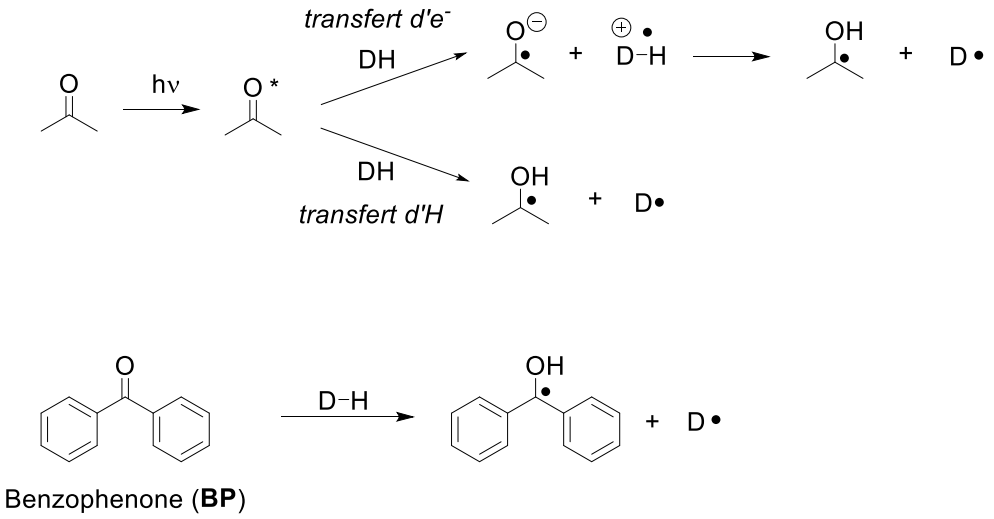

Figure IA-3 *: Exemple d'amorçage par photoamorceur Norrish Type II.*

III. 3. Système photoamorceur à trois composants

Enfin, afin d'améliorer l'efficacité des systèmes de type II, il est possible d'utiliser un troisième composant (additif A) en plus de photosensibilisateur et du co-amorceur (Co) [11,12]. Cet additif va réagir par oxydoréduction avec les sous-produits de la réaction avec le co-amorceur pour produire des radicaux supplémentaires (**Figure IA-4**). Suivant le type de photosensibilisateur et de réaction, il est possible de régénérer le PS, formant ainsi un système photocatalytique.

Système à trois composants

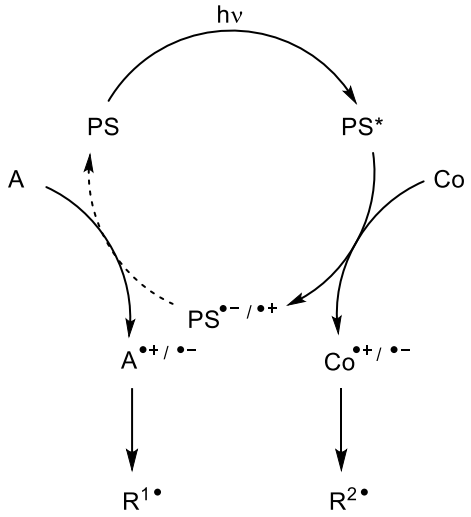

Figure IA-4 *: Mécanisme d'un système à trois composants.*

Afin d'éviter l'ambiguïté entre les termes, les molécules absorbant la lumière dans les systèmes seront qualifiés de photoamorceur dans le sens large du terme c'est-à-dire définie comme une

molécule capable d'absorber la lumière pour permettre de créer des espèces réactives soit seule, ou en présence de co-amorceurs, sans distinction entre les termes photoamorceurs et photosensibilisateurs.

Un photoamorceur doit répondre à un certain nombre de critères pour permettre un bon amorçage de la polymérisation. Il doit tout d'abord posséder une bonne absorption à la longueur d'onde de travail, pour maximiser l'absorption lumineuse. De plus, les états excités doivent avoir un temps de vie suffisamment long pour permettre la réaction. Les temps de vie des états triplets étant naturellement plus longs que ceux des états singulets (τ_T = [10^{-3} – 100] s, et τ_S = [10^{-9} – 10^{-6}] s), la probabilité de réaction est meilleure sur les états triplets. Il est donc préférable d'avoir un PA possédant un bon rendement quantique de croisement inter-système pour favoriser la conversion de l'état singulet en état triplet.

III. 4. Utilisation de la lumière visible

La photopolymérisation se base sur une rupture de liaisons, ce qui est généralement associé à de hautes énergies et donc à de basses longueurs d'onde comme les UV. C'est pourquoi de nombreux systèmes photoamorceurs nécessitent l'emploi d'UV. Cependant ces basses longueurs d'onde sont néfastes sur plusieurs niveaux.

La manipulation de ces lampes peut être dangereuse pour l'utilisateur, car une exposition de la peau ou des yeux peut causer des brûlures, voir des dommages à l'ADN ce qui peut entraîner des tumeurs [13]. Les lampes UV sont traditionnellement très consommatrices en énergie (comme les lampes à mercure) et produisent de l'ozone [14]. L'exposition à une irradiation UV peut entraîner de la production de chaleur, et donc endommager les composés actifs présents dans le polymère, voir la structure du matériau en lui-même [15]. De plus, les UV ne permettent pas la polymérisation d'un système épais, l'épaisseur de pénétration de la lumière étant d'autant plus grande que la longueur d'onde est élevée [16]. En effet, une irradiation à 800 nm permet une polymérisation jusqu'à 5 cm, là où une irradiation à 400 nm ne permet que quelques millimètres. Il paraît donc important de développer de nouveaux systèmes, capables d'absorber la lumière dans la gamme du visible.

IV. Polymérisation radicalaire

De nombreuses polymérisations sont possibles en photopolymérisation [17,18], comme les polymérisations cationique ou anionique, mais nous allons nous concentrer sur différents types de photopolymérisations radicalaires. Comme leurs noms l'indiquent, les espèces réactives produites lors de l'amorçage sont des espèces radicalaires.

IV. 1. Photopolymérisation radicalaire FRP

La photopolymérisation radicalaire (en anglais, Free-Radical Polymerization, ou FRP) permet de polymériser des fonctions acrylates ou alcènes par propagation des radicaux formés lors de l'étape d'amorçage. Elle se compose de plusieurs étapes (**Figure 6**). Tout d'abord, l'étape d'amorçage permet de former le radical ($A^{\bullet}$) en irradiant un système photoamorceur, comme vu précédemment (**Section III**). Le radical formé va ensuite réagir sur un monomère (M) pour former le premier centre actif radicalaire $AM^{\bullet}$. Lors de l'étape de propagation, cet oligoradical va encore réagir sur des unités monomériques pour former le polymère radicalaire $RM_n^{\bullet}$. Enfin, l'étape de terminaison peut se dérouler de deux façons par réaction entre deux chaînes polymériques radicalaires $RM_n^{\bullet}$ et $RM_m^{\bullet}$. Soit par recombinaison, pour former une liaison covalente à partir de ces deux radicaux, et obtenir un

polymère plus long (RM_n–RM_m), soit par dismutation, impliquant un transfert d'hydrogène entre les deux chaînes, donnant lieu à la formation d'une chaîne possédant une insaturation à son extrémité.

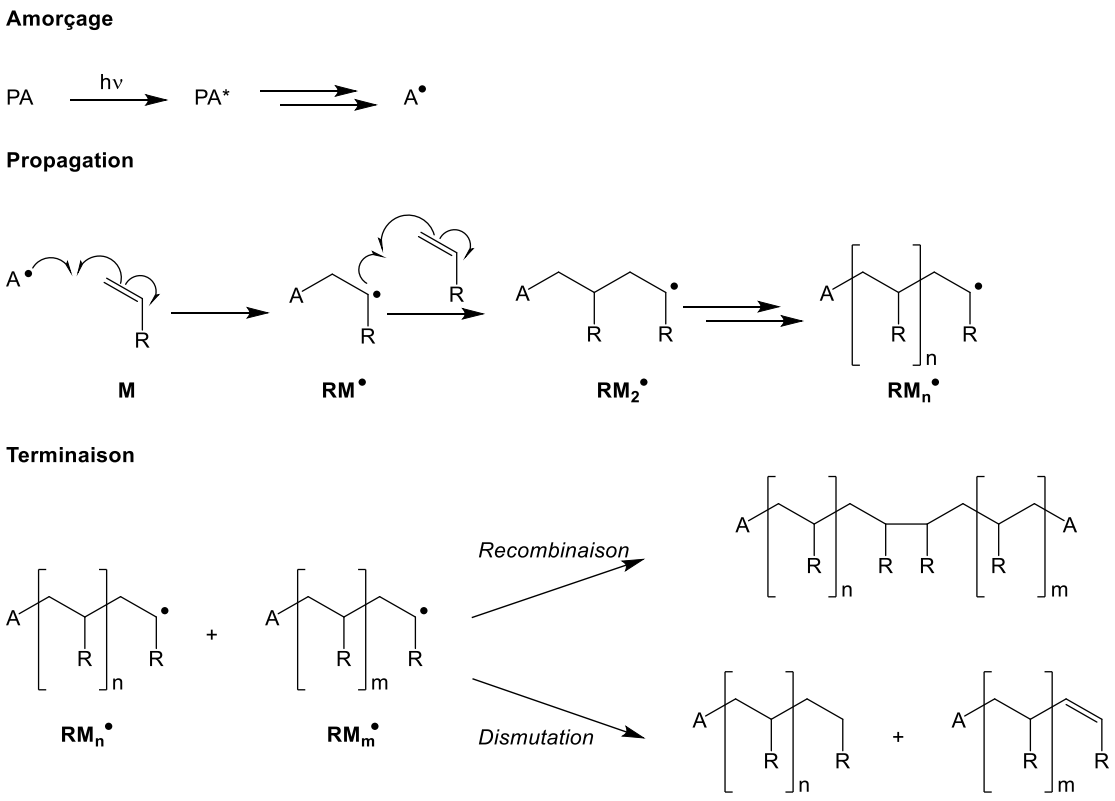

***Figure IA-5** : Étapes de la polymérisation radicalaire.*

IV. 2. Photopolymérisation radicalaire sous lumière visible

Comme vu dans la section précédente (**Section III. 4**), l'utilisation d'une source d'irradiation UV pose différents problèmes, aussi bien d'un point de vue écologique, qu'économique. Le remplacement de cette source lumineuse par une irradiation dans la gamme du visible peut donc être pertinent. Le photoamorceur doit cependant être capable d'absorber la lumière à des longueurs d'ondes qui coïncident avec le spectre d'émission de la source lumineuse. Pour cela, différentes stratégies ont été mises en place.

Tout d'abord, plusieurs équipes de recherche ont mis à profit des complexes métalliques, à base de germanium [19–21], de titane [22], d'étain [23,24] ou de silicium [25] pour permettre un amorçage efficace de la polymérisation par génération de radicaux sous irradiation visible.

Une deuxième stratégie consiste à utiliser les photoamorceurs efficaces sous UV, en leur greffant des fonctions aromatiques, qui permettra au photoamorceur de décaler son spectre d'absorption vers les longueurs d'ondes du visible. Des dérivés de benzophénone ont par exemple été utilisés pour permettre une photopolymérisation radicalaire dans le visible [26,27], de même que des dérivés de thioxanthones [28–32] (structures en **Figure IA-3**).

De plus, il est possible d'utiliser des produits organiques naturels absorbant dans le visible en tant que photoamorceurs, comme l'anthraquinone [33], la camphorquinone [34], la chalcone [35], la coumarine modifiée [36], la lawsone [37] ou la quinizarine [38,39] (structures en **Figure IA-6**).

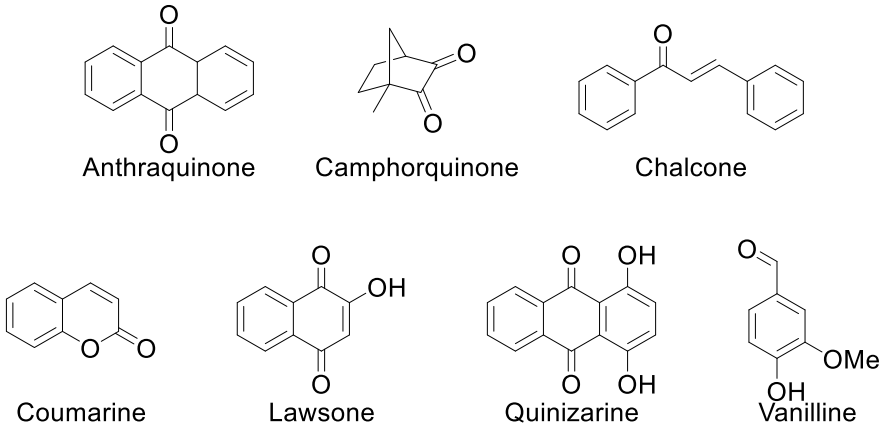

Figure IA-6 : *Structure des colorants naturel.*

Il est également possible d'utiliser des nouveaux chromophores de synthèse, comme l'anthracène modifié [26,40], l'éosine [41], la naphthalimide [42], la phénothiazine [43] ou le pyrène modifié [44] (structures en **Figure IA-7**). Enfin, des structures à base de porphyrines ont également été développées pour la FRP, et ce sujet sera développé dans la **partie B** de ce chapitre.

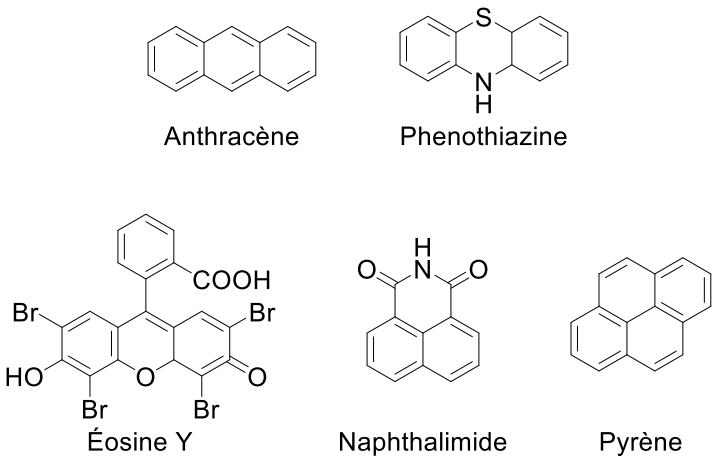

Figure IA-7 *: Structure des colorants synthétiques.*

L'emploi de ces molécules absorbant à plus grande longueur d'onde que les amorceurs UV classiques ont permis l'utilisation de lampes économes en énergie comme les LEDs ou les diodes laser, mais l'utilisation de l'irradiation solaire serait encore plus avantageuse. Cependant, le spectre d'émission du soleil comporte majoritairement des rayonnements infra-rouges [45]. Plusieurs systèmes ont permis une polymérisation efficace sous des longueurs d'ondes dans le proche infra-rouge, comme à λ_{exc} = 785 nm pour des composés à base de cyanines [46], et plus particulièrement des heptamethines [47] permettant une polymérisation sous des longueurs d'ondes de λ_{exc} = 850 et 940 nm, ou des azacalixphyrins [48] initiant la polymérisation à des longueurs d'ondes de λ_{exc} = 800 nm. D'autres systèmes permettant d'amorcer une polymérisation sous lumière solaire ont également été proposés [49].

Des systèmes absorbant la lumière visible ont donc pu être développés, mais l'une des limites majeures est la coloration persistante des matériaux après polymérisation. En effet, une fois le polymère synthétisé, le photoamorceur reste en général piégé à l'intérieur de la matrice du réseau, procurant une coloration au matériau. Cet aspect n'est généralement pas préjudiciable, mais certaines

applications, comme la dentisterie [50] nécessite un matériau incolore ou de couleur neutre. Pour lutter contre ce problème, des systèmes photoamorceurs photodégradables ont été développés [51].

La polymérisation FRP est très efficace pour former des polymères avec des monomères acrylates ou alcènes. Cependant, les monomères acrylates naturels sont assez rares, et la meilleure façon d'obtenir des monomères biosourcés est donc d'acrylater des monomères naturels. De plus, ce type de polymérisation ne permet pas un contrôle du poids moléculaire ni de la polydispersité. C'est pourquoi différentes polymérisations radicalaires contrôlées ont été développées, comme nous allons le voir dans la prochaine partie.

IV. 3. Polymérisation radicalaire contrôlée

La polymérisation radicalaire contrôlée (PRC, ou RDRP en anglais pour Reversible Desactivation Radical Polymerization) est basée sur un processus d'activation ou de désactivation (**Figure IA-8**) [52]. Le polymère en formation P—X est considéré comme dormant, et doit être activé par un stimulus thermique, photochimique ou chimique pour former le radical P•. Une fois sous forme radicalaire, la forme active, dite propageante, peut réagir avec le monomère M pour agrandir la chaîne polymérique lors de la propagation, jusqu'à désactivation pour former à nouveau le polymère dormant P—X. Cette méthode permet d'obtenir des chaînes polymériques de tailles homogènes si les cycles d'activation-désactivation sont suffisamment fréquents. De plus, les chaînes dormantes en fin de réaction peuvent être réutilisées dans une nouvelle polymérisation avec d'autres monomères pour permettre la synthèse de copolymères à blocs.

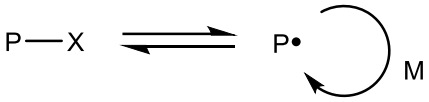

***Figure IA-8** : Principe de la polymérisation radicalaire contrôlée.*

Trois principales voies de contrôle ont émergé, dépendantes de la nature du type d'activation-désactivation en jeu (**Figure IA-9**). D'autres voies plus minoritaires peuvent également être utilisées [53].

- La NMP (polymérisation radicalaire contrôlée par les nitroxydes), développée en 1995 [54,55] permet une dissociation des deux parties du polymère dormant par rupture homolytique d'une liaison C–O, conduisant au radical propageant $P_n^{\bullet}$ ainsi qu'un radical nitroxyde, stabilisé par délocalisation. Le radical reste en solution jusqu'à désactivation de l'espèce propageante.

- L'ATRP (polymérisation radicalaire contrôlée par transfert d'atome) repose sur une réaction d'oxydo-réduction entre l'amorceur sous forme d'un halogénure d'alcane et un catalyseur à base d'un métal de transition comme du cuivre. Développée en 1995 [56] , les applications sont très nombreuses, car une grande variété de monomères peut être utilisée.

- La polymérisation RAFT (polymérisation par transfert réversible par addition-fragmentation) est développée par Moad *et al.* [57] en 1998. Elle permet de polymériser un grand nombre de monomères, tout en évitant l'ajout de cuivre. Cette méthode nécessite l'emploi d'un agent de transfert de type thiocarbonylthio, qui va permettre d'activer une espèce dormante et désactiver une espèce propageante.

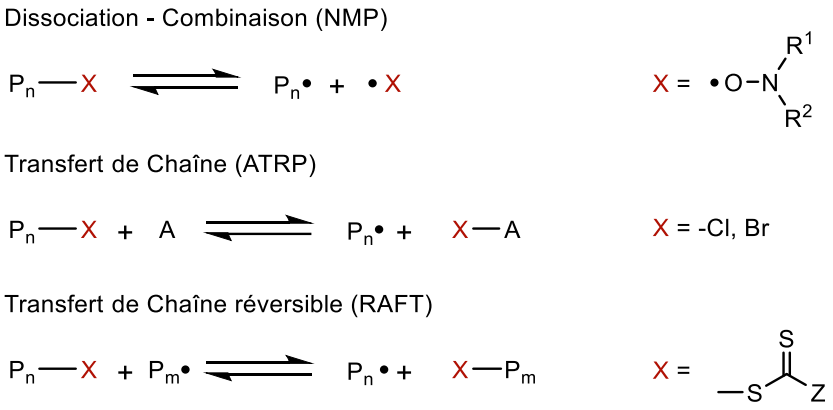

Figure IA-9 *: Types de polymérisation radicalaire contrôlée.*

Chaque méthode présente ses avantages ainsi que ces inconvénients, mais dans le cadre de cette étude, nous allons nous restreindre à la polymérisation RAFT. Le principal avantage de la RAFT est le large éventail de monomères compatibles, ce qui permet une grande variété de propriétés, sans utilisation de cuivre comme de l'ATRP et sans chauffage comme la NMP.

IV. 4. RAFT

Le mécanisme de la polymérisation RAFT est similaire au mécanisme de polymérisation radicalaire classique avec ajout d'un agent de transfert. Cet agent de transfert, aussi appelé « agent RAFT » va permettre de contrôler la formation des chaînes de polymère et donc de contrôler la taille de celles-ci. Lors de l'amorçage de la polymérisation, un radical primaire $I^{\bullet}$ est généré sous l'action d'un stimulus (thermique, chimique ou photochimique). Celui-ci va réagir sur un monomère pour former un premier oligoradical $P_n^{\bullet}$. L'oligoradical formé va réagir avec un agent RAFT moléculaire, en s'additionnant sur la liaison C=S, lors d'une première réaction d'addition (**Figure IA-10**). L'espèce radicalaire intermédiaire obtenue va pouvoir soit redonner l'oligoradical, soit se fragmenter lors d'une β-scission, en formant un oligomère fonctionnalisé thiocarbonylthio ainsi qu'un radical formé de sa chaîne latérale $R^{\bullet}$. La réactivité de la liaison C=S de l'agent de transfert étant plus élevée que celle de la liaison C=C du monomère, les premiers radicaux consommeront préférentiellement l'agent RAFT avant l'étape de propagation. Le radical $R^{\bullet}$ va ensuite être capable de réagir sur les monomères pour former des chaînes oligoradicalaires $P_m^{\bullet}$.

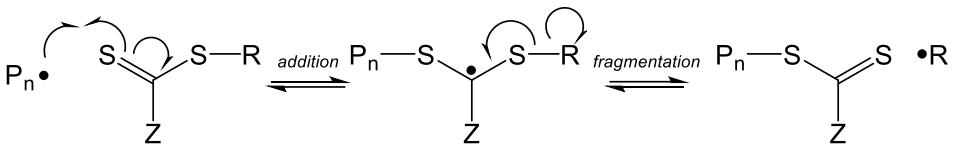

Figure IA-10 *: Mécanisme d'addition fragmentation d'un oligoradical avec l'agent RAFT moléculaire.*

Enfin, l'étape de propagation fait intervenir l'oligoradical $P_m^{\bullet}$ ainsi qu'un agent RAFT macromoléculaire composé de la chaîne précédemment additionnée $P_n^{\bullet}$ (**Figure IA-11**). Lors de ces équilibres d'addition-fragmentation, les chaînes oligoradicalaires générées vont pouvoir tour à tour croître en réagissant avec des monomères.

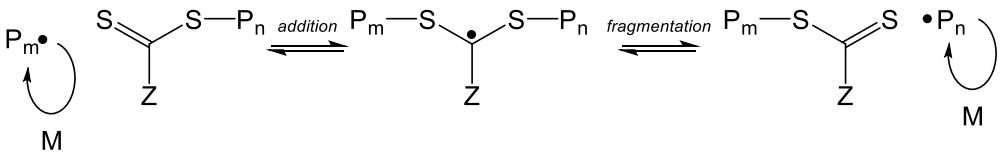

Figure IA-11 *: Mécanisme d'addition-fragmentation de la polymérisation RAFT.*

Enfin, même si la polymérisation RAFT permet de protéger en partie les radicaux formés vis-à-vis de la terminaison, cette méthode n'est pas parfaite, et les mêmes réactions de terminaison que pour la FRP sont observées : la dismutation et la recombinaison.

Lors d'une polymérisation RAFT, l'agent de transfert joue un rôle principal. C'est une espèce soufrée composée de deux parties (**Figure IA-12**). Un premier groupement dit activateur (noté Z), intervient principalement dans l'étape d'addition, tandis que le deuxième groupement, dit partant (noté R) va permettre une fragmentation efficace. Les agents de transfert sont organisés en fonction de la nature du groupe Z. On peut ainsi obtenir des dithioesters (avec des groupements alkyles ou aryles en position Z), des xanthates (groupements alkoxy), des dithiocarbamate (groupement amines) ou des trithiocarbonates (groupements thiolate). Le choix du type d'agent RAFT se fait en fonction de la nature des monomères impliqués [58–60].

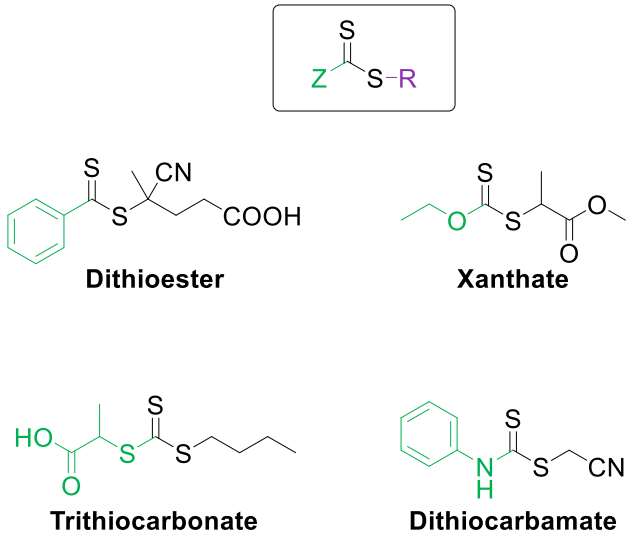

Figure IA-12 *: Structure et exemples de l'agent de transfert.*

IV. 5. Photo-RAFT

Historiquement, les radicaux initiant la polymérisation RAFT étaient générés de manière thermique [61], mais cette méthode risque de décomposer les agents RAFT et entraîner la création de chaînes de polymère non contrôl ées. De ce fait, comme pour la polymérisation radicalaire, les méthodes de polymérisation radicalaires contrôlées se sont tournées vers l'utilisation de lumière pour permettre d'amorcer ou de contrôler la polymérisation. Plusieurs méthodes sont disponibles en fonction du mécanisme impliqué [62]:

- La polymérisation RAFT photoamorcée. Elle nécessite l'emploi d'un photoamorceur pour former les radicaux sous irradiation [63]. Le mécanisme est équivalent à la polymérisation RAFT thermique.

- La polymérisation RAFT par photodissociation de l'agent de transfert. Dans ce cas, l'irradiation sous lumière UV [64–66] ou visible [67,68] permet de photolyser l'agent RAFT pour générer les radicaux propageants.
- La polymérisation PET-RAFT avec ajout de photocatalyseur. Dans ce cas, l'amorçage de la polymérisation est entraîné par la réaction entre l'agent de transfert et le photocatalyseur (PC).

La photopolymérisation PET-RAFT a été développée par Boyer en s'inspirant des travaux de Hawker sur la photo-ATRP et son utilisation de catalyseur *fac*-Ir(ppy)$_3$ [69]. Il repose sur l'oxydation du photocatalyseur, et la réduction du polymère dormant en espèce propageante (**Figure IA-13**). L'équilibre espèce dormante – espèce propageante est contrôlée par irradiation [70].

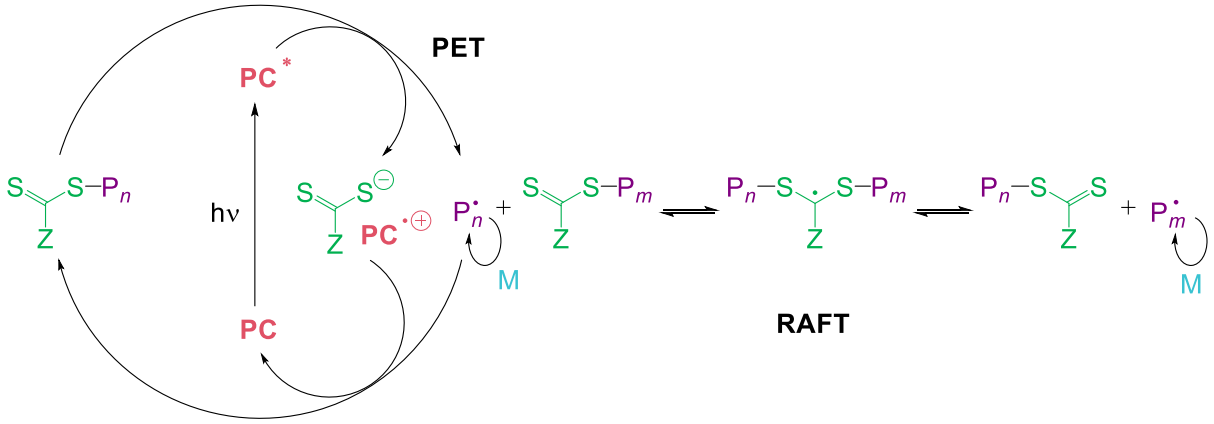

***Figure IA-13** : Mécanisme de PET-RAFT.*

Les premiers essais ont été réalisés avec le même complexe que celui utilisé par Hawker et ont permis une polymérisation efficace d'une large variété de monomères ((méth)acrylates, (méth)acrylamide, styrène et ester vinylique) grâce à différents agents RAFT sous irradiation à 460 nm [71–75]. Les capacités de photoamorçage du catalyseur Ru(bpy)$_3$Cl$_2$ sous irradiation à 435 nm ont également été démontrées [76–78]. Même si une perte d'efficacité a été observée en milieu organique par rapport au complexe d'iridium, son intérêt persiste dans les milieux aqueux [79].

L'utilisation de ces composés ne permettant une polymérisation qu'avec une lumière bleue (λ = 435 et 460 nm), d'autres systèmes ont été développés. En effet, en plus des avantages procurés par l'irradiation à grande longueur d'onde évoqué précédemment, l'agent RAFT risque une photolyse sous lumière bleue. Des composés organométalliques ont été utilisés comme photocatalyseur, comme par exemple des systèmes à base de phthalocyanine [80]. Dans ce système, le photocatalyseur est réduit par le solvant pour former les espèces réactives et permet une polymérisation sous diverses longueurs d'ondes d'irradiation entre 460 et 850 nm. De plus, de nombreux systèmes à base de porphyrines ou de dérivés porphyriniques ont été utilisés, mais seront développés dans la **partie B** de ce chapitre.

Enfin, l'exploitation de différents composés organiques sans métal a été réalisé, comme l'utilisation de 10-phenylphenothiazine (PTH) sous lumière visible [81,82] ou de l'éosine Y sous lumière bleue (λ = 461 nm) [83]. Des systèmes à base d'amine tertiaire ont également été développés, sans ajout de photoamorceur traditionnel sous irradiation UV (λ = 365 nm) [84,85] permettant l'essor de nouveaux systèmes hétérogènes [86].

V. Polymérisation sous oxygène

V. 1. Inhibition de la FRP

La présence d'oxygène dans le milieu peut perturber la polymérisation radicalaire. En effet, l'oxygène peut réagir sur les espèces réactives, et inhiber la polymérisation. Plusieurs mécanismes peuvent être responsables de cet effet (**Figure IA-14**). L'état triplet du photoamorceur peut être désactivé par l'oxygène, naturellement à l'état triplet, par échange énergétique pour aboutir au photoamorceur dans son état fondamental (a), ainsi que de l'oxygène singulet [87]. De plus, les radicaux formés peuvent être désactivés pour former des peroxydes avec l'oxygène (b). Ces peroxydes ne seront plus réactifs vis-à-vis des monomères et inhibent donc la polymérisation [88,89].

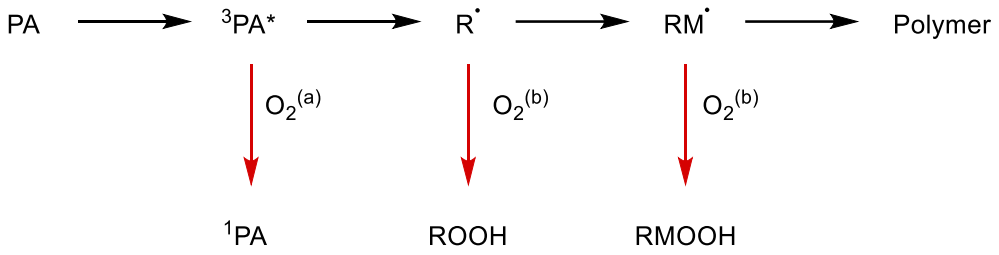

***Figure IA-14** : Inhibition de la polymérisation par l'oxygène à différents stades de la polymérisation.*

Diverses solutions ont été apportées pour lutter contre ce problème [87]. Il est possible de limiter la présence d'oxygène en le remplaçant par un gaz inerte, ou en empêchant son arrivée par une barrière physique comme en utilisant un film de polypropylène à la surface du système. Cependant ces solutions sont difficiles à mettre en œuvre d'un point de vue industriel. D'autres solutions peuvent être envisagées. Tout d'abord, il est possible d'amplifier les réactions d'initiation pour diminuer la concentration d'oxygène au début de la réaction de polymérisation. Pour cela, il est possible d'augmenter le nombre de radicaux formés en augmentant l'intensité lumineuse ou la concentration en photoamorceur. Enfin, l'utilisation de composés spécifiques permet de limiter l'inhibition de la polymérisation, comme l'utilisation de composés permettant la conversion d'oxygène en oxygène singulet (bleu de méthylène, rose Bengale, porphyrine or phthalocyanine), l'utilisation de photoamorceurs capable de se décomposer en CO_2 [33], des donneurs d'hydrogènes (comme les amines, les thiols ou les silanes) ou des agents réducteurs (composés borés ou phosphorés).

V. 2. Cas de la PET-RAFT

Malgré la présence d'espèces actives communes avec la polymérisation radicalaire, la polymérisation RAFT n'est pas aussi sensible que la polymérisation radicalaire. En effet, Boyer *et al.* ont montré que l'oxygène présent dans la solution est réduit en ion hydroxyle.[77] Ainsi une période d'inhibition peut être observée pour des systèmes fermés, le temps que tout l'oxygène ait été consommé. Cependant, dans certains cas l'oxygène peut également être nécessaire dans les réactions de polymérisation en permettant des réactions qui ne sont pas efficaces sous gaz inerte, et en jouant le rôle de co-amorceur.[90]

VI. Conclusion

Finalement, de nombreux systèmes pour la photopolymérisation radicalaire classique ou contrôlée ont été développés, permettant un amorçage efficace dans les longueurs d'onde du visible.

Toutefois, une famille de molécule montre un intérêt particulier pour la photopolymérisation et fera l'objet de la **partie B** de ce chapitre, les porphyrines. En effet, ces molécules sont des molécules qui absorbent dans le visible et dans le proche infra-rouge, faisant d'elles de très bonnes candidates en tant que photoamorceurs pour la photopolymérisation. De plus, elles possèdent un grand système conjugué, pouvant stabiliser les radicaux formés.

VII. Références

1 N. Corrigan, J. Yeow, P. Judzewitsch, J. Xu and C. Boyer, Angewandte Chemie International Edition, 2019, 58, 5170–5189.
2 J.-P. Fouassier and J. Lalevée, Photoinitiators for Polymer Synthesis: Scope, Reactivity, and Efficiency, John Wiley & Sons, 2012.
3 M. A. Tehfe, F. Louradour, J. Lalevée and J.-P. Fouassier, Applied Sciences, 2013, 3, 490–514.
4 B. P. Chan, Tissue Engineering Part B: Reviews, 2010, 16, 509–522.
5 J. W. Stansbury, Journal of Esthetic and Restorative Dentistry, 2000, 12, 300–308.
6 Y. Yagci, S. Jockusch and N. J. Turro, Macromolecules, 2010, 43, 6245–6260.
7 D. He, H. Susanto and M. Ulbricht, Progress in Polymer Science, 2009, 34, 62–98.
8 N. Oda, K. Tsuji and A. Ichimura, ANALYTICAL SCIENCES.
9 R. G. W. Norrish and C. H. Bamford, Nature, 1937, 140, 195–196.
10 Y. Tang, Y. Zhang, J. Yang and J. Nie, Journal of Polymer Science Part A: Polymer Chemistry, 2017, 55, 313–320.
11 C. Grotzinger, D. Burget, P. Jacques and J. P. Fouassier, Polymer, 2003, 44, 3671–3677.
12 O. I. Tarzi, X. Allonas, C. Ley and J.-P. Fouassier, Journal of Polymer Science Part A: Polymer Chemistry, 2010, 48, 2594–2603.
13 K. J. Gromkowska-Kępka, A. Puścion-Jakubik, R. Markiewicz-Żukowska and K. Socha, J of Cosmetic Dermatology, 2021, 20, 3427–3431.
14 H. Claus, Photochemistry and Photobiology, 2021, 97, 471–476.
15 H. Kaczmarek, Polymer, 1996, 37, 547–553.
16 Z. Wu, K. Jung and C. Boyer, Angewandte Chemie International Edition, 2020, 59, 2013–2017.
17 P. Xiao, J. Zhang, F. Dumur, M. A. Tehfe, F. Morlet-Savary, B. Graff, D. Gigmes, J. P. Fouassier and J. Lalevée, Progress in Polymer Science, 2015, 41, 32–66.
18 C. Dietlin, S. Schweizer, P. Xiao, J. Zhang, F. Morlet-Savary, B. Graff, J.-P. Fouassier and J. Lalevée, Polym. Chem., 2015, 6, 3895–3912.
19 B. Ganster, U. K. Fischer, N. Moszner and R. Liska, Macromolecular Rapid Communications, 2008, 29, 57–62.
20 J. Lalevée, X. Allonas and J. P. Fouassier, Chemical Physics Letters, 2009, 469, 298–303.
21 J. Radebner, A. Eibel, M. Leypold, C. Gorsche, L. Schuh, R. Fischer, A. Torvisco, D. Neshchadin, R. Geier, N. Moszner, R. Liska, G. Gescheidt, M. Haas and H. Stueger, Angewandte Chemie International Edition, 2017, 56, 3103–3107.
22 L. Breloy, V. Brezová, J.-P. Malval, A. Rios de Anda, J. Bourgon, T. Kurogi, D. J. Mindiola and D.-L. Versace, Macromolecules, 2019, 52, 3716–3729.
23 M. Mitterbauer, P. Knaack, S. Naumov, M. Markovic, A. Ovsianikov, N. Moszner and R. Liska, Angewandte Chemie International Edition, 2018, 57, 12146–12150.
24 J. Radebner, A. Eibel, M. Leypold, N. Jungwirth, T. Pickl, A. Torvisco, R. Fischer, U. K. Fischer, N. Moszner, G. Gescheidt, H. Stueger and M. Haas, Chemistry – A European Journal, 2018, 24, 8281–8285.
25 M. Bouzrati-Zerelli, J. Kirschner, C. P. Fik, M. Maier, C. Dietlin, F. Morlet-Savary, J. P. Fouassier, J.-M. Becht, J. E. Klee and J. Lalevée, Macromolecules, 2017, 50, 6911–6923.

26 Z. El Hajj, L. Pierau, J.-P. Malval, J. Marrot, P.-E. Mazeran, D. Naoufal, M.-H. Ha-Thi, K. Steenkeste, A. Dolbecq, S. Floquet, O. Oms, D.-L. Versace and P. Mialane, Macromolecules, 2023, 56, 6105–6116.

27 P. Xiao, F. Dumur, B. Graff, D. Gigmes, J. P. Fouassier and J. Lalevée, Macromolecules, 2013, 46, 7661–7667.

28 D. K. Balta, G. Temel, G. Goksu, N. Ocal and N. Arsu, Macromolecules, 2012, 45, 119–125.

29 L. Breloy, R. Losantos, D. Sampedro, M. Marazzi, J.-P. Malval, Y. Heo, J. Akimoto, Y. Ito, V. Brezová and D.-L. Versace, Polym. Chem., 2020, 11, 4297–4312.

30 H. Tar, D. Sevinc Esen, M. Aydin, C. Ley, N. Arsu and X. Allonas, Macromolecules, 2013, 46, 3266–3272.

31 D. Tunc and Y. Yagci, Polymer Chemistry, 2011, 2, 2557–2563.

32 G. Yilmaz, B. Aydogan, G. Temel, N. Arsu, N. Moszner and Y. Yagci, Macromolecules, 2010, 43, 4520–4526.

33 C. Elian, N. Sanosa, N. Bogliotti, C. Herrero, D. Sampedro and D.-L. Versace, Polym. Chem., 2023, 14, 3262–3269.

34 J. Jakubiak, X. Allonas, J. P. Fouassier, A. Sionkowska, E. Andrzejewska, L. Å. Linden and J. F. Rabek, Polymer, 2003, 44, 5219–5226.

35 M.-A. Tehfe, F. Dumur, P. Xiao, M. Delgove, B. Graff, J.-P. Fouassier, D. Gigmes and J. Lalevée, Polym. Chem., 2013, 5, 382–390.

36 M. Abdallah, A. Hijazi, B. Graff, J.-P. Fouassier, G. Rodeghiero, A. Gualandi, F. Dumur, P. G. Cozzi and J. Lalevée, Polym. Chem., 2019, 10, 872–884.

37 C. Elian, V. Brezová, P. Sautrot-Ba, M. Breza and D.-L. Versace, Polymers, 2021, 13, 2015.

38 L. Breloy, V. Brezová, Z. Barbieriková, Y. Ito, J. Akimoto, A. Chiappone, S. Abbad-Andaloussi, J.-P. Malval and D.-L. Versace, ACS Appl. Polym. Mater., 2022, 4, 210–228.

39 P. Sautrot-Ba, S. Jockusch, J.-P. Malval, V. Brezová, M. Rivard, S. Abbad-Andaloussi, A. Blacha-Grzechnik and D.-L. Versace, Macromolecules, 2020, 53, 1129–1141.

40 M.-A. Tehfe, J. Lalevée, F. Morlet-Savary, B. Graff, N. Blanchard and J.-P. Fouassier, ACS Macro Lett., 2012, 1, 198–203.

41 P. Sautrot-Ba, A. Contreras, S. A. Andaloussi, T. Coradin, C. Hélary, N. Razza, M. Sangermano, P.-E. Mazeran, J.-P. Malval and D.-L. Versace, J. Mater. Chem. B, 2017, 5, 7572–7582.

42 A.-H. Bonardi, S. Zahouily, C. Dietlin, B. Graff, F. Morlet-Savary, M. Ibrahim-Ouali, D. Gigmes, N. Hoffmann, F. Dumur and J. Lalevée, Catalysts, 2019, 9, 637.

43 M. Abdallah, T.-T. Bui, F. Goubard, D. Theodosopoulou, F. Dumur, A. Hijazi, J.-P. Fouassier and J. Lalevée, Polym. Chem., 2019, 10, 6145–6156.

44 M.-A. Tehfe, J. Lalevée, S. Telitel, E. Contal, F. Dumur, D. Gigmes, D. Bertin, M. Nechab, B. Graff, F. Morlet-Savary and J.-P. Fouassier, Macromolecules, 2012, 45, 4454–4460.

45 B. Diffey, Photochemistry and Photobiology, 2015, 91, 553–557.

46 H. Mokbel, G. Noirbent, D. Gigmes, F. Dumur and J. Lalevée, Beilstein J. Org. Chem., 2021, 17, 2067–2076.

47 C. Elian, B. Mourot, C. Benbouziyane, J.-P. Malval, S. Lajnef, F. Peyrot, F. Massuyeau, O. Siri, D. Jacquemin, S. Pascal and D.-L. Versace, Angewandte Chemie International Edition, 2023, 62, e202305963.

48 L. Breloy, R. Mhanna, J.-P. Malval, V. Brezová, D. Jacquemin, S. Pascal, O. Siri and D.-L. Versace, Chem. Commun., 2021, 57, 8973–8976.

49 F. Dumur, European Polymer Journal, 2023, 189, 111988.

50 F. A. Rueggeberg, M. Giannini, C. A. G. Arrais and R. B. T. Price, Braz. oral res., 2017, 31, e61.

51 F. Dumur, European Polymer Journal, 2023, 186, 111874.

52 K. Matyjaszewski and T. P. Davis, .

53 A. Ohtsuki, L. Lei, M. Tanishima, A. Goto and H. Kaji, J. Am. Chem. Soc., 2015, 137, 5610–5617.

54 C. J. Hawker, A. W. Bosman and E. Harth, Chem. Rev., 2001, 101, 3661–3688.

55 G. Moad and E. Rizzardo, Macromolecules, 1995, 28, 8722–8728.

56 J.-S. Wang and K. Matyjaszewski, J. Am. Chem. Soc., 1995, 117, 5614–5615.
57 J. Chiefari, Y. K. (Bill) Chong, F. Ercole, J. Krstina, J. Jeffery, T. P. T. Le, R. T. A. Mayadunne, G. F. Meijs, C. L. Moad, G. Moad, E. Rizzardo and S. H. Thang, Macromolecules, 1998, 31, 5559–5562.
58 A. Favier and M.-T. Charreyre, Macromolecular Rapid Communications, 2006, 27, 653–692.
59 G. Moad, E. Rizzardo and S. H. Thang, Aust. J. Chem., 2005, 58, 379.
60 G. Moad, E. Rizzardo and S. H. Thang, Polymer, 2008, 49, 1079–1131.
61 G. Moad, Polymer Chemistry, 2017, 8, 177–219.
62 J. Wang, X. Hu, N. Zhu and K. Guo, Chemical Engineering Journal, 2021, 420, 127663.
63 L. Lu, N. Yang and Y. Cai, Chem. Commun., 2005, 5287–5288.
64 M. Hartlieb, Macromolecular Rapid Communications, 2022, 43, 2100514.
65 L. Lu, H. Zhang, N. Yang and Y. Cai, Macromolecules, 2006, 39, 3770–3776.
66 T. Otsu, Journal of Polymer Science Part A: Polymer Chemistry, 2000, 38, 2121–2136.
67 W. Jiang, L. Lu and Y. Cai, Macromolecular Rapid Communications, 2007, 28, 725–728.
68 J. Xu, S. Shanmugam and C. Boyer, ACS Macro Lett., 2015, 4, 926–932.
69 B. P. Fors and C. J. Hawker, Angew. Chem. Int. Ed., 2012, 51, 8850–8853.
70 N. D. Dolinski, Z. A. Page, F. Eisenreich, J. Niu, S. Hecht, J. Read de Alaniz and C. J. Hawker, ChemPhotoChem, 2017, 1, 125–131.
71 C. Fu, J. Xu, M. Kokotovic and C. Boyer, ACS Macro Lett., 2016, 5, 444–449.
72 K. Jung, J. Xu, P. B. Zetterlund and C. Boyer, ACS Macro Lett., 2015, 4, 1139–1143.
73 S. Shanmugam, J. Xu and C. Boyer, Macromolecules, 2014, 47, 4930–4942.
74 J. Xu, K. Jung, A. Atme, S. Shanmugam and C. Boyer, J. Am. Chem. Soc., 2014, 136, 5508–5519.
75 P. Yang, P. Pageni, M. P. Kabir, T. Zhu and C. Tang, ACS Macro Lett., 2016, 5, 1293–1300.
76 J. Christmann, A. Ibrahim, V. Charlot, C. Croutxé-Barghorn, C. Ley and X. Allonas, ChemPhysChem, 2016, 17, 2309–2314.
77 J. Xu, K. Jung and C. Boyer, Macromolecules, 2014, 47, 4217–4229.
78 J. Xu and C. Boyer, Macromolecules, 2015, 48, 520–529.
79 J. Xu, K. Jung, N. A. Corrigan and C. Boyer, Chem. Sci., 2014, 5, 3568–3575.
80 N. Corrigan, J. Xu and C. Boyer, Macromolecules, 2016, 49, 3274–3285.
81 M. Chen, M. J. MacLeod and J. A. Johnson, ACS Macro Lett., 2015, 4, 566–569.
82 J. R. Tumbleston, D. Shirvanyants, N. Ermoshkin, R. Janusziewicz, A. R. Johnson, D. Kelly, K. Chen, R. Pinschmidt, J. P. Rolland, A. Ermoshkin, E. T. Samulski and J. M. DeSimone, Science, 2015, 347, 1349–1352.
83 J. Xu, S. Shanmugam, H. T. Duong and C. Boyer, Polym. Chem., 2015, 6, 5615–5624.
84 M. L. Allegrezza, Z. M. DeMartini, A. J. Kloster, Z. A. Digby and D. Konkolewicz, Polym. Chem., 2016, 7, 6626–6636.
85 Q. Fu, T. G. McKenzie, S. Tan, E. Nam and G. G. Qiao, Polym. Chem., 2015, 6, 5362–5368.
86 Q. Fu, T. G. McKenzie, J. M. Ren, S. Tan, E. Nam and G. G. Qiao, Sci Rep, 2016, 6, 20779.
87 S. C. Ligon, B. Husár, H. Wutzel, R. Holman and R. Liska, Chem. Rev., 2014, 114, 557–589.
88 C. Decker and A. D. Jenkins, Macromolecules, 1985, 18, 1241–1244.
89 A. K. O'Brien and C. N. Bowman, Macromolecules, 2006, 39, 2501–2506.
90 L. Zhang, C. Wu, K. Jung, Y. H. Ng and C. Boyer, Angew Chem Int Ed, 2019, 58, 16811–16814.

Partie B : Article 1 – Influence of porphyrin functionalization on properties for visible-light photopolymerization.

Fanny Schnetz[a], Yusuf Yagci[b], Sebastien Richeter[c], Davy-Louis Versace[a*]

[a] Institut de Chimie et des Matériaux Paris-Est (ICMPE), UMR CNRS-UPEC 7182, 2-8 rue Henri Dunant, 94320 Thiais, France.

[b] Istanbul Technical University, Faculty of Science and Letters, Department of Chemistry, Maslak, 34469, Turkey.

[c] Institut Charles Gerhardt Montpellier, UMR 5253 CNRS-UM2-ENSCM-UM1, Equipe Chimie Moléculaire et Organisation du Solide, CC1701 Place Eugène Bataillon, 34095, Montpellier Cedex 05, France.

***Corresponding author**: versace@icmpe.cnrs.fr

Abstract

Photopolymerization using visible light represents a significant progress in the synthesis of materials, providing a more economical and ecological method. However, it is necessary to develop new and more effective photoinitiators. Thanks to their high absorption, their ability to form reactive species under irradiation and their low toxicity in the dark, porphyrins are particularly attractive candidates. The convenience of their functionalization, allowing optimization of their photophysical and photochemical properties, makes them particularly interesting for developing new photoinitiators that are effective under visible irradiation. The aim of this review is to explore the various aspects that need to be anticipated in order to obtain optimised photoinitiators. The different routes for synthesising and functionalising porphyrins will first be presented. The effect of these groups will then be highlighted on the various properties, such as the absorption of the fundamental state, the influence on the excited states, and finally on the redox capacities of these molecules. Finally, particular attention will be attached to studies using porphyrins for photopolymerization, whether free-radical, cationic or PET-RAFT polymerization.

Graphical abstract

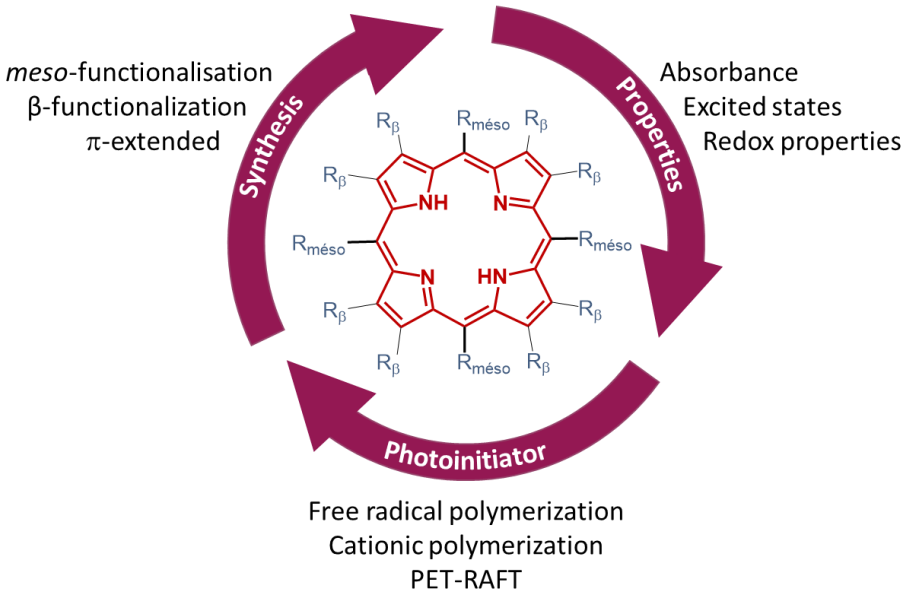

I. Introduction

Photochemistry has increasingly gained interests over the last ten years and is widely used in different domains including adhesives, coatings, dental restoratives, or 3D (photo)printing process.[1–3] It offers several advantages over the thermal polymerization such as rapid curing, temporal and spatial control of the polymerization without the use of harmful solvent [4–6]. One of the key component used to drive the photopolymerization process under light irradiation remains the photo-initiator. To date many examples of UV-absorbing photo-initiating systems have been described in literature,[7,8] however, and due to UV-handling safety issues,[9,10] their use should be limited. In this context, a particular attention has been paid to the design of multifunctional and visible/NIR-light absorbing photo-initiating systems. Notably, many relevant reviews or investigations have described the free-radical (FRP) and cationic photopolymerization (CP) using type I or type II photo-initiators including natural dyes [11–13], synthetic dyes [14,15] or phthalocyanins [11].

Surprisingly, porphyrins-based-photo initiating systems remain rare despite their broad absorption range in the visible spectrum, and their high molar absorption coefficients between 10^3 and 10^6 $L.mol^{-1}.cm^{-1}$. Porphyrins are 18π aromatic macrocyclic compounds consisting of four pyrrole units and four bridging carbon atoms in a planar conformation. For instance, various types of porphyrin derivatives can be found in nature such as chlorophylls which are chlorins and play essential roles in photosynthesis and hemes which are the key molecules for oxygen carriers in the blood. Porphyrins constitute a huge playground for innovation and for the synthesis of new performed initiating systems. Indeed, they are employed in multiple areas of scientific research and are the cornerstone of a wide range of applications including organic photovoltaic [16] photodynamic therapy [17] bioimaging [18] and so forth. To achieve these fascinating functions, and obtain the desired spectroscopic and electrochemical properties, different synthetic pathways concerning the modification of porphyrin macro ring have been developed and are well documented. We are convinced that the increasing research on

porphyrins and their modifications could be of great importance for the development of innovative photo-initiating systems under visible and NIR light irradiation.

This review reports the main current synthetic methods of porphyrin synthesis and modifications for extending their absorbance spectrum in the NIR range for photopolymerization applications. Through an intensive discussion on some structural characteristics of porphyrins, we identified the main factors that could improve the absorbance, the redox and the photophysical properties of porphyrins at the ground and excited states. Interestingly, some innovative porphyrin-based photo-initiating systems used for PET-RAFT, free-radical and cationic photopolymerization under visible and NIR light irradiation are also exemplified.

II. Synthesis and modification of porphyrins

In this paragraph, some important methods of synthesis of porphyrins and simple reactions in order to functionalize them are presented with a view to modifying their photophysical and electrochemical properties.

II. 1. Nomenclature

Two nomenclature systems have been actually accepted for porphyrins. In 1937, a simple numbering system was proposed by Hans Fischer [19] where the α-pyrrolic positions were numbered from 1–8 and the α, β, γ, δ positions were thus called *meso*-positions (**Figure 1A**). The weakness of the Hans Fisher's nomenclature system is that some carbon atoms remain unassigned in complicated porphyrin structures. Therefore, *IUPAC* adopted a new system which involved the numbering of all carbon atoms (**Figure 1B**).

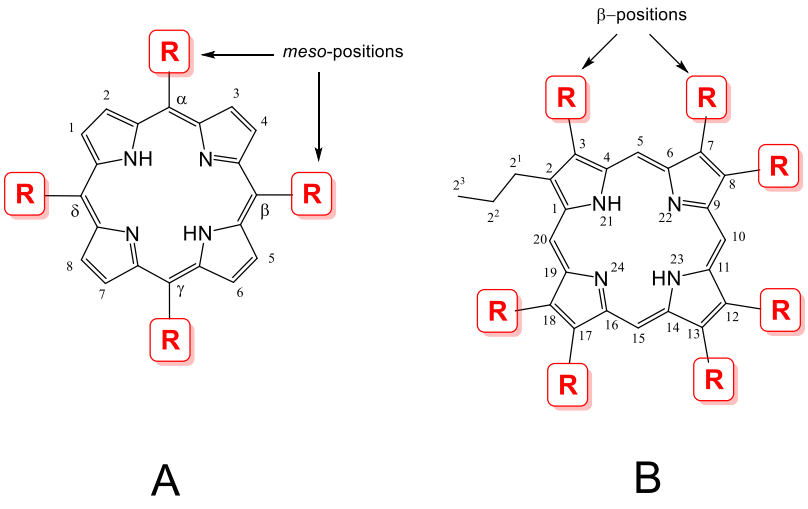

***Figure 1**: Nomenclature of porphyrins according to A) Hans Fisher and B) IUPAC.*

II. 2. Important synthetic procedures to obtain porphyrin macrocycles in few steps

The structures of porphyrin derivatives used as photo-initiators are usually rather simple and possess aryl groups on their *meso* positions. Aryl groups are used as *meso* substituents because the obtained chromophores are very stable and, more importantly, they can be prepared in high-yields through one-

pot procedures. This is an important prerequisite to target practical or industrial applications in the future. *Meso* tetraarylporphyrins are considered as workhorses to develop new porphyrin derivatives because the chemistry of these substituents is most of the time easy to control. *Meso* aryl groups are not coplanar with the aromatic core of the porphyrin because of the existence of steric interactions with the neighboring C(*β*)-H groups (**Figure 2A**). The tilted orientation of the *meso* aryl groups is an advantage to prevent strong aggregation between the porphyrins and improve their solubility in organic solvents. Water soluble porphyrins can also be obtained by functionalizing the *meso* aryl positions with cationic or anionic groups such as *N*-methylpyridinium or p(sulfonate)phenyl groups, respectively (**Figure 2B** and **Figure 2C**) [20]. The aim of the next paragraphs is not to make an exhaustive list of reactions allowing the functionalization porphyrins, but to give the reader an overview of short synthetic pathways (from 1 to 5 steps maximum) giving access to monomeric porphyrins with desired properties to potentially use them as photo-initiators. There is notably a focus on short synthetic pathways allowing the formation of porphyrinoids absorbing in the red or near infrared region (NIR).

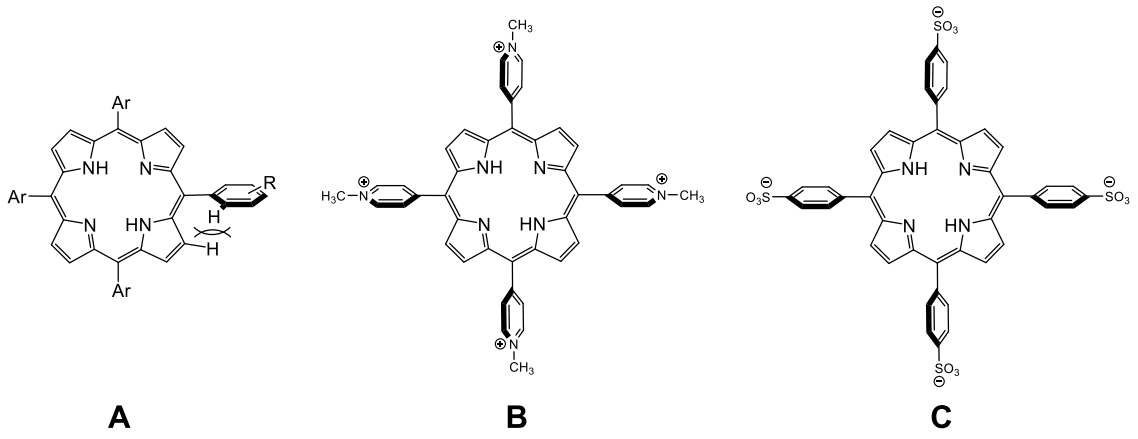

Figure 2: *Left: structure of meso-tetraarylporphyrins showing steric interactions between meso aryl groups and C(β)-H groups. Middle and right: structures of water-soluble porphyrins with meso cationic and anionic aryl groups, respectively.*

II.2.a. Synthesis of symmetric A_4 porphyrins

The simplest porphyrins to synthesize are totally symmetrical, namely of the A_4-type, in which the four *meso* aryl groups are the same. In mid-1930, Rothemund *et al*. reported the synthesis of *meso* 5,10,15,20-tetraphenylporphyrin (H_2TPP, **Figure 3** top) by reacting pyrrole and benzaldehyde in a sealed bomb at 150 °C for 24 hours [21,22]. These conditions were improved in 1965 by Adler and Longo who developed a milder synthetic procedure consisting in reacting pyrrole and benzaldehyde under reflux in propionic acid [23] (**Figure 3** bottom). The porphyrinogen resulting from the polycondensation reaction is then oxidized to porphyrin by ambient oxygen.

This straightforward procedure makes it possible to vary the aromatic groups present on the *meso* positions using various aromatic aldehydes and is still routinely used nowadays to obtain A_4-porphyrins, especially when the purification of the compounds is facilitated by their crystallization in the reaction mixture. For example, the *meso* 5,10,15,20-tetraphenylporphyrin is easily obtained at the gram scale with yields of around 20% following this procedure. Later, Lindsey *et al*. have improved the reactions yields (40 – 50%) by developing much milder reaction conditions in a two-step procedure also allowing the use of more sensitive aldehydes [24,25] (**Figure 3** bottom). Their procedure consists in reacting pyrrole with aromatic aldehydes in the presence of BF_3:OEt_2 or TFA acting as a Lewis acid under inert atmosphere. Then, the *in situ* generated porphyrinogens are oxidized using quinone derivatives such as dichlorodicyanoquinone (DDQ) or *p*-chloranil. Column chromatography separations are necessary here to obtain the A_4-type porphyrins as pure compounds. The choice of Adler or Lindsey

conditions is made according to the nature and the substituents on the *meso* aryl groups, which are more or less sensitive to Lewis or Brönsted acids and/or strong oxidizing agents like DDQ or *p*-chloranil.

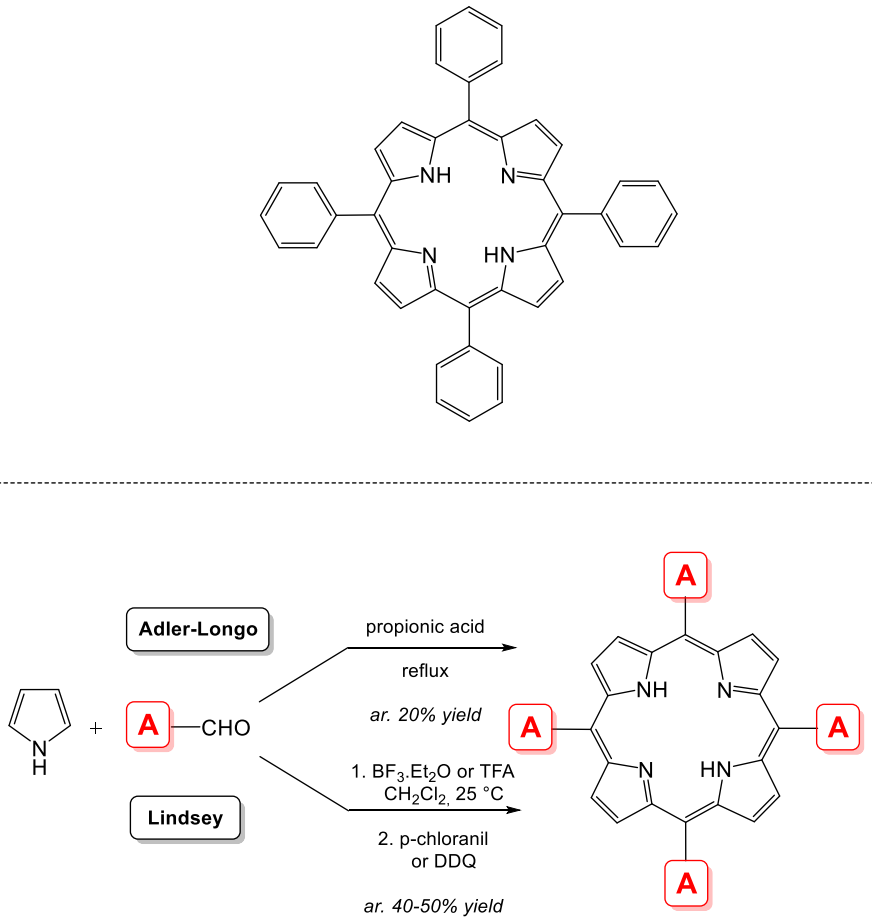

Figure 3: Top: *Structure of* meso-*5,10,15,20-tetraphenylporphyrin (H_2TPP).* ***Bottom:*** *Synthesis of meso-tetraarylporphyrins through Adler-Longo and Lindsey conditions. Yields are indicated for the synthesis of H2TPP (A = phenyl).*

II.2.b. Synthesis of A-type and *trans*-A_2-type porphyrins

Many applications with porphyrins generally require unsymmetrically substituted macrocycles to bring additional functionalities: one or more anchoring groups for surface functionalization, donor and/or acceptor groups for solar energy conversion, or chiral unit(s) for enantioselective catalysis. Many synthetic procedures can be used to obtain such compounds and we summarize here some of the most important ones (**Figure 4**). The simplest A-type porphyrin with only one *meso* substituent can be obtained in 2-12% yield by first synthetizing the dipyrromethane and then by reacting this compound with 2-formylpyrrole and suitable A-CHO aldehyde [26]. This strategy reported by Senge *et al*. works quite well but other isomers like the *trans*-A_2-type porphyrin can also be obtained due to scrambling and they should be removed by column chromatography. The A-type porphyrin can also be synthesized from the unsubstituted porphin, but the lack of solubility may be an issue in this case [27]. The *trans*-A_2-type porphyrin with two opposed identical *meso* substituents can be obtained by condensing the dipyrromethane with one equivalent of the desired aldehyde A-CHO. This procedure generally works well with high yields up to ~40% [28].

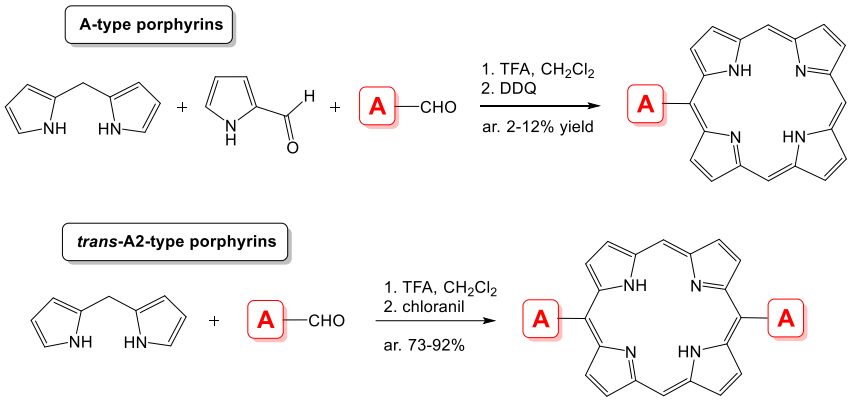

Figure 4: *Synthesis of A-type and trans-A2-type porphyrins.*

II.2.c. Synthesis of A_xB_y-type porphyrins.

Unsymmetrically substituted porphyrins of A_xB_y-type can be obtained by condensing two aldehydes with pyrrole under Lindsey's equilibrium conditions to yield a mixture of different isomers (**Figure 5**) [24]. Pyrrole and the desired two aldehydes react reversibly at room temperature with trace acid catalysis to form cyclic tetraphenylporphyrinogen at thermodynamic equilibrium (**Figure 5**, top). Then, an oxidant is added in the reaction mixture and irreversibly convert porphyrinogens into porphyrins. In these conditions, all possible porphyrins can be obtained in one step including A_3B porphyrins, and *trans*- and *cis*-A_2B_2-type porphyrins isomers (**Figure 5**, bottom). Of course, the use of column chromatography to separate these compounds may be a serious issue here, especially if important quantities of porphyrins are needed. Chromatographic separations are easier when the two *meso* aryl possess different polarities.

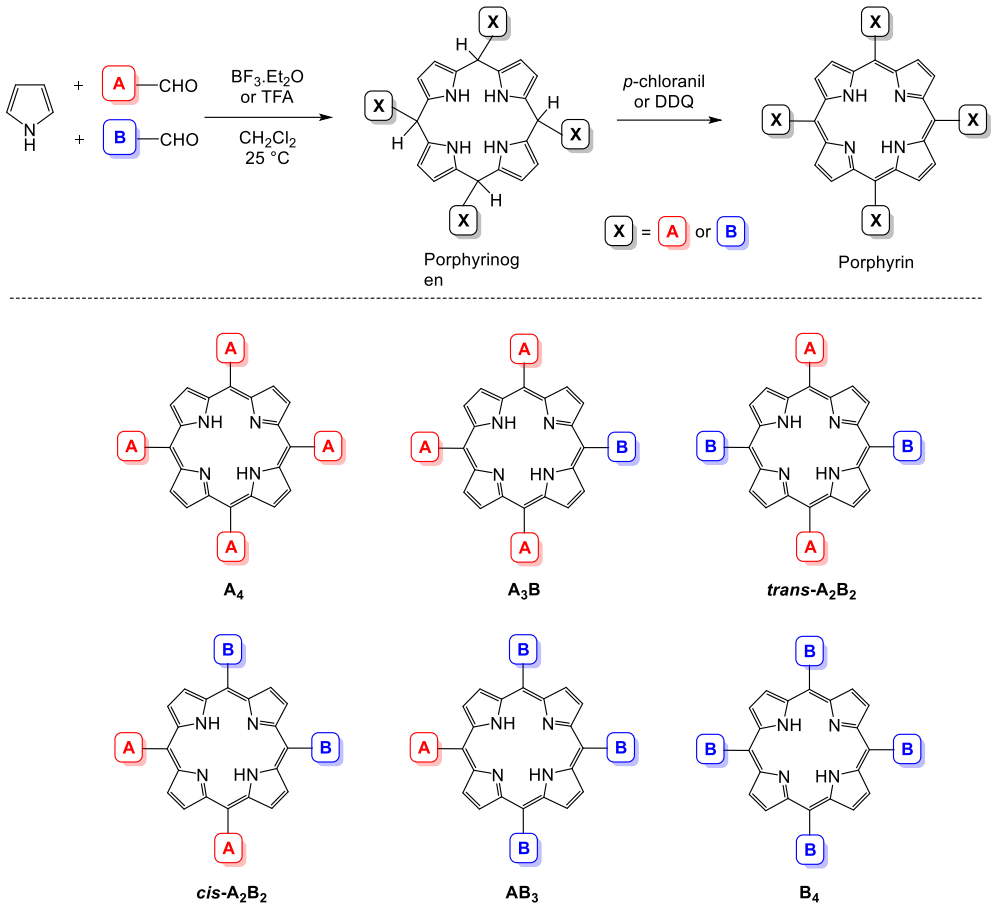

Figure 5: Synthesis of meso-tetraarylporphyrins under equilibrium conditions.

To improve the synthesis of trans-A_2B_2-type porphyrins, Macdonald and co-worker [29] have developed a new methodology. This involves two dipyrromethane condensed with an aldehyde, forming a [2+2] condensation (**Figure 6**). Initially, pyrrole is condensed with a first aldehyde A-CHO under acid condition to form the dipyrromethane intermediate. Then, this intermediate is condensed with the second aldehyde B-CHO, to form the porphyrin after oxidation with chloranil or DDQ. The method has been widely studied by Lindsey *et al.* [30] to minimize the formation of undesired product, specifically the *cis*-A_2B_2 isomer. In order to maximize the formation of the desired porphyrins, several conditions have been studied, as the order of insertion of the aldehydes, their concentration or the nature of the acids used as catalysts.

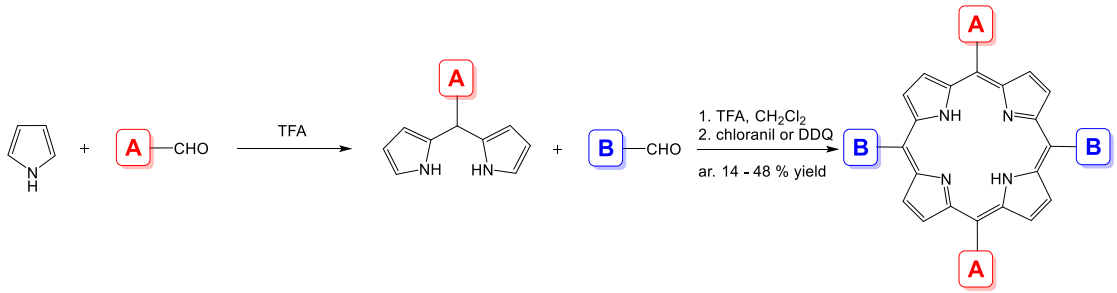

Figure 6: Synthesis of trans-A_2B_2-type porphyrin following the MacDonald's pathway.

II.2.d. Synthesis of *beta*-substituted porphyrin

Even if porphyrins with *meso* aryl groups are preferred for photopolymerization, it can be noted that β-functionalized porphyrins also present interesting properties which will be explored in section II and III. The synthesis of these molecules is therefore introduced here.

In the same way that TPP is the simplest *meso* porphyrin, OEP (octaethylporphyrin, **Figure 7**) is used as a model of β-functionalized porphyrin. Two major routes can be used to synthesis it. The first one is comparable to the synthesis of TPP, where the 3,4-diethylpyrrole is cyclised with formaldehyde which provided the methine carbons, leading to a yield of 55-75% [31]. The second route implied the presence of the methine carbon on the pyrrole, and therefore, the use of a 5-(CH_2-R)-substituted pyrrole.

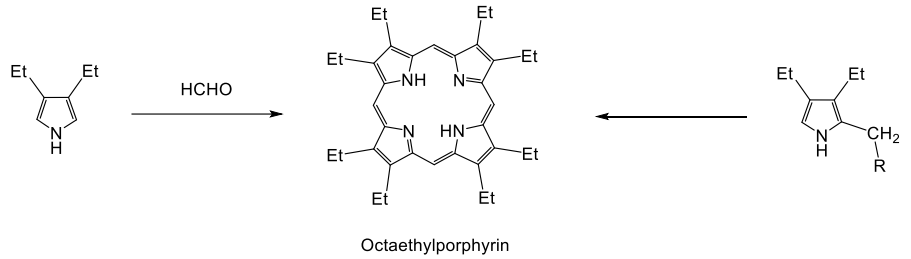

***Figure 7**: Structure of OEP*

II. 3. Functionalization of porphyrin macrocycles

II.3.a. Functionnalization of the *meso* aryl groups.

Meso-tetraarylporphyrins can be functionalized either on their *meso* aryl groups or directly on their macrocycle. In the case where chemical functions are introduced on *meso* aryl groups, these chemical functions can be introduced before the synthesis of the porphyrin, *i.e.* on the aldehydes used for the synthesis of the porphyrin. In this case, these chemical functions should be tolerant towards the reaction conditions used for the synthesis of the porphyrins under Adler's (refluxing propionic acid) or Lindsey's conditions. If it is not the case, alternative synthetic procedures should be found to prepare the expected compound. For example, it is not possible to directly synthesize the *meso*-tetra(*p*-aminophenyl)porphyrin (TAPP, **Figure 8**) from the corresponding *p*-aminobenzaldehyde with BF_3.Et2O catalyst, because amino groups will strongly interact with the Lewis acid. In this case, there are two possible alternatives requiring one additional synthetic step to obtain the desired compound. The first alternative is to synthesize the *meso*-tetra(*p*-acetamidophenyl)porphyrin from the corresponding *p*-acetamidobenzaldehyde and then to deprotect the amino groups under acidic conditions [32]. The second alternative is to synthesize the *meso*-tetra(*p*-nitrophenyl)porphyrin from the *p*-nitrobenzaldehyde and then to reduce the nitro functions to the corresponding amino functions [33]. This example illustrates well that sensitive functions such as amino groups should be introduced on the *meso* aryl groups after the formation of the porphyrin macrocycle. However, numerous chemical functions such as esters or halogens, for example, and allowing easy further transformations can be introduced on the aldehydes used for the synthesis of the porphyrin macrocycle.

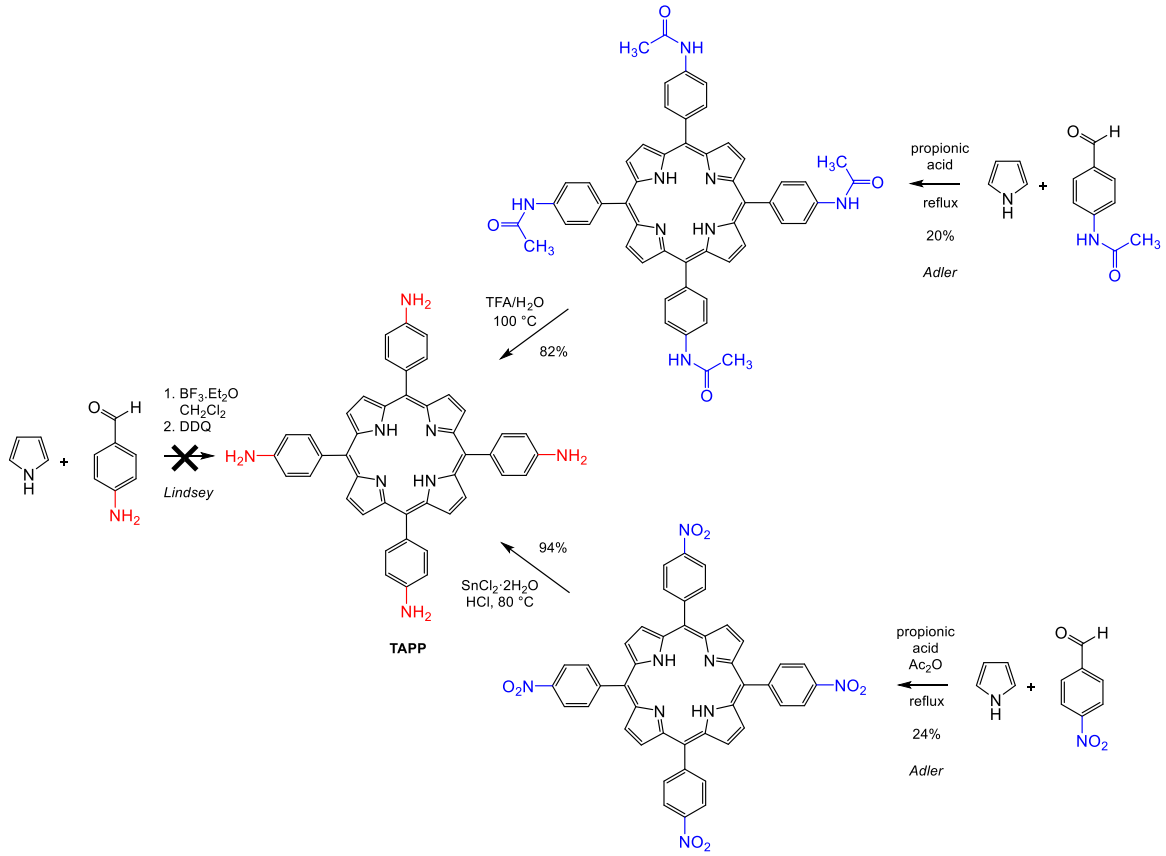

Figure 8: *Synthesis of meso-tetra(p-aminophenyl)porphyrin.*

II.3.b. Functionnalization of the porphyrin core.

During the last 50 years, there was an extensive development of β-pyrrolic and *meso* functionalization of porphyrins. One of the most important reactions to post-functionalize the A_4-type *meso*-tetraarylporphyrins is the bromination in β positions of the pyrrolic rings (**Figure 9**). Among all brominating agents, *N*-bromossucinimide (NBS) is probably one of the most convenient and easy to handle. Single bromination is generally performed with NBS in refluxing $CHCl_3$ as initially reported by Callot [34]. Modified procedure of Zhang *et al.* by using pyridine as additive and slow addition of NBS allowed the obtention of the monobrominated porphyrin in more than 70-80% yields [35]. This compound is a starting material of choice for the synthesis of β-functionalized porphyrins *via* palladium-catalyzed C-N, C-S or C-O bonds formation. The formation of polybrominated species may be an issue when purifiying the monobrominated species. Continuous flow techniques with additive free Callot's conditions is probably one of the most efficient procedure to obtain monobrominated porphyrin [36]. Interestingly, when polybromination reaction performed on the free base *meso* tetraarylporphyrin, the first four bromine atoms take place on the two antipodal β-pyrrolic double bonds which are not involved in the aromatic system of the porphyrin macrocycle. The 2,3,2,13-tetrabromoporphyrin can be obtained in about 80% yield when using a slight excess of NBS in refluxing $CHCl_3$ [37]. Up to eight bromine atoms can be added to the porphyrin core with NBS in refluxing $CHCl_3$ or Br_2 in $CHCl_3/CCl_4$ [38]. Best yields are obtained with metalloporphyrins (M = Ni or Cu). The post-functionalization of porphyrins through the bromination in β-position of the pyrrolic rings is a relevant transformation because the resulting bromo derivatives are useful synthons to functionalize the porphyrin core. For example, it is possible to substitute bromine atoms by a cyano functions by reacting the corresponding brominated porphyrin with CuCN, for example [39,40] (**Figure 10**, top). Two other important and simple reactions to functionalize β-pyrrolic positions of porphyrins are Vilsmeier-Haack

formylation reaction [41] and nitration reactions [42] (**Figure 10**, middle and bottom). Mono-functionnalization of a β-pyrrolic position can be easily performed in these conditions and the corresponding porphyrins are obtained in high yields. They are also excellent starting materials to obtain π–extended porphyrins by ring-fusion (*vide infra*).

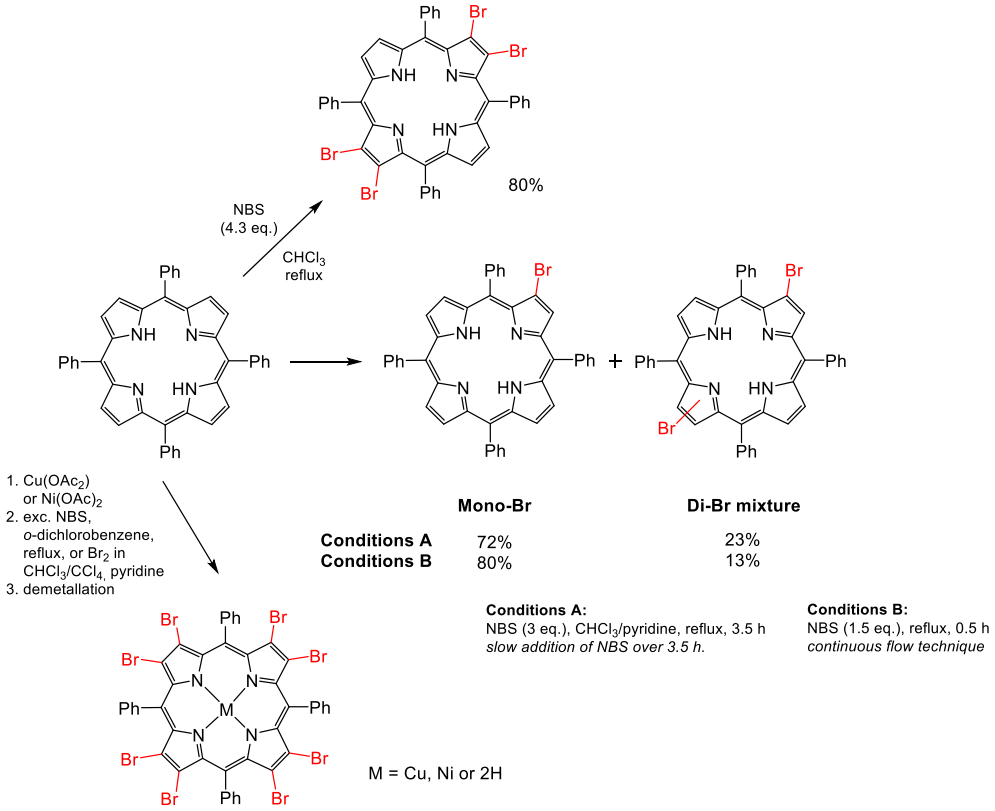

Figure 9: *Bromination reactions of meso-tetraarylporphyrins*

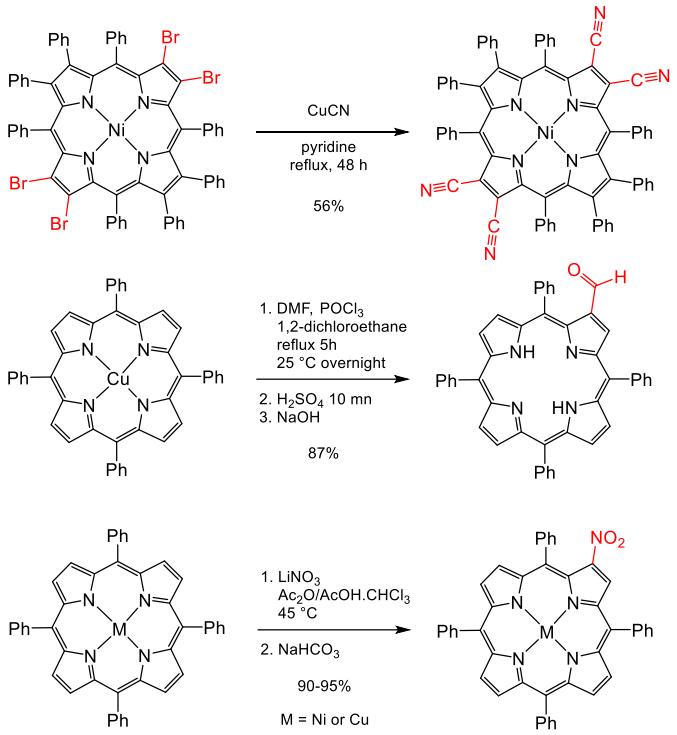

Figure 10: *Some important reactions on β-pyrrolic positions: cyanation (top), formylation (middle) and nitration (bottom) reactions*

A_3- and *trans*-A_2-type porphyrins possess one or two free *meso* positions, respectively, which are more reactive compared to the β-pyrrolic positions. Indeed, bromine [43], formyl [44] or nitro [45] groups can be regioselectively introduced on this *meso* position (**Figure 11**). The obtained compounds can be used as precursors to obtain A_2B_x π-extended porphyrins and multiporphyrinic systems. Indeed, *meso*-bromoporphyrins are key intermediates to obtain high-values porphyrins with advanced photophysical properties.

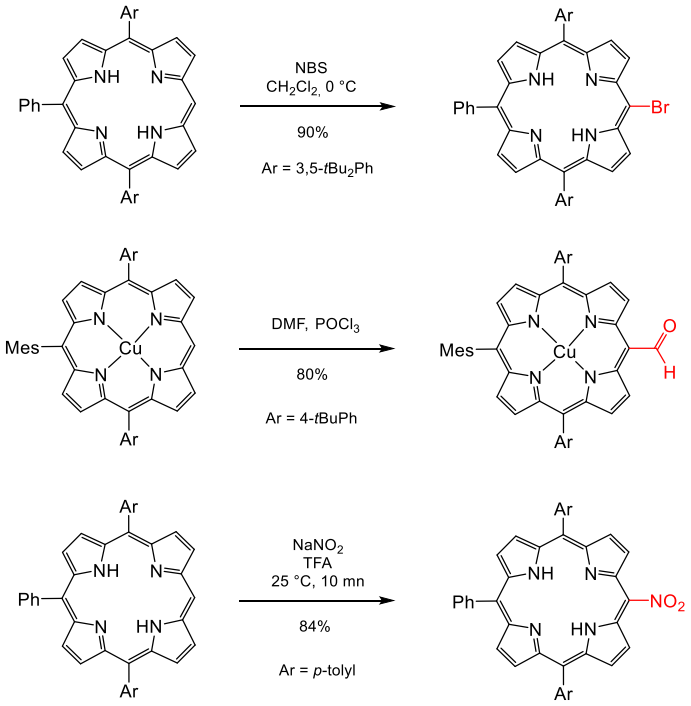

Figure 11: *Some important reactions on* meso *positions: bromination (top), formylation (middle) and nitration (bottom) reactions.*

As an illustration, *trans*-A_2-type porphyrin can be used as starting material and substituents B can be attached on one or two remaining *meso* positions through bromination (96% yield [46]) and transition-metal catalyzed reactions (**Figure 12**). Brominated porphyrin can be obtained from a variety of methods, as reviewed by Chumakov *et al*. [47]) in order to allowed different cross-coupling reactions (see review [48]).

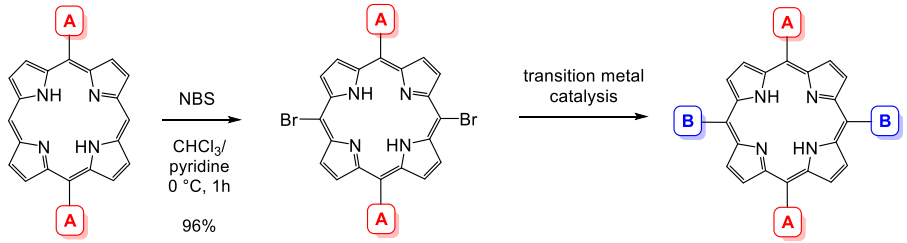

Figure 12: *Synthesis of* trans-A_2B_2*-type porphyrin.*

A sequential addition of bromo function can be used to obtain dissymmetrical porphyrins. A representative example is depicted in **Figure 13** as a *push-pull* porphyrin [49]. The donor-π-bridge-acceptor zinc(II) porphyrin was used as sensitizer in dye-sensitized solar cells (DSSCs) and was obtained starting from the corresponding *trans*-A_2-type porphyrins. The synthetic strategy consists in using *meso* bromoporphyrins to successively introduce the alkyne group and the tertiary amine *via* cross-coupling reactions. Numerous compounds of this type were used in DSSCs [50]. A nice review of Senge *et al*. summarizes such procedures to obtain unsymmetrically *meso* substituted porphyrins [51].

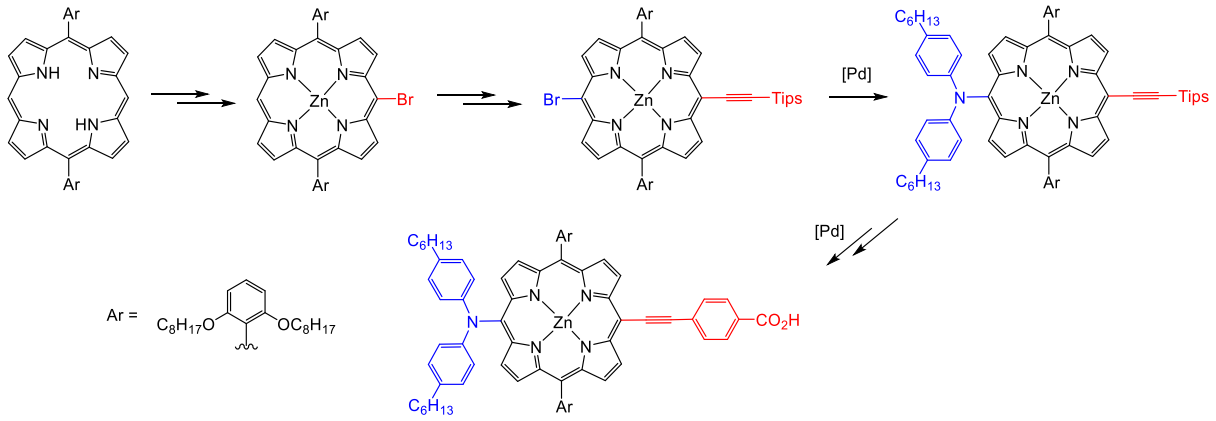

Figure 13: *Synthesis of a donor-π-bridge-acceptor zinc(II) porphyrin used as sensitizer in DSSCs (donor part in blue, acceptor part in red).*

II. 4. Synthetic strategies towards π-extended porphyrins

II.4.a. Ring fusion strategy between *meso* aryl groups and *β*-pyrrolic positions.

As previously shown, aryl groups of *meso* tetraarylporphyrins are not coplanar and thus poorly conjugated with the aromatic core of the porphyrin because of the existence of steric interactions with the neighbouring C(*β*)-H groups. However, forcing these *meso* aryl groups to be coplanar with the porphyrin core is a nice way to quickly obtain π-extended porphyrins [52] and some useful transformations are presented below to connect *meso*-aryl groups with *β*-pyrrolic positions in few synthetic steps starting from simple porphyrin precursors, which were presented in the previous section. One of the first reaction involving an intramolecular cyclization reaction is the formation of so-called naphtoketoporphyrins from *β*-formylporphyrins (**Figure 14**) [53,54]. These compounds are formed upon protonation of the formyl group with TFA followed by a nucleophilic attack of the neighboring *meso* aryl group. Dismutation of the obtained intermediate secondary alcohol afforded the naphtoketoporphyrins accompanied with reduced species. The yield of the naphtoketoporphyrins could be increased up to 50% upon adding an oxidant in the reaction mixture. Interestingly, these naphotketoporphyrins possess strong absorption bands in the red region of the visible spectrum (between 700-800 nm for the free-base naophtoketoporphyrin). Dolphin also reported the formation of an additional five-membered ring when donor groups such as meta-methoxy groups are present on the meso aryl groups [55].

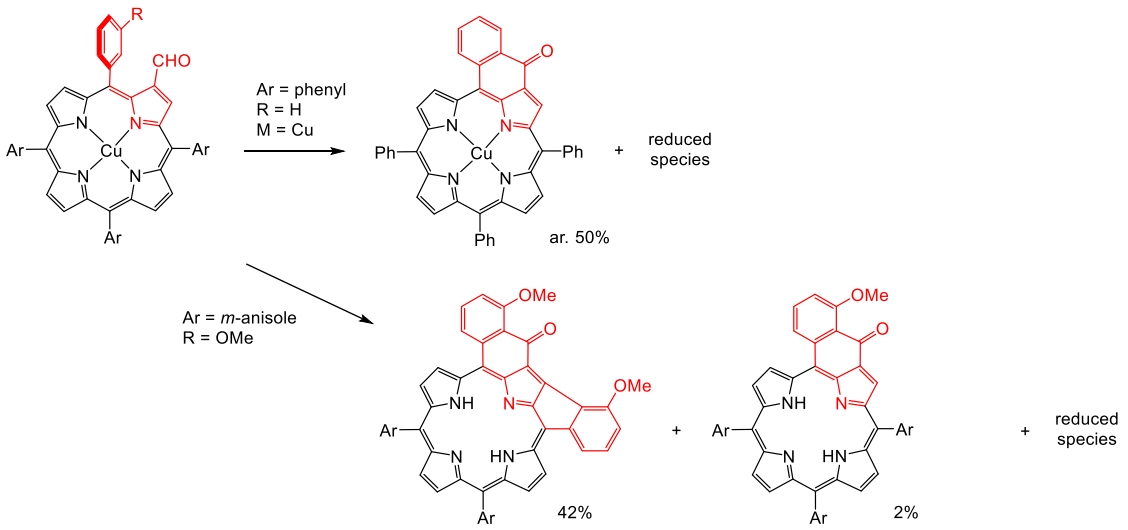

Figure 14: *Synthesis of a naphtoketoporphyrins from β-formylporphyrins.*

β-Cyanoporphyrins are also excellent precursors to obtain such naphtoketoporphyrins. Indeed, cyano group can be converted into carboxylic acid group (**Figure 15**, top). The corresponding porphyrin bearing an acyl chloride group can be used in intramolecular Friedel-Crafts reaction affording the expected naphtoketoporphyrin in a excellent in yield of 90% [56]. Another strategy consists in using porphyrins equipped with *meso* orthobenzoic esters (**Figure 15**, top). A similar intramolecular Friedel-Crafts procedure allows the formation of naphotketoporphyrins [57]. Bis(naphtoketo)porphyrins could also be obtained through double intramolecular Friedel–Crafts reactions starting from porphyrins equipped with two carboxylic acid groups (**Figure 15**, bottom). Lower energy absorption bands of these compounds are in the red and near-infrared region [56].

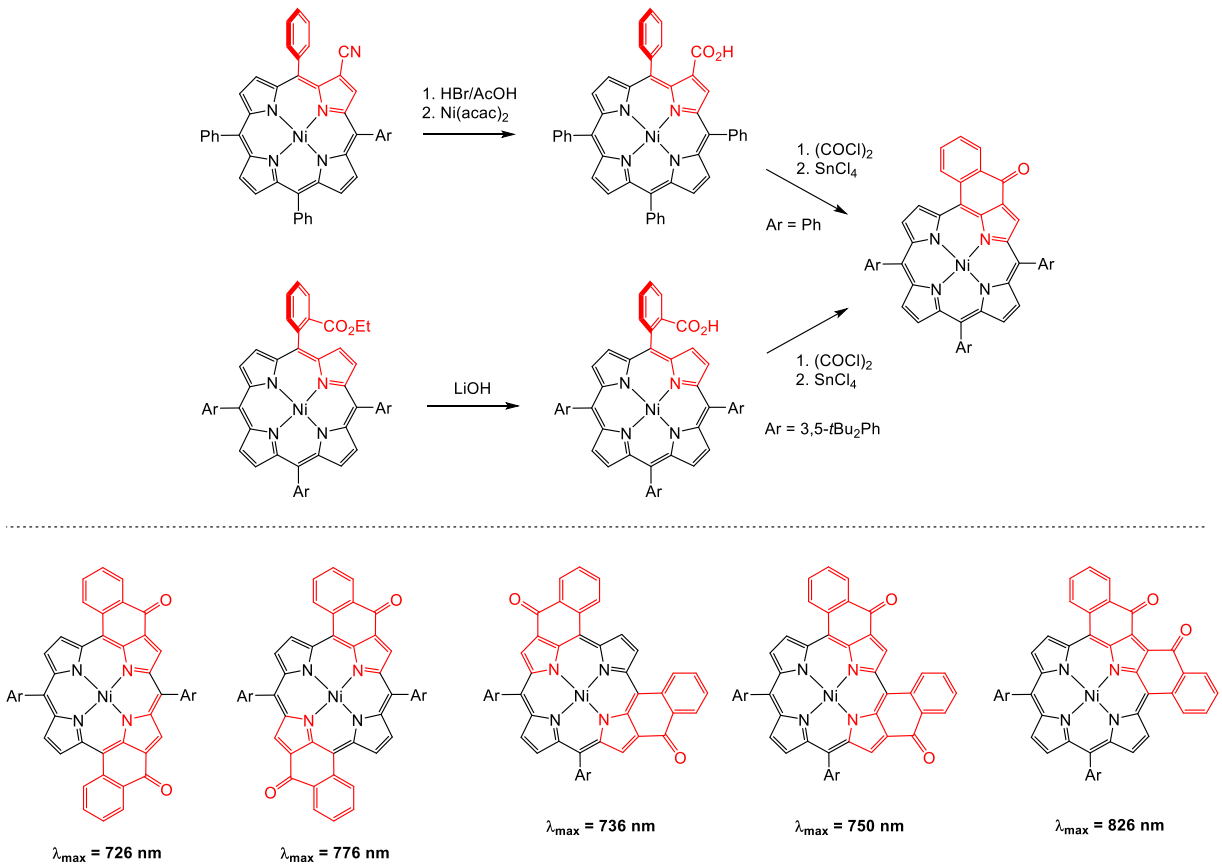

Figure 15: *Synthesis of a mono- and bis-naphtoketoporphyrins from porphyrins bearing carboxylic acid functions on β- or meso-carbon atoms.*

Other heteroatom such as nitrogen atoms can be used as connectors between *meso*-aryl groups and *β*-pyrrolic positions and *β*-nitroporphyrins can be used as starting material (**Figure 16**). Intramolecular cyclization reaction occurred in 75% yield using the Cadogan cyclization reaction conditions [42]. In this case, the cyclized *meso* aryl group is also forced to be coplanar and conjugated with the porphyrin macrocycles. Other compounds of this type were synthesized starting from *β*-azidoporphyrin [58] and *β*-anilinoporphyrin [59]. Double cyclization reactions leading to the formation of biquinolinoporphyrin and naphtalenequinolinoporphyrin were later described.

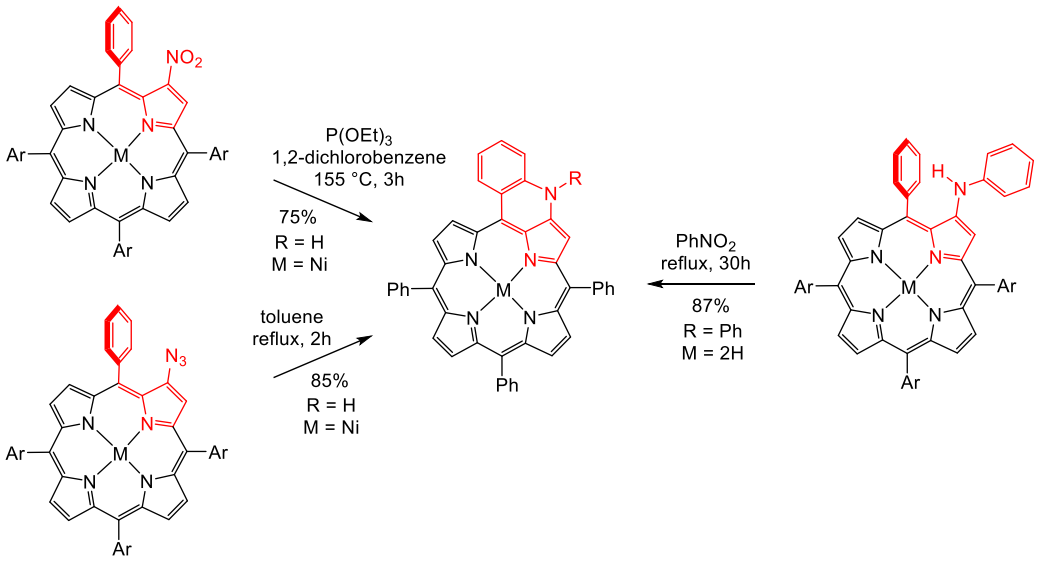

Figure 16: *Synthesis of enaminoporphyrins.*

Imahori and coworkers developed an elegant strategy to obtain unsymmetrically π-extended porphyrins for TiO_2-based DSSCs [60] (**Figure 17**). They first synthesized a A_3B-type porphyrin namely nickel(II) 5-(4-carbomethoxynaphth-1-yl)-10,15,20-tris(2,4,6-trimethylphenyl) porphyrin and ring fusion was achieved by the treatment of this porphyrin with $FeCl_3$. The obtained *meso*,*β*-naphthyl doubly fused porphyrin could then be dematalated and rematalated with zinc (II). Extension of the π-system and loss of symmetry dramatically improve light absorption since broad and intense Soret and Q-bands bands are observed in the UV-visible spectra of the naphthyl fused compounds. Gryko, Kadish and coworkers also reported the convenient and straightforward synthesis of similar compounds through an electrochemical oxidation process [61,62].

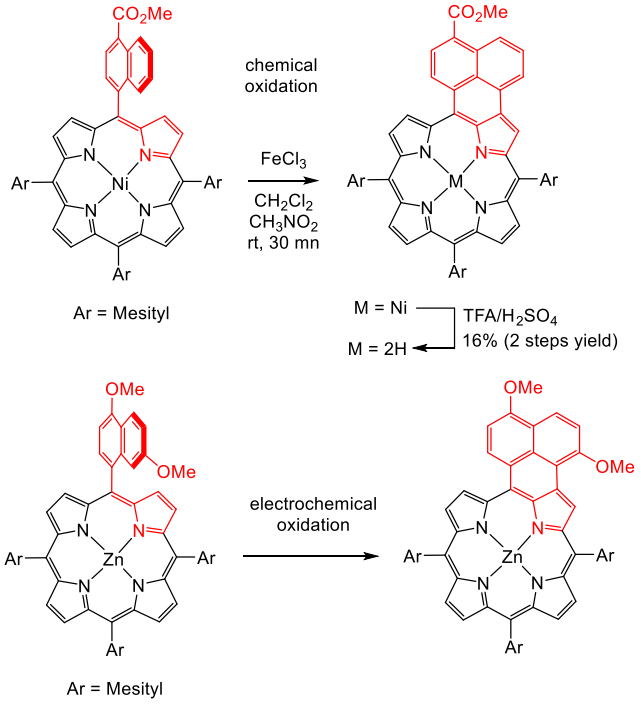

Figure 17: *Synthesis of meso, β-naphthyl doubly fused porphyrins.*

Ring fusion strategy was also used by Anderson and coworkers to synthesize *β,meso,β*-anthracene triply fused and *β,meso*-anthracene doubly fused porphyrins through oxidative intramolecular ring closure of meso-(9-anthryl)porphyrins and meso-(1-anthryl)porphyrins in 80-82% yields (**Figure 18**) [63]. In this case, it is important to have electron-donating alkoxy groups on the anthryl unit to favor the oxidative ring closure. As expected, the important red-shift of the UV-visible absorption bands and the reduced electrochemical HOMO-LUMO gaps of the anthracene doubly and triply fused porphyrins can be attributed to the extension of the π-conjugation. Following a similar strategy, Anderson and coworkers obtained porphyrins fused to two [64] and to four [65] anthracenes. This compound with four fused anthracene units exhibit an intense and red-shifted absorption spectrum (λ_{max} = 1417 nm) and a very small electrochemical HOMO−LUMO gap of 0.61 eV. Following a similar ring fusion strategy, Müllen, Narita and coworkers synthesized two triply fused porphyrin-nanographene conjugates by the cyclodehydrogenation of benzo[m]tetraphene-substituted porphyrins (**Figure 19**) [66]. Their UV-vis-near infrared absorption spectra demonstrated broad and largely red-shifted absorption spectra extending up to 866 and 1176 nm, respectively, indicating the important extension of the π-conjugated systems. These compounds red-shifted absorption in the near infrared (NIR) are potentially useful NIR dyes for optoelectronic applications such as infrared sensing.

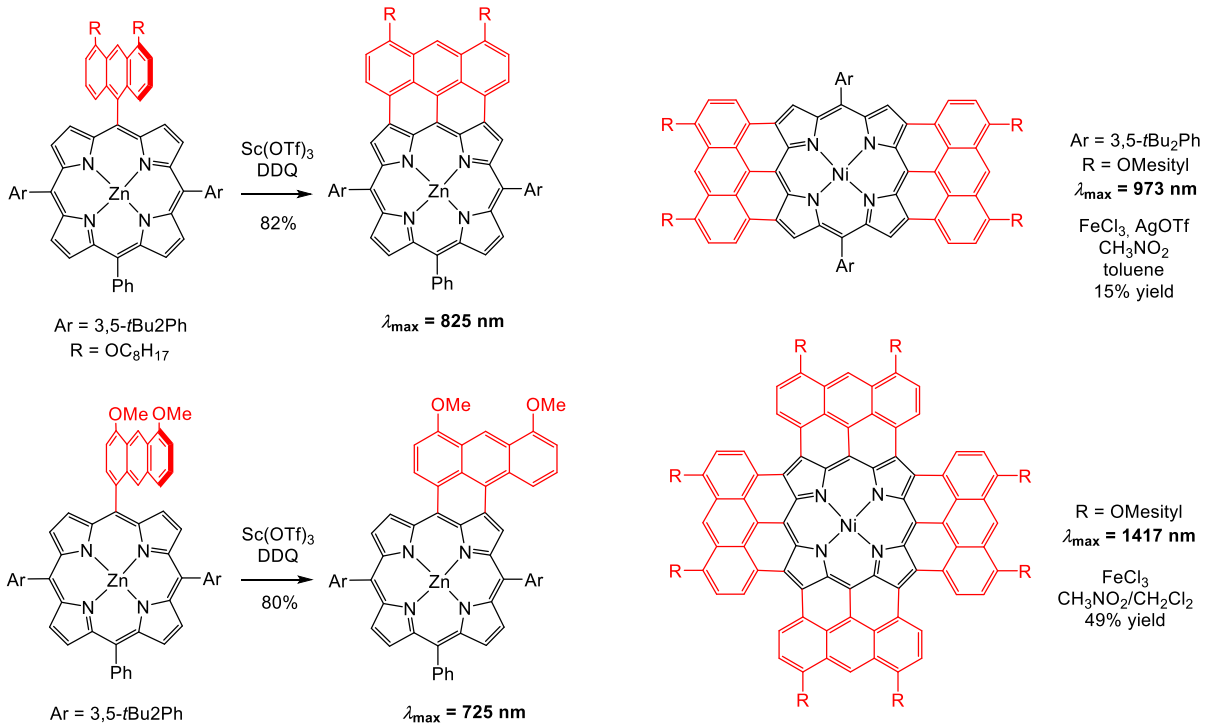

Figure 18: *Synthesis of β,meso, β-anthracene triply fused and β,meso-anthracene doubly fused porphyrins.*

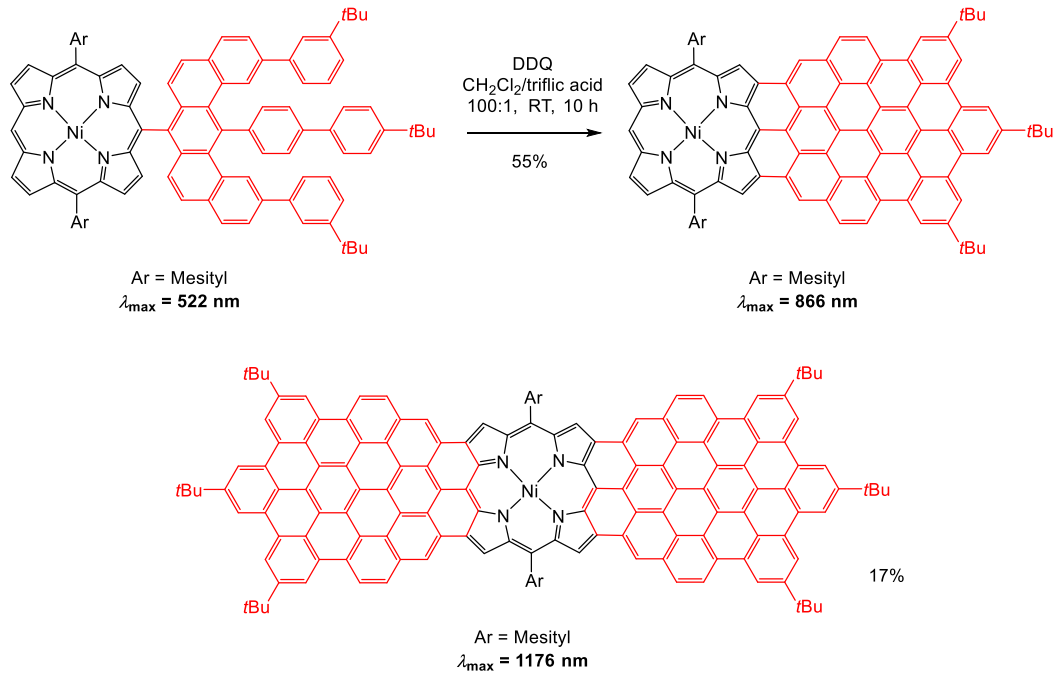

Figure 19: *Synthesis of β,meso, β-nanographene triply fused porphyrins.*

II.4.b. Ring fusion strategy on *β*-pyrrolic carbons.

Ring fusion strategy involving only *β*-pyrrolic carbons implies the synthesis of suitable pyrrolic precursors or the functionalization of the *β*-pyrrolic carbons of the porphyrin core [67]. Benzoporphyrins are the archetype of π-extended porphyrins where pyrrole rings are fused to benzene rings. They can be obtained following different procedures involving few synthetic steps starting from suitable pyrrolic precursors (**Figure 20**). The first method relies on the reaction of isoindole with an aldehyde in the presence of metal ion playing the role of template to assist the reaction and bring about cyclization [68]. Knowing that unsubstituted isoindole are relatively unstable for the preparation of such compounds, 4,7-dihydro-4,7-ethano-2H-isoindole can be used as starting material for the preparation of benzoporphyrins. Lindsey's condensation reaction of 4,7-dihydro-4,7-ethano-2H-isoindole with an aldehyde followed by oxidation gave the corresponding *meso*-tetraarylated porphyrin. After metalation reaction (Zn), this porphyrin can be converted into the corresponding benzoporphyrin by heating it at 200 °C for 10 minutes [69]. An analogous synthetic procedure consists in using 4,5,6,7-tetrahydroisoindole as starting material. Lindsey's condensation reaction of 4,5,6,7-tetrahydroisoindole with an aldehyde followed by oxidation with DDQ at room temperature gave the corresponding tetracyclohexenoporphyrin derivative. After metalation reaction (Pt), oxidation with DDQ in refluxing toluene afforded the corresponding benzoporphyrin [70,71].

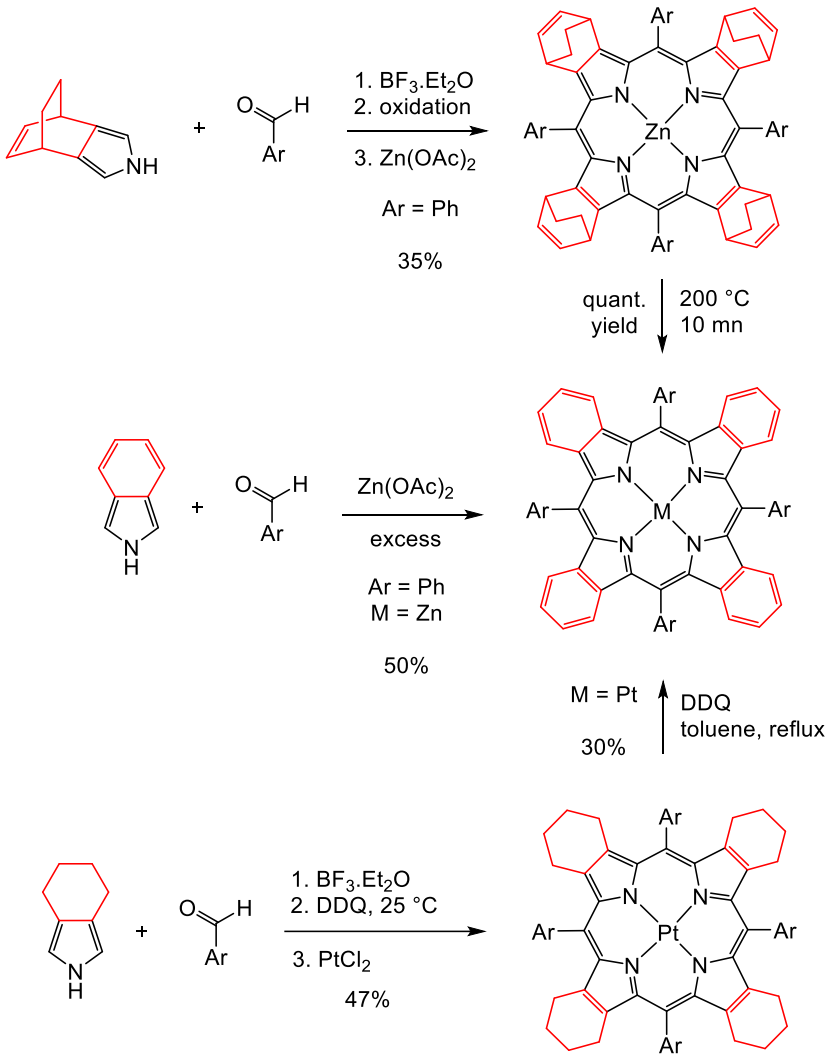

Figure 20: *Synthesis of benzoporphyrins.*

Another elegant strategy to obtain π-extended porphyrins was developed by Crossley and consists in doing condensation reactions with carbonyl groups (**Figure 21**) [37,72–75]. This method allows the stepwise annelation of heteroaromatic residues onto the porphyrin core. The starting material is a *β*-nitroporphyrin which is reduced into the corresponding *β*-aminoporphyrin. Photooxidation of the later and mild hydrolysis of the intermediate imine afforded the corresponding dioxochlorin. Condensation reaction with 1,2 diamino-benzene afforded the corresponding pyrazine annelated porphyrin. This strategy can be repeated up to four times to obtain four annelated pyrazine systems.

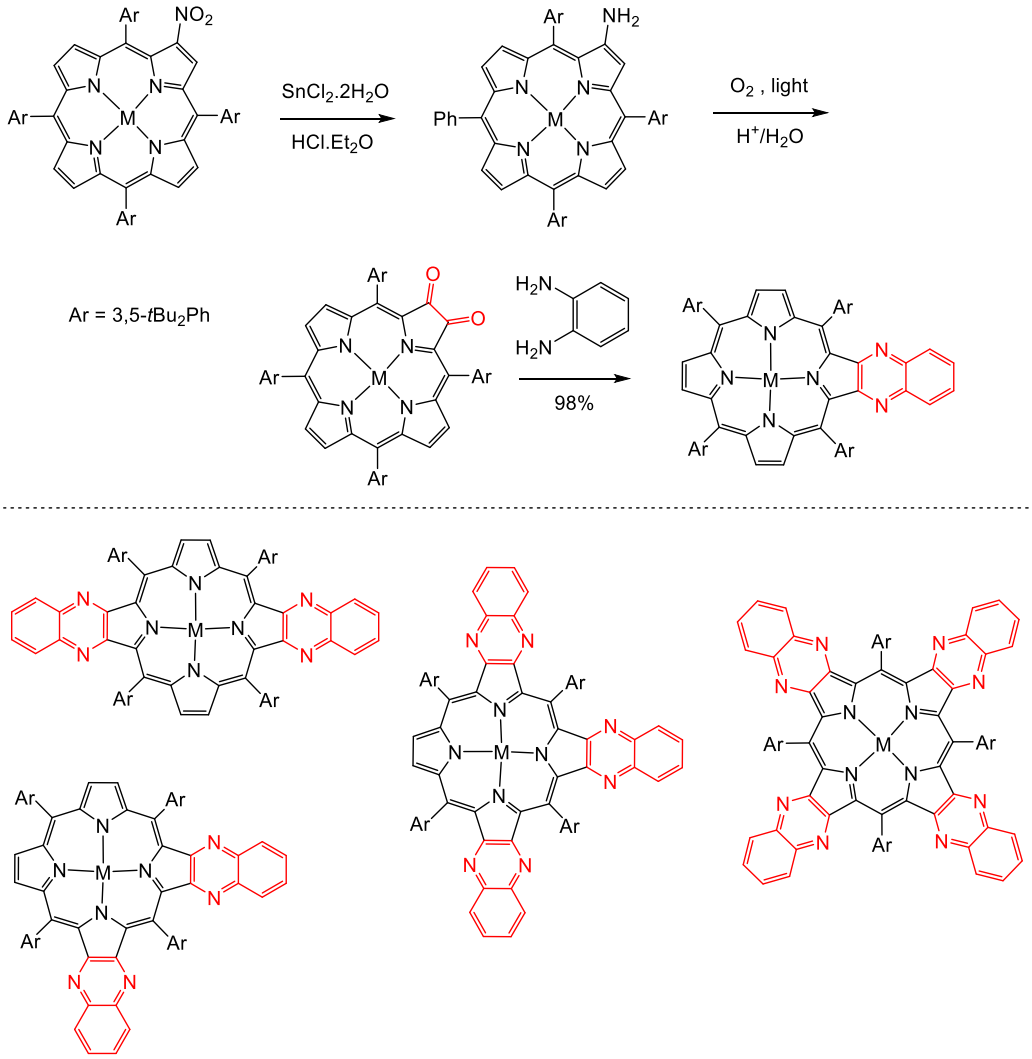

Figure 21: *Synthesis of porphyrins annelated to pyrazine systems.*

II. 5. Hemisynthetic strategies and use of porphyrin derivates

The production of valuable chemicals and materials from biomass resources has developed rapidly in recent years and will become a ubiquitous challenge of our future with economic and environmental benefits. Chlorophyll derivatives are the most abundant class of porphyrinoids in nature. Like porphyrins, they are tetrapyrrolic macrocycles, but one of their C_β-C_β bond is reduced. This structural change confers chlorophyll derivatives different optical properties compared to porphyrins, notably a more intense and redshifted lowest energy Q-band around 650 nm. These natural compounds thus possess optical properties which are sometimes desired when considering π-extended porphyrins (redshifted intense Q bands in the red or NIR region, vide supra). An important biomass resource developed all over the world is spirulina, a green algae mainly used as food supplement. One of the most valuable chlorophyll derivatives which can be easily extracted from spirulina is chlorophyll a (**Figure 22**). It can be easily extracted with ethanol as solvent and Soxhlet extractor from dried powder of commercially available spirulina. Then, magnesium (II) ion was removed under acidic conditions (HCl, acetone). Transesterification reaction (MeOH, H_2SO_4) was performed to obtain the methylpheophorbide a. Then, decarboxylation reaction with collidine at reflux and subsequent treatment under acidic conditions (HCl, acetone) afforded the expected pyropheophorbide a [76–79]. This hemisynthetic compound and its zinc (II) complex are chlorin derivatives and possess strong absorption

bands in the 600-700 nm region. They were successfully used as visible-light photosensitizers notably under red light for free-radical photopolymerization [80].

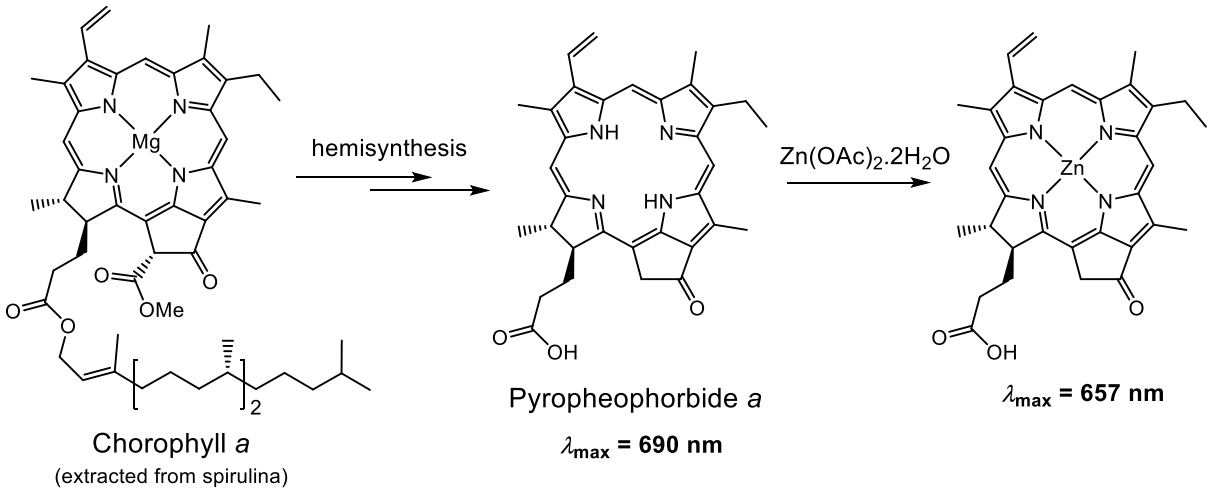

Figure 22: *Synthesis of pyropheophorbide a and its Zn (II) complex.*

Other porphyrin derivatives can be employed, like chlorin and bacteriochlorin, which have one or two reduced double bond respectively (**Figure 23**) resulting in a wider absorption spectrum. The transformation of tetraphenylporphyrin (TPP) into tetraphenylchlorin (TPC) and tetraphenylbacteriochlorin (TPB) can be achieved through sequential treatment of porphyrin with hydrazine as reducing agent in a basic medium [81,82]. The reaction leads to a mixture of chlorin and bacteriochlorin, although the addition of excess hydrazine enables the selective formation of bacteriochlorin, which can be oxidized again to regenerate chlorin [83].

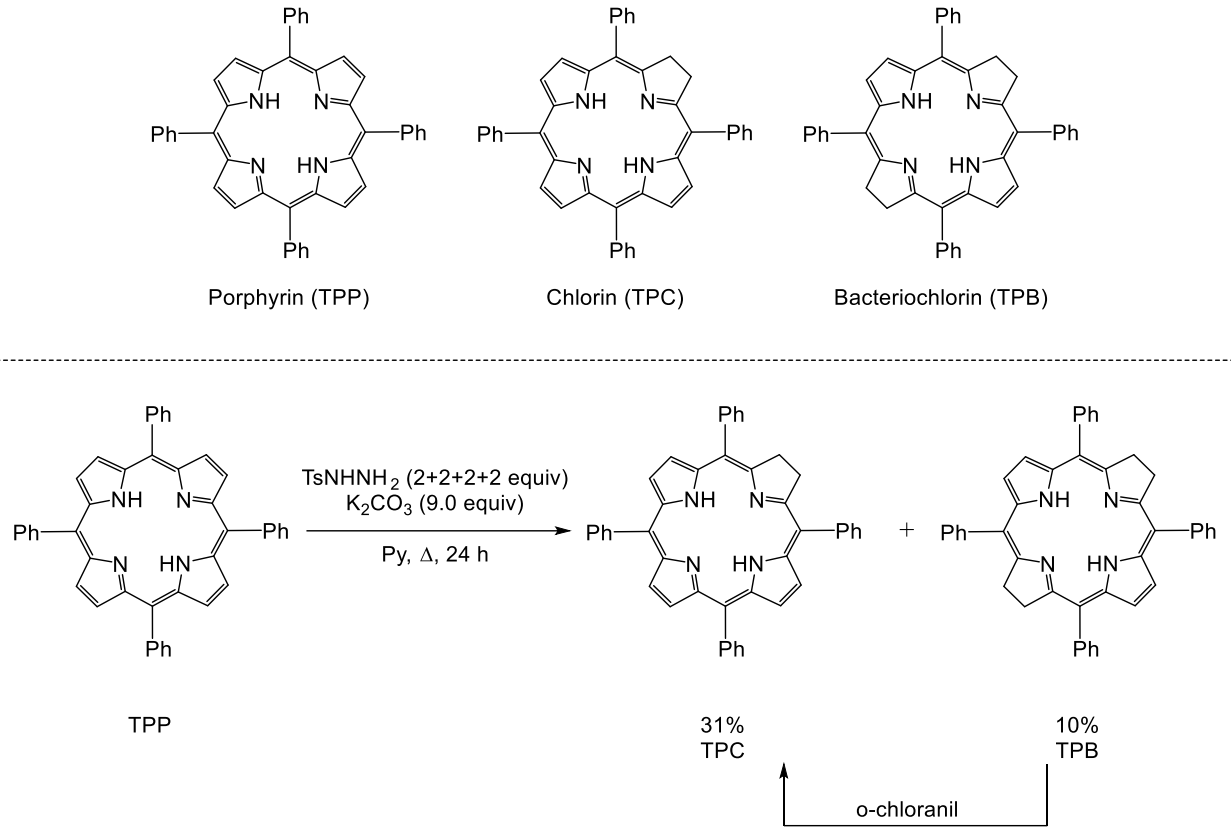

***Figure 23**: Structure of chlorin and bacteriochlorin in comparison with porphyrin (TPP)*

III. Electronic state of porphyrins

The photochemistry of porphyrins and their derivatives have been widely studied for their relevance in photocatalysis, molecular electronics or dye-sensitized solar cells. The study of the electronic states has been addressed by many reviews, articles and books. A comprehensive and brief overview of the electronic states of porphyrins is described in the following paragraph.

A meaningful model for interpreting the electronic state of porphyrins was proposed by Gouterman in the 60's. This model also called "four orbital model" [84] is based on the two higher occupied molecular orbitals (HOMO) and the two lower unoccupied molecular orbitals (LUMO). In free-metal porphyrins, the two hydrogens bonded to the two-opposing central nitrogen atoms in the pyrrole ring lead to a D_{2h} symmetry whereas metalloporphyrins assume a planar D_{4h} geometry. Both HOMOs are labelled a_{1u} and a_{2u} in D_{4h} geometry, and a_u and b_{1u} in D_{2h} symmetry. The two LUMOs correspond to e_{gx} and e_{gy} in D_{4h} and b_{2g} and b_{3g} in D_{2h} according to **Figure 24**. In porphyrins, some allowed optical transitions are observed: 1) a pair of low energy transitions (Q_x and Q_y) between 500 and 650 nm corresponding to $S_1 \leftarrow S_0$ transition, and 2) another high energy transitions (B_x and B_y) which are often observed between 400-420 nm as a single intense and large band called Soret band and corresponding to $S_2 \leftarrow S_0$. As the two components x and y correspond to the porphyrin symmetry axis, Q_x and Q_y, and B_x and B_y are equivalent in D_{4h} porphyrins, leading to a unique Q transition in metalloporphyrins, and a couple of two transition for free-base porphyrin. As demonstrated by Shelnutt and coworkers [85], Q bands can be splitted into different bands, noted Q(a,b), where "a" and "b" correspond to the vibrational quantum numbers in the electronically excited state and ground state respectively (example of the absorption spectrum of TPP and ZnTPP in **Figure 25**).

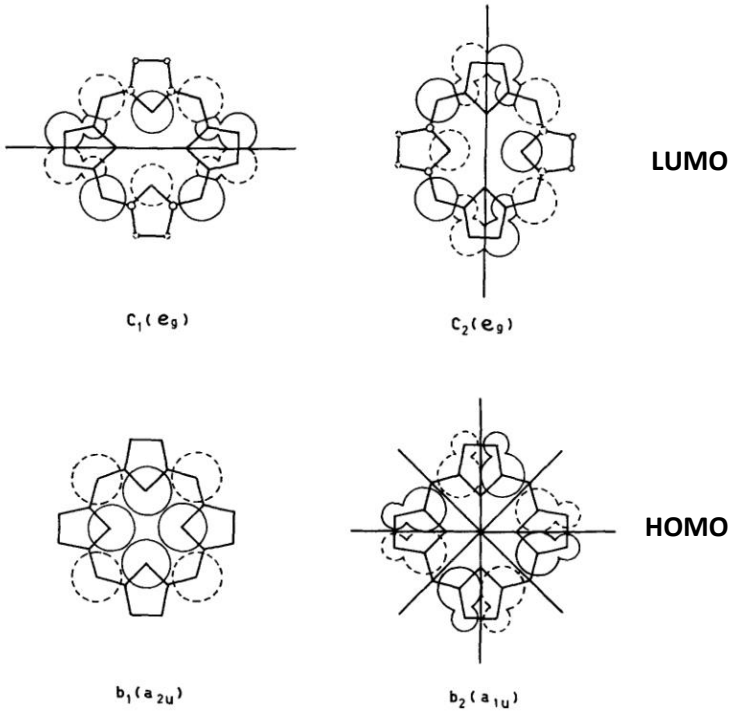

***Figure 24**: HOMO and LUMO for D_4h porphyrin. Reprinted with permission from [84].*

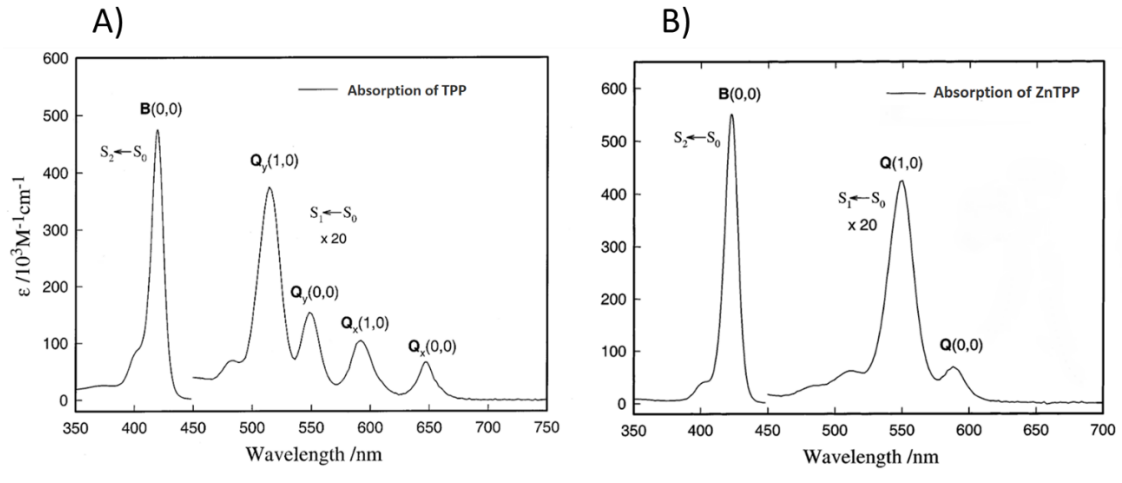

***Figure 25**: Ground-state absorption of TPP (A) and ZnTPP (B) in benzene. Adapted with permission from [86,87].*

1. Modification of the absorption spectra

To be able to initiate the polymerization upon irradiation, PIs must be able to absorb light at the emission wavelength of the illumination source. In order to modify the absorption wavelength or the molar absorption coefficient of their absorption bands, the structure of the porphyrin core can be modified to obtain the desired absorption properties (**Table 1** and **Table 2**).

Absorption spectrum of the porphyrin can be modified by several methods. The first method to be used is the modification of the substituents in *meso* or β positions, which will modify the porphyrin geometry and thus influence the absorption spectrum. Besides, insertion of metal ion in the porphyrin core can usually intensifies this effect and provide modification on the absorption spectrum. Moreover, the presence of electron-withdrawing/donating groups can modify the π-conjugated system.

III.1.a. Structural modifications

The addition of the substituents at the β-pyrrolic positions of the porphyrins leads to a skeletal distortion of the porphyrin core. Steric repulsions between β-substituents then lead to the destabilization of the HOMOs and result to the non-planarity in the macrocyclic system and induce a bathochromic shift in the absorption bands [88]. Several configurations of distortion can be found, and the most common configurations are depicted in **Figure 26**. Indeed, Rathi *et al*. observed a significant bathochromic shift in the absorption spectra of *meso*-tetraphenylporphyrin derivatives ($\Delta\lambda_{max}$ = 53-61 nm in the Soret band and $\Delta\lambda_{max}$ = 90-95 nm in the Q band) by appending both electron donor and acceptor substituents at the β-positions of the porphyrin skeleton, leading to a saddle shape conformation.

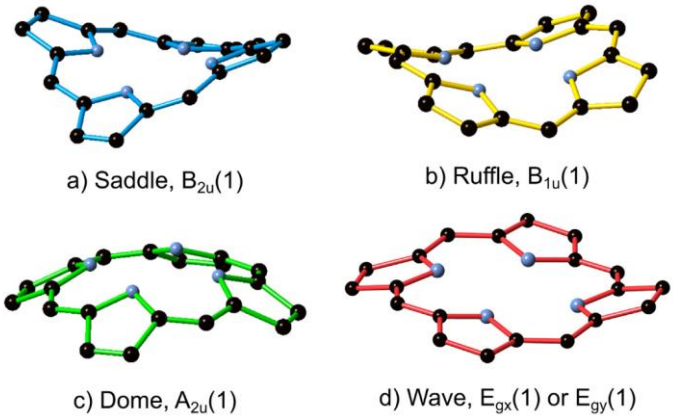

***Figure 26**: Deformation of porphyrin core. Reprinted with permission from [89].*

Also, Fonda *et al*. demonstrated that the increase of the alkyl chain length in the β-position of the alkyl-substituted porphyrins lead to severe distortions from planarity, thus inducing red shifts in the absorption spectra [90]. A similar effect was also observed by Barkigia *et al* [91] by comparing absorption spectra of zinc (II) octaethyltetraphenylporphyrin (ZnOETPP) and zinc (II) tetraphenylporphyrin (ZnTPP). They explained that puckering destabilizes the π system of the porphyrin, raising the HOMO levels with a small perturbation of the LUMO ones. Thus, the decrease of the energy gap between the HOMO and the LUMO levels induces concomitantly a red shift of the absorption band.

Another structural parameter is of great importance for tailoring the absorption properties of porphyrin derivatives, *i.e.* the dihedral angles. The addition of groups in the *ortho* position of a phenyl group close to the porphyrin ring (**Figure 27**), tend to increase the dihedral angle between the porphyrin core and the substituent, thus reducing the conjugation with the porphyrin core and causing a blue-shift of the Soret absorption band [90,92,93]. The opposite phenomenon can also be highlighted by reducing the size of the group in the *meso* position. Indeed, the addition of thienyl groups instead of phenyl ones allows a better rotation of the group (**Figure 27**)favouring the resonance interactions between the tetra pyrrole and the thienyl groups and, inducing thus a red shift [92] of both Soret and Q absorption bands.

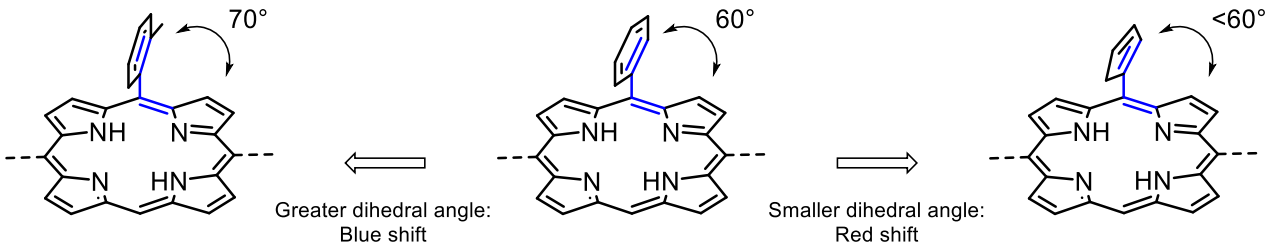

Figure 27: *Dihedral angle between porphyrin core and aromatic substituent.*

III.1.b. Complexation with different metal ions

From the four-orbital-model theory developed by Gouterman [94], the asymmetric structure of the porphyrin core without central metal ion and the split of the degenerated orbital energy levels lead to four absorption peaks of Q-band. Theoretically, the Q bands correspond to the $a_{2u}(\pi) \rightarrow eg^*(\pi)$ transition and the Soret band of metalloporphyrin arises from the $a_{1u}(\pi) \rightarrow eg^*(\pi)$ transition [95]. After metalation of the porphyrin core, both Soret and Q absorption bands are strongly affected according to the different electronic characters of the metal ion [96]. For example, the coordination of *tetra*-triphenylamine porphyrins (TPA-Ps) with metal ions increases the electronic energy level degeneracy inducing the decrease of electronic transition types and hence the number of Q-bands [97]. Therefore, metal ions can be separated into two main groups, those with a full or half-full d-shell like Zn and Mn, and the others (Co, Ni, Cu, Pd and Pt). Metal ions with full d-shell tend to donate electrons, and increasing thus the electron density on porphyrin core [98–100]. Sun *et al*. [101] reported that the introduction of a Mn^{3+} ion on methoxy-triphenylamine porphyrins will significantly redshift the Soret band by 50 nm and present the largest shift of Q band to longer wavelength comparing to the other TPA-Ps. The authors explained this phenomenon by a strong interaction between the d_{x2-y2} orbitals of Mn^{3+} with the π porphyrin orbitals. In the other hand, metals with an unfilled d-shell (Co, Ni, Cu, Pd and Pt) attract electrons to them, decreasing thus the electron density on the porphyrin core, leading to a blue-shift of the Soret band [98,100–103].

Noteworthy, the chelation of porphyrins by a metal ion greatly modifies their geometry, particularly altering the planarity of the porphyrin ring. Indeed, depending on the size of the inserted metal ion, the coordination could be either in-plane or out-of-plane (see **Figure 28**) [104]. Metal ion with an ionic radius comprises between 55 and 80 pm can fit into the porphyrin core, leading thus to an in-plane geometry [105]. Stabilization of the HOMO level is observed without any modification of the LUMO one, inducing a blue shift of the Soret band compared to the corresponding free-base porphyrin. On the contrary, the introduction of a metal with higher ionic radius causes different porphyrin core distortions, as dome, saddle, ruffled or wave distortion (see **Figure 26**). In these out-of-plane geometries, the corresponding metal stabilizes the LUMO level and in a lesser extent the HOMO level, resulting in a decrease of the energy gap, increasing thus the Soret wavelength. In addition, and according to Marcille [100] and Sun [101] investigations, porphyrins containing Mn and Zn metal ions are no longer planar, causing the redshift of the Soret band.

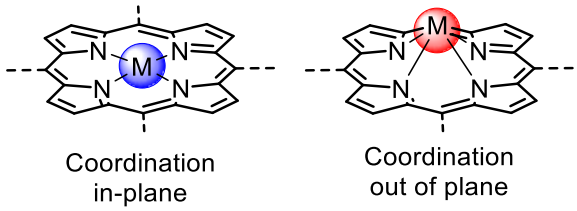

***Figure 28**:* Metal coordination in porphyrin

III.1.c. Electron withdrawing/donating groups.

Compared to free- base *meso* tetraphenylporphyrin (H_2TPP), the absorption bands of *meso* tetrathienyl porphyrins are red shifted by 10–15 nm. The induction effect of the S atom in thiophene group enrich electron density of the π-porphyrin system. According to Gouterman's four orbital model, the electron contributions of the different substituents at *meso*-position of porphyrin derivatives affect energy of a_{2u} energy level (HOMO orbit) [84]. Electron donating substituents cause an increase in a_{2u} orbit electron density and consequently leads a_{2u} level to shift to higher energy, inducing thus a red shift in absorption. Interestingly the addition of methyl group at the 3'-position of the thiophene ring close to tetrapyrrole ring in the *meso* tetra(3-methylthienyl)porphyrin leads to a less important red-shift of the absorption bands: the author explained that methyl groups decrease both the extent of co-planarity and conjugation of the system. Therefore, red shift of the absorption bands could be observed by extending the conjugation on aryl substituted porphyrins. For instance, increasing the size and the number of the aromatic groups from thienyl [92] to naphthalene[90], anthracene[90] and fluorene [106,107] lead to a significant red shift of both Soret and Q absorption bands[107,108] (**Figure 29**).

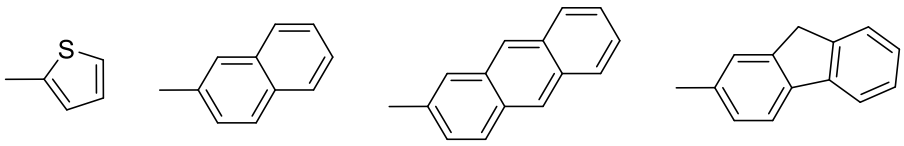

***Figure 29:** Structure of the different substituents by size, from thienyl, naphthalene, anthracene to fluorene.*

In order to modify the maximum absorbance wavelength, it is also possible to synthesize so-called push-pull systems, which will improve the displacement of electrons over the entire conjugated system. Maufroy *et al.* [109] compared a system incorporating an electron withdrawing group (nitrophenyl) and an electron donor group (benzoic acid) (ZnP-CO_2H-NO_2) (**Figure 30**). This new porphyrin derivative highlighted an interesting absorbance redshift to 423 nm for the Soret band and to 551 nm for the first Q band. In the same study, an ethynyl group has been added between a *meso* position of the porphyrin and an aryl substituent to improve the electronic communication between the parts. Two porphyrins have been design, ZnP-CO_2H-eNO_2 and ZnP-eCO_2H-NO_2. This leads to a better planarity of the phenyl groups and an extension of conjugation of. Two effects are observed: it redshifts the Soret and Q absorption bands to approximatively 445 and 570 nm, respectively, and the relative intensity of the Qx and Qy vibronic bands are inverted. Logically, these effects are more important for porphyrins with two ethynyl groups. Indeed, Soret absorption band is red shift to 459 nm and the lowest energy Q bands to 660 nm.

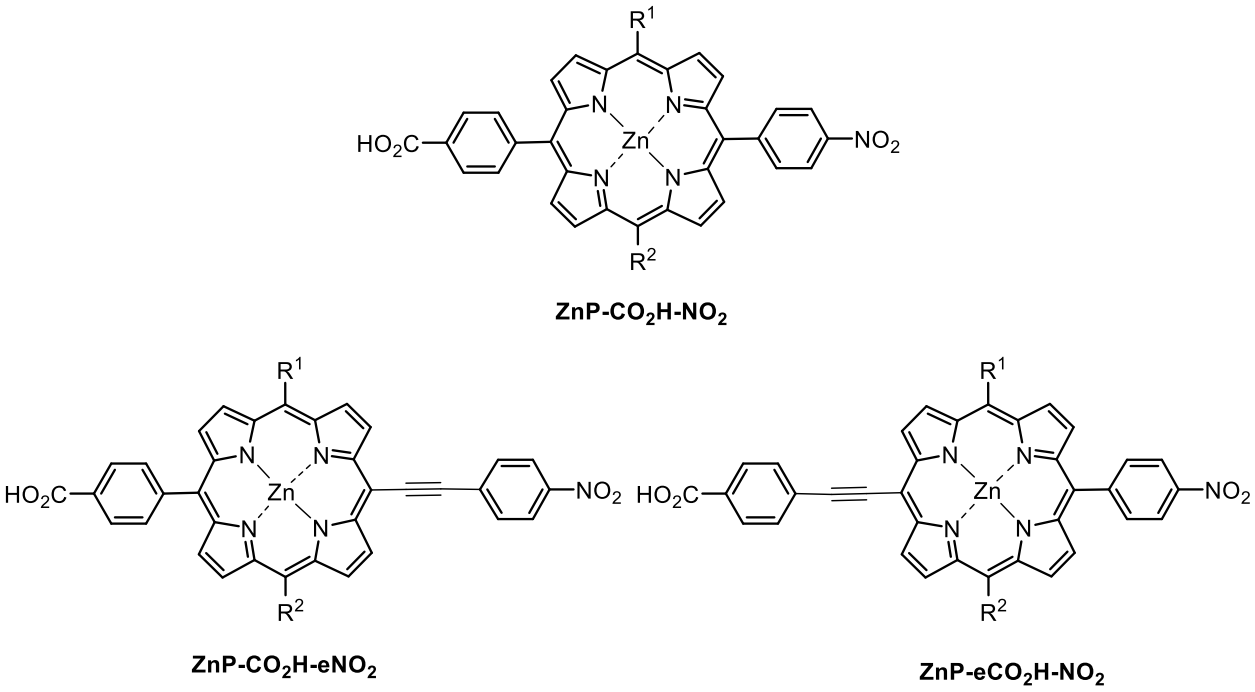

***Figure 30**: Exemples of Push-Pull porphyrins.*

III.1.d. Influence of concentration and solvent on porphyrin absorption spectra.

Porphyrins are prone to agglomeration in concentrated solutions by π-stacking, which may induce changes in the porphyrin absorption spectrum. In free-based porphyrin, the C-H---N intermolecular hydrogen bonds favour face-to-face interactions, and form so-called H-type aggregates (**Figure 31A**, from [110]) [111] which leads to a blue-shift in the absorption spectrum. Such observations are in full accordance with *meso*-tetra-thienyl porphyrins or *meso*-tetrakis(1- methylpyridinium-4-yl)porphyrin chloride which have been respectively described by Sun *et al.* [92] and Vasilopoulou *et al.* [112]. On the contrary, the edge-to-edge interactions favor the so-called *J*-aggregates which induce red shift absorption spectra in solution [92,113]. Such a behavior is also observed in Zinc derivated porphyrins containing pyridine groups as ZnTPyP [110]. The self-assembled *J*-aggegates are formed *via* Zn–N coordination bonds between the central Zn ion of one porphyrin and the nitrogen atom in the pyridine side chain of a neighboring porphyrin (see **Figure 31B**)

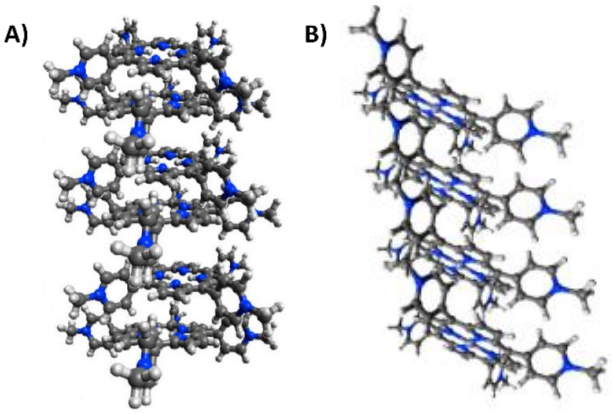

***Figure 31**: H-type (A) et J-type (B) aggregate. Reprinted with permission from [110].*

Interestingly, the nature of the solvent may also influence the UV-vis absorption properties of porphyrins. For instance, the increase of solvent polarity leads to the red-shift of the Soret and Q bands due to the stabilization of the S_2 excited energy of porphyrins containing high density electronic groups [92]. Furthermore, protic solvents can create hydrogen bonds with the porphyrin core, thus creating a deformation of the porphyrin planarity, and leading to a slight redshift of the UV-absorption spectra of porphyrins, compared to the solvent with the similar polar media. This is particularly true with water molecules up to an upper limit concentration where porphyrins derivatives form H-aggregates according to face-to-face interaction due to their poor solubility in water [92].

IV. Photophysical properties at excited states

IV. 1. Fluorescence

TPA-metalloporphyrins (**Figure 32**) show negligible fluorescence because of the significant fluorescence quenching effect [101] by the paramagnetic central metal ions (Mn^{3+} , Fe^{2+}, Co^{2+}, Ni^{2+} and Cu^{2+}), which enhance the spin-orbit coupling and promote the non-radiative deactivation process. Such a phenomenon was also observed with the addition of Ge(IV) in the core of H_2TPP [114] where the fluorescence lifetime and quantum yield are reduced. These changes in photophysical properties have been explained in terms of nonradiative (k_{nr}) and radiative (k_r) decay rates. The estimated values of k_{nr} and k_r are calculated from the following equations:

$$k_r = \frac{\Phi_f}{\tau_f} \quad \text{and} \quad k_{nr} = k_f - k_r$$

with τ_f is the fluorescence lifetime, k_f (= $1/\tau_f$) is the fluorescence decay rate and Φ_f is the fluorescence quantum yield.

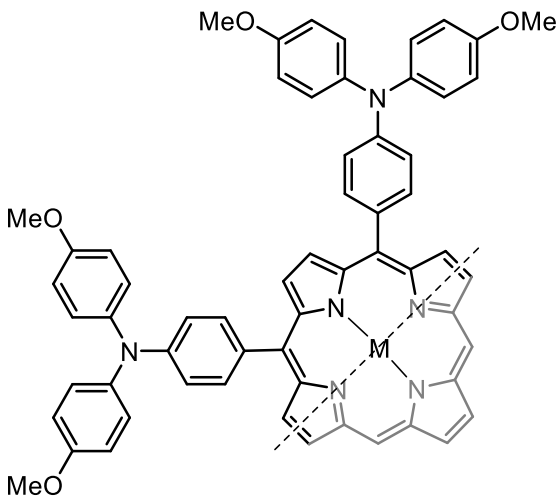

***Figure 32**: Structure of TPA.*

Therefore, by tuning the fluorescence decay rate, the nonradiative (k_{nr}) and radiative processes may be favoured. For instance, the addition of electron-donating groups such as OH, CH_3 and OCH_3 when substituted in the *para* position of the phenyl porphyrin ring were reported to decrease the fluorescence lifetimes and increase the fluorescence quantum yields [114], favouring the radiative pathway. This phenomenon was easily correlated by the more enhanced extent of π-conjugation in the excited state than that of the ground state, thus increasing the k_r value [90]. However, the addition of metal ion enhances the non-radiative decay rates concomitantly with a decrease of the fluorescence quantum yield, due to the spin-orbit coupling and the structural distortion of the porphyrin core [114,115].

Barkigia *et al*. [91] also demonstrated that the distortions from planarity of the porphyrins macrocycles lead to very low fluorescence yields and higher values of k_{nr} favoring the intersystem crossing (isc). This effect has been confirmed by Rathi *et al*. [88] where bromo and nitro β-substituted porphyrins present very weak emission and low quantum yield caused by the distortion from planarity, as well as a heavy atom effect of brome.

IV. 2. Intersystem crossing efficiency and triplet state

The influence of porphyrins functional groups on their triplet lifetimes has been fairly studied but the main parameters controlling this photophysical property are described in the following paragraph.

The triplet quantum yield is closed related to the fluorescence quantum yield, the radiative and non-radiative decay rates and the intersystem crossing efficiency as described in the following equation:

$$\Phi_T = \Phi_f \times \frac{k_{ISC}}{k_r}$$

where k_{ISC} is the intersystem crossing efficiency, k_r the radiative decay rate and Φ_f the fluorescence quantum yield.

According to Souza *et al*. [115] the addition of strong electron donating groups on porphyrins (such as methoxyphenyl groups) causes a reduction of π-electron delocalization leading to a high decrease of the radiative decay rate, favouring the increase of the intersystem crossing efficiency and thus the increase of the triplet quantum yield. The presence of the central metal ion is also a parameter to take into consideration to design new porphyrin derivatives with high intersystem crossing efficiency [116]. Indeed, metalation of H_2TPP with Zn or Mn promotes both the decrease of Φ_f and the increase of the intersystem crossing efficiency favouring the population of the triplet levels relative to TPP.

V. Redox properties of porphyrins

The reactions between the co-initiator and the porphyrin derivatives usually involve electron transfer reactions. Thus, the redox properties of the porphyrins are an important parameter to consider for obtaining the most efficient photo-initiating systems. They can be easily tuned by modifying the chemical nature of the β–substituents, their number, and the nature of the central metal ions (**Table 3** and **Table 4**).

V. 1. Chemical nature and numbers of the β-substituents

Some studies have highlighted the variations in electrochemical properties of porphyrins simply by changing the number and the nature of β and *meso* substituents on porphyrin core [117]. Gross *et al*. reported the effects of β-substituents on the redox potentials of *meso*-tetraphenylporphyrins (TPP). Remarkably, the addition of electron-withdrawing substituents make the reduction easier and the oxidation of *meso* tetraphenylporphyrins more difficult. The difficulty of *meso* tetraphenylporphyrins to be oxidized increases according to the following sequence of mono substitution: OEt < H < Br < Cl < NO_2 < CN. The clear-cut difference between the oxidation and the reduction potentials of porphyrins may be ascribed primarily to a difference in the reaction sites. The reduction process is described as a direct electron transfer to the π electrons of the conjugated systems with which β-substituents of the pyrroles are in direct resonant interactions. On the contrary, the oxidation capability of porphyrins is related to an electron transfer from the π electron systems involving the lone electron pairs of the pyrrolic nitrogens. In other words, the addition of electron withdrawing substituents directly on the π-

conjugated system of the porphyrin core decreases its electron density, enhancing the electron affinity of the porphyrins: reduction should become easier on the contrary to the oxidation [118]. Interestingly, the addition of electron-withdrawing groups on the peripheral phenyl moieties of *meso* tetraphenylporphyrins, which are not directly bound to the π-conjugated system, has a few influences on their reduction properties [119,120].

As a major of concern, the polysubstitution of *meso* tetraphenylporphyrins by electron-withdrawing bromine groups lead to an improvement of the reduction potential [121] and an anodic half-wave potential shift. Results appear similar to what was previously described with polysubstituted cyano-based TPP [122]. However, and contrary to cyano substitution, no cumulative effect was observed with the addition of bromine groups on TPP: the reduction potential for three bromine substituents on *meso* tetraphenylporphyrins shifted to 0.3-0.4 V whereas this shift increases to 0.75 V with three -CN groups. This interesting result reasonably highlighted that steric hindrance is also a key parameter to consider: the addition of -bromine atoms groups gradually induce a structural deformation between pyrroles and *meso* bridges which tend to decrease reduction potential.

The addition of strongly electron-donating substituents attached at a *meso* position of porphyrins significantly influence its electrochemical properties. For instance, Hsieh *et al.* [123] studied a series of porphyrins with electron-donating group (*e.g*. diphenylamino groups) and demonstrated that the addition of such moieties results in an electronic coupling between the porphyrin ring and the diphenylamino group, thus increasing the energy level of the HOMO and reducing the HOMO-LUMO energy gap. This phenomenon leads the electronic distribution into the π-system of the porphyrin ring and the electron-donating group favouring the oxidation of the porphyrin dyes.

V. 2. Nature of the central metal ion

Metalation of free base porphyrins is also a mean to tailor their electrochemical properties. Several authors have demonstrated that the energy required to oxidize metalloporphyrins may depend on the electronegativity of the central metal ions introduced into a porphyrin and its number of d electrons. Furhop *et al.* [124] demonstrated a linear relationship when plotted either the reduction or the oxidation potentials of metalloporphyrins *vs* electronegativity of the corresponding metal ions. Thus, the lower the electronegativity, the easier the oxidation and vice versa for the reduction potential. However similar trend is not obvious for metal central ions with oxidation number 3+ and 4+. More recent studies highlighted that concomitant parameters (d-shell, amine character of the pyrrolic nitrogen) can account for the tunability of the redox properties of the metalloporphyrins. For instance, the electrochemical oxidations of metalloporphyrin with Zn^{II} or Cu^{II} are easier than ones with Pd^{II} or Mn^{II} according to Giraudeau's study [117].

VI. Porphyrins as new visible photo-initiating systems

As previously specified, porphyrins strongly absorb in the visible range which make them suitable dyes for initiating free-radical or cationic polymerization under visible light irradiation. The use of porphyrins as photo-initiators was first reported in 1994 by Wayland *et al*. [125]. This article highlighted that organometallic derivatives of cobalt (II) meso tetramesitylporphyrin could promote a living radical polymerization of methylacrylate under argon atmosphere with polydispersities ranging from 1.1 and 1.3. In the 2000s, organocobalt porphyrins experienced an incredible expansion and were extensively used for living radical polymerization of acrylates and vinyl acetate monomers under visible-light

irradiation. Organocobalt complexes with a weak metal–carbon bond undergoes photo-cleavage of the Co–C bond to generate both an organic radical, which initiate polymerization, and a persistent cobalt-centered radical [126]. Thus, organo-cobalt porphyrins appear to be the ideal candidate to promote photo-induced living radical polymerization [127]. Zhao *et al*. demonstrated an unprecedented opportunity to obtain multifunctional block copolymers through the photo-induced living radical polymerization (LRP) of various acrylamide monomers mediated by organocobalt porphyrins under visible light irradiation [127]. In 2014, the same team reported the visible-light induced LRP of a series of hydrophilic and hydrophobic monomers including methyl acrylate, *n*-butyl acrylate, *tert*-butyl acrylate and 2-hydroxyethyl acrylate. Thus, various multiblock copolymers containing acrylate segments with controlled molecular weight and narrow polydispersity were synthesized by means of organocobalt porphyrin complexes. Interestingly, the light-induced processes involving the polymerization were regulated by tuning the light intensities [128].

More recently, researchers have focused their attention on zinc(II) 5,10,15,20-tetraphenylporphyrin (ZnTPP) which has been described as a good candidate for sensitizing iodonium salts for free-radical and cationic photopolymerization [129]. Thus, Stansbury *et al*. have developed a new three-component photo-oxidable system including ZnTPP as a photosensitizer, diphenyliodonium chloride (DPI) as an electron acceptor and *N*-methyldiethanol amine (MDEA, DH) as an electron donor [129]. Interestingly, the oxidation of ZnTPP by DPI under UV irradiation leads to both initiating radicals, *i.e.* the dye-based radical cation ZnTPP•+ and the phenyl radical. In a second step reaction, ZnTPP•+ reacts with DH to subsequently regenerate ZnTPP and form a new initiating radical, D•. This original photo-initiating system (ZnTPP/MDEA/DPI) promoted the free-radical photopolymerization of 2-hydroxyethyl methacrylate with 90% of acrylate conversion after only 90s of irradiation. Recently, Lalevée *et al*. demonstrated the high free-radical and cationic initiating performance of ZnTPP when combined with *bis*(4-*tert*-butylphenyl) iodonium hexafluorophosphate (Iod) under visible-light exposure using LEDs at 405, 455, 477, and 530 nm [130]. Remarkably, 3D and thick epoxy films from the following photosensitive formulation *i.e.* ZnTPP/Iod/(3,4-Epoxycyclohexane)methyl 3,4-epoxycyclohexylcarboxylate), were obtained under air using LED@405 nm projector (see **Figure 33**).

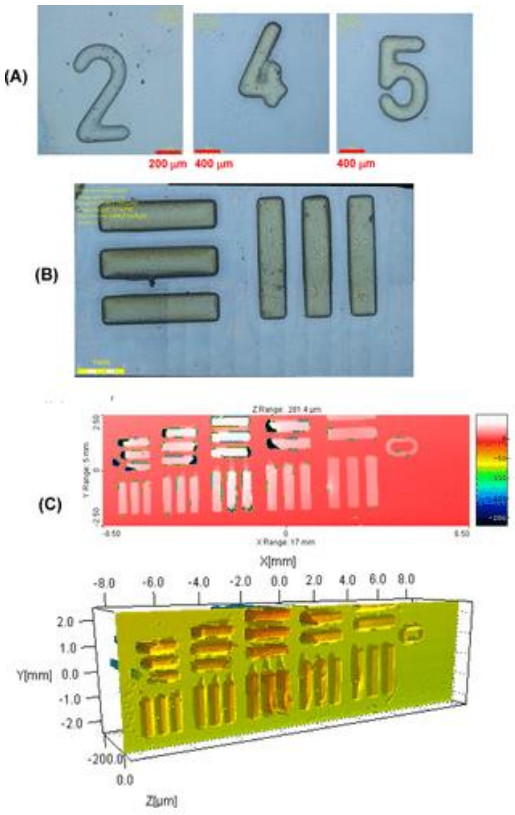

***Figure 33**: 3D-Photopolymerization experiments using projector LED@405 nm: different numbers (2, 4, 5) in part A or patterns in part B written can be easily observed by a numerical optical microscope; in part C, the patterns are characterized in 3D by profilometry. Reprinted with permission from [130].*

ZnTPP was also used as photoredox catalysts for the photoinduced electron/energy transfer-reversible addition-fragmentation chain transfer (PET-RAFT) polymerization of styrene, (meth)acrylates and (meth)acrylamides with trithiocarbonate compounds over a wide range of visible wavelengths up to 655 nm [102]. ZnTPP exhibits outstanding initiation properties under air and allow to regulate LRP without giving up living behavior despite the presence of oxygen which is known as a radical scavenger.

In the 2010's, new porphyrin derivatives have been designed for promoting PET-RAFT [99,131,132] and free-radical polymeriation (FRP). For instance, the aqueous PET-RAFT polymerization of *N,N*-dimethylacrylamide (DMA) was conducted under green LED light irradiation with Zn (II) *meso*-tetra(4-naphthalylmethylpyridyl)porphyrin (ZnTPOR) in combination with a chain transfer agent [99] (see **Figure 34**).

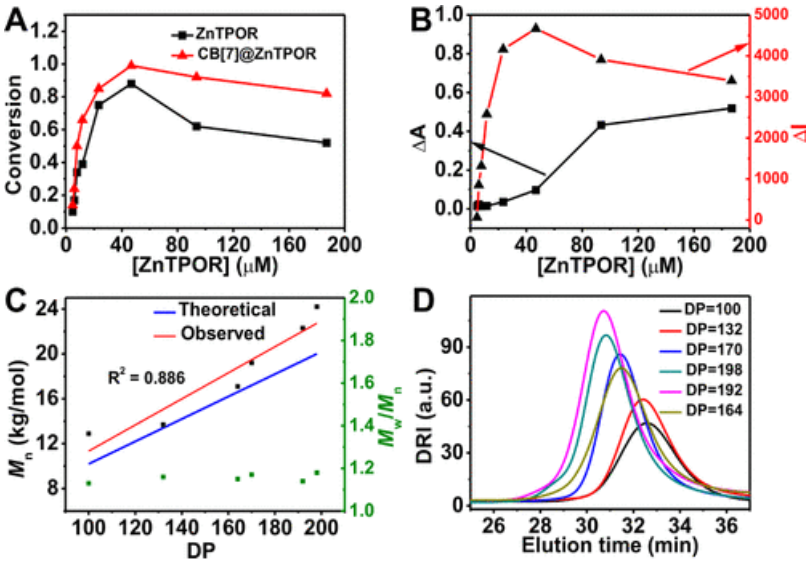

***Figure 34**: Results of polymerization of DMA (30% w/v) in water catalyzed by different concentrations of ZnTPOR and CB[7]@ZnTPOR, [ETTC]/[DMA] = 1:200, [CB[7]]/[ZnTPOR] = 4:1, green LED light, 8 w, 520 nm, 20 °C, 4 h. (A) Dependence of monomer conversion on concentration of ZnTPOR; (B) Differences in UV–vis absorbance at 566 nm (ΔA) and fluorescence intensity at 637 nm (ΔI) between CB[7]@ZnTPOR and ZnTPOR versus concentration of ZnTPOR, ΔA = ACB[7]@ZnTPOR – AZnTPOR, ΔI = ICB[7]@ZnTPOR – IZnTPOR; (C) Dependence of molecular weight on DP in the presence of CB[7]; (D) GPC traces of PDMAs corresponding to different CB@ZnTPOR concentrations. Reprinted with permission from [99].*

This method was successfully extended with other acrylate monomers such as poly(ethylene glycol) methyl ether methacrylate and poly(ethylene glycol) methyl ether acrylate, where high acrylate conversions (> 90%) were obtained after only 5h. The resulting supramolecular catalyst-containing NPs opened new opportunities in phototherapy and catalysis. In order to promote green chemistry and enhance PET-RAFT process in biological applications, photopolymerization in aqueous conditions is highly sought after. Thus, a water soluble zinc porphyrin, Zn(II) *meso* tetra(4-sulfonatophenyl) porphyrin [133] was employed to initiate PET-RAFT of DMA in aqueous medium under red light activation (λ_{max} = 635 nm). Remarkably, the RAFT photopolymerization rate of DMA was tuned by simply modifying the pH and light intensity considering that the maximum rate was reached in basic conditions. As a new concept, a series of new organic electron donor-acceptor (EDA) molecules containing RAFT agent and free base porphyrin was designed [132]. Upon green and red-light excitation (λ_{max} = 530 nm and λ_{max} = 635 nm), an electron transfer reaction occurs straightforward in the single molecule from the porphyrin to the RAFT agent, subsequently promoting the generation of radicals and increasing the living radical polymerization rates of vinyl monomers in comparison to donor/acceptor mixture (see **Figure 35**).

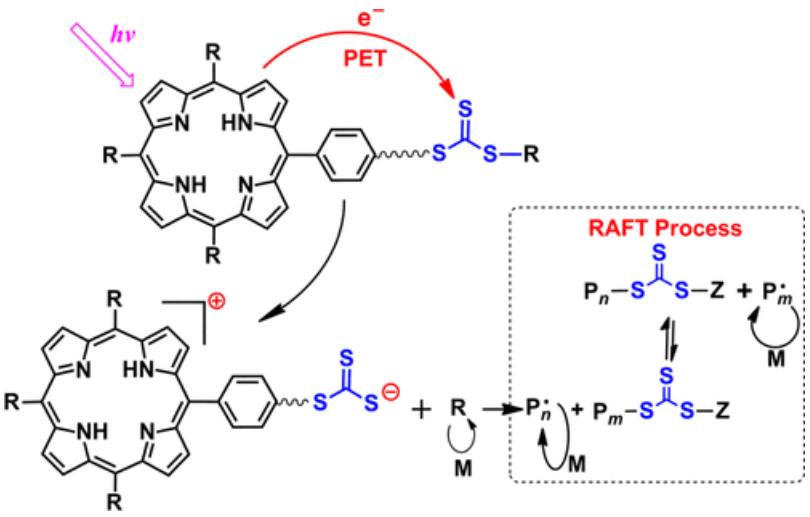

***Figure 35**: Designed Electron Donor–Acceptor (EDA) Photoredox Catalyst and Its Plausible Electron Transfer Mechanism. Reprinted with permission from [132].*

Recently, Boyer *et al*. [134] make a screening of the efficiency of ten different RAFT agents *i.e.* (2-(n-Butyltrithiocarbonate)propionic acid, Methyl 2-((ethoxycarbonothioyl)thio)propanoate,4-cyano-4 [(dodecylsulfanylthiocarbonyl)sulfanyl]pentanoic acid, 2-(dodecylthiocarbonothioylthio)-2-methylpropionic acid, 4-cyano-4-(phenylcarbonothioylthio)pentanoic acid, cyanomethyl (3,5-dimethyl-1H-pyrazole)-carbodithioate, 2-cyanobutan-2-yl 4-chloro-3,5-dimethyl-1H-pyrazole-1-carbodithioate, 2-cyanobutan-2-yl methyl(pyridin-4-yl)carbamodithioate, cyanomethyl methyl(4-pyridyl)carbamodithioate, and cyanomethyl methyl(phenyl)carbamodithioate, four porphyrin catalysts *i.e.* ZnTPP, zinc(II) *meso* 5,10,15,20-tetra(4-chlorophenyl)porphyrin, zinc(II) *meso* 5,10,15,20-tetra(pentafluorophenyl)porphyrin) and zinc(II) *meso* 5,10,15,20-tetra(4-carboxyphenyl)porphyrin on the polymerization of four different model monomers, namely N,N-dimethylacrylamide, benzyl acrylate, benzyl methacrylate and 2-hydroxypropyl methacrylamide. The effects of the RAFT agents and porphyrin derivatives were evaluated during their photopolymerization using green LED light (λ_{max} = 530 nm, 5.5 mW.cm^{-2}) under air condition. They highlighted the effects of the stabilizing Z and leaving R groups on the rate of polymerization and demonstrated the significant catalytic efficiency of the zinc metalated porphyrins on the polymerization rate of the monomers.

Despite the ongoing research on PET-RAFT process, few examples of biobased molecules have demonstrated its effectiveness as photoredox catalyst for the synthesis of polymeric materials via LRP [135,136]. A new approach in the synthesis of precise macromolecular architectures was developed through a selective visible-light photoactivation of RAFT agents with two photoredox catalysts, pheophorbide *a* and ZnTPP [136]. This orthogonal chemistry leads by switching the light wavelength to the synthesis of complex macromolecules. Thus, pheophorbide *a* selectively displays the activation of 4-cyanopentanoic acid dithiobenzoate (a dithiobenzoate) under red light irradiation for the polymerization of methacrylates whereas ZnTPP leads to the polymerization of acrylates side chains *via* the activation of trithiocarbonate group under green light irradiation. Recently, a light trigger control of the polymerization of (meth)acrylamide and (meth)acrylate monomers containing different functional groups (-COOH, -NH_2, -OH, and glycidyl group) was successfully conducted within a few hours in the presence of chlorophyll *a* (Chl *a*) and RAFT agents, leading to the synthesis of well-defined polymers with controlled molecular weights and narrow polydispersity [135]. This study opened new opportunities towards the design of novel sustainable and non-transition metal photocatalysts. For instance, Boyer *et al*. [137] reported in 2016 the first controlled/living radical polymerization by PET-RAFT under NIR (λ = 850 nm, light intensity = 23.75 mWcm^2) and far-red light (λ = 780 nm, light intensity = 19.74 mWcm^2) irradiation with Bacteriochlorophyll *a* (Bachl *a*) in combination with a RAFT transfer

agent *i.e.* cyanopentanoic acid dithiobenzoate (CPADB). This photoinitiating system proved to be highly efficient to promote the polymerization of methyl methacrylate (MMA) with an excellent control over its molecular weight (I_p < 1.25).

In light of these results, new photo-initiating systems based on bio-based pyropheophorbide *a* (Pyro), and its corresponding zinc (II) complex (Zn-Pyro) (see **Figure 36**) have been used to perform free-radical polymerization (FRP) under visible and NIR irradiation when combined with dimethylphenyl iodonium salt (Iod) and the bio-sourced thiol-amine cysteamine (Cys) [80]. According to the remarkable absorption properties of Pyro and Zn-Pyro, very promising results have been obtained in FRP under blue and red-light irradiation (LEDs@405nm, @455nm, @625nm and @660nm). More than 80% of the acrylate of PEG-diacrylate were consumed with the three-component photo-initiating system, Zn-Pyro/Iod/Cys. These interesting kinetic performances represent a promising step for the design of fully bio-based photo-initiating system.

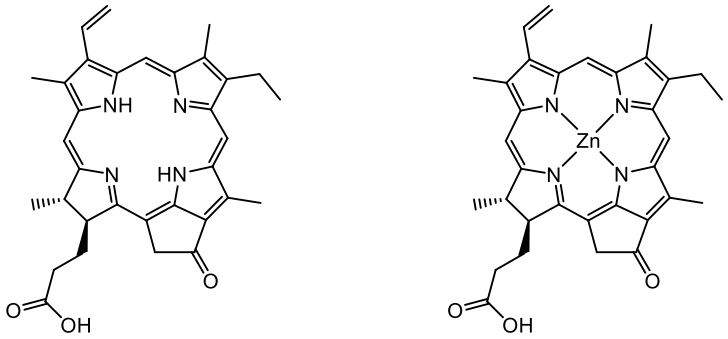

Pyro Zn-Py

***Figure 36**: Structure of Pyro and Zn-Pyro.*

In order to move further in the NIR irradiation, bacteriochlorin can also be used [138,139]. The absorption of these structure between 700 and 780 nm allows the use of far-red wavelength for the photopolymerization, at λ_{max} = 740 nm. Cao *et al.* present a polymerization rate of methyl methacrylate of 89% in presence of the photocatalyst RTPP (reduced *meso* tetraphenylporphyrin) (**Figure 37**) and a RAFT agent after 12 h of irradiation. Ma *et al.* work with the fluorinated version of the photocatalyst and monomer and observe a conversion of 78% of the trifluoromethyl methacrylate in presence of *meso* tetra(pentafluorophenyl)bacteriochlorin (FBC) (**Figure 37**) and a RAFT agent after 28 h of irradiation.

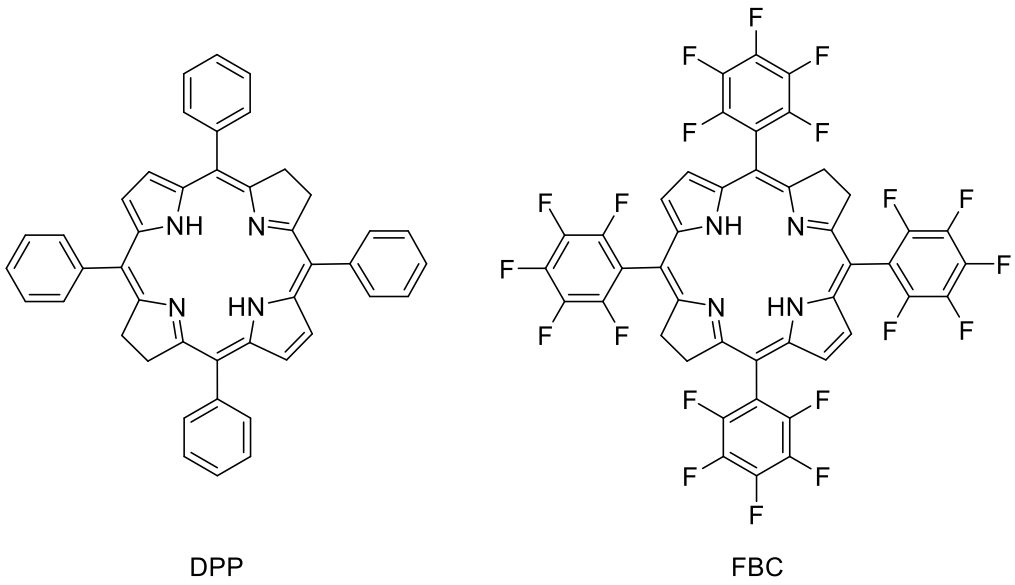

***Figure 37**: Structure of RTPP and FBC.*

Recently, a series of metalloporphyrins based on Pd^{2+}, Cu^{2+}, Zn^{2+}, Fe^{2+} complexation have been tested to initiate FRP of a methacrylate resin (Mix-MA) in oxygen conditions at 405 nm and 785 nm [98,140]. Despite the high absorption properties of the porphyrin derivatives, the final methacrylate conversion is low (< 30%) under LED@405 nm excitation as oxygen inhibits the polymerization. However, the combination of porphyrin derivatives with iodonium salt, 4-(diphenylphosphino)benzoic acid (a phosphine derivative) as oxygen consumer and the thermal initiator BlocBuilder®MA allows to promote the FRP of acrylate monomers under laser diode emitting at 785 nm. Interestingly, an electron transfer reaction process occurred from the excited porphyrin to iodonium salt leading to its photoreduction and the formation of initiating phenyl radicals. Subsequently, porphyrin derivatives also convert NIR light into heat to permit the decomposition of the BlocBuilder®MA for generating additional initiating radicals. The presence of the phosphine derivative allows to convert the non-initiating peroxy radicals into reactive alkoxy radicals in a first step, but also contribute to both reduce the oxidation of the porphyrin dyes and its regeneration. Such a photochemical mechanism was evidenced by a relatively high final methacrylate conversion (~50%) after 1000s of irradiation under LED@785 nm and under air (see **Figure 38**).

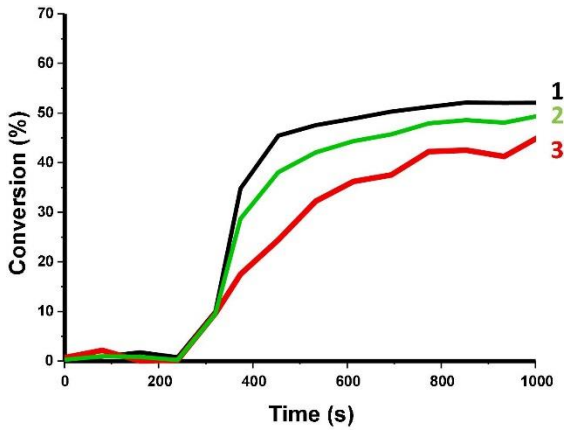

***Figure 38**: Photopolymerization profiles for Mix-MA in air (methacrylate function conversion vs. irradiation time) in the presence of Ar2I+/PF6− (3 wt%), 4-dppba (2 wt%), BlocBuilder® MA (2 wt%), and (1) Fe-Porph_1 (0.1 wt%), (2) Zn-Porph_2 (0.1 wt%) and (3) Zn-Porph_4 (0.1 wt%), using a laser diode @785 nm (I = 2.5 W.cm−2); thickness = 1.4 mm; the irradiation starts at t = 17 s. Reprinted with permission from [98].*

Marcille *et al*. also contributed to the development of FRP under visible-light irradiation by using new diphenyl functional porphyrins (DPP and Zn-DPP) [100] (see **Figure 39**). For the first time, the capability of new porphyrins to initiate various photochemical reactions such as FRP, cationic polymerization and thiolene process under multiple wavelengths between 385 to 530 nm has been highlighted. The kinetic profiles for the FRP and CP of acrylate and epoxy monomers respectively demonstrated that the initiating properties of zinc metalated diphenyl porphyrin is much more efficient than that of common photosensitizers such as camphorquinone or benzophenone. Cationic photopolymerization is particularly interesting as 90% of epoxy functional groups are consumed after 800s irradiation under LED@405 nm in air conditions.

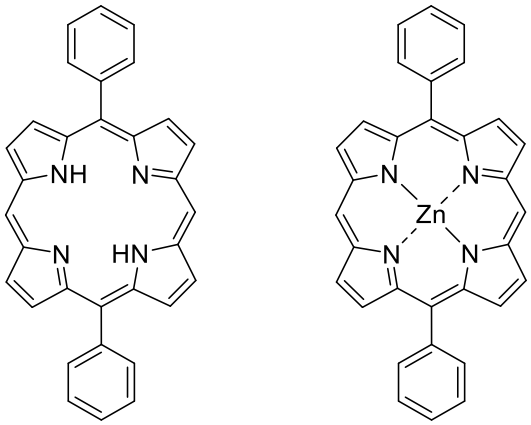

***Figure 39**: Structure of DPP and Zn-DPP.*

Based on these results, Schnetz *et al*. [141] also carried out a study on porphyrins containing benzophenone groups (PBP and its zinc complex PBPZn **Figure 40**), which are more effective for photopolymerization [142]. These new photoinitiators have been used for the FRP of a bio-based monomers, SOA, a derivative of soybean oil, in combination with different co-initiators such as MDEA or Iod, but also with two bio-based co-initiators, N-acetylcysteine (NAC) and cysteamine, which make it possible to obtain more environmentally friendly materials. Quite high conversion were obtained, up to 90% and 60% for PBPZn/MDEA under LED@405 nm exposure and PBPZn/NAC under LED@530 nm respectively.

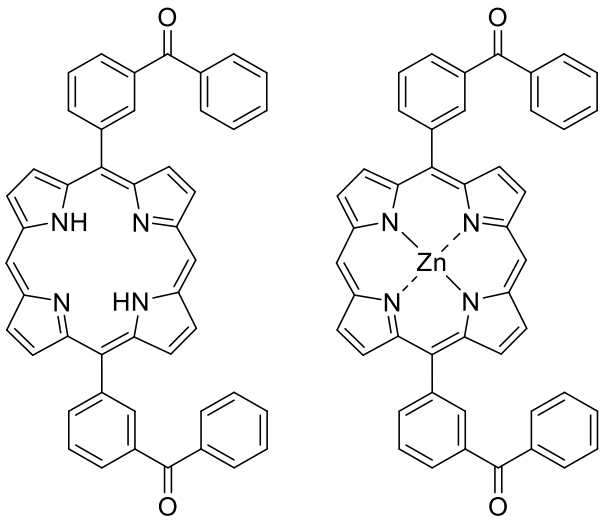

***Figure 40**: Structure of PBP and Zn-PBP.*

VII. Conclusion

The design of porphyrin derivatives is a hot topic in (bio)chemistry and material science, that scientists have been addressing in recent years. What makes them special is that these compounds are intensively used in many fields, as photodynamic therapy agents in cancer treatment, solar cells, and recently as photosensitizers for photoinduced electron/energy transfer-reversible addition-fragmentation chain transfer (PET-RAFT) polymerization of various (meth)acrylate monomers, free-radical, cationic photopolymerization or thiolene process. Many potential applications *i.e.* biomedical applications, industrial coatings, electronic devices which are high-added-value products, photoresist technology, photolithographic applications, adhesives, and high-performance composites are potentially concerned. The amazing variety of applications of porphyrin derivatives is attributed to their unique absorption, electrochemical and photophysical properties which can be easily tuned by appropriate modifications of their structures by changing for instance the nature of the organic groups in the β– or *meso*-positions and/or by complexing the porphyrin ring with different metal ions.

The aim of this review is to present both fundamental and applied research on the development of new porphyrin derivatives implied in photochemistry process, under UV-visible and NIR irradiation. Through this review, scientists will have an overview of the improvements needed to the synthesis of new visible/NIR absorbing porphyrins for photopolymerization applications which have increasingly gained a growing interest in the polymer field for decades. The first part of the review covers the synthesis and functionalization strategies of porphyrins and described the major modifications of porphyrin structures to easily tune their photophysical/photochemical properties to enhance the photo-initiating process. In a second part, we discussed the relative contribution of the structural modifications of porphyrins, the effect of electron withdrawing/donating groups and the nature of the solvent on their absorbance properties. These results give some keys to the readers to understand the relationship between the photo-initiating efficiency of porphyrins and their structures. Finally, a series of photopolymerization applications involving porphyrins are also described. The uses of porphyrins as photosensitizers are exemplified in detail in literature for PET-RAFT, free-radical promoted cationic polymerization, cationic and free-radical photopolymerization. Depending on their chemical structures, porphyrins can act as photosensitizers in broad wavelength ranges from visible to NIR. We strongly believe that this review is of great importance for scientists working on porphyrin

chemistry for medical (PDT for cancer therapy) or photocatalysts research but also represents an interesting contribution to researchers working in the photopolymerization field and in the synthesis of innovative materials related to antibacterial PDT.

Declaration of Competing Interest

The authors declare that they have no known competing financial interests or personal relationships that could have appeared to influence the work reported in this paper.

***Table 1**: Photochemical and photophysical parameters of selected* meso*-substituted porphyrins.*

Structure 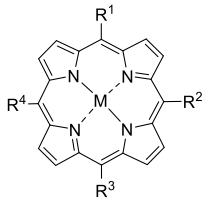		Absorption wavelength in nm of the Soret bands $Q_{(y)}(1,0)$ $Q_{(x)}(0,0)$	Emission	Solvent	References
Metal – M	Substituent – R^{1-4}				
No metal	R^{1-4} = 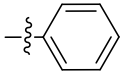	413 512		Acetonitrile	[140]
Cu	R^{1-4} = 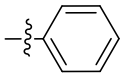	412 555			
Pd	R^{1-4} = 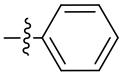	412 520			
Zn	R^{1-4} = 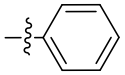	424	ϕt = 0.88	HEMA monomer	[129]
Zn	R^{1-4} = 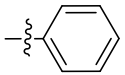	420 552		Dichloromethane	[130]
No metal	R^{1-4} = 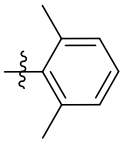	420 532			
Pd	R^{1-4} = 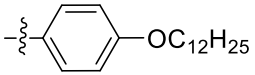	421		Chloroform	[98]
Zn	R^{1-4} = 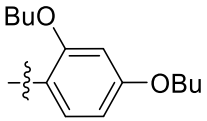	425			

Cu	R^{1-4} = 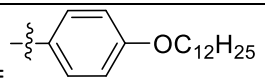	420			
Zn	R^{1-4} = 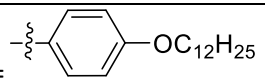	427			
Fe	R^{1-4} = 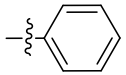	417			
Fe	R^{1-4} = 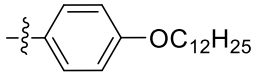	425			
No metal	R^{1-4} = 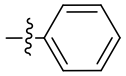	420 510 643	Φ_f = 0.13 τs = 13.6 ns ϕt = 0.82	BTPA	[135]
Zn	R^{1-4} = 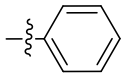	425 560	Φ_f = 0.04 τs = 2.7 ns ϕt = 0.88		
Ni	R^{1-4} = 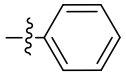	415 530			
Co	R^{1-4} = 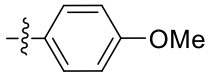	418 540			
Fe	R^{1-4} = 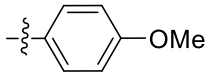	420 535			
Zn	R^{1-4} = 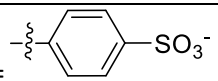	416 556 600	Φf = 0.042 τs = 1.7 ns ϕt = 0.85 τt = 1.4 ns	Water	[131,133]
No metal	R^{1-4} = 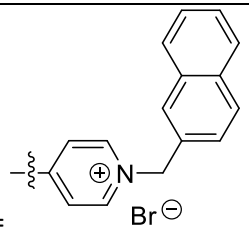	426		Water	[99]

Zn	R^{1-4} = 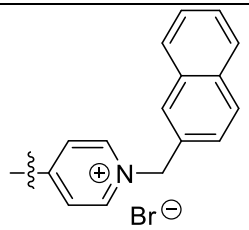	444			
No metal	R^{1-4} = 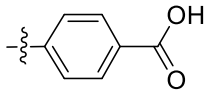	417	λ_f = 646 nm Φf = 0.25 τs = 4.21 ns	DMSO	[143]
No metal	R^{1-4} = 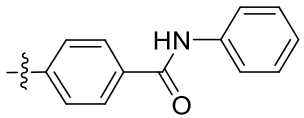	420	λ_f = 647 nm Φf = 0.42 τs = 11.33 ns		
No metal	R^{1-4} = 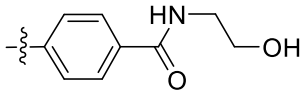	422	λ_f = 649 nm Φf = 0.52 τs = 11.81 ns		
No metal	R^{1-4} = 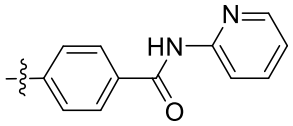	419	λ_f = 644 nm Φf = 0.39 τs = 11.13 ns		
No metal	R^{1-4} = 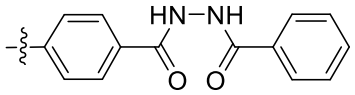	418	λ_f = 646 nm Φf = 0.35 τs = 10.82 ns		
No metal	R^{1-4} = 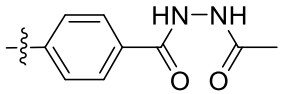	421	λ_f = 648 nm Φf = 0.41 τs = 10.98 ns		

No metal	R^{1-4} = 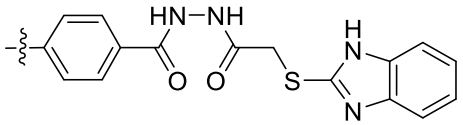	418	λ_f = 647 nm Φf = 0.28 τs = 10.76 ns		
No metal	R^{1-4} = 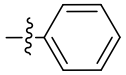	427	λ_f = 650 nm Φf = 0.12 τs = 8.25 ns	DMF	144
No metal	R^{1-4} = 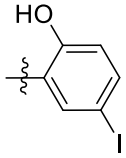	423	λ_f = 647 nm Φf = 0.17 τs = 6.16 ns		
No metal	R^{1-4} = 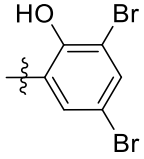	422	λf= 644 nm Φf = 0.15 τs = 6.12 ns		
No metal	R^{1-4} = 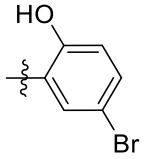	424	λf= 648 nm Φf = 0.18 τs = 6.17 ns		
No metal	R^{1-4} = 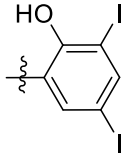	420	λ_f = 644 nm Φf = 0.14 τs = 6.11 ns		
No metal	R^{1-4} = 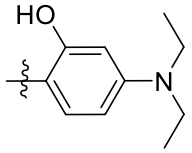	433	λ_f = 657 nm Φf = 0.22 τs = 9.37 ns		

No metal	R^{1-4} = 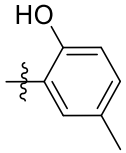	430	λ_f = 653 nm Φf = 0.2 τs = 8.96 ns		
No metal	R^{1-4} = 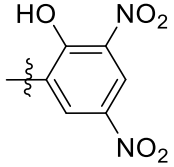	428	λ_f = 644 nm Φf = 0.16 τs = 6.14 ns		
No metal	R^{1-4} = 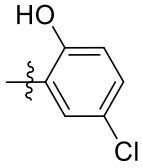	424	λ_f = 647 nm Φf = 0.18 τs = 6.2 ns		
No metal	R^{1-4} = 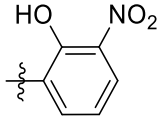	428	λ_f = 649 nm Φf = 0.18 τs = 6.22 ns		
Zn	$R^1 = R^3$ = 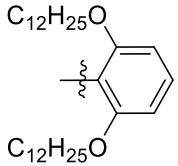 R^2 = 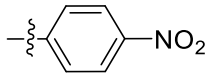 R^4 = 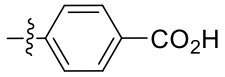	423 551 594	λ_f = 601 & 643 nm	Dichloromethane	[109]

Zn	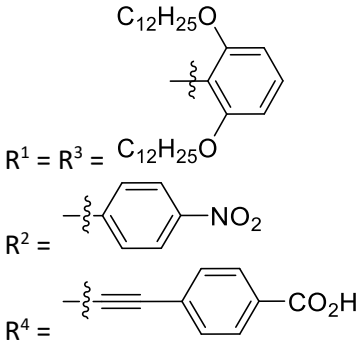	444 568 619	λ_f = 629 & 680 nm		
Zn	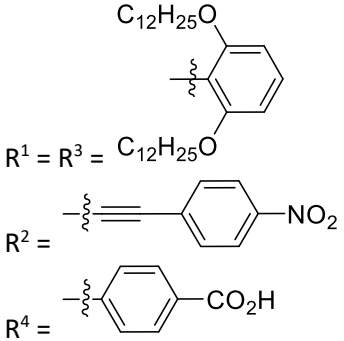	446 570 623	λ_f = 630 & 682 nm		
Zn	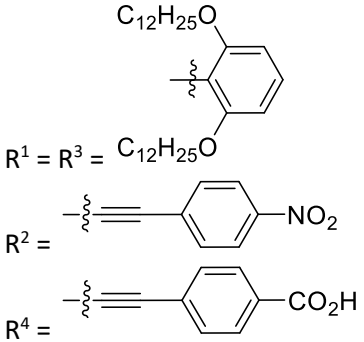	459 558 660	λ_f = 664 & 730 nm		

Zn	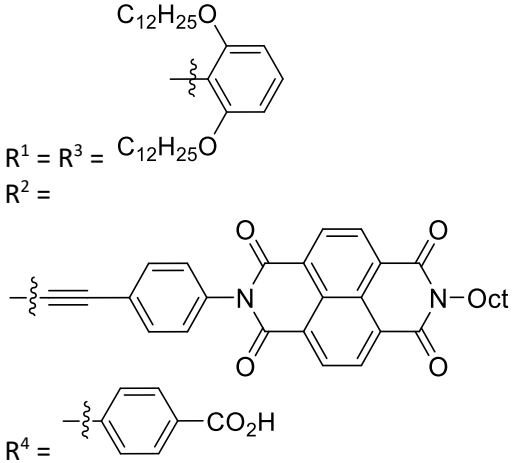	441 567 614	λf= 625 & 670 nm		
Zn	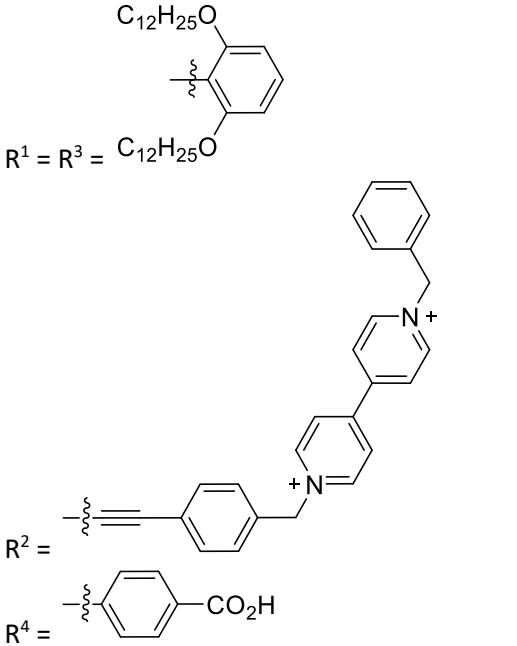	425 557 600	λ_f = 610 & 662 nm		
No metal	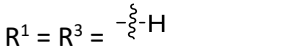	407 536	Φ_f = 0.034 τs = 69 ms	Dichloromethane	[100]

	$R^2 = R^4 =$ 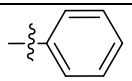				
Zn	$R^1 = R^3 =$ $R^2 = R^4 =$ 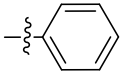	405 505	$\Phi_f = 0.022$ $\tau s = 28$ ms		
Cu	$R^1 = R^3 =$ $R^2 = R^4 =$ 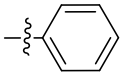	401 525	$\tau s = 0.44$ ms		
No metal	$R^1 = R^3 =$  $R^2 = R^4 =$ 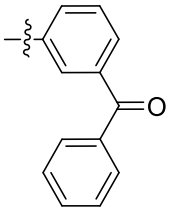	406 501 536 574 629	$\lambda_f = 633$ & 697 nm	Dichloromethane	[141]
Zn	$R^1 = R^3 =$ $R^2 = R^4 =$ 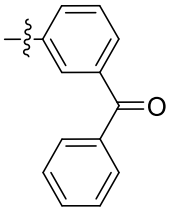	411 539 575	$\lambda_f = 588$ & 638 nm		
No metal	$R^{1-4} =$ 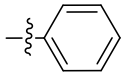	415 514 645	$\Phi f = 0.11$ $\tau s = 9.8$ ns	Dichloromethane	[92]
No metal	$R^{1-4} =$ 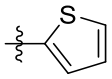	425 522 659	$\Phi f = 0.012$ $\tau s = 1.11$ ns		

No metal	R^{1-4} = 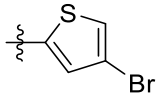	425 521 663	Φf = 0.017 τs = 1.2 ns		
No metal	R^{1-4} = 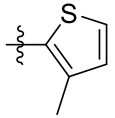	422 520 653	Φf = 0.013 τs = 1.47 ns		
No metal	R^{1-4} = 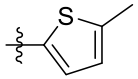	430 525 662	Φf = 0.014 τs = 1.31 ns		
No metal	R^{1-4} = 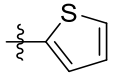	421	λ_f = 664 nm	n-hexane	
No metal	R^{1-4} = 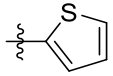	462	λ_f = 667 nm	THF	
No metal	R^{1-4} = 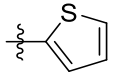	426	λ_f = 668 nm	DMF	
No metal	R^{1-4} = 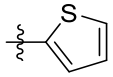	422	λ_f = 663 nm	Ethanol 100%	
No metal	R^{1-4} = 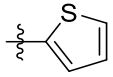	422		Ethanol 25%	
No metal	R^{1-4} = 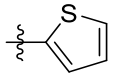	431		Ethanol 50%	
No metal	R^{1-4} = 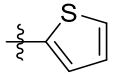	425		Ethanol 75%	
No metal	R^{1-4} = 	396 488 616	λ_f = 618 & 684 nm Φ_f = 0.07 τs = 15.5 ns	Benzene	[90]

No metal	R^{1-4} = 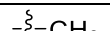	418 520 666	λf = 668 & 741 nm Φf = 0.08 τs = 11 ns		
No metal	R^{1-4} = 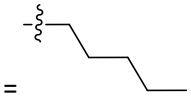	418 52 662	λ_f = 665 & 738 nm Φf = 0.08 τs = 10.8 ns		
No metal	R^{1-4} = 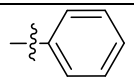	418 514 648	λ_f = 652 & 720 nm Φf = 0.13 τs = 12.3 ns		
No metal	R^{1-4} = 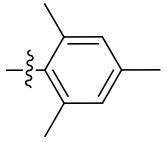	418 514 650	λ_f = 652 & 723 nm Φf = 0.12 τs = 14.1 ns		
No metal	R^{1-4} = 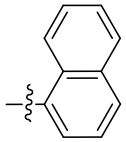	420 514 646	λ_f = 651 & 718 nm Φf = 0.11 τs = 14 ns		
No metal	R^{1-4} = 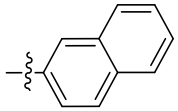	420 518 652	λ_f = 659 & 724 nm Φf = 0.16 τs = 11.8 ns		

No metal	R^{1-4} = 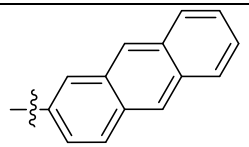	432 522 656	λ_f = 666 & 729 nm Φf = 0.17 τs = 11.4 ns		
No metal	R^{1-4} = 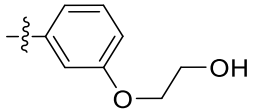	419 515 644		Chloroform	[145]
No metal	R^{1-4} = 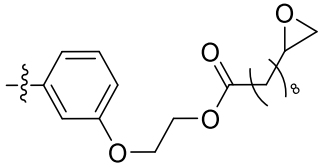	415 512 644			
No metal	R^1 = 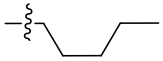 R^3 = 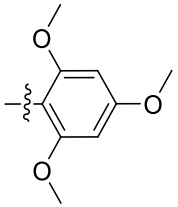 $R^2 = R^4$ = 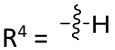	407 503 629	λ_f = 637 nm Φf = 0.037 τs = 13.1 ns Φt = 0.6	DMSO	[115]
No metal	R^1 = 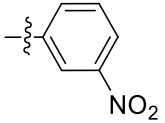 R^2 = 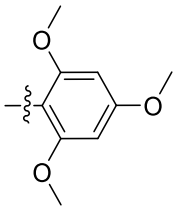	415 510 638	λ_f = 645 nm Φf = 0.01 τs = 4.6 ns ϕt = 0.3		

	R^3 =  R^4 = 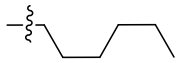				
No metal	$R^1 = R^3$ = 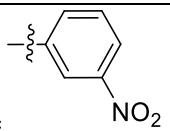 R^2 = 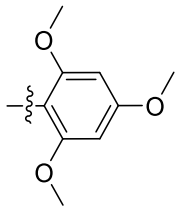 R^4 = 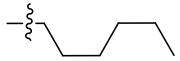	422 517 647	λ_f = 655 nm Φf = 0.026 τs = 7.7 ns ϕt = 0.37		
No metal	$R^1 = R^3$ = 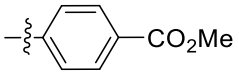 R^2 = 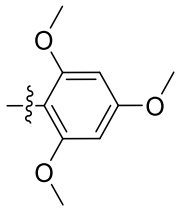 R^4 = 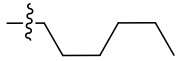	421 517 648	λ_f = 656 nm Φf = 0.054 τs = 12.6 ns ϕt = 0.52		
No metal	$R^1 = R^3$ = 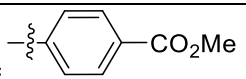 $R^2 = R^4$ = 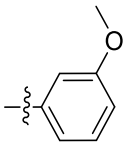	421 514 644	λ_f = 652 nm Φf = 0.074 τs = 11.5 ns ϕt = 0.51		

No metal	R^1 = 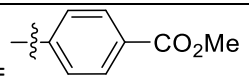 $R^{2\text{-}4}$ = 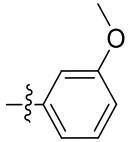	420 514 643	λ_f = 652 nm Φf = 0.058 τs = 12.4 ns ϕt = 0.52		
No metal	R^1 = 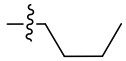 $R^2 = R^4$ = 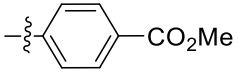 R^3 = 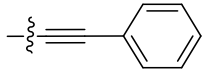	435 535 668	λ_f = 675 nm Φf = 0.026 τs = 11.5 ns ϕt = 0.5		
No metal	R^1 = 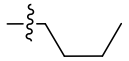 $R^2 = R^4$ = 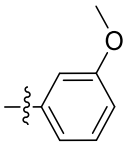 R^3 = 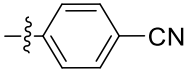	419 515 646	λ_f = 654 nm Φf = 0.055 τs = 13.4 ns ϕt = 0.59		
No metal	$R^1 = R^3$ = 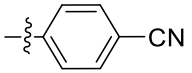 $R^2 = R^4$ = 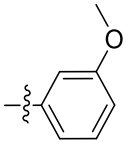	420 514 643	λ_f = 652 nm Φf = 0.054 τs = 12.5 ns ϕt = 0.6		
No metal	$R^1 = R^2$ = 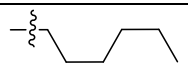 $R^3 = R^4$ = 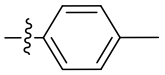	418 516 653	λ_f = 658 nm Φf = 0.036 τs = 11.4 ns ϕt = 0.5		

No metal	R^1 = 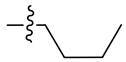 $R^2 = R^4$ = 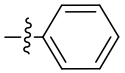 R^3 = 	413 509 640	λ_f = 646 nm Φf = 0.04 τs = 12.5 ns ϕt = 0.53		
No metal	$R^1 = R^4$ =  $R^2 = R^3$ = 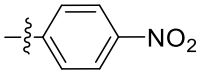	422 517 646	λ_f = 655 nm Φf = 0.031 τs = 10.2 ns ϕt = 0.43		
No metal	$R^1 = R^3 = R^4$ = 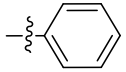 R^3 = 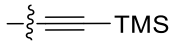	428 528 661	λ_f = 667 nm Φf = 0.017 τs = 11.4 ns ϕt = 0.45		
No metal	R^1 = 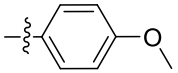 $R^2 = R^4$ =  R^3 = 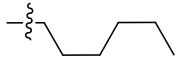	408 505 639	λ_f = 639 nm Φf = 0.038 τs = 14.8 ns ϕt = 0.6		
No metal	R^1 =  R^2 = 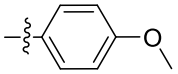 $R^3 = R^4$ = 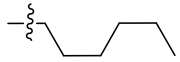	414 511 643	λ_f = 650 nm Φf = 0.053 τs = 12 ns ϕt = 0.7		
No metal	R^1 = 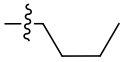	414 509 639	λ_f = 646 nm Φf = 0.038 τs = 14.4 ns ϕt = 0.75		

	$R^2 = R^4 =$ 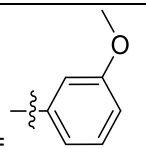 $R^3 =$				
No metal	$R^1 =$ 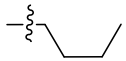 $R^{2-4} =$ 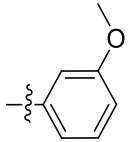	419 515 647	λ_f = 654 nm Φf = 0.035 τs = 13.4 ns ϕt = 0.81		
Zn	$R^1 = R^2 =$ 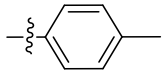 $R^3 =$ 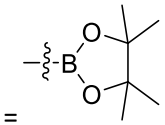 $R^4 =$ 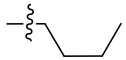	426 559 599	λ_f = 609 & 657 nm Φf = 0.033 τs = 3.1 ns ϕt = 0.46		
Zn	$R^1 = R^3 =$ 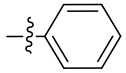 $R^2 =$ 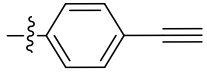 $R^4 =$	423 554 592	λ_f = 603 nm Φf = 0.025 τs = 2.9 ns ϕt = 0.44		
No metal	$R^{1-4} =$ 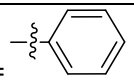	418 515			146
Co	$R^{1-4} =$ 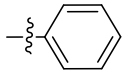	410 528			
Ni	$R^{1-4} =$ 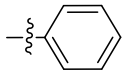	415 528			

Cu	R^{1-4} = 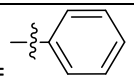	415 539			
Zn	R^{1-4} = 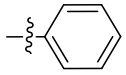	424 557			
No metal	R^{1-3} = 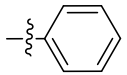 R^4 = 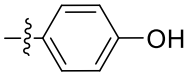	420 515 650	λ_f = 653 & 719 nm Φf = 0.207	Chloroform	[103]
Mn	R^{1-3} = 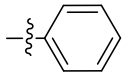 R^4 = 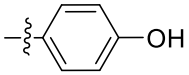	480 585 620			
FeCl	R^{1-3} = 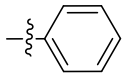 R^4 = 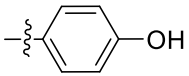	420 514			
Co	R^{1-3} = 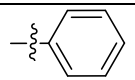 R^4 = 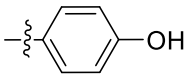	415 545			
Ni	R^{1-3} = 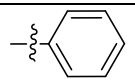 R^4 = 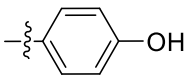	415 530			
Cu	R^{1-3} = 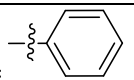 R^4 = 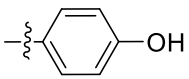	415 540			

Zn	R^{1-3} = 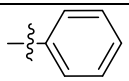 R^4 = 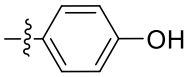	425 555	λ_f = 604 & 654 nm Φf = 0.176		
No metal	R^{1-3} = 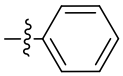 R^4 = 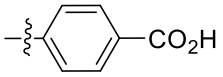	420 515 650	λ_f = 653 & 717 nm Φf = 0.05		
Zn	R^{1-3} = 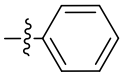 R^4 = 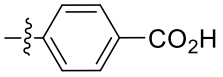	425 555 590	λ_f = 603 & 653 nm Φf = 0.154		
No metal	R^{1-4} = 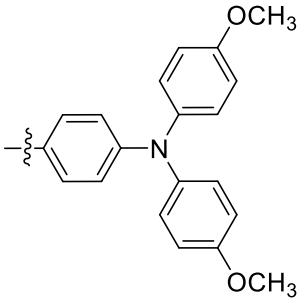	444 528 784	Φf = 0.002 τs = 1.73 ns	Chloroform	[101]
Mn	R^{1-4} = 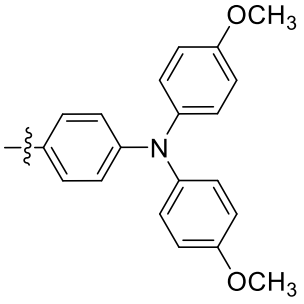	493 600 651	Φf undetected τs = 1.68 ns		

Fe	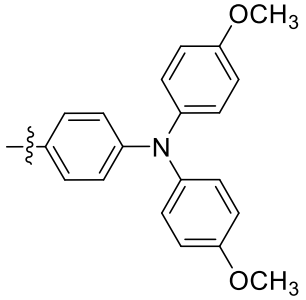 R^{1-4} =	445 562 722	Φf undetected τs = 1.54 ns		
Co	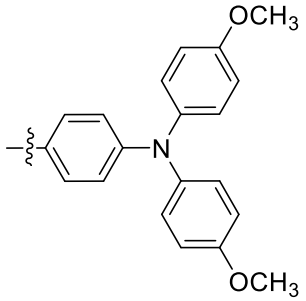 R^{1-4} =	440 540 579	Φf undetected τs = 1.42 ns		
Ni	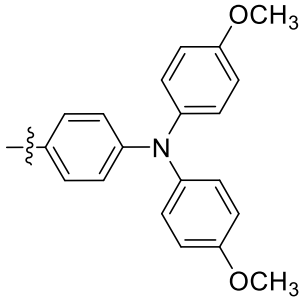 R^{1-4} =	444 540 582	Φf undetected τs = 1.46 ns		

Cu	R^{1-4} = 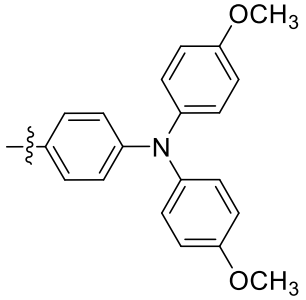	442 549 593	Φf undetected τs = 1.29 ns		
Zn	R^{1-4} = 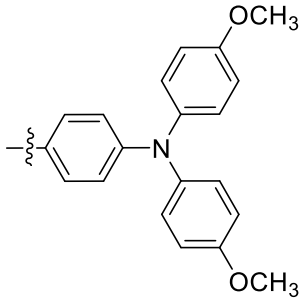	446 560 607	Φf = 0.007 τs = 1.29 ns		
No metal	R^{1-4} = 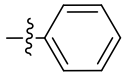	418 513 648	λ_f = 653 nm Φf = 0.11 τs = 10.9 ns	DMSO	[147]
Zn	R^{1-4} = 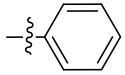	423 550 588	λ_f = 596 nm Φf = 0.03 τs = 2.04 ns		
No metal	R^{1-4} = 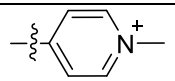	422 521 642	λ_f = 662 & 702 nm τs = 9.8 ns	Ethanol : Water	[148]

Mn(III)	R^{1-4} = 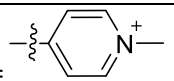	463 565 594	λ_f = 632 & 668 nm τs = 3.9 ns		
Mn(II)	R^{1-4} = 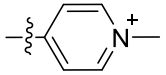	445 575 625			
No metal	R^{1-4} = 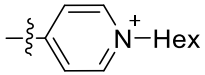	426 519 642	λ_f = 663 & 702 nm τs = 9.2 ns		
Mn(III)	R^{1-4} = 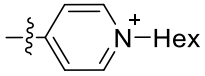	463 562 596	λ_f = 631 & 665 nm τs = 4.6 ns		
Mn(II)	R^{1-4} = 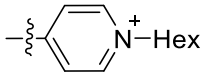	452 576 623			
No metal	R^{1-4} = 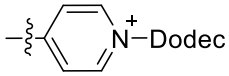	428 519 648	λ_f = 652 & 712 nm τs = 8.7 ns		
Mn(III)	R^{1-4} = 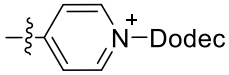	463 568 600	λ_f = 628 & 671 nm τs = 6.6 ns		
Mn(II)	R^{1-4} = 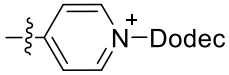	456			
No metal	R^{1-4} = 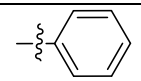	417 514 646		DMF	[149]

No metal	R^{1-4} = 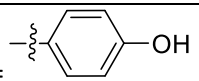	424 519 653			
No metal	R^{1-4} = 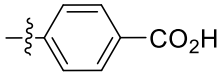	420 516 647			
No metal	R^{1-4} = 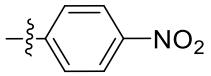	423 516 646			
No metal	R^{1-4} = 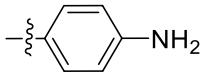	436 575 666			
Cu	R^{1-4} = 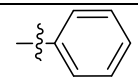	415 542			
Li	R^{1-4} = 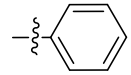	416 515 649			
No metal	R^{1-4} = 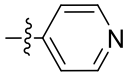	417 513	λ_f = 650 nm Φf = 1.61 x 10^{-2} τs = 7.2 ns	Chloroform	[150]
No metal	R^{1-4} = 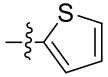	426 523	λ_f = 670 nm Φf = 0.44 x 10^{-2} τs = 0.95 ns		
No metal	R^{1-4} = 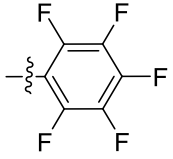	413 506	λ_f = 640 nm Φf = 1.79 x 10^{-2} τs = 9.13 ns		

No metal	R^{1-4} = 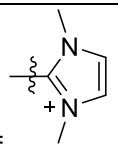	435 546 625	ϕt = 0.004	DMF	[151]
Zn	R^{1-4} = 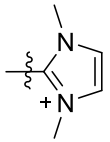	432 561 596	ϕt = 0.001		
No metal	R^{1-4} = 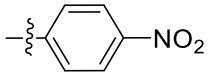	424		Dichloromethane	[152]
No metal	R^{1-4} = 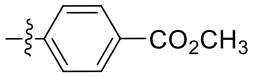	418			
No metal	R^{1-4} = 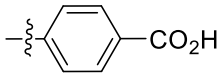	420 (DMSO)			
No metal	R^{1-4} = 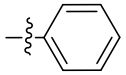	416			
No metal	R^{1-4} = 	417			
No metal	R^{1-4} = 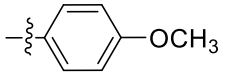	421			
No metal	R^{1-4} = 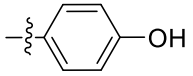	419			
No metal	R^{1-4} = 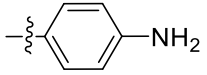	427			
No metal	R^{1-4} = 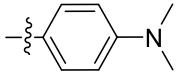	436			
No metal	R^{1-4} = 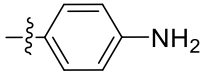	436 670	λ_f = 686 nm Φf = 0.18	DMF	[93]

			τs = 7.49 ns ϕt = 0.58		
No metal	R^{1-4} = 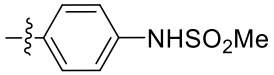	422 650	λ_f = 655 & 716 nm Φf = 0.15 τs = 11.26 ns ϕt = 0.53		
No metal	R^{1-4} = 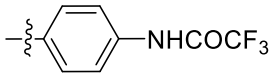	421 649	λ_f = 652 & 718 nm Φf = 0.15 τs = 11.68 ns ϕt = 0.45		
No metal	R^{1-4} = 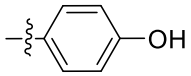	423 653	λ_f = 660 & 724 nm Φf = 0.17 τs = 10.27 ns ϕt = 0.57		
No metal	R^{1-4} = 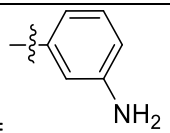	423 649	λ_f = 651 & 715 nm Φf = 0.09 τs = 8.95 ns ϕt = 0.4		
No metal	R^{1-4} = 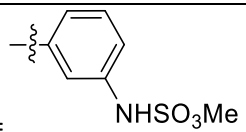	419 647	λ_f = 648 & 714 nm Φf = 0.12 τs = 12.38 ns ϕt = 0.62		

No metal	R^{1-4} = 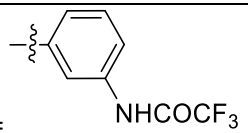	419 646	λ_f = 649 & 714 nm Φf = 0.12 τs = 11.54 ns ϕt = 0.45		
No metal	R^{1-4} = 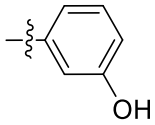	419 647	λ_f = 649 & 715 nm Φf = 0.11 τs = 11.64 ns ϕt = 0.54		
No metal	R^{1-4} = 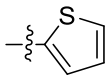	426 661	λ_f = 665 & 718 nm Φf = 0.012 τs = 2.09 ns ϕt = 0.65		
No metal	R^{1-4} = 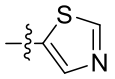	423 662	λ_f = 664 & 725 nm Φf = 0.01 τs = 1.96 ns ϕt = 0.62		
Pt	R^{1-4} = 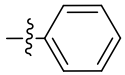	400 508 538	λ_f = 668 & 734 nm ϕt = 4.6 τt = 59 μs	Dichloromethane	[106]
Pt	R^{1-4} = 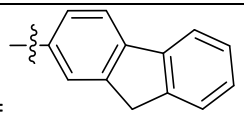	409 512 541	λ_f = 679 & 741 nm ϕt = 2 τt = 22 μs		

Pd	R^{1-4} = 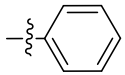	415 522 553	λ_f = 705 & 776 nm ϕt = 1.2 τt = 443 µs		
Pd	R^{1-4} = 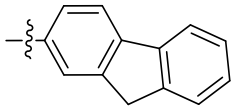	423 526 560	λ_f = 715 & 785 nm ϕt = 0.9 τt = 248 µs		
No metal	R^{1-4} = 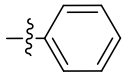	417 513 646	λf= 650 & 714 nm Φf = 0.13 τs = 8.6 ns	Dichloromethane	[107]
No metal	R^1 = R^3 = 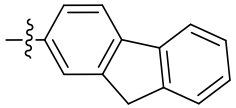 R^2 = R^4 = 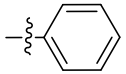	421 516 647	λf= 657 & 722 nm Φf = 0.17 τs = 8.3 ns		
No metal	R^1 = R^3 = 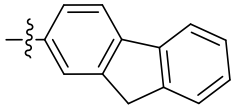 R^2 = R^4 = 	411 505 633	λ_f = 640 & 704 nm Φf = 0.14 τs = 8.3 ns		
No metal	R^{1-4} = 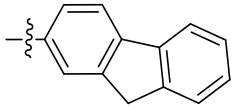	426 519 649	λ_f = 661 & 725 nm Φf = 0.24 τs = 8 ns		

***Table 2**: Photochemical and photophysical parameters of selected* meso and *β substituted porphyrins.*

Structure 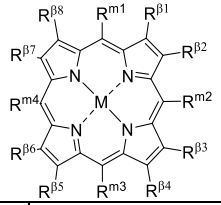		Absorption Soret $Q_{(y)}(1,0)$ $Q_{(x)}(0,0)$	Emission	Solvent	Référence
Metal – M	Substituent – R^{1-4}				
No metal	$R^{m1-4} = R^{\beta1-7} =$ $R^{\beta8} =$ 	426 525 661	λ_f = 690 nm Φf = 0.06 τs = 2.86 ns	DMSO	[147]
Zn	$R^{m1-4} = R^{\beta1-7} =$ $R^{\beta8} =$ 	432 558 602	λ_f = 641 nm Φf = 0.061 τs = 1.09 ns		
No metal	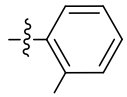 $R^{\beta1-8} =$ 	422 516 652			
No metal	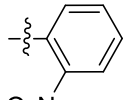 $R^{\beta1-7} =$  $R^{\beta8} =$	434 531 676	λ_f = 660 nm Φf = 0.048 τs = 2.96 ns		

Zn	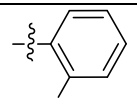 R^{m1-4} = O_2N $R^{\beta1-7}$ = -H $R^{\beta8}$ = $-NO_2$	446 575 628	λ_f = 667 nm Φf = 0.03 τs = 1.18 ns		
Zn	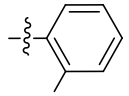 R^{m1-4} = O_2N $R^{\beta2}$ = $R^{\beta4-8}$ = -H $R^{\beta1}$ = $R^{\beta3}$ = $-NO_2$	449 573 623	λ_f = 655 nm Φf = 0.002 τs = 1.25 ns		
No metal	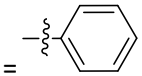 R^{m1-4} = $R^{\beta1-2}$ = $R^{\beta3-5}$ = $R^{\beta7-8}$ = $-Br$ $R^{\beta6}$ = $-NO_2$	477	λ_f = 816 nm Φf = 0.003 τs = 0.0985 ns	Dichloromethane	[88]
No metal	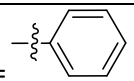 R^{m1-4} = $R^{\beta1-2}$ = $R^{\beta3-8}$ = $-Br$	469	λ_f = 808 nm τs = 0.0059 ns		
Zn	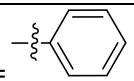 R^{m1-4} = $R^{\beta1-2}$ = $R^{\beta3-5}$ = $R^{\beta7-8}$ = $-Br$ $R^{\beta6}$ = $-NO_2$	472	λ_f = 769 & 807 nm Φf = 0.001 τs = 0.0503 ns		
Zn	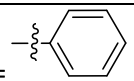 R^{m1-4} = $R^{\beta1-2}$ = $R^{\beta3-8}$ = $-Br$	463	λ_f = 720 nm Φf = 0.0016 τs = 0.1760 ns		

Table 3: *Redox properties of selected* meso*-substituted porphyrins.*

Structure 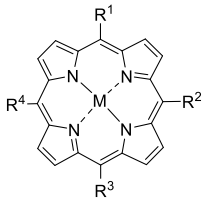		Redox properties	Solvent	Reference
Metal – M	Substituent – R^{1-4}			
Zn	$R^1 = R^3 =$ 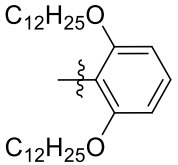 $R^2 =$ 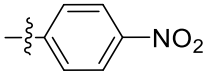 $R^4 =$ 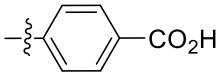	E_{ox} = 0.72 V vs SCE E_{red} = -1.14 V vs SCE	Dichloromethane	[109]
Zn	$R^1 = R^3 =$ 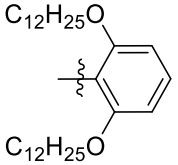 $R^2 =$ 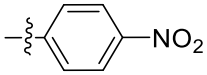 $R^4 =$ 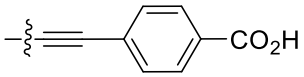	E_{ox} = 0.77 V vs SCE E_{red} = -1.12 V vs SCE		

Zn	$R^1 = R^3 =$ 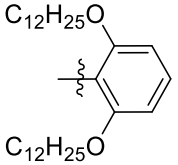 $R^2 =$ 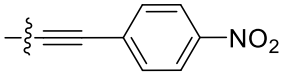 $R^4 =$ 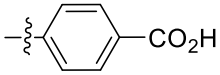	E_{ox} = 0.74 V vs SCE E_{red} = -1.07 V vs SCE		
Zn	$R^1 = R^3 =$ 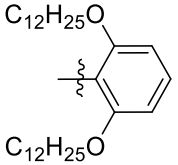 $R^2 =$ 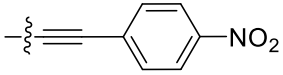 $R^4 =$ 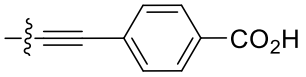	E_{ox} = 0.75 V vs SCE E_{red} = -1.05 V vs SCE		
Zn	$R^1 = R^3 =$ 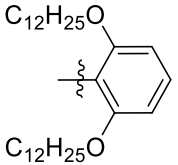 $R^2 =$ 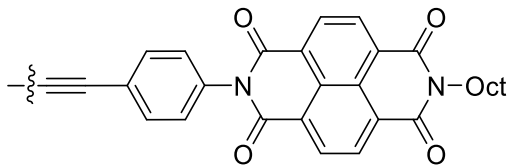 $R^4 =$ 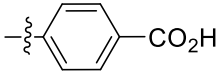	E_{ox} = 0.75 V vs SCE E_{red} = -1.46 V vs SCE		

Zn	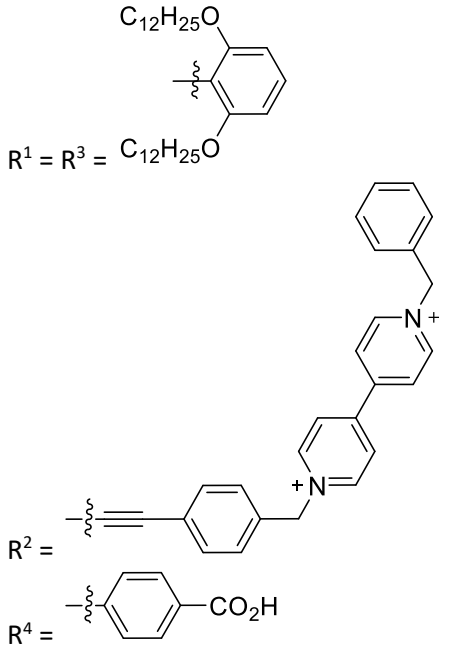	E_{ox} = 0.73 V vs SCE E_{red} = -1.52 V vs SCE		
No metal	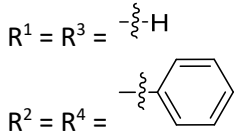	E_{ox} = 1.15 V vs SCE E_{red} = -1.23 V vs SCE	Dichloromethane	[100]
Zn	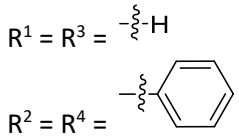	E_{ox} = 0.87 V vs SCE E_{red} = -1.57 V vs SCE		
No metal	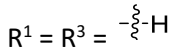	E_{ox} = 1.47 V vs SCE E_{red} = -1.18 V vs SCE	*N*,*N*-diméthylformamide	[141]

	$R^2 = R^4 =$ 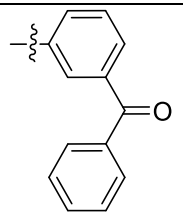			
Zn	$R^1 = R^3 =$  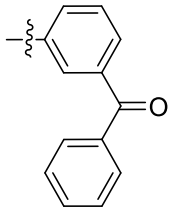 $R^2 = R^4 =$	E_{ox} = 1.09 V vs SCE E_{red} = -1.48 V vs SCE		
No metal	$R^{1-4} =$ 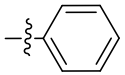	E_{ox} = 1.04 V vs SCE E_{red} = -1.16 V vs SCE	Dichloromethane	92
No metal	$R^{1-4} =$ 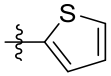	E_{ox} = 0.92 V vs SCE E_{red} = -1.22 V vs SCE		
No metal	$R^{1-4} =$ 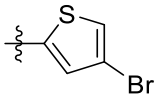	E_{ox} = 0.96 V vs SCE E_{red} = -1.13 V vs SCE		
No metal	$R^{1-4} =$ 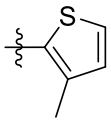	E_{ox} = 0.88 V vs SCE E_{red} = -1.20 V vs SCE		
No metal	$R^{1-4} =$ 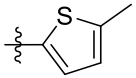	E_{ox} = 0.90 V vs SCE E_{red} = -1.23 V vs SCE		
No metal	$R^{1-4} =$ 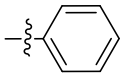	E_{ox} = 0.98 V vs SCE E_{red} = -1.23 V vs SCE	Benzene	90

No metal	R^{1-4} = 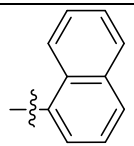	E_{ox} = 1.03 V vs SCE E_{red} = -1.20 V vs SCE		
No metal	R^{1-4} = 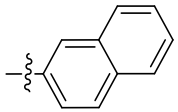	E_{ox} = 0.92 V vs SCE E_{red} = -1.21 V vs SCE		
No metal	R^{1-4} = 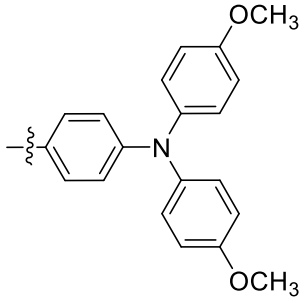	E_{ox} = 0.78 V vs Ag/AgCl	Chloroform	[101]
Mn	R^{1-4} = 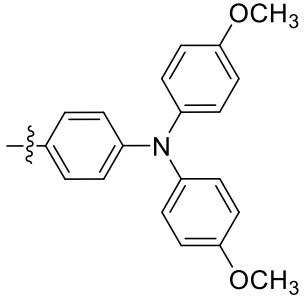	E_{ox} = 0.86 V vs Ag/AgCl		

Fe	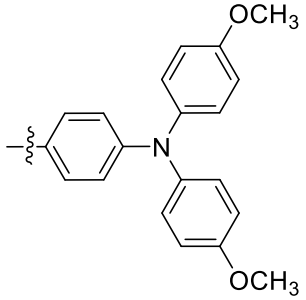 R^{1-4} =	E_{ox} = 0.85 V vs Ag/AgCl		
Co	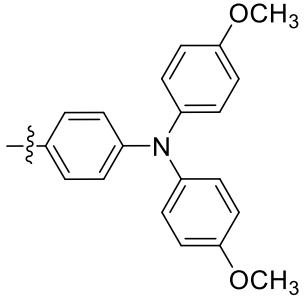 R^{1-4} =	E_{ox} = 0.84 V vs Ag/AgCl		
Ni	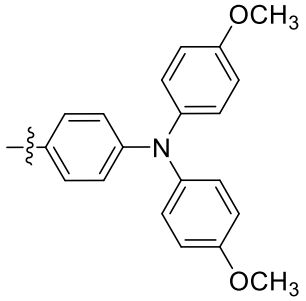 R^{1-4} =	E_{ox} = 0.83 V vs Ag/AgCl		

Cu	R^{1-4} = 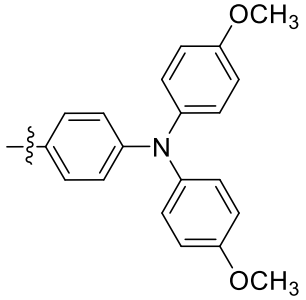	E_{ox} = 0.82 V vs Ag/AgCl		
Zn	R^{1-4} = 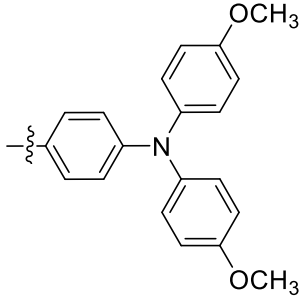	E_{ox} = 0.81 V vs Ag/AgCl		
No metal	R^{1-4} = 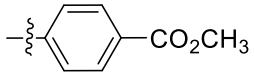	E_{ox} = 1.14 V vs SCE E_{red} = -0.92 V vs SCE	Dichloromethane	[152]
No metal	R^{1-4} = 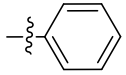	E_{ox} = 1.04 V vs SCE E_{red} = -1.03 V vs SCE		
No metal	R^{1-4} = 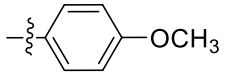	E_{ox} = 0.94 V vs SCE E_{red} = -1.08 V vs SCE		
No metal	R^{1-4} = 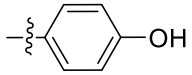	E_{ox} = 0.75 V vs SCE E_{red} = -1.12 V vs SCE		
No metal	R^{1-4} = 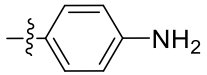	E_{ox} = 0.48 V vs SCE E_{red} = -1.18 V vs SCE		

***Table 4**: Redox properties of selected* meso and *β substituted porphyrins.*

Structure		Redox properties	Solvent	Reference
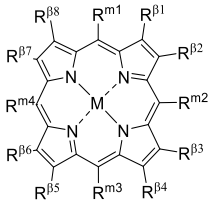				
Metal – M	Substituent – R^{1-4}			
No metal	R^{m1-4} = 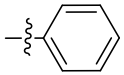 $R^{\beta1-8}$ = 	E_{ox1} = 1.00 V vs Ag/AgCl E_{ox2} = 1.28 V vs Ag/AgCl E_{red1} = -1.23 V vs Ag/AgCl E_{red2} = -1.54 V vs Ag/AgCl	Dichloromethane	[88]
No metal	R^{m1-4} = 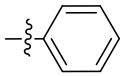 $R^{\beta2-8}$ =  $R^{\beta1}$ = 	E_{ox1} = 1.10 V vs Ag/AgCl E_{ox2} = 1.28 V vs Ag/AgCl E_{red1} = -0.87 V vs Ag/AgCl E_{red2} = -1.08 V vs Ag/AgCl		
No metal	R^{m1-4} = $R^{\beta1-2}$ = 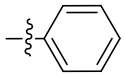 $R^{\beta3-5}$ = $R^{\beta7-8}$ =  $R^{\beta6}$ = 	E_{ox1} = 1.00 V vs Ag/AgCl E_{ox2} = 1.13 V vs Ag/AgCl E_{red1} = -0.85 V vs Ag/AgCl E_{red2} = -1.03 V vs Ag/AgCl		
No metal	R^{m1-4} = $R^{\beta1-2}$ = 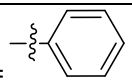 $R^{\beta3-5}$ = $R^{\beta7-8}$ =  $R^{\beta6}$ = 	E_{ox1} = 1.27 V vs Ag/AgCl E_{ox2} = 1.63 V vs Ag/AgCl E_{red1} = -1.06 V vs Ag/AgCl E_{red2} = -1.29 V vs Ag/AgCl		
No metal	R^{m1-4} = $R^{\beta1-2}$ = 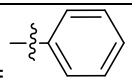	E_{ox1} = 0.84 V vs Ag/AgCl E_{ox2} = 1.16 V vs Ag/AgCl		

	$R^{\beta 3\text{-}8}$ =	E_{red1} = -0.80 V vs Ag/AgCl E_{red2} = -1.17 V vs Ag/AgCl		
Co	$R^{1\text{-}4}$ =	E_{ox1} = 1.06 V vs Ag/AgCl E_{ox2} = 1.31 V vs Ag/AgCl E_{red1} = -1.38 V vs Ag/AgCl		
Co	$R^{m1\text{-}4}$ = $R^{\beta 2\text{-}8}$ = $R^{\beta 1}$ =	E_{ox1} = 1.17 V vs Ag/AgCl E_{ox2} = 1.42 V vs Ag/AgCl E_{red1} = -1.30 V vs Ag/AgCl		
Co	$R^{m1\text{-}4}$ = $R^{\beta 1\text{-}2}$ = $R^{\beta 3\text{-}5}$ = $R^{\beta 7\text{-}8}$ = $R^{\beta 6}$ =	E_{ox1} = 1.13 V vs Ag/AgCl E_{ox2} = 1.34 V vs Ag/AgCl E_{red1} = -1.29 V vs Ag/AgCl		
Co	$R^{m1\text{-}4}$ = $R^{\beta 1\text{-}2}$ = $R^{\beta 3\text{-}5}$ = $R^{\beta 7\text{-}8}$ = $R^{\beta 6}$ =	Eox1 = 1.33 V vs Ag/AgCl Eox2 = 1.47 V vs Ag/AgCl Ered1 = -1.16 V vs Ag/AgCl Ered2 = -1.64 V vs Ag/AgCl		
Co	$R^{m1\text{-}4}$ = $R^{\beta 1\text{-}2}$ = $R^{\beta 3\text{-}8}$ =	E_{ox1} = 1.35 V vs Ag/AgCl E_{red1} = -1.38 V vs Ag/AgCl		
Ni	$R^{1\text{-}4}$ =	E_{ox1} = 1.02 V vs Ag/AgCl E_{ox2} = 1.32 V vs Ag/AgCl E_{red1} = -1.28 V vs Ag/AgCl E_{red2} = -1.72 V vs Ag/AgCl		
Ni	$R^{m1\text{-}4}$ = $R^{\beta 2\text{-}8}$ =	E_{ox1} = 1.19 V vs Ag/AgCl E_{ox2} = 1.32 V vs Ag/AgCl		

	$R^{\beta1}$ =	E_{red1} = -0.95 V vs Ag/AgCl E_{red2} = -1.21 V vs Ag/AgCl		
Ni	R^{m1-4} = $R^{\beta1-2}$ = 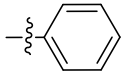 $R^{\beta3-5}$ = $R^{\beta7-8}$ = 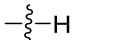 $R^{\beta6}$ =	E_{ox1} = 1.12 V vs Ag/AgCl E_{ox2} = 1.24 V vs Ag/AgCl E_{red1} = -0.94 V vs Ag/AgCl E_{red2} = -1.20 V vs Ag/AgCl		
Ni	R^{m1-4} = $R^{\beta1-2}$ = 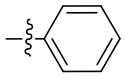 $R^{\beta3-5}$ = $R^{\beta7-8}$ = 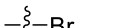 $R^{\beta6}$ =	E_{ox1} = 1.27 V vs Ag/AgCl E_{ox2} = 1.95 V vs Ag/AgCl E_{red1} = -0.77 V vs Ag/AgCl E_{red2} = -1.03 V vs Ag/AgCl		
Ni	R^{m1-4} = $R^{\beta1-2}$ = 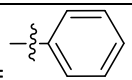 $R^{\beta3-8}$ =	E_{ox1} = 1.22 V vs Ag/AgCl E_{red1} = -0.92 V vs Ag/AgCl E_{red2} = -1.24 V vs Ag/AgCl		
Cu	R^{1-4} = 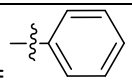	E_{ox1} = 0.99 V vs Ag/AgCl E_{ox2} = 1.36 V vs Ag/AgCl E_{red1} = -1.36 V vs Ag/AgCl E_{red2} = -1.73 V vs Ag/AgCl		
Cu	R^{m1-4} = 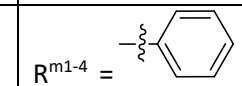 $R^{\beta2-8}$ = $R^{\beta1}$ =	E_{ox1} = 1.08 V vs Ag/AgCl E_{ox2} = 1.44 V vs Ag/AgCl E_{red1} = -0.97 V vs Ag/AgCl E_{red2} = -1.22 V vs Ag/AgCl		
Cu	R^{m1-4} = $R^{\beta1-2}$ = 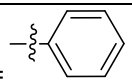 $R^{\beta3-5}$ = $R^{\beta7-8}$ =  $R^{\beta6}$ =	E_{ox1} = 0.96 V vs Ag/AgCl E_{ox2} = 1.38 V vs Ag/AgCl E_{red1} = -0.96 V vs Ag/AgCl E_{red2} = -1.21 V vs Ag/AgCl		

Cu	$R^{m1-4} = R^{\beta1-2} =$ 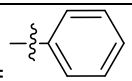 $R^{\beta3-5} = R^{\beta7-8} =$  $R^{\beta6} =$	E_{ox1} = 0.98 V vs Ag/AgCl E_{ox2} = 1.55 V vs Ag/AgCl E_{red1} = -0.74 V vs Ag/AgCl E_{red2} = -1.01 V vs Ag/AgCl		
Cu	$R^{m1-4} = R^{\beta1-2} =$ 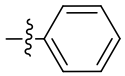 $R^{\beta3-8} =$	E_{ox1} = 0.88 V vs Ag/AgCl E_{ox2} = 1.46 V vs Ag/AgCl E_{red1} = -0.91 V vs Ag/AgCl E_{red2} = -1.19 V vs Ag/AgCl		
Zn	$R^{1-4} =$ 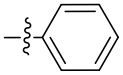	E_{ox1} = 0.84 V vs Ag/AgCl E_{ox2} = 1.15 V vs Ag/AgCl E_{red1} = -1.36 V vs Ag/AgCl E_{red2} = -1.77 V vs Ag/AgCl		
Zn	$R^{m1-4} =$ 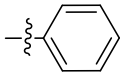 $R^{\beta2-8} =$  $R^{\beta1} =$ 	E_{ox1} = 0.91 V vs Ag/AgCl E_{ox2} = 1.22 V vs Ag/AgCl E_{red1} = -1.05 V vs Ag/AgCl E_{red2} = -1.19 V vs Ag/AgCl		
Zn	$R^{m1-4} = R^{\beta1-2} =$ 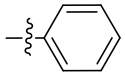 $R^{\beta3-5} = R^{\beta7-8} =$  $R^{\beta6} =$	E_{ox1} = 0.85 V vs Ag/AgCl E_{ox2} = 1.07 V vs Ag/AgCl E_{red1} = -1.06 V vs Ag/AgCl E_{red2} = -1.20 V vs Ag/AgCl		
Zn	$R^{m1-4} = R^{\beta1-2} =$ 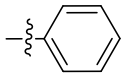 $R^{\beta3-5} = R^{\beta7-8} =$  $R^{\beta6} =$	E_{ox1} = 0.89 V vs Ag/AgCl E_{ox2} = 1.17 V vs Ag/AgCl E_{red1} = -0.98 V vs Ag/AgCl E_{red2} = -1.22 V vs Ag/AgCl		
Zn	$R^{m1-4} = R^{\beta1-2} =$ 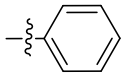	E_{ox1} = 0.84 V vs Ag/AgCl E_{ox2} = 1.07 V vs Ag/AgCl		

	$R^{\beta 3\text{-}8} = -\!\!\!

VIII. References

1 B. P. Chan, Tissue Eng. Part B Rev., 2010, 16, 509–522.
2 J. W. Stansbury, J. Esthet. Restor. Dent., 2000, 12, 300–308.
3 Y. Yagci, S. Jockusch and N. J. Turro, Macromolecules, 2010, 43, 6245–6260.
4 N. Corrigan, J. Yeow, P. Judzewitsch, J. Xu and C. Boyer, Angew. Chem. Int. Ed., 2019, 58, 5170–5189.
5 J.-P. Fouassier and J. Lalevée, Photoinitiators for Polymer Synthesis: Scope, Reactivity, and Efficiency, John Wiley & Sons, 2012.
6 M. A. Tehfe, F. Louradour, J. Lalevée and J.-P. Fouassier, Appl. Sci., 2013, 3, 490–514.
7 C. Mendes-Felipe, J. Oliveira, I. Etxebarria, J. L. Vilas-Vilela and S. Lanceros-Mendez, Adv. Mater. Technol., 2019, 4, 1800618.
8 V. Shukla, M. Bajpai, D. K. Singh, M. Singh and R. Shukla, Pigm. Resin Technol., 2004, 33, 272–279.
9 H. Claus, Photochem. Photobiol., 2021, 97, 471–476.
10 K. J. Gromkowska-Kępka, A. Puścion-Jakubik, R. Markiewicz-Żukowska and K. Socha, J. Cosmet. Dermatol., 2021, 20, 3427–3431.
11 L. Breloy, V. Brezová, A. Blacha-Grzechnik, M. Presset, M. S. Yildirim, I. Yilmaz, Y. Yagci and D.-L. Versace, Macromolecules, 2020, 53, 112–124.
12 C. Elian, V. Brezová, P. Sautrot-Ba, M. Breza and D.-L. Versace, Polymers, 2021, 13, 2015.
13 P. Sautrot-Ba, S. Jockusch, J.-P. Malval, V. Brezová, M. Rivard, S. Abbad-Andaloussi, A. Blacha-Grzechnik and D.-L. Versace, Macromolecules, 2020, 53, 1129–1141.
14 A.-H. Bonardi, S. Zahouily, C. Dietlin, B. Graff, F. Morlet-Savary, M. Ibrahim-Ouali, D. Gigmes, N. Hoffmann, F. Dumur and J. Lalevée, Catalysts, 2019, 9, 637.
15 Z. El Hajj, L. Pierau, J.-P. Malval, J. Marrot, P.-E. Mazeran, D. Naoufal, M.-H. Ha-Thi, K. Steenkeste, A. Dolbecq, S. Floquet, O. Oms, D.-L. Versace and P. Mialane, Macromolecules, 2023, 56, 6105–6116.
16 Ö. Birel, S. Nadeem and H. Duman, J. Fluoresc., 2017, 27, 1075–1085.
17 T. Dai, Y.-Y. Huang and M. R. Hamblin, Photodiagnosis Photodyn., 2009, 6, 170–188.
18 H. Lang and T. Rueffer, Applications of Porphyrinoids as Functional Materials, Royal Society of Chemistry, 2021.
19 H. Fischer and H. Orth, Die Chemie des Pyrrols, 1937.
20 K. E. Martin, Y. Tian, T. Busani, C. J. Medforth, R. Franco, F. van Swol and J. A. Shelnutt, Chem. Mater., 2013, 25, 441–447.
21 P. Rothemund, J. Am. Chem. Soc., 1936, 58, 625–627.
22 P. Rothemund, J. Am. Chem. Soc., 1939, 61, 2912.
23 A. D. Adler, F. R. Longo, J. D. Finarelli, J. Goldmacher, J. Assour and L. Korsakoff, J. Org. Chem., 1967, 32, 476–476.
24 J. S. Lindsey, I. C. Schreiman, H. C. Hsu, P. C. Kearney and A. M. Marguerettaz, J. Org. Chem., 1987, 52, 827–836.
25 J. S. Lindsey, The Porphyrin Handbook, Volume 1, Elsevier, K. M. Kadish, K. M. Smith and R. Guilard., 2000.
26 A. Wiehe, C. Ryppa and M. O. Senge, Org. Lett., 2002, 4, 3807–3809.
27 C. Ryppa, M. O. Senge, S. S. Hatscher, E. Kleinpeter, P. Wacker, U. Schilde and A. Wiehe, Chem. - Eur. J., 2005, 11, 3427–3442.
28 J. S. Manka and D. S. Lawrence, Tetrahedron Lett., 1989, 30, 6989–6992.
29 G. P. Arsenault, E. Bullock and S. F. MacDonald, J. Am. Chem. Soc., 1960, 82, 4384–4389.
30 B. J. Littler, Y. Ciringh and J. S. Lindsey, J. Org. Chem., 1999, 64, 2864–2872.
31 M. Vicente and K. Smith, Curr. Org. Synth., 2014, 11, 3–28.
32 T. Ikeda, T. Tsukahara, R. Iino, M. Takeuchi and H. Noji, Angew. Chem. Int. Ed., 2014, 53, 10082–10085.

33 S. Meng, Z. Xu, G. Hong, L. Zhao, Z. Zhao, J. Guo, H. Ji and T. Liu, Eur. J. Med. Chem., 2015, 92, 35–48.
34 H. J. Callot, Tetrahedron Lett., 1973, 14, 4987–4990.
35 G.-Y. Gao, J. V. Ruppel, D. B. Allen, Y. Chen and X. P. Zhang, J. Org. Chem., 2007, 72, 9060–9066.
36 P. Zardi, M. Maggini and T. Carofiglio, J. Flow Chem., 2021, 11, 163–169.
37 M. J. Crossley, P. L. Burn, S. S. Chew, F. B. Cuttance and I. A. Newsom, J. Chem. Soc., Chem. Commun., 1991, 1564–1566.
38 G. A. Spyroulias, A. P. Despotopoulos, C. P. Raptopoulou, A. Terzis, D. de Montauzon, R. Poilblanc and A. G. Coutsolelos, Inorg. Chem., 2002, 41, 2648–2659.
39 L. Jaquinod, R. G. Khoury, K. M. Shea and K. M. Smith, Tetrahedron, 1999, 55, 13151–13158.
40 P. Bhyrappa, M. Sankar and B. Varghese, Inorg. Chem., 2006, 45, 4136–4149.
41 E. E. Bonfantini, A. K. Burrell, W. M. Campbell, M. J. Crossley, J. J. Gosper, M. M. Harding, D. L. Officer and D. C. W. Reid, J. Porphyr. Phthalocya., 2002, 06, 708–719.
42 S. Richeter, C. Jeandon, J.-P. Gisselbrecht, R. Graff, R. Ruppert and H. J. Callot, Inorg. Chem., 2004, 43, 251–263.
43 R. D. Hartnell, A. J. Edwards and D. P. Arnold, J. Porphyr. Phthalocya., 2002, 06, 695–707.
44 I. V. Sazanovich, A. Balakumar, K. Muthukumaran, E. Hindin, C. Kirmaier, J. R. Diers, J. S. Lindsey, D. F. Bocian and D. Holten, Inorg. Chem., 2003, 42, 6616–6628.
45 C. H. Devillers, S. Hebié, D. Lucas, H. Cattey, S. Clément and S. Richeter, J. Org. Chem., 2014, 79, 6424–6434.
46 C. J. P. Monteiro, M. M. Pereira, M. G. H. Vicente and L. G. Arnaut, Tetrahedron, 2012, 68, 8783–8788.
47 D. E. Chumakov, A. V. Khoroshutin, A. V. Anisimov and K. I. Kobrakov, Chem. Heterocycl. Compd., 2009, 45, 259–283.
48 S. Hiroto, Y. Miyake and H. Shinokubo, Chem. Rev., 2017, 117, 2910–3043.
49 A. Yella, H.-W. Lee, H. N. Tsao, C. Yi, A. K. Chandiran, Md. K. Nazeeruddin, E. W.-G. Diau, C.-Y. Yeh, S. M. Zakeeruddin and M. Grätzel, Science, 2011, 334, 629–634.
50 K. Zeng, Z. Tong, L. Ma, W.-H. Zhu, W. Wu and Y. Xie, Energy Environ Sci., 2020, 13, 1617–1657.
51 M. O. Senge, Chem. Commun., 2011, 47, 1943–1960.
52 A. M. V. M. Pereira, S. Richeter, C. Jeandon, J.-P. Gisselbrecht, J. Wytko and R. Ruppert, J. Porphyr. Phthalocya., 2012, 16, 464–478.
53 K. Henrick, P. G. Owston, R. Peters, P. A. Tasker and A. Dell, Inorg. Chim. Acta, 1980, 45, L161–L163.
54 H. J. Callot, E. Schaeffer, R. Cromer and F. Metz, Tetrahedron, 1990, 46, 5253–5262.
55 L. Barloy, D. Dolphin, D. Dupre and T. P. Wijesekera, J. Org. Chem., 1994, 59, 7976–7985.
56 S. Richeter, C. Jeandon, N. Kyritsakas, R. Ruppert and H. J. Callot, J. Org. Chem., 2003, 68, 9200–9208.
57 S. Richeter, C. Jeandon, J.-P. Gisselbrecht, R. Ruppert and H. J. Callot, J. Am. Chem. Soc., 2002, 124, 6168–6179.
58 D.-M. Shen, C. Liu and Q.-Y. Chen, Eur. J. Org. Chem., 2007, 2007, 1419–1422.
59 A. M. V. M. Pereira, C. M. A. Alonso, M. G. P. M. S. Neves, A. C. Tomé, A. M. S. Silva, F. A. A. Paz and J. A. S. Cavaleiro, J. Org. Chem., 2008, 73, 7353–7356.
60 M. Tanaka, S. Hayashi, S. Eu, T. Umeyama, Y. Matano and H. Imahori, Chem. Commun., 2007, 2069–2071.
61 P. Chen, Y. Fang, K. M. Kadish, J. P. Lewtak, D. Koszelewski, A. Janiga and D. T. Gryko, Inorg. Chem., 2013, 52, 9532–9538.
62 Y. Fang, D. Koszelewski, K. M. Kadish and D. T. Gryko, Chem. Commun., 2014, 50, 8864–8867.
63 N. K. S. Davis, M. Pawlicki and H. L. Anderson, Org. Lett., 2008, 10, 3945–3947.
64 N. K. S. Davis, A. L. Thompson and H. L. Anderson, Org. Lett., 2010, 12, 2124–2127.
65 N. K. S. Davis, A. L. Thompson and H. L. Anderson, J. Am. Chem. Soc., 2011, 133, 30–31.
66 Q. Chen, L. Brambilla, L. Daukiya, K. S. Mali, S. De Feyter, M. Tommasini, K. Müllen and A. Narita, Angew. Chem. Int. Ed., 2018, 57, 11233–11237.

67 A. D. Cheprakov, The Porphyrin Handbook, K. M. Kadish, K. M. Smith and R. Guilard., 2011, vol. 13.
68 D. E. Remy, Tetrahedron Lett., 1983, 24, 1451–1454.
69 S. Ito, T. Murashima, N. Ono and H. Uno, Chem. Commun., 1998, 1661–1662.
70 O. S. Finikova, A. V. Cheprakov, I. P. Beletskaya, P. J. Carroll and S. A. Vinogradov, J. Org. Chem., 2004, 69, 522–535.
71 C. Borek, K. Hanson, P. I. Djurovich, M. E. Thompson, K. Aznavour, R. Bau, Y. Sun, S. R. Forrest, J. Brooks, L. Michalski and J. Brown, Angew. Chem. Int. Ed., 2007, 46, 1109–1112.
72 M. J. Crossley and L. G. King, J. Chem. Soc., Chem. Commun., 1984, 920–922.
73 M. J. Crossley, P. L. Burn, S. J. Langford, S. M. Pyke and A. G. Stark, J. Chem. Soc., Chem. Commun., 1991, 1567–1568.
74 T. Khoury and M. J. Crossley, New J. Chem., 2009, 33, 1076–1086.
75 T. Khoury and M. J. Crossley, Chem. Commun., 2007, 4851–4853.
76 K. M. Smith, D. A. Goff and D. J. Simpson, J. Am. Chem. Soc., 1985, 107, 4946–4954.
77 H. Tamiaki, M. Amakawa, Y. Shimono, R. Tanikaga, A. R. Holzwarth and K. Schaffner, Photochem. Photobiol., 1996, 63, 92–99.
78 H. Tamiaki, K. Fukai, H. Shimazu and S. Shoji, Photochem. Photobiol., 2014, 90, 121–128.
79 M. Chevrier, A. Fattori, L. Lasser, C. Kotras, C. Rose, M. Cangiotti, D. Beljonne, A. Mehdi, M. Surin, R. Lazzaroni, P. Dubois, M. F. Ottaviani, S. Richeter, J. Bouclé and S. Clément, Molecules, 2020, 25, 198.
80 L. Breloy, V. Brezová, S. Richeter, S. Clément, J.-P. Malval, S. A. Andaloussi and D.-L. Versace, Polym. Chem., 2022, 13, 1658–1671.
81 M. Varamo, B. Loock, P. Maillard and D. S. Grierson, Org. Lett., 2007, 9, 4689–4692.
82 W. Zhu, Y.-H. Gao, P.-Y. Liao, D.-Y. Chen, N.-N. Sun, P. A. Nguyen Thi, Y.-J. Yan, X.-F. Wu and Z.-L. Chen, Eur. J. Med. Chem., 2018, 160, 146–156.
83 B. F. O. Nascimento, A. M. d'A. Rocha Gonsalves and M. Pineiro, Inorg. Chem. Commun., 2010, 13, 395–398.
84 M. Gouterman, G. H. Wagnière and L. C. Snyder, J. Mol. Spectrosc., 1963, 11, 108–127.
85 J. A. Shelnutt, J. Porphyr. Phthalocya., 2001, 05, 300–311.
86 H.-Z. Yu, J. S. Baskin and A. H. Zewail, J. Phys. Chem. A, 2002, 106, 9845–9854.
87 J. S. Baskin, H.-Z. Yu and A. H. Zewail, J. Phys. Chem. A, 2002, 106, 9837–9844.
88 P. Rathi, R. Butcher and M. Sankar, Dalton Trans., 2019, 48, 15002–15011.
89 C. J. Kingsbury and M. O. Senge, Coord. Chem. Rev., 2021, 431, 213760.
90 H. N. Fonda, J. V. Gilbert, R. A. Cormier, J. R. Sprague, K. Kamioka and J. S. Connolly, J. Phys. Chem., 1993, 97, 7024–7033.
91 K. M. Barkigia, M. D. Berber, J. Fajer, C. J. Medforth, M. W. Renner and K. M. Smith, J. Am. Chem. Soc., 1990, 112, 8851–8857.
92 X. Sun, J. Zhang and B. He, J. Photochem. Photobiol. A: Chem., 2005, 172, 283–288.
93 A. B. Ormond and H. S. Freeman, Dyes Pigm., 2013, 96, 440–448.
94 M. Gouterman, The Porphyrins V3: Physical Chemistry, Part A, Elsevier, 2012.
95 D. Wang, J. Zhang, T. Shi, B. Wang, X. Cao and T. Li, J. Photochem. Photobiol. A: Chem., 1996, 93, 21–25.
96 C.-W. Huang, K. Y. Chiu and S.-H. Cheng, Dalton Trans., 2005, 2417–2422.
97 R. Pudi, C. Rodríguez-Seco, A. Vidal-Ferran, P. Ballester and E. Palomares, Eur. J. Org. Chem., 2018, 2018, 2064–2070.
98 G. Noirbent, Y. Xu, A.-H. Bonardi, D. Gigmes, J. Lalevée and F. Dumur, Eur. Polym. J., 2020, 139, 110019.
99 L. Shen, Q. Lu, A. Zhu, X. Lv and Z. An, ACS Macro Lett., 2017, 6, 625–631.
100 H. Marcille, J.-P. Malval, M. Presset, N. Bogliotti, A. Blacha-Grzechnik, V. Brezová, Y. Yagci and D.-L. Versace, Polym. Chem., 2020, 11, 4237–4249.
101 T. Sun, Z. Zhang, J. Xu, L. Liang, C.-L. Mai, L. Ren, Q. Zhou, Y. Yu, B. Zhang and P. Gao, Dyes Pigm., 2021, 193, 109469.
102 S. Shanmugam, J. Xu and C. Boyer, J. Am. Chem. Soc., 2015, 137, 9174–9185.

103 W. Zheng, N. Shan, L. Yu and X. Wang, Dyes Pigm., 2008, 77, 153–157.
104 Z. Valicsek and O. Horváth, Microchem. J., 2013, 107, 47–62.
105 O. Horváth, R. Huszánk, Z. Valicsek and G. Lendvay, Coord. Chem. Rev., 2006, 250, 1792–1803.
106 S. Drouet, C. O. Paul-Roth, V. Fattori, M. Cocchi and J. A. G. Williams, New J. Chem., 2011, 35, 438–444.
107 C. O. Paul-Roth, J. A. G. Williams, J. Letessier and G. Simonneaux, Tetrahedron Lett., 2007, 48, 4317–4322.
108 Y.-H. Zhang, W.-J. Ruan, Z.-Y. Li, Y. Wu and J.-Y. Zheng, Chem. Phys., 2005, 315, 201–213.
109 A. Maufroy, L. Favereau, F. B. Anne, Y. Pellegrin, E. Blart, M. Hissler, D. Jacquemin and F. Odobel, J. Mater. Chem. A, 2015, 3, 3908–3917.
110 M. Vasilopoulou, A. M. Douvas, D. G. Georgiadou, V. Constantoudis, D. Davazoglou, S. Kennou, L. C. Palilis, D. Daphnomili, A. G. Coutsolelos and P. Argitis, Nano Res., 2014, 7, 679–693.
111 R. N. Sampaio, A. E. H. Machado, E. Piovesan, P. J. Gonçalves, R. De Paula, J. A. S. Cavaleiro and N. M. Barbosa Neto, Dyes Pigm., 2014, 100, 73–78.
112 M. Vasilopoulou, D. G. Georgiadou, A. M. Douvas, A. Soultati, V. Constantoudis, D. Davazoglou, S. Gardelis, L. C. Palilis, M. Fakis, S. Kennou, T. Lazarides, A. G. Coutsolelos and P. Argitis, J. Mater. Chem. A, 2013, 2, 182–192.
113 T. H. Tran-Thi, J. F. Lipskier, P. Maillard, M. Momenteau, J. M. Lopez-Castillo and J. P. Jay-Gerin, J. Phys. Chem., 1992, 96, 1073–1082.
114 J.-H. Ha, S. I. Yoo, G. Y. Jung, I. R. Paeng and Y.-R. Kim, J. Mol. Struct., 2002, 606, 189–195.
115 T. G. B. de Souza, M. G. Vivas, C. R. Mendonça, S. Plunkett, M. A. Filatov, M. O. Senge and L. De Boni, J. Porphyr. Phthalocya., 2016, 20, 282–291.
116 A. Harriman, J. Chem. Soc., Faraday Trans. 1, 1980, 76, 1978–1985.
117 A. Giraudeau, H. J. Callot and M. Gross, Inorg. Chem., 1979, 18, 201–206.
118 S. E. Jones and H. N. Po, Inorg. Chim. Acta, 1980, 42, 95–99.
119 K. M. Kadish, M. M. Morrison, L. A. Constant, L. Dickens and D. G. Davis, J. Am. Chem. Soc., 1976, 98, 8387–8390.
120 K. M. Kadish and M. M. Morrison, J. Am. Chem. Soc., 1976, 98, 3326–3328.
121 A. Giraudeau, H. J. Callot, J. Jordan, I. Ezhar and M. Gross, J. Am. Chem. Soc., 1979, 101, 3857–3862.
122 H. J. Callot, A. Giraudeau and M. Gross, J. Chem. Soc. Perkin Trans. 2, 1975, 1321–1324.
123 C.-P. Hsieh, H.-P. Lu, C.-L. Chiu, C.-W. Lee, S.-H. Chuang, C.-L. Mai, W.-N. Yen, S.-J. Hsu, E. Wei-Guang Diau and C.-Y. Yeh, J. Mater. Chem., 2010, 20, 1127–1134.
124 J. H. Furhop, K. M. Kadish and D. G. Davis, J. Am. Chem. Soc., 1973, 95, 5140–5147.
125 B. B. Wayland, G. Poszmik, S. L. Mukerjee and M. Fryd, J. Am. Chem. Soc., 1994, 116, 7943–7944.
126 C. Detrembleur, D.-L. Versace, Y. Piette, M. Hurtgen, C. Jérôme, J. Lalevée and A. Debuigne, Polym. Chem., 2012, 3, 1856–1866.
127 Y. Zhao, M. Yu and X. Fu, Chem. Commun., 2013, 49, 5186–5188.
128 Y. Zhao, M. Yu, S. Zhang, Y. Liu and X. Fu, Macromolecules, 2014, 47, 6238–6245.
129 D. Kim and J. W. Stansbury, J. Polym. Sci. A Polym. Chem., 2009, 47, 3131–3141.
130 A. Al Mousawi, C. Poriel, F. Dumur, J. Toufaily, T. Hamieh, J. P. Fouassier and J. Lalevée, Macromolecules, 2017, 50, 746–753.
131 S. Shanmugam, J. Xu and C. Boyer, Macromolecules, 2016, 49, 9345–9357.
132 J. Xu, S. Shanmugam and C. Boyer, ACS Macro Lett., 2015, 4, 926–932.
133 S. Shanmugam, J. Xu and C. Boyer, Polym. Chem., 2016, 7, 6437–6449.
134 G. Ng, K. Jung, J. Li, C. Wu, L. Zhang and C. Boyer, Polym. Chem., 2021, 12, 6548–6560.
135 S. Shanmugam, J. Xu and C. Boyer, Chem. Sci., 2015, 6, 1341–1349.
136 J. Xu, S. Shanmugam, C. Fu, K.-F. Aguey-Zinsou and C. Boyer, J. Am. Chem. Soc., 2016, 138, 3094–3106.
137 S. Shanmugam, J. Xu and C. Boyer, Angew. Chem., 2016, 128, 1048–1052.
138 H. Cao, G. Wang, Y. Xue, G. Yang, J. Tian, F. Liu and W. Zhang, ACS Macro Lett., 2019, 8, 616–622.
139 Q. Ma, W. Wang, L. Zhang and H. Cao, Macromol. Rapid Commun., 2022, 43, 2200122.

140 A. Bonardi, F. Bonardi, G. Noirbent, F. Dumur, C. Dietlin, D. Gigmes, J.-P. Fouassier and J. Lalevée, Polym. Chem., 2019, 10, 6505–6514.
141 F. Schnetz, I. Knysh, D. Jacquemin, S. A. Andaloussi, M. Presset, S. Lajnef, F. Peyrot and D.-L. Versace, Polym. Chem., , DOI:10.1039/D4PY00126E.
142 P. Xiao, F. Dumur, B. Graff, D. Gigmes, J. P. Fouassier and J. Lalevée, Macromolecules, 2013, 46, 7661–7667.
143 P. G. Mahajan, N. C. Dige, B. D. Vanjare, A. R. Phull, S. J. Kim, S.-K. Hong and K. H. Lee, J. Fluoresc., 2018, 28, 871–882.
144 P. G. Mahajan, N. C. Dige, B. D. Vanjare, C.-H. Kim, S.-Y. Seo and K. H. Lee, J. Fluoresc., 2020, 30, 397–406.
145 K. Lintinen, L. Storbacka, A. Efimov, S. Hietala, R. Ahorinta, N. Tkachenko and H. Lemmetyinen, J. Polym. Sci., Part A: Polym. Chem., 2009, 47, 6095–6103.
146 M. Gamboa, M. Campos and L. A. Torres, J. Chem. Thermodyn., 2010, 42, 666–674.
147 C. Farley, A. Aggarwal, S. Singh, A. Dolor, P. To, A. Falber, M. Crossley and C. M. Drain, J. Comput. Chem., 2018, 39, 1129–1142.
148 M. A. Fodor, O. Horváth, L. Fodor, K. Vazdar, G. Grampp and A. Wankmüller, J. Photochem. Photobiol. A: Chem., 2016, 328, 233–239.
149 M. Lan, H. Zhao, H. Yuan, C. Jiang, S. Zuo and Y. Jiang, Dyes Pigm., 2007, 74, 357–362.
150 J. M. S. Lopes, J. R. T. Reis, A. E. H. Machado, T. H. O. Leite, A. A. Batista, T. V. Acunha, B. A. Iglesias, P. T. Araujo and N. M. Barbosa Neto, Spectroc. Acta A, 2020, 238, 118389.
151 A. E. H. Machado, W. R. Gomes, D. M. S. Araújo, H. S. Miglio, L. T. Ueno, R. D. Paula, J. A. S. Cavaleiro and N. M. B. Neto, Molecules, 2011, 16, 5807–5821.
152 J. R. Weinkauf, S. W. Cooper, A. Schweiger and C. C. Wamser, J. Phys. Chem. A, 2003, 107, 3486–3496.

Partie C : Applications pour les matériaux

I. Formation des espèces réactives de l'oxygène

Les molécules photosensibles comme les photoamorceurs, et donc les porphyrines, sont capables de réagir sous irradiation avec l'oxygène pour produire des espèces réactives de l'oxygène, les ROS (Reactive Oxygen Species), comme l'oxygène singulet ($^1O_2$), l'ion superoxyde ($O_2^{\bullet-}$), le peroxyde d'hydrogène (H_2O_2) ou le radical hydroxyle ($HO^\bullet$) (**Figure IC-1**).

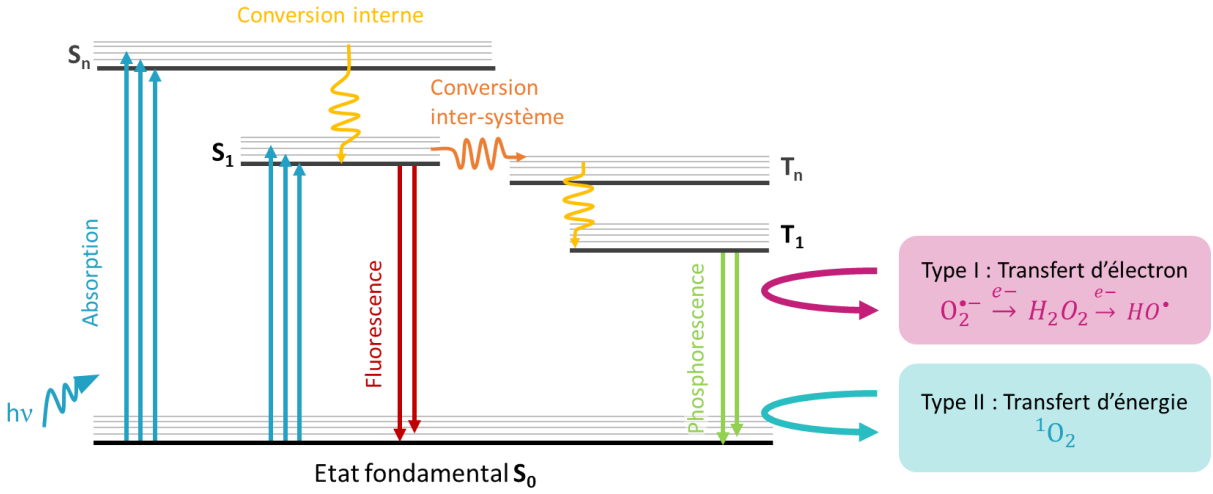

***Figure IC-1** : Diagramme de Perrin-Jablonski précisant les types de réactions possibles avec l'oxygène pour la formation des ROS.*

I. 1. Principe

Les photosensibilisateurs excités peuvent réagir avec l'oxygène par différents mécanismes. Ces mécanismes photophysiques et photochimiques ont été largement étudiés [1,2].

La molécule photosensible doit d'abord être excitée par de la lumière pour passer de son état fondamental S_0 à un état excité singulet S_n depuis lequel, un croisement intersystème est possible, pour passer dans un état excité triplet T_n (Eq. **C1–1** et **C1–2**). Le temps de vie de l'état triplet étant plus long, il est généralement admis que les réactions prennent place à ce niveau d'énergie, car plus probables.

Étape de photosensibilisation :

$$PS \xrightarrow{h\nu} {}^1PS^* \qquad (C1-1)$$

$${}^1PS^* \rightarrow {}^3PS^* \qquad (C1-2)$$

Ensuite, deux mécanismes sont possibles : les réactions de type I ou II. Lors d'une réaction de type II, un transfert énergétique a lieu entre le photosensibilisateur et l'oxygène, conduisant à la formation d'oxygène singulet, et au retour dans son état fondamental du photosensibilisateur (Eq. **B–3**). Il semble admis que le mécanisme de type II est prédominant pour les porphyrines [1].

Mécanisme de type II :

$$^3PS^* + {}^3O_2 \rightarrow {}^1PS + {}^1O_2 \qquad (C1-3)$$

Les réactions de type I impliquent un transfert d'électron avec un autre composé excité pour former deux radicaux ioniques (Eq. **C1–4**). Le radical anionique est en mesure de réagir avec l'oxygène moléculaire pour former l'ion superoxyde $O_2^{\bullet -}$ (Eq. **C1–6**).

Mécanisme de type I :

$$^3PS^* + {}^{3\ or\ 1}PS^* \rightarrow PS^{\bullet -} + PS^{\bullet +} \qquad (C1-4)$$

$$^3PS^* + \text{Substrate} \rightarrow PS^{\bullet -} + \text{Substrate}^{\bullet +} \qquad (C1-5)$$

$$PS^{\bullet -} + O_2 \rightarrow PS + O_2^{\bullet -} \qquad (C1-6)$$

L'ion superoxyde peut ensuite être réduit en H_2O_2 en présence d'un donneur d'électron et/ou d'hydrogène (Eq. **C1–7**). Puis le peroxyde d'hydrogène est capable de former des radicaux hydroxyles $HO^{\bullet}$ par réaction avec le radical anionique du photosensibilisateur (Eq. **C1–8**), par réaction avec l'ion superoxyde (Eq. **C1–9**), ou plusieurs autres moyens qui seront détaillées dans la **section III. 2** de cette partie.

$$O_2^{\bullet -} \xrightarrow{H^+/\,e-} H_2O_2 \qquad (C1-7)$$

$$PS^{\bullet -} + H_2O_2 \rightarrow PS + HO^{\bullet} + HO^- \qquad (C1-8)$$

$$O_2^{\bullet -} + H_2O_2 \rightarrow {}^1O_2 + HO^{\bullet} + HO^- \qquad (C1-9)$$

I. 2. Définitions et détections des espèces réactives de l'oxygène

Les espèces réactives de l'oxygène sont l'ensemble des espèces formées à partir de l'excitation de l'oxygène moléculaire et donnant lieu à un ensemble de sous réactions complexes. Les ROS comprennent de nombreuses espèces, incluant également les dérivés d'azotes, que nous n'allons pas aborder ici. Les ROS peuvent être produits sous rayonnement lumineux, ou dans une cellule, comme sous-produit du métabolisme. Les ROS vont produire des dommages aux molécules environnantes, en transférant des électrons dans des réactions en chaînes. Ces dégradations vont pouvoir être valorisées dans des applications telles que la lutte contre les bactéries ou la dégradation des polluants présents dans l'eau.

I.2.a. Oxygène singulet

L'oxygène singulet est une forme excitée de l'oxygène moléculaire. Les deux électrons de l'oxygène sont non-appariés pour l'oxygène moléculaire (état triplet), alors que dans le cas de l'oxygène singulet, les deux électrons possèdent des spins opposés (**Figure IC-2**). Les deux premiers états excités de l'oxygène sont sous forme singulet, et relativement bas en énergie. Le plus bas en énergie est communément appelé oxygène singulet. Une fois excité, l'oxygène peut passer dans une forme $^1\Sigma_g^+$ (31.5 kcal), qui pourra à son tour se désexciter en oxygène singulet $^1\Delta_g$. La transition entre les deux états se fait rapidement, mais le retour à l'état fondamental (22.5 kcal) est plus long, dû au fait que la transition soit interdite.

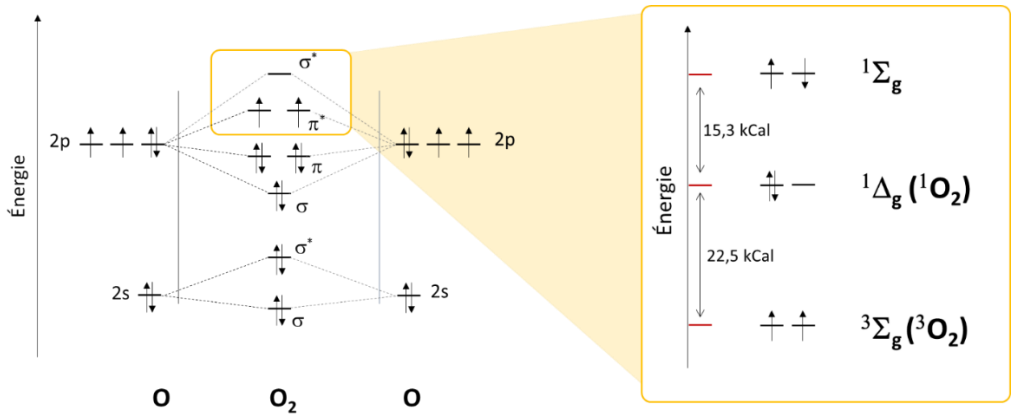

Figure IC-2 *: Représentation des orbitales moléculaires des états excités les plus bas de l'oxygène.*

L'oxygène singulet est très réactif. Il peut soit réagir avec une autre molécule pour revenir à son état fondamental par quenching physique ($^1O_2$ + A → $^3O_2$ + A), où aucune modification n'est observée, ou par quenching chimique, en réagissant avec une espèce chimique ($^1O_2$ + A → P) par exemple par addition [4+2] sur des diènes.

L'oxygène singulet peut être détecté par des méthodes directes, comme la détection de la bande d'émission à 1260 nm. Cette méthode est surtout qualitative, et difficile à mettre en œuvre étant donné la très courte durée de vie de l'espèce.

Une autre méthode plus efficace consiste à utiliser des piéges spécifiques, et d'observer leur modification. On peut citer par exemple le diphényl-iso-benzofuranne (DPBF), qui est une molécule fluorescente présentant un pic d'absorption à 410 nm [3]. En contact avec l'oxygène singulet, une réaction de Diels-Alder forme une un composé bicyclique instable dont l'ouverture de cycle conduit au dibenzoylbenzène qui n'absorbe plus dans la gamme du visible (**Figure IC-3**). Lorsque le DPBF est en contact avec de l'oxygène singulet, on peut donc suivre par spectroscopie UV-visible une baisse de l'absorbance à 410 nm correspondant à la dégradation du DPBF.

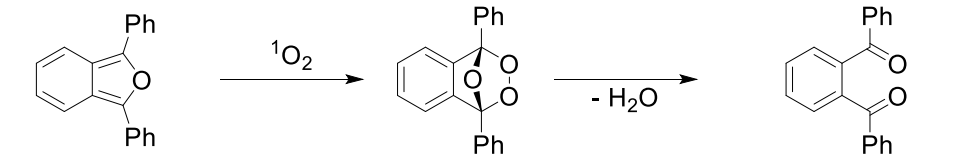

DPBF
jaune (410 nm)

Dibenzoylbenzène
incolore

Figure IC-3 *: Mécanisme de dégradation du DPBF.*

Le DPBF possède cependant deux inconvénients majeurs : il n'est pas spécifique à l'oxygène singulet car il peut se dégrader en présence d'autres espèces oxydantes et il se photolyse sous irradiation, ne permettant pas de quantifier précisément sa réaction avec l'oxygène singulet. D'autres sondes moléculaires ont donc été utilisées, comme le TPCPD (tétraphénylcyclopentadione), dont le mécanisme est basé sur le même principe (**Figure IC-4**), mais de manière plus spécifique et sans réaction compétitives [4]. C'est cette méthode qui sera utilisée préférentiellement dans les travaux de cette thèse.

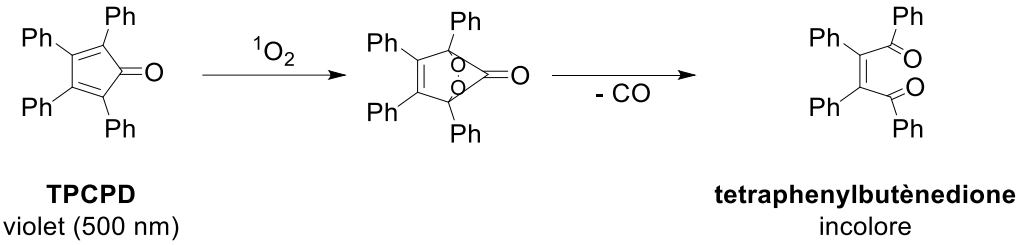

***Figure IC-4** : Mécanisme de dégradation du TPCPD.*

I.2.b. Ion superoxyde

L'ion superoxyde se forme par transfert électronique avec l'oxygène moléculaire, ce qui implique l'apparition d'un électron non apparié. *In vivo*, l'ion superoxyde est neutralisé par des enzymes spécifiques, la superoxyde dismutase (SOD), qui catalyse la transformation de l'ion superoxyde en peroxyde d'hydrogène et en oxygène. Hors de la cellule, l'ion superoxyde peut également se réduire en O_2^{2-} pour ensuite former du peroxyde d'hydrogène dans des conditions acides.

Plusieurs méthodes permettent de détecter l'ion superoxyde. Comme il s'agit d'une espèce radicalaire, il est possible de la détecter par RPE, grâce au spin-trap DMPO. De plus, comme pour l'oxygène singulet, des méthodes optiques permettent de mettre en évidence la présence d'ion superoxyde dans le milieu étudié. La réduction du NBT (nitroblue tetrazolium chloride) mène à la formation du monoformazan (MF), puis une seconde réduction forme le diformazan (DF) (**Figure IC-5**) [5]. L'ensemble de ces deux produits est qualifié de formazan.

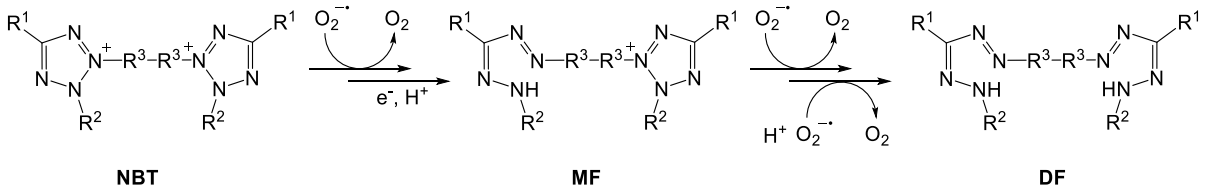

***Figure IC-5** : Mécanisme de dégradation du NBT en monoformazan et en diformazan.*

II. Application antibactérienne

II. 1. Les bactéries

Les bactéries sont des microorganismes procaryotes unicellulaires. La cellule est protégée par une membrane cytoplasmique, elle-même protégée par une paroi cellulaire. Le type de paroi cellulaire dépend du type de bactérie. En effet, il est possible de diviser les bactéries en deux groupes en fonction de la composition chimique et de la structure de leur paroi (**Figure IC-6**). Leur type est déterminé par un test appelé coloration de Gram.

- Les bactéries Gram négatif (Gram -) : La paroi cellulaire de ce type de bactéries est composée d'une membrane externe à base d'une bicouche phospholipidique (environ 8 nm), suivi d'une couche de peptidoglycane (environ 3 nm), et enfin de la membrane cytoplasmique (environ 10 nm) (par exemple : *Escherichia coli* ou *Pseudomonas aeruginosa*).
- Les bactéries Gram positif (Gram +) : La paroi ne comprend pas de membrane externe, mais la couche peptidoglycane est plus épaisse (de 20 à 80 nm) (par exemple : *Staphylococcus aureus*).

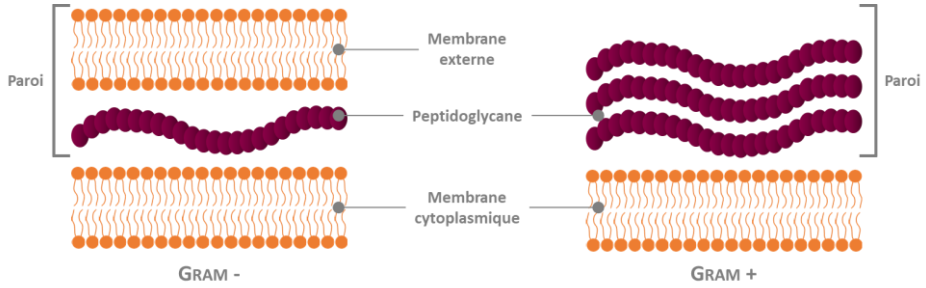

***Figure IC-6** : Schématisation de deux types de parois cellulaires bactériennes Gram négatif et positif*

Les bactéries ont la capacité d'adhérer sur une surface et de proliférer. Elles forment dans ce cas des structures hydratées appelées biofilms [6]. Elles peuvent adhérer sur toutes sortes de surfaces, comme les sols, les surfaces ou les dispositifs médicaux (cathéters, prothèses). Les environnements humides sont propices au développement des biofilms, qui se déroule en plusieurs étapes (**Figure IC-7**). Les bactéries entrant en contact avec le substrat vont être capables de s'adhérer lors de l'étape d'adhésion réversible (1). Elles vont ensuite adhérer à la surface de façon irréversible (2), s'organiser en amas, et produire une matrice protectrice, composée de protéines spécifiques et de polysaccharides. L'étape de maturation du biofilm va permettre aux micro-colonies de croître en surface (3), puis en multicouche (4) jusqu'à devenir macroscopiques. Enfin, des micro-organismes peuvent être relargués du biofilm lors de l'étape de détachement (5) afin de développer une nouvelle colonie.

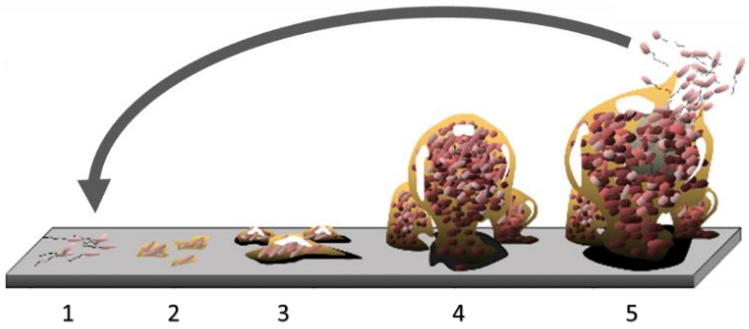

***Figure IC-7** : Développement du biofilm.*[7]

Le développement du biofilm est régulé avec la densité de bactérie, par la détection du quorum ou (*quorum sensing en anglais)* [8]. Il s'agit d'un mécanisme de communication entre les bactéries lors de la variation de la densité de cellule. Les bactéries sont en effet capables de sécréter et détecter de petites molécules leur permettant d'adapter leur comportement et ainsi favoriser la survie de la colonie. En fonction du type de bactéries, les molécules de communication mises en jeu sont différentes. Ainsi, pour les bactéries Gram -, il s'agit d'homosérine lactones (lactone portée par un amide) alors que les bactéries Gram + produisent des peptides.

II. 2. Infections bactériennes

Les bactéries sont présentes en grand nombre dans le corps humain, et la plupart d'entre elles sont inoffensives, voire même bénéfiques. Cependant, certaines bactéries sont pathogènes, et peuvent cibler différentes parties de l'organisme. Les infections qu'elles provoquent peuvent être bégnines, comme l'angine bactérienne ciblant la gorge, ou mortelles comme les endocardites bactériennes visant le cœur.

Les infections bactériennes peuvent survenir en milieux hospitalier, entrainant alors ce qu'on appelle des infections nosocomiales. Les sources de contamination peuvent être les germes présents sur les gants chirurgicaux, lors la pose de sonde (gastrique ou urinaires) ou d'implants, ou présents sur des surfaces touchées directement par le patient ou indirectement par le personnel. La moitié des infections nosocomiales sont causées par trois principales souches bactériennes : *Escherichia coli* à 26%, *Staphylococcus aureus* à 16% et *Pseudomonas aeruginosa* à 8,4%. Ces bactéries peuvent adhérer sur les surfaces sèches pendant des mois : jusqu'à 16 mois pour *E. coli* et *P. aeruginosa*, et 7 mois pour *S. aureus* [9].

Les infections nosocomiales sont une préoccupation majeure de santé publique, puisqu'elles touchent environ un patient hospitalisé sur vingt en 2022.[10] Ces infections entrainent un rallongement d'environ 4 jours du temps d'hospitalisation, et qui peuvent être estimés à plus de 2 milliards d'euros en France en 2006.

Dans le type d'infection, le traitement le plus courant est la prise d'antibiotiques. Malheureusement, cette solution favorise l'émergence de nouvelles souches bactériennes résistantes aux différentes familles d'antibiotiques. Il est donc nécessaire de trouver de nouvelles solutions pour soigner ces patients, et surtout miser sur la prévention afin de diminuer les contaminations.

II. 3. Stratégies de lutte contre les biofilms bactériens

Le problème du développement de biofilm touche de nouveaux domaines en plus du milieu hospitalier, comme les industries alimentaires [11] ou de composants électroniques [12].

Les méthodes de désinfection classique, comme l'utilisation de désinfectants, sont efficaces. Elles reposent sur l'utilisation de produits permettant d'inhiber les fonctions enzymatiques ou de compromettre l'intégrité membranaire des bactéries. Les désinfectants à base d'aldéhydes (comme le formaldéhyde) vont par exemple permettre une alkylation des amines primaires des protéines et des acides nucléiques, ce qui aura comme fonction de modifier la structure des protéines, et d'altérer l'ADN. Par ailleurs, les désinfectants à base d'ammonium quaternaires vont se lier aux groupements phosphates des lipides de la membrane cellulaire, conduisant à une altération de sa structure et une fuite des constituants cellulaires [13].

Cependant, ces méthodes requièrent une action humaine, ce qui ne permet pas de les utiliser fréquemment. De nouvelles recherches portent donc sur le développement de surfaces antibactériennes, qui peuvent être classées en plusieurs catégories : les surfaces antiadhésives qui empêchent la formation du biofilm ; les surfaces limitant la prolifération bactérienne ; les surfaces bactéricides, qui vont tuer les bactéries en contact ou proche de la surface [14].

- Les surfaces antiadhésives luttent contre les infections bactériennes en empêchant l'interaction entre la surface et les bactéries ou les protéines formant le biofilm [15]. Pour cela, il est possible de modifier le caractère hydrophile de la surface. En effet, des surfaces rendues très hydrophobes par leur nano-structuration (comme la feuille de lotus), ne permettent pas une adhésion efficace de la colonie. De même, les revêtements très hydrophiles vont former une couche hydratée autour du matériau, empêchant ainsi le dépôt de protéine sur la surface [16].

- Les matériaux permettant de limiter la prolifération bactérienne peuvent par exemple empêcher la communication bactérienne. Certains matériaux, comme des nanoparticules à base de lutéoline [17] ont montré une bonne efficacité.

- Enfin, les surfaces bactéricides sont basées sur l'utilisation de composés antibactériens. Ils peuvent être incorporés de façon covalente au support, ou libérés de façon continue.

Dans les deux prochaines parties, nous allons nous intéresser aux différentes surfaces bactéricides.

II.3.a. Surfaces bactéricides

Plusieurs types de matériaux antibactériens ont été développés depuis de nombreuses années.

Tout d'abord, les matériaux à base de métaux, comme le cuivre [18] ou l'argent [19] ont démontré leur efficacité pour des activités antibactériennes. Cependant, le coût imposé par leur utilisation à grande échelle ainsi que les controverses vis-à-vis de leur innocuité limitent son expansion. Des matériaux à base de nanocomposites, comme des nanoparticules de métaux tels que l'argent [20], ou le cuivre [21,22], ou d'oxydes métalliques (oxyde de cuivre [23], de fer [24] ou de magnésium [25]) sont alors apparus, permettant une économie de métal sans incidence sur l'efficacité. Les mécanismes impliqués comprennent des dommages aux enzymes ou aux protéines membranaires et la production de ROS [26]. De ce point de vue, les nano-composites permettent une très bonne activité antibactérienne, avec un moindre risque de résistance.

La paroi cellulaire des bactéries étant chargée négativement, de nombreuses études ont porté sur l'utilisation de polymères chargés positivement, pour altérer l'intégrité membranaire par interaction électrostatique. Les polymères contenant des ammonium quaternaires sont largement utilisés [27], mais d'autres méthodes sont également possibles, comme l'utilisation de sels de phosphonium [28], de chitosan pour les milieux acides [29], ou de berbérine [30].

L'utilisation de produits naturellement antibiotiques comme les huiles essentielles a été largement étudiée [31,32]. Les huiles essentielles sont généralement composées de plusieurs constituants avec des mécanismes différents, permettant une large gamme d'action [33]. Les mécanismes font intervenir une rupture de la paroi cellulaire et de la membrane cytoplasmique, entrainant une fuite des composants de la cellule. De plus, les différents composants d'une huile essentielle peuvent avoir des effets additifs, synergiques ou antagonistes.

Enfin, une méthode permettant de lutter contre la prolifération bactérienne consiste à exploiter la capacité de certaines molécules à réagir avec l'oxygène sous lumière pour former des ROS. Il est possible de créer des matériaux incorporant ces photosensibilisateurs, pour une utilisation de surfaces antibactériennes photoactivables [34].

II.3.b. Surfaces photoactivables

II.3.b.i. Mode d'action

Les matériaux à base de photosensibilisateurs ont permis d'exploiter la production de ROS pour la dégradation des bactéries. Une fois les ROS générés, ils vont être capables de cibler de nombreux mécanismes de survie de la bactérie, entraînant sa mort par nécrose et apoptose [35]. Les quatre types de ROS (l'oxygène singulet ($^1O_2$), l'ion superoxyde ($O_2^{\bullet-}$), le peroxyde d'hydrogène (H_2O_2) et le radical hydroxyl ($HO^\bullet$)) vont affecter la bactérie. Même si des études ont tenté de déterminer quel ROS est le plus actif, c'est bien la combinaison de toutes les espèces qui permet la meilleure efficacité [36–38]. Les mécanismes mis en jeu[39,40] ciblent principalement *i*) l'ADN, par oxydation des acides nucléiques, *ii*) les protéines, en oxydant les acides aminés les composants et permettant ainsi d'induire des pertes de fonctionnalisation[41], ainsi que *iv*) la membrane cytoplasmique, en s'attaquant aux triglycérides, aux phospholipides ou au cholestérol [42–44], permettant une perte de structure de la paroi cellulaire, induisant une fuite des composants ou une entrée possible des ROS [45,46].

On peut également noter que des mécanismes de défense de la bactérie existent pour l'ion superoxyde et le peroxyde d'hydrogène, respectivement la superoxyde dismutase et la catalase, mais qu'aucune méthode ne lui permet de lutter contre l'oxygène singulet ou le radical hydroxyl [47,48]. L'utilisation de surfaces photoactives semble donc particulièrement indiquée pour éviter l'émergence de nouvelles bactéries multi-résistantes.

II.3.b.ii. Matériaux photo-antibactériens

Les premières utilisations de molécules photosensibles pour ses applications en médecine remontent aux années 1960, quand par exemple Bellin *et al*. [49] a efficacement utilisé différents colorants pour la photo-désactivation de tumeur. Il a réussi à montrer un effet cytotoxique de certains colorants dans le noir, comme le rose Bengale ou le cristal violet, et d'autres avec un effet cytotoxique uniquement sous irradiation, comme l'éosine ou le bleu de méthylène. Ces travaux ont été précédés de nombreuses études permettant de mettre en lumière l'action de ces colorants sous irradiation sur le corps humain en développant la thérapie photodynamique (PDT) [50].

La recherche a également utilisé cette méthode pour la lutte contre la prolifération bactérienne, avec les premiers travaux de Raab et von Tappeiner dans les années 1900 sur le micro-organisme *Paramecium caudatum*. Mais les avancées dans ce domaine se sont surtout accentuées vers les années 1980, où l'apparition de bactéries multi-résistantes a imposé de diversifier les méthodes antibactériennes, permettant l'essor de la chimiothérapie photodynamique antibactérienne (ou *PhotoAntimicrobial ChemoTherapy* ou PACT en anglais) [51]. Finalement, cette méthode a été transposée aux surfaces pour prévenir l'apparition de biofilms, et donc les risques d'infection.

- Tout comme pour la photopolymérisation, les matériaux à base de métaux ont montré de bons résultats pour lutter contre les bactéries. Des polymère à base de ruthénium (II) [52] ont démontré un effet bactéricide sous lumière solaire. De la même façon, les matériaux à base de TiO_2 ont démontré des propriétés antibactériennes sous irradiation lumineuse, permettant la production des textiles antibactériens [53].

- L'utilisation de colorants utilisés pour la PDT a également été reprise pour l'élimination de bactéries. Cet usage a été largement étudié à travers différentes revues [54,55], quelques exemples sont résumés ici. L'utilisation de photosensibilisateurs absorbant les irradiations UV, comme la benzophénone et l'anthraquinone, est aussi possible. Ces deux composés et leurs dérivés ont été utilisés pour développer des tissus antibactériens. Certains dérivés de benzophénone ont permis d'obtenir des taux de réduction de colonies bactériennes > 99.99% pour *S. aureus* et *E. coli* [56]. L'utilisation d'anthraquinone [57] a démontré une durabilité des fonctions antibactériennes après un cycle de 10 lavages, avec la même efficacité de 99 ,99% pour *E. coli*, mais descendu à 60% pour *S. aureus*.

- Des colorants à base de phénothiazine ou de xanthène ont permis de développer des surfaces antibactériennes. Le bleu de méthylène, un colorant à base de phénothiazine a montré une action antibactérienne contre *S. aureus* en utilisant un matériau polymère comme support pour un relargage progressif [58]. L'utilisation de colorants à base de xanthène, comme l'éosine, est également possible. Ce colorant est connu comme antibactérien, et très utilisé dans le soin de plaies quotidiennes. Sa combinaison avec un polymère cationique a permis d'obtenir de très bons résultats contre *S. aureus et E. coli* [59].

- L'utilisation de riboflavine supporté sur chitosan a permis la réalisation de films antibactériens efficaces contre différentes souches bactériennes pathogènes après 2 h d'irradiation. Elle est également compatible avec une utilisation pour des films alimentaires pour l'emballage de saumon par exemple [60].

- Les phthalocyanines permettent d'obtenir des surfaces antibactériennes sous irradiation avec des longueurs d'onde plus hautes grâce à son absorption proche de l'infra-rouge [61]. Des matériaux à base de phthalocyanines supportés sur papier filtre ont permis d'obtenir une bonne dégradation des bactéries *E. coli* après 1 h d'irradiation [62]. De plus, des propriétés supplémentaires d'anti-encrassement ont été obtenues par combinaison avec un polymère de ε-poly-lysine, entraînant une élimination de 98% du nombre de colonies bactériennes en 10 min d'irradiation.

II.3.b.iii. Matériaux photo-antibactériens photo-synthétisés

Il est également possible d'attribuer un double rôle au colorant : comme développé dans la première partie de ce chapitre (**Partie A : Photopolymérisation**), le colorant peut servir de photoamorceur pour la photopolymérisation (**Figure IC-8A**), puis une fois le polymère formé, le

colorant sera piégé dans la matrice du polymère et pourra servir de photosensibilisateur pour réagir avec l'oxygène pour former des ROS (**Figure IC-8B**) et donner au matériau un effet antibactérien.

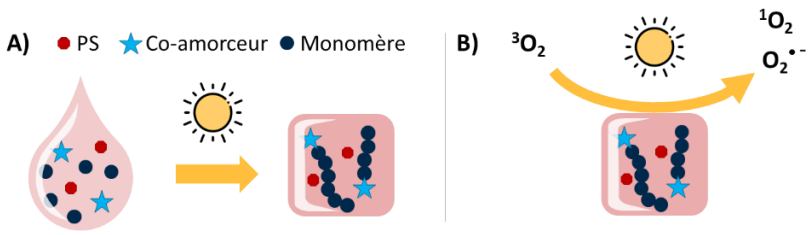

***Figure IC-8** : Principe du double rôle de la molécule photoactive : **A**) en tant que photoamorceur pour la polymérisation et **B**) en tant que phosensibilisateur pour les applications.*

Cet aspect a été largement étudié par Versace *et al*. La curcumine a été utilisée pour développer des polymères d'huile de soja époxydée obtenus par photopolymérisation cationique, avec une conversion finale des fonctions époxy de 80% en 600 s. Ces matériaux ont ensuite été utilisés pour évaluer leur activité antibactérienne et ont présenté une très bonne efficacité de 99% et 95% de réduction de colonies bactériennes de *S. aureus* et *E. coli* après incubation de 48 h [63]. Ce modèle a ensuite été utilisé pour le développement de micro-cages à base de monomère acrylaté chargé en curcumine [64]. Son efficacité contre *S. aureus* a atteint 95% de mortalité en seulement 10 min d'irradiation.

Le paprika, un autre colorant naturel, a efficacement amorcé la photopolymérisation cationique de l'acide gallique époxydé avec 90% de conversion du monomère en 1200 s d'irradiation sous lampe au xénon [65]. L'efficacité antibactérienne de ces matériaux a été évaluée et montre une élimination totale des bactéries *S. aureus* et *E. coli* après 6 h d'incubation. Plusieurs colorants présents dans le paprika sont responsables de cet effet : la capsanthine, la capsorubine et la cryptocapsine.

Des matériaux à base de quercétine ont également été développés [66], en exploitant le double rôle du colorant pour atteindre 75% de conversion des fonctions époxy du glycérol modifié, et une inhibition de 99% du nombre de colonies pour *S. aureus* après 2 h d'irradiation. Cependant, aucune efficacité n'a pu être observée contre *E. coli*.

Des phthalocyanines et leurs dérivés ont également montré des propriétés d'amorçage de polymérisation et de photoactivité. Une phthalocyanine couplée avec de l'anthraquinone [67] a présenté de bonnes cinétiques de polymérisation, en co-polymérisant deux monomères acrylatés et époxydés, à hauteur de 80% et 40% de conversion des fonctions réactives respectives. De plus, une bonne activité antibactérienne a été démontrée par production d'oxygène singulet par la phthalocyanine.

L'utilisation de matériaux à base d'éosine [68] a permis de mettre en évidence le problème de relargage du PS. En effet, ce matériau présente une bonne activité antibactérienne, mais qui est associé à la diffusion de l'éosine dans le milieu. D'autres études ont donc porté sur la modification de photoamorceurs efficaces pour insérer des fonctions polymérisables. Ainsi, dans une étude de 2021 [69], la purpurine a été fonctionnalisée, permettant sa liaison covalente au réseau du polymère. En plus d'un très bon effet d'amorçage en photopolymérisation radicalaire, une bonne inhibition de *S. aureus* a été remarqué même après trois cycles de tests antibactériens.

Une nouvelle stratégie permettant d'augmenter l'effet antibactérien du matériau a été l'introduction d'huile essentielle dans les matériaux photosynthétisés, pour permettre de réduire le nombre de bactéries à la surface des matériaux, même sans irradiation. Ainsi, des matériaux contenant

de l'eugénol et synthétisés grâce à un systèmes photoamorceur composé de β-carotène,[70] a permis de diminuer le nombre de colonies à la surface des matériaux.

Finalement, Elian *et al.*[71] ont développé des matériaux photopolymérisés par des dérivés d'alizarine fonctionnalisés. Ceci a permis d'éviter le relargage du photosensibilisateur hors du polymère. De plus, des monomères eugénol également fonctionnalisés ont permis une diminution du nombre de bactéries à la surface des matériaux dans le noir, tandis que la photoactivité de l'alizarine a permis une élimination totale des bactéries après 1 h d'irradiation.

II.3.b.iv. Matériaux photo-antibactériens contenant des porphyrines

Un grand nombre de différents photosensibilisateurs ont été développés dans la recherche de nouveaux matériaux antibactériens. Cependant, de nombreux photosensibilisateurs sont des composés polycycliques, posant problème quant à leur possible toxicité. En effet, ces molécules peuvent être métabolisées en fonctions toxiques pour l'organisme, comme des phénols, et donc présenter des risques cancérigènes s'il est relargué hors du matériau.

Les porphyrines sont des colorants naturellement présents dans le corps humain, comme dans l'hémoglobine ou sous forme dérivée comme dans la vitamine B12. De plus, elles ne semblent pas présenter de toxicité si elles ne sont pas irradiées[72], permettant leur utilisation dans des matériaux en limitant le risque de toxicité. Elles sont également indiquées pour une utilisation en tant qu'agent théranostique,[73] et les premières utilisations de la thérapie photodynamique ont été réalisées sur des porphyrines, comme la photofrin II [74] et l'hematoporphyrine [35] (**Figure IC-9**).

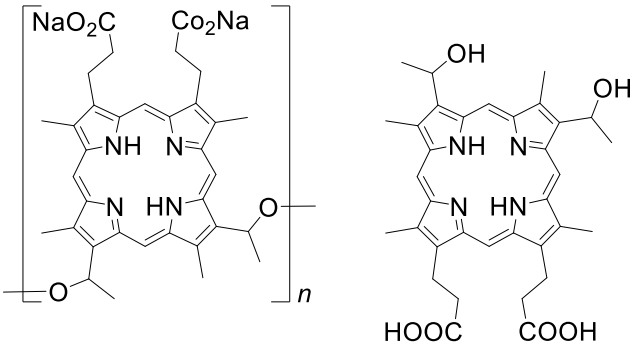

Photofrin II **Hématoporphyrine**

***Figure IC-9** : Structure de Photofrin II et hématoporphyrine*

De nombreux exemples d'utilisation de porphyrines pour la lutte contre les bactéries ont fait l'objet de revues [54]. Mais nous nous intéresserons ici uniquement à l'usage de porphyrines pour des matériaux antibactériens.

Les porphyrines ont été utilisées pour développer des tissus antibactériens, à base de nylon par l'utilisation de protoporphyrines IX libres ou métallées [75]. Ces matériaux ont présenté des effets antibactériens contre *S. aureus* et *E. coli* sous irradiation. D'autres tissus ont été développés à base de TAPP et de ZnTAPP (**Figure IC-10**) à base de cellulose [76]. Les résultats des tests antibactériens démontrent que les matériaux présentent des taux de photo-inhibition dépendant de la nature des bactéries et de la concentration des porphyrines sur le matériau. En effet, la diminution de la concentration de porphyrine ZnTAPP de 10^{-4} M, à 10^{-5} M puis 10^{-4} M, fait passer la photoactivité de 100%, à 20% puis 10% respectivement en 30 minutes pour une souche de *S. aureus*.

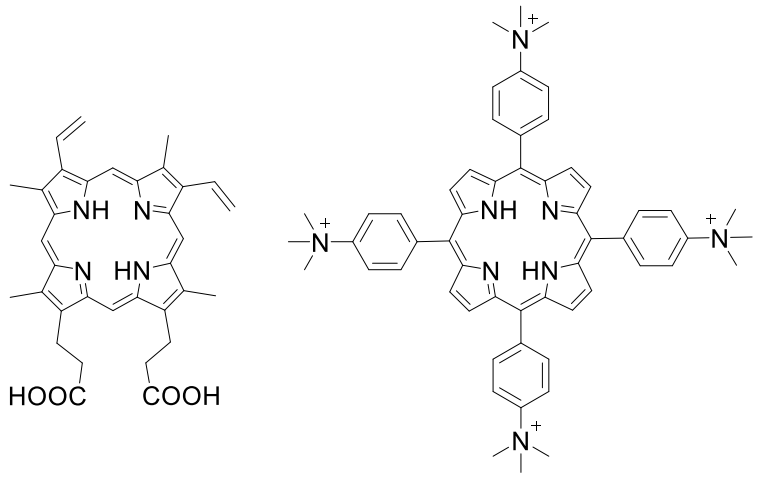

Figure IC-10 *: Structure des porphyrines protoporphyrine IX et TAPP.*

Les porphyrines ont également été employées dans des matériaux supportés par des polymères. Un polymère à base de poly-S-lysine a été développé [77] contenant une porphyrine meso-tetrasubstituée contenant un groupement permettant l'ancrage de la porphyrine au polymère et trois groupements pyridine ou pyridinium (**Figure IC-11**). Un effet antibactérien sur *S. aureus* a été observé avec toutes les porphyrines étudiées et également sur *E. coli* mais uniquement avec les porphyrines chargées. De la même façon, des porphyrines chargées positivement ont été développées [78] liées de façon covalente à un réseau composé de polyéthylène téréphtalate (PET).

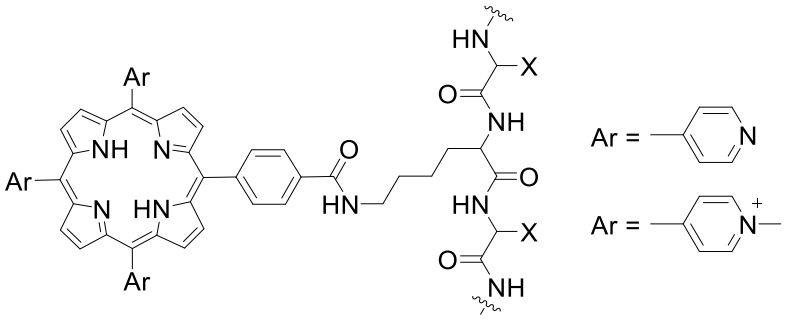

Figure IC-11 *: Structure du polymère à base de porphyrine de Tomé* et al. [77]

De nombreux polymères biosourcés ont également permis de développer des surfaces antibactériennes, comme la chitine [79], la gélatine [80], le chitosan [81] ou la cellulose estérifiée par l'acide laurique pour permettre l'obtention d'un matériau plastique [82]. Dans ce dernier cas, aucune colonie de *S. aureus* n'a été détectée après 24 h d'incubation en utilisant des matériaux contenant une fraction à partir de 0.19% de protoporphyrine IX par unité de glucose, mais une charge plus élevée à 0.52% de porphyrine par unité de glucose a dû être employée pour l'élimination des colonies de *E. coli*.

Finalement, des porphyrines ont pu également être combinées à des supports sans liaison covalente, comme dans le cas de la formation d'hydrogel à base de HEMA (2-hydroxyethyl méthacrylate) et d'acide méthacrylique [83,84]. Les porphyrines TPPS et TMPyP (**Figure IC-12**) respectivement chargées négativement et positivement, ont démontré un effet antiadhésif avec une

réduction de 91.76 ± 5.99% contre *S. epidermidis* dans le noir, et jusqu'à 99.02 ± 0.42% sous irradiation intense.

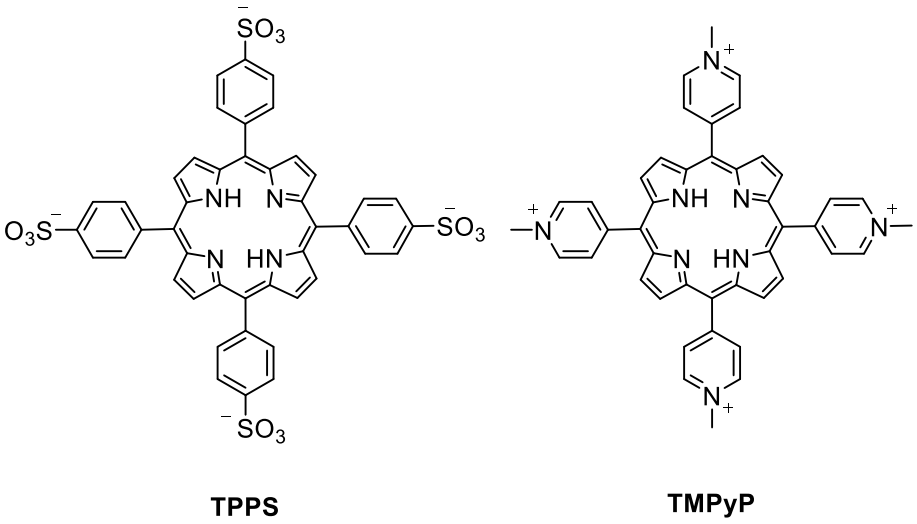

***Figure IC-12** : Structures de TPPS et TMPyP.*

II.3.b.v. Matériaux photo-antibactériens photosynthétisés contenant des porphyrines

L'utilisation de porphyrines pour la préparation de matériaux présente l'avantage de combiner les effets de photoamorçage de la porphyrine ainsi que sa photoactivité contre les bactéries. Les exemples présents dans la littérature sont assez peu nombreux. [85,86]

Tout d'abord, les porphyrines ont permis d'obtenir des polymères antibactériens par polymérisation PET-RAFT. Les polymères obtenus étant linéaires et sans réticulation, il a été nécessaire de greffer la porphyrine au monomère [85]. Cela a permis l'autocatalyse de la polymérisation, et ont donné des résultats antibactériens très satisfaisant, puisqu'une inhibition > 99.99% est observée en 30 min d'irradiation sur *S. aureus*.

Enfin, Marcille *et al.* [86] ont développé des polymères par photopolymérisation radicalaire, cationique ou par thiol-ène en utilisant deux porphyrines PP et PPZn (**Figure IC-13**), qui a permis de développer des matériaux contenant des porphyrines avec des propriétés antibactériennes. En effet, sous irradiation, aucune colonie de *S. aureus* n'a été observée à la surface des matériaux.

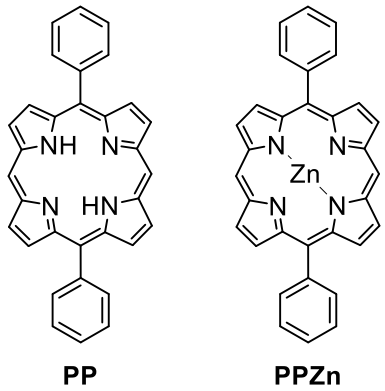

***Figure IC-13** : Structure de PP et PPZn.*

Grâce aux bons résultats obtenus pour la double utilisation de colorants en tant que photoamorceur et agent antibactérien, d'autres application ont été envisagées. En utilisant le même principe de photogénération de ROS, les matériaux pourraient permettre de dépolluer l'eau.

II. 4. Conclusion

De nombreuses méthodes sont disponibles pour le développement de surfaces présentant des propriétés antibactériennes. Cependant, les matériaux photoactifs permettent de produire des ROS sous irradiation lumineuse, et présentent ainsi la possibilité d'empêcher la résistance des bactéries, en ayant de nombreux modes d'actions.

Parmi les matériaux photoactifs, les colorants présentent un double rôle : en tant que photoamorceur pour la synthèse du polymère, et également en tant que photosensibilisateur, pour la production de ROS et donc responsable de l'activité antibactérienne. Cette stratégie permet une simplification de la composition des matériaux, en combinant les deux actions sur le même composé.

Finalement, les porphyrines ont prouvé qu'elles possèdent de bonnes applications pour la lutte contre les bactéries, en étant efficaces contre plusieurs souches responsables des maladies nosocomiales. De plus, contrairement à de nombreux composés polycycliques, elles ne semblent pas présenter de toxicité dans le noir, ce qui est compatible avec la réalisation de matériaux où le relargage des composants semble inévitable sur de longues périodes.

III. Dépollution de l'eau

III. 1. Pollution de l'eau

III.1.a. Pollution de l'eau dans le monde et en France

La disponibilité des ressources en eau potable est un problème grandissant. En effet, les besoins en eau augmentent d'1% par an dans le monde depuis les années 1980. Cela est dû à la croissance démographique, au développement de l'industrie et au dérèglement climatique. [87]

Dans le monde, en 2023, on compte 2 milliards de personnes n'ayant pas accès à une eau potable gérée de façon sûre, soit 26% de la population mondiale. De plus, 46% de population, soit 3.6 milliards de personnes ne disposent pas de services d'assainissement gérés de façon sûre [87]. Ces problèmes ne touchent pas que les pays en voie de développement, puisqu'en Europe, et également en France, de nombreux épisodes de sècheresse mettent à mal les réserves en eau dans les nappes phréatiques. La diminution des ressources en eau appelle à une meilleure réutilisation des eaux usées traitées (REUT), en retraitant les eaux de sortie de stations d'épurations pour des utilisations directes comme l'irrigation ou l'industrie [88].

Les eaux usées sont traitées en station d'épuration avant d'être rejetées en milieu naturel, tandis que les boues de traitements, riches en nutriments, sont réutilisées pour l'agriculture. Cependant, même si les traitements sur les eaux usées permettent de dégrader une majorité de polluants [89], certaines substances sont plus difficiles à dégrader, avec jusqu'à 87% de produit résiduel [90]. Certaines études ont montré la présence de polluants résiduels dans les rivières européennes, démontrant que 90% d'entre elles sont polluées. Les principaux polluants sont des analgésiques ou des pesticides. Des médicaments comme le diclofénac ou l'atrazine ont été retrouvés à des concentrations de l'ordre du ng/L au µg/L, prouvant que les eaux traitées ne le sont pas entièrement [91,92].

Ceci démontre que la réutilisation directe des eaux usées traitées n'est pas encore possible, et que des efforts pour la dépollution de l'eau doivent encore être déployés pour s'assurer de la bonne qualité des eaux rejetées.

III.1.b. Les sources de pollution

La pollution de l'eau est causée par une utilisation massive de produits divers : médicaments dans les eaux urbaines, fertilisants dans les eaux agricoles, colorants et médicaments dans les eaux industrielles [93,94]. La principale source de contamination des eaux vient de l'agriculture et de l'élevage. Ces deux pôles consomment 70% de l'eau utilisée dans le monde, et rejettent pesticides, engrais, déjections animales et résidus de vaccins et d'antibiotiques. Les rejets urbains, représentant 8% de la consommation en eau, sont produits par les villes et leurs habitants. Ils sont en général mieux traités que les eaux issues de l'agriculture, puisqu'ils rejoignent directement les stations d'épurations. Cependant, la concentration en produits plus difficilement traitables, comme les médicaments [90] est plus élevée. Enfin, les eaux rejetées par les industries (22% de la consommation en eau) produisent des déchets plus dangereux, mais ces industries sont soumises à des réglementations et doivent traiter l'eau en amont de leur retraitement en station d'épuration. Les rejets peuvent contenir des métaux lourds, des micro-organismes ou des composés organiques comme des résidus d'industries pétrochimiques ou pharmaceutiques ou des colorants des industries textiles ou agroalimentaires.

Les colorants, et principalement les colorants azoïques, sont beaucoup utilisés dans les industries, que ce soit les imprimeries, les industries alimentaires ou cosmétiques, mais surtout dans le domaine des textiles. Les colorants de synthèse (dont les colorants azoïques représentent 60%) sont produits à hauteur de 700 000 tonnes par an, et une partie est rejetés lors des étapes de fabrication, soit 105 000 tonnes par an [95].

III.1.c. Effets de la pollution

Les risques sanitaires liés à la présence des substances polluantes dans l'eau sont nombreux. Les effets sur la santé ont été considérés par l'ANSES (Agence nationale de sécurité sanitaire de l'alimentation, de l'environnement et du travail), qui ont développé des directives sur les valeurs toxicologiques de références (VTR) permettant de relier les valeurs limites de contact avec des substances toxiques ou cancérigènes, comme l'arsenic ou le benzène [96]. De plus, l'arrêté du 11 janvier 2007 présente une liste d'une quarantaine de substances dont des limites de concentration sont fixées pour l'eau distribuée au consommateur [97].

Les risques liés à la présence de micro-organismes par contamination directe peuvent causer des maladies comme le choléra ou la fièvre typhoïque. Environ 3 millions de morts par an dans le monde sont liées à la mauvaise qualité de l'eau, principalement dans les pays en voie de développement. Cependant, en France aussi, la mauvaise qualité de l'eau peut entraîner des gastro-entérites aigües, qui peuvent entrainer des complications comme la dyspepsie, l'arthrite réactive, des hépatites virales A ou E, ou des gastrites qui peuvent se compliquer en ulcère ou en cancer de l'estomac.

De même, les polluants chimiques peuvent causer des dérèglements dans l'organisme entraînant des maladies, comme du saturnisme en cas de trop forte concentration en plomb ou des empoisonnements à l'arsenic. De plus, les résidus médicamenteux, comme les vaccins ou les pesticides, présentent des effets encore méconnus, mais peuvent provoquer des troubles du système hormonal à des concentrations de l'ordre du nano ou du microgramme [91]. Enfin, certains colorants azoïques peuvent être toxiques ou mutagènes, et même s'ils ne le sont pas, leurs produits de métabolisation peuvent l'être (phénols par exemple). [98–101]

En plus des effets sur la santé humaine, les risques environnementaux causés par le rejet d'eaux encore polluée peuvent avoir des conséquences sur la faune et la flore aquatique. Les composés pharmaceutiques peuvent par exemple avoir des effets sur la faune aquatique, comme des perturbateurs endocriniens sur les poissons ou des déséquilibres dans la répartition des sexes chez les reptiles. Enfin, la coloration de l'eau par les colorants rejetés n'est pas seulement un problème esthétique, mais elle interfère aussi avec la diffusion de la lumière dans l'eau, bloquant la photosynthèse des plantes aquatiques, et impactant ainsi toute la biodiversité.

III. 2. Solutions existantes

Afin de traiter l'eau polluée et de lutter contre la diminution des ressources hydriques, plusieurs méthodes de traitements des eaux ont été développées. Une partie est d'ailleurs mise en application dans les stations d'assainissement de l'eau. On peut compter par exemple la filtration [102], la coagulation [103] ou l'adsorption [94].

Ces méthodes sont cependant basées sur un principe de séparation des polluants de l'eau, et ne permet donc pas de les détruire. Un traitement des déchets, potentiellement toxiques est donc à prévoir en aval de la dépollution de l'eau. D'autres méthodes de dépollution sont donc envisagées,

dont les processus d'oxydation avancés (Advanced Oxidation Processes (AOPs)) [104]. Cette méthode est basée sur la production d'espèces très réactives oxydantes, comme par exemple $HO^{\bullet}$, qui permet de dégrader la majorité des polluants présents dans l'eau par minéralisation complète (CO_2, H_2O …). Diverses méthodes permettent de mettre en place ces AOP :

- La photolyse du peroxyde d'hydrogène sous irradiation UV :

$$H_2O_2 + h\nu \rightarrow 2\,HO^{\bullet} \qquad (C3-1)$$

- La réaction de Fenton permet de produire des radicaux hydroxyles en présence de fer (II). Le Fe^{3+} est généralement reconverti en Fe^{2+} à la suite de plusieurs réactions non présentées ici.

$$H_2O_2 + Fe^{2+} \rightarrow HO^{\bullet} + HO^{-} + Fe^{3+} \qquad (C3-2)$$

Le Fe^{3+} peut être hydrolysé pour obtenir le complexe $Fe(OH)^{2+}$. Dans le cas de la photo-Fenton [105], ce complexe est reconverti en Fe^{2+} plus efficacement que dans le cas de la Fenton classique :

$$Fe(OH)^{2+} + h\nu \rightarrow HO^{\bullet} + Fe^{2+} \qquad (C3-3)$$

- L'utilisation d'ozone :

$$3\,O_3 + H_2O \rightarrow 2\,HO^{\bullet} + 4\,O_2 \qquad (C3-4)$$

L'ajout de peroxyde d'hydrogène dans le milieu améliore l'efficacité. On parle de peroxonation :

$$O_3 + H_2O_2 \rightarrow HO^{\bullet} + HO_2^{\bullet} + O_2 \qquad (C3-5)$$

La combinaison de l'ozonolyse avec l'irradiation UV permet de générer *in situ* du peroxyde d'hydrogène. Le peroxyde d'hydrogène pourra soit réagir avec l'ozone (**C3–5**), soit avec le rayonnement UV pour former des radicaux hydroxyle (**C3–1**).

$$O_3 + H_2O + h\nu \rightarrow H_2O_2 + O_2 \qquad (C3-6)$$

- La sonolyse est une méthode qui fait partie des techniques émergentes pour la dépollution de l'eau. Le principe est d'utiliser des ultrasons qui génèrent des microbulles de cavitation. Ces bulles vont ensuite se propager, et lors de leur éclatement, une forte pression est observée, conduisant à des réactions de dégradation :

$$H_2O +))) \rightarrow HO^{\bullet} + H^{\bullet} \qquad (C3-7)$$

- D'autres méthodes plus exotiques ont aussi trouvé leur place dans les procédés d'oxydation avancés, comme l'association microonde/H_2O_2, les rayons X ou gamma, l'utilisation d'eau supercritique ou l'oxydation électrochimique.

- Enfin, la méthode à laquelle nous allons plus particulièrement nous intéresser est la photodégradation. Plusieurs méthodes sont disponibles en fonction du type de composé utilisé. L'utilisation de photosensibilisateur induit une formation de ROS par les mécanismes présentés plus tôt (**Section I. 1**), alors que les photocatalyseurs comme le TiO_2 induisent la création d'une paire d'électron/trou, entrainant la formation des ROS.

III.2.a. Photocatalyse

Les oxydes métalliques tels que TiO_2 [106,107] ou ZnO [108–113] ont été largement étudiés pour leurs applications en photocatalyse, notamment dans la dépollution de l'eau. Le mécanisme impliqué est résumé en **Figure IC-14**. Pour amorcer la photocatalyse, le semi-conducteur doit être irradié avec une lumière de longueur d'onde d'énergie supérieure au gap électronique du semi-conducteur. Un électron passe alors de la bande de valence, en laissant un trou (ou hole en anglais, h^+), à la bande de conduction où il y aura donc présence d'un électron (**Eq. C3–8**). Il se crée alors une paire électron/trou (e^-/h^+). Le trou va réagir avec l'eau en photo-oxydation (**Eq. C3–9 et C3–10**) pour former directement le radical hydroxyle, et l'électron va réagir avec l'oxygène en photo-réduction pour former le radical hydroxyle après plusieurs étapes (**Eq. C3–11 et C3–15**).

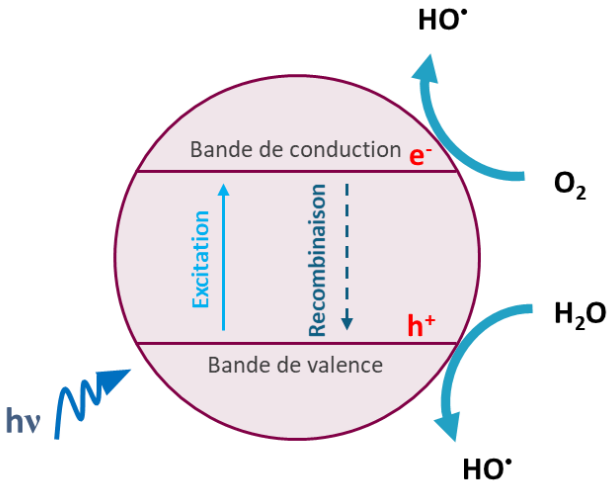

***Figure IC-14** : Schéma du principe de la photocatalyse.*

$$TiO_2 + h\nu \rightarrow TiO_2\,(e^-) + TiO_2\,(h^+) \qquad (C3-8)$$

En photo-oxydation :

$$TiO_2\,(h^+) + H_2O \rightarrow TiO_2 + HO^\bullet + H^+ \qquad (C3-9)$$

$$TiO_2\,(h^+) + HO^- \rightarrow TiO_2 + HO^\bullet \qquad (C3-10)$$

En réduction :

$$TiO_2\,(e^-) + O_2 \rightarrow TiO_2 + {O_2}^{\bullet-} \qquad (C3-11)$$

$${O_2}^{\bullet-} + H^+ \rightarrow {HO_2}^\bullet \qquad (C3-12)$$

$$2\,{HO_2}^\bullet \rightarrow H_2O_2 + O_2 \qquad (C3-13)$$

$$TiO_2\,(e^-) + H_2O_2 \rightarrow HO^\bullet + HO^- \qquad (C3-14)$$

$$H_2O_2 + {O_2}^{\bullet-} \rightarrow HO^\bullet + HO^- + O_2 \qquad (C3-15)$$

D'autres catalyseurs ont également été développés pour la photodégradation de polluants, comme des oxydes métalliques (WO_3 [114]), des sulfures de métaux (ZnS [115,116] ou MoS_2 [117]), des titanates (BaTiO3 [118]), des tungstates (Bi_2WO_6 [119]), d'autres métallates (BiVO4 [120]) ou des semi-conducteurs non métalliques (g-C_3N_4 [121]).

Une autre méthode consiste à utiliser des polymères conducteurs. En effet, certains polymères sont dits conducteurs car ils possèdent des cycles aromatiques et/ou des doubles liaisons conjuguées permettant la fusion des niveaux énergétiques, et conduisant à une structure similaire à celle des semi-conducteurs inorganiques comme le silicium [122]. Ces polymères ont montré des capacités de dépollution par adsorption (comme le poly-aniline ou le poly-pyrrole) [123], ou en utilisant les mêmes mécanismes de paire électron/trou que les oxydes de métaux (comme le poly-éthylènedioxythiophène) [124] [125] (**Figure IC-15**).

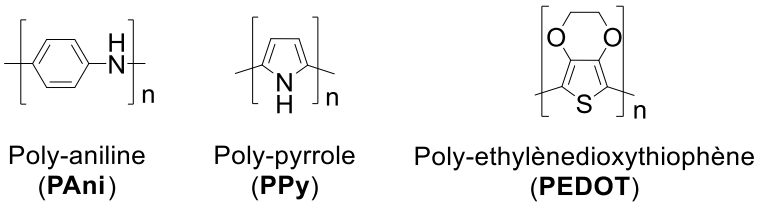

Poly-aniline (**PAni**) | Poly-pyrrole (**PPy**) | Poly-ethylènedioxythiophène (**PEDOT**)

***Figure IC-15** : Structure des polymères conducteurs présentés.*

De plus, la combinaison de polymères avec des photocatalyseurs permet une meilleure efficacité de dépollution, que ce soit avec l'utilisation de polymères conducteurs [126,127], grâce à un transfert de charge entre le polymère et le photocatalyseur, ou avec l'utilisation de polymères classiques acrylatés [128].

Les photocatalyseurs ont été largement utilisés pour la dépollution des eaux, mais leur usage nécessite généralement de travailler sous irradiation UV. Des études se sont penchées sur les méthodes pour permettre une photodégradation des polluants dans le visible.

Une des solutions est l'utilisation de nanoparticules greffées avec des métaux nobles, qui a déplacé le spectre d'absorption maximale de TiO_2 vers les longueurs d'onde du visible. Des nanoparticules de TiO_2 dopées en zirconium et en argent ont permis de dégrader des polluants présents dans l'eau tels que le nitrophénol, l'orange de méthyl et le bleu de méthylène en 30 minutes sous irradiation visible, en présence de borohydrure de sodium en tant qu'agent de réduction.[129] L'utilisation de nanoparticules d'or recouvertes de TiO_2 a également permis de très bonnes dégradation de polluants, en dégradant à 93% le phénol présent en solution après 180 min d'irradiation solaire. [130]

Enfin, tout comme pour les applications en antibactérien, l'utilisation de photosensibilisateurs produisant des ROS rend possible l'émergence de la photodégradation des composés organiques considérés comme des polluants dans le visible.

III.2.b. Photosensibilisation

Tout comme pour les applications des surfaces antibactériennes, les molécules possédant les propriétés de photosensibilisation, et donc capable de former des ROS, présentent un intérêt pour la photodégradation des polluants.

Des molécules connues pour être des photosensibilisateurs efficaces ont été utilisés pour la photodégradation homogène de polluants. Diverses phthalocyanines métallées (Al(III), Zn(Zn), Ga(III)), le rose Bengale, le bleu de méthylène, des diimides tétracarboxiliques chargées positivement ainsi que la porphyrine tétra-carboxyphényle ont participé à l'oxydation de différents phénols [131]. Des phénomènes d'agrégation des PS ont néanmoins contribué à la diminution de leur efficacité. Le

mécanisme proposé implique la formation d'oxygène singulet produit par les photosensibilisateurs, puis leur addition sur le phénol.

Plus tard, en 2001, Ozoemena *et al.* confirma la participation des mécanismes de type II pour la dégradation de phénol en présence de phthalocyanines, mais proposa également une contribution du mécanisme de type I selon la concentration en polluants.[132]

Divers photosensibilisateurs ont été utilisés en système homogène pour la dépollution de l'eau, comme le rose Bengale et la riboflavine pour la dégradation d'un fongicide (le carbendazine)[133], ou le bleu de méthylène pour la dégradation de médicaments (le diclofénac, le propranolol et le sulfaméthoxazole) [134]. La dégradation de ces médicaments a été très inégale, de 100%, 80% à 15% respectivement, et s'est montrée dépendante de la concentration initiale de bleu de méthylène, puisqu'une augmentation de la concentration à partir de 0.1 mg/L jusqu'à environ 2 mg/L a permis une augmentation de la dégradation.

Afin d'éviter le problème d'agrégation, et de permettre une meilleure récupération et une réutilisation des photosensibilisateurs, des systèmes comportant un PS supporté sur polymère ont vu le jour [126]. On peut citer par exemple une phthalocyanine greffée dans les pores d'une bentonite modifiée [135]. La bentonite est un adsorbant efficace pour les polluants organiques, qui va permettre de rapprocher le polluant, ici du phénol et des chlorophénols, de la phthalocyanine, capable de les dégrader par production d'oxygène singulet.

III.2.c. Porphyrines pour la dépollution de l'eau

Les porphyrines, ayant déjà prouvé leur propriété de photosensibilisateur dans le cas des surfaces antibactériennes, ont également été mises à profit pour le développement de surface dépolluantes. En effet, la simplicité de leur fonctionnalisation rend possible leur intégration dans de nombreux matériaux, et leur stabilité sous irradiation les rends pertinentes pour une utilisation dans de nombreux cycle de traitement des eaux.

Un polymère à base de porphyrines (PSBAZnPP) (**Figure IC-16**) [136] a montré une efficacité importante contre trois colorants organiques, à savoir l'orange de méthyl, le rouge de méthyl et le rouge Congo. Des dégradations de 96%, 95% et 94% respectivement ont été observées après seulement 60 minutes d'irradiation.

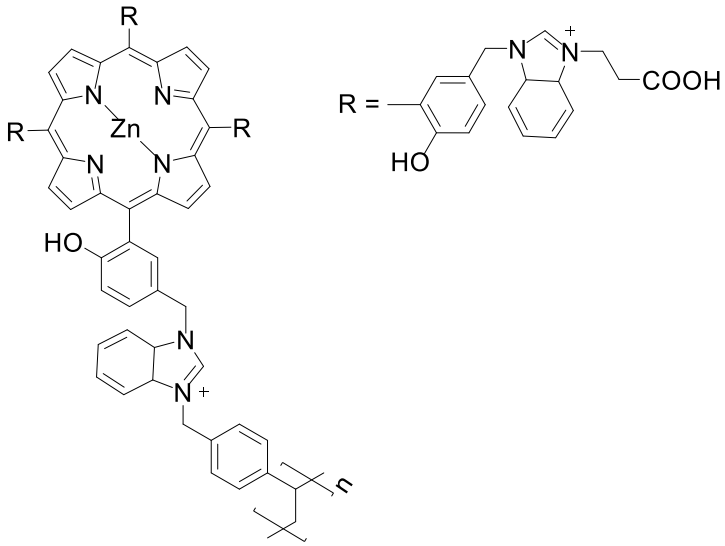

Figure IC-16 *: Structure du PSBAZnPP*

De même, l'étude de Gao *et al.* [137] présente le développement d'un polymère à base de porphyrines contenant du fer (FePPOP-1) (**Figure IC-17**), pour une combinaison des effets de photo-dégradation et de photo-Fenton. Les auteurs observent une dégradation de 100% de bleu de méthylène en 80 min.

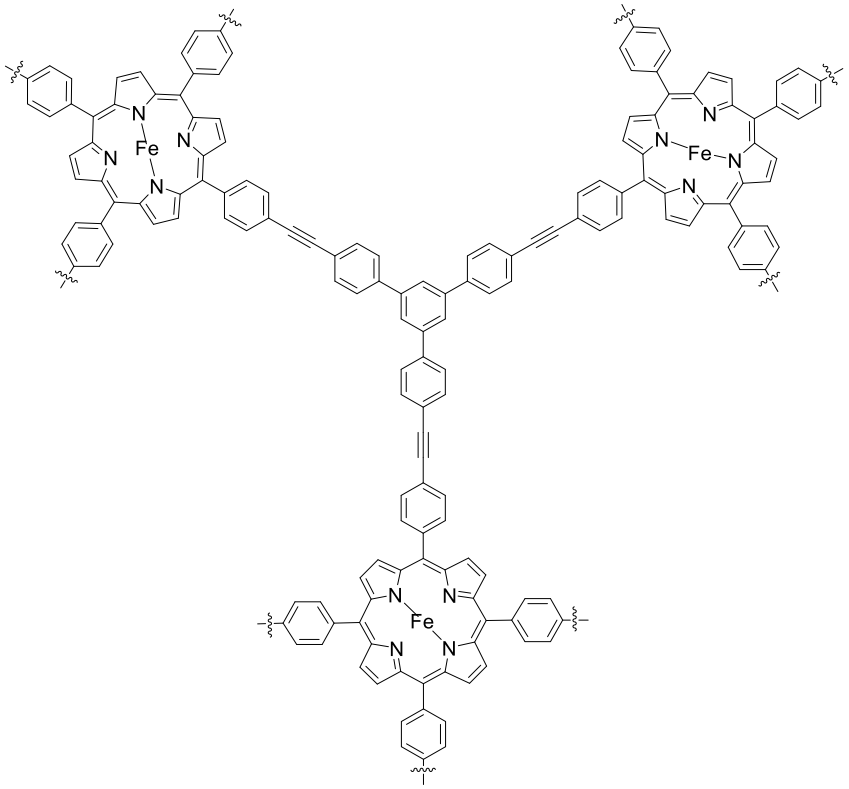

Figure IC-17 *: Structure de FePPOP-1*

Enfin, Lyubimenko *et al.* ont présenté la dépollution du bleu de méthylène à partir de la porphyrine de palladium Pd-TFPP (**Figure IC-18**) [138] incorporée dans un polymère de poly(vinylidène

fluoride) (PVDF). La dégradation du bleu de méthylène par formation d'oxygène singulet a atteint 83% en flux sous lumière verte de 528 nm. En 2022, la même équipe a présenté la dégradation de l' estradiol (une hormone stéroïdienne) [139] à partir de M-TFPP métallée avec différents métaux (Pd, Zn, Mn ou base libre) en flux et sous irradiation. En utilisant une lampe dont le spectre et l'intensité est équivalent au soleil, la dégradation de l'estradiol atteint 77% et 85% avec la porphyrine au zinc et sous forme de base libre respectivement, ce qui est équivalent à la porphyrine palladée. Cependant, sous irradiation réduite, la porphyrine complexée au zinc présente une moins bonne efficacité, mais une meilleure stabilité que celle au palladium.

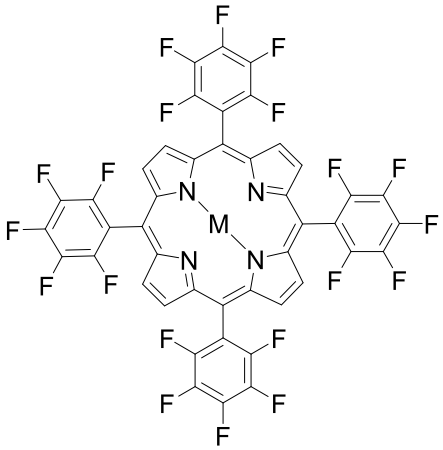

***Figure IC-18** : Structure de M-TFPP*

La photocatalyse de pesticides, colorants et médicaments utilisant des porphyrines supportées a fait l'objet d'une revue. [140] Il en ressort plusieurs critères importants. Tout d'abord, l'importance du métal à l'intérieur de la porphyrine a été évaluée. En effet, les porphyrines à base de cuivre greffées sur TiO_2 ont montré une meilleure capacité de dépollution du nitrophénol que les mêmes porphyrines à base de zinc ou de nickel greffées au TiO_2.[141] Cette différence est attribuée à un potentiel d'excitation plus proche de la bande de conduction de TiO_2 pour le cuivre. D'autres études arrivent aux mêmes résultats en comparant le cuivre avec le cobalt, le manganèse ou le fer [142–144] indiquant que Cu(II) donne de meilleurs taux de dégradation. Il semble que le cuivre ait tendance à gagner plus facilement un électron pour atteindre un état stable, et permet de séparer plus facilement ses paires électron-trou, donnant lieu à de meilleures capacités de photocatalyse. Enfin, l'ajout d'une faible quantité d'additif, comme le peroxyde d'hydrogène permet d'obtenir de meilleures photodégradations, car il permet une meilleure génération de ROS [136,145].

Les porphyrines ont déjà prouvé leur efficacité en production de ROS et la pertinence de leur utilisation en dépollution. Mais une autre propriété des porphyrines peut également être exploitée : leurs propriétés d'adsorption. En effet, la présence d'un cycle aromatique, permet des liaisons π-π avec des polluants, favorisant ainsi leur adsorption. Cet effet a été exploité pour la réalisation de polymères poreux organiques (POPs) à base de porphyrines [146], comme par exemple d'adsorption de bleu de méthylène par un polymère à base de porphyrines liées entre elles par des fonctions dihydroxynaphtalène [147]. De même, la présence d'atomes d'azotes dans les pyrroles des porphyrines libres peut induire la chélation d'un métal. Ainsi, dans leur étude sur l'extraction d'ions Cu (II) par des porphyrines, Jeong *et al.* ont pu démontrer par comparaison des spectres UV-Visible que le métal absorbé est bien chelaté aux atomes d'azotes de la porphyrine, traduisant la capacité des porphyrines

libres à purifier des eaux polluées par des métaux lourds. Enfin, ces deux effets peuvent être combinés, pour donner lieu à un système permettant de dépolluer des colorants (par exemple la rhodamine B) et des métaux en même temps [148] .

III. 3. Conclusion

La purification de l'eau représente un enjeu important, et la photodégradation des polluants se présente comme une solution efficace. Le principal avantage de cette stratégie est la dégradation spontanée des polluants, sans besoin d'un second traitement des boues en aval de la purification de l'eau. Les matériaux photoactifs entrainent des dégradations importantes des polluants, tout en permettant une réutilisation des composés actifs.

Plusieurs matériaux ont été développés, à base de photocatalyseurs, comme TiO_2 ou ZnO, ou de photosensibilisateurs. Les porphyrines ont montré une bonne efficacité, mais semblent n'avoir été que peu exploitées. De plus, même si des systèmes polymériques contenant des porphyrines ont démontré une certaine efficacité, aucun système photosynthétisé n'a encore été développé pour la dépollution de l'eau.

IV. Références

1 W. M. Sharman, C. M. Allen and J. E. van Lier, Drug Discov. Today, 1999, 4, 507–517.
2 M. Ochsner, J. Photochem. Photobiol. B: Biol., 1997, 39, 1–18.
3 K. Żamojć, M. Zdrowowicz, P. B. Rudnicki-Velasquez, K. Krzymiński, B. Zaborowski, P. Niedziałkowski, D. Jacewicz and L. Chmurzyński, Free Radic. Res., 2017, 51, 38–46.
4 A. Blacha-Grzechnik, M. Krzywiecki, R. Motyka and M. Czichy, J. Phys. Chem. C, 2019, 123, 25915–25924.
5 B. H. J. Bielski, G. G. Shiue and S. Bajuk, J. Phys. Chem., 1980, 84, 830–833.
6 G. O'Toole, H. B. Kaplan and R. Kolter, Annu. Rev. Microbiol., 2000, 54, 49–79.
7 D. Monroe, PLoS Biol., 2007, 5, e307.
8 M. B. Miller, .
9 A. Kramer, I. Schwebke and G. Kampf, BMC Infect. Dis., 2006, 6, 130.
10 Santé Publique France, Principaux résultats de l'enquête nationale de prévalence 2022 des infections nosocomiales et des traitements anti-infectieux en établissement de santé, 2023.
11 S. Quintavalla and L. Vicini, Meat Sci., 2002, 62, 373–380.
12 V. Vishwakarma, J. Basic Microbiol., 2020, 60, 198–206.
13 W. A. Rutala, 2008, 163.
14 X. Yang, J. Hou, Y. Tian, J. Zhao, Q. Sun and S. Zhou, Sci. China Technol. Sci., 2022, 65, 1000–1010.
15 A. M. C. Maan, A. H. Hofman, W. M. De Vos and M. Kamperman, Adv. Funct. Mater., 2020, 30, 2000936.
16 S. I. Jeon, J. H. Lee, J. D. Andrade and P. G. De Gennes, J. Colloid Interface Sci., 1991, 142, 149–158.
17 J. Hu, Y. Ding, B. Tao, Z. Yuan, Y. Yang, K. Xu, X. Li, P. liu and K. Cai, Bioact. Mater., 2022, 18, 228–241.
18 J. O. Noyce, H. Michels and C. W. Keevil, J. Hosp. Infect., 2006, 63, 289–297.
19 N. Silvestry-Rodriguez, E. E. Sicairos-Ruelas, C. P. Gerba and K. R. Bright, Rev. Environ. Contam. T, 2007, 191, 23–45.
20 B. Le Ouay and F. Stellacci, Nano Today, 2015, 10, 339–354.
21 P. Sautrot-Ba, A. Al Mousawi, J. Lalevee, P.-E. Mazeran, S. J. Park, I.-K. Kang, M. Laurent-Brocq, V. Langlois and D.-L. Versace, Chem. Afr., 2019, 2, 241–251.
22 L. Tamayo, M. Azócar, M. Kogan, A. Riveros and M. Páez, Mater. Sci. Eng. C, 2016, 69, 1391–1409.
23 N.-F. Chen, Y.-H. Liao, P.-Y. Lin, W.-F. Chen, Z.-H. Wen and S. Hsieh, Int. J. Mol. Sci., 2021, 22, 12913.
24 M. Thukkaram, S. Sitaram, S. kumar Kannaiyan and G. Subbiahdoss, Int. J. Biomater., 2014, 2014, e716080.
25 S. Hayat, S. Muzammil, M. H. Rasool, Z. Nisar, S. Z. Hussain, A. N. Sabri and S. Jamil, J Microbiol Immunol Infect, 2018, 62, 211–220.
26 R. Rawashdeh and Y. Haik, .
27 P. Makvandi, R. Jamaledin, M. Jabbari, N. Nikfarjam and A. Borzacchiello, Dent. Mater. J., 2018, 34, 851–867.
28 A. Popa, C. M. Davidescu, R. Trif, Gh. Ilia, S. Iliescu and Gh. Dehelean, React. Funct. Polym., 2003, 55, 151–158.
29 F. Ferrero, M. Periolatto, C. Vineis and A. Varesano, Carbohydr. Polym., 2014, 103, 207–212.
30 M. J. Al-Awady, A. Fauchet, G. M. Greenway and V. N. Paunov, J. Mater. Chem. B, 2017, 5, 7885–7897.
31 C. Elian, S. A. Andaloussi, R. Moilleron, J.-W. Decousser, C. Boyer and D.-L. Versace, J. Mater. Chem. B, 2022, 10, 9081–9124.
32 T. Modjinou, D. L. Versace, S. Abbad Andaloussi, V. Langlois and E. Renard, Bioeng., 2020, 7, 13.
33 M. L. Faleiro, .
34 M. R. Hamblin and T. Hasan, Photochem. Photobiol. Sci., 2004, 3, 436–450.
35 X. Ding, Q. Xu, F. Liu, P. Zhou, Y. Gu, J. Zeng, J. An, W. Dai and X. Li, Cancer Lett., 2004, 216, 43–54.

36 M. Cho, H. Chung, W. Choi and J. Yoon, Appl. Environ. Microbiol., 2005, 71, 270–275.
37 Solar Energy, 2008, 82, 1107–1117.
38 J. C. Ireland, P. Klostermann, E. W. Rice and R. M. Clark, Appl. Environ. Microbiol., 1993, 59, 1668–1670.
39 D. Mitoraj, A. Jańczyk, M. Strus, H. Kisch, G. Stochel, P. B. Heczko and W. Macyk, Photochem. Photobiol. Sci., 2007, 6, 642–648.
40 K. Sunada, T. Watanabe and K. Hashimoto, J. Photochem. Photobiol. A: Chem., 2003, 156, 227–233.
41 M. J. Davies, BBRC, 2003, 305, 761–770.
42 H. S. El-Beltagi and H. I. Mohamed, Not. Bot. Horti. Agrobo., 2013, 41, 44–57.
43 J. Kiwi and V. Nadtochenko, J. Phys. Chem. B, 2004, 108, 17675–17684.
44 H. R. Rawls and P. J. Van Santen, J. Am. Oil Chem. Soc., 1970, 47, 121–125.
45 Y. W. Cheng, R. C. Y. Chan and P. K. Wong, Water Res., 2007, 41, 842–852.
46 J. A. Ibáñez, M. I. Litter and R. A. Pizarro, J. Photochem. Photobiol. A: Chem., 2003, 157, 81–85.
47 T. Maisch, Photochem. Photobiol. Sci., 2015, 14, 1518–1526.
48 F. Vatansever, W. C. M. A. de Melo, P. Avci, D. Vecchio, M. Sadasivam, A. Gupta, R. Chandran, M. Karimi, N. A. Parizotto, R. Yin, G. P. Tegos and M. R. Hamblin, FEMS Microbiol. Rev., 2013, 37, 955–989.
49 J. S. Bellin, S. C. Mohos and G. Oster, Cancer Res., 1961, 21, 1365–1371.
50 M. D. Daniell and J. S. Hill, ANZ J. Surg., 1991, 61, 340–348.
51 T. Dai, Y.-Y. Huang and M. R. Hamblin, Photodiagnosis Photodyn., 2009, 6, 170–188.
52 M. E. Jiménez-Hernández, F. Manjón, D. García-Fresnadillo and G. Orellana, Solar Energy, 2006, 80, 1382–1387.
53 G. Carré, L. Garnier, J. Moeller-Siegert, J.-P. Gies, V. Keller, P. André and N. Keller, RSC Adv., 2015, 5, 38859–38867.
54 L. Jiang, C. R. R. Gan, J. Gao and X. J. Loh, Small, 2016, 12, 3609–3644.
55 D.-L. Versace, L. Breloy, E. Palierse and T. Coradin, J. Mater. Chem. B, 2021, 9, 9624–9641.
56 K. H. Hong and G. Sun, Carbohydr. Polym., 2008, 71, 598–605.
57 J. Zhuo and G. Sun, ACS Appl. Mater. Interfaces, 2013, 5, 10830–10835.
58 L. El-Khordagui, N. El-Sayed, S. Galal, H. El-Gowelli, H. Omar and M. Mohamed, Int. J. Pharm., 2017, 520, 139–148.
59 Y. Zhu, C. Xu, N. Zhang, X. Ding, B. Yu and F.-J. Xu, Adv. Funct. Mater., 2018, 28, 1706709.
60 L. Su, J. Huang, H. Li, Y. Pan, B. Zhu, Y. Zhao and H. Liu, Int. J. Biol. Macromol., 2021, 172, 231–240.
61 L. George, A. Hiltunen, V. Santala and A. Efimov, J. Inorg. Biochem., 2018, 183, 94–100.
62 L. George, A. Müller, B. Röder, V. Santala and A. Efimov, Dyes Pigm., 2017, 147, 334–342.
63 M. Condat, P.-E. Mazeran, J.-P. Malval, J. Lalevée, F. Morlet-Savary, E. Renard, V. Langlois, S. A. Andalloussi and D.-L. Versace, RSC Adv., 2015, 5, 85214–85224.
64 D.-L. Versace, G. Moran, M. Belqat, A. Spangenberg, R. Méallet-Renault, S. Abbad-Andaloussi, V. Brezová and J.-P. Malval, ACS Appl. Mater. Interfaces, 2020, 12, 5050–5057.
65 P. Sautrot-Ba, J.-P. Malval, M. Weiss-Maurin, J. Paul, A. Blacha-Grzechnik, S. Tomane, P.-E. Mazeran, J. Lalevée, V. Langlois and D.-L. Versace, ACS Sustain. Chem. Eng., 2018, 6, 104–109.
66 M. Condat, J. Babinot, S. Tomane, J.-P. Malval, I.-K. Kang, F. Spillebout, P.-E. Mazeran, J. Lalevée, S. A. Andalloussi and D.-L. Versace, RSC Adv., 2016, 6, 18235–18245.
67 L. Breloy, V. Brezová, A. Blacha-Grzechnik, M. Presset, M. S. Yildirim, I. Yilmaz, Y. Yagci and D.-L. Versace, Macromolecules, 2020, 53, 112–124.
68 P. Sautrot-Ba, A. Contreras, S. A. Andaloussi, T. Coradin, C. Hélary, N. Razza, M. Sangermano, P.-E. Mazeran, J.-P. Malval and D.-L. Versace, J. Mater. Chem. B, 2017, 5, 7572–7582.
69 P. Sautrot-Ba, V. Brezová, J.-P. Malval, A. Chiappone, L. Breloy, S. Abbad-Andaloussi and D.-L. Versace, Polym. Chem., 2021, 12, 2627–2642.
70 L. Breloy, C. A. Ouarabi, A. Brosseau, P. Dubot, V. Brezova, S. Abbad Andaloussi, J.-P. Malval and D.-L. Versace, ACS Sustain. Chem. Eng., 2019, 7, 19591–19604.

71 C. Elian, B. Quienne, S. Lajnef, F. Peyrot, R. Moilleron, S. Abbad Andaloussi, S. Caillol and D.-L. Versace, Eur. Polym. J., 2023, 112369.
72 N. Tsolekile, S. Nelana and O. S. Oluwafemi, Molecules, 2019, 24, 2669.
73 Y. Zhang and J. F. Lovell, Theranostics, 2012, 2, 905–915.
74 M. Athar, H. Mukhtar and D. R. Bickers, J. Invest. Dermatol., 1988, 90, 652–657.
75 J. Bozja, J. Sherrill, S. Michielsen and I. Stojiljkovic, J. Polym. Sci., Part A: Polym. Chem., 2003, 41, 2297–2303.
76 R. Rahimi, F. Fayyaz and M. Rassa, Mater. Sci. Eng. C, 2016, 59, 661–668.
77 J. P. C. Tomé, M. G. P. M. S. Neves, A. C. Tomé, J. A. S. Cavaleiro, M. Soncin, M. Magaraggia, S. Ferro and G. Jori, J. Med. Chem., 2004, 47, 6649–6652.
78 S. F. Musolino, F. Shatila, G. M. O. Tieman, A. C. Masarsky, M. C. Thibodeau, J. E. Wulff and H. L. Buckley, ACS Omega, 2022, 7, 29517–29525.
79 K. Li, P. Berton, S. P. Kelley and R. D. Rogers, Biomacromolecules, 2018, 19, 3291–3300.
80 J. Mosinger, K. Lang, J. Hostomský, J. Franc, J. Sýkora, M. Hof and P. Kubát, J. Phys. Chem. B, 2010, 114, 15773–15779.
81 V. Lukseviciute and Z. Luksiene, J. Photochem. Photobiol. B: Biol., 2020, 202, 111721.
82 M. Krouit, R. Granet, P. Branland, B. Verneuil and P. Krausz, BMCL, 2006, 16, 1651–1655.
83 C. Brady, S. E. J. Bell, C. Parsons, S. P. Gorman, D. S. Jones and C. P. McCoy, J. Phys. Chem. B, 2007, 111, 527–534.
84 C. Parsons, C. P. McCoy, S. P. Gorman, D. S. Jones, S. E. J. Bell, C. Brady and S. M. McGlinchey, Biomater., 2009, 30, 597–602.
85 P. R. Judzewitsch, N. Corrigan, E. H. H. Wong and C. Boyer, Angew. Chem., 2021, 133, 24450–24458.
86 H. Marcille, J.-P. Malval, M. Presset, N. Bogliotti, A. Blacha-Grzechnik, V. Brezová, Y. Yagci and D.-L. Versace, Polym. Chem., 2020, 11, 4237–4249.
87 R. Connor and M. Miletto, UN World Water Development Report 2023, 2023.
88 D. Bixio, C. Thoeye, J. De Koning, D. Joksimovic, D. Savic, T. Wintgens and T. Melin, Desalination, 2006, 187, 89–101.
89 A. Joss, S. Zabczynski, A. Göbel, B. Hoffmann, D. Löffler, C. S. McArdell, T. A. Ternes, A. Thomsen and H. Siegrist, Water Res., 2006, 40, 1686–1696.
90 Y. Luo, W. Guo, H. H. Ngo, L. D. Nghiem, F. I. Hai, J. Zhang, S. Liang and X. C. Wang, Sci. Total Environ., 2014, 473–474, 619–641.
91 M. J. M. Bueno, M. J. Gomez, S. Herrera, M. D. Hernando, A. Agüera and A. R. Fernández-Alba, Environmental Pollution, 2012, 164, 267–273.
92 R. Loos, B. M. Gawlik, G. Locoro, E. Rimaviciute, S. Contini and G. Bidoglio, Environ. Pollut., 2009, 157, 561–568.
93 D. Fatta-Kassinos, S. Meric and A. Nikolaou, Anal. Bioanal. Chem., 2011, 399, 251–275.
94 M. Grassi, L. Rizzo and A. Farina, Environ. Sci. Pollut. Res., 2013, 20, 3616–3628.
95 C. Bauer, P. Jacques and A. Kalt, J. Photochem. Photobiol. A: Chem., 2001, 140, 87–92.
96 Liste des Valeurs Toxicologiques de Référence (VTR) de l'Anses, https://www.anses.fr/fr/content/liste-des-valeurs-toxicologiques-de-r%C3%A9f%C3%A9rence-vtr-de-l%E2%80%99anses, (accessed October 29, 2023).
97 Legifrance, Arrêté du 11 janvier 2007 relatif aux limites et références de qualité des eaux brutes et des eaux destinées à la consommation humaine mentionnées aux articles R. 1321-2, R. 1321-3, R. 1321-7 et R. 1321-38 du code de la santé publique - Légifrance, 2007.
98 H. B. Mansour, D. Barillier, D. Corroler, K. Ghedira, L. Chekir-Ghedira and R. Mosrati, Environ. Toxicol. Chem., 2009, 28, 489–495.
99 N. Puvaneswari, J. Muthukrishnan and P. Gunasekaran, Indian J Exp Biol.
100 A. Gottlieb, C. Shaw, A. Smith, A. Wheatley and S. Forsythe, J. Biotechnol., 2003, 101, 49–56.
101 A. Gičević, L. Hindija and A. Karačić, in CMBEBIH 2019, eds. A. Badnjevic, R. Škrbić and L. Gurbeta Pokvić, Springer International Publishing, Cham, 2020, vol. 73, pp. 581–587.

102 H. Zhou and D. W. Smith, Can. J. Civ. Eng., 2001, 28, 49–66.
103 K. A. Yongabi, .
104 Y. Deng and R. Zhao, Curr. Pollut. Rep., 2015, 1, 167–176.
105 M. Moradi, A. Elahinia, Y. Vasseghian, E.-N. Dragoi, F. Omidi and A. Mousavi Khaneghah, J. Environ. Chem. Eng., 2020, 8, 104330.
106 N. Daneshvar, D. Salari and A. R. Khataee, J. Photochem. Photobiol. A: Chem., 2003, 157, 111–116.
107 S. Nouacer and R. Djellabi, Environ. Sci. Pollut. Res., , DOI:10.1007/s11356-022-23772-5.
108 M. Le Pivert, B. Zerelli, N. Martin, M. Capochichi-Gnambodoe and Y. Leprince-Wang, Constr Build Mater, 2020, 257, 119592.
109 K. M. Lee, C. W. Lai, K. S. Ngai and J. C. Juan, Water Res., 2016, 88, 428–448.
110 N. Martin, V. Lacour, C. M.-T. Perrault, E. Roy and Y. Leprince-Wang, React. Chem. Eng., 2022, 7, 750–757.
111 Y. G. Habba, M. Capochichi-Gnambodoe, L. Serairi and Y. Leprince-Wang, Phys. Status Solidi B Basic Res., 2016, 253, 1480–1484.
112 Y. Leprince-Wang, N. Martin, Y. Ghozlane Habba, M. L. Pivert and M. Capochichi-Gnambodoe, NanoWorld J, , DOI:10.17756/nwj.2019-074.
113 M. Le Pivert, R. Poupart, M. Capochichi-Gnambodoe, N. Martin and Y. Leprince-Wang, Microsyst. Nanoeng., 2019, 5, 1–7.
114 S. G. Kumar and K. S. R. K. Rao, Appl. Surf. Sci., 2017, 391, 124–148.
115 G.-J. Lee and J. J. Wu, Powder Technol., 2017, 318, 8–22.
116 C. Mondal, A. Singh, R. Sahoo, A. K. Sasmal, Y. Negishi and T. Pal, New J. Chem., 2015, 39, 5628–5635.
117 C. Wang, H. Lin, Z. Xu, H. Cheng and C. Zhang, RSC Adv., 2015, 5, 15621–15626.
118 M. Rastogi, H. S. Kushwaha and R. Vaish, Electron. Mater. Lett., 2016, 12, 281–289.
119 J. Zhang, X. Yuan, L. Jiang, Z. Wu, X. Chen, H. Wang, H. Wang and G. Zeng, J. Colloid Interface Sci., 2018, 511, 296–306.
120 S. M. Thalluri, S. Hernández, S. Bensaid, G. Saracco and N. Russo, Appl. Catal. B: Environ., 2016, 180, 630–636.
121 C. Zhang, Y. Li, D. Shuai, Y. Shen, W. Xiong and L. Wang, Chemosphere, 2019, 214, 462–479.
122 P.-H. Aubert and C. Plesse, L'actualité scientifique, 2017.
123 J. Stejskal, Chem. Pap., 2020, 74, 1–54.
124 S. Ghosh, N. A. Kouame, S. Remita, L. Ramos, F. Goubard, P.-H. Aubert, A. Dazzi, A. Deniset-Besseau and H. Remita, Sci. Rep., 2016, 5, 18002.
125 C. Lei, Y. Guo, W. Guan and G. Yu, J. Polym. Sci., 2021, 59, 3084–3099.
126 M. Nowakowska and K. Szczubiałka, Polym. Degrad. Stab., 2017, 145, 120–141.
127 U. Riaz, S. M. Ashraf and J. Kashyap, Mater. Res. Bull., 2015, 71, 75–90.
128 M. Benltifa, C. Brahmi, F. Dumur, L. Limousy, L. Bousselmi and J. Lalevée, Eur. Polym. J., 2022, 181, 111660.
129 S. Naraginti, F. B. Stephen, A. Radhakrishnan and A. Sivakumar, Spectroc. Acta A, 2015, 135, 814–819.
130 A. Shet and S. K. Vidya, Solar Energy, 2016, 127, 67–78.
131 R. Gerdes, D. Wöhrle, W. Spiller, G. Schneider, G. Schnurpfeil and G. Schulz-Ekloff, J. Photochem. Photobiol. A: Chem., 1997, 111, 65–74.
132 K. Ozoemena, N. Kuznetsova and T. Nyokong, J. Photochem. Photobiol. A: Chem., 2001, 139, 217–224.
133 J. P. Escalada, A. Pajares, J. Gianotti, W. A. Massad, S. Bertolotti, F. Amat-Guerri and N. A. García, Chemosphere, 2006, 65, 237–244.
134 Y. Ye, Y. Luo, H. Bruning, D. Yntema and H. H. M. Rijnaarts, J. Photochem. Photobiol. A: Chem., 2017, 348, 96–101.
135 Z. Xiong, Y. Xu, L. Zhu and J. Zhao, Environ. Sci. Tech., 2005, 39, 651–657.
136 V. B. Khajone and P. R. Bhagat, Res. Chem. Intermed., 2020, 46, 783–802.

137 W. Gao, J. Tian, Y. Fang, T. Liu, X. Zhang, X. Xu and X. Zhang, Chemosphere, 2020, 243, 125334.
138 R. Lyubimenko, D. Busko, B. S. Richards, A. I. Schäfer and A. Turshatov, ACS Appl. Mater. Interfaces, 2019, 11, 31763–31776.
139 R. Lyubimenko, B. S. Richards, A. I. Schäfer and A. Turshatov, J. Membr. Sci, 2022, 642, 119981.
140 S. Silvestri, A. R. Fajardo and B. A. Iglesias, Environ. Chem. Lett., 2022, 20, 731–771.
141 W. Sun, J. Li, G. Yao, F. Zhang and J.-L. Wang, Appl. Surf. Sci., 2011, 258, 940–945.
142 G. Granados-Oliveros, E. A. Páez-Mozo, F. M. Ortega, C. Ferronato and J.-M. Chovelon, Appl. Catal. B: Environ., 2009, 89, 448–454.
143 X. Zhao, X. Liu, M. Yu, C. Wang and J. Li, Dyes Pigm., 2017, 136, 648–656.
144 X.-T. Zhou, H.-B. Ji and X.-J. Huang, Molecules, 2012, 17, 1149–1158.
145 G. Yao, J. Li, Y. Luo and W. Sun, J. Mol. Catal. A: Chem., 2012, 361–362, 29–35.
146 Y. Wang, X. Cui, P. Zhang, Y. Wang and W. Lu, Environ. Technol. Innov., 2023, 29, 102972.
147 T. Liu, L. Jing, L. Cui, Q. Liu and X. Zhang, Chemosphere, 2018, 212, 1038–1046.
148 Y. Chen, Y. Fang, J. Yu, W. Gao, H. Zhao and X. Zhang, J. Hazard. Mater., 2021, 406, 124769.

Partie D : Méthodes de chimie quantique

Afin de comprendre la relation structure-propriété et de prévoir les propriétés photochimiques, pour en déduire les capacités de photopolymérisation des molécules synthétisées dans le cadre de ce travail, une approche par modélisation de ces propriétés des systèmes moléculaires étudiés présente de nombreux avantages. En effet, une étude préparatoire permet de prédire les propriétés physico-chimiques des composés, et donc d'éliminer les candidats à priori non intéressants pour l'application visée et ainsi d'éviter des synthèses et analyses expérimentales, plus longues et plus coûteuses.

I. Introduction à la chimie théorique

I. 1. Les méthodes de chimie quantique

La chimie quantique repose sur la résolution de l'équation de Schrödinger. Cette équation décrit le mouvement des électrons et des noyaux dans une molécule. Le système étudié, ici une porphyrine, est composée de *n* électrons et de *N* noyaux de masses respectives m_e et m_N. L'état électronique de ce système est décrit par une fonction d'onde Ψ. La fonction d'onde se calcule en résolvant l'équation de Schrödinger ici écrite indépendante du temps :

$$\hat{\mathrm{H}}\Psi = \left[-\frac{\bar{h}^2}{2m}\nabla^2 + V(r)\right]\Psi(\mathrm{r}) = \mathrm{E}\Psi \qquad (D-1)$$

En prenant en compte l'hamiltonien :

$$\hat{\mathrm{H}} = -\frac{\bar{h}^2}{2m}\nabla^2 + V(r) \qquad (D-2)$$

Où le premier terme représente l'énergie cinétique de la particule, et le deuxième terme correspond aux forces d'attraction ou de répulsion appliquées à la particule.

L'équation de Schrödinger ne peut être résolue exactement que pour un système à un électron. Des approximations sont donc faites pour résoudre l'équation d'un système avec plusieurs composants. Une des principales approximations est celle de Born-Oppenheimer, qui permet de simplifier drastiquement l'équation de Schrödinger. Elle permet de découpler le mouvement des électrons de celui des noyaux, du fait de leurs masses très différentes. En effet, les noyaux ont un mouvement très lent comparé aux électrons, et le déplacement de ceux-ci peut donc être considéré comme instantané par rapport à celui des noyaux. On peut donc simplifier l'équation de Schrödinger en résolvant la partie purement électronique :

$$\widehat{\mathrm{H_e}}\Psi_\mathrm{e} = \mathrm{E_e}\Psi_\mathrm{e} \qquad (\mathrm{D}-3)$$

$$\text{avec } \widehat{\mathrm{H_e}} = \hat{\mathrm{T}}_\mathrm{e} + \hat{\mathrm{V}}_\mathrm{Ne} + \hat{\mathrm{V}}_\mathrm{ee} \qquad (D-4)$$

Cependant, cette simplification n'est pas suffisante pour pouvoir résoudre l'équation, et deux principales méthodes de calculs ont été développées. Les méthodes *ab-initio* qui se concentrent sur la fonction d'onde électronique, avec pour principale méthode la méthode de Hartree-Fock et ses méthodes de corrections dites post-Hartree-Fock, et les méthodes basées sur la densité électronique (théorie de la fonctionnelle de la densité (DFT)) que nous avons utilisé pour ces travaux de thèse.

I. 2. Théorie de la fonctionnelle de densité (DFT)

La théorie de la fonctionnelle de densité (DFT) est basée sur les travaux préliminaires de Thomas et Fermi [1] dans les années 30, qui ont considéré la densité électronique globale de la molécule au lieu de considérer chaque électron individuellement. Ces travaux ont ensuite été repris par Hohenberg et Kohn en 1964 [2] qui ont montré un lien entre l'énergie fondamentale d'un système et sa densité électronique. En 1965, ces travaux sont complétés par une série d'équations monoélectroniques par Kohn et Sham, ce qui permet d'obtenir la densité électronique d'un système et ainsi en déduire son énergie totale [3]. Cette méthode permet de corriger une approximation dans la méthode de Hartree-Fock, qui sous-estime l'énergie d'interaction entre les électrons. Kohn et Sham définissent alors l'énergie d'échange-corrélation, qui prend mieux en compte cette interaction. Le terme échange vient principalement de l'exclusion de Pauli et correspond aux interactions entre électrons de même spin alors que le terme corrélation correspond aux interactions de répulsion entre deux électrons, indépendamment de leurs spins. Une fonction a été développée pour approximer ces énergies, qui correspond à la fonction d'échange-corrélation.

Différentes méthodes de DFT ont été développées au cours du temps, en fonction des approximations de la fonctionnelle d'échange-corrélation. Leur nom correspond généralement aux initiales des auteurs. Deux principales méthodes sont utilisées :

- L'approximation de la densité locale : Cette méthode suppose une densité électronique localement uniforme (*Local Density Approximation*), comme dans le cas d'un gaz uniforme d'électrons. Un deuxième modèle, LSDA (*Local Spin Density Approximation*) permet des calculs sans contrainte de spin (*unrestricted*). Différentes méthodes existent comme SVWN (en échange : Slater, et en corrélation : Vosko, Wilk, Nusair [4]) ou SVWN5. Ces méthodes permettent d'obtenir de bonnes propriétés moléculaires comme la géométrie ou les fréquences, mais d'assez mauvaises données énergétiques.

- L'approximation du gradient généralisé et les fonctionnelles hybrides : Ces méthodes permettent de prendre en compte le gradient électronique en plus de sa valeur locale. La partie échange peut être basée sur la fonctionnelle de Becke (B), et la partie corrélation sur la fonctionnelle de Lee, Yang et Parr (LYP [5]) ou celle de Perdew-Wang (PW) pour donner les fonctionnelles BLYP, BPW86 ou BPW91. Enfin, la combinaison empirique de différentes méthodes ont permis l'essor des méthodes hybrides, comme la méthode de « Becke à trois paramètres » (B3), et ont ainsi permis le développement de différentes fonctionnelles hybrides. On peut compter par exemple la B3LYP, la CAM-B3LYP [6] qui prend en compte les interactions à longue distance, et d'autres comme la M06-2X [7], ou les PBE0 [8] et HSE06 [9] qui prennent en compte les corrections dîtes de PBE (Perdew, Burke et Ernzerhof [10]). La fonctionnelle B3LYP est souvent utilisée pour la modélisation de l'état fondamental des porphyrines [11–16], même si d'autres méthodes sont aussi utilisées [16–18].

I. 3. Bases utilisées

Les bases utilisées sont les ensembles de fonctions utilisées pour modéliser les orbitales moléculaires. Plusieurs bases peuvent être utilisées, comme les bases de Slater ou les bases gaussienne, qui sont plus adaptées pour la description de la densité électronique, en particulier, les bases de Pople. Ces bases, notées X-YZg, correspondent à un nombre X de gaussiennes primitives pour les orbitales atomiques de cœurs, et à une combinaison de deux fonctions, la première composée d'un nombre Y de fonctions gaussiennes primitives et la deuxième d'un nombre Z de fonctions gaussiennes.

Ces bases X-YZg sont qualifiées de bases double zêta à valence séparées, mais peuvent être augmentées à des bases triples ou quadruples zêta notées X-YZWg et X-YZWVg pour des niveaux plus complexes. Classiquement, on peut retrouver les bases 3-21g, 6-31g ou 6-311g.

Les bases peuvent également être complétées par l'ajout de fonctions diffuses ou de polarisation afin d'affiner les résultats des espèces étudiées.

Les fonctions de polarisation permettent d'augmenter la précision de la base en prenant en compte la déformation des orbitales de valence. Ceci est particulièrement utile pour décrire les déformations du nuage électronique lors d'une réaction. Elles sont notées avec un astérisque (*). Par exemple, dans la base 6-31G*, les fonctions polarisées sont ajoutées uniquement sur les atomes lourds, et sont ajoutées également sur les atomes légers (hydrogène et hélium) pour les bases doublement polarisées comme 6-31G**. Notons enfin que ces bases peuvent également être notées 6-31G(d) et 6-31G(d,p) respectivement.

Enfin, les fonctions diffuses permettent d'augmenter la taille du nuage électronique pour décrire les électrons fortement éloignés des noyaux atomiques, comme pour les molécules contenant des charges ou des doublets non liants. Les fonctions diffuses sont notées avec un signe plus (+). De la même façon que pour les fonctions diffuses, les bases contenant un seul + permettent uniquement de prendre en compte les atomes lourds, comme la base 6-31+G, là où la base 6-31++G prendra également en compte les bases diffuses des atomes légers.

I. 4. Fonctionnelle DFT en fonction du temps : TD-DFT

La DFT permet de calculer les énergies, la structure optimisée du système (celle de plus basse énergie), et de nombreuses propriétés de la molécule dans son état fondamental. Mais les molécules peuvent également présenter des états électroniques excités. Il est donc nécessaire d'utiliser une méthode de DFT dépendante du temps, la TD-DFT (Time-Dependent Density Functional Theory) [19], qui permet de décrire la densité électronique du système soumis à potentiel extérieur (donc une irradiation) et donc de décrire les états électroniquement excités.

La méthode de la TD-DFT permet d'obtenir les spectres électroniques d'absorption ou d'émission des molécules. Les spectres sont obtenus en calculant les énergies de transitions verticales des états excités, depuis les structures optimisées des états fondamentaux ou excités (**Figure ID-1A**). Le spectre est ensuite simulé avec une convolution gaussienne, en choisissant arbitrairement (ou afin d'être proche des largeurs de spectres expérimentaux) une valeur d'écart type σ (**Figure ID-1B**).

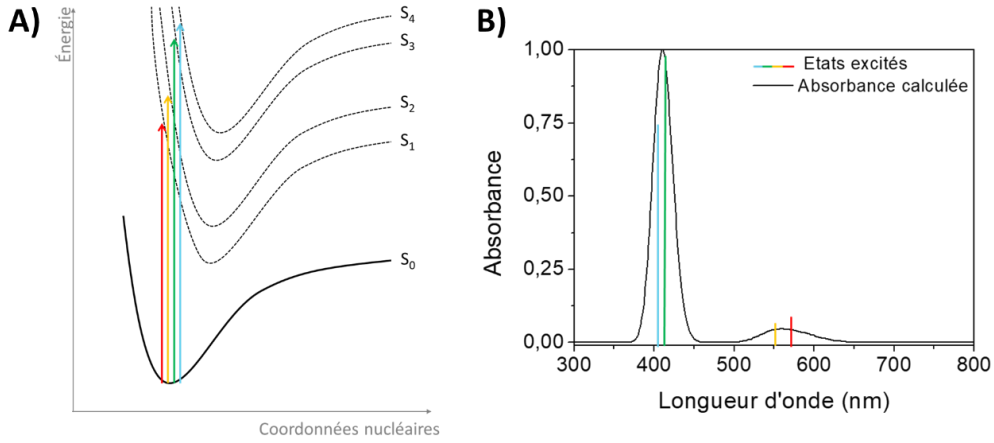

Figure ID-1 *: A) Schématisation des transitions verticales des différents états excités. B) Spectre d'absorption obtenus par déconvolution des énergies des états excités.*

I. 5. Vibration

Cependant, la méthode de TD-DFT ne permet pas de rendre parfaitement compte des spectres d'absorption et d'émission des molécules. En effet, cette méthode ne prend en compte que les énergies de transitions verticales, et néglige les effets de vibrations de la molécule. Pour y remédier, il faut considérer les états vibroniques pour chaque état excité (représentés en jaune dans la **Figure ID-2**). Dans la méthode TD-DFT, l'énergie prise en compte pour la transition $S_0 \rightarrow S_1$ correspond à l'énergie de la transition verticale qui permet de passer de la courbe de l'état électronique S_0 à celle de la courbe de l'état électronique S_1 à la géométrie d'équilibre de S_0 et donc correspond à la longueur de la flèche verticale sur le diagramme qui part du minimum de la courbe S_0 (approximation de Franck-Condon) et s'arrête lorsque la droite coupe la courbe de l'état S_1 (voir **Figure 74**). Lors d'un calcul de spectre résolu en vibration, on prend en compte les différents niveaux vibrationnels associés au nombre quantique vibrationnel ν' ($\nu' = 0, 1, 2$, etc.) pour l'état excités. Dans une première approximation, l'approximation de Franck-Condon (FC), les transitions associées sont faites à partir de la position d'équilibre de l'état fondamental (flèche vert) au point zéro d'énergie (zero point energy ZPE en anglais), niveau vibronique $\nu'' = 0$. Une deuxième approximation, l'approximation de Herzberg-Teller (HT), permet également une variation de la position des noyaux atomique dans l'état fondamental. Schématiquement, elle prend en compte une gamme plus large de transition (rectangle bleu dans la **Figure ID-2**).

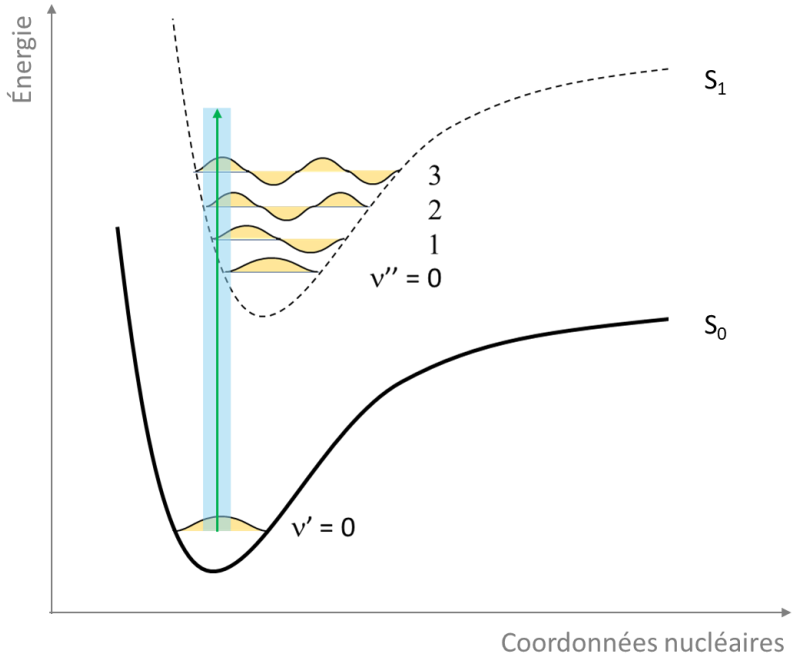

Figure ID-2 *: Schématisation des approximations de Franck-Condon (en vert) et de Herzberg-Teller (en bleu).*

I. 6. Effet du solvant

Dans les méthodes de calcul présentées ci-dessus, les molécules sont considérées comme dans un état gazeux, sans interaction avec le milieu. Cependant, les effets du solvant sont très importants pour les propriétés structurales ou d'absorption. Il est donc essentiel de prendre ces effets en compte. Deux modèles de solvatation peuvent être considérés. Le premier est le modèle explicite. Dans ce cas, les molécules de solvants sont considérées individuellement, et les interactions avec le système étudié

sont prises en compte, comme les liaisons hydrogène par exemple. Cette méthode requiert beaucoup de temps de calcul étant donné le nombre de molécules et d'interactions à considérer.

Dans le deuxième cas, la méthode implicite, le système étudié est placé dans une cavité de taille définie et le solvant est considéré comme un continuum. Le modèle que nous avons utilisé ici est le modèle PCM (Polarizable Continuum Model) [20]. La forme de la cavité de ce modèle est basée sur les sphères de van der Waals centrées sur chaque atome, et détermine une surface de contact avec le solvant. L'effet du solvant peut ensuite être considéré en prenant en compte la polarisation du solvant sur cette surface. La méthode est appelée avec le mot clef SCRF (« Self Consistent Reaction Field ») car le potentiel du solvant est obtenu de façon auto-consistante avec le calcul de la densité de charge du soluté.

I. 7. Programme de calcul utilisé

Gaussian est un logiciel de chimie quantique créé en 1970 par John Pople [21]. Son nom provient du choix de Pople d'utiliser des orbitales gaussiennes plutôt que les orbitales de Slater, ce qui a permis d'accélérer les calculs. Ce logiciel permet la description de plusieurs propriétés physico-chimiques, comme la détermination de la structure moléculaire de l'état fondamental ou des états excités (structure la plus basse en énergie), les orbitales moléculaires décrivant le système, les propriétés spectroscopiques, comme les spectres d'absorption ou d'émission, ou les effets de solvatation. La version utilisée a été la version g16, révision B.01.

II. Description de la méthode de calcul

La modélisation des porphyrines par les méthodes de chimie théorique décrites précédemment permet de décrire certaines propriétés de la molécule. Dans un premier temps, on peut déterminer la géométrie de la molécule dans son état fondamental, c'est-à-dire trouver la géométrie qui correspond au minimum d'énergie électronique calculée avec par exemple la méthode DFT. On peut alors calculer les modes de vibration de la molécule par le calcul des fréquences au minimum local du système dans une approximation harmonique. Différentes propriétés vont en découler, comme la simulation d'un spectre infra-rouge, les énergies des liaisons, ou la valeur des niveaux énergétiques et la nature des orbitales moléculaires. Le calcul de l'optimisation de la géométrie dans l'état fondamental par calculs de DFT est symbolisé en jaune dans la **Figure ID-3**.

Ensuite, la TD-DFT permet de calculer les énergies des transitions verticales entre l'état fondamental et les états excités singulets à la géométrie optimisée à l'état fondamental (approximation de Franck-Condon). L'énergie des transitions électroniques (en bleu si on prend en compte le ZPE dans la **Figure ID-3**) et de la force d'oscillateur associées permettent de simuler le spectre d'absorbance de la porphyrine, d'analyser des changements de densité électrique pendant l'excitation. Il est possible d'optimiser la géométrie du système dans un état excité, et en particulier dans le premier état excité (symbolisé en orange dans la **Figure ID-3**). La transition électronique (en rouge dans la **Figure ID-3**) et sa force d'oscillateur calculée en TD-DFT du système dans cette géométrie permet de simuler le spectre d'émission de fluorescence.

De la même façon, le calcul avec la méthode TD-DFT des états excités triplets permet d'obtenir leur niveau d'énergie, et après optimisation, leur structure de plus basse énergie et les énergies de phosphorescence (en vert dans la **Figure ID-3**). Ce dernier calcul sera particulièrement intéressant, car il permettra de calculer l'énergie de transition $T_n \rightarrow S_0$, et donc de déterminer si l'énergie du photon émis est suffisante pour exciter l'oxygène de l'air pour former de l'oxygène singulet.

Enfin, des calculs de vibration ont été effectués pour prendre en compte les couplages ro-vibroniques dans la simulation du spectre d'absorption de la porphyrine.

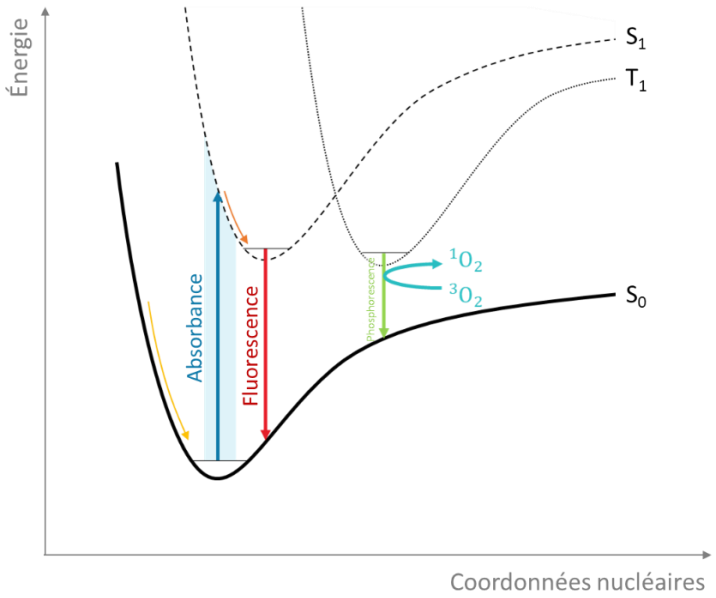

***Figure ID-3** : Diagramme énergie*

III. Références

1 L. H. Thomas, *Math. Proc. Camb. Philos. Soc.*, 1927, **23**, 713–716.
2 P. Hohenberg and W. Kohn, *Phys. Rev.*, 1964, **136**, B864–B871.
3 W. Kohn and L. J. Sham, *Phys. Rev.*, 1965, **140**, A1133–A1138.
4 L. Wilk, M. Nusair and S. H. Vosko, *Can. J. Phys.*, 1981, **59**, 585–595.
5 C. Lee, W. Yang and R. G. Parr, *Phys. Rev. B*, 1988, **37**, 785–789.
6 T. Yanai, D. P. Tew and N. C. Handy, *Chem. Phys. Lett.*, 2004, **393**, 51–57.
7 Y. Zhao and D. G. Truhlar, *Theor. Chem. Acc.*, 2008, **120**, 215–241.
8 C. Adamo and V. Barone, *J. Chem. Phys.*, 1999, **110**, 6158–6170.
9 J. Heyd and G. E. Scuseria, *J. Chem. Phys.*, 2004, **121**, 1187–1192.
10 J. P. Perdew, K. Burke and M. Ernzerhof, *Phys. Rev. Lett.*, 1996, **77**, 3865–3868.
11 S. Daoudi, A. Semmeq, M. Badawi, X. Assfeld, Y. Arfaoui and M. Pastore, *J. Comput. Chem.*, 2019, **40**, 2530–2538.
12 Y. Gao and V. N. Nemykin, *J. Mol. Graph. Model.*, 2013, **42**, 73–80.
13 O. Loboda, *Quantum-chemical studies on Porphyrins, Fullerenes and Carbon Nanostructures*, Springer Berlin Heidelberg, Berlin, Heidelberg, 2013.
14 H. Marcille, J.-P. Malval, M. Presset, N. Bogliotti, A. Blacha-Grzechnik, V. Brezová, Y. Yagci and D.-L. Versace, *Polym. Chem.*, 2020, **11**, 4237–4249.
15 S. Perun, J. Tatchen and C. M. Marian, *Chemphyschem*, 2008, **9**, 282–292.
16 N. A. Sánchez-Bojorge, S. Flores-Armendáriz, M. E. Fuentes-Montero, V. H. Ramos-Sánchez, G. Zaragoza-Galán and L. M. Rodríguez-Valdez, *J. Porphyr. Phthalocya.*, 2017, **21**, 88–102.
17 J. M. S. Lopes, J. R. T. Reis, A. E. H. Machado, T. H. O. Leite, A. A. Batista, T. V. Acunha, B. A. Iglesias, P. T. Araujo and N. M. Barbosa Neto, *Spectroc. Acta A*, 2020, **238**, 118389.
18 A. Maufroy, L. Favereau, F. B. Anne, Y. Pellegrin, E. Blart, M. Hissler, D. Jacquemin and F. Odobel, *J. Mater. Chem. A*, 2015, **3**, 3908–3917.
19 E. Runge and E. K. U. Gross, *Phys. Rev. Lett.*, 1984, **52**, 997–1000.
20 S. Miertuš, E. Scrocco and J. Tomasi, *Chem. Phys.*, 1981, **55**, 117–129.

21 M. J. Frisch, G. W. Trucks, H. B. Schlegel, G. E. Scuseria, M. A. Robb, J. R. Cheeseman, G. Scalmani, V. Barone, G. A. Petersson, H. Nakatsuji, X. Li, M. Caricato, A. V. Marenich, J. Bloino, B. G. Janesko, R. Gomperts, B. Mennucci, H. P. Hratchian, J. V. Ortiz, A. F. Izmaylov, J. L. Sonnenberg, D. Williams-Young, F. Ding, F. Lipparini, F. Egidi, J. Goings, B. Peng, A. Petrone, T. Henderson, D. Ranasinghe, V. G. Zakrzewski, J. Gao, N. Rega, G. Zheng, W. Liang, M. Hada, M. Ehara, K. Toyota, R. Fukuda, J. Hasegawa, M. Ishida, T. Nakajima, Y. Honda, O. Kitao, H. Nakai, T. Vreven, K. Throssell, J. A. Montgomery Jr., J. E. Peralta, F. Ogliaro, M. J. Bearpark, J. J. Heyd, E. N. Brothers, K. N. Kudin, V. N. Staroverov, T. A. Keith, R. Kobayashi, J. Normand, K. Raghavachari, A. P. Rendell, J. C. Burant, S. S. Iyengar, J. Tomasi, M. Cossi, J. M. Millam, M. Klene, C. Adamo, R. Cammi, J. W. Ochterski, R. L. Martin, K. Morokuma, O. Farkas, J. B. Foresman and D. J. Fox, 2016.

Conclusions du Chapitre I

Les matériaux photoactifs permettent de lutter contre deux problèmes actuels, qui sont la prolifération des bactéries, principalement en milieu hospitalier, ainsi que la pollution de l'eau par des polluants organiques.

Il a été montré que la photopolymérisation permet d'obtenir ce type de matériau de façon plus économique et respectueuse de l'environnement que d'autres matériaux photoactifs. De plus, l'élargissement de la gamme d'irradiation vers les longueurs d'onde du visible a permis l'utilisation de lampes LED plus économes encore en énergie, et moins dangereuses à manipuler.

Dans ce contexte, les porphyrines ont montré un intérêt particulier, puisqu'elles présentent une grande variété de propriétés qu'il est possible de moduler par leur simple fonctionnalisation, faisant d'elles des candidates pertinentes en tant que photoamorceur.

De plus, les porphyrines ont été largement étudiées pour leurs propriétés en tant que photosensibilisateur, permettant la production de ROS, et leur utilisation dans une large gamme d'applications. Elles ont présenté notamment des applications pour la réalisation de surfaces antibactériennes et de dépollution de l'eau.

Chapitre II

Utilisation de photosensibilisateurs pour la création de matériaux dépolluants de l'eau

Contexte

Le chapitre précédent a souligné l'importance du développement de matériaux photoactifs pour des applications en dépollution de l'eau. En effet, les solutions actuelles mises en place ne sont pas assez efficaces, comme en témoignent les résidus de polluants présents dans les eaux en Europe. Diverses recherches considèrent des alternatives, avec une attention particulière portée sur la photodégradation des polluants, apporté par les procédés d'oxydation avancés qui utilisent les ROS comme espèces actives.

Il a été montré que les porphyrines étaient capables de produire ces ROS et également de servir pour la synthèse de matériaux par photopolymérisation. Il a donc été envisagé de coupler ces deux actions.

Les porphyrines utilisées dans la première partie (**Figure II-1**) ont été sélectionnées pour différentes raisons. L'ajout d'un atome de brome sur la porphyrine **P3** est supposée améliorer l'efficacité de son croisement intersystème, en favorisant la conversion des états singulet en états triplet,[1] possédant une durée de vie plus longue et donc de meilleures probabilités de réaction. La porphyrine **P4** quant à elle possède des fonctions vinyles sur deux positions méso. Ces fonctions vont réagir de la même façon que les fonctions acrylate présentes sur le monomère. La création de liaisons covalentes avec le réseau polymérique est donc probable, permettant d'empêcher le relargage de la porphyrine du matériau.

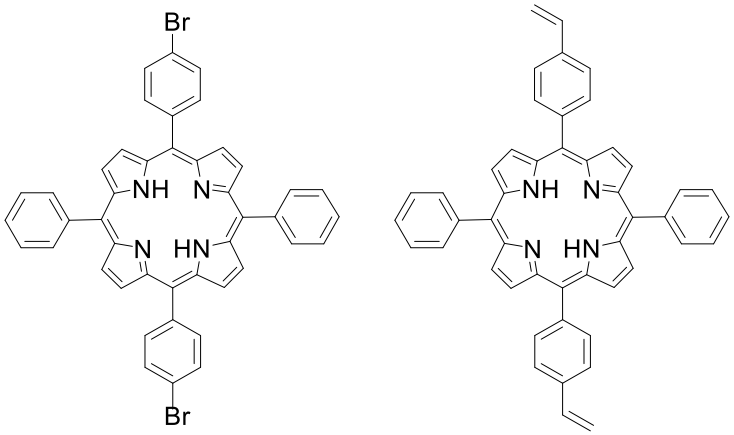

P3 **P4**

***Figure II-1**: Structures des porphyrines P3 et P4 utilisées dans la **partie A**.*

Dans cet article, la modélisation des porphyrines puis leur synthèse seront d'abord présentées. Les porphyrines seront ensuite mises en présence d'un co-amorceur pour former le système photoamorceur, et les interactions entre les deux composés seront étudiées. Pour cela, le comportement de son absorption en solution sous irradiation sera étudié par spectroscopie UV-visible pour suggérer la présence d'une interaction. Ensuite, des études de fluorescence ou par laser nanoseconde permettront de localiser cette interaction dans l'état singulet ou triplet respectivement. Enfin, des expériences de RPE permettront de déterminer la nature des espèces produites sous irradiation. Les capacités de photoamorçage de ces systèmes seront ensuite étudiées dans le cadre de la photopolymérisation radicalaire, et les meilleurs systèmes permettront de synthétiser des

matériaux. Ils seront enfin exploités pour la dépollution de l'eau sous irradiation UV, où de l'azorubine (acid red 14 en anglais ou AR14) sera utilisée en tant que polluant modèle des colorants azoïques.

Pour la seconde partie, les porphyrines utilisées (**Figure II-2**) possèdent un spectre d'absorption plus large, afin d'obtenir une absorption plus efficace dans les longueurs d'onde du visible et ainsi entreprendre une étude de photodégradation sous irradiation dans le visible. En effet, les nombreux cycles aromatiques de la porphyrine **P8** permettent une extension du système conjugué et engendrent un déplacement de la bande de Soret. L'ajout d'un ion zinc (II) dans une deuxième porphyrine, **P8Zn**, doit permettre d'améliorer les capacités de photoamorçage de la porphyrine, ce constat ayant déjà été observé pour de nombreuses études. [2–4] En effet, en plus de permettre un déplacement vers les longueurs d'onde du visible de la bande de Soret, la présence du métal augmente le taux de croisement intersystème, et, tout comme pour **P3**, permet de favoriser la formation d'états triplet.

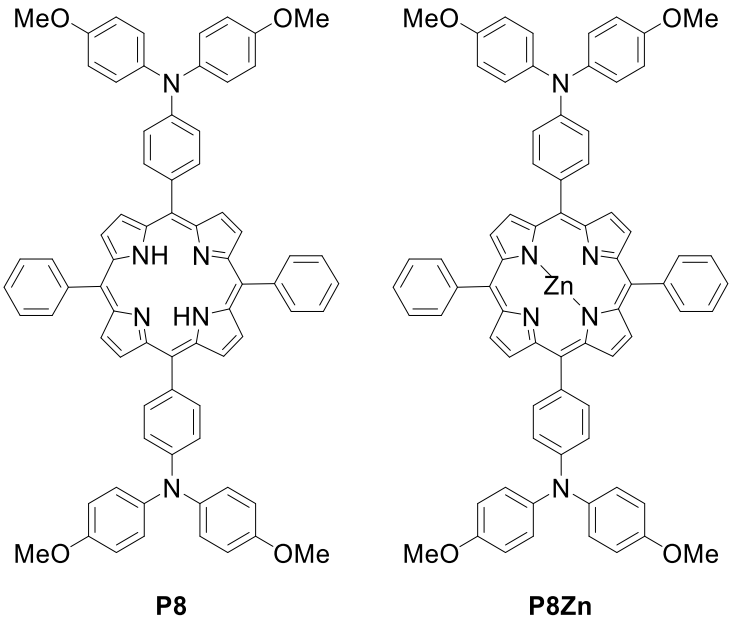

***Figure II-2** : Structures des porphyrines P8 et P8Zn utilisées dans la **partie B**.*

Références

1 R. Bonnett, A. Harriman and A. N. Kozyrev, J. Chem. Soc., Faraday Trans., 1992, 88, 763–769.
2 S. Shanmugam, J. Xu and C. Boyer, J. Am. Chem. Soc., 2015, 137, 9174–9185.
3 H. Marcille, J.-P. Malval, M. Presset, N. Bogliotti, A. Blacha-Grzechnik, V. Brezová, Y. Yagci and D.-L. Versace, Polym. Chem., 2020, 11, 4237–4249.
4 G. Noirbent, These de doctorat, Aix-Marseille, 2021.

Partie A : Article 2 – New porphyrins for water depollution under UV irradiation

Abstract.

The photoinitiation properties of two novel porphyrins were evaluated for the photopolymerization of a bio-based acrylated monomer, *i.e.* soybean oil acrylated (SOA). They were combined with a co-initiators, such as a tertiary amine as electron donor (MDEA), an iodonium salt as electron acceptor (Iod), or two biosourced co-initiators used as H-donors, cysteamine and *N*-acetylcysteine. The reaction mechanisms between photoinitiators and co-initiators were determined by steady state photolysis, fluorescence, laser flash photolysis (LFP) and electron paramagnetic resonance spin-trapping (EPR-SP). High monomer conversions were obtained with these different systems at different irradiation wavelengths (LEDs@385 nm, 405 nm, 455 nm and 530 nm), in the presence or absence of oxygen. The prepared materials were used for the photodegradation of an azo-dye in water under UV irradiation, in order to design mostly bio-based depolluting coating. These coating have been involved in three successive depollution cycles without reduction of their efficiency.

I. Introduction

Photopolymerization has received an increasing attention in recent years [1], and is applied to a wide range of applications, including bioengineering [2], electronic components and coatings [1]. The use of visible light to initiate polymerisation has gained considerable attention, from both economic and environmental aspects [3–5]. The use of dyes to initiate polymerisation, including eosin [6], anthracene [7] or phthalocyanines [8], makes the production of photopolymerised materials possible even under such low-energy irradiation. However, despite their high absorption of visible light, porphyrins are not commonly used in such processes. In addition to their ability to photoinitiate polymerization of various monomers by free radical or cationic polymerization [9–13] as well as PET-RAFT polymerization [14–17], porphyrins are known to react with environmental oxygen to form reactive oxygen species [18–21], which are highly oxidative species used in various applications such as advanced oxidation processes (AOPs) [22]. Coatings using porphyrins have already been used in our laboratory to produce antibacterial materials [11], but no application in water purification has been reported so far.

Azo dyes represent a significant source of pollution from textile or food industries [23]. They are sometimes toxic and non-biodegradable, thus representing a potential threat to marine biodiversity by limiting the required light absorption for photosynthesis. Current depollution methods, like coagulation [24], filtration [22] or absorption [25], have numerous limitations, whereas AOPs allow pollutants to be locally degraded [26]. Materials based on metal oxides like TiO_2 [27,28] or ZnO [29] have already demonstrate their efficiency in the degradation of azo pollutants, and notable results have been obtained with ZnO nanowires [30–34].

Research has also focused on the use of polymers for depollution, either through absorption or photocatalytic degradation [35]. The use of porphyrins usually requires co-catalysts or complexation with noble metals for effective degradation [36 37]. Free base porphyrins have not been deeply used due to their lower photodegradation activity [38], but present remove heavy metals [39,40].

In this context, two new porphyrins have been developed with the aim of using them in two complementary ways: *i*) as photoinitiators for radical polymerisation, *ii*) as photosensitisers for the photooxidation of water pollutants. The properties of these porphyrins have been computed by

Density Functional Theory (DFT) and Time-Dependent Density Functional Theory (TD-DFT) to determine their ground state structure and their theoretical vertical energy, leading to the absorption spectrum. They have been used to imitate photopolymerization in combination with various co-initiators like electron donor or acceptor (*i.e.* tertiary amine and iodonium salt respectively) or H-donor molecule (*i.e.* cysteamine or *N*-acetylcysteine). The photo-reactivity of these systems were studied using various methods. Steady state photolysis were used to follow the absorption behaviour under irradiation, whereas fluorescence and nanosecond laser were used to localize the effect on singlet or triplet state respectively. The different radical species produced under irradiation were identified using electronic paramagnetic resonance spin-trapping (EPR-SP). Photo-initiating capacities of such systems have been determined for free-radical polymerization of acrylated soy bean oil (SOA), a bio-sourced monomer under low-intensity blue LED (405 and 455 nm) and green LED (530 nm) irradiation, and followed by Real-Time Fourier-Transformed Infrared spectroscopy (RT-FTIR). The more effective systems were used to generate photo-induced materials from photopolymerization of SOA which have been used for the photodegradation of azo dyes in water.

II. Materiel & Methods

Material. Solvents (acetic acid, methanol, dichloromethane = DCM, petroleum ether (PE) and acetone) were used as received. Tetrahydrofuran (THF) for Suzuki-Miyaura coupling reactions was distilled under argon using sodium and benzophenone. Pyrrole, para-formaldehyde, 2,3-dichloro-5,6-dicyano-1,4-benzoquinone (DDQ), trifluoroacetic acid (TFA), *N*-bromosuccinimide (NBS), bromophenylboronic acid, vinylphenylboronic acid, potassium carbonate, tetraphenylcyclopentadienone (TPCPD) were purchased from TCI. Benzaldehyde, trimethylamine, pyridine, [1,1'-bis(diphenylphosphino)ferrocene]dichloropalladium(II) ($PdCl_2$(dppf)), heptanal, bromobenzaldehyde, SOA, *N*-methyldiethanolamine (MDEA), 4-(2-methylpropyl)phenyliodonium hexafluorophosphate (Iod), cysteamine, 5,5-dimethylpyrroline-*N*-oxide (DMPO), acid red 14 (AR14) were provided from Merck. All the compounds were used as received. The chemical structures of the monomer, co-initiators, porphyrin derivatives used for free-radical polymerization are described in **Table IIA-1**.

***Table IIA-1**: Chemical structures of the photoinitiating systems, monomers and used pollutant.*

Name	Chemical structure
P3 5,15-diphenyl-10,20-bis(4-bromophenyl) porphyrin	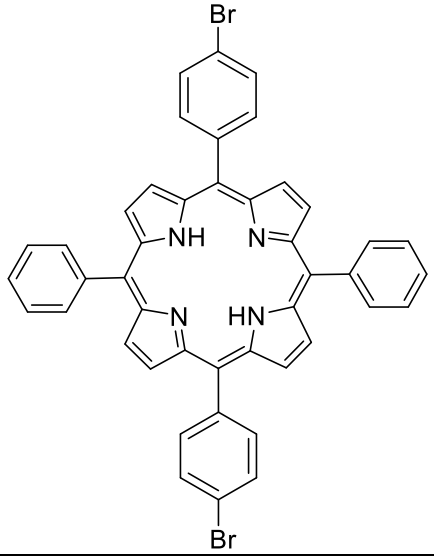

P4 5,15-diphenyl-10,20-bis(4-vinylphenyl) porphyrin	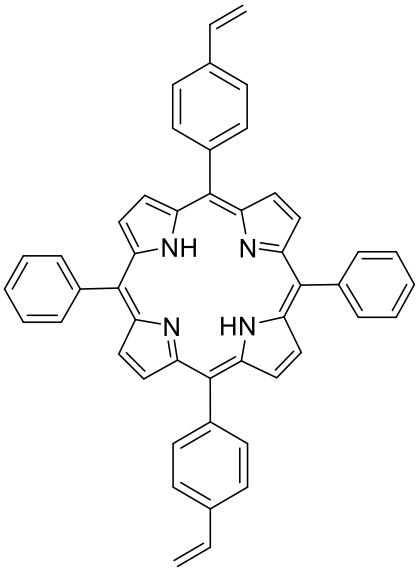
MDEA *N*-methyldiethanol amine	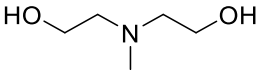
Iod *Bis*(4-methylphenyl) iodonium hexafluorophosphate	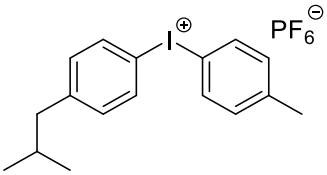
Cysteamine	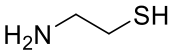
***N*-acetylcysteine**	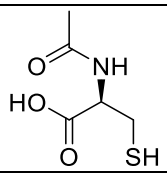
SOA soybean oil acrylate	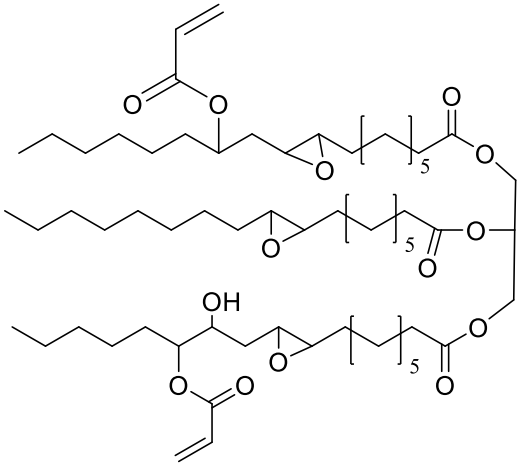
Acid red 14 disodium 4-hydroxy-2-[(*E*)-(4-sulfonato-1-naphthyl)diazenyl]naphthalene-1-sulfonate	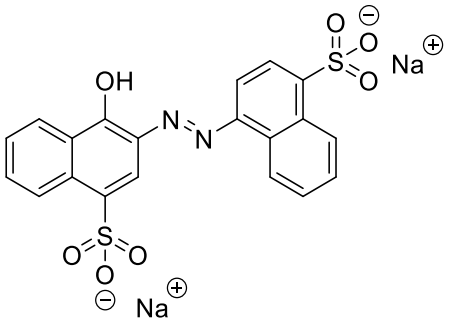

Characterization. Analytical thin layer chromatography (TLC) was performed on silica gel plates (0.25 mm) precoated with a fluorescent indicator (Merck 60F254) and revelation was performed using ultraviolet light (λ = 254 nm) or an aqueous solution of $KMnO_4$. Flash chromatography was performed on 40–63 µm silica gel with mixture of solvents. NMR spectra were recorded using a Bruker Avance II 400 MHz spectrometer at room temperature. Results are presented as the following: chemical shift δ (ppm), multiplicity (*s* = singlet, *d* = doublet, *t* = triplet, *q* = quartet, *quint* = quintet, *hept* = heptuplet, *m* = multiplet, *br* = broad), coupling constant J (Hz), integration. Chemical shifts were referenced to the residual $CDCl_3$ non-deurerated signal (δ^1H = 7.26 ppm and δ^{13}C = 77.16 ppm). Infrared spectra were recording using a Brucker Tensor 27 spectrometer in ATR mode. UV-Visible absorption spectra were recorded using a PerkinElmer Lambda 2 UV-vis spectrophotometer. High-Resolution Mass Spectra were obtained at the ICOA of the University of Orléans by electrospray ionization using a Q-TOF analyzer.

Synthesis of dipyrromethane. In air, a 500 mL rounded-bottomed flask equipped with a stirring bar is charged with pyrrole (130 mL, 1.87 mol, 4.0 equiv), paraformaldehyde (1.41 g, 0.47 mol, 1.0 equiv), acetic acid (200 mL) and methanol (65 mL). The flask is closed with a septum and the reaction is stirred at room temperature for 16 h. Then, the reaction mixture is diluted with DCM (400 mL), and the resulting solution is washed with water (2 x 200 mL) and 1.0 M aq NaOH (2 x 200 mL). The organic layer is dried over Na_2SO_4 and the solvent and the excess of pyrrole are successively removed by evaporation under reduced pressure. The residue is purified by flash chromatography (silica, DCM/PE: 5/5) to afford the expected product (1.923 g, 7%) as a white solid, which turn black under air. **^{1}H NMR** (400 MHz, $CDCl_3$): δ 7.63 (s, 2 H), 6.61 (dd, J = 4.2, 2.6 Hz, 2 H), 6.21 (dd, J = 5.7, 2.8 Hz, 2 H), 6.09 (d, J = 0.6 Hz, 2 H), 3.94 (s, 2 H). **^{13}C NMR** (100 MHz, $CDCl_3$): δ 129.2 (2 C), 117.4 (2 CH), 108.4 (2 CH), 106.6 (2 CH), 26.4 (CH_2).

Synthesis of 5,15-diphenylporphyrin (1). A 1 L rounded-bottomed flask equipped with a stirring bar, purged with argon, and protected from light by an aluminium foil is charged with dipyrromethane (1 g, 6.8 mmol, 1.0 equiv), benzaldehyde (0.72 mL, 7.1 mmol, 1.05 equiv) and DCM (1 L). The solution is degassed by argon bubbling for 15 min, and TFA (0.42 mL, 5.4 mmol, 0.8 equiv) is added. The reaction is stirred at room temperature for 18 h. DDQ (2.2 g, 9.52 mmol, 1.4 equiv) is then added and the mixture is stirred at room temperature for 30 min. After addition of triethylamine (5 mL), the solvent is removed under reduced pressure and the residue was purified by flash chromatography (silica, DCM/PE: 5/5) to afford the desired product as a purple solid (1.5 g, 39%). **^{1}H NMR** (400 MHz, $CDCl_3$): δ (ppm) 10.33 (s, 2H), 9.41 (d, J = 4.6 Hz, 4H), 9.10 (d, J = 4.6 Hz, 4H), 8.29 (dd, J = 6.5, 2.9 Hz, 4H), 7.83–7.81 (m, 6H), −3.11 (s, 2H). **^{13}C NMR** (100 MHz, $CDCl_3$): δ (ppm) 147.4 (4C), 145.4 (4C), 141.6 (2C), 135.0 (4CH), 131.8 (4CH), 131.2 (4CH), 127.9 (4CH), 127.1 (2CH), 119.3 (2C), 105.4 (2CH).

Synthesis of 5,10-diphenyl-10,20-dibromoporphyrin (2). A 1 L rounded-bottom flask equipped with a stirring bar is charged with 5,15-diphenylporphyrin (1.2 g, 2.5 mmol, 1.0 equiv), DCM (870 mL) and pyridine (1.17 mL). The mixture is treated with NBS (945 mg, 5.3 mmol, 2.1 equiv) at 0 °C for 3 h and monitored by TLC [until the full conversion is reached, NBS (90 mg, 0.5 mmol, 0.2 equiv) is added every hour]. The reaction is quenched with acetone (60 mL), the solvent are removed under reduced pressure and the residue is triturated in methanol and filtered several times to afford the desired product (1.29 g, 82%) as a purple solid.

^{1}H NMR (400 MHz, $CDCl_3$): δ 9.62 (d, J = 4.7 Hz, 4H), 8.84 (d, J = 4.6 Hz, 4H), 8.16 (d, J = 7.1 Hz, 4H), 7.91 – 7.68 (m, 6H), -2.73 (s, 2H). **^{13}C NMR** (100 MHz, $CDCl_3$): δ 141.51 (4C), 134.65 (4CH), 128.20 (2CH),

126.98 (4CH), 121.56 (2C), [16C not detected]. **HRMS (ESI/Q-TOF)**: *m/z* [M + H^+] calcd for $C_{32}H_{21}N_4Br_2$ 619.01127; found 619.0118.

Synthesis of 5,15-diphenyl-10,20-bis(4-bromophenyl) porphyrin (P3). A 25 mL rounded-bottomed flask equipped with a stirring bar is charged with 5,10-diphenyl-10,20-dibromoporphyrin (50 mg, 0.08 mmol, 1.0 equiv), bromophenylboronic acid (35 mg, 0.176 mmol, 2.2 mmol), K_2CO_3 (66 mg, 0.48 mmol, 6 equiv), THF (7.2 mL) and water (0.8 mL). The reaction mixture is flushed with Ar, $PdCl_2(PPh_3)_2$ (6 mg, 0.008 mmol, 0.1 equiv) is added and then the reaction is heated to reflux for 16 h. The resulting solution is washed with water (2 x 10 mL) and brine (10 mL). The solvent is removed under reduced pressure and the residue is purified by flash chromatography (silica, DCM/PE: 3/7) to afford the desired product as a purple solid (39 mg, 63%). **^{1}H NMR** (400 MHz, $CDCl_3$): δ 8.85 (dd, J = 17.4, 4.2 Hz, 8H), 8.21 (d, J = 7.1 Hz, 4H), 8.08 (d, J = 7.9 Hz, 4H), 7.89 (d, J = 8.0 Hz, 4H), 7.80–7.75 (m, 6H), -2.82 (s, 2H). **^{13}C NMR** (100 MHz, $CDCl_3$): δ 142.15 (2C), 142.06 (4C), 141.16 (4C), 135.98 (4CH), 135.21 (4CH), 134.67 (4CH), 130.02 (4CH), 127.97 (4CH), 126.88 (4CH), 125.21 (2CH), 122.60 (2C), 120.63 (2C), 120.55 (2C), 118.78 (2C) (**Figure S1** and **S2**). **HRMS (ESI/Q-TOF)**: *m/z* [M + H^+] calcd for $C_{44}H_{29}N_4Br_2$ 771.0753; found 771.0751. ν_{max} (ATR)/cm^{-1}: 3319, 3040, 2704, 2336, 1564, 1470, 1340, 1169, 1063, 974, 789, 714.

Synthesis of 5,15-diphenyl-10,20-bis(4-vinylphenyl) porphyrin (P4). A 25 mL rounded-bottomed flask equipped with a stirring bar is charged with 5,10-diphenyl-10,20-dibromoporphyrin (50 mg, 0.08 mmol, 1.0 equiv), vinylphenylboronic acid (26 mg, 0.176 mmol, 2.2 mmol), K_2CO_3 (66 mg, 0.48 mmol, 6 equiv), THF (7.2 mL) and water (0.8 mL). The reaction mixture is flushed with Ar, $PdCl_2$dppf (6 mg, 0.008 mmol, 0.1 equiv) is added and then the reaction is heated to reflux for 16 h. The resulting solution is washed with water (2 x 10 mL) and brine (10 mL). The solvent is removed under reduced pressure and the residue is purified by flash chromatography (silica, DCM/PE: 3/7) to afford the desired product as a purple solid (30 mg, 57 %). **^{1}H NMR** (400 MHz, CDCl3): δ 9.01 – 8.67 (m, 8H), 8.27 – 8.17 (m, 8H), 7.82 – 7.75 (m, 10H), 7.07 (dd, J = 17.6, 10.9 Hz, 2H), 6.08 (d, J = 17.6 Hz, 2H), 5.50 (d, J = 10.7 Hz, 2H), -2.77 (s, 2H). **^{13}C NMR** (100 MHz, CDCl3): δ 136.84(4 CH), 134.99 (4 CH), 134.69 (4 CH), 127.87(4 CH), 126.84 (4 CH), 124.74 (4 CH), 114.81 (2CH), [22C not detected] (**Figure S3** and **S4**). **HRMS (ESI/Q-TOF)**: *m/z* [M + H^+] calcd for $C_{48}H_{35}N_4$ 667.2856; found 667.2853; *m/z* [M + 2H^+] calcd for $C_{48}H_{35}N_4$ 334.1465; found 335.1465. ν_{max} (ATR)/cm^{-1}: 3319, 2947, 2704, 2355, 1458, 1256, 1080, 1013, 791, 719.

Theoretical calculation. Density functional theory (DFT) and time-dependent density functional theory (TD-DFT) calculations were carried out with Gaussian 16 package [41]. The functional B3LYP combined with 6-31(g) basis set was used for the optimization of the porphyrin structures and for frequencies calculations. Lack of imaginary frequencies were controlled to confirm the true minima of the optimization. The TD-DFT using the same level of theory were used to compute UV-visible absorption spectra. The solvent effect were considered in the polarizable continuum model (PCM).

Irradiation source. Four light emitting diodes (LEDs) were used for the photopolymerization experiments: LED@385 nm (35.3 mW/cm^2), LED@405 nm (118 mW/cm^2), LED@455 nm (23.8 mW/cm^2), and LED@530 nm (14.6 mW/cm^2). An UV lamp was used for the observation of reactive oxygen species (ROS) and water depollution experiment (Hamamatsu-LC8, 35 mW/cm^2, λ = 365 nm).

Steady state photolysis. Photolysis experiments were performed in dichloromethane, under air and under LED@405 nm irradiationThe absorbace of **P3** and **P4** solutions with an without the presence of co-initiators (*i.e.* MDEA, Iod, cysteamine or *N*-acetylcysteine) was followed upon light irradiation. [**P3**] = 1.85 x 10^{-5} mol/L, [**P4**] = 2.9 x 10^{-6} mol/L, [MDEA] = 2.8 x 10^{-2} mol/L, [Iod] = 2.9 x 10^{-5} mol/L, [cysteamine] = 1.7 x 10^{-4} mol/L.

Steady state fluorescence measurement. Fluorescence experiments were performed using FluoroMax + spectrofluorometer from Horiba. Emission spectra were obtained after the excitation of **P3** and **P4** at 649 and 646 nm respectively.

Laser Flash Photolysis. Nanosecond flash photolysis were performed using a nanosecond Nd:TAG laser (Powerlite 9010, Continuum) operating at 5 Hz with 7-8 ns impulsion time and working at 385 nm, as described previously [42]. Measurements were performed under a saturated argon atmosphere at room temperature.

Electronic Paramagnetic Resonance (EPR). The EPR spectra were recorded *in situ* upon/after a defined exposure as described previously in ref. [42] and [8]. The solutions were prepared in chloroform (for spectroscopy Uvasol®, Merck) and carefully saturated with argon were irradiated at 295 K directly in the EPR resonator using a LED@400 nm source (λ_{max} = 400 nm; Bluepoint LED, Hönle UV Technology). The 5,5-dimethyl-1-pyrroline N-oxide (DMPO, Merck, distilled and stored at –20°C before the application) was applied as the spin trapping agent. The X-band cw-EPR spectra (modulation frequency of 100 kHz) were monitored using the EMX*plus* spectrometer (Bruker) equipped with the High Sensitivity Probe-head (Bruker) in a small quartz flat cell (Wilmad-LabGlass, WG 808-Q). The *g*-factors were determined with an uncertainty of ±0.0001 exploiting a nuclear magnetic resonance teslameter (ER 036TM, Bruker) and integrated frequency counter. The experimental EPR spectra were analyzed by the WinEPR software (Bruker) and the calculations of spin-Hamiltonian parameters and relative concentrations of individual DMPO-adducts were performed with the EasySpin toolbox working on MatLab® platform [Stoll]. The standard EPR spectrometer settings: microwave frequency, ~ 9.43 GHz; microwave power, 10.80 mW; center field, ~336.0 mT; sweep width, 4–10 mT; gain, 2.00 x 10^5; modulation amplitude, 0.025–0.1 mT; sweep time, 45 s; time constant, 10.24 ms; number of scans, 5–10.

Cyclic voltammetry. The cyclic voltammograms of **P3** and **P4** were obtained using an AUTOLAB potentiometer/galvanometer employing GPES electrochemical software 4.9 (Utrecht, The Netherlands). Three-electrode cell configuration was employed, with glassy electrode as working electrode, saturated calomel electrode (SCE) as reference one and gold wire electrode as counter electrode. DMF solution of nBu$_4$NBF$_4$ (0.1M) was used as supporting electrolyte.

Kinetic studies. Photosensitive formulations were layed on a BaF_2 pellet (thickness of the layer = 12 μm) and irradiated with various LEDs in laminate or under air. The absorbance decrease of the SOA acrylate function was followed by Real-Time Fourier Transform InfraRed spectroscopy (RT-FTIR, Jasco) at 1636 cm^{-1}, allowing thus to determine the final acrylate conversions and polymerization rate.

Pellet preparation. The photosensitive formulation (**P3**/MDEA/SOA and **P4**/MDEA/SOA (0.5/5% wt.wt.)) were poured in a round silicon mold of 15 mm diameter and 1.3 mm thickness. Both systems have been irradiated for 10 min each side under LED@405 nm in laminate.

Release experiments. Pellets obtained from the polymerization **P4**/MDEA/SOA and **P3**/MDEA/SOA (0.5%/5% wt.wt) was immerged in 3 mL of solvent and stirred by orbital stirring for 5 h. The release of the porphyrin from the pellet was monitored by UV-Visible spectroscopy at fixed time. The percentage of **P3** and **P4** release was determined using Beer-Lambert's law at maximum absorption wavelength and compared with TPP based sample using the Eq. 1. Each experiment was done in triplicate.

$$R(\%) = \frac{C_t^P \times V \times M^{PS}}{m_{sample}} \times 100 \quad (1)$$

Where C_t^P is the concentration of porphyrin in the solution, V is the volume of the solution, M^{PS} is the molecular weight of the porphyrin and m_{sample} corresponds to the mass of the pellet.

Coating preparation. The photosensitive formulations (**P3**/MDEA/SOA and **P4**/MDEA/SOA (0.5%/5% wt.wt.)) were firstly deposited on a glass substrate freshly cleaned with acetone and ethanol. Formulations have been then irradiated for10 min under LED@405 nm in laminate.

Detection of singlet oxygen. The photogeneration of reactive oxygen species (ROS) of coatings were determined. A solution of TPCPD in methanol (3.4×10^{-4} M) was used to investigate the photogeneration of singlet oxygen. Coating is embedded in 30 mL of TPCPD solution and irradiated with an UV light source. The singlet oxygen formation is followed by the absorbance decrease of TPCPD at 510 nm.

Depolluting. Glass sample coated with porphyrin was immerged in 30 mL of an aqueous solution of AR14 with an initial concentration of 10 µM and irradiated under UV-light. Experiments were carried out in dynamic mode, *i.e.* the sample is continuously under stirring to ensure a constant supply of AR14 molecules on the surface of the coating. This dynamic fluid regime can also maximize the removal of the formed reaction products from the catalyst surface [33]. The photodegradation reaction was monitored by UV-visible spectrophotometry, measured by using a sample of the solution taken every 15 min for 5 hours, allowing then to determine the photodegradation rate of the pollutant in the water. In order to compare the photodegradation efficiency, we use the degradation rate (X%) in aqueous solutions was determined using Eq. 2.

$$X(\%) = \frac{A_0 - A_t}{A_0} \times 100 \qquad (2)$$

Where A_0 and A_t stand respectively for the maximum absorbance peak *i.e.* λ = 515 nm for AR14 before illumination (t = 0 min=, and at time t during the irradiation process.

In order to highlight the photocatalytic properties of synthesized based-porphyrin materials, a photolysis test, without any sample, was carried out. Furthermore, an adsorption test without UV-light was also performed to determine if the absorbance decrease of the pollutant is only due to the adsorption of AR14 on the surface of materials.

III. Results

Synthesis. The preparation of **P3** and **P4** required the synthesis of *meso-substituted* A_2B_2-*trans*-porphyrins. In order to have a method based on a common precursor, we focus our attention on the use of Suzuki-Miyaura cross-coupling reaction between diphenyl-dibromo-*trans*-porphyrin **2** and arylboronic acids [43,44]. Indeed, the intermediate molecule **2** could be easily obtained in a 94% yield by dibromation of 5,15-diphenylporphyrin **1** [45] with *N*-bromosuccinimide (NBS) in chloroform in the presence of pyridine (**Figure IIA-1**) [46,47].

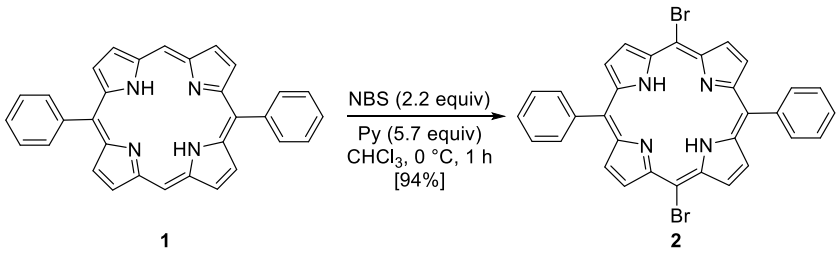

***Figure IIA-1**: Dibromation of 5,15-diphenylporphyrin **1**.*

The functionalization of **2** with arylboronic acids could be efficiently achieved using palladium catalysis (**Figure IIA-2**). Indeed, the use of standard conditions (10 mol% of $PdCl_2(PPh_3)_2$ with 8.0 equiv of Na_2CO_3) allowed the double Suzuki-Miyaura cross-coupling of **2** with 4-bromoboronic acid. The use of an excess of this last reagent was essential to ensure the introduction of the two aryl groups, thus simplifying the isolation of **P3** with a good 63% yield. Even if these conditions revealed to be less efficient with 4-vinylphenylboronic acid (30% isolated yield), a slight modification of the reaction conditions, notably with the use of $PdCl_2$(dppf) as a catalyst, delivered **P4** in a similarly good 57% yield with only a slight excess (2.2 equiv) of the boronated reagent.

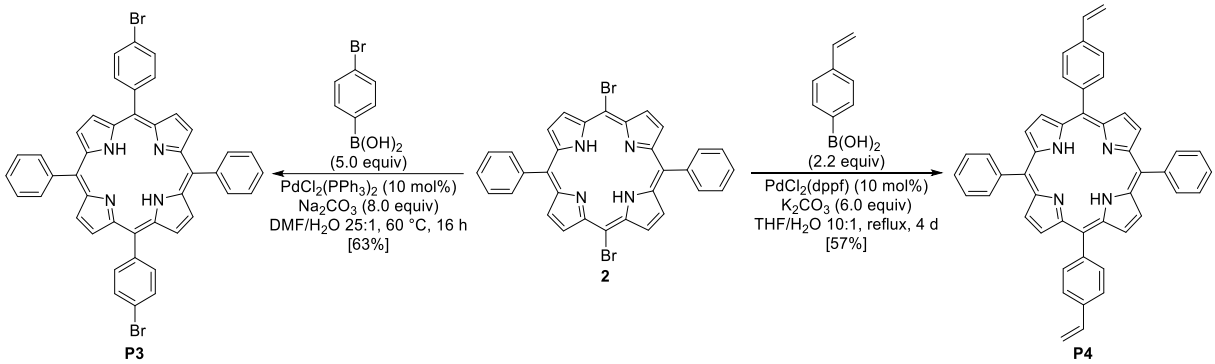

***Figure IIA-2**: Synthesis of **P3** and **P4**.*

Absorption and fluorescence spectra. The UV-visible absorption spectrum and the normalized emission spectrum of **P3** and **P4** are illustrated in **Figure IIA-3**. The absorption and emission properties of both porphyrins are depicted in **Table IIA-2**. The absorbance spectra of **P3** and **P4** present classical π-π* transition [48]. The Soret band absorbing at 418 nm and 419 nm for **P3** and **P4** respectively, corresponds to the $S_0 \rightarrow S_3$ and $S_0 \rightarrow S_4$ transitions. Q bands are assigned to the $S_0 \rightarrow S_1$ and $S_0 \rightarrow S_2$ transitions and their corresponding vibronic overtones are localized between 500-600 nm. The fluorescence spectrum of **P3** and **P4** present two bands, corresponding to the $S_1 \rightarrow S_0$ transition and its vibronic band, are separated by 63 nm and 62 nm respectively, which is in adequation with the literature [49].

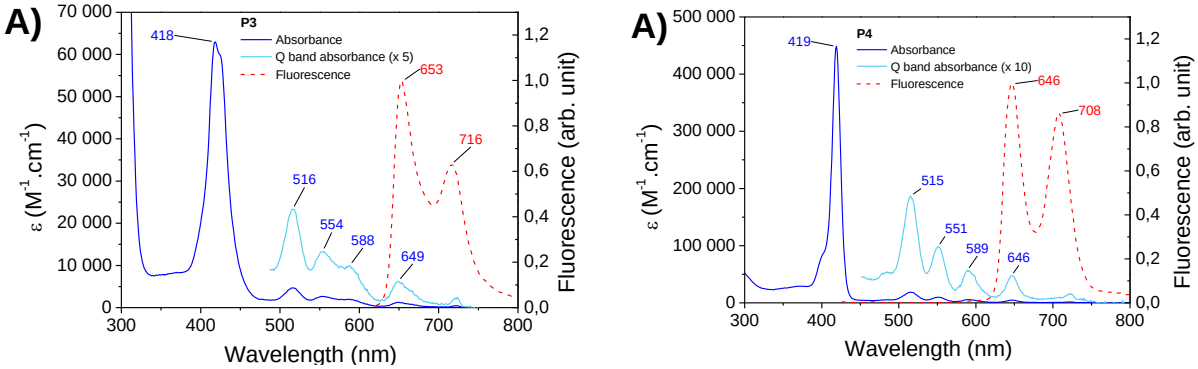

***Figure IIA-3**: Experimental absorption and fluorescence spectra of **A) P3** and **B) P4** in DCM.*

***Table IIA-2**: Absorption and emission properties of **P3** and **P4**.*

Porphyrin	Soret band: λ_{abs} / nm (ε /$M^{-1}.cm^{-1}$)	Q bands: λ_{abs} / nm (ε /$M^{-1}.cm^{-1}$)	λ_{em} / nm (normalized unit)
P3	418 (62 825)	516 (4 660) 554 (2 660) 588 (1 993) 649 (1 241)	653 (1), 717 (0.63)
P4	419 (448 666)	515 (18 665) 551 (9 832) 589 (5 682) 646 (4 723)	646 (1), 708 (0.86)

The optimized geometry of **P3** and **P4** in the ground state and their first excited states in DCM have been computed using DFT calculations at the B3LYP level using 6-31G+(d) basis set to explore the influence of the substituents on the porphyrin core. Different geometry can be obtained for the porphyrin core, as previously illustrated [50]. The optimized structures in the ground state reveal a relatively planar saddle conformation for the porphyrins core (C7-C8-C9-C10) (175.8° and 177° for **P3**, 174.7° and 176° for **P4**) (**Figure IIA-4**). The phenyl groups are twisted by a dihedral angle (C11-C12-C13-C14) of 70.1° for **P3**, and 65.4° for **P4**. The dihedral angle with substituted aryl groups (C8-C7-C1-C2) follow the same tend, but are more accentuated: 71.1° for bromo-phenyl of **P3** and 63.6° for vinyl-phenyl of **P4**.

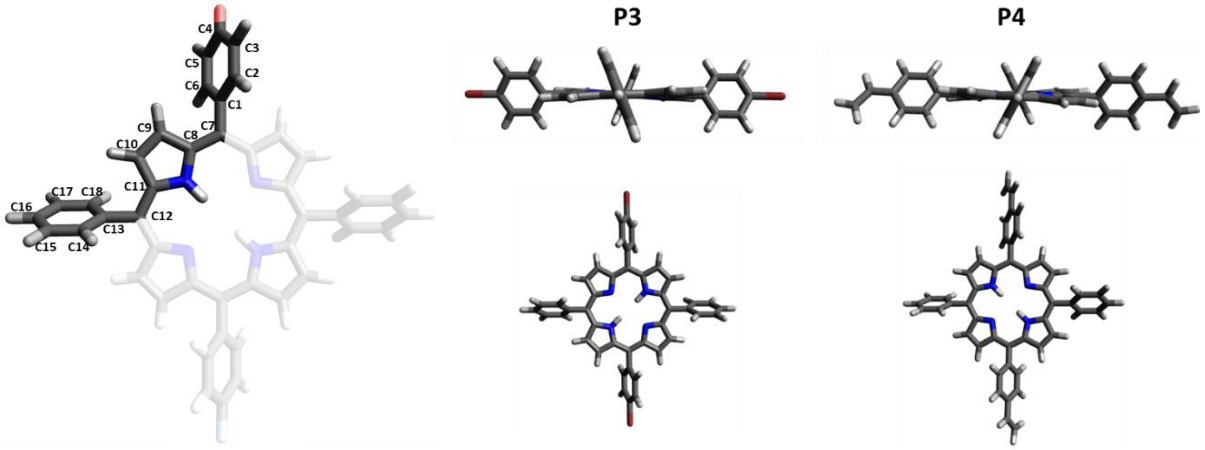

***Figure IIA-4**: A) Labelling of carbons in used porphyrin. Red part correspond to the substituted part of the porphyrin, corresponding to brome for **P3** and vinyl group for **P4**. B) Molecular geometry of the ground state of **P3** and **P4** optimized in DCM at the B3LYP level using 6-31G+(d) basis set.*

The electron-density distribution of the four frontier molecular orbitals (MOs) of **P3** and **P4** with their associated energies are presented in **Figure IIA-5**. For all porphyrins, LUMO and LUMO+1 are very close in energy, which is coherent with previous studies [51]. The electronic distributions of the different MOs are similar for **P3** and **P4** and are mainly located on porphyrin core. This explains the slight difference in absorption spectra between **P3** and **P4** as the transition density is not located on the substituents.

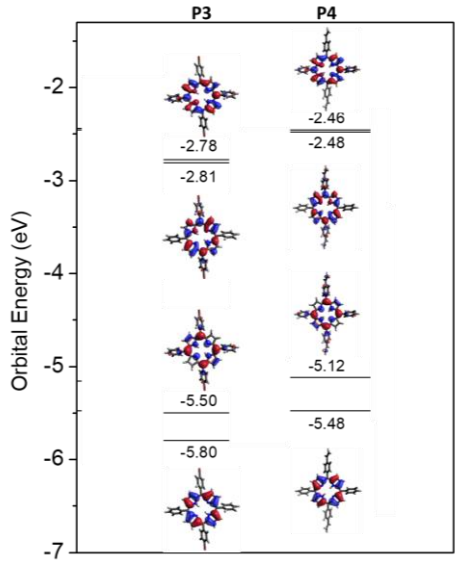

***Figure IIA-5**: Representation of the frontier orbitals for **P3** and **P4**.*

For the calculation of excited states, a benchmark has been performed on **P3** to choose the most reliable method (functional and basis set) in the case of the substituted porphyrin. Different density functional theory methods have been tested, *i.e*. B3LYP, CAM-B3LYP, M06-2X, PBE0 and HSE06, with different basis set combinations, *i.e*. 6-31G(d), 6-31+G(d), 6-311++G(d,p) and DZVP. The calculated Soret band determined by the different methods are summarized in **Table S1**. The 6-31+G(d) basis set provides reliable results at a reasonable computational cost. The choice of B3LYP that is widely used for porphyrin computing [11,52–56] is also reasonable. Finally, as several publications presented different functional/base combinations for optimisation calculations and then TDDFT calculations [54,57,58], two series of calculations were carried out using a combination of these theories. The best agreement with the experiment was achieved using B3LYP/6-31+G(d) for both the DFT and TDDFT calculations

The computed electronic transitions (**Table IIA-3**) are in good agreement with experimental data. Indeed, transition energies associated with their oscillation strengths (*f*) reveal two low-intensity transitions, located approximately at 600 nm, corresponding to the Q bands (without their vibronic overtones), as well as two high-intensity transitions, which correspond to the Soret band. In addition, the Soret wavelength are in good adequation with the theoretical values, indeed the variations observed for the experimental Soret band compared with the TDDFT predictions are neglectable. However, it can be noted that TDDFT calculations predict significantly lower wavelengths for the Q-bands compared to those experimentally observed. Indeed, the lowest energetic peak reveals a significant difference of 69 nm for **P3** and 62 nm for **P4**.

***Table IIA-3**: Excitation energies (λ) and oscillator strengths (f) for different excited states transitions of **P3** and **P4** determined by TD-DFT using B3LYP/6-31G(d) basis set.*

Porphyrin	transition	λ_{abs} (nm)	*f* (a.u.)
P3	$S_0 \rightarrow S_1$	580.23	0.0415
	$S_0 \rightarrow S_2$	544.40	0.0476
	$S_0 \rightarrow S_3$	411.48	1.4566
	$S_0 \rightarrow S_4$	405.86	1.7718
P4	$S_0 \rightarrow S_1$	584.96	0.0744
	$S_0 \rightarrow S_2$	549.73	0.1146
	$S_0 \rightarrow S_3$	413.58	1.7850
	$S_0 \rightarrow S_4$	405.39	1.5069

Reactivity of P3 and P4 under light irradiation in the presence of co-initiators.

a) Porphyrin characterization. P3 and **P4** were used as part of new photoinitiating systems when combined with co-initiators, *i.e.* MDEA, Iod, cysteamine and *N*-acetylcysteine, to achieve free-radical polymerization of SOA. In order to suggest a mechanism involving the porphyrin-based photoinitiating systems under irradiation, we described in detail their photochemical properties by steady-state photolysis, fluorescence, laser flash photolysis, EPR-ST experiments. All these properties are summarized in **Table S2** including the redox properties (E_{ox} and E_{red}) of both porphyrins (**Figure S5**), and the energies of the excited singlet (E_S) and triplet states (E_T) determined by fluorescence and laser flash photolysis experiments respectively. These results were used to determine the free energy changes (ΔG_S and ΔG_T at the singlet and triplet excited state respectively) according to Rehm-Weller equation (**Equation S1**) and given in **Table IIA-4**, confirming thus that the electron transfer reactions may be favourable or not.

Table IIA-4*: Free energy changes (in kJ.mol^{-1}) at the singlet excited (ΔG_S) and triplet excited (ΔG_T) state for different photo-initiating systems involving **P3**, **P4**, BP and CQ in the presence of MDEA, Iod, cysteamine and N-acetylcysteine as co-initiators.*

	MDEA		Iod		cysteamine		*N*-acetylcysteine	
	ΔG_S	ΔG_T	ΔG_S	ΔG_T	ΔG_S	ΔG_T	ΔG_S	ΔG_T
P3	4.0	-82.9	-59.7	23.3	23.3	-63.6	10.7	-76.1
P4	-25.0	-100.0	-82.0	-5.7	-5.7	-80.6	-18.3	-93.2
BP		-44.7				-25.4		-37.8
CQ		-21.2				-1.9		-14.5

Used alone, and under LED@405 nm irradiation, the absorbance of both porphyrins does not change, demonstrating their high stability (**Figure S6**). However, the irradiation of P3 and P4 in the presence of DMPO leads to a superposition of individual signals of DMPO-adducts generated *via* reaction of DMPO with free radicals. The spin-Hamiltonian parameters of corresponding DMPO-adducts elucidated from the simulations are as follows: *i*) •DMPO-$CHCl_2$ (a_N = 1.401 mT, a_H^β = 1.997 mT; *g* = 2.0061), *ii*) •DMPO-CCl_3 (a_N = 1.363 mT, a_H^β = 1.585 mT; *g* = 2.0062) and iii) •DMPO-CR (a_N = 1.483 mT, a_H^β = 2.157 mT; *g* = 2.0059), assigned to a DMPO-adduct of carbon-centered radical produced most probably from porphyrins (**Figure S7**).

Transient absorption spectra of **P3** and **P4** are determined by Laser Flash Photolysis (LFP) between 350 and 750 nm under laser excitation at λ = 385 nm (**Figure S8A and B**). The absorption maxima corresponding to the triplet excited states of **P3** and **P4** are observed at 444 nm and 460 nm respectively. As expected, the triplet states of both porphyrins are highly sensitive to oxygen, and results in a tremendous decrease of their lifetime going from τ = 25.7 µs to τ = 0.95 µs and from τ = 28.2 µs to τ = 0.63 µs for **P3** and **P4** respectively (**Figure S8C and D**).

b) Effect of the addition of MDEA. Under irradiation, the addition of MDEA significantly decreases the absorbance of both porphyrins (**Figure IIA-6**). The absorbance of **P3** is divided by a third in 10 minutes, while the absorbance of **P4** decreases by a half in only 140 s. These results are in good agreement with a possible electron transfer reaction between the porphyrins and MDEA. According to **Table 4**, calculation of the electron-transfer Gibbs energy ΔG between **P3** in its singlet state and MDEA in its ground state is thermodynamically unfavourable (ΔG_S^{MDEA}(**P3**) = 4.0 eV > 0) contrary to **P4** (ΔG_S^{MDEA}(**P4**) = -25.0 eV < 0). Experimental investigation of the singlet state upon addition of MDEA by fluorescence is consistent with these low ΔG values. Indeed, both porphyrins exhibit a low quenching

of their singlet state in the presence of MDEA (**Figure S9**), with fluorescence quenching rates of K_{SV}^{MDEA} (**P3**) = 9.8 M^{-1} and K_{SV}^{MDEA} (**P4**) = 0.9 M^{-1}.

Interestingly, the addition of MDEA to both porphyrin solutions leads to an increase of their triplet lifetime (from τ = 25.7 µs to τ = 32.8 µs for **P3** and from τ = 28.2 µs to τ = 49.2 µs for **P4**) highlighting the formation of new species. The favourable electron-transfer Gibbs energies ΔG (ΔG_T^{MDEA}(**P3**) = -82.9 kJ.mol^{-1} and ΔG_T^{MDEA} (**P4**) = -100.0 kJ.mol^{-1}) are in accordance with an electron transfer reaction between MDEA and the triplet excited state of porphyrins. The irradiation of both porphyrins at λ = 405 nm in the presence of MDEA and DMPO shows some individual DMPO-adducts: with a dominant signal of •DMPO-C(α-aminoalkyl) characterized by the spin-Hamiltonian parameters a_N = 1.509 mT, a_H^{β} = 1.730 mT, a_H^{γ} = 0.183 mT, a_H^{γ} = 0.0730 mT; g = 2.0057 [59] and two less-abundant signals of DMPO-adduct with a carbon-centered radical (a_N = 1.500 mT, a_H^{β} = 2.164 mT; g = 2.0059) and •DMPO-$CHCl_2$ reflecting interaction of photo-initiating system with solvent (**Figure S11**).

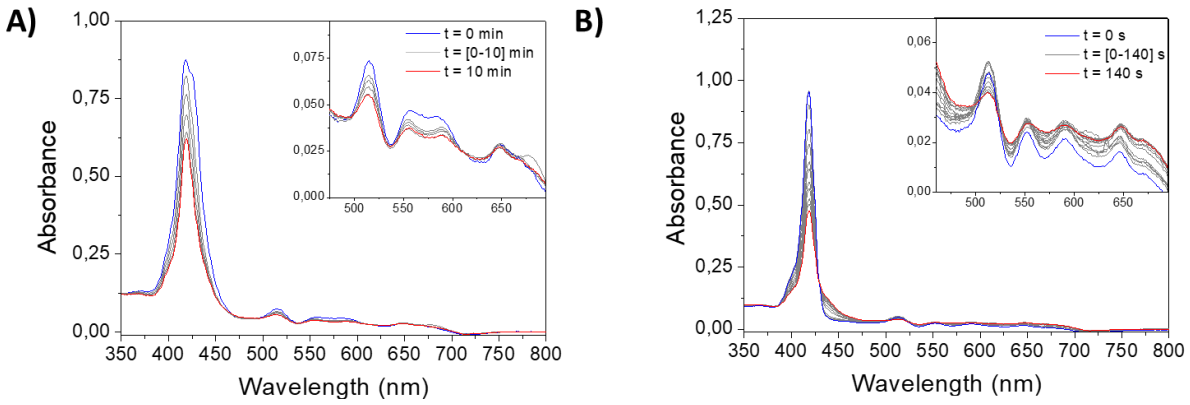

***Figure IIA-6**: Steady state photolysis of a DCM solution of **A) P3** and **B) P4** in the presence of MDEA under air after LED @405 nm irradiation. [**P3**] = 1.9 x 10^{-5} mol.L^{-1}, [**P4**] = 2.9 x 10^{-6} mol.L^{-1}, [MDEA] = 2.8 x 10^{-2} mol.L^{-1}.*

c) Effect of the addition of Iod. The addition of Iod has a strong effect on the absorbance of both porphyrins (**Figure IIA-7**). The absorbance of **P3** significantly decreases after only 10 s, whereas the one of **P4** remains slower than that observed with **P3**. Interestingly, and concomitantly to the decrease of the absorbance of both porphyrins, an increase of the absorbance can be observed at 450 nm, indicating thus the formation of new absorbing products.

The singlet state study of the porphyrins revealed a quenching upon addition of Iod (**Figure S11)**. The Stern-Volmer constants are relatively high (K_{SV}^{Iod} (**P3**) = 2600 M^{-1} and K_{SV}^{Iod} (**P4**) = 1756 M^{-1}), indicating a rapid exchange between the components. This results is consistent with the low values of free energy change, corresponding to a favourable reaction: ΔG_S^{Iod}(**P3**) = -59.7 kJ.mol^{-1} and ΔG_S^{Iod} (**P4**) = -82.0 kJ.mol^{-1}. At triplet state, the Rehm-Weller predict a lower reactivity (ΔG_T^{Iod}(**P3**) = 23.3 kJ.mol^{-1} and ΔG_T^{Iod} (**P4**) = -5.7 kJ.mol^{-1}), which is consistent with the poor interaction observed using LFP (**Figure S13**). EPR spectra obtained upon irradiation of **P3** and **P4** in the presence of Iod in $CHCl_3$ under argon present broad signals with unresolved hyperfine structures (**Figure S14**), which can be assigned to the corresponding porphyrin radical cations, **P3**$^{\bullet+}$ and **P4**$^{\bullet+}$ (g=2.0040 and g=2.0032 for **P3**/Iod and **P4**/Iod respectively).

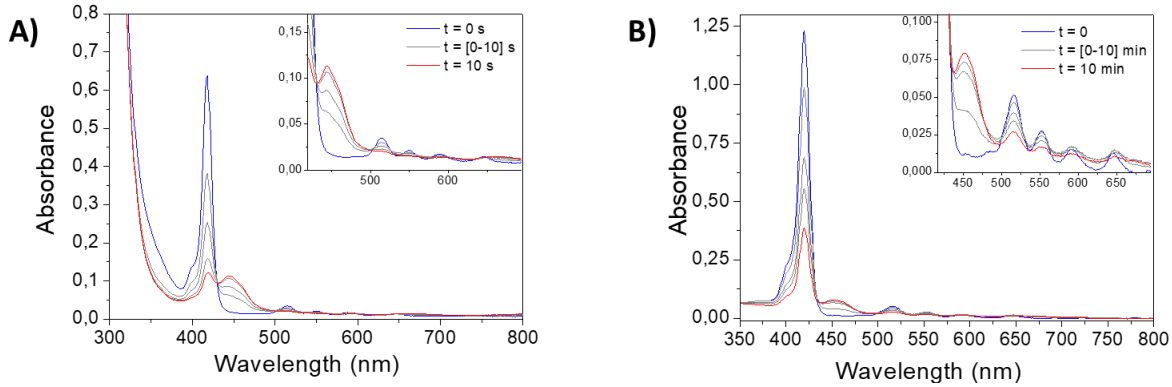

***Figure IIA-7**: Steady state photolysis of **A**) **P3** and **B**) **P4** in presence of Iod under air after LED @405 nm exposure. [**P3**] = 1.9 x 10^{-5} mol/L, [**P4**] = 2.9 x 10^{-6} mol/L, [Iod] = 2.9 x 10^{-5} mol/L. Solvent = DCM*

d) Effect of the addition of cysteamine. The addition of cysteamine has no significant influence on the evolution of porphyrin absorption after 10 minutes of irradiation (**Figure S15**). However, despite a less favourable free energy change at singlet state ($\Delta G_S^{cysteamine}$(**P3**) = 23.3 kJ.mol^{-1} and $\Delta G_S^{cysteamine}$ (**P4**) = -5.7 kJ.mol^{-1}), the study of the singlet state shows an interaction between porphyrins and cysteamine, with a high quenching constant of $K_{SV}^{cysteamine}$ (**P3**) = 235 M^{-1} and $K_{SV}^{cysteamine}$ (**P4**) = 351 M^{-1} for **P3** and **P4** respectively (**Figure S16**). The EPR spectra confirmed this interaction, by revealing the formation of a signal of limited stability, typical for •DMPO-SR spin-adduct (a_N = 1.369 mT, a_H^{β} = 1.247 mT, a_H^{γ} = 0.094 mT, a_H^{γ} = 0.082 mT; g = 2.0059 [8,60]) when irradiated with DMPO (**Figure S18**). The study of interaction between cysteamine and porphyrins a triplet state reveal a limited modification for **P4**, and a small increase in lifetime of the excited state of **P3** (**Figure S17**). These results indicate a photoinduced electron transfer between excited porphyrins and cysteamine coupled with the formation of porphyrin radical anions.

d) Effect of the addition of *N*-acetylcysteine.
The effect of the addition of *N*-acetylcysteine on the photochemical properties of porphyrins is less pronounced. Steady state photolysis (**Figure S19**) does not reveal any interaction, since the absorbance of both porphyrins remains stable during an irradiation of 10 min, without the appearance of new peaks. The study of singlet excited state reveals fluorescence quenching upon gradual addition of *N*-acetylcysteine to a solution of **P3** (**Figure S20**), with a Stern-Volmer constant of $K_{SV}^{\mathbf{P3}/N\text{-acetylcysteine}}$ = 216 M^{-1}. In contrast, the addition of *N*-acetylcysteine to a solution of **P4** results in an increase of fluorescence intensity, suggesting the presence of a new species. In the triplet state, cysteamine has no quenching effect, but an increase in the lifetime of excited species is observed for **P3** (**Figure S21**). Indeed, it can be observed that the decay traces require a longer time to reach zero, implying the presence of a more stable porphyrin excited state. For **P4**, on the other hand, no significant change is observed. The EPR-SP study revealed the presence of a DMPO-SR adduct upon irradiation of porphyrin solutions in the presence of *N*-acetylcysteine and BMPO, consistent with the presence of a thiyl radical (**Figure S22**). The Hamiltonian parameters of this adduct are a_N = 1.417 mT, a_H^{β} = 1.409 mT, a_H^{γ} = 0.086 mT, a_H^{γ} = 0.063 mT; g = 2.0061. It should be noted that this adduct is also present without irradiation, which can be explained by the formation of a Forrester-Hepburn mechanism (**Figure S23**), but this adduct is present in much smaller quantities.

Free radical polymerization. Free radical polymerization have been carried out using a porphyrin in combination with MDEA, Iod, cysteamine or *N*-acetylcysteine and using SOA as a monomer. Kinetic profiles of experiment under LED@405 nm irradiation under laminate and under air are shown in **Figure IIA-8** and final monomer conversion after 800 s are presented in **Table IIA-5**. As previously seen, porphyrins can be reactive toward co-initiator to produce radical species, suggesting the possibility of

FRP on acrylated functions of the monomer. Interestingly, high final conversion of monomer are obtained using porphyrin and MDEA (0.5%/5% wt.wt) under a wide range of irradiation. Maximal monomer conversion are obtained at LED@405 nm irradiation corresponding to their maximal absorption, *i.e.* 91% for both porphyrin under laminate and 93% and 80% for **P3** and **P4** respectively under an oxygen atmosphere. In the same condition, CQ only afforded 56% and 38% of acrylate conversion under laminate and oxygen respectively. Upon higher wavelength irradiation, porphyrin/MDEA allow polymerization around 60% and 40% for both porphyrin at 455 nm under laminate and under oxygen respectively. At 530 nm, the conversion of the monomer still reach around 45% under laminate and 26% under oxygen atmosphere. Systems containing 5% cysteamine were found to polymerise at room temperature in the absence of light. To achieve optimal conditions, the cysteamine concentration had to be reduced to 1%. It should be noted that cysteamine is not soluble in SOA, requiring the incorporation of a small amount of ethanol to achieve homogeneity of the photoinitiating solution before evaporation of solvent. This can explain the low monomer conversion of 61 and 70% for **P3** and **P4** respectively at 405 nm under laminate. Monomer conversions for *N*-acetylcysteine-containing systems are particularly high when polymerised at 405 nm in air, reaching 96% and 85% for **P3** and **P4** respectively. Finally, systems based on Iod are particularly interesting for high wavelength applications. When irradiated at 405nm, the final monomer conversion shows a good conversion of 86% for **P3** but only 70% for **P4**. However, Iod-based system enables higher conversion rates than other co-initiator to be achieved at 530 nm, reaching 70% under laminate for **P3**.

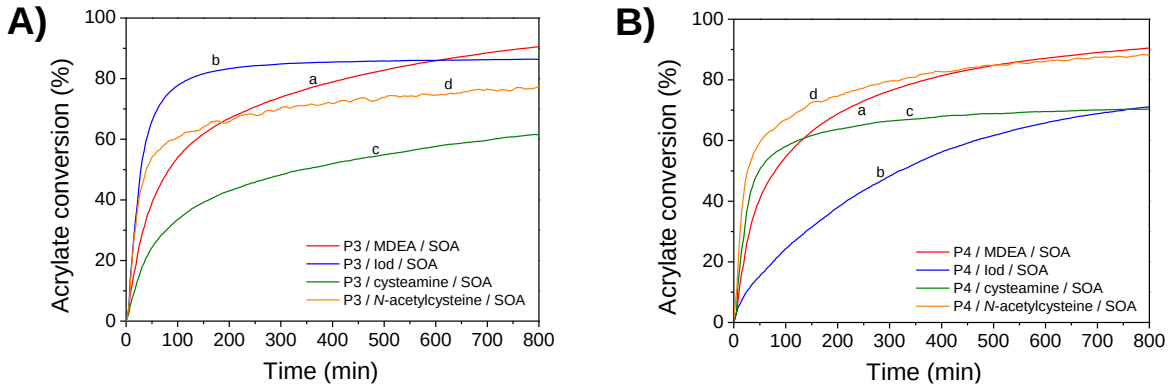

***Figure IIA-8**: Kinetic profiles of FRP of SOA under laminate for **A) P3** and **B) P4** in the presence of (a) MDEA (0.5%/5% w/w), (b) Iod (0.5%/2.5% w/w), (c) cysteamine (0.5%/1% w/w) and (d) N-acetylcysteine (0.5%/5% w/w) under LED@405 nm exposure.*

***Table IIA-5**: Acrylate conversion (%) of SOA determined by IR after 800 s of irradiation under LEDs@385 nm, 405 nm, 455 nm and 530 nm of different photoinitiating system containing porphyrins (0.5% w) under laminate (a) or under air (b).*

	Final conversion (%)							
Photoinitiating systems	385 nm		**405 nm**		455 nm		530 nm	
P3/MDEA(5%)/SOA	73 [a]	55 [b]	**91** [a]	**93** [b]	64 [a]	40 [b]	43 [a]	26 [b]
P4/MDEA(5%)/SOA	76 [a]	48 [b]	**91** [a]	**80** [b]	66 [a]	40 [b]	47 [a]	26 [b]
CQ/MDEA(5%)/SOA	28 [a]	np [b]	**56** [a]	**38** [b]	68 [a]	44 [b]	40 [a]	np [b]
P3/Iod(2.5%)/SOA	77 [a]	30 [b]	**86** [a]	**46** [b]	66 [a]	13 [b]	70 [a]	13 [b]
P4/Iod(2.5%)/SOA	62 [a]	28 [b]	**70** [a]	**46** [b]	51 [a]	9 [b]	43 [a]	2 [b]
CQ/Iod(2.5%)/SOA	79 [a]	13 [b]	**84** [a]	**51** [b]	81 [a]	64 [b]	73 [a]	np [b]
P3/cysteamine(1%)/SOA	47 [a]	30 [b]	**61** [a]	**58** [b]	29 [a]	26 [b]	21 [a]	15
P4/cysteamine(1%)/SOA	45 [a]	25 [b]	**70** [a]	**53** [b]	31 [a]	10 [b]	17 [a]	np [b]
CQ/cysteamine(1%)/SOA	Polymerization at Rt							
P3/cysteine(5%)/SOA	99 [a]	37 [b]	**78** [a]	**96** [b]	82 [a]	np [b]	50 [a]	np [b]

P4/cysteine(5%)/SOA	92 [a]	np [b]	**78** [a]	**85** [b]	92 [a]	np [b]	61 [a]	np [b]
CQ/cysteine(5%)/SOA	78 [a]	14 [b]	**98** [a]	**33** [b]	95 [a]	44 [b]	52 [a]	np [b]

[a] under laminate, [b] under air, np : no polymerization

Application. The results obtained in photopolymerization with MDEA and SOA provide an opportunity to synthetize biosourced coatings for water depollution (**Figure S24**).

Release study. Release experiment have been done with **P4** base materials (**P4**/MDEA/SOA 0.5/5 wt.wt) were carried out to demonstrate the advantage of adding vinyl functions to create covalent bond between monomer and porphyrin. Materials containing TPP have been used as reference. The different pellets have been immerged into ethanol and the percentage of porphyrin release have been determined by UV-visible spectroscopy by following the absorbance band at 419 nm. The results are displayed in **Figure IIA-9A**. The addition of vinyl function on P4 limits the release of porphyrin derivative from the materials after 5 h. Indeed only 10% of P4 is released in comparison with TPP-based materials which TPP percentage release reaches 55% in the same experimental conditions. These results highlight that vinyl group on P4 allow to make covalent bonds with the polymer network, probably leading to a long-lasting efficacy.

Considering that **P3** contains no function enabling it to be covalently bonded to the polymer network, its release in ethanol is not relevant. However, we can see from release experiments in water (**Figure IIA-9B**) that the material remain stable during 5 hours of immersion: there is no sign of degradation as in the case with TPP in ethanol. However, a small amount of SOA was released.

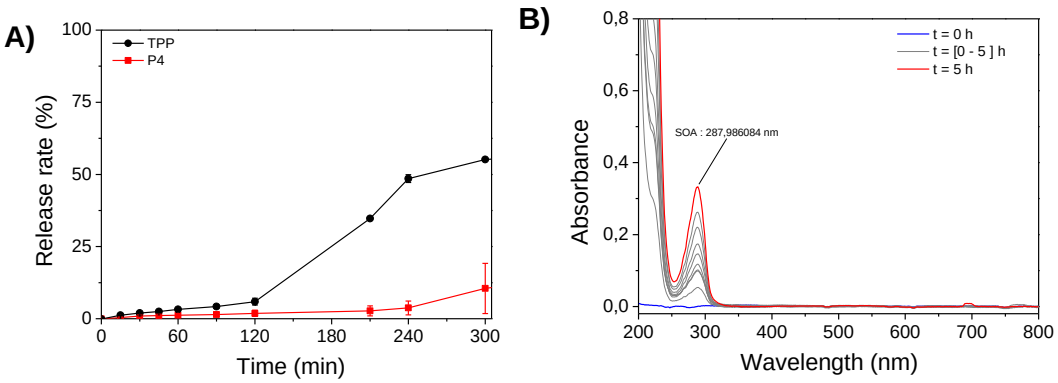

*Figure IIA-9: **A**) Release rate of **P4** and TPP in ethanol. **B**) Absorption spectrum of a **P3** coating in water during 5 hours.*

Adhesion. The production of pellets is possible, but requires a considerable amount of material. Alternatively, coatings can be developed to cover surfaces, providing photoactive properties while minimising material consumption. Glass initially adheres well (**Figure IIA-10**), but tends to delaminate after prolonged immersion. To overcome this problem, a Teflon film is used to reinforce adhesion on each side of the film.

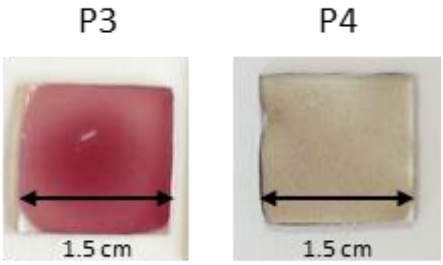

Figure IIA-10: *Pictures of **P3** and **P4** coating (0.5%wt.wt, MDEA5% wt.wt, SOA) on glass surface.*

Formation of singlet oxygen under UV light. In order to anticipate the depollution capacity of the porphyrin-based materials, ROS formation tests have been carried out. The energy transfer between the porphyrin in the material and the oxygen, and therefore the formation of singlet oxygen, was monitored with the TPCPD probe (mechanism in **Figure S25**). A decrease in absorbance is detected by UV-Visible spectroscopy, and after 10 minutes, a decrease of 32% was observed without any material, while materials based on **P3** and **P4** allowed a decrease of 92% (**Figure IIA-11**). We can therefore conclude that both materials lead to the formation of singlet oxygen under UV irradiation. The following mechanism can therefore be proposed:

$$\mathrm{P} \xrightarrow{h\nu} {}^{3}\mathrm{P}^{*} \qquad (3-a)$$

$${}^{3}\mathrm{P}^{*} + {}^{3}\mathrm{O}_2 \rightarrow {}^{1}\mathrm{P} + {}^{1}\mathrm{O}_2 \qquad (3-b)$$

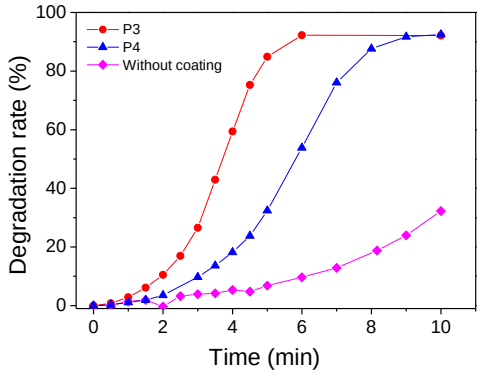

Figure IIA-11: *Degradation of TPCPD at 510 nm, indicating formation of singlet oxygen, in presence of **P3** or **P4** coating under UV lamp ($\lambda_{maximum}$ = 365 nm) in an open air system. [TPCPD] = 3.4 x 10^{-4} mol.L^{-1} in methanol.*

Degradation study. The photodegradation capacity of these materials for water decontamination was next evaluated. Studies were carried out on Acid Red 14, a dye used in textile and food industries. The coating was immerged in an aqueous solution of AR14 and irradiated by an UV lamp with a maximum wavelength of 365 nm. The degradation of the dye was monitored by UV-Visible spectroscopy every 15 minutes, until total degradation was achieved (**Figure IIA-12A** for **P3** coating and **Figure IIA-12B** for **P4** coating).

The photodegradation results are shown in **Figure IIA-12C**. It can be seen that good levels of degradation are obtained for the both **P3-** and **P4-based** materials compared with photolysis. Indeed, a large difference in degradation can be seen after 2 hours of irradiation, with around 30% difference in the degradation rate between **P3** or **P4** and photolysis 32% and 27% respectively. In addition, a 90% degradation rate is reached in around 3 hours for materials containing **P3** or **P4**, whereas more than 5

hours are needed for photolysis alone. Finally, after 5 h, all the dye had been degraded, which is not the case for photolysis alone. Adsorption tests without a lamp were carried out (**Figure IIA-12D**), proving that the decrease in absorbance was not due to absorption of the dye by the material, but rather to degradation of the material.

These results are difficult to compare with the literature, as many parameters can affect depollution, such as the type and size of the material or the type of structure, the concentration and the volume of the pollutant to degrade. However, two methods can be used to compare photocatalytic efficiencies: *i*) by rationalising the quantity of pollutant degraded per unit of time and surface area of the material, or *ii*) by determining the first-order constant k_{app} of the systems.

A review proposes to compare the efficiency of different polymers loaded with photoactive molecules [61] on the degradation of acid black (AB). The result shows that acid black decomposes more rapidly than acid red under photolysis, with a k_{app} (AB) = 0.005 compared with k_{app}(AR14) = 0.003, suggesting a lower stability of this molecule. As a result, the systems studied allow degradation with a k_{app} = [0.03 - 0.10], presenting a degradation 6 to 20 times greater than photolysis, whereas porphyrin-based polymers show degradation 2 times greater than photolysis, but with a lower charge of photoactive molecule (0.5% for porphyrins and 1% for the review) and a different azo-dye.

However, some polymeric systems, based on MOFs such as MIL-53(Cr) and HKUST-1(Cu)[62] or perovskites (LaTiO3 or Nd0.9TiO3)[63] allow degradation of 6.4 µmol.min^{-1}.m^{-2}, and 12. 2 µmol.min^{-1}.m^{-2}, where porphyrin-based materials allow slightly lower degradation, at 4.4 µmol.min^{-1}.m^{-2}, but with a lower loading of photoactive molecule, at 0.5%, where most of these systems are loaded at 2%.

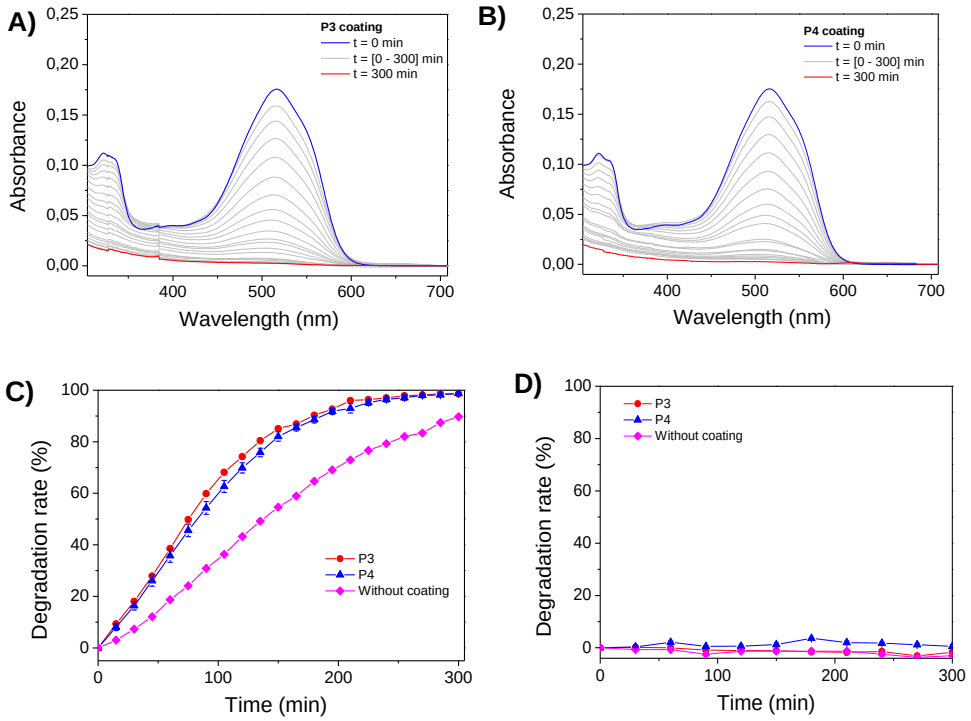

***Figure IIA-12**: Photodegradation of AR14 under UV irradiation UV lamp ($\lambda_{maximum}$ = 365 nm) in an open air system for **A)** **P3** and **B)** **P4**. **C)** Associated degradation rate of AR14 for **P3** coating, **P4** coating and without coating. **D)** Adsorption of AR14 on surface of **P3** or **P4** without light. The controls without coating and without light are presented to control the stability of solution.*

The reusability of the films was also determined with **P4-based** coating. After an initial irradiation, the sample was rinsed with water and ethanol and air-dried. A second and third degradation cycle were

then carried out. The results are shown in **Figure IIA-13**. It can be seen that the efficiency drops slightly at the start of the experiment, but after two hours of irradiation, the efficiency is restored.

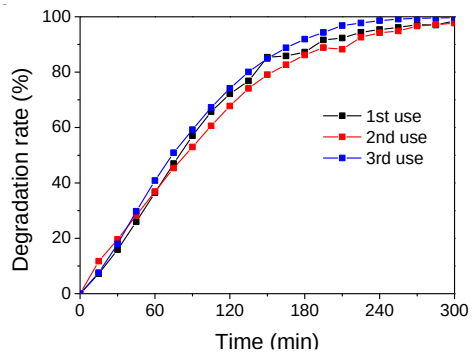

***Figure IIA-13**: Degradation rate of AR14 for **P4** coating after several reuse..*

IV. Conclusion

In this article, two new free base porphyrins are presented for their potential use as photoagents, with the ability to act as a photoinitiator to initiate free-radical polymerization and then to act as a photosensitizer for water depollution. Synthesis and computing of porphyrins, characterisation of photoactives systems, polymer synthesis and their use in pollutant photodegradation are presented. Their preparation is based on the use of a dibrominated synthon for a functionalization by a Suzuki coupling. Interactions between these porphyrins and several co-initiators (MDEA, Iod and cysteamine) were studied by steady state photolysis, fluorescence, laser flash photolysis, EPR and cyclic voltammetry, and revealed the intervention of an electron transfer reaction. Porphyrins **P3** and **P4** were used to initiate FRP in combination with co-initiator. MDEA-based systems achieved polymerisation with a final conversion of monomer of 91% for both porphyrins under irradiation at LED@405 nm. Systems based on Iod allow a final conversion of 84% and 70% for **P3** and **P4**, and a fast initiation, reaching 90% of monomer conversion in 100 s and 190 s respectively. The advantage of the presence of phenyl groups on the porphyrins was demonstrated by comparison with 2 and P6 porphyrins. The materials obtained are based on acrylated soya oil, and **P4** demonstrated its capacity to form covalent bonds with the acrylate functions of the monomer, making possible to improve the stability and reusability of the material. These materials demonstrated an ability to form ROS, and were used for the photodegradation of dyes in water. They showed similar activities, for a total degradation of 30 mL of a 10 µM solution of AR14. The **P4**-based material showed possible reuse without loss of efficiency, after only rinsing the material with water and ethanol.

V. References

1 Y. Yagci, S. Jockusch and N. J. Turro, Macromolecules, 2010, 43, 6245–6260.
2 B. P. Chan, Tissue Engineering Part B: Reviews, 2010, 16, 509–522.
3 H. Claus, Photochemistry and Photobiology, 2021, 97, 471–476.
4 K. J. Gromkowska-Kępka, A. Puścion-Jakubik, R. Markiewicz-Żukowska and K. Socha, J of Cosmetic Dermatology, 2021, 20, 3427–3431.
5 H. Kaczmarek, Polymer, 1996, 37, 547–553.
6 P. Sautrot-Ba, A. Contreras, S. A. Andaloussi, T. Coradin, C. Hélary, N. Razza, M. Sangermano, P.-E. Mazeran, J.-P. Malval and D.-L. Versace, J. Mater. Chem. B, 2017, 5, 7572–7582.
7 D. K. Balta, G. Temel, G. Goksu, N. Ocal and N. Arsu, Macromolecules, 2012, 45, 119–125.
8 L. Breloy, V. Brezová, A. Blacha-Grzechnik, M. Presset, M. S. Yildirim, I. Yilmaz, Y. Yagci and D.-L. Versace, Macromolecules, 2020, 53, 112–124.

9 A. Al Mousawi, C. Poriel, F. Dumur, J. Toufaily, T. Hamieh, J. P. Fouassier and J. Lalevée, Macromolecules, 2017, 50, 746–753.
10 D. Kim and J. W. Stansbury, J. Polym. Sci. A Polym. Chem., 2009, 47, 3131–3141.
11 H. Marcille, J.-P. Malval, M. Presset, N. Bogliotti, A. Blacha-Grzechnik, V. Brezová, Y. Yagci and D.-L. Versace, Polym. Chem., 2020, 11, 4237–4249.
12 G. Noirbent, Y. Xu, A.-H. Bonardi, D. Gigmes, J. Lalevée and F. Dumur, European Polymer Journal, 2020, 139, 110019.
13 B. B. Wayland, G. Poszmik, S. L. Mukerjee and M. Fryd, J. Am. Chem. Soc., 1994, 116, 7943–7944.
14 N. Corrigan, D. Rosli, J. W. J. Jones, J. Xu and C. Boyer, Macromolecules, 2016, 49, 6779–6789.
15 G. Ng, K. Jung, J. Li, C. Wu, L. Zhang and C. Boyer, Polym. Chem., 2021, 12, 6548–6560.
16 S. Shanmugam, J. Xu and C. Boyer, Polym. Chem., 2016, 7, 6437–6449.
17 S. Shanmugam, J. Xu and C. Boyer, J. Am. Chem. Soc., 2015, 137, 9174–9185.
18 M. Athar, H. Mukhtar and D. R. Bickers, Journal of Investigative Dermatology, 1988, 90, 652–657.
19 X. Ding, Q. Xu, F. Liu, P. Zhou, Y. Gu, J. Zeng, J. An, W. Dai and X. Li, Cancer Letters, 2004, 216, 43–54.
20 L. M. Rossi, P. R. Silva, L. L. R. Vono, A. U. Fernandes, D. B. Tada and M. S. Baptista, Langmuir, 2008, 24, 12534–12538.
21 W. M. Sharman, C. M. Allen and J. E. van Lier, Drug Discovery Today, 1999, 4, 507–517.
22 H. Zhou and D. W. Smith, Can. J. Civ. Eng., 2001, 28, 49–66.
23 C. Bauer, P. Jacques and A. Kalt, Journal of Photochemistry and Photobiology A: Chemistry, 2001, 140, 87–92.
24 K. A. Yongabi, .
25 M. Grassi, L. Rizzo and A. Farina, Environ Sci Pollut Res, 2013, 20, 3616–3628.
26 Y. Deng and R. Zhao, Curr Pollution Rep, 2015, 1, 167–176.
27 N. Daneshvar, D. Salari and A. R. Khataee, Journal of Photochemistry and Photobiology A: Chemistry, 2003, 157, 111–116.
28 S. Nouacer and R. Djellabi, Environ Sci Pollut Res, , DOI:10.1007/s11356-022-23772-5.
29 K. M. Lee, C. W. Lai, K. S. Ngai and J. C. Juan, Water Research, 2016, 88, 428–448.
30 M. Le Pivert, B. Zerelli, N. Martin, M. Capochichi-Gnambodoe and Y. Leprince-Wang, Construction and Building Materials, 2020, 257, 119592.
31 N. Martin, V. Lacour, C. M.-T. Perrault, E. Roy and Y. Leprince-Wang, React. Chem. Eng., 2022, 7, 750–757.
32 Y. G. Habba, M. Capochichi-Gnambodoe, L. Serairi and Y. Leprince-Wang, physica status solidi (b), 2016, 253, 1480–1484.
33 Y. Leprince-Wang, N. Martin, Y. Ghozlane Habba, M. L. Pivert and M. Capochichi-Gnambodoe, NanoWorld J, , DOI:10.17756/nwj.2019-074.
34 M. Le Pivert, R. Poupart, M. Capochichi-Gnambodoe, N. Martin and Y. Leprince-Wang, Microsyst Nanoeng, 2019, 5, 1–7.
35 M. Nowakowska and K. Szczubiałka, Polymer Degradation and Stability, 2017, 145, 120–141.
36 S. Silvestri, A. R. Fajardo and B. A. Iglesias, Environ Chem Lett, 2022, 20, 731–771.
37 R. Lyubimenko, D. Busko, B. S. Richards, A. I. Schäfer and A. Turshatov, ACS Appl. Mater. Interfaces, 2019, 11, 31763–31776.
38 R. Lyubimenko, B. S. Richards, A. I. Schäfer and A. Turshatov, Journal of Membrane Science, 2022, 642, 119981.
39 Y. Chen, Y. Fang, J. Yu, W. Gao, H. Zhao and X. Zhang, Journal of Hazardous Materials, 2021, 406, 124769.
40 E.-Y. Jeong, M. B. Ansari, Y.-H. Mo and S.-E. Park, Journal of Hazardous Materials, 2011, 185, 1311–1317.
41 M. J. Frisch, G. W. Trucks, H. B. Schlegel, G. E. Scuseria, M. A. Robb, J. R. Cheeseman, G. Scalmani, V. Barone, G. A. Petersson, H. Nakatsuji, X. Li, M. Caricato, A. V. Marenich, J. Bloino, B. G. Janesko, R. Gomperts, B. Mennucci, H. P. Hratchian, J. V. Ortiz, A. F. Izmaylov, J. L. Sonnenberg, D. Williams-Young, F. Ding, F. Lipparini, F. Egidi, J. Goings, B. Peng, A. Petrone, T. Henderson, D. Ranasinghe, V.

G. Zakrzewski, J. Gao, N. Rega, G. Zheng, W. Liang, M. Hada, M. Ehara, K. Toyota, R. Fukuda, J. Hasegawa, M. Ishida, T. Nakajima, Y. Honda, O. Kitao, H. Nakai, T. Vreven, K. Throssell, J. A. Montgomery Jr., J. E. Peralta, F. Ogliaro, M. J. Bearpark, J. J. Heyd, E. N. Brothers, K. N. Kudin, V. N. Staroverov, T. A. Keith, R. Kobayashi, J. Normand, K. Raghavachari, A. P. Rendell, J. C. Burant, S. S. Iyengar, J. Tomasi, M. Cossi, J. M. Millam, M. Klene, C. Adamo, R. Cammi, J. W. Ochterski, R. L. Martin, K. Morokuma, O. Farkas, J. B. Foresman and D. J. Fox, 2016.

42 L. Breloy, V. Brezová, J.-P. Malval, A. Rios de Anda, J. Bourgon, T. Kurogi, D. J. Mindiola and D.-L. Versace, Macromolecules, 2019, 52, 3716–3729.

43 S. Hiroto, Y. Miyake and H. Shinokubo, Chem. Rev., 2017, 117, 2910–3043.

44 B. Vaz, R. Alvarez, M. Nieto, A. I. Paniello and A. R. de Lera, Tetrahedron Letters, 2001, 42, 7409–7412.

45 R. W. Boyle, C. Bruckner, J. Posakony, B. R. James and D. Dolphin, in Organic Syntheses, John Wiley & Sons, Ltd, 2003, pp. 287–287.

46 L. R. Nudy, H. G. Hutchinson, C. Schieber and F. R. Longo, Tetrahedron, 1984, 40, 2359–2363.

47 O. B. Locos and D. P. Arnold, Org. Biomol. Chem., 2006, 004, 902–916.

48 M. Gouterman, G. H. Wagnière and L. C. Snyder, Journal of Molecular Spectroscopy, 1963, 11, 108–127.

49 A. K. Mandal, M. Taniguchi, J. R. Diers, D. M. Niedzwiedzki, C. Kirmaier, J. S. Lindsey, D. F. Bocian and D. Holten, J. Phys. Chem. A, 2016, 120, 9719–9731.

50 C. J. Kingsbury and M. O. Senge, Coordination Chemistry Reviews, 2021, 431, 213760.

51 L. G. Arnaut, in Advances in Inorganic Chemistry, eds. R. van Eldik and G. Stochel, Academic Press, 2011, vol. 63, pp. 187–233.

52 S. Daoudi, A. Semmeq, M. Badawi, X. Assfeld, Y. Arfaoui and M. Pastore, Journal of Computational Chemistry, 2019, 40, 2530–2538.

53 S. Perun, J. Tatchen and C. M. Marian, Chemphyschem, 2008, 9, 282–292.

54 N. A. Sánchez-Bojorge, S. Flores-Armendáriz, M. E. Fuentes-Montero, V. H. Ramos-Sánchez, G. Zaragoza-Galán and L. M. Rodríguez-Valdez, J. Porphyrins Phthalocyanines, 2017, 21, 88–102.

55 Y. Gao and V. N. Nemykin, Journal of Molecular Graphics and Modelling, 2013, 42, 73–80.

56 O. Loboda, Quantum-chemical studies on Porphyrins, Fullerenes and Carbon Nanostructures, Springer Berlin Heidelberg, Berlin, Heidelberg, 2013.

57 A. Maufroy, L. Favereau, F. B. Anne, Y. Pellegrin, E. Blart, M. Hissler, D. Jacquemin and F. Odobel, J. Mater. Chem. A, 2015, 3, 3908–3917.

58 J. M. S. Lopes, J. R. T. Reis, A. E. H. Machado, T. H. O. Leite, A. A. Batista, T. V. Acunha, B. A. Iglesias, P. T. Araujo and N. M. Barbosa Neto, Spectrochimica Acta Part A: Molecular and Biomolecular Spectroscopy, 2020, 238, 118389.

59 A. Boulmier, M. Haouas, S. Tomane, L. Michely, A. Dolbecq, A. Vallée, V. Brezová, D.-L. Versace, P. Mialane and O. Oms, Chemistry – A European Journal, 2019, 25, 14349–14357.

60 M. Conte, K. Wilson and V. Chechik, Org. Biomol. Chem., 2009, 7, 1361–1367.

61 M. Benltifa, C. Brahmi, F. Dumur, L. Limousy, L. Bousselmi and J. Lalevée, European Polymer Journal, 2022, 181, 111660.

62 C. Brahmi, M. Benltifa, C. Vaulot, L. Michelin, F. Dumur, F. Millange, M. Frigoli, A. Airoudj, F. Morlet-Savary, L. Bousselmi and J. Lalevée, European Polymer Journal, 2021, 154, 110560.

63 C. Brahmi, , DOI:10.1016/j.eurpolymj.2021.110641.

VI. Supporting information

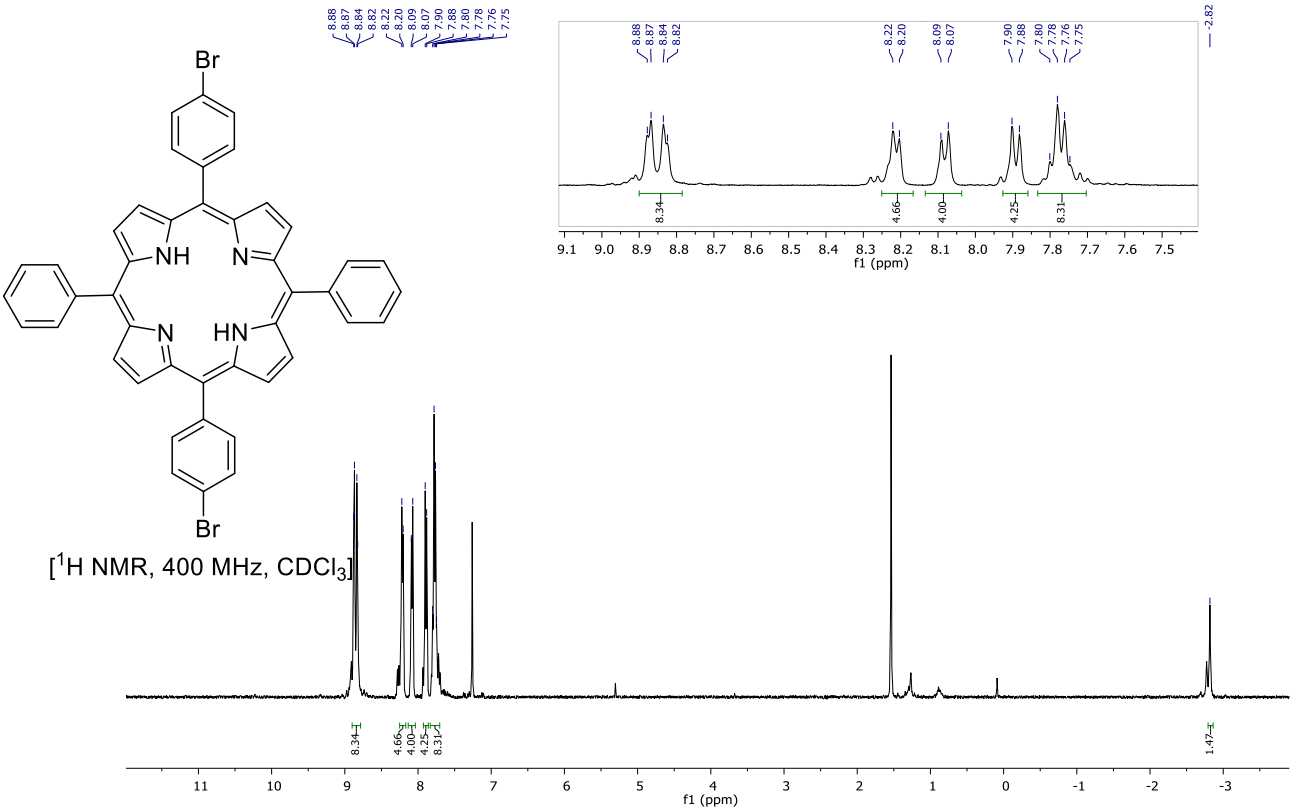

***Figure S1**: ^{1}H NMR spectrum of **P3** in $CDCl_3$.*

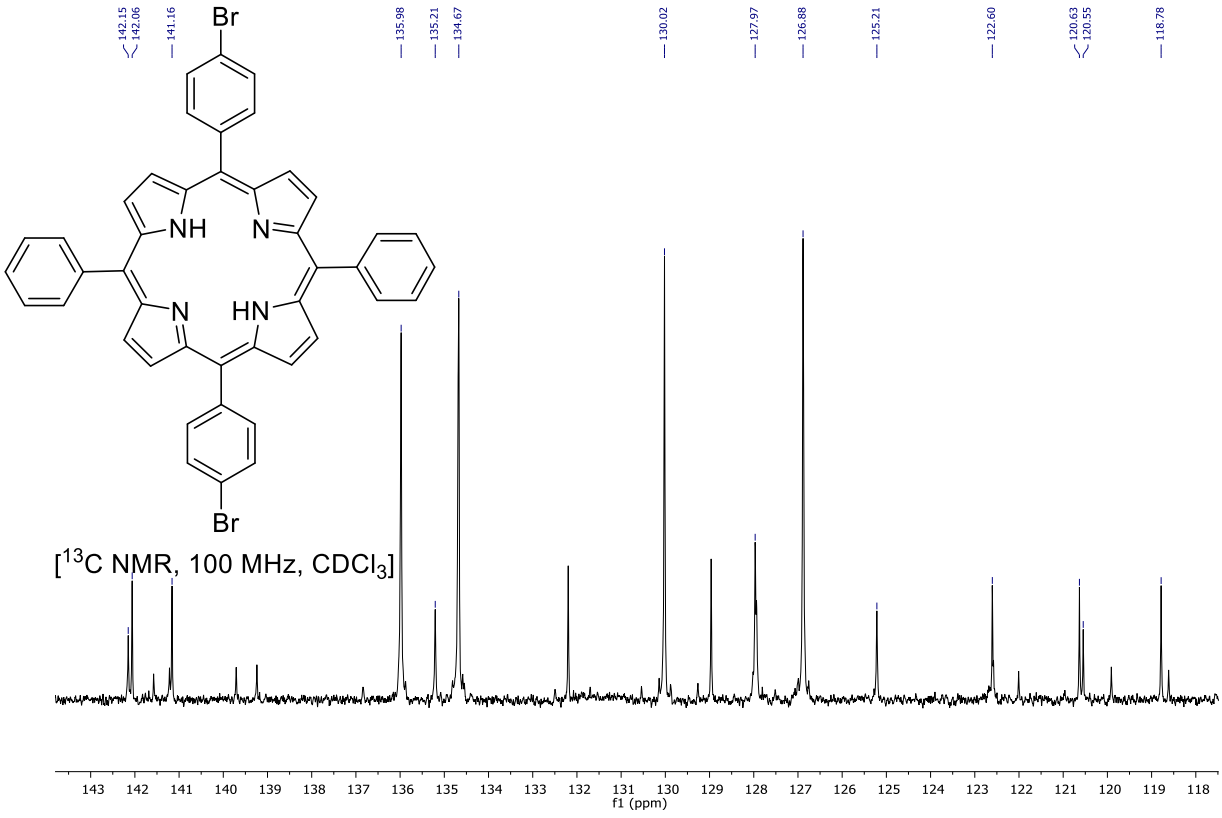

***Figure S2**: ^{13}C NMR spectrum of **P3** in $CDCl_3$.*

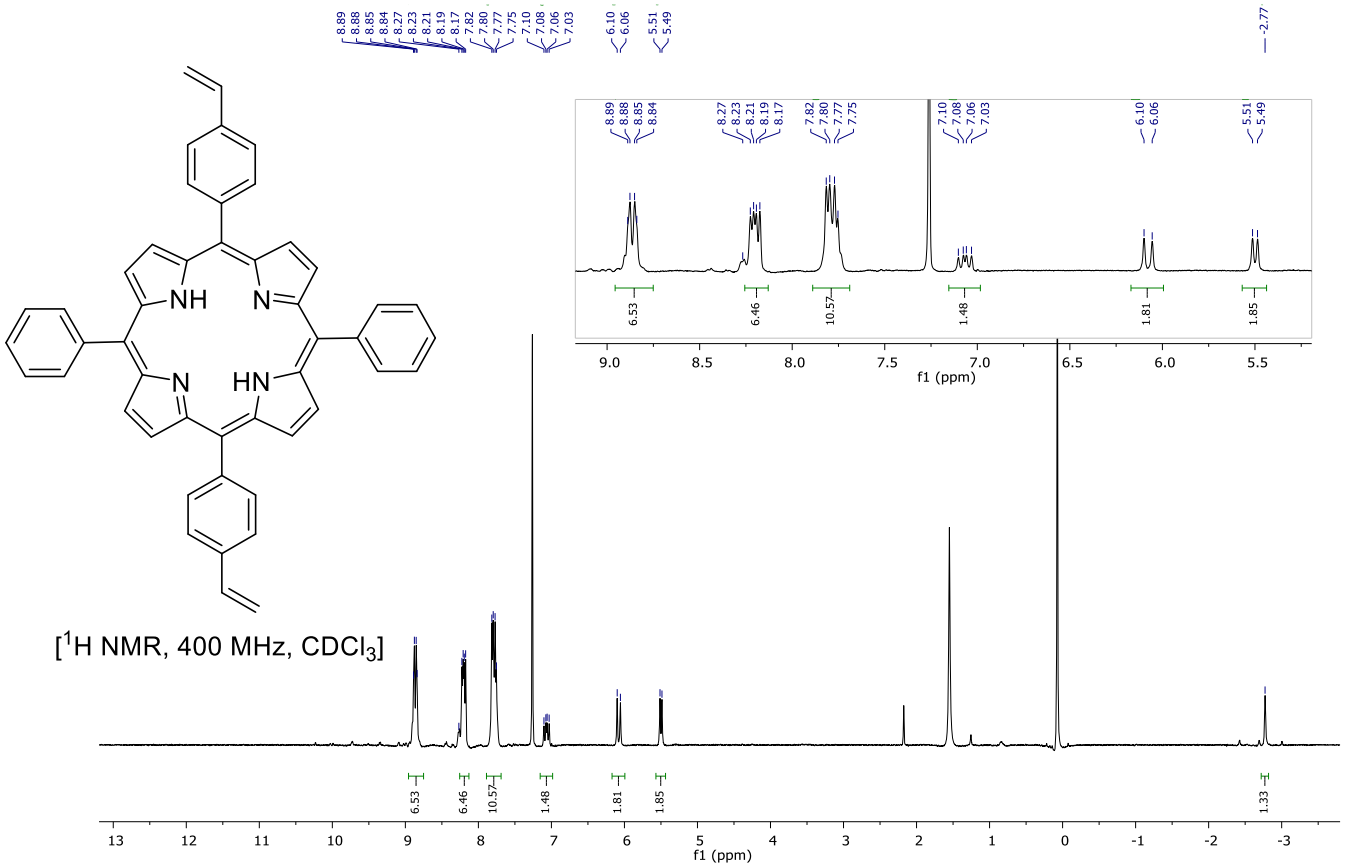

***Figure S3**: ^{1}H NMR spectrum of **P4** in $CDCl_3$.*

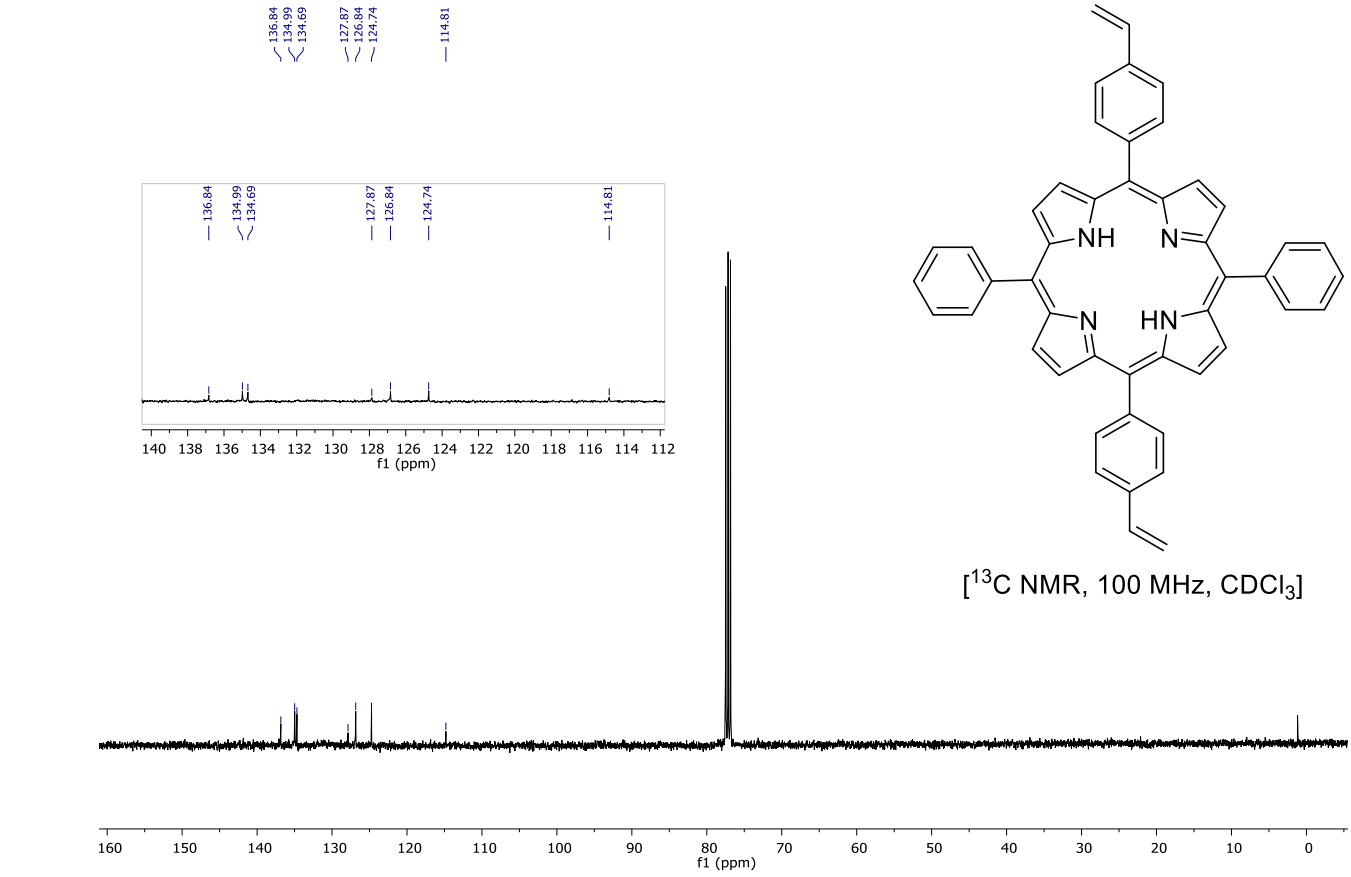

***Figure S4**: ^{13}C NMR spectrum of **P4** in $CDCl_3$.*

Table S1: *Wavelength (nm) of the S0 → S3 transition of P3 using different level of theory. The first column indicates the level of theory use of the optimization of the structure (row 1-8), and the following column indicates the level of theory used for the TDDFT computation (column A-H).*

		A	B	C	D	E	F	G	H
	TD-DFT DFT	B3LYP 6-31G(d)	B3LYP 6-31+G(d)	B3LYP 6-311++G(d, p)	B3LYP DZVP	CAM-B3LYP 6-31+G(d)	PBE0 6-31+G(d)	M062X 6-31+G(d)	HSE06 6-31+G(d)
1	B3LYP 6-31G(d)	406.82							
2	B3LYP 6-31+G(d)		**411.48**		411	387	403	391	407
3	B3LYP 6-311++G(d,p)			411.19					
4	B3LYP DZVP4		410		410.74				
5	CAMB3LYP 6-31+G(d)		405			386.90			
6	PBE0 6-31+G(d)		410				402.68		
7	M062X 6-31+G(d)		409					389.90	
8	HSE06 6-31+G(d)		410						406.93

Photochemical properties:

Table S2*: Photochemical properties of porphyrins. [a] determined by peak potential using cyclic voltammetry. [b] calculated from the wavelength at the intersection of the absorption and emission spectra (λ_{inter}), according to : $E_S = 1240/\lambda_{inter}$. [c] calculated from the wavelength at the maximum absorption of transient absorption spectrum ($\lambda_{triplet}$), according to: $E_T = 1240/\lambda_{triplet}$.*

Molecules	E_{ox}[a] (eV)	E_{red}[a] (eV)	E_S[b] (eV)	E_T[c] (eV)
P3	1,08	-1,22	1.90	2.80
P4	0,87	-0,94	1.92	2.70
BP	0.16 [1]	-1.20 [1]		2.38 [1]
CQ	0.12 [1]	-1.25 [1]		2.21 [1]
MDEA	0.72 [1]		-	-
Iod	-	-0.2 [1]	-	-
cysteamine	0.92 [1]		-	-
N-acetylcysteine	0.79 [1]		-	-

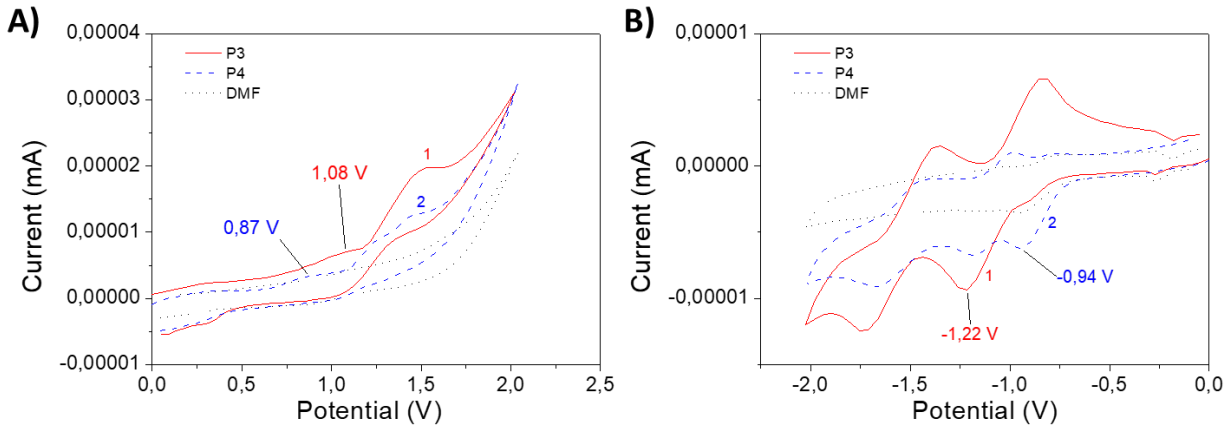

***Figure S5**: Cyclic voltammetry of 1) **P3** and 2) **P4** in DMF ([**P3**] = [**P4**] = [$N_4Et_4BF_4$] = 10^{-3} M) between **A**) 0 V and 2 V to determine the oxidation peak potential E_{ox} and **B**) 0 V and -2 V to determine reduction peak potential E_{red}.*

Rehm-Weller equation.

$$\Delta G_{S \text{ or } T} = F(E_{ox} - E_{red}) - E_{s\,(or\,T)} + \Delta E_c$$

***Equation S1**: Determination of energy change at singlet ΔG_S or triplet state ΔG_T of the electron transfer between a donor and an acceptor under irradiation. Where F is the Faraday constant, E_{ox} is the oxidation reduction of the donor, E_{red} is the reduction potential of the acceptor, $E_{S\,(or\,T)}$ is the excited singlet (or triplet) state of the photoinitiator (**P3** or **P4**) and ΔE_c is the Coulombic stabilization energy, which is negligible for most systems.*

Photostability of porphyrin.

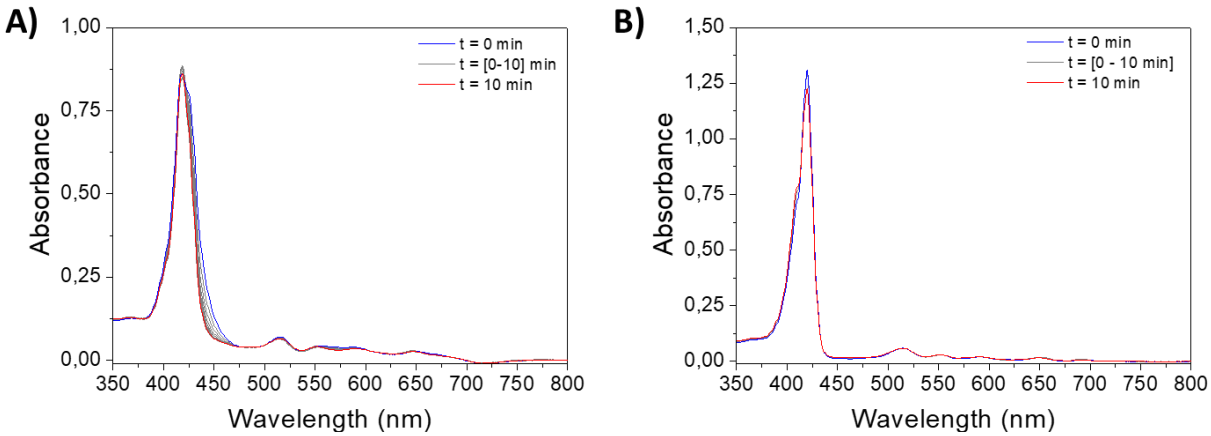

***Figure S6**: Steady state photolysis of different photoinitiating systems under air after LED @405 nm exposure of **A) P3** and **B) P4**. [**P3**] = 1.85 x 10^{-5} mol/L, [**P4**] = 2.9 x 10^{-6} mol/L in DCM.*

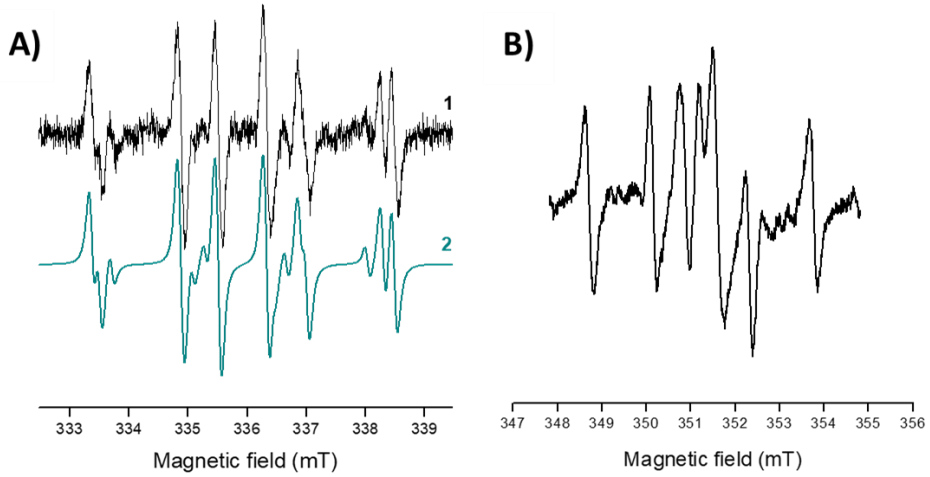

***Figure S7**: The normalized experimental (1) and simulated (2) EPR spectrum obtained upon continuous in situ LED@400 nm exposure of **A) P3** and **B) P4** in chloroform under argon in the presence of DMPO spin trapping agent.*

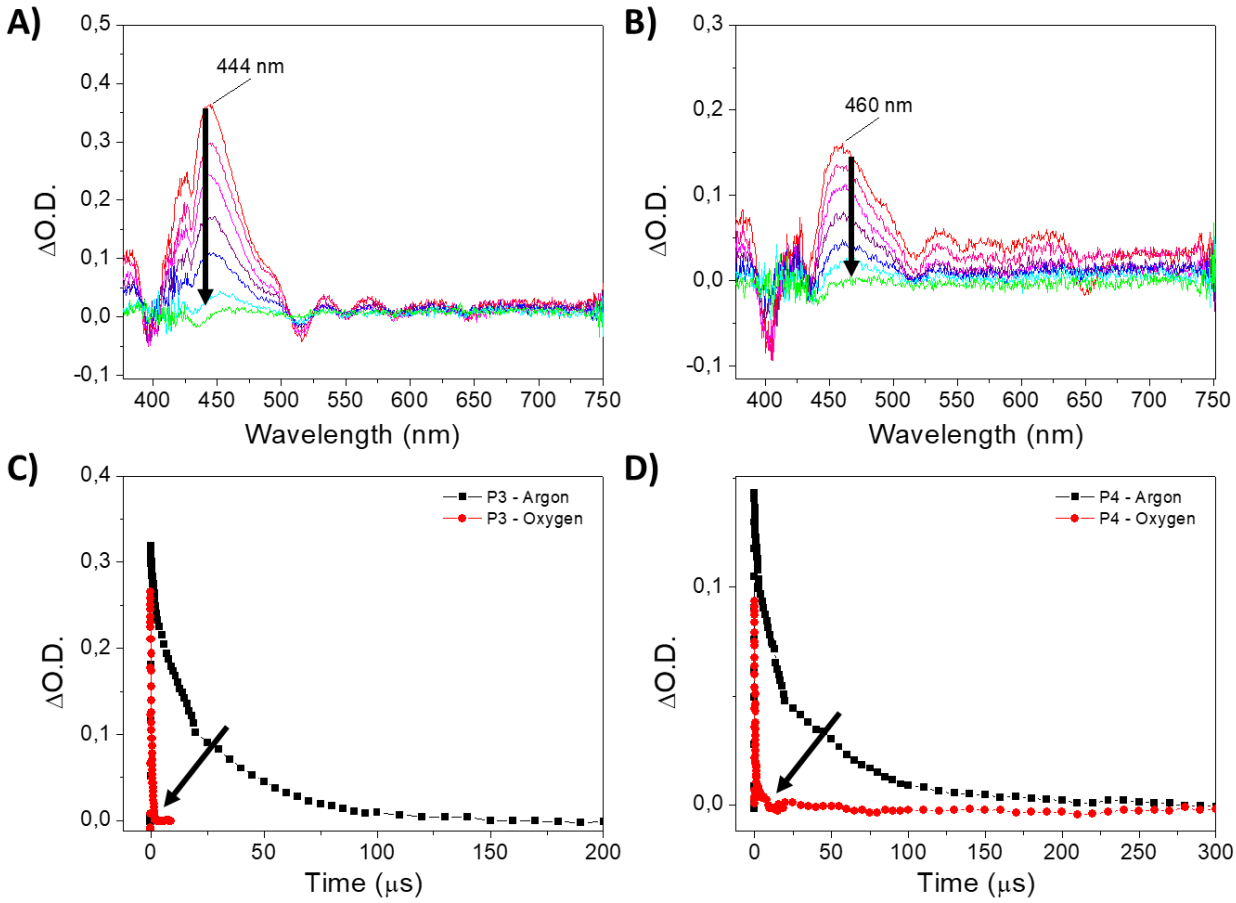

***Figure S8**: Transient absorption spectra of **A)** **P3** and **B)** **P4** in a deoxygenated DCM solution after laser pulse (λ = 385 nm). Decay traces of **C)** **P3** at 444 nm and **D)** **P4** at 460 nm by LFP with and without O_2. [**P3**] = 7.0 x 10^{-5} mol.L^{-1}; [**P4**] = 3.0 x 10^{-5} mol.L^{-1}.*

Reactivity with MDEA:

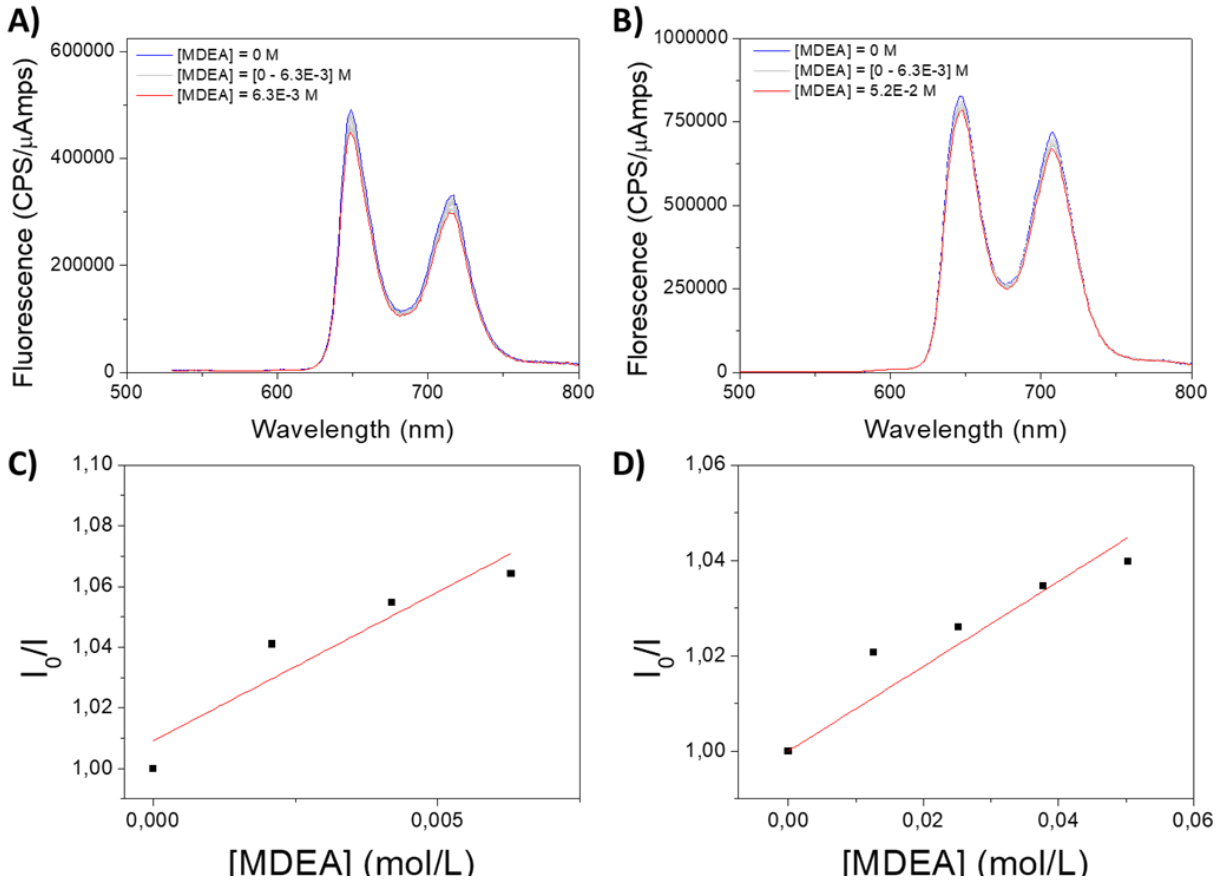

***Figure S9**: Quenching fluorescence of **A) P3** and **B) P4** after a gradual addition of MDEA. [**P3**] = 4.63 x 10-6 mol/L, [**P4**] = 6.17 x 10-7 mol/L. Insert: Corresponding Stern-Volmer plot ($K_{SV}^{P3/MDEA}$ = 9.8 M^{-1}, $K_{SV}^{P4/MDEA}$ = 0.9 M^{-1}). Excitation at λ = 649 and 646 nm for **P3** and **P4** respectively.*

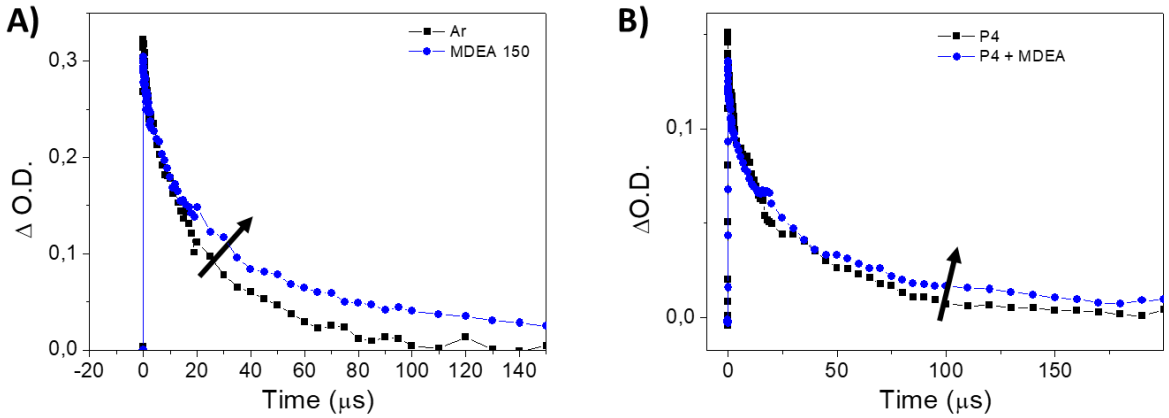

***Figure S10**: Decay traces of **A) P3** and **B) P4** triplet state after a laser pulse (λ_{ex} = 385 nm) with a gradual addition of MDEA. [**P3**] = 7.0 x 10^{-5} mol.L^{-1}; [**P4**] = 3.0 x 10^{-5} mol.L^{-1}, [MDEA] = 4.4 x 10^{-1} mol.L^{-1} in DCM.*

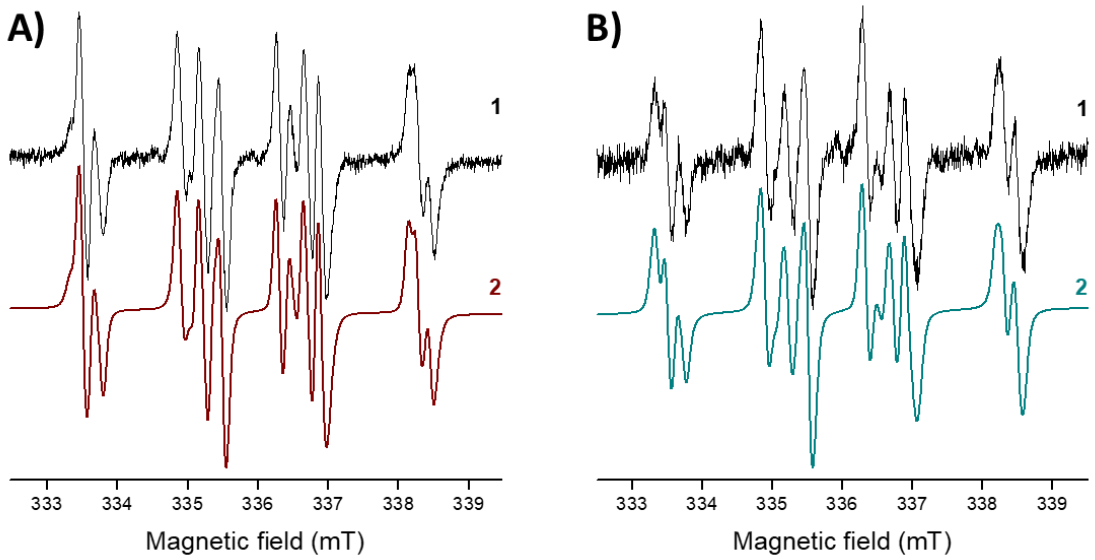

***Figure S11**: The normalized experimental (1) and simulated (2) EPR spectra obtained upon continuous in situ LED@400 nm exposure of porphyrin derivatives in chloroform under argon in the presence of DMPO spin trapping agent and MDEA: **A**) **P3** and **B**) **P4**.*

Reactivity with Iod:

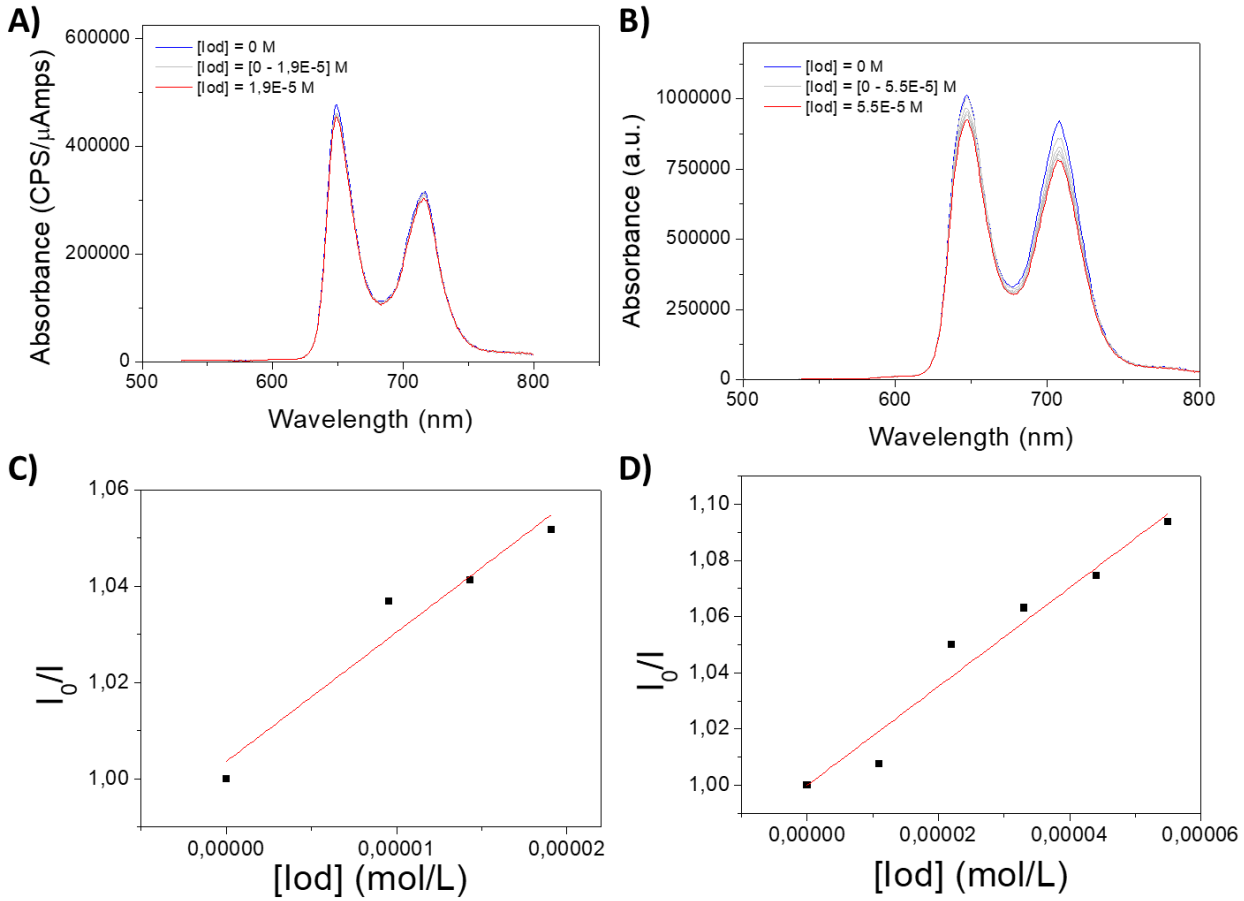

***Figure S12**: Quenching fluorescence of **A) P3** and **B) P4** after a gradual addition of Iod. [**P3**] = 4.63 x 10-6 mol/L, [**P4**] = 6.17 x 10-7 mol/L. Corresponding Stern-Volmer plot for **C) P3** ($K_{SV}^{P3/IOD}$ = 2600 M^{-1}) and **D) P4** ($K_{SV}^{P4/IOD}$ = 1756 M^{-1}). Excitation at λ = 649 and 646 nm for **P3** and **P4** respectively.*

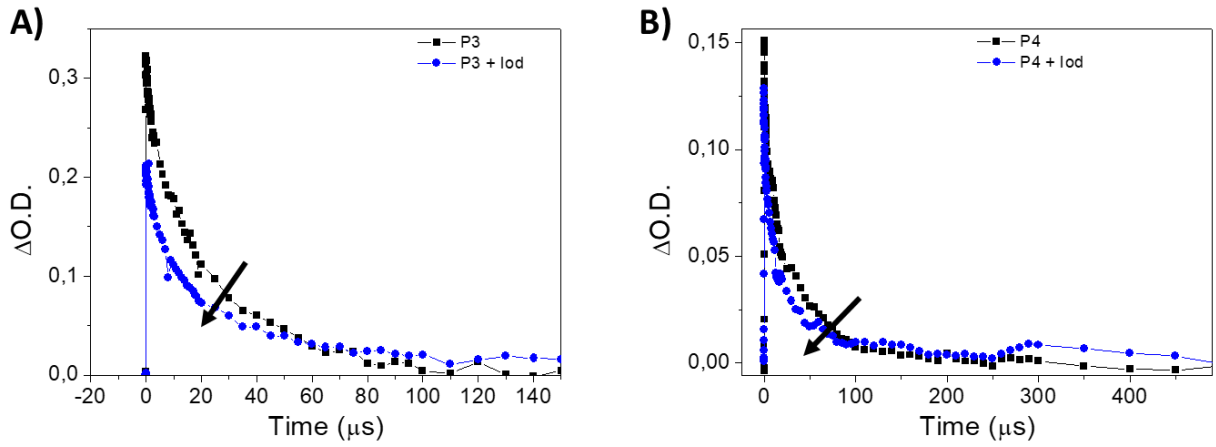

***Figure S13**: Decay traces of **A) P3** and **B) P4** triplet state after a laser pulse (λ_{ex} = 385 nm) with a gradual addition of Iod. [**P3**] = 7.0 x 10^{-5} mol.L^{-1}; [**P4**] = 3.0 x 10^{-5} mol.L^{-1}, [Iod] = 2.2 x 10^{-3} mol.L^{-1} in DCM.*

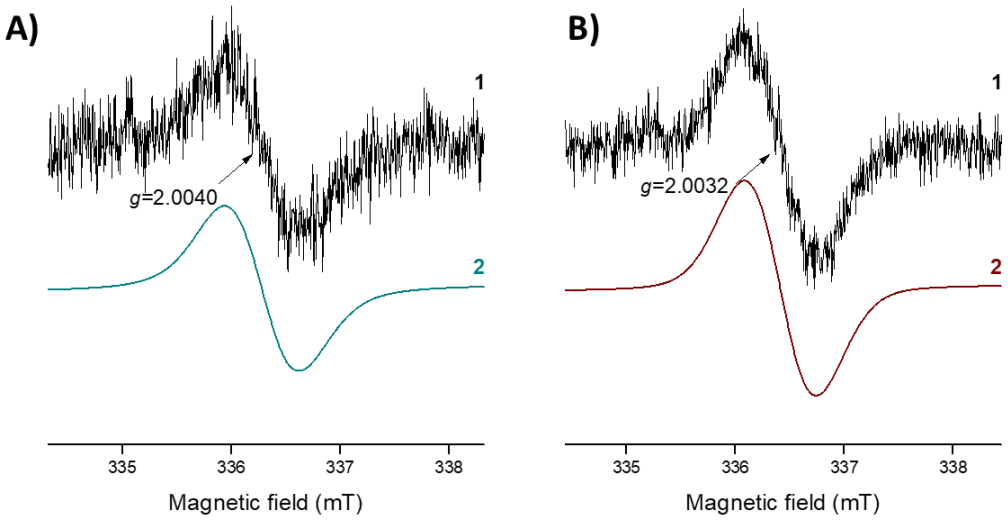

***Figure S14**: The normalized experimental (1) and simulated (2) EPR spectra obtained upon continuous in situ LED@400 nm exposure of porphyrin derivatives in chloroform under argon in the presence Iod: **A) P3** and **B) P4**.*

Reactivity with cysteamine:

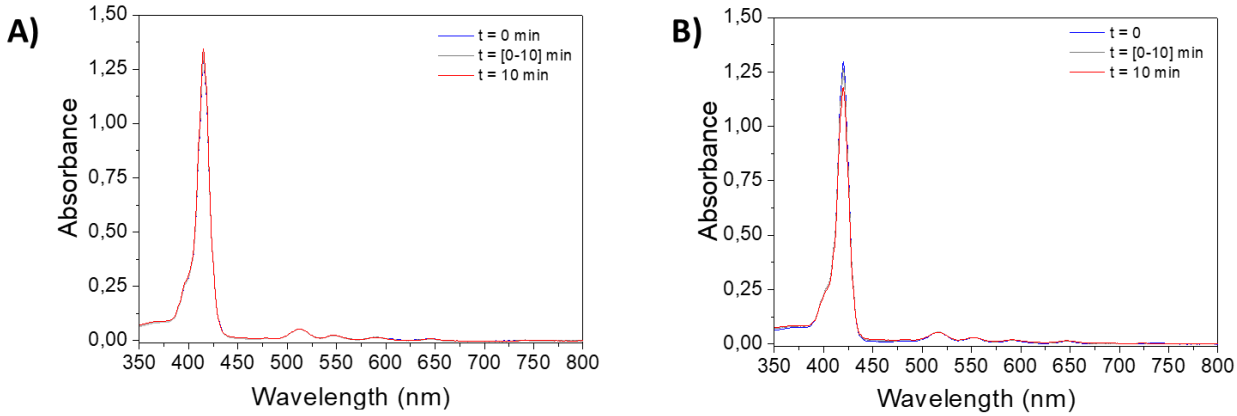

***Figure S15**: Steady state photolysis of **A) P3** and **B) P4** in presence of cysteamine systems under air after LED @405 nm exposure. [**P3**] = 1.85 x 10^{-5} mol/L, [**P4**] = 2.9 x 10^{-6} mol/L, [cysteamine] = 1.7 x 10^{-4} mol/L. Solvent = DCM*

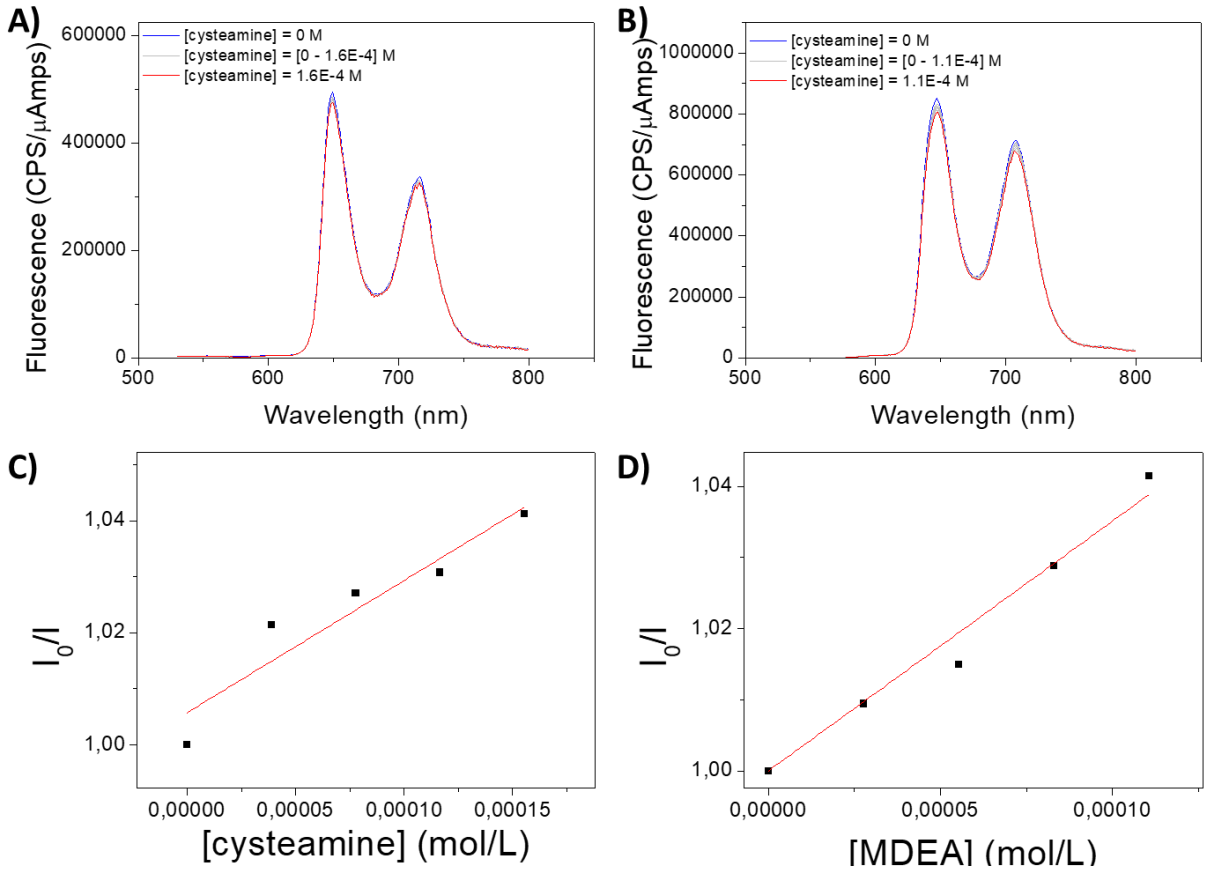

***Figure S16**: Quenching fluorescence of **A) P3** and **B) P4** after a gradual addition of cysteamine. [**P3**] = 4.63 x 10^{-6} mol.L^{-1}, [**P4**] = 6.17 x 10^{-7} mol.L^{-1}. Corresponding Stern-Volmer plot for **C) P3** ($K_{SV}^{P3/cysteamine}$ = 235 M^{-1}) and **D) P4** ($K_{SV}^{P4/cysteamine}$ = 351 M^{-1}). Excitation at λ = 649 and 646 nm for **P3** and **P4** respectively.*

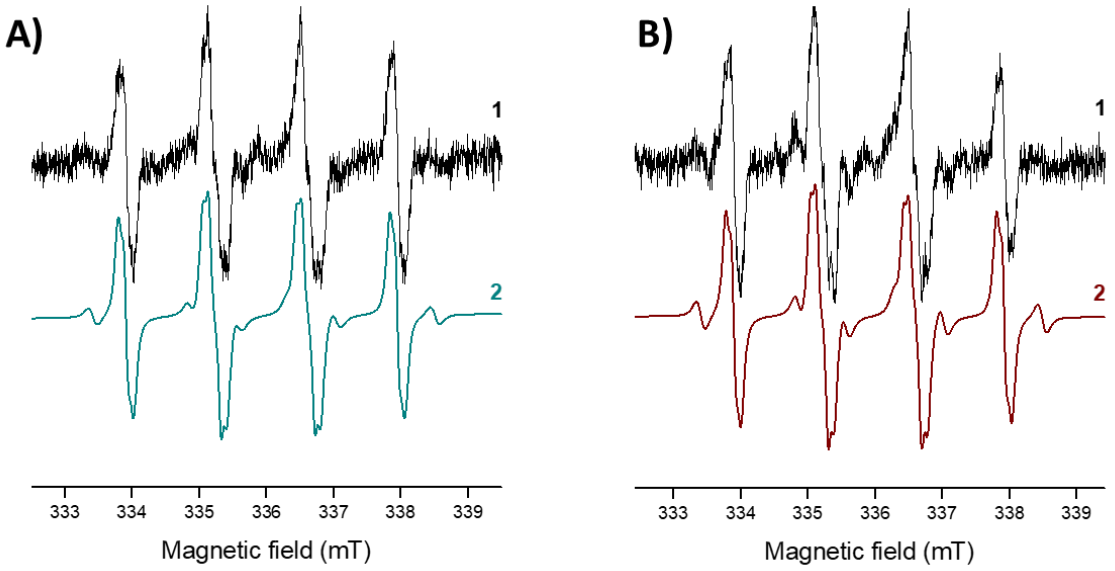

Figure S17: *The normalized experimental (1) and simulated (2) EPR spectra obtained upon continuous in situ LED@400 nm exposure of porphyrin derivatives in chloroform under argon in the presence of DMPO spin trapping agent and cysteamine:* ***A)*** ***P3*** *and* ***B)*** ***P4****.*

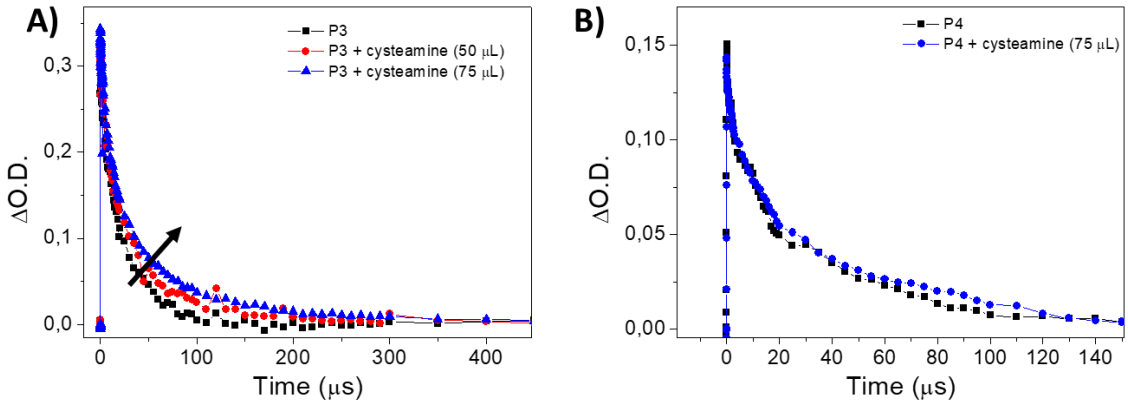

Figure S18*: Decay traces of* ***A)*** ***P3*** *and* ***B)*** ***P4*** *triplet state after a laser pulse (λ_{ex} = 385 nm) with a gradual addition of cysteamine. [****P3****] = 7.0 x 10^{-5} mol.L^{-1}; [****P4****] = 3.0 x 10^{-5} mol.L^{-1}, [cysteamine] = 1.3 x 10^{-1} mol.L^{-1} in DCM.*

Reactivity with *N*-acetylcysteine:

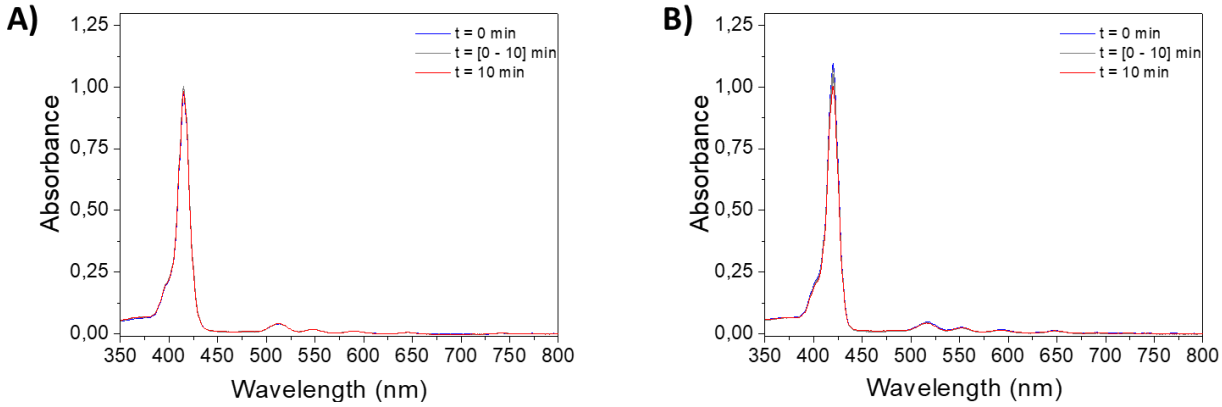

***Figure S19**: Steady state photolysis of **A) P3** and **B) P4** in presence of cysteine systems under air after LED @405 nm exposure. [**P3**] = 1.85 x 10^{-5} mol.L^{-1}, [**P4**] = 2.9 x 10^{-6} mol.L^{-1}L, [cysteine] = 1.1 x 10^{-4} mol.L^{-1}. Solvent = DCM*

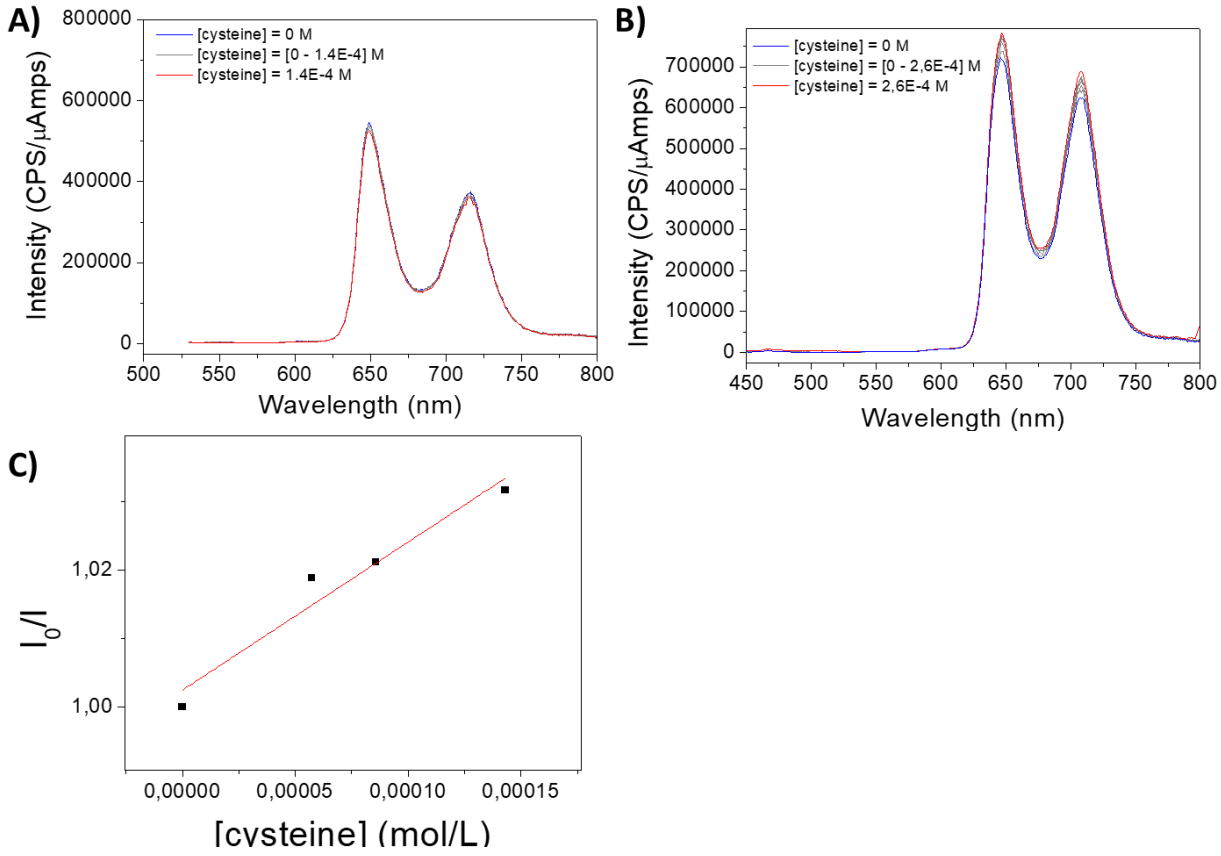

***Figure S20**: Quenching fluorescence of **A) P3** and **B) P4** after a gradual addition of cysteine. [**P3**] = 4.63 x 10^{-6} mol.L^{-1}, [**P4**] = 6.17 x 10^{-7} mol.L^{-1}. Corresponding Stern-Volmer plot for **C) P3** ($K_{SV}^{P3/cysteine}$ = 216 M^{-1}). Excitation at λ = 649 and 646 nm for **P3** and **P4** respectively.*

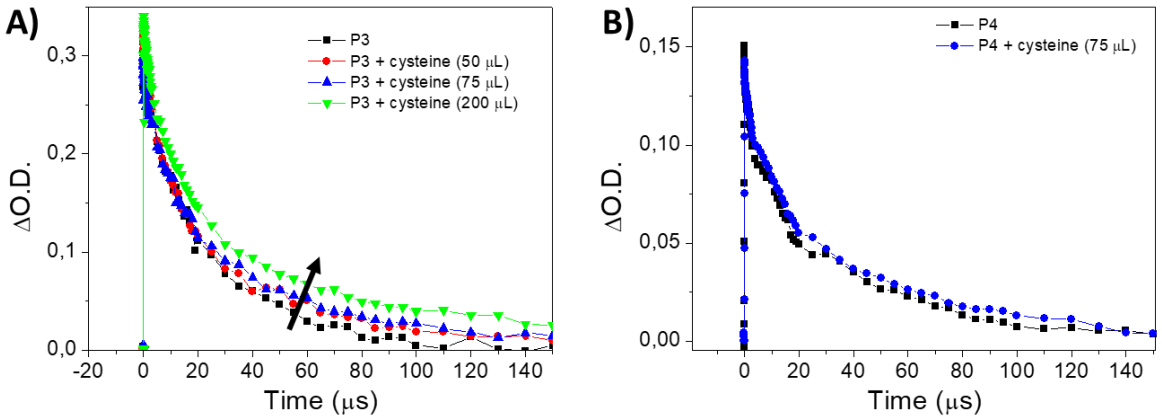

***Figure S21**: Decay traces of **A**) **P3** and **B**) **P4** triplet state after a laser pulse (λ_{ex} = 385 nm) with a gradual addition of cysteine. [[**P3**] = 7.0 x 10^{-5} mol.L^{-1}; [**P4**] = 3.0 x 10^{-5} mol.L^{-1}, [cysteine] = 8.3 x 10^{-2} mol.L^{-1} in DCM.*

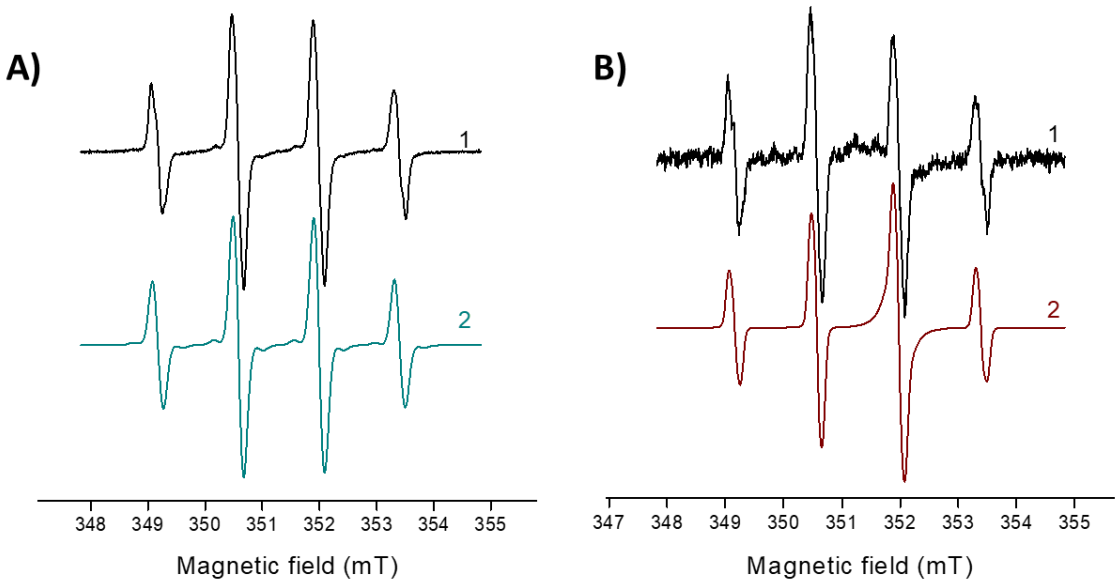

***Figure S22**: The normalized experimental (1) and simulated (2) EPR spectra obtained upon continuous in situ LED@400 nm exposure of porphyrin derivatives in chloroform under argon in the presence of DMPO spin trapping agent and cysteine: **A**) **P3** and **B**) **P4**.*

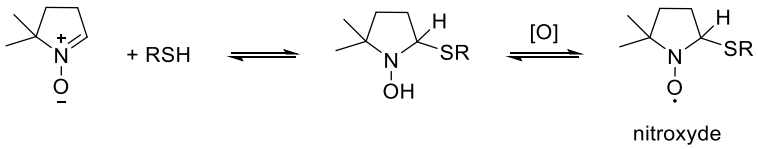

***Figure S23**: Forrester-Hepburn mechanism.*

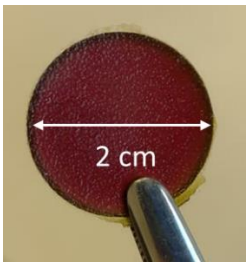

***Figure S24**: Picture of **P4** pellet*

Mechanisms with ROS probe:

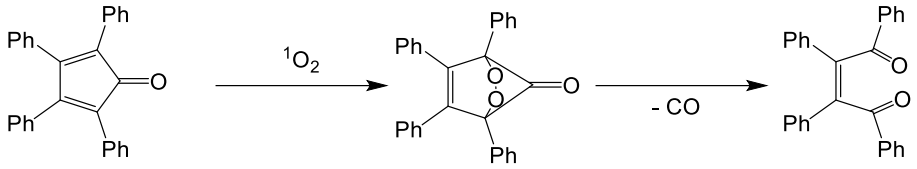

***Figure S25**: Degradation of TPCPD under singlet oxygen condition*

1 H. Marcille, J.-P. Malval, M. Presset, N. Bogliotti, A. Blacha-Grzechnik, V. Brezová, Y. Yagci and D.-L. Versace, Polym. Chem., 2020, 11, 4237–4249.
2 B. H. J. Bielski, G. G. Shiue and S. Bajuk, J. Phys. Chem., 1980, 84, 830–833.

Transition

Dans cette première partie, l'utilisation de deux nouvelles porphyrines non complexées a permis de développer de nouveaux matériaux photosynthétisés sous irradiation visible à partir d'un monomère biosourcé, avec de bonnes cinétiques de polymérisation. De plus, ces matériaux ont été exploités pour la photodégradation de polluants présents dans l'eau sous irradiation UV avec des cinétiques de dégradations efficaces. Cette étude a prouvé l'intérêt de l'utilisation de porphyrines possédant une double action : en tant que photoamorceur pour la synthèse de matériaux à base de bioressources par photopolymérisation, mais également en tant que photosensibilisateur pour la photodégradation de polluants présents dans l'eau.

Toutefois, l'intérêt des porphyrines pour le développement de matériaux photoactifs est leur capacité à absorber la lumière visible et donc de pouvoir dépolluer l'eau sous irradiation dans la gamme du visible. Les porphyrines **P3** et **P4** présentant une absorption limitée dans le visible, de nouvelles porphyrines, **P8** et **P8Zn**, possédant une absorption très large sur des longueurs d'onde entre 400 et 700 nm ont été développées, permettant l'exploitation de toute la gamme du visible pour les applications en dépollution de l'eau.

Dans cette deuxième partie, ces nouvelles porphyrines vont être utilisées pour leur propriétés de photoamorceurs, en se limitant au système porphyrine/MDEA/SOA qui a présenté les meilleurs résultats dans la première partie. L'application de ces matériaux pour la dépollution de l'eau a de nouveau été déterminé sous irradiation UV, puis le mécanisme sous irradiation visible a été étudié pour entreprendre une dépollution sous irradiation visible.

Partie B : Article 3 – New porphyrins for the depollution of water under visible irradiation

Abstract.

In this study, we reported the use of two new porphyrins, **P8** and **P8Zn**, used both as an H-abstraction photoinitiator and as photosensitizer for pollutants degradation. The polymerization is performed through a free-radical polymerization, using acrylated bio-based monomer in the presence of amine as co-initiator under visible irradiation reaching 89% and 87% under LED@405 nm irradiation. The photodegradation properties of water pollutant have been determined for the obtained coating. Good degradation of AR14, an azo dye, have been obtained both materials under UV irradiation, and promising degradation have been obtained in presence of H_2O_2 under visible irradiation. ROS formation mechanisms and activity under degradation have been established to a better understanding of the depollution process.

I. Introduction

The pollution of water is attributed to a number of different factors. Indeed, heavy metal ion, pharmaceutical products, or dyes for example are released from numerous industries, like textile, food, cosmetic or paper industries. One source of pollution presenting particular concern is the production of azo dyes. These substances, composed of a N=N bond, are particularly problematic. Indeed, they present toxicity to aquatic life, like algae, bacteria and fish, and animals, and also present carcinogenic and mutagenic properties to mammal cells. [1–3] Their toxicity are linked to their complete structure, but also to the compounds obtained after their partial degradation, when the azo bond is cleaved by solar photolysis or by intestinal bacteria, leading to the formation of polyphenol. Despite their toxicity, there are widely used – up to 60% of the synthesized dyes are azo dyes [4] – and are difficult to degrade. The development of methods for the complete degradation of these dyes is therefore necessary. A large range of solutions are available for the removal of pollutants, including membranes filtration [5], coagulation [6] or adsorption [7], but these solutions simply displace the pollution, without removing it. One of the promising solution is the development of advanced oxidative processes (AOP) including photoactive surfaces. [8] The use of metal oxide, like TiO_2 or ZnO allow the production of hydroxyl radical under irradiation for the degradation of pollutants and their complete mineralization.[9,10] However, these compounds require the use of UV irradiation, whereas adequate photosensitizer can be efficient under visible irradiation, allowing the use of more economical and safer lamps. [11,12] Indeed, photosensitizer are photoactives molecules, able to interact with molecular oxygen under irradiation to form reactive oxygen species (ROS), including singlet oxygen, superoxide ion or hydroxyl radical. These molecules have presented promising degradation rate under visible light.[13–15]

In addition, the photoactive molecule can have a dual role. Indeed, by excitation under irradiation, these molecules can also react to initiate photopolymerization, by forming reactive species, like radical, cation or anion species. Several compounds have been reported to have efficient photoinitiator properties, like anthracene,[16] phthalocyanine [17] or alizarin [18]. Several examples have been used for a comparable application to the water depollution *i.e* antibacterial material,[18–20] where the biocide properties are provided by ROS production. Therefore, the photoactive molecule used as photoinitiator for the polymerization can also be used as photosensitizer for the pollutant degradation. Porphyrins have prior been used as photoinitiator, [21,22] as dual photoactive molecule, inducing a

photopolymerization and antibacterial activities,[23] and as photosensitizer for water pollution [24–27]. They are therefore been chosen for the development of photosynthesized coating for water depollution.

In this context, two new porphyrins have been synthesized. They have been used as photoinitiator in presence of MDEA as electron donor co-initiator, for the polymerization of acrylated bio-based monomer, *i.e.* acrylated soybean oil. The reactivity between porphyrins and MDEA has been investigated using steady-state photolysis, fluorescence, laser flash photolysis, and electronic paramagnetic resonance spin-trapping (EPR ST). The polymerization have been followed by Real-Time Fourier-Transformed Infrared spectroscopy (RT-FTIR) under various visible-range LED, and the final monomer conversion of system containing porphyrin and MDEA have been evaluated. Finally, the application of these coating for the depollution of water have been investigated under UV and visible irradiation.

II. Experimental part

Materials. Solvent (acetic acid, acetone, chloroform, dichloromethane (DCM), methanol, methyl acetate and petroleum ether) were used as received. THF was freshly distilled using benzophenone and sodium under argon before use for Suzuki-Miyaura coupling. Reactant for synthesis, 2,3-dichloro-5,6-dicyano-1,4-benzoquinone (DDQ), N-bromosuccinimide (NBS), paraformaldehyde, potassium carbonate, pyrrole trifluoroacetic acid (TFA) and zinc acetate were provided by Sigma-Aldrich and benzaldehyde, [4-[Bis(4-methoxyphenyl)amino]phenyl]boronic acid, $PdCl_2$dppf, pyridine and triethylamine were provided by TCI and used as received. Soybean oil acrylated (SOA) and N-methyldiethanol (MDEA) were provided by Sigma-Aldrich and used as monomer and co-initiator respectively. Analysis species, i.e. spin trapping agent *N*-*tert*-Butyl-α-phenylnitrone (PBN, Sigma-Aldrich) and 5-*tert*-Butoxycarbonyl-5-methyl-1-pyrroline-N-oxide (BMPO), supporting electrolyte tetrabutylammonium tetrafluoroborate (Alpha aesar, 99%), ROS detector tetraphenylcyclopentadienone (TPCPD, Sigma-Aldrich), nitro blue tetrazolium chloride (NBT, Sigma-Aldrich) and azo-dye acid red 14 (AR14, Sigma-Aldrich) were used as received.

Table IIB-1*: Chemical structure of photoinitiating system, monomer and used pollutant.*

Name	Chemical structure
P8 5,15-diphenyl-10,20-di(4-(*N*,*N*-dianisolamine)phenyl)porphyrin	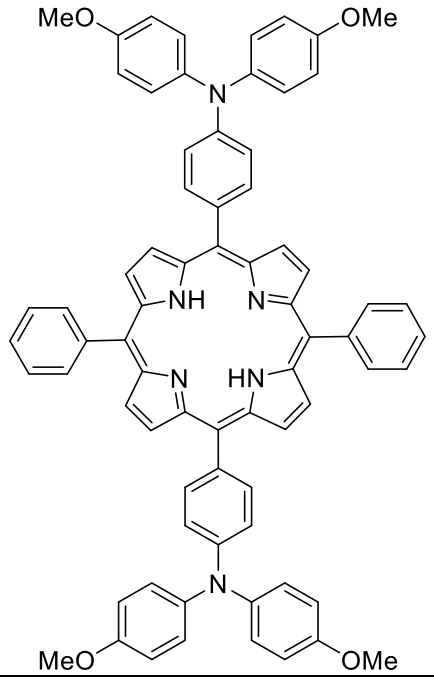
P8Zn Zinc (II) 5,15-diphenyl-10,20-di(4-(*N*,*N*-dianisolamine)phenyl)porphyrin	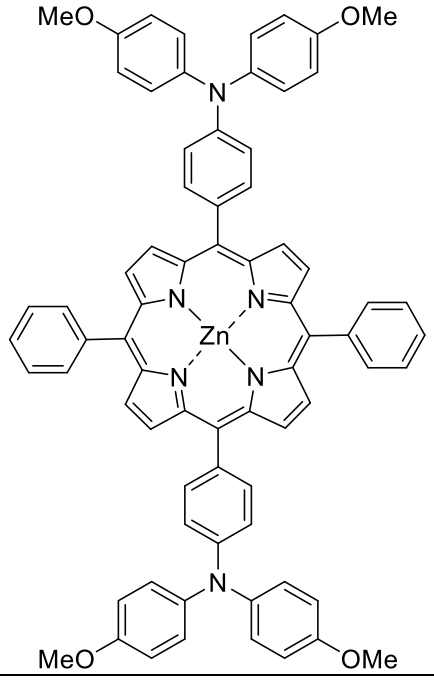
MDEA *N*-methyldiethanol amine	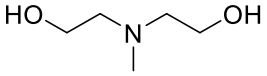

SOA soybean oil acrylate	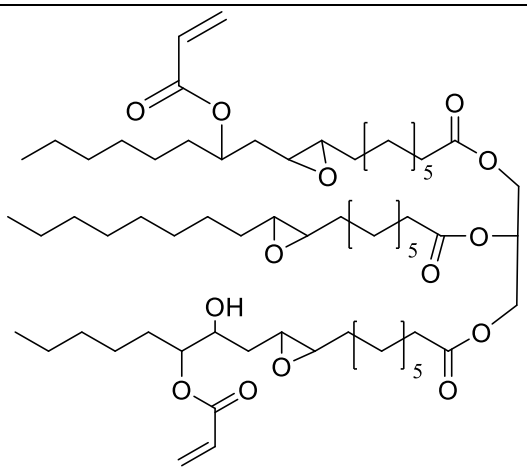
AR14 Acid red 14	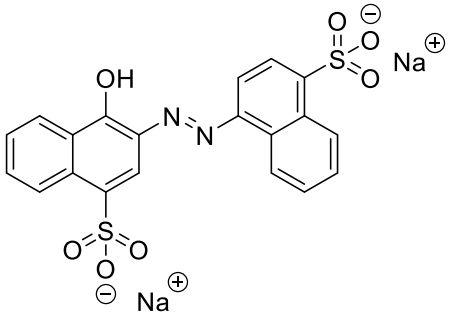

Characterization. Reaction monitoring was performed using thin layer chromatography (TLC) on a silica gel plates (0.25 mm) precoated with a fluorescent indicator (Merck 60F254). The revelation was performed using ultraviolet light (λ = 254 nm). NMR spectra were recorded using a Brucker Avance II 400 MHz spectrometer, and the results present the chemical shift (δ) in ppm, the multiplicity, the coupling constant and the integration. High-Resolution Mass Spectra were obtained by electrospray ionization using a Q-TOF analyzer from the ICOA of the University of Orléans.

Synthesis of 5,15-diphenyl-10,20-bis(4-N,N-dianisolaminophenyl) porphyrin (P8). A 25 mL rounded-bottomed flask equipped with a stirring bar is charged with 5,10-diphenyl-10,20-dibromoporphyrin (50 mg, 0.08 mmol, 1.0 equiv), [4-[Bis(4-methoxyphenyl)amino]phenyl]boronic acid (62 mg, 0.177 mmol, 2.2 mmol), K_2CO_3 (67 mg, 0.48 mmol, 6 equiv), THF (7.3 mL) and water (0.8 mL). The reaction mixture is flushed with Ar, $PdCl_2$dppf (6 mg, 0.008 mmol, 0.1 equiv) is added and then the reaction is heated to reflux for 16 h. The resulting solution is washed with water (2 x 10 mL) and brine (10 mL). The solvent is removed under reduced pressure and the residue is triturated in methyl acetate to afford the desired product as a purple solid (64 mg, 74%).

^{1}H NMR (400 MHz, CDCl3): δ 8.98 (d, J = 4.9 Hz, 4H), 8.83 (d, J = 4.7 Hz, 4H), 8.22 (d, J = 6.8 Hz, 4H), 7.99 (d, J = 7.8 Hz, 4H), 7.82 – 7.72 (m, 6H), 7.36 (d, J = 8.3 Hz, 8H), 7.29 (d, J = 8.2 Hz, 4H), 6.97 (d, J = 8.3 Hz, 8H), 3.86 (s, 12H), -2.71 (s, 2H). **^{13}C NMR (100 MHz, $CDCl_3$):** δ 172.46 ($4C_q$), 170.13 ($4C_q$), 163.06 ($4C_q$), 156.19 (4CH), 148.41 ($4C_q$), 141.00 (4CH), 135.55 (4CH), 134.71 (4CH), 133.85 ($2C_q$), 127.70 (2CH), 127.19 (8CH), 126.71 (4CH), 120.43 ($2C_q$), 118.09 (4CH), 114.95 (8CH), 55.63 ($4CH_3$) [6 C_q not detected]. (**Figure S1** and **S2**). **HRMS (ESI/Q-TOF):** *m/z* [M + H^+] calcd for $C_{72}H_{57}N_6O_4$ 1069.4436; found 1069.4435; *m/z* [M + $2H^+$] calcd for $C_{72}H_{58}N_6O_4$ 535.2254; found 535.2254. ν_{max} (ATR)/cm^{-1}: 3315, 2956, 1596, 1487, 1245, 1082, 1018, 794, 709, 518.

Synthesis of Zinc (II) complex of 5,15-diphenyl-10,20-bis(4-N,N-dianisolaminophenyl) porphyrin (P8Zn). In air, a 25 mL rounded-bottomed flask equipped with a stirring bar is charged with **P8** (64 mg, 0.060 mmol, 1.0 equiv), $Zn(OAc)_2$ (26 mg, 0.12 mmol, 2.0 equiv), chloroform (9 mL) and methanol

(3 mL). The reaction is stirred under reflux for 1.5 h. Solvents are removed under reduced pressure and the residue is triturated in methanol and filtered several times to afford the desired product (44 mg, 64%) as a purple solid.

^{1}H NMR (400 MHz, CDCl3): δ 8.98 (d, J = 4.5 Hz, 4H), 8.82 (d, J = 4.7 Hz, 4H), 8.19 (d, J = 6.3 Hz, 4H), 7.96 (d, J = 8.1 Hz, 4H), 7.74 (s, 6H), 7.32 (d, J = 8.1 Hz, 8H), 7.25 (d, J = 7.8 Hz, 4H), 6.96 (d, J = 8.1 Hz, 8H), 3.79 (s, 12H). **^{13}C NMR (100 MHz, $CDCl_3$):** δ 157.48 ($4C_q$), 151.37 ($4C_q$), 150.78 ($4C_q$), 149.18 ($2C_q$), 144.68 ($2C_q$), 144.87 ($4C_q$), 136.13 (4CH), 135.40 (4CH), 132.31 (4CH), 131.92 (4CH), 128.01 (2CH), 127.95 (8CH), 127.13 (4CH), 125.39 ($2C_q$), 121.67 ($2C_q$), 121.21 ($2C_q$), 118.37 (4CH), 115.61 (8CH), 55.61 ($4CH_3$). (**Figure S3** and **S4**). **HRMS (ESI/Q-TOF):** *m/z* [M + H^+] calcd for $C_{72}H_{55}N_6O_4Zn$ 1131.3571; found 1131.3535. ν_{max} (ATR)/cm^{-1}: 2958, 1596, 1492, 1249, 1068, 1014, 790, 690.

UV-Visible spectrum. UV-Visible absorption spectra were recorded on a PerkinElmer Lambda 2 UV-vis spectrophotometer.

Irradiation Source. Eight light emitting diodes (LEDs) with emission wavelengths at 385 nm (35.3 mW.cm^{-2}), 405 nm (118 mW.cm^{-2}), 455 nm (56.8 mW.cm^{-2}), 470 nm (41.3 mW.cm^{-2}), 505 nm (20.8 mW.cm^{-2}), 530 nm (14.6 mW.cm^{-2}) and 625 nm (51.0 mW.cm^{-2}) provided by Thorlabs have been used for photopolymerization and mechanistic studies. A UV-lamp Hamamatsu-LC8 (4500 mW/cm^2, λ = 365 nm) have been used for depollution and ROS detection under UV irradiation.

Steady State Photolysis. The photolysis of **P8** and **P8Zn** were solution in DCM were carried out by placing the porphyrin solutions ([**P8**] = 6.2 x 10^{-6} M and [**P8Zn**] = 3.2 x 10^{-6} mol.L^{-1}) in quartz cuvette of 1 cm at 10 cm from the irradiation source (LED@405 nm). The experiments were conducted without or with MDEA ([**MDEA**] = 1.0 × 10^{-4} mol.L^{-1}) and their absorption behavior was studies.

Electron Paramagnetic Resonance experiment. EPR spectra were obtained using porphyrins in deoxygenated DCM in a 4 mm quartz tube. The addition of PBN and BMPO enable to highlight the radical production by spin-trapping (EPR-SP) with or without addition of MDEA. The spectra were compiled before (5 spectra) and during (15 spectra) LED@405 nm irradiation outside the resonator. The experiments were carried out using an Elexsys E500 EPR spectrometer (Bruker) operating at X-band (9.8 GHz) and equipped with an SHQ high-sensitivity cavity. The setting used are detailed in ref [18]. Spectra processing was carried out using Bruker software and the determination of Hamiltonian parameters was carried out on MatLab platform using Easyspin toolbox.

Cyclic voltammetry. Cyclic voltammograms were performed on a Radiometer Voltalab 6 potentiostat to determine reduction peak potentials and recorded using a three electrode cell using glassy carbon electrode as working electrode, saturated calomel electrode as reference and a gold wire electrode as counter electrode. The porphyrin solution were prepared in deoxygenated DMF at 10^{-3} M, using tetrabutylammonium hexafluorophosphate ($(nBu)_4NPF_6$) as supporting electrolyte.

Fluorescence. Fluorescence spectra and quenching fluorescence after the addition of MDEA were carried out on FluoroMax + spectrofluorometer from Horiba. The solutions of **P8** ([**P8**] = 1.3 x 10^{-6} mol.L^{-1}) were excited at 420 nm and 553 nm for **P8Zn** ([**P8Zn**] = 1.4 x 10^{-6} mol.L^{-1}).

Laser Flash Photolysis experiment. The transient spectra of porphyrins were obtained on nanosecond Nd:TAG laser (Powerlite 9010, Continuum) set up at 5 Hz and 7–8 ns impulsion time. The solutions of the porphyrins in deoxygenated DCM ([**P8**] = 3.32 x 10^{-5} mol.L^{-1} and [**P8Zn**] = 1.35 x 10^{-5} mol.L^{-1}) were excited at 385 nm. The decay spectra were monitored at 470 nm for **P8** and 480 nm for **P8Zn**.

Photopolymerization kinetic studies. The photosensitive systems containing 0.5% of porphyrin and 5% of MDEA in SOA were placed on BaF_2 pellets, and irradiated with different lamps under air or

protected from oxygen by a polypropylene film (under laminate). The polymerization of the monomer was monitored by following the decrease in the signal corresponding to the acrylate function at 1636 cm^{-1} by Real-Time Fourier Transformation Infrared spectroscopy (RT-FTIR) on a JASCO FTIR 4700 Instrument, in order to determine the kinetic profiles and the final acrylate conversion after 800 s of irradiation.

Coating synthesis. **P8**/MDEA/SOA and **P8Zn**/DMEA/SOA (0.5%/5% w/w) blend mixtures were placed on glass plates to reach the size of 1.5 x 1.5 cm side, placed under laminate, and irradiated at 10 cm of the 405 nm source of irradiation for 10 min. The coating was fixed on glass surface by Teflon film to prevent its peeling in water.

ROS detection. The capability of coating to form oxygen reactive species (ROS) have been determined using common ROS probe in solution under irradiation at 10 cm of LED@405 nm and followed by UV-Visible spectrometry. The formation of singlet oxygen ($^1O_2$) was monitored using tetraphenylcyclopentadione (TPCPD) solution ([TPCPD] = 3.4 x 10^{-4} M in methanol). The oxidation of TPCPD by singlet oxygen leads to the decrease of its absorbance at 510 nm. The formation of superoxide ion ($O_2^{\bullet-}$) is followed using nitroblue tetrazolium chloride (NBT) solution ([NBT] = 6.0 x 10^{-5} M in ethanol). This colorless product is oxidized by superoxide ion into formazan, a purple mix of product absorbing at 570 nm.

Depollution assay. The photodegradation of azo-dye of **P8** and **P8Zn** coating have been determined using acid red 14 (AR14) as model pollutant. Sample was immerged at middle-height of 30 mL of AR14 solution ([AR14] = 10 μM) and placed at 10 cm of the irradiation source. The photodegradation was carried out in dynamic mode, using a magnetic stirring to create fluid turbulences in the solution, in order to maintain a homogeneous distribution of the pollutant on the surface of the photoactivatable coating and maximize the pollutant degradation [10]. The photodegradation of the azo-dye was monitored by following the decrease of the maximum absorption peak of AR14 (λ_{max} = 515 nm) by UV-Visible spectroscopy every 15 min for 5 hours. The degradation rate (X%) is determined using **Eq. 1**.

$$X(\%) = \frac{A_0 - A_t}{A_0} \times 100 \qquad (1)$$

Where A_0 and A_t represent the absorption at 515 nm of the solution before irradiation and during a time t of irradiation respectively.

III. Results and Discussion

Synthesis. The synthesis of **P8** and **P8Zn** has been achieved following the same strategy developed for the preparation of others *meso-substituted* A_2B_2-*trans*-porphyrins (**Figure IIB-1**) (Ref Article P3/P4). A Suzuki-Miyaura cross-coupling between diphenyl-dibromo-*trans*-porphyrin **1** and arylboronic acid **2** delivered **P8** in a good 74% yield, using 10 mol% of $Pd(PPh_3)_4$ with 6.0 equiv of K_2CO_3 in THF/H_2O at reflux. The corresponding zinc complex **P8Zn** was next easily obtained by treating **P8** with zinc acetate in a chloroform/methanol mixture, leading to the expected product in 64% yield.

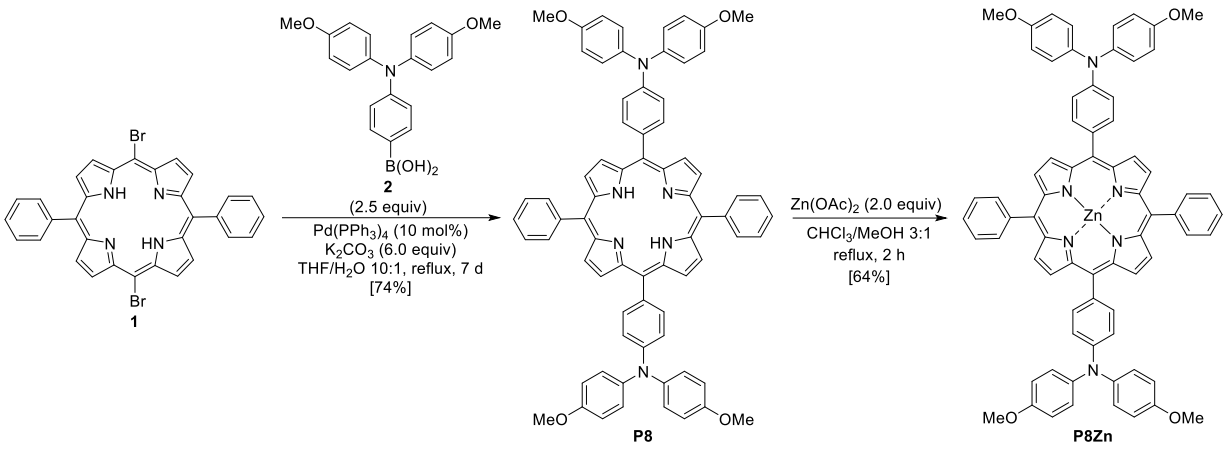

*Figure IIB-1: Synthesis of **P8** and **P8Zn**.*

Absorption properties. The UV-Visible absorption spectrum of **P8** and **P8Zn** in DCM are shown in **Figure IIB-2**. The absorption characteristics are displayed in **Table IIB-2**. Porphyrins show an intense peak around 400 nm corresponding to the $a_{1u}(\pi)$-$e_g^*(\pi)$transition localised at 414 nm for **P8**. Four weaker bands in the visible range are present between 520 and 655 nm and are assigned to $a2u(\pi)$-$e_{eg}^*(\pi)$ transition. The metalation of **P8** to **P8Zn** has two effects: *i*) a slight redshift of the Soret band to 428 nm for **P8Zn** due to the increase of electron density in the porphyrin core, and *ii*) the symmetrisation of the porphyrin, leading to the degeneration of molecular orbital and thus, to the reduction of the four Q bands to two bands.

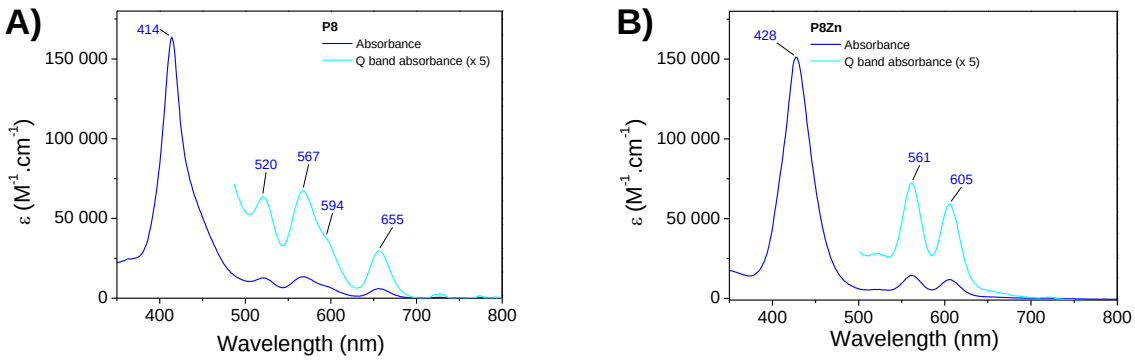

*Figure IIB-2: UV-Visible absorption spectrum and emission spectrum of **A**) **P8** and **B**) **P8Zn**.*

Both porphyrins present a large Soret band, absorbing in a wide range in visible spectrum, compared to **P3** and **P4**. These broad absorptions enable porphyrins to be used as photoinitiators for free-radical photopolymerization, allowing a wild range of visible-light LED to be used, *i.e.* 385 nm, 405 nm, 455 nm and 470 nm for the absorption of Soret band, and mild visible range LEDs at 505 nm, 530 nm, 590 nm and 625 nm for the Q bands. As previous studies have shown that the best final acrylated conversion for SOA were obtained with MDEA as co-initiator, only this system will be investigated.

***Table IIB-2**: Absorption characteristic of **P8** and **P8Zn**.*

Porphyrin	Soret band λ / nm (ε / $M^{-1}.cm^{-1}$)	Q bands λ / nm (ε / $M^{-1}.cm^{-1}$)	Absorption at LED wavelength ε / $M^{-1}.cm^{-1}$
P8	414 (163 679),	520 (12 731) 567 (13 478) 594 (7 614) 655 (5 934)	385 nm: 34 648 405 nm: 114 789 455 nm: 44 108 470 nm: 26 113 505 nm: 10 532 530 nm: 10 582 590 nm: 8 233 625 nm: 1 538
P8Zn	428 (151 390)	561 (14 475) 605 (11 790)	385 nm: 17 802 405 nm: 62 579 455 nm: 53479 470 nm: 22 497 505 nm: 5 484 530 nm: 5 435 590 nm: 6 191 625 nm: 4 083

Reactivity with MDEA as co-initiators. Reactivities of porphyrins toward MDEA under irradiation have been first studied by steady-state photolysis (**Figure IIB-3**) using UV-Visible spectroscopy. First, the irradiation of **P8** alone at under LED@405 nm (**Figure IIB-3A**) reveals the stability of free-base porphyrin under irradiation, in contrary of **P8Zn** (**Figure IIB-3C**) which undergoes into a total degradation after 15 min of irradiation. Interestingly, when **P8** and **P8Zn** are combined with MDEA (**Figure IIB-3B** and **Figure IIB-3D**), their absorbance decrease is modified, proving an interaction between the two components. Indeed, a low photobleaching can be observed for **P8** in presence of MDEA, whereas for **P8Zn**, the decrease is initially slower than **P8Zn** alone before an acceleration of the photobleaching. New species formation is observed for **P8Zn**, as it can be observed by an increase of absorbance around 500 nm.

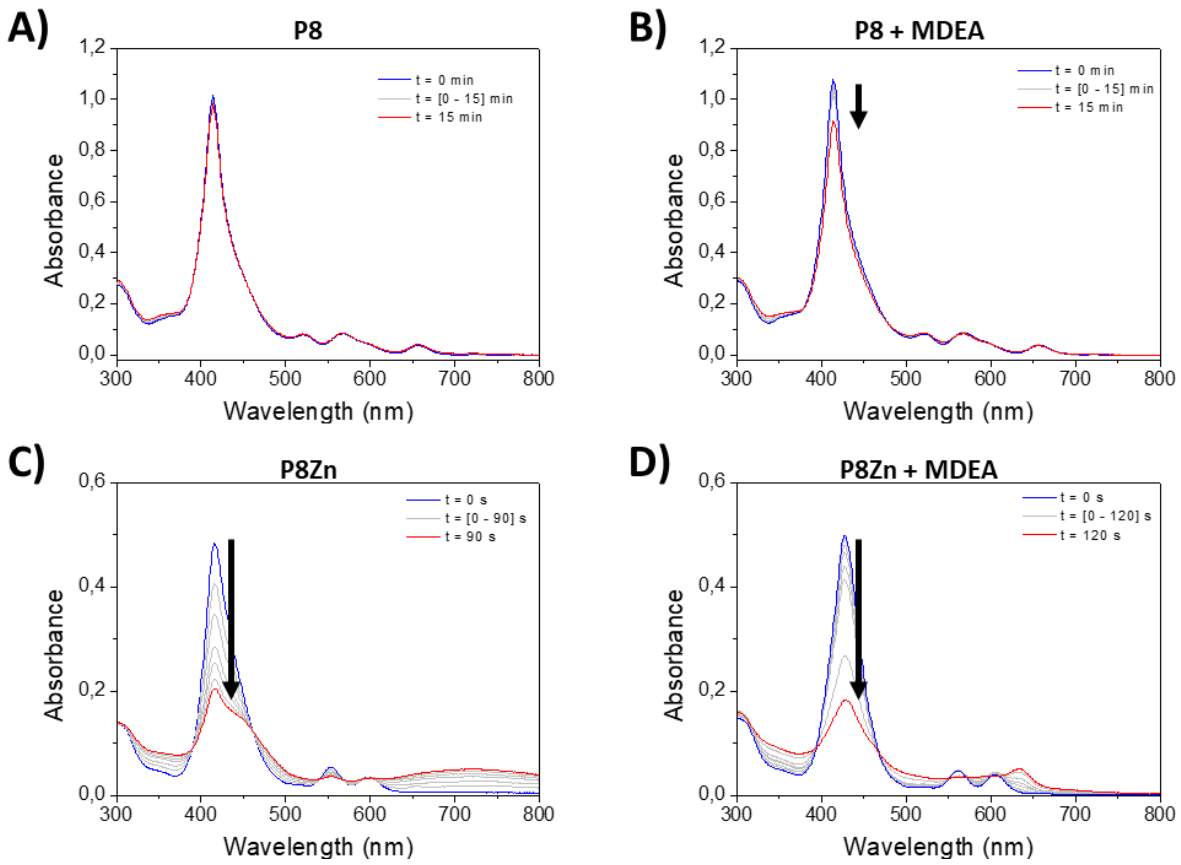

***Figure IIB-3**: Steady-state photolysis of A) **P8**, B) **P8** in presence of MDEA, C) **P8Zn**, D) **P8Zn** in presence of MDEA in DCM after 15 min of LED@405 nm irradiation. [**P8**] = 6.2 x 10^{-6} M. [**P8Zn**] = 3.2 x 10^{-6} mol.L^{-1}, [**MDEA**] = 1.0 × 10^{-4} mol.L^{-1}.*

EPR-ST experiments have been used for the identification of the radical species formed during the interaction between the photoinitiator and the co-initiator. All experiment have been performed in deoxygenated DCM (**Figure IIB-4**). The irradiation of both porphyrins with MDEA and PBN have highlight the formation of a PBN-adduct of α-aminoalkyl radical, which is consistent with the electron transfer between porphyrins and MDEA and the formation of MDEA radical [23] promoting the radical polymerization. The Hamiltonian parameter of PBN-adduct of α-aminoalkyl radical for **P8Zn** is a_N = 1.525 mT, a_H = 0.3515 mT, a_C = 1.116 mT, a_C = 0.540 mT, g = 2.0059, whereas for **P8**, the signal is characterized with a_N = 1.517 mT, a_H = 0.470 mT, g = 2.0056 and is superimposed to a signal corresponding to PBP-adduct of a carbon centered radical (a_N = 1.491 mT, a_H = 0.267 mT, g = 2.0056).

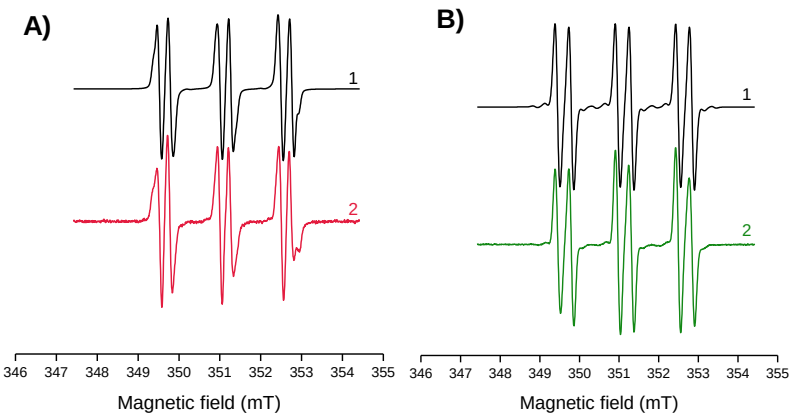

***Figure IIB-4**: Simulated (1) and experimental (2) EPR spectra of the α-aminoalkyl spin adduct obtained after LED@@405 nm exposure of **A**) **P8**/MDEA/PBN and **B**) **P8Zn**/MDEA/PBN in DCM under argon.*

In order to investigate further the mechanism of formation of the identified radical, the reactivity of porphyrins and MDEA has been studied in the singlet excited state of porphyrins by fluorescence and the triplet excited state by laser flash photolysis experiment. Rehm-Weller equation was used to determine the probability of electron transfer from the singlet state and from the triplet state of photoinitiator, by calculating the free Gibbs energy (**Eq. S1**) using reduction potential of photoinitiators E_{red}(**P8**) = -0.68 V/SCE and E_{red}(**P8Zn**) = -0.85 V/SCE determined by cyclic voltammetry (**Figure S5**) and oxidation potential of MDEA as found in literature E_{ox}(MDEA) = 0.72 V/SCE [23]. The negative value of free energy for both porphyrin at singlet states (ΔG_S(**P8**/MDEA) = -45.10 eV and ΔG_S(**P8Zn**/MDEA) = -39.90 eV) and triplet state (ΔG_T(**P8**/MDEA) = -119.48 eV and ΔG_T(**P8Zn**/MDEA) = -96.81 eV) highlight a favorable reaction at singlet state and triplet state (**Table IIB-3**).

***Table IIB-3**: Photophysical properties of **P8** and **P8Zn**. [a] determined by peak potential using cyclic voltammetry. [b] calculated from the wavelength at the intersection of the absorption and emission spectra (λ_{inter}), according to : $E_S = 1240/\lambda_{inter}$. [c] calculated from the wavelength at the maximum absorption of transient absorption spectrum ($\lambda_{triplet}$), according to: $E_T = 1240/\lambda_{triplet}$. [d] Calculated from Rehm-Weller equation (see **Eq. S1**)*

Molecules	E_{red}[a] (V/SCE)	E_S[b] (eV)	E_T[c] (eV)	$\Delta G_S^{MDEA, d}$ (eV)	$\Delta G_T^{MDEA, d}$ (eV)
P8	-0.68	1.87	2.64	-45.10	-119.48
P8Zn	-0.85	1.99	2.58	-39.90	-96.81
BP	-1.20 [23]		2.38 [23]		-44.65
CQ	-1.25 [23]		2.21 [23]		-21.20

Fluorescence spectra have been recorded in DCM (**Figure S6**) and present a maximum of emission at 673 nm for **P8** and 621 nm for **P8Zn**. It can be noted that the maximum emission of **P8Zn** is weaker due to the increase of intersystem crossing due to zinc complexation [28] favouring the population of triplet state instead of singlet state. The ratio of the two peaks are consistent with the pattern of tetra-phenyl porphyrin [29]. A quenching of **P8** fluorescence is observed when a graduating quantity of MDEA is added (**Figure IIB-5A**), with a high constant of Stern-Volmer, K_{SV}^{MDEA}(**P8**) = 233 M^{-1}. In contrary, no fluorescence quenching is observed with **P8Zn** (**Figure IIB-5B**), which is consistent with a lower population of singlet state. However the increase of fluorescence intensity can confirm the formation of a new fluorescent specie.

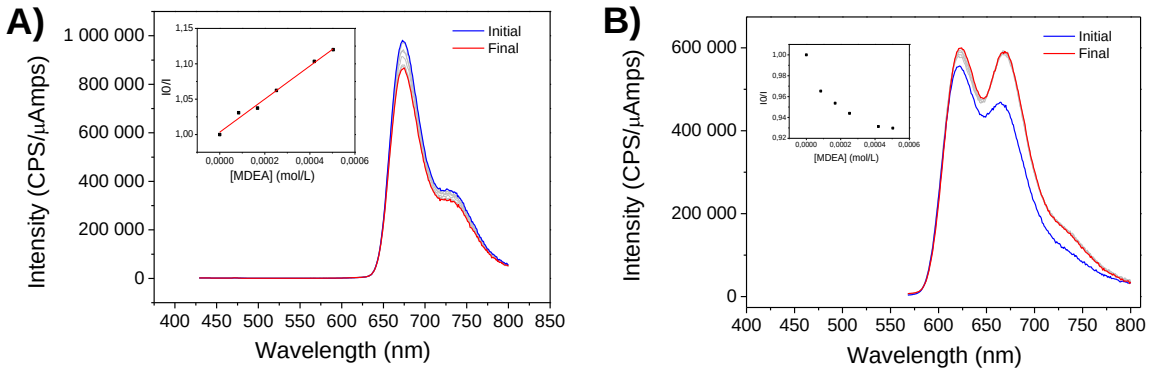

***Figure IIB-5**: Quenching of fluorescence of **A) P8** and **B) P8Zn** solution in DCM with a gradual addition of MDEA in DCM (λ_{exc}^{P8} = 414 nm & λ_{exc}^{PZn8} = 428 nm). Insert: Stern-Volmer plot I_0/I in function of [MDEA]. [**P8**] = 1.3 x 10^{-6} mol.L^{-1}, [**P8Zn**] = 1.4 x 10^{-6} mol.L^{-1}.*

The study of the excited triplet state of porphyrins have been made by lase flash photolysis (LFP) in deoxygenated DCM, with an excitation at 385 nm. Transient absorption spectra of photoinitiators are given in **Figure S7A** for **P8** and **Figure S7B** for **P8Zn**, and allow to identify the triplet states at 470 nm and 480 nm for **P8** and **P8Zn** respectively localised as the maximum absorption. The lifetime of the triplet state are calculated from de decay trace at their maximum absorption, and lead to τ(**P8**) = 16 µs and τ(**P8Zn**) = 18 µs. The triplet states are sensitive to oxygen, and lead to a severe decrease of lifetime, to τ_{O2}(**P8**) = 0.38 µs and τ_{O2}(**P8Zn**) = 0.81 µs (**Figure S7C** and **D**).

The reactivity at triplet state have been demonstrated by adding MDEA to the porphyrins solution, leading in both case to an increase of the triplet state lifetime (**Figure IIB-6**). Indeed, the lifetime of the triplet state are increase to τ_{MDEA}(**P8**) = 42 µs and τ_{MDEA}(**P8Zn**) = 51 µs.

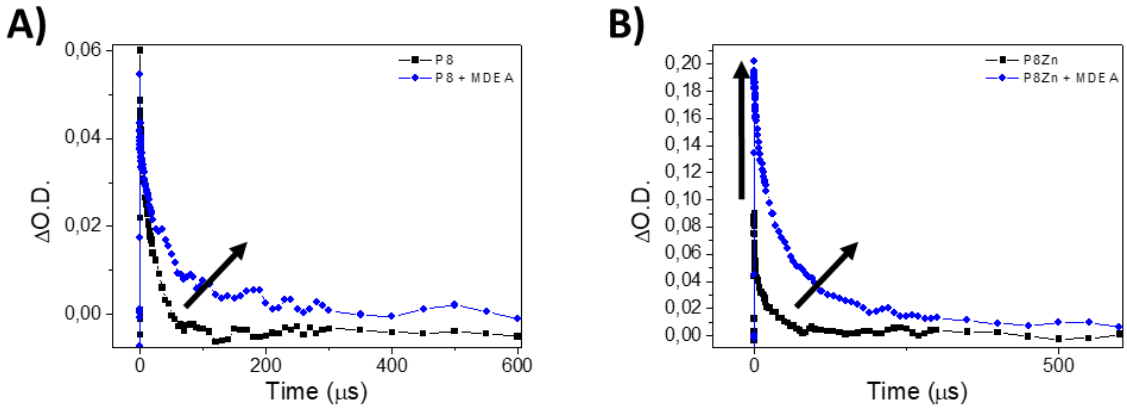

***Figure IIB-6**: Decay trace of A) **P8** at 470 nm and B) **P8Zn** at 480 nm by LFP alone and in presence of MDEA in deoxygenated DCM. [MDEA] = 4.4 x 10^{-1} mol.L^{-1}.*

This study tend to prove the interaction between MDEA and porphyrins at both triplet and singlet state by an electron transfer to form radical MDEA, which is able to initiate radical polymerization.

Free radical polymerization. Free radical polymerization experiment is carried out using porphyrin/MDEA/SOA (0.5%/5% w/w) mixture. Kinetics profiles of the polymerization are followed by RT-FTIR at different wavelength of irradiation and results are shown in **Figure IIB-7** for **P8** and **Figure IIB-8** for **P8Zn**. Final monomer conversion after 800 s of irradiation are displayed in **Table IIB-4**.

According to the results, both **P8**/MDEA and **P8Zn**/MDEA exhibit excellent monomer conversion. Maximum monomer conversion is achieved by irradiation with a light source whose wavelength is as close as possible to the maximum absorption wavelength of the porphyrin. Indeed, where **P8** has a

maximum absorption at 414 nm, maximum monomer conversion peaks occurred at 405 nm, giving a yield of 89%. Similar results were observed for **P8Zn**, which showed maximum conversion at 405 nm (87%) and at 455 nm (77%), due to the mid-position of its maximal absorbance peak at 428 nm.

It should be noted that the broad absorption range of **P8** and **P8Zn** covering the entire visible spectrum enabled correct conversion to be achieved at all the wavelengths tested (*i.e.* 385 nm, 405 nm, 455 nm, 470 nm, 505 nm, 530 nm, 590 nm and 625 nm). For example, under the illumination of a lamp at 625 nm, conversion reached up to 44% for **P8Zn**, compared with 25% for **P8**, in the context of experimental conditions under lamination.

It should be noted that, with the exception of **P8Zn** at 470 nm, where the two conversion rates of 36% and 41% are relatively close, the conversions obtained in the presence of oxygen are generally lower than those obtained under laminate conditions. This difference can be explained by the fact that the oxygen reacts on the initiating radicals (R°) formed to generate peroxyl radical (ROO°), which inhibits the polymerisation [30–32].

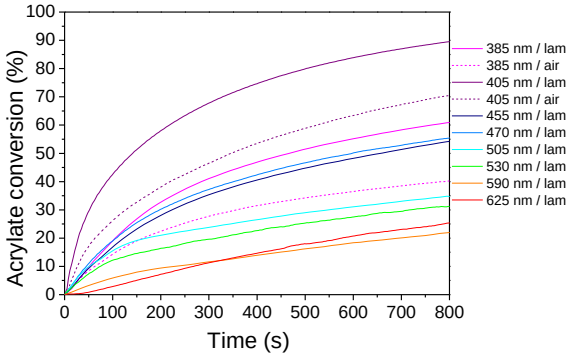

***Figure IIB-7**: Kinetic profiles of **P8**/MDEA/SOA (0.5%/5% w.w) under laminate (lam) or oxygen atmosphere (air).*

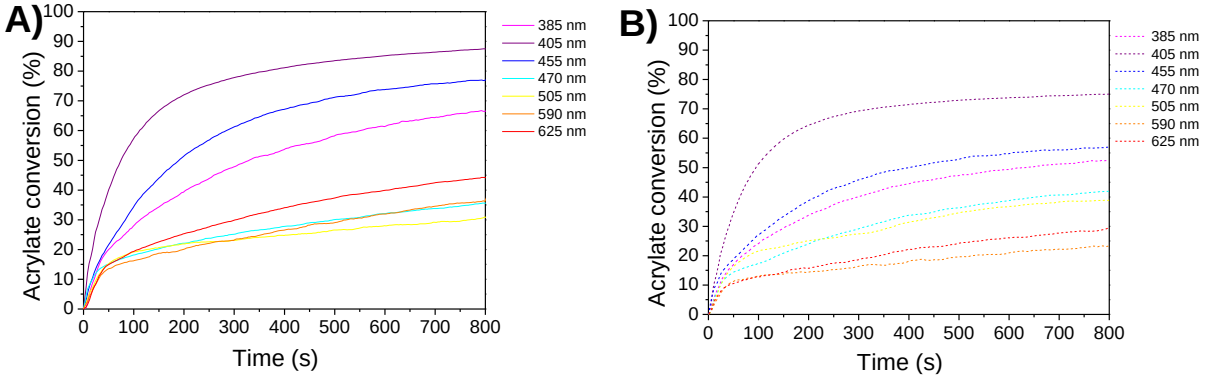

***Figure IIB-8**: Kinetic profiles of **P8Zn**/MDEA/SOA (0.5%/5% w.w) under **A**) laminate **B**) oxygen atmosphere.*

***Table IIB-4**: Final conversion of polymerization*

	Lam							
	385	405	455	470	505	530	590	625
P8 MDEA SOA	61	89	54	55	35	31	22	25
P8Zn MDEA SOA	67	87	77	36	30	38	37	44

	Air							
	385	405	455	470	505	530	590	625

P8 MDEA SOA	40	70	44	32	6	5	15	10
P8Zn MDEA SOA	50	75	57	41	np	np	22	29

np = no polymerization

ROS formation and water depollution. In light of their high photoinitiating ability, **P8** and **P8Zn** can be used as photoinitiators to synthesized biosourced polymers. These polymers can then be used to depollute water under visible light.

a) Formation of ROS under UV irradiation. The ability of porphyrins to create ROS have been investigated to understand the mechanisms involved under UV irradiation. To determine the capacity to form singlet oxygen, a solution of **P8** (or **P8Zn**) was mixed with a solution of TPCPD under UV irradiation. The degradation reaction of TPCPD in presence of singlet oxygen (see mechanism in **Figure S8**) is monitored by UV-visible spectroscopy, and results are presented in **Figure IIB-9A**. For determination of superoxide ion generation, formation of formazan from NBT (see mechanism in **Figure S9**) is followed by UV-visible spectroscopy and results are shown in **Figure IIB-9B**.

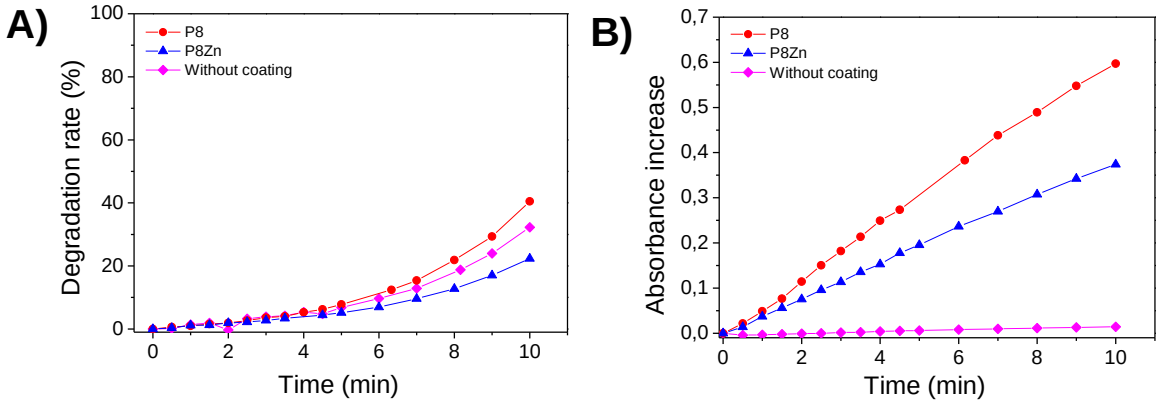

***Figure IIB-9**: A) Degradation of TPCPD, indicating formation of singlet oxygen. B) Absorption increase at 530 nm using NBT, indicating the formation of formazan, and formation of ion superoxide.*

The following mechanism is proposed [33,34]:

$$P \xrightarrow{h\nu} {}^3P^* \qquad (1-a)$$

Type I mechanism:

$${}^3P^* + {}^3O_2 \rightarrow {}^1P + {}^1O_2 \qquad (1-b)$$

Type II mechanism:

$$P \xrightarrow{h\nu} {}^3P^* \qquad (2-a)$$

$${}^3P^* + {}^3P^* \rightarrow P^{\bullet+} + P^{\bullet-} \qquad (2-b)$$

$$P^{\bullet-} + O_2 \rightarrow P + O_2^{\bullet-} \qquad (2-c)$$

$$2O_2^{\bullet-} + 2H^+ \rightarrow H_2O_2 + O_2 \qquad (2-d)$$

$$H_2O_2 + P^{\bullet-} \rightarrow PS + HO^{\bullet} + HO^- \qquad (2-e)$$

b) Depollution of AR14 under UV irradiation. The ability of **P8** and **P8Zn**-based coatings to depollute water was investigated using AR14, a dye used in textile and pharmaceutical industry, as pollutant [4]. The coating was immerged in an aqueous solution of AR14 and irradiated by a UV lamp emitting at a maximum wavelength of 365 nm. Degradation of the dye is monitored by UV-Visible spectroscopy at 15-minute intervals. Irradiation is maintained 5 hours until the pollutant is completely degraded.

Results of photodegradation of AR14 in presence of **P8** or **P8Zn** are presented in **Figure IIB-10A** as well as photolysis of AR14 under UV irradiation alone. **P8**- and **P8Zn**-based coatings showed good performance for degradation of AR14. It is worth noticing that the results obtained are comparable to those observed with **P3**- and **P4**-based coatings, demonstrating the efficiently of our materials for photodegradation. The maximum difference between photolysis and photodegradation was observed at 180 minutes for **P8** material (Δ_{max} = 34%), while for **P8Zn** material, this maximum difference was reached after 120 minutes (Δ_{max} = 36%). Both coatings achieved a significant 90% degradation after 165 minutes, compared to the 5+ hours required for photolysis. Finally, total degradation (> 99%) was achieved for **P8** and **P8Zn** coatings after 255 minutes of irradiation. Adsorption tests were also carried out (the results are shown in **Figure IIB-10B**), confirming that the dye was not adsorbed on the surface of our coatings. Thus, the observed decrease in absorbance can be attributed to chemical photodegradation rather than simple adsorption.

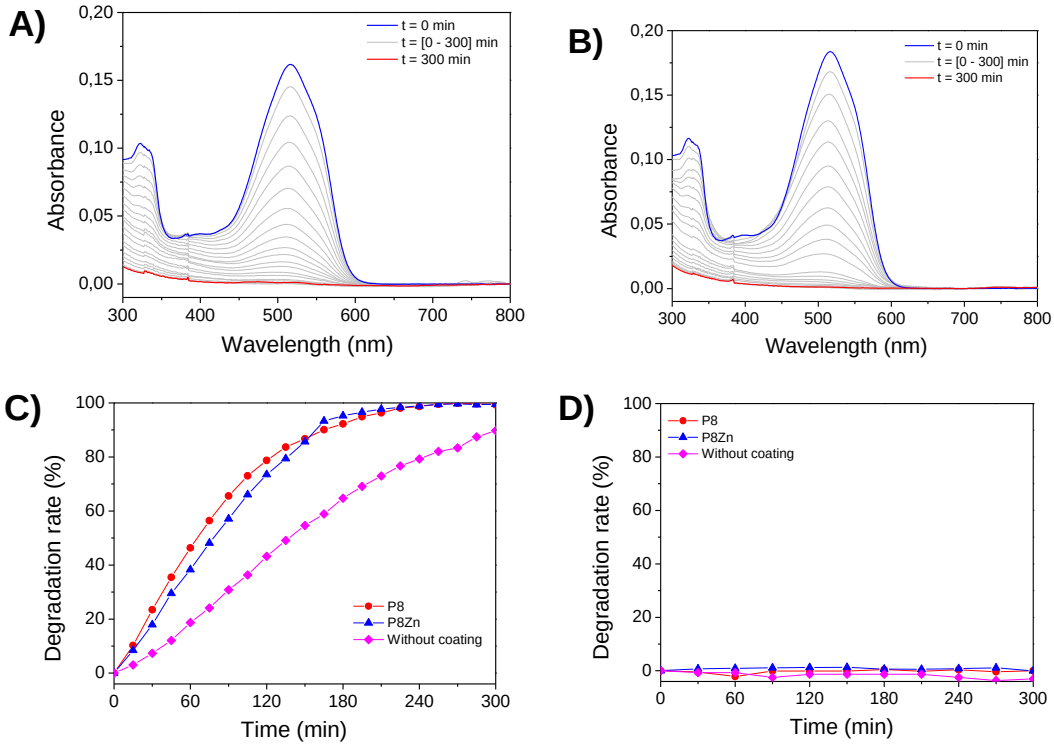

***Figure IIB-10**: Photodegradation of AR14 under UV irradiation UV lamp ($\lambda_{maximum}$ = 365 nm) in an open air system for **A)** **P8** and **B)** **P8Zn**. **C)** Associated degradation rate of AR14 for **P8** coating, **P8Zn** coating and without coating. **D)** Adsorption of AR14 on surface of **P8** or **P8Zn** without light. The controls without coating and without light are presented to control the stability of solution.*

Porphyrin-based materials have been used to depollute water under UV irradiation, demonstrating their ability to produce ROS with sufficient energy to degrade azo dye. However, porphyrins present the major interest of absorbing light in the visible range, which would provide a safer and more energy-efficient alternative to UV lamps.

c) Formation of ROS under visible light. In order to determine the ability of porphyrin to create ROS under visible irradiation, the same experiment than under UV irradiation are made, using LED@405 nm irradiation. Under visible exposure, it can be seen that **P8** and **P8Zn** have approximately the same ability to form singlet oxygen (**Figure IIB-11A**). **P8** is faster but reaches a maximum after 15 minutes with 80% degradation of TPCPD. For the formation of superoxide ions (**Figure IIB-11B**), **P8Zn** is the only one able to form superoxide, since it requires the presence of a metal ion for the electron transfer [35,36]. We can therefore conclude that **P8** only allows a type I mechanism in the presence of oxygen, whereas **P8Zn** allows both mechanisms.

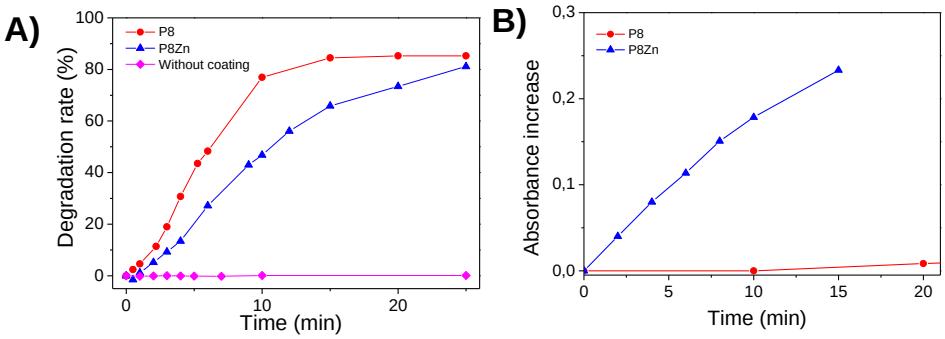

*Figure IIB-11: A) Degradation of TPCPD followed by visible spectroscopy (formation of singlet oxygen). B) Formation of formazan followed by visible spectroscopy (formation of superoxide ion) in contact with **P8** or **P8Zn** solution.*

d) Depollution of AR14 under visible irradiation. From the results obtained for the formation of ROS under visible irradiation, it appears that only **P8Zn** can form adequate quantities of superoxide ion to perform depollution. The same procedure was used for the depollution of AR14 under visible irradiation as under UV irradiation.

Firstly, the results obtained by 405 nm irradiation of **P8** (**Figure IIB-12A**) and **P8Zn Figure IIB-12B**) showed that no significant degradation of AR14 was observed after one hour of irradiation, in contrast to those observed under UV irradiation. The results of the singlet oxygen formation experiments on **P8** show that singlet oxygen is not energetic enough to initiate AR14 degradation. Similarly, experiments demonstrating the formation of superoxide ion by **P8Zn** led to the conclusion that it is not reactive towards AR14. In contrast to the results obtained under UV irradiation, no significant transformation of the superoxide ion into hydrogen peroxide was observed.

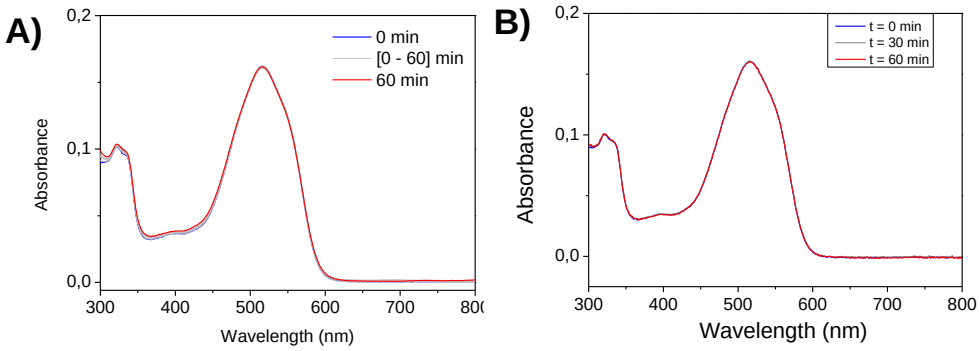

*Figure IIB-12: Absorbance of a solution of AR14 (C = 10 µM) in contact with a **A) P8** or **B) P8Zn** coating under 60 minutes of irradiation (λ = 405 nm).*

In order to improve the efficiency of degradation by materials under visible irradiation, an additive seems to be necessary to facilitate the conversion of superoxide ion into hydrogen peroxide, inspired by previous studies [34]. For this purpose, acetic acid was added to allow proton exchange. The results are shown in **Figure IIB-13A**. A decrease in the absorbance of the AR14 solution can be observed, suggesting possible degradation. However, examination of the sample at the end of the experiment revealed a pink coloration, suggesting possible adsorption of the dye on the surface of the coating. This hypothesis was validated by an experiment without light, which showed the same rate of decrease in AR14. Other experiments at different pH levels were also carried out (**Figure IIB-13B**), but without any improvement in degradation.

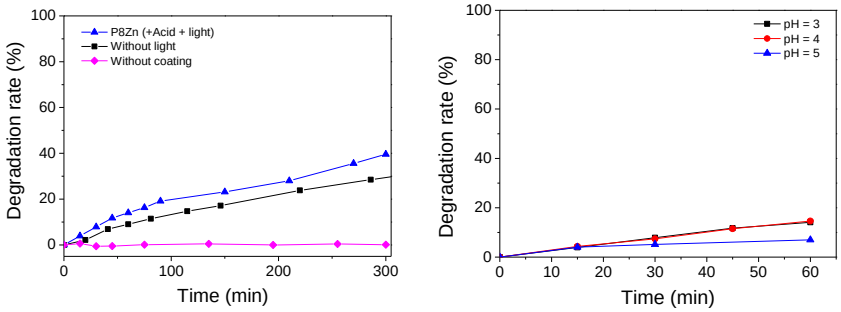

***Figure IIB-13**: Diminution of AR14 with **P8Zn** coating with acetic acid at **A**) pH = 3 with control without light or without coating, and **B**) at different pH.*

To remove the dye from the material, ultrasound was applied to the setup. For this, the beaker was placed inside an ultrasound bath and secured with tweezers to prevent it from moving. This approach showed that (**Figure IIB-14**) although good degradation was observed with the addition of light, it is important to note that without material (*i.e.* just ultrasound and light), the same rate of degradation was observed, indicating that the combination of the two parameters was responsible of the degradation of AR14, and not the effect of the material.

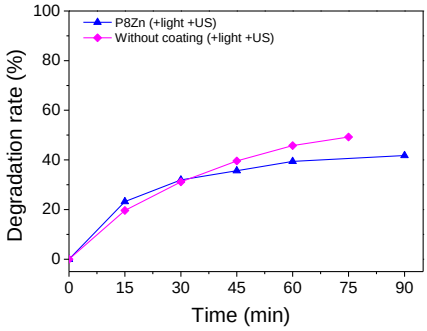

***Figure IIB-14**: Degradation of AR14 in presence of **P8Zn** coating with ultrasound.*

The introduction of ascorbic acid to bring electrons to the reaction was evaluated, but the results showed similar degradation (**Figure IIB-15**). Indeed, despite the fact that the dye is not adsorbed by the material, the same degradation is observed with and without the material. This proves that the combination of light and ascorbic acid is effective on its own in degrading AR14.

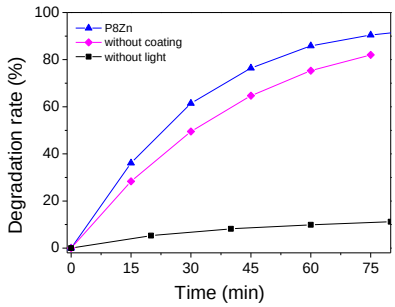

***Figure IIB-15**: Degradation of AR14 in presence of **P8Zn** coating with ascorbic acid. [acid ascorbic] = 8.1 x 10^{-6} M.*

Finally, the direct addition of hydrogen peroxide revealed significant differences between the two control experiments (without light and without material) and the experiment combining our material with light (**Figure IIB-16**). These results clearly indicate the formation of radical porphyrin, reacting with hydrogen peroxide to form hydroxyl radicals. This procedure can also be used with a porphyrin that does not produce superoxide ions, such as **P8** (**Figure IIB-16B**).

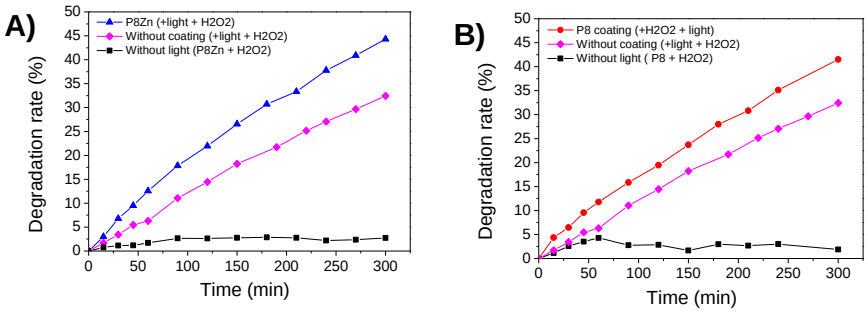

***Figure IIB-16**: Degradation of AR14 in presence of **P8Zn** (A) and **P8** (B) coatings with hydrogen peroxide. [H_2O_2] = 2.4 x 10^{-1} M.*

The direct addition of hydrogen peroxide proved the feasibility of equation 2. Although the transformation of the superoxide ion into hydrogen peroxide has not yet been possible, it should be noted that the rest of the equation is possible.

IV. Conclusion

This study reports the synthesis of two new porphyrins that showed good photoinitiator properties as H-abstractors with a tertiary amine as co-initiator for the photopolymerisation of acrylated soybean oil, a bio-based monomer. The final conversion of acrylated function of SOA reach 89% and 87% under LED@405 nm and the system also provided a substantial conversion of 25% and 44% under LED@625 nm irradiation for **P8** and **P8Zn** respectively. The porphyrin photodegradation properties using acid red 14 as pollutant model of azo dye, were determined under UV and visible irradiation.

It has been demonstrated that under UV irradiation, significant degradation rates have been obtained, comparable to other porphyrins already developed (P3/P4). In addition, the mechanism of ROS formation under visible irradiation (LED@405 nm) was investigated, revealing the possibility of superoxide ion formation via metalled porphyrin. However, it appears that the superoxide ion formed is not converted to hydrogen peroxide. It is possible that the superoxide ion is not sufficiently stable to diffuse into the medium to form hydrogen peroxide, or that the amount formed is insufficient.

V. References

1 N. Puvaneswari, J. Muthukrishnan and P. Gunasekaran, INDIAN J EXP BIOL.
2 A. Gottlieb, C. Shaw, A. Smith, A. Wheatley and S. Forsythe, Journal of Biotechnology, 2003, 101, 49–56.
3 A. Gičević, L. Hindija and A. Karačić, in CMBEBIH 2019, eds. A. Badnjevic, R. Škrbić and L. Gurbeta Pokvić, Springer International Publishing, Cham, 2020, vol. 73, pp. 581–587.
4 C. Bauer, P. Jacques and A. Kalt, Journal of Photochemistry and Photobiology A: Chemistry, 2001, 140, 87–92.
5 H. Zhou and D. W. Smith, Can. J. Civ. Eng., 2001, 28, 49–66.
6 K. A. Yongabi, .
7 M. Grassi, L. Rizzo and A. Farina, Environ Sci Pollut Res, 2013, 20, 3616–3628.
8 Y. Deng and R. Zhao, Curr Pollution Rep, 2015, 1, 167–176.
9 S. Nouacer and R. Djellabi, Environ Sci Pollut Res, , DOI:10.1007/s11356-022-23772-5.
10 Y. Leprince-Wang, N. Martin, Y. Ghozlane Habba, M. L. Pivert and M. Capochichi-Gnambodoe, NanoWorld J, , DOI:10.17756/nwj.2019-074.
11 K. J. Gromkowska-Kępka, A. Puścion-Jakubik, R. Markiewicz-Żukowska and K. Socha, J of Cosmetic Dermatology, 2021, 20, 3427–3431.
12 H. Claus, Photochemistry and Photobiology, 2021, 97, 471–476.
13 R. Gerdes, D. Wöhrle, W. Spiller, G. Schneider, G. Schnurpfeil and G. Schulz-Ekloff, Journal of Photochemistry and Photobiology A: Chemistry, 1997, 111, 65–74.
14 K. Ozoemena, N. Kuznetsova and T. Nyokong, Journal of Photochemistry and Photobiology A: Chemistry, 2001, 139, 217–224.
15 M. Nowakowska and K. Szczubiałka, Polymer Degradation and Stability, 2017, 145, 120–141.
16 D. K. Balta, G. Temel, G. Goksu, N. Ocal and N. Arsu, Macromolecules, 2012, 45, 119–125.
17 L. Breloy, V. Brezová, A. Blacha-Grzechnik, M. Presset, M. S. Yildirim, I. Yilmaz, Y. Yagci and D.-L. Versace, Macromolecules, 2020, 53, 112–124.
18 C. Elian, B. Quienne, S. Lajnef, F. Peyrot, R. Moilleron, S. Abbad Andaloussi, S. Caillol and D.-L. Versace, European Polymer Journal, 2023, 112369.
19 D.-L. Versace, G. Moran, M. Belqat, A. Spangenberg, R. Méallet-Renault, S. Abbad-Andaloussi, V. Brezová and J.-P. Malval, ACS Appl. Mater. Interfaces, 2020, 12, 5050–5057.
20 P. Sautrot-Ba, A. Contreras, S. A. Andaloussi, T. Coradin, C. Hélary, N. Razza, M. Sangermano, P.-E. Mazeran, J.-P. Malval and D.-L. Versace, J. Mater. Chem. B, 2017, 5, 7572–7582.
21 G. Noirbent, Y. Xu, A.-H. Bonardi, D. Gigmes, J. Lalevée and F. Dumur, European Polymer Journal, 2020, 139, 110019.
22 A. Bonardi, F. Bonardi, G. Noirbent, F. Dumur, C. Dietlin, D. Gigmes, J.-P. Fouassier and J. Lalevée, Polym. Chem., 2019, 10, 6505–6514.
23 H. Marcille, J.-P. Malval, M. Presset, N. Bogliotti, A. Blacha-Grzechnik, V. Brezová, Y. Yagci and D.-L. Versace, Polym. Chem., 2020, 11, 4237–4249.
24 V. B. Khajone and P. R. Bhagat, Res Chem Intermed, 2020, 46, 783–802.
25 G.-Y. Gao, J. V. Ruppel, D. B. Allen, Y. Chen and X. P. Zhang, J. Org. Chem., 2007, 72, 9060–9066.
26 R. Lyubimenko, B. S. Richards, A. I. Schäfer and A. Turshatov, Journal of Membrane Science, 2022, 642, 119981.
27 R. Lyubimenko, D. Busko, B. S. Richards, A. I. Schäfer and A. Turshatov, ACS Appl. Mater. Interfaces, 2019, 11, 31763–31776.
28 A. Harriman, J. Chem. Soc., Faraday Trans. 1, 1980, 76, 1978–1985.
29 A. K. Mandal, M. Taniguchi, J. R. Diers, D. M. Niedzwiedzki, C. Kirmaier, J. S. Lindsey, D. F. Bocian and D. Holten, J. Phys. Chem. A, 2016, 120, 9719–9731.
30 C. Decker and A. D. Jenkins, Macromolecules, 1985, 18, 1241–1244.
31 C. J. Kingsbury and M. O. Senge, Coordination Chemistry Reviews, 2021, 431, 213760.
32 A. K. O'Brien and C. N. Bowman, Macromolecules, 2006, 39, 2501–2506.
33 W. M. Sharman, C. M. Allen and J. E. van Lier, Drug Discovery Today, 1999, 4, 507–517.

34 P. Mroz, J. Bhaumik, D. K. Dogutan, Z. Aly, Z. Kamal, L. Khalid, H. L. Kee, D. F. Bocian, D. Holten, J. S. Lindsey and M. R. Hamblin, Cancer Letters, 2009, 282, 63–76.
35 M. Tezuka, Y. Ohkatsu and T. Osa, BCSJ, 1975, 48, 1471–1474.
36 K. Yamamoto and T. Kwan, Journal of Catalysis, 1970, 18, 354–356.

VI. Supporting information

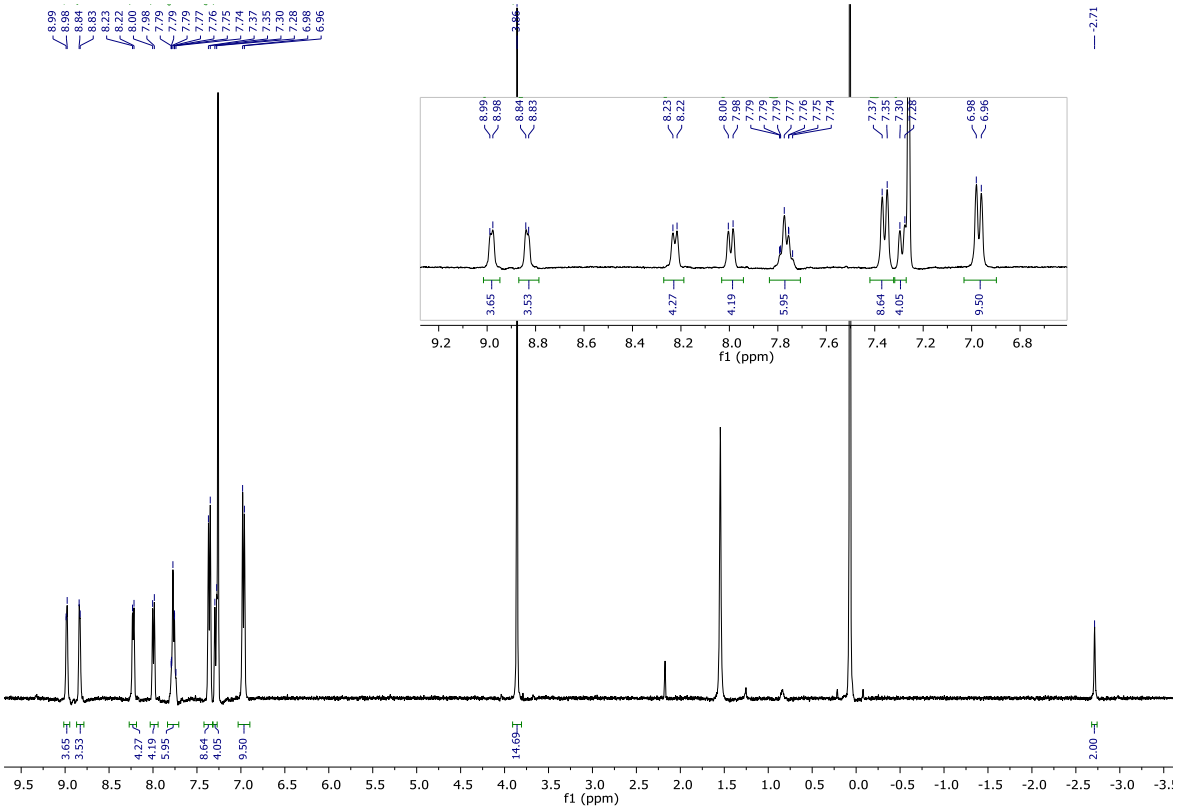

***Figure S1**: ^{1}H NMR of **P8** in $CDCl_3$.*

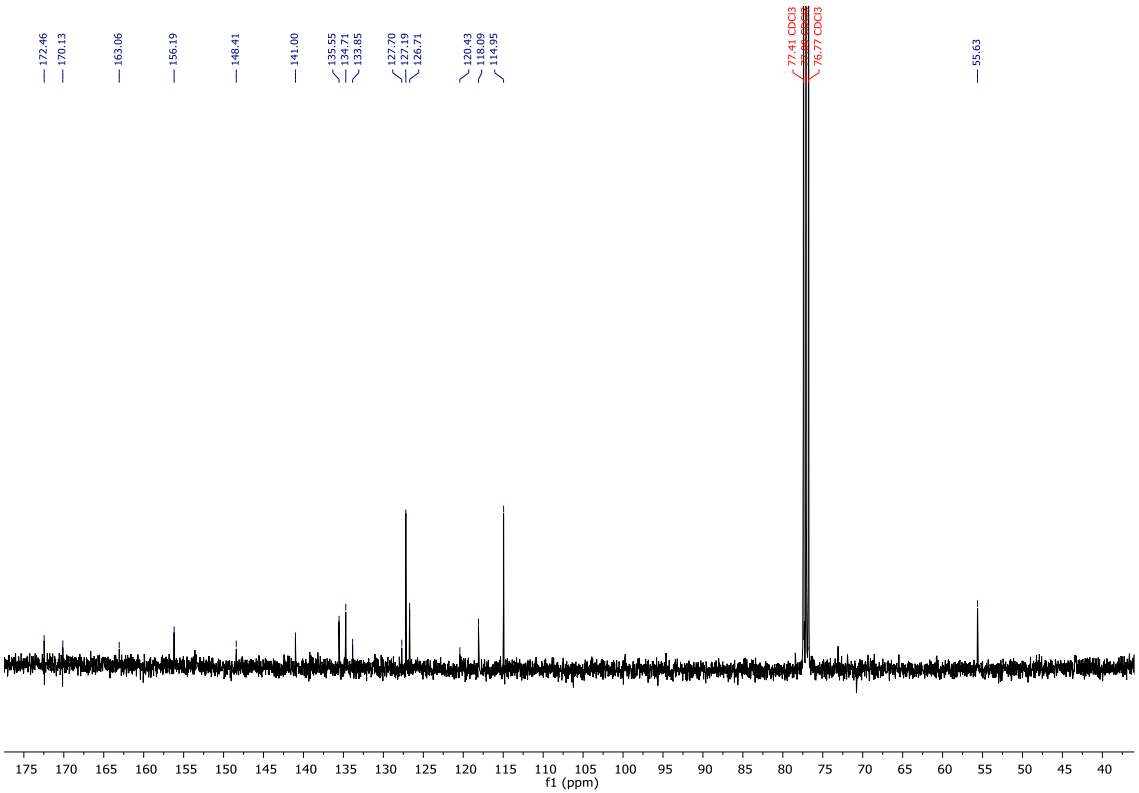

***Figure S2**: ^{13}C NMR of **P8** in $CDCl_3$.*

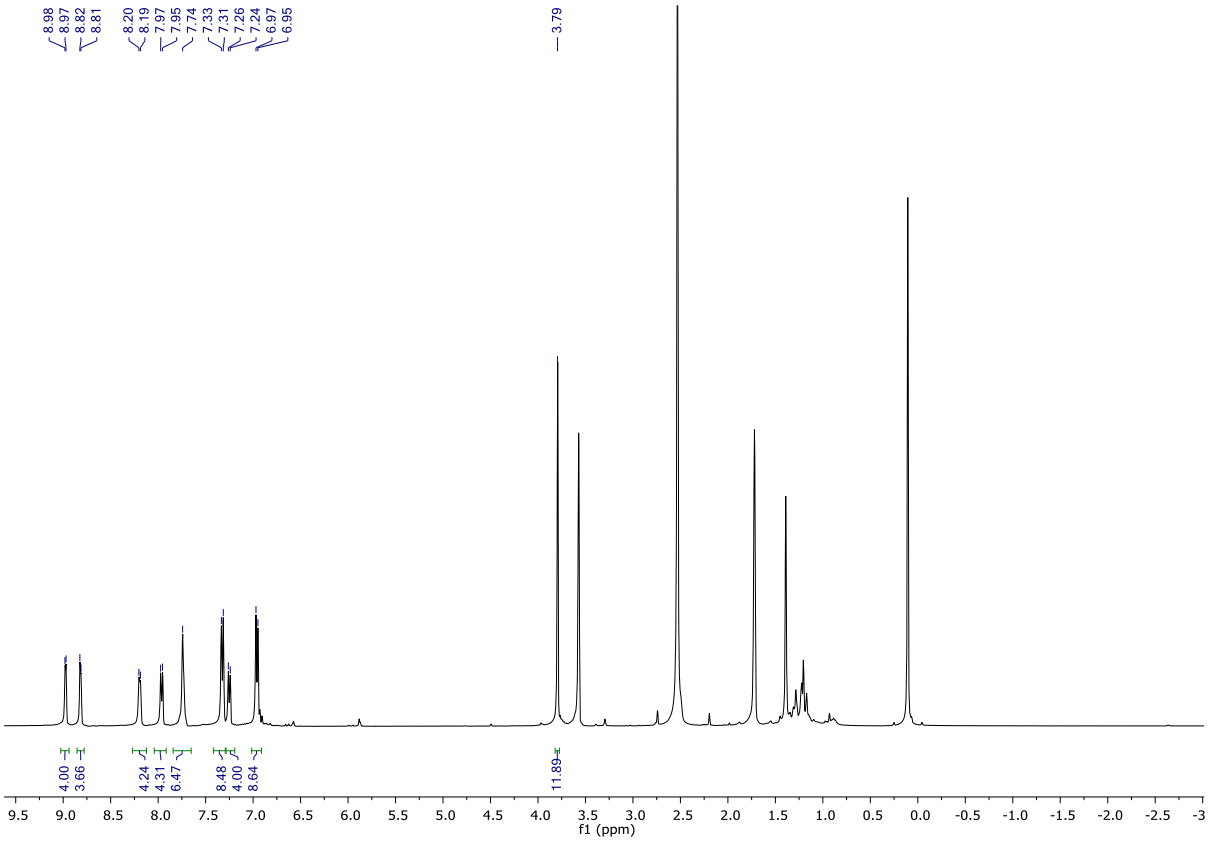

***Figure S3**: ^{1}H NMR of **P8Zn** in $CDCl_3$.*

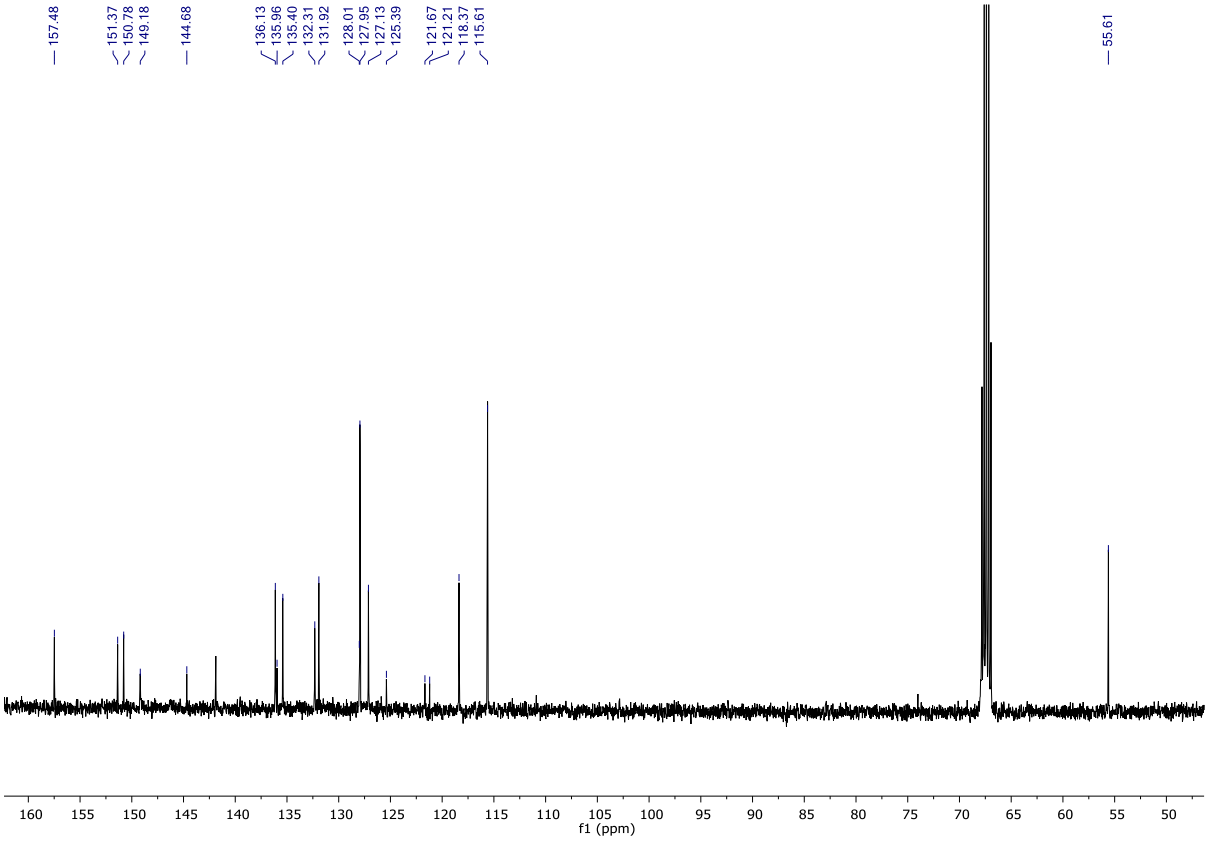

***Figure S4**: ^{13}C NMR of **P8Zn** in $CDCl_3$.*

Photochemical properties:

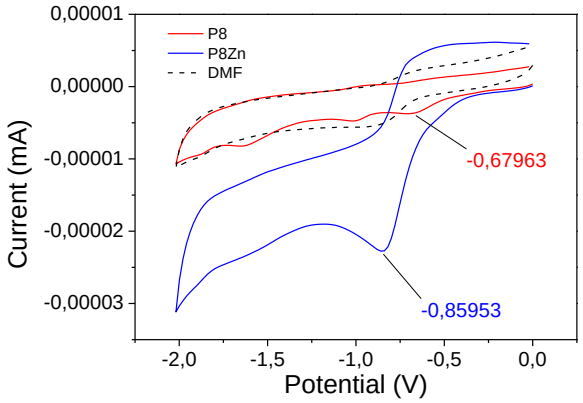

***Figure S5**: Cyclic voltammogram of **P8** and **P8Zn** in DMF + 0.05 M Bu_4NBF_4. [**P8**] = [**P8Zn**] = 10^{-3} M.*

Rehm-Weller equation.

$$\Delta G_{S\ or\ T} = F(E_{ox} - E_{red}) - E_{s\ (or\ T)} + \Delta E_c \quad (1)$$

***Equation S1**: Determination of energy change at singlet ΔG_S or triplet state ΔG_T of the electron transfer between a donor and an acceptor under irradiation. Where F is the Faraday constant, E_{ox} is the oxidation reduction of the donor (MDEA) E_{ox}^{MDEA} = 0.72 eV, E_{red} is the reduction potential of the acceptor, $E_{S\ (or\ T)}$ is the excited singlet (or triplet) state of the photoinitiator (**P8** or **P8Zn**) and ΔE_c is the Coulombic stabilization energy, which is negligible for most systems.*

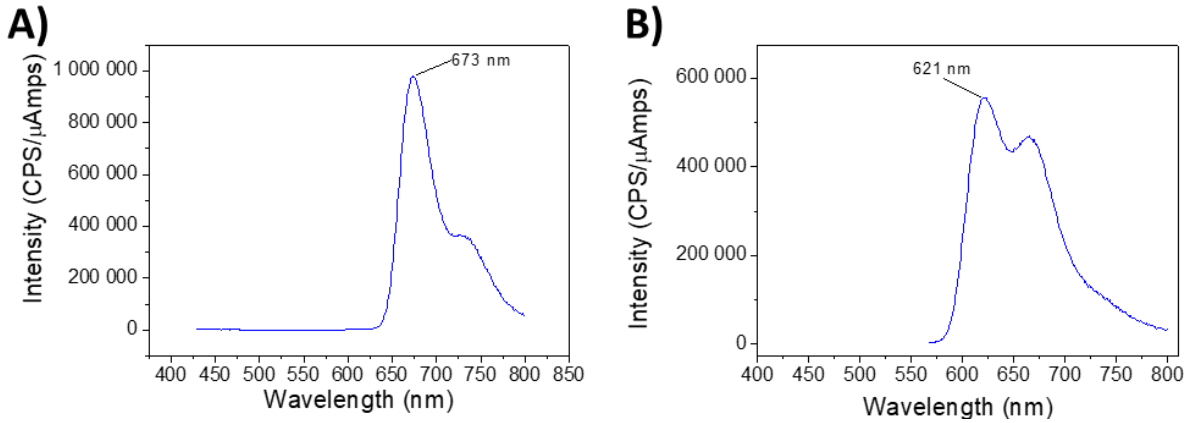

***Figure S6**: Emission spectra of **A) P8** and **B) P8Zn** in DCM. [**P8**] = 1.3 x 10^{-6} mol.L^{-1}, [**P8Zn**] = 1.4 x 10^{-6} mol.L^{-1}.*

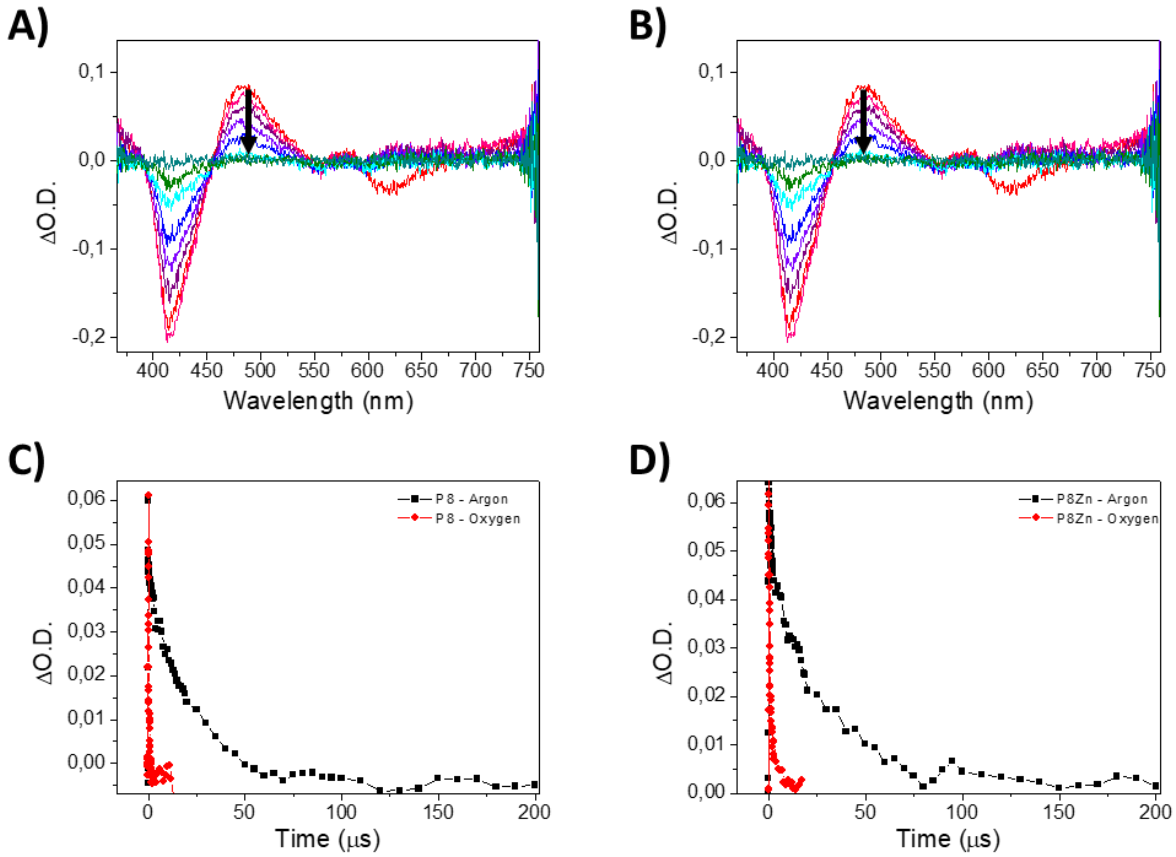

***Figure S7**: Transient absorption spectra of P8 and P8Zn in a deoxygenated DCM solution after laser pulse (λ = 385 nm). Decay trace of P8 at 470 nm and P8Zn at 480 nm by LFP with and without O_2. [**P8**] = 3.32 x 10^{-5} mol.L^{-1} and [**P8Zn**] = 1.35 x 10^{-5} mol.L^{-1}.*

ROS mechanisms probe

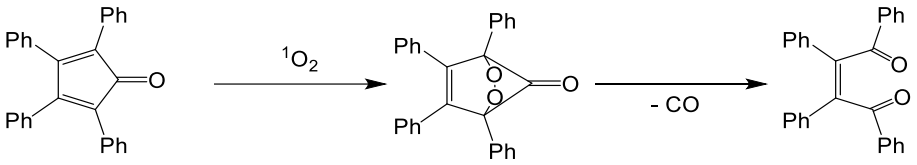

***Figure S8**: Degradation of TPCPD under singlet oxygen condition*

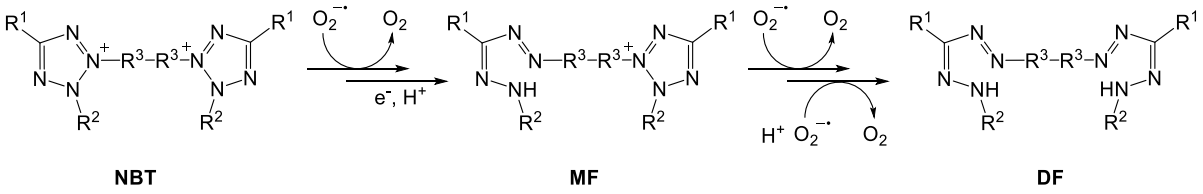

***Figure S9**: Degradation of nitro blue tetrazolium (NBT) into monoformazan (MF) and diformazan (DF) under ion superoxide condition [10]*

Conclusions du Chapitre II

Dans ce chapitre, l'intérêt de deux couples de porphyrines a été montré, en prenant en considération leur capacité à amorcer la polymérisation en tant que photoamorceur dans différents systèmes, et également leur capacité à dégrader un polluant modèle en tant que photosensibilisateur.

Il a été constaté que les porphyrines répondaient aux attentes. En effet, **P3** et **P4** ont donné d'excellents résultats d'amorçage de la polymérisation sous différentes longueurs d'onde dans le visible en combinaison avec différents co-amorceurs. De plus, **P8** et **P8Zn** possèdent bien un spectre d'absorption plus large que celui habituellement obtenu pour des porphyrines.

Les porphyrines ont ensuite été utilisées pour développer des matériaux présentant une bonne efficacité pour les applications de dépollution de l'eau sous irradiation UV, et donnent des résultats encourageants sous irradiation visible. En effet, même si aucune dégradation n'est observée sous irradiation visible, l'ajout de peroxyde d'hydrogène permet de dégrader le polluant, et les mécanismes de formation des ROS ont été déterminés.

Chapitre III

Modélisation et synthèse des porphyrines

Contexte

Dans le chapitre précédent, la modélisation des propriétés des porphyrines **P3** et **P4** a été réalisée par calcul DFT et TDDFT. Cela a permis de mettre en lumière les bonnes corrélations entre les données théoriques et expérimentales. La méthode de calcul employée pour ces deux molécules sera appliquée à d'autres porphyrines de type A_2B_2 (**Figure III-1**) dans la première partie de ce chapitre. La simulation des spectres d'absorption des différents candidats ainsi que la prise en compte des propriétés chimiques attendues permettront de sélectionner les meilleurs candidats au photoamorçage. Ces candidats seront synthétisés et les données spectroscopiques expérimentales et théoriques seront comparées.

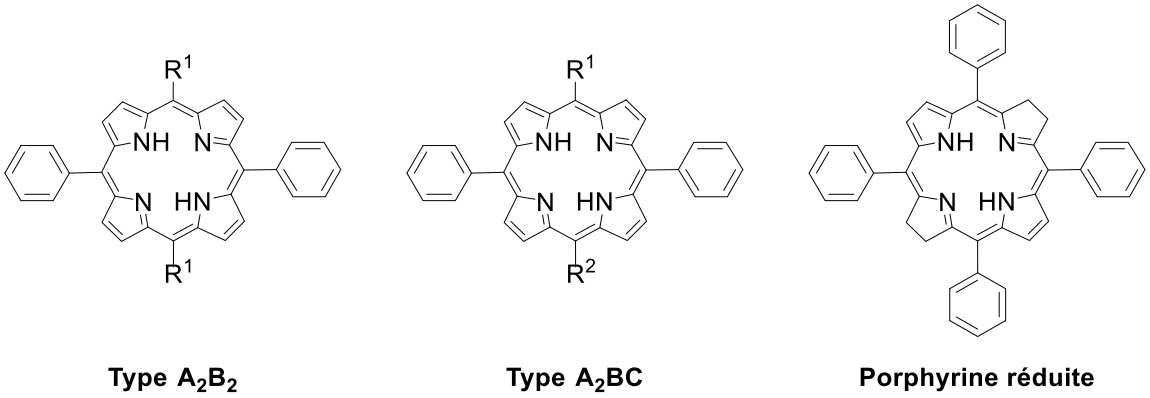

***Figure III-1** : Type de structures employées dans le chapitre III.*

Dans la deuxième partie de ce chapitre, des porphyrines de type A_2BC (**Figure III-1**) seront également modélisées pour simuler leurs propriétés. Ces porphyrines possèdent un groupement donneur (R^1) et attracteur (R^2), sont dîtes push pull, et devraient permettre ainsi un meilleur transfert électronique. De plus, la réduction d'une et deux liaisons sur le noyau porphyrinique a été envisagée, créant des chlorines et bactériochlorines respectivement.

Partie A : Design of new porphyrins for photopolymerization assisted by modelisation

I. Introduction

Porphyrins are macromolecules used in a wide variety of applications, from the development of solar cells,[1] or materials[2] to the use in photomedicine[3]. Their applications are mainly associated to their spectroscopic properties, which have been extensively studied. Many studies focusing on the reactivity of porphyrins for different applications also involve a theoretical study of their properties.[4–6] Porphyrins have also shown particular interest in the development of new photoinitiator systems for use in photopolymerization under visible irradiation.[5,7–9] Some studies have focused on their theoretical properties to investigate the origin of their properties, and determined with accuracy the mechanisms involved. In particular, it is possible to obtain the optimized geometry of molecules, the characterisation of frontier orbitals, the properties of excited states, the nature of the electronic transitions and the spectroscopic properties.

One of the methods used to model porphyrins is based on Time-dependent density-functional theory TDDFT.[10] Different functional have been used, as B3LYP[11–14], M06[15] or PBE0[4], for the determination of structural, electronic or optical properties. When compared to experimental values (*i.e* Qx and Qy wavelength as well as $E_{0\text{-}0}$, HOMO and LUMO values), B3LYP present the smallest deviations from experimental results.[16,17] Calculations on porphyrins have been performed using different basis sets, such as 3-21G(d),[11] 6-31G(d),[18] 6-31++G**[19] or 6-311G(d)[17]. Different basis sets have also been compared.[20] The geometry obtained using a relatively small basis set B3LYP/3-21G and a more complex one B3LYP/6-31G* present only a slight difference, less than 0.016 Å and 1.1° for the bond length ad angle.[20]

Finally, a combination of different levels of theory can be used for the optimization of geometry in one hand and the calculation of the TD-DFT electronic transitions in the other hand. For example, two studies[4,19] have used B3LYP (resp. PBE0/6-31G(d)) for the optimization of geometry, followed by wB97XQ (resp. CAM-B3LYP/6-31+G(d)) for the vertical transition energies.

The experimental absorption spectrum of porphyrins is composed of different types of bands. The Soret band (also known as the B band), a very intense single band around 400 nm, and a series of weaker bands between 500 and 800 nm known as the Q bands. As the free base porphyrin is asymmetric (due to the protonation states of nitrogen atoms present in the porphyrin nucleus), the B and Q transitions are polarised, resulting in the formation of the B_x and B_y bands, and the Q_x and Q_y bands respectively.

The four orbital theory of Gouterman in 1963 [21] interpreted the origin of these bands based on the two highest occupied molecular orbitals (HOMO and HOMO-1) and the two lowest unoccupied molecular orbitals (LUMO and LUMO+1). Thus, the Q bands (Q_x and Q_y) are composed of transitions from the two occupied bands (respectively from HOMO-1 and HOMO) to LUMO, while the B bands (B_x and B_y) are due to transitions between the two occupied bands (respectively from HOMO-1 and HOMO) to LUMO+1. These Q_x and Q_y transitions correspond to low-intensity transitions from ground state (S_0) to n^{th} singlet electronic excited states S_n ($S_0 \rightarrow S_1$ and $S_0 \rightarrow S_2$), respectively. In addition, the Q_x and Q_y bands are both vibrationally split due to vibrational coupling of the excited state.[22] These bands were then assigned to their respective transitions $Q_x(0,0)$ and $Q_x(1,0)$ for Q_x and $Q_y(0,0)$ and $Q_y(1,0)$ for Q_y (see **Figure IIIA-1**). The Soret band, composed of two transitions B_x and B_y corresponds to the transitions $S_0 \rightarrow S_3$ and $S_0 \rightarrow S_4$.

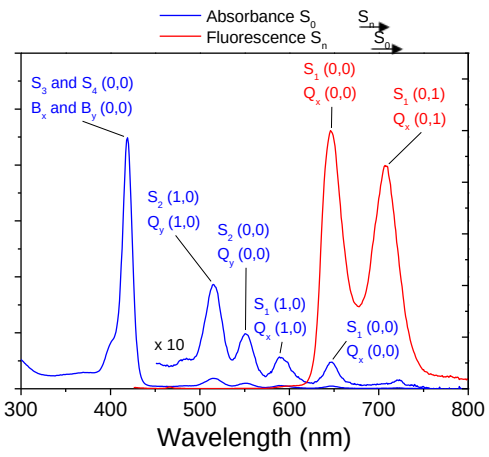

***Figure IIIA-1**: Correspondence between the notation of vertical transition (S_n) and corresponding absorption peak (B and Q) for the experimental absorption and emission spectra of **P4** in DCM.*

TDDFT calculation gives the energies of the excited states relatively to the ground state. At the optimized ground state geometry, the vertical transition energies and the associated oscillator strengths give information on the absorbance wavelengths of the molecules and their associated relative intensity. In standard TDDFT studies, no vibronic coupling is taken into account, and only the $Q_x(0,0)$ and $Q_y(0,0)$ bands are obtained. Studies have been conducted to investigate the harmonic vibrational frequencies and vibronic intensities of the absorption spectrum.[22,23] TDDFT can also be used to study the excited states of porphyrins. Indeed, the study of the first excited singlet state can lead to the determination of fluorescence emission spectrum[24], whereas the study of triplet states can lead to the determination of intersystem conversion[25], radiative lifetime [26] and vibronic analysis of phosphorescence [27].

In a previous study (Chapter II, part A), the spectroscopic properties of porphyrins **P3** and **P4** were modelled and compared with experimental results. These porphyrins were then used for photopolymerization. In order to better understand the relationship between spectroscopic data and photoactive activity, this part focuses on the modelling of a series of porphyrins. The method of computation developed with the previous part using the **P3** benchmark will be used to compute the spectroscopic properties of these porphyrins. The absorption properties will be compared, to select the porphyrin with the best absorption in visible range. These porphyrins will then be synthesised, and their experimental absorption spectra will be compared to theoretical results. Finally, the porphyrins will be used to develop new systems for radical photopolymerization.

II. Experimental part

Computational details.

Gaussian 16 package [28] was used for the Density Functional Theory (DFT) and Time Dependent Density Functional Theory (TD-DFT) calculations. The structure optimization has been computed by DFT using B3LYP/6-31G theory and have been followed by control of lack of imaginary vibrational frequencies. The determination of vertical excitation energy at TD-DFT level was determined on the optimized geometries using the same level of theory using six or ten excited states, depending on the number needed to reach the UV range. The simulation have been performed using the polarizable continuum (PCM) model for dichloromethane to consider the effect of the solvent.

General procedure for Suzuki-Miyaura coupling (4).

A 25 mL rounded-bottomed flask equipped with a stirring bar is charged with 5,10-diphenyl-10,20-dibromoporphyrin (100 mg, 0.16 mmol, 1.0 equiv), boronic acid (0.35 mmol, 2.2 mmol), K_2CO_3 (133 mg, 0.96 mmol, 6 equiv), THF (14 mL) and water (1.5 mL). The reaction mixture is flushed with Ar, $PdCl_2$dppf (12 mg, 0.016 mmol, 0.1 equiv) is added and then the reaction is heated to reflux for 16 h. The resulting solution is washed with water (2 x 20 mL) and brine (20 mL). The solvent is removed under reduced pressure.

Synthesis of 5,15-diphenyl-10,20-*N,N*-dimethylaminophenylporphyrin (P5). Dimethylaminophenylboronic acid **i** (58 mg) was used, and the crude residue is purified by flash chromatography (silica, DCM/PE: 60/40) to afford the desired product as a purple solid (64 mg, 70%). **^{1}H NMR (400 MHz, CDCl3):** δ 8.94 (d, J = 4.8 Hz, 4H), 8.81 (d, J = 4.8 Hz, 4H), 8.22 (d, J = 6.7 Hz, 4H), 8.09 (d, J = 8.0 Hz, 4H), 7.92 – 7.64 (m, 6H), 7.11 (d, J = 8.0 Hz, 4H), 3.24 (s, 12H), -2.68 (s, 2H). **^{13}C NMR** (100 MHz, CDCl3): δ 135.89 (4CH), 134.72 (4CH), 126.75 (4CH), 110.84 (4CH), 40.91 ($4CH_3$) (**Figures S7** and **S8**). **HRMS (ESI/Q-TOF)**: *m/z* [M + H^+] calcd for $C_{48}H_{41}N_6$ 701.3387; found 701.3390. ν_{max} (ATR)/cm^{-1}: 3308, 2896, 2341, 1596, 1487, 142, 1178, 1056, 960, 796, 734.

Synthesis of 5,15-diphenyl-10,20-*N,N*-dimethylaminophenylporphyrin (P6). Carbazolboronic acid **h** (101 mg) was used, and the crude residue is triturated in methyl acetate to afford the desired product as a purple solid (102 mg, 67%). **^{1}H NMR (400 MHz, CDCl3):** δ 9.02 (s, 4H), 8.97 (s, 4H), 8.48 (d, J = 7.8 Hz, 4H), 8.28 (m, 8H), 8.01 (d, J = 7.8 Hz, 4H), 7.86 (d, J = 8.2 Hz, 4H), 7.84 – 7.78 (m, 6H), 7.60 (t, J = 7.7 Hz, 4H), 7.42 (t, J = 7.5 Hz, 4H), -2.67 (s, 2H). **^{13}C NMR** (100 MHz, CDCl3): δ 136.07, 134.82, 128.02, 126.94, 126.32, 125.26, 123.86, 120.68, 120.42, 110.17 (**Figures S9** and **S10**). **HRMS (ESI/Q-TOF)**: *m/z* [M + H^+] calcd for $C_{68}H_{45}N_6$ 945.3700; found 945.3708. ν_{max} (ATR)/cm^{-1}: 3307, 2910, 2345, 1726, 1587 ,1494, 1460, 1330, 1220, 975, 796, 723.

Synthesis of 5,15-diphenyl-10,20-isopropylphenylporphyrin (P7). Dibromoporphyrin (81 mg, 0.13 mmol), isoporpylphenylboronic acid **f** (47 mg, 0.28 mmol), K_2CO_3 (107 mg, 0.78 mmol), THF (12 mL), water (1.2 mL) and $PdCl_2$(dppf) (9.5 mg, 0.013 mmol) were used, and the crude residue is purified by flash chromatography (silica, DCM/PE: 60/40) to afford the desired product as a purple solid (65 mg, 72%). **^{1}H NMR (400 MHz, CDCl3):** δ 8.91 (d, J = 4.0 Hz, 4H), 8.86 (d, J = 4.2 Hz, 4H), 8.25 (d, J = 7.2 Hz, 4H), 8.15 (d, J = 7.3 Hz, 4H), 7.77 (d, J = 7.0 Hz, 6H), 7.61 (d, J = 7.1 Hz, 4H), 3.27 (p, J = 6.8 Hz, 2H), 1.56 (dd, J = 7.0, 1.7 Hz, 12H), -2.73 (s, 2H). **^{13}C NMR** (100 MHz, CDCl3): δ 148.36, 142.43, 139.63, 134.81, 134.75, 127.79, 126.80, 124.91, 120.49, 120.11 (**Figures S11** and **S12**). **HRMS (ESI/Q-TOF)**: *m/z* [M + H^+] calcd for $C_{50}H_{43}N_4$ 699.3482; found 699.3482. ν_{max} (ATR)/cm^{-1}: 3311, 2945, 2343, 1797, 1697, 1546, 1458, 1346, 1259, 1170, 1039, 964, 798, 715.

Synthesis of 5,15-diphenyl-10,20-methoxynaphtaleneporphyrin (P9).

Isopropylphenylboronic acid **g** (71 mg) was used, and the crude residue is triturated in methyl acetate to afford the desired product as a purple solid (100 mg, 81%). **^{1}H NMR (400 MHz, CDCl3):** δ 8.f85 (d, J = 8.4 Hz, 8H), 8.60 (s, 2H), 8.36 (d, J = 8.3 Hz, 2H), 8.23 (d, J = 6.6 Hz, 4H), 8.09 (d, J = 8.4 Hz, 2H), 7.99 (d, J = 8.8 Hz, 2H), 7.75 (d, J = 6.8 Hz, 6H), 7.48 (s, 2H), 7.39 (d, J = 9.0 Hz, 2H), 4.10 (s, 7H), -2.67 (s, 2H). **^{13}C NMR** 134.46, 134.38, 133.35, 133.09, 129.82, 127.53, 126.51, 124.55, 119.67, 105.62, 55.38 (**Figures S13** and **S14**). **HRMS (ESI/Q-TOF)**: *m/z* [M + H^+] calcd for $C_{54}H_{39}N_4O_2$ 775.3068. ν_{max} (ATR)/cm^{-1}: 3315, 2896, 2345, 1593, 1469, 1336, 1211, 1161, 1022, 966, 910, 798, 717.

Photopolymerization kinetic studies.

Porphyrins have been used as photoinitiators for free-radical polymerization of acrylated soybean oil (SOA) under visible light in combination with MDEA (*N*-methyldiethanolamine) as co-initiator. The photopolymerization have been conduct by deposing the photosensitive formulation

(porphyrin/MDEA/SOA (0.5%:5% wt.wt.)) on a BaF_2 pellet and irradiated with various LEDs (LED@385 nm (35.3 mW·cm^2), LED@405 nm (118 mW·cm^2), LED@455 nm (23.8 mW·cm^2), and LED@530 nm (14.6 mW·cm^2)) in laminate or under air. The polymerization was monitoring by following the decrease of acrylated function of SOA by Real-Time Fourier Transformation InfraRed spectroscopy (RT-FTIR, Jasco) at 1636 cm^{-1} to determine the final monomer conversion.

III. Results and Discussion

Theoretical study of porphyrins allows various properties to be predicted, in order to design the best structures for photopolymerization. The wavelength at the maximum of the absorption spectra need to be determined in order to check if the absorption is effective in the visible range.

III. 1. Design and computation of new porphyrins

III.1.a. Porphyrin design

In order to optimise the photopolymerization and photoactive properties of porphyrins, a series of new molecules have been designed. The strategy adopted is to maintain the porphyrin core and add two types of functional group on *meso* position (positions 5, 10, 15 and 20 of **Figure IIIA-2**). For all molecules, phenyl functions are added in positions 5 and 15 to obtain a porphyrin with good absorption. For each molecule the difference is on the functional group that is added on position 10 and 20 via a Suzuki-Miyaura coupling.

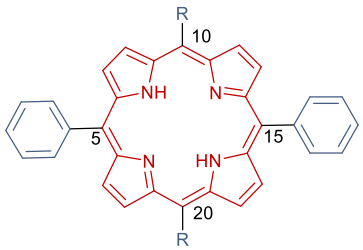

***Figure IIIA-2**: Structure of new porphyrin. The porphyrin core is represented in red and the meso positions are put with numbers. Functional groups that differ from each molecule are represented by R.*

Different molecules were synthetized depending on the availability of the boronic acid with the functional groups (**Figure IIIA-3**). Firstly, it was envisaged to synthesise porphyrins with a reactive group enabling them to be linked to the polymer network (**Figure IIIA-3 part A**). Indeed, the vinyl (A1), acrylamide (B2) and thiol (B3) functions are able to react in the same way as a monomer during free-polymerisation, and thus enable the porphyrin to be linked to the polymer network by covalent bonds. This strategy reduces the release of porphyrins from the network, to preserve the photoactive functions over time.

In addition, different groups have been considered for more efficient initiation of photopolymerization (**Figure IIIA-3 part B**). They can also improve the photophysical or photochemical proprieties. For example, bromo function (B1 and B2) may be able to improve the intersystem crossing, in order to maximise the formation of more statistically reactive triplet state[29]. In addition, some aromatic function, like carbazol[30] (B4), triphenylamine[31] (B7) or anthracene[32] (B9), are already used as photoinitiator for polymerization, as their can form or stabilise the radicals more effectively, and therefore enable faster or longer-lasting initiation.

Finally, the last functions considered are groups that could improve the absorption properties of porphyrin (**Figure IIIA-3 part C**), either by allowing absorption at greater wavelengths, or by improving absorption capacity.

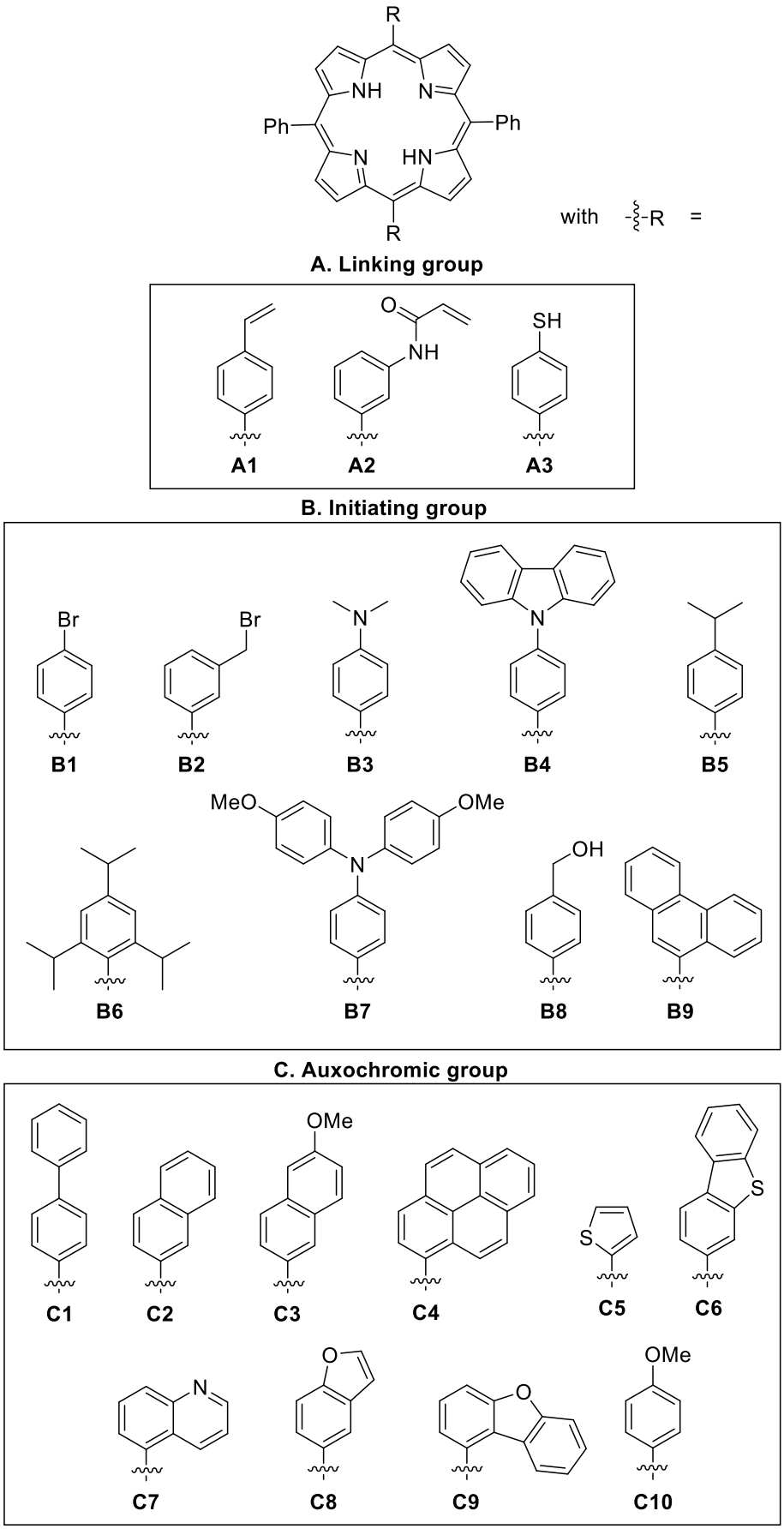

***Figure IIIA-3**: Overview of the different groups on porphyrins*

III.1.b. Ground state computation

Frontier orbitals. The energies of the HOMO and LUMO orbitals have been determined and reported in **Table IIIA-1**. It can be seen that the porphyrins with the lowest HOMO LUMO gap include molecules containing tertiary amine groups B3, B4 and B7.

***Table IIIA-1**: Molecular orbital energy levels (eV) calculated at B3LYP/6-31G(d) in DCM (PCM). For each compound (system), the group R is specified with the numerotation of **Figure IIIA-3**.*

Porphyrin	Group	HOMO-1	HOMO	LUMO	LUMO+1	$\Delta_{HOMO-LUMO}$
P4	A1	-5.49	-5.12	-2.48	-2.46	2.64
Pm12	A2	-5.50	-5.28	-2.40	-2.33	2.88
Pm14	A3	-5.33	-5.10	-2.53	-2.40	2.56
P3	B1	-5.55	-5.10	-2.48	-2.44	2.63
Pm13	B2	-5.51	-5.24	-2.33	-2.32	2.91
P5	B3	-5.04	-4.47	-2.40	-2.20	2.08
P6	B4	-5.22	-4.89	-2.50	-2.28	2.39
P7	B5	-5.42	-4.93	-2.43	-2.35	2.50
Pm17	B6	-5.43	-5.02	-2.32	-2.24	2.71
P8	B7	-4.80	-4.54	-2.40	-2.19	2.14
Pm16	B8	-5.39	-5.09	-2.68	-2.15	2.41
Pm4	B9	-5.46	-5.09	-2.41	-2.23	2.68
Pm1	C1	-5.28	-4.83	-2.22	-2.19	2.60
Pm2	C2	-5.49	-5.07	-2.43	-2.26	2.64
P9	C3	-5.41	-4.96	-2.33	-2.28	2.62
Pm5	C4	-5.47	-5.19	-2.49	-2.47	2.70
Pm10	C5	-5.48	-4.83	-2.58	-2.44	2.25
Pm11	C6	-5.19	-5.05	-2.47	-2.36	2.58
Pm7	C7	-5.53	-5.14	-2.46	-2.31	2.69
Pm8	C8	-5.32	-5.03	-2.44	-2.38	2.59
Pm9	C9	-5.46	-5.12	-2.40	-2.26	2.73
Pm6	C10	-5.36	-5.05	-2.60	-2.17	2.45

III.1.c. Vertical transition energies

The vertical transition energies of the studied molecules are calculation at the TDDFT level and reported in **Table IIIA-2**. The transitions have been attributed depending different conditions. Indeed, Q bands have been attributed to $S_0 \rightarrow S_1$ and $S_0 \rightarrow S_2$ in every molecules. They have been represented in yellow in **Table IIIA-2**. Soret band have been attributed to the more intense bands, usually associated to transitions $S_0 \rightarrow S_3$ and $S_0 \rightarrow S_4$, but they can be shifted to transitions $S_0 \rightarrow S_7$ and $S_0 \rightarrow S_8$ in the case of **P5**, **P8**, **P9**, Pm4 and Pm5, and even to transitions $S_0 \rightarrow S_7$ and $S_0 \rightarrow S_{10}$ for **P6**. These transition have been represented in blue in **Table IIIA-2**. Finally, some porphyrins present intermediate transition, represented in green.

Analysis of NTOs [17] can be used to highlight the displacement of electrons during a vertical transition, by proposing a hole-particle pair, allowing better visualisation of transitions that are mainly mixed in the case of porphyrins. It is then possible to compare hole-particle pairs to understand the mechanisms involved. Porphyrins generally comprise four transitions in visible range, as in the case of **P3**, whose NTOs are shown in **Figure IIIA-4**.

According to the NTO analysis of the additional transition on the porphyrins containing the groups B3, B4, B7, B9, C3 and C4, these transitions correspond to electron transfer from the particularly electron-rich moieties at the periphery to the porphyrin core (**Figures S1-4**).

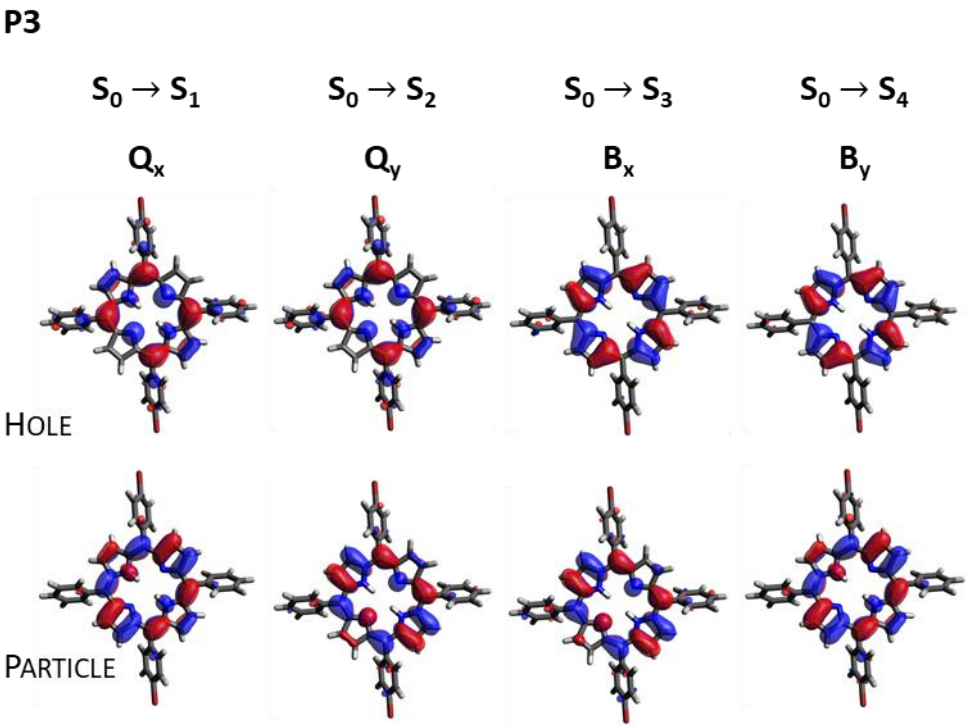

***Figure IIIA-4**: Electronic transition of NTO for TPP, and assigned absorption band.*

***Table IIIA-2** : Wavelength (λ in nm) and oscillator strength (f) associated to transition from ground state, to the excited state S_n. The transitions have been attributed according the following colour: the Q bands are represented in yellow, the Soret band in blue, and the additional bands in green.*

Porphyrin	Group	S_1	S_2	S_3	S_4	S_5	S_6	S_7	S_8/S_{10}[a]
P4	A1	584.96	549.73	413.58	405.39	382.13	377.34		
		0.0744	0.1146	1.7850	1.5069	0.0004	0.0000		
Pm12	A2	575.28	538.90	406.33	398.69	373.29	368.59		
		0.0352	0.0481	1.2863	1.6431	0.0005	0.0633		
Pm14	A3	576.35	540.23	409.78	401.98	391.94	385.54		
		0.0446	0.0636	1.3993	1.2923	0.0000	0.0002		
P3	B1	580,1	543,81	406,82	399,38	374,18	356,82		
		0,0521	0,0745	1,4551	1,7953	0	0,4844		
Pm13	B2	579.65	542.93	406.23	399.30	373.61	355.59		
		0.0504	0.0627	1.4149	1.7249	0.0000	0.4810		
P5	B3	618.92	587.12	507.84	498.82	484.10	474.41	400.88	392.17
		0.1342	0.3067	0.0000	0.0000	0.2175	0.2183	1.1730	1.4939
P6	B4	575.27	539.50	464.07	463.54	456.23	454.92	403.10	394.46
		0.0478	0.0698	0.0000	0.1307	0.0001	0.0197	1.3881	1.7851
P7	B5	574.77	538.31	403.68	395.97	371.68	354.60		
		0.0392	0.0533	1.4012	1.7182	0.0000	0.3623		
Pm17	B6	579.24	541.78	408.66	399.60	372.96	366.36		
		0.0339	0.0392	1.1997	1.7074	0.0000	0.0031		
P8	B7	625.49	609.23	590.40	584.07	545.29	520.26	403.99	395.42
		0.1780	0.1653	0.0000	0.0001	0.0046	0.0089	1.6709	1.7907
Pm16	B8	577.42	540.95	404.74	397.23	372.28	354.37		
		0.0448	0.0623	1.4015	1.7428	0.0000	0.4504		
Pm4	B9	574.89	538.28	432.19	424.95	419.98	411.91	394.03	388.78
		0.0265	0.0322	0.3538	0.0004	0.7690	0.0018	0.8325	1.3440
Pm1	C1	581.22	544.39	397.17	385.05	376.36	362.90		
		0.0368	0.0716	1.2571	1.4051	0.0000	0.2350		
Pm2	C2	581.89	548.89	416.39	412.53	407.31	400.23		
		0.0582	0.1042	1.2234	1.0778	0.0042	0		
P9	C3	591.31	553.21	449.11	448.04	439.56	438.96	400.16	394.06
		0.0886	0.1323	0.0039	0.5191	0.0006	0.3895	1.0665	1.4391
Pm5	C4	573.98	537.47	484.95	484.58	474.35	474.25	410.64	401.69
		0.0393	0.0417	0.0196	0.0013	0.0110	0.0033	1.6110	1.5984
Pm10	C5	588.71	551.55	413.72	406.55	381.78	378.15		
		0.0648	0.0777	1.3195	1.6089	0.0002	0.0002		
Pm11	C6	575.22	539.86	411.79	407.08	398.45	391.24		
		0.0456	0.0723	1.5386	1.1554	0.0019	0.4923		
Pm7	C7	571.88	535.60	405.20	396.85	384.22	383.97		
		0.0262	0.0337	1.2712	1.6730	0.0000	0.0077		
Pm8	C8	574.15	537.06	406.03	399.30	379.30	374.02		
		0.0353	0.0397	1.2611	1.5773	0.0001	0.0003		
Pm9	C9	577.19	540.06	411.21	401.57	386.28	380.63		
		0.0361	0.0552	1.2063	1.6029	0.0008	0.1777		
Pm6	C10	587.31	551.50	413.87	406.15	392.36	389.99		
		0.0713	0.1118	1.5161	1.2837	0.0002	0.0002		

[a] For all compounds the intense transition is reported in this column. For **P5**, **P8**, **P9**, Pm4 and Pm5, transition $S_0 \rightarrow S_8$ is reported, for **P6** the $S_0 \rightarrow S_{10}$ is reported as the transition to S_8 at 397.12 nm shows a *f* value of 0.0044, to S_9 at 397.11 nm with *f* 0.0020 and to S_{10} at 394.46 with *f* 1.7851

III.1.d. Selection of porphyrins for synthesis

In order to select the most promising porphyrins for photopolymerization, several factors were taken into account.

Firstly, particular attention was paid to porphyrins with additional absorption bands in addition to the Q and Soret bands. When looking at the calculated transitions (**Table IIIA-2**) and the absorption spectra (**Figures S5** and **S6**), Porphyrins **P5**, **P6**, **P9** and Pm4 have absorption bands between 440 and 480 nm with relatively high intensity. This would make it possible to obtain photoinitiator systems that perform better at visible wavelengths. However, unlike **P5**, **P6** and **P9**, the Soret band of Pm4 is in the near UV, indicating its poor performance for visible initiation. In addition, although Pm5 and **P8** have additional bands, their intensities are too low (small oscillator strengths for $S_0 \rightarrow S_1$ and $S_0 \rightarrow S_2$) to provide significant absorption in the visible range. Pm5 will therefore be excluded from the synthesis. **P8**, on the other hand, has a Q band at a particularly high wavelength, allowing it to be selected.

Independent of the capacity of the porphyrin to absorb light, another important point is the nature of the functional group present on the porphyrin. Groups that promote network bonding, such as the acrylamide and thiol groups of porphyrins Pm12 and Pm14, are of interest in preventing porphyrins from leaching out of the polymer, as with the vinyl function of **P4**. In addition, the porphyrin **P7** has an isopropyl group, which would make it a good photoinitiator system because of its ease to form radicals. These three molecules will therefore be synthesised, despite a negligible absorption in the visible range, leading to a lower interest for the photopolymerization.

Finally, the other porphyrins (Pm1, Pm2, Pm6, Pm7, Pm8, Pm9, Pm10, Pm11, Pm13, Pm16 and Pm17) were excluded from the screening because they did not show any particularly promising characteristics, either in terms of absorption or the nature of the added groups.

As a result, only porphyrins **P5**, **P6**, **P9**, **P8**, Pm12, Pm14 and **P7** are selected for further study.

III. 2. Synthesis of porphyrin

The synthesis of *meso-substituted* A_2B_2-*trans*-porphyrins was envisioned to be achieved via a modular strategy (**Figure IIIA-5**). First, the porphyrin core would be assembled either by condensation of dipyrromethane with an aldehyde, leading to a 5,15-disubstituted porphyrin **1** [33–35]. After bromination of the unsubstituted *meso* positions, the two other groups would be introduced by a double Suzuki−Miyaura cross-coupling with an arylboronic acid [36,37], affording the expected *meso*-tetrasubstitued porphyrin **3**. This approach offers multiple advantages such as the variety of groups that could be introduced on both 5,15 and 10,20 positions thanks to the large number of aldehydes and arylboronic acids commercially available. Moreover, once intermediate **1** brominated, the resulting intermediate **2** could be used with different boronic acids, which make easier the elaboration of various structures.

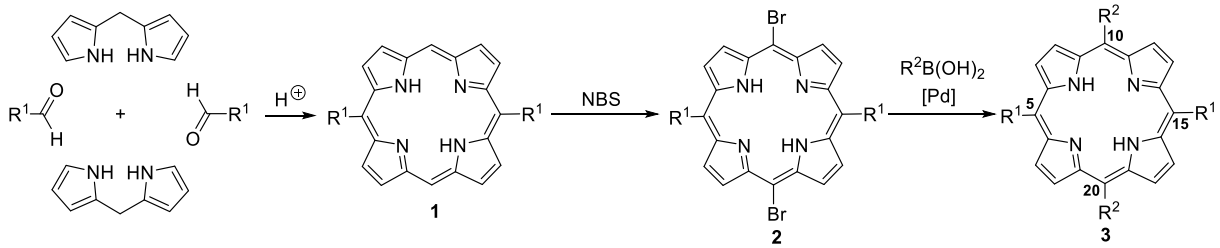

***Figure IIIA-5**: General approach to meso-tetrasubstitued porphyrin.*

We first turned our attention to the preparation of 5,15-diphenylporhyrin **1**, as a model target for the first step (**Figure IIIA-6**). Our initial plan to assemble the porphyrin ring was the condensation of benzaldehyde **c** with dipyrromethane **a** (path **a** of **Figure IIIA-6**). This latter could be obtained by treating paraformaldehyde with a large excess of pyrrole under acidic conditions. Whereas the use of a catalytic amount of trifluoroacetic acid (TFA) suffered from reproducibility issues with yields ranging from 9% to 34% in our hands, a more reliable method was to perform the reaction in an acetic acid / methanol mixture which delivered a 45% isolated yield of **a**. Whatever the method used, the excess of pyrrole required to avoid the appearance of higher oligomers could be recovered by distillation. Cyclization was next achieved by treatment of dipyrromethane **a** with benzaldehyde **c** in the presence of a Brønsted acid, followed by an oxidation *in situ*. Interestingly, the use of either a catalytic amount of TFA and DDQ as an oxidant or montmorillonite as a heterogenous acid source followed by a treatment with p-chloranil delivered an equally good 40% isolated yield of porphyrin **1**. Nevertheless, the product obtained by this second method revealed easier to purify. We also envisioned the complementary strategy based on the use of the *meso*-substituted dipyrromethane **b** (path **b** of **Figure IIIA-6**). This substrate has been prepared in a similar manner to the unsubstituted derivative **a** by treating benzaldehyde **c** with an excess of pyrrole in the presence of TFA, which proved to be very efficient as a very good 93% isolated yield was obtained. In this second route, the porphyrin has been assembled by condensation with trimethyl orthoformate in the presence of TFA followed by an oxidation by exposure to air after neutralization with pyridine. This alternative strategy led to 13% of the expected 5,15-diphenylporhyrin **1**, corresponding to a 12% overall yield from pyrrole slightly better than the 8% obtained in path a.

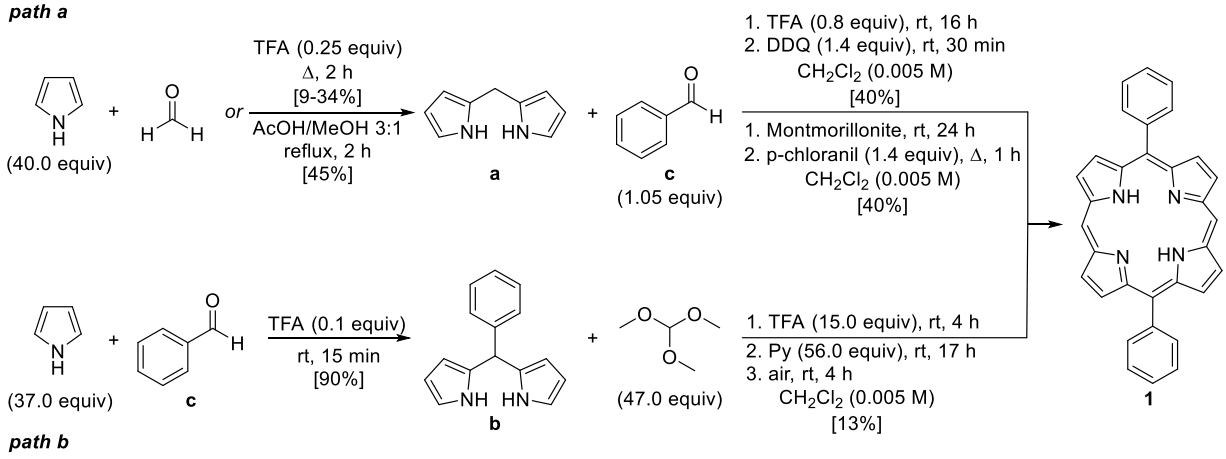

***Figure IIIA-6**: Synthesis of 5,15-diphenylporhyrin **1**.*

Bromination of 5,15-diphenylporhyrin **1** was next investigated (**Figure IIIA-7**). Its reaction with an excess (2.2 equiv) of *N*-bromosuccinimide (NBS) in the presence of pyridine (Py) in chloroform delivered an excellent 94% of the *meso*-dibrominated product **2** [38,39].

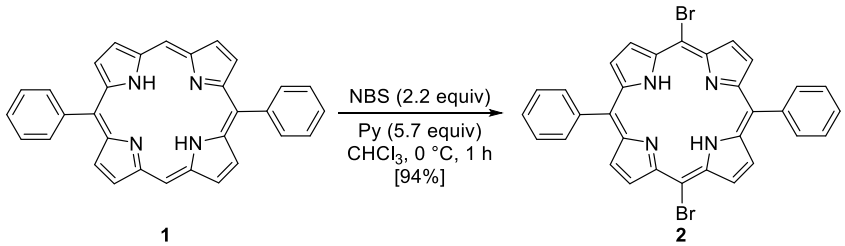

***Figure IIIA-7**: Bromination of 5,15-diphenylporhyrin **2**.*

Once compound **2** in hands, we began the investigation of the second functionalization step, the double Suzuki-Miyaura cross-coupling reaction, by an optimization of the reaction conditions. We thus performed a study of the influence of various parameters (catalyst, base, solvent) on the reaction yield between **2** and a slight excess of 4-vinylphenylboronic acid **d** (**Table IIIA-3**). When $PdCl_2(PPh_3)_2$ was used as a pre-catalyst, encouraging yields in the double cross-coupled product have been obtained and the nature of the base seems to have only a limited influence on the reaction outcome (K_3PO_4: 35%; K_2CO_3: 30% - entries 1-2). Regarding the nature of the ligand for palladium (entries 3-5), P(*o*-Tol)$_3$ (55%) and dppf (57%) appeared to be more efficient than PPh_3 and Xantphos (6%, entry 4). In the case of $PdCl_2$(dppf), the addition of K_2CO_3 or K_3PO_4 as a base has again a limited influence (57% and 51%, respectively), even if the former delivered a slightly higher yield (entries 5-6).

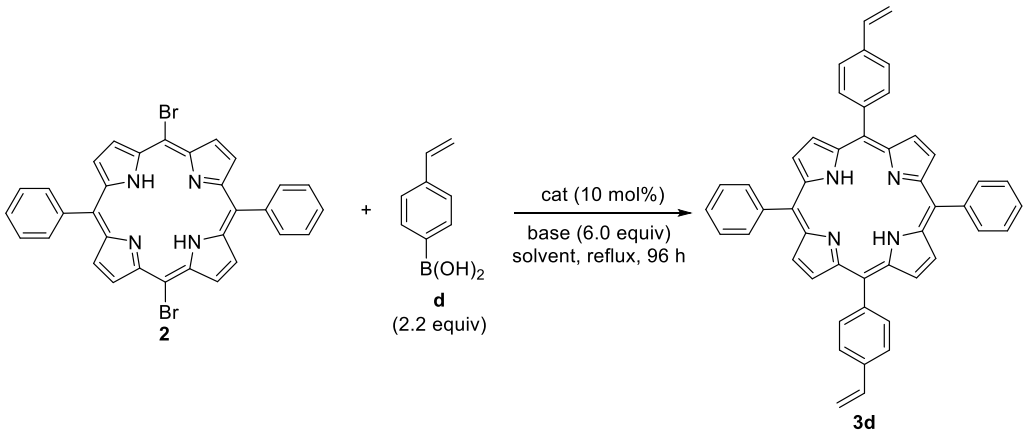

entry	cat	base	solvent	isolated yield (%)
1	$PdCl_2(PPh_3)_2$	K_3PO_4	THF	35
2	$PdCl_2(PPh_3)_2$	K_2CO_3	THF/H_2O 10:1	30
3	$Pd(OAc)_2$ + P(*o*-Tol)$_3$	K_2CO_3	THF/H_2O 10:1	55
4	$Pd(OAc)_2$ + Xantphos	K_2CO_3	THF/H_2O 10:1	6
5	**$PdCl_2$(dppf)**	**K_2CO_3**	**THF/H_2O 10:1**	**57**
6	$PdCl_2$(dppf)	K_3PO_4	THF/H_2O 10:1	51

***Table IIIA-3**: Optimization of the double Suzuki-Miyaura cross-coupling reaction.*

The scope of the reaction was next investigated using *meso*-dibrominated porphyrin **2** and different arylboronic acids **e** (**Table IIIA-4**). In comparison with 4-vinylphenylboronic acid (57%, entry 1), arylboronic acids bearing an electron-donating group delivered higher yields. Indeed, when 4-*iso*-propylphenylboronic acid was used as the reaction partner, a higher 72% yield of the expected porphyrin was obtained (entry 2). The reaction was even more productive using 6-methoxy-2-naphthaleneboronic acid which led to 81% yield of the desired product (entry 3). We also investigated the use of arylboronic acids bearing nitrogenated groups (entries 4 to 6). Only tertiary amine derivatives were found to be suitable in the reaction conditions allowing the preparation of porphyrins bearing carbazole (58%, entry 4) and dimethylamino (41%, entry 5) groups. The presence of electron-donating groups on 4-[Bis(4-methoxyphenyl)amino]phenyl leads to a higher conversion (74%, entry 6). The introduction of 4-bromophenyl groups thanks to this method was also possible and the expected tetrasubstituted porphyrin was isolated in 63% yield using $PdCl_2(PPh_3)_2$ as a catalyst (entry 7).

The synthesis of porphyrins containing acrylamide and thiol functions (entries 8 and 9) was unsuccessful. Indeed, even if the product of the coupling of **2** with a boronic acid bearing an acrylamide group was detected by NMR analysis of the crude reaction mixture, its purification on silica gel reveals to be impossible. On the other hand, the porphyrin bearing thiol functions could not be obtained in an useful amount, because of the formation of disulphides upon heating of the coupling reaction, thus

leading to insoluble porphyrin polymers. As the synthesis of these new photoinitiators had to be efficient, these two porphyrins were discarded.

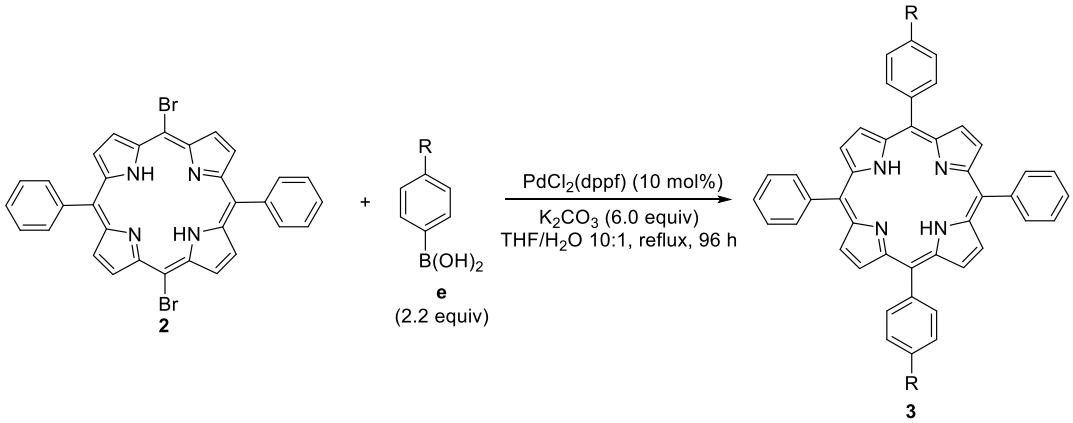

entry	arylboronic acid (e)		isolated yield (%)	Porphyrin
1	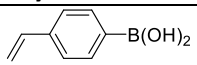	**d**	57	**P4**
2	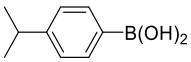	**f**	72	**P7**
3	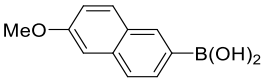	**g**	81	**P9**
4	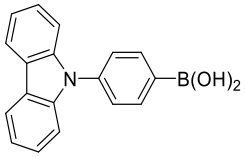	**h**	58	**P6**
5[a]	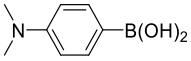	**i**	41	**P5**
6	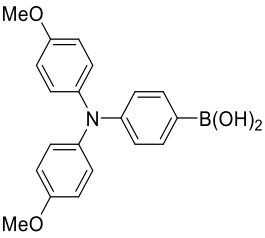	**j**	74	**P8**
7[a,b]	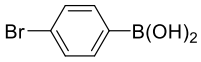	**k**	63	**P3**
8	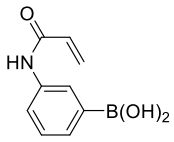	**l**	0	-
9	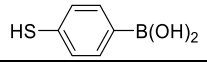	**m**	0	-

***Table IIIA-4**: Scope of arylboronic acids. [a]$PdCl_2(PPh_3)_2$ (10 mol%) and K_2CO_3 (4.5 equiv) were used. [b]Reaction performed in DMF/H_2O 25:1.*

III. 3. Comparison of simulated and experimental absorption spectra

The vertical transitions were used to trace a theoretical spectrum by calculating Gaussian functions with a full width at half maximum (σ) of 0.2 cm^{-1}. The effect of the DCM solvent was taken into account using the polarizable continuum (PCM). The experimental spectra were carried out in DCM. For each synthetized porphyrin, **Figure IIIA-8** shows the calculated vertical transitions, the normalised simulated spectrum calculated from the transitions and the normalised experimental spectrum. **Table IIIA-5**

reports the values of the wavelengths and molar extinction coefficient of the maxima from experimentally spectra corresponding to Soret band and Q bands. For the theoretical data, the wavelength of the maxima of the simulated absorption spectra corresponding to the Soret band is reported and compared to the experimental data. For the Q bands, as the shape of the spectra shows four bands for the experimental spectra and only two transitions have been calculated for the theoretical spectra, the absorption wavelength of the electronic vertical transitions have been reported.

In general, the simulated theoretical maximum of the Soret band is blue-shifted compared to the experimental one (between 11 and 27 nm). As no vibronical coupling was taken into account, the four picks of the Q band are not well reproduced but the two transitions are in the vicinity of the experimental band and the relative intensity compared to the Soret band is well reproduced.

In the spectrum of **P5**, the experimental Soret band is quite broad (45 nm of width at half height). This can be explained by the additional theoretical electronic transitions found between the Q transitions and the Soret transitions. The transition to S_5 and S_6 are as intense as the one to S_1 and S_2 (**Table IIIA-2**). On the other hand, **P6**, **P8** and **P9** show also some supplementary transitions between Q and Soret band. However, the experimental spectra of **P6** and **P9** have a thin Soret band. **P8** shows a broad experimental Soret band but the supplementary calculated transitions between 500 and 600 nm have a weak oscillation strength. The theory can then not explain the experimental shape.

Table IIIA-5 *: Wavelengths of principal bands of computed and theoretical of porphyrins absorption spectra.* $\lambda_{maximum\ computed\ Soret}$ *correspond to the wavelength of the maximum of computed absorption spectra, whereas* $\lambda_{Q\ electronic\ transition\ computed}$ *correspond to the computed vertical transition wavelengths. Electronic transitions and computed absorption spectra were performed at the B3LYP/6-31+G(d) with PCM for DCM solvent. The experimental spectra have been performed in DCM.*

Porphyrin	Group	$\lambda_{maximum\ computed\ Soret}$ **in nm**	$\lambda_{Soret\ experimental}$ **in nm**	$\Delta\lambda_{exp-theo}$ **in nm**	$\lambda_{Q\ electronic\ transition\ computed}$ **in nm** (normalized oscillator strength)	$\lambda_{Q\ experimental}$ **in nm** (molar extinction coefficient)
P3	B1	403	418	15	544 (0.0745) 580 (0.0521)	516 (4 660) 554 (2 660) 588 (1 993) 649 (1 241)
P4	A1	408	419	11	550 (0.1146) 585 (0.0744)	515 (18 665) 551 (9 832) 589 (5 682) 646 (4 723)
P5	B3	395	422	27	587 (0.3067) 619 (0.1342)	520 (6 181) 564 (5 989) 596 (3 071) 656 (2 842)
P6	B4	398	420	22	540 (0.0698) 575 (0.0478)	516 (30 397) 551 (18375) 590 (9 706) 646 (7 526)
P7	B5	399	418	19	538 (0.0533) 575 (0.0392)	514 (18 287) 551 (9 322) 591 (5 703) 647 (5 226)
P8	B7	399	414	15	609 (0.1653) 625 (0.1780)	520 (12 731) 567 (13 478) 590 (8 233) 655 (5 934)
P9	C3	397	422	25	554 (0.1323) 591 (0.0886)	518 (11 389) 553 (6 381) 593 (3 497) 648 (3 156)

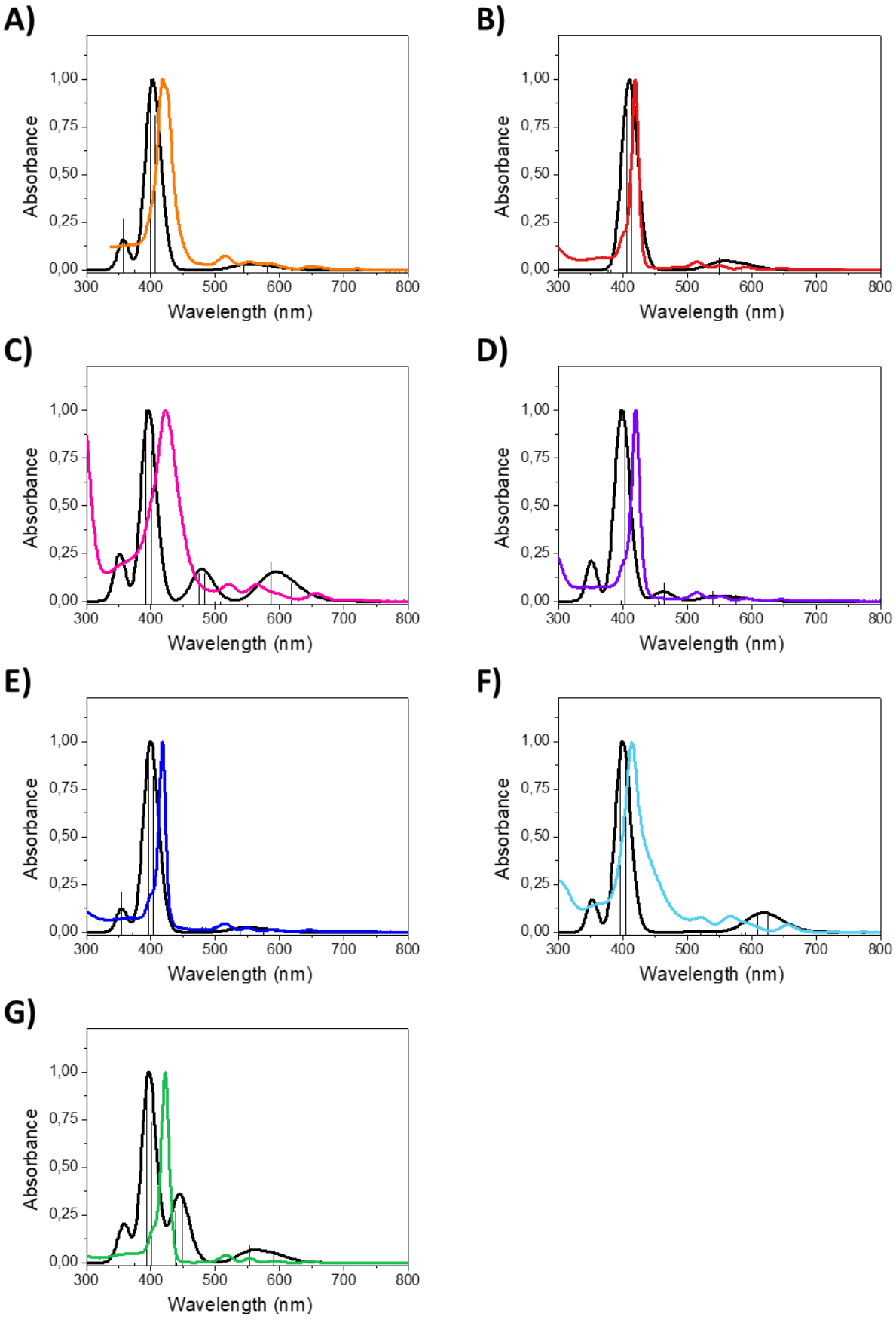

Figure IIIA-8: Vertical transition energies (corresponding to the one reported

Table IIIA-2*) and experimental (in color) and theoretical (in black) absorption spectra of* ***A) P3****,* ***B) P4****,* ***C) P5****,* ***D) P6****,* ***E) P7****,* ***F) P8*** *and* ***G) P9****.*

III. 4. Free-radical photopolymerization

The photoinitiator properties of these porphyrins have been investigated for free-radical photopolymerization, using MDEA as electron donor co-initiator, and acrylated soybean oil (SOA) as bio-based monomer. Photopolymerization are followed by Real Time Fourier Transformation Infrared spectroscopy (RT-FTIR). Kinetics profiles of polymerization are represented in **Figure IIIA-9**. The final conversion of acrylated function of SOA after 800 s of various wavelength irradiation are reported in **Table 6**. The maximum final monomer conversion of each system is obtained under an irradiation of 405 nm, which corresponds to the lamp at the closest wavelength to the Soret band, the maximum absorption of all porphyrins. As expected, conversions are higher under laminate than under oxygen for all wavelength of irradiation. This is due to the fact that oxygen is likely to quench the radicals present in the system to form peroxides. For **P3**, it can be noted that the conversion at 405 nm is slightly higher under air, but only corresponds to a slight variation.

Under LED@405 nm irradiation, porphyrins **P3**, **P4** and **P8** exhibit the highest final monomer conversion, respectively 91%, 91% and 89% under laminate. However, porphyrins **P5** and **P7** have very similar values, with conversions reaching 86%. At other wavelengths, only systems based on **P3**, **P4**, **P5** and **P7** allow the highest conversion. On the other hand, the lowest values are obtained for **P9**, and particularly **P6** which does not allow a better conversion than TPP. It can be noted that porphyrins-based systems present higher final conversion than those obtained with system based on commonly used photoinitiators CQ and BP under higher wavelength.

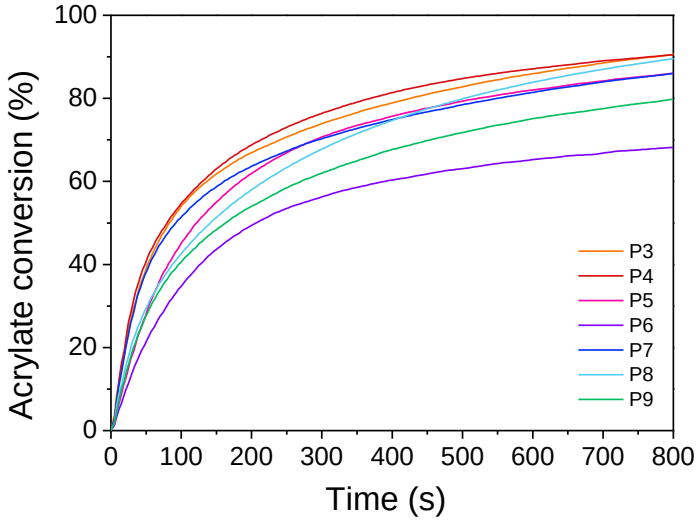

Figure IIIA-9*: Polymerization profiles (acrylate function conversion vs. irradiation time) for SOA in presence of different porphyrins (0.5% wt.) in laminate upon LED@405 nm in presence of MDEA (5% wt.).*

***Table IIIA-6**: Acrylate conversion of SOA (%) with different porphyrins (0.5% wt.) in presence of MDEA (5% wt.), upon different LED (nm)*

Photoinitiating systems	Final conversion (%)							
	385 nm		405 nm		455 nm		530 nm	
P3/MDEA/SOA	73 [a]	55 [b]	**91** [a]	93 [b]	64 [a]	40 [b]	43 [a]	26 [b]
P4/MDEA/SOA	76 [a]	48 [b]	**91** [a]	80 [b]	66 [a]	40 [b]	47 [a]	26 [b]
P5/MDEA/SOA	60 [a]	29 [b]	**86** [a]	78 [b]	69 [a]	50 [b]	36 [a]	np [b]
P6/MDEA/SOA	46 [a]	np [b]	**68** [a]	40 [b]	28 [a]	np [b]	20 [a]	np [b]
P7/MDEA/SOA	70 [a]	52 [b]	**86** [a]	83 [b]	65 [a]	36 [b]	40 [a]	14 [b]
P8/MDEA/SOA	61 [a]	40 [b]	**89** [a]	70 [b]	54 [a]	44 [b]	31 [a]	5 [b]
P9/MDEA/SOA	66 [a]	19 [b]	**80** [a]	52 [b]	54 [a]	34 [b]	np [a]	np [b]
TPP/MDEA/SOA	34 [a]	35 [b]	**81** [a]	85 [b]	29 [a]	np [b]	15 [a]	np [b]
CQ/MDEA/SOA	28 [a]	np [b]	**56** [a]	38 [b]	68 [a]	44 [b]	np [a]	np [b]
BP/MDEA/SOA	96 [a]	95 [b]	**99** [a]	82 [b]	np [a]	np [b]	np [a]	np [b]

[a] under laminate, [b] under air, np: no polymerization

IV. Conclusion

In conclusion, the method for the computing of porphyrins **P3** and **P4** developed previously have been used to simulate the absorbance properties of around twenty porphyrins, which were then selected on the basis of their theoretical spectroscopic properties or the importance of their functional groups. These porphyrins were then synthesised using a common dibrominated synthon, to quickly arrive at the desired molecules with a yield between 57% and 81%. The study of the theoretical spectra enabled to obtain results consistent with the experimental spectra and to explain the differences between the absorption of the porphyrins based on the NTO analysis.

The selected porphyrins have then be used for photopolymerization, and have presented good final monomer conversion under visible irradiation. However, no significant correlation can be found between the theoretical absorption and the photoinitiating capacities of the different porphyrins.

V. Références.

1 Ö. Birel, S. Nadeem and H. Duman, J. Fluoresc., 2017, 27, 1075–1085.
2 W. Ji, T.-X. Wang, X. Ding, S. Lei and B.-H. Han, Coord. Chem. Rev., 2021, 439, 213875.
3 H. Huang, W. Song, J. Rieffel and J. F. Lovell, Front. Phys.
4 A. Maufroy, L. Favereau, F. B. Anne, Y. Pellegrin, E. Blart, M. Hissler, D. Jacquemin and F. Odobel, J. Mater. Chem. A, 2015, 3, 3908–3917.
5 H. Marcille, J.-P. Malval, M. Presset, N. Bogliotti, A. Blacha-Grzechnik, V. Brezová, Y. Yagci and D.-L. Versace, Polym. Chem., 2020, 11, 4237–4249.
6 C. Wu, H. Chen, N. Corrigan, K. Jung, X. Kan, Z. Li, W. Liu, J. Xu and C. Boyer, J. Am. Chem. Soc., 2019, 141, 8207–8220.
7 G. Noirbent, Y. Xu, A.-H. Bonardi, D. Gigmes, J. Lalevée and F. Dumur, Eur. Polym. J., 2020, 139, 110019.
8 A. Bonardi, F. Bonardi, G. Noirbent, F. Dumur, C. Dietlin, D. Gigmes, J.-P. Fouassier and J. Lalevée, Polym. Chem., 2019, 10, 6505–6514.
9 A. Al Mousawi, C. Poriel, F. Dumur, J. Toufaily, T. Hamieh, J. P. Fouassier and J. Lalevée, Macromolecules, 2017, 50, 746–753.
10 E. Runge and E. K. U. Gross, Phys. Rev. Lett., 1984, 52, 997–1000.

11 M. E. Zandler and F. D'Souza, C. R. Chim., 2006, 9, 960–981.
12 Y. F. Liu, J. Guan, D. Hu, L. Du, H. Sun, J. Gao, J. Zhao and Z. Lan, J. Phys. Chem. C, 2015, 119, 8417–8430.
13 T. Fransson, T. Saue and P. Norman, J. Chem. Theory Comput., 2016, 12, 2324–2334.
14 L. Rintoul, S. R. Harper and D. P. Arnold, Phys. Chem. Chem. Phys., 2013, 15, 18951–18964.
15 Y. Zhao and D. G. Truhlar, Theor. Chem. Acc., 2008, 120, 215–241.
16 S. Daoudi, A. Semmeq, M. Badawi, X. Assfeld, Y. Arfaoui and M. Pastore, J. Comput. Chem., 2019, 40, 2530–2538.
17 X. Gu and Q. Sun, Phys. Chem. Chem. Phys., 2013, 15, 15434–15440.
18 F. Bureš, RSC Adv., 2014, 4, 58826–58851.
19 A. K. Mandal, M. Taniguchi, J. R. Diers, D. M. Niedzwiedzki, C. Kirmaier, J. S. Lindsey, D. F. Bocian and D. Holten, J. Phys. Chem. A, 2016, 120, 9719–9731.
20 X. D. Gong, H. M. Xiao and H. Tian, Int. J. Quantum Chem., 2002, 86, 531–540.
21 M. Gouterman, G. H. Wagnière and L. C. Snyder, J. Mol. Spectrosc., 1963, 11, 108–127.
22 B. Minaev, Y.-H. Wang, C.-K. Wang, Y. Luo and H. Ågren, Spectroc. Acta A, 2006, 65, 308–323.
23 M. H. Perrin, M. Gouterman and C. L. Perrin, J. Chem. Phys., 2003, 50, 4137–4150.
24 B. Minaev and M. Lindgren, Sensors, 2009, 9, 1937–1966.
25 S. Perun, J. Tatchen and C. M. Marian, Chemphyschem, 2008, 9, 282–292.
26 O. Loboda, I. Tunell, B. Minaev and H. Ågren, Chem. Phys., 2005, 312, 299–309.
27 B. Minaev and H. Ågren, Chem. Phys., 2005, 315, 215–239.
28 M. J. Frisch, G. W. Trucks, H. B. Schlegel, G. E. Scuseria, M. A. Robb, J. R. Cheeseman, G. Scalmani, V. Barone, G. A. Petersson, H. Nakatsuji, X. Li, M. Caricato, A. V. Marenich, J. Bloino, B. G. Janesko, R. Gomperts, B. Mennucci, H. P. Hratchian, J. V. Ortiz, A. F. Izmaylov, J. L. Sonnenberg, D. Williams-Young, F. Ding, F. Lipparini, F. Egidi, J. Goings, B. Peng, A. Petrone, T. Henderson, D. Ranasinghe, V. G. Zakrzewski, J. Gao, N. Rega, G. Zheng, W. Liang, M. Hada, M. Ehara, K. Toyota, R. Fukuda, J. Hasegawa, M. Ishida, T. Nakajima, Y. Honda, O. Kitao, H. Nakai, T. Vreven, K. Throssell, J. A. Montgomery Jr., J. E. Peralta, F. Ogliaro, M. J. Bearpark, J. J. Heyd, E. N. Brothers, K. N. Kudin, V. N. Staroverov, T. A. Keith, R. Kobayashi, J. Normand, K. Raghavachari, A. P. Rendell, J. C. Burant, S. S. Iyengar, J. Tomasi, M. Cossi, J. M. Millam, M. Klene, C. Adamo, R. Cammi, J. W. Ochterski, R. L. Martin, K. Morokuma, O. Farkas, J. B. Foresman and D. J. Fox, 2016.
29 R. Bonnett, A. Harriman and A. N. Kozyrev, J. Chem. Soc., Faraday Trans., 1992, 88, 763–769.
30 F. Dumur, European Polymer Journal, 2020, 125, 109503.
31 F. Dumur, European Polymer Journal, 2022, 166, 111036.
32 F. Dumur, European Polymer Journal, 2022, 169, 111139.
33 R. W. Boyle, C. Bruckner, J. Posakony, B. R. James and D. Dolphin, in Organic Syntheses, John Wiley & Sons, Ltd, 2003, pp. 287–287.
34 J. S. Manka and D. S. Lawrence, Tetrahedron Lett., 1989, 30, 6989–6992.
35 A. Treibs and N. Häberle, Liebigs Ann., 1968, 718, 183–207.
36 S. Hiroto, Y. Miyake and H. Shinokubo, Chem. Rev., 2017, 117, 2910–3043.
37 B. Vaz, R. Alvarez, M. Nieto, A. I. Paniello and A. R. de Lera, Tetrahedron Lett., 2001, 42, 7409–7412.
38 L. R. Nudy, H. G. Hutchinson, C. Schieber and F. R. Longo, Tetrahedron, 1984, 40, 2359–2363.
39 O. B. Locos and D. P. Arnold, Org. Biomol. Chem., 2006, 004, 902–916.
, 2006, 65, 308–323.
15 M. H. Perrin, M. Gouterman and C. L. Perrin, The Journal of Chemical Physics, 2003, 50, 4137–4150.
16 B. Minaev and M. Lindgren, Sensors, 2009, 9, 1937–1966.
17 O. Loboda, I. Tunell, B. Minaev and H. Ågren, Chemical Physics, 2005, 312, 299–309.
18 B. Minaev and H. Ågren, Chemical Physics, 2005, 315, 215–239.
19 S. Perun, J. Tatchen and C. M. Marian, Chemphyschem, 2008, 9, 282–292.
20 H. Marcille, J.-P. Malval, M. Presset, N. Bogliotti, A. Blacha-Grzechnik, V. Brezová, Y. Yagci and D.-L. Versace, Polym. Chem., 2020, 11, 4237–4249.

21 N. A. Sánchez-Bojorge, S. Flores-Armendáriz, M. E. Fuentes-Montero, V. H. Ramos-Sánchez, G. Zaragoza-Galán and L. M. Rodríguez-Valdez, J. Porphyrins Phthalocyanines, 2017, 21, 88–102.
22 O. Loboda, Quantum-chemical studies on Porphyrins, Fullerenes and Carbon Nanostructures, Springer Berlin Heidelberg, Berlin, Heidelberg, 2013.
23 A. Maufroy, L. Favereau, F. B. Anne, Y. Pellegrin, E. Blart, M. Hissler, D. Jacquemin and F. Odobel, J. Mater. Chem. A, 2015, 3, 3908–3917.
24 J. M. S. Lopes, J. R. T. Reis, A. E. H. Machado, T. H. O. Leite, A. A. Batista, T. V. Acunha, B. A. Iglesias, P. T. Araujo and N. M. Barbosa Neto, Spectrochimica Acta Part A: Molecular and Biomolecular Spectroscopy, 2020, 238, 118389.
25 J. M. S. Lopes, K. Sharma, R. N. Sampaio, A. A. Batista, A. S. Ito, A. E. H. Machado, P. T. Araújo and N. M. Barbosa Neto, Spectrochimica Acta Part A: Molecular and Biomolecular Spectroscopy, 2019, 209, 274–279.
26 R. W. Boyle, C. Bruckner, J. Posakony, B. R. James and D. Dolphin, in Organic Syntheses, John Wiley & Sons, Ltd, 2003, pp. 287–287.
27 J. S. Manka and D. S. Lawrence, Tetrahedron Letters, 1989, 30, 6989–6992.
28 A. Treibs and N. Häberle, Justus Liebigs Annalen der Chemie, 1968, 718, 183–207.
29 S. Hiroto, Y. Miyake and H. Shinokubo, Chem. Rev., 2017, 117, 2910–3043.
30 B. Vaz, R. Alvarez, M. Nieto, A. I. Paniello and A. R. de Lera, Tetrahedron Letters, 2001, 42, 7409–7412.
31 L. R. Nudy, H. G. Hutchinson, C. Schieber and F. R. Longo, Tetrahedron, 1984, 40, 2359–2363.
32 O. B. Locos and D. P. Arnold, Org. Biomol. Chem., 2006, 004, 902–916.

VI. Supporting information

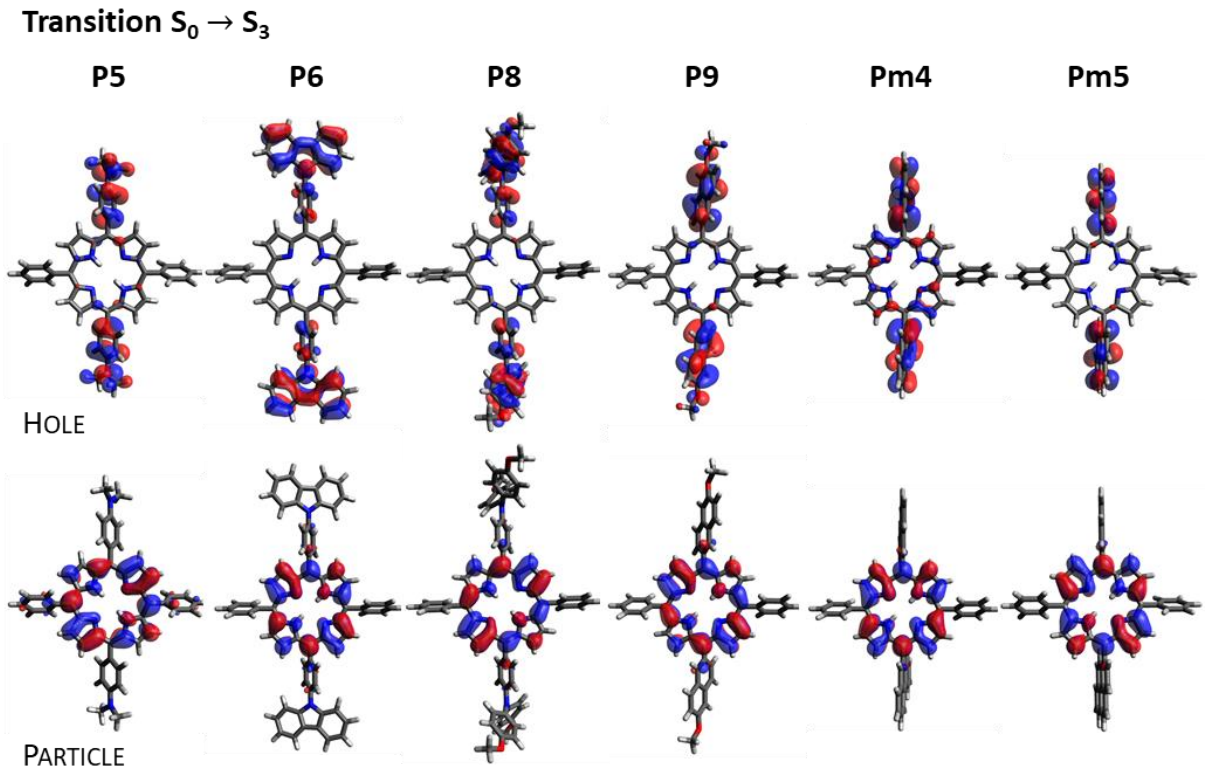

***Figure S1**: Electron densities of "hole" and "particles" NTO pairs for $S_0 \rightarrow S_3$ transition.*

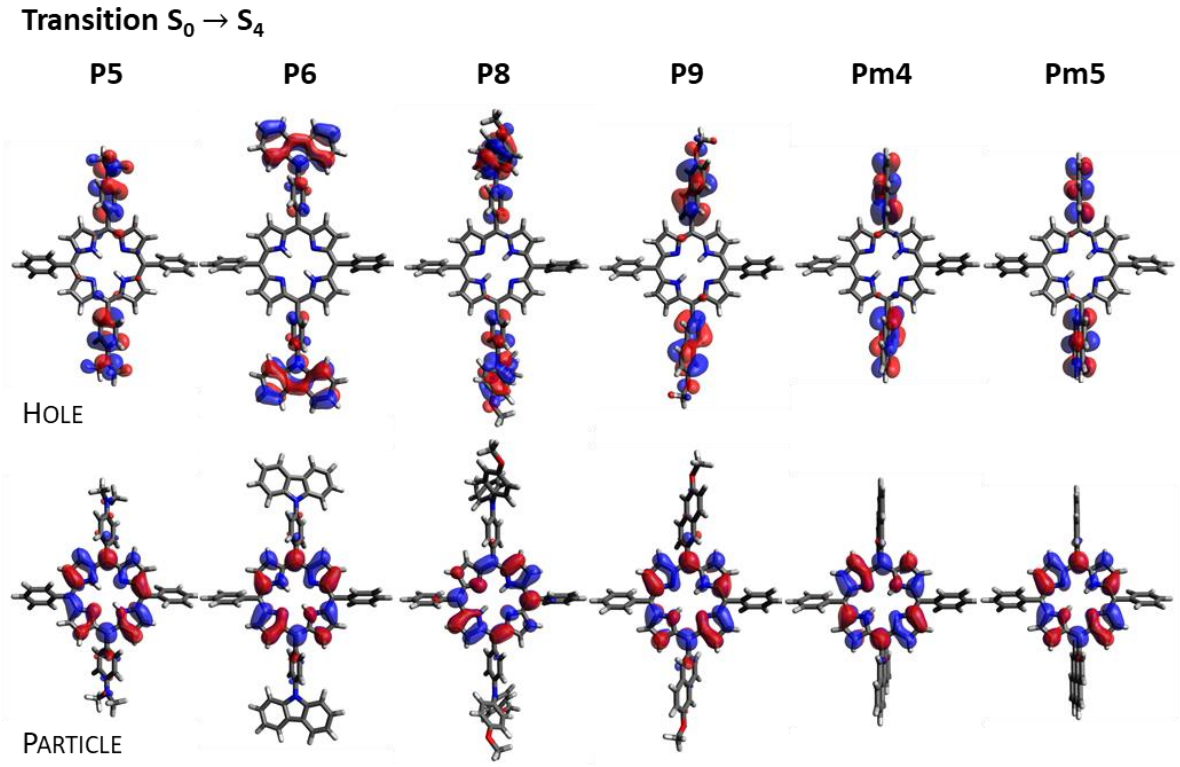

***Figure S2**: Electron densities of "hole" and "particles" NTO pairs for $S_0 \rightarrow S_4$ transition.*

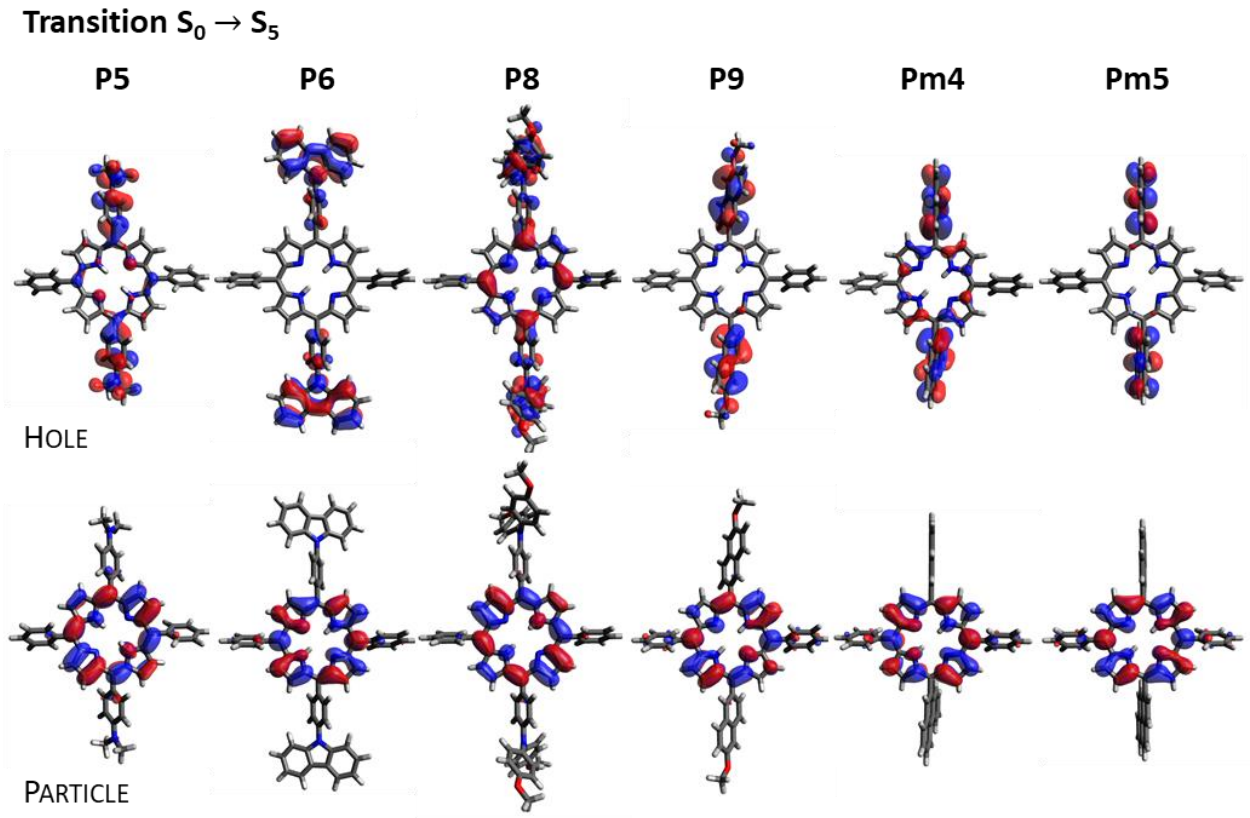

***Figure S3**: Electron densities of "hole" and "particles" NTO pairs for $S_0 \rightarrow S_5$ transition.*

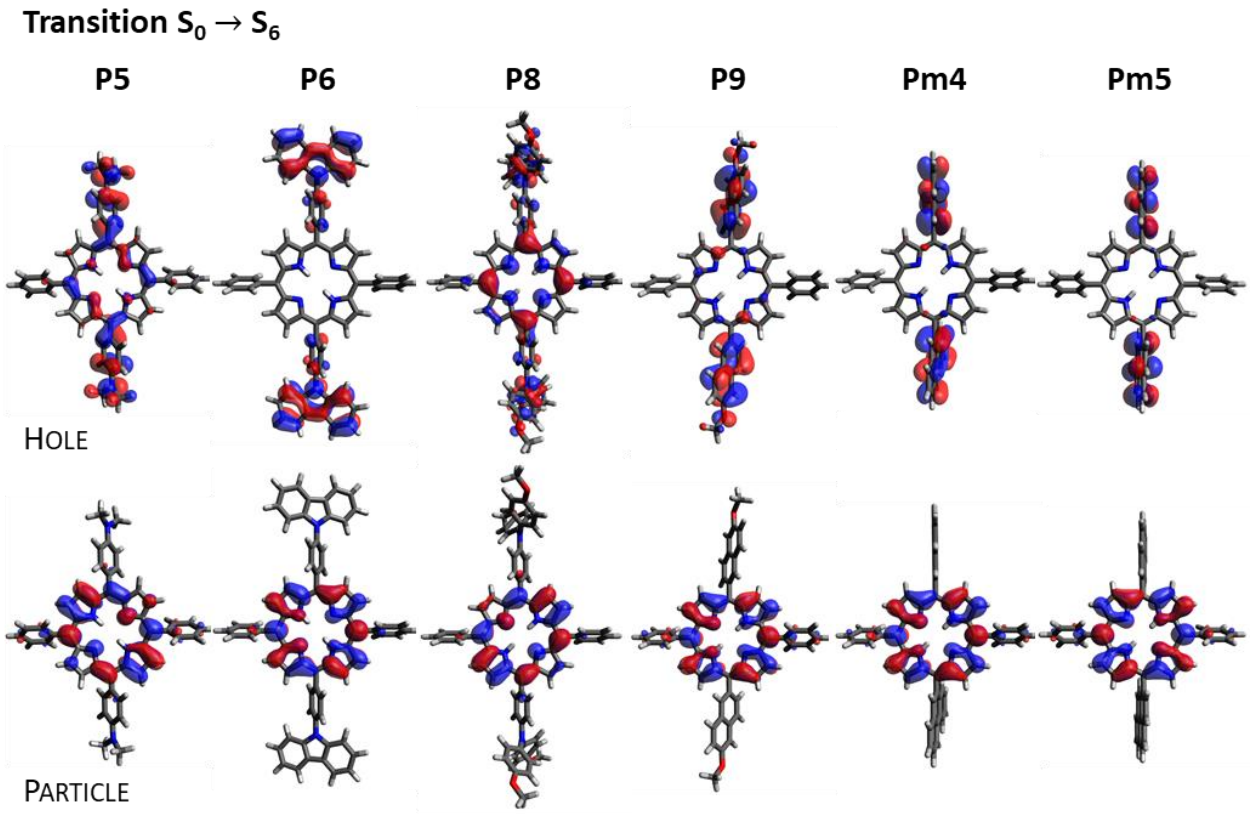

***Figure S4**: Electron densities of "hole" and "particles" NTO pairs for $S_0 \rightarrow S_6$ transition.*

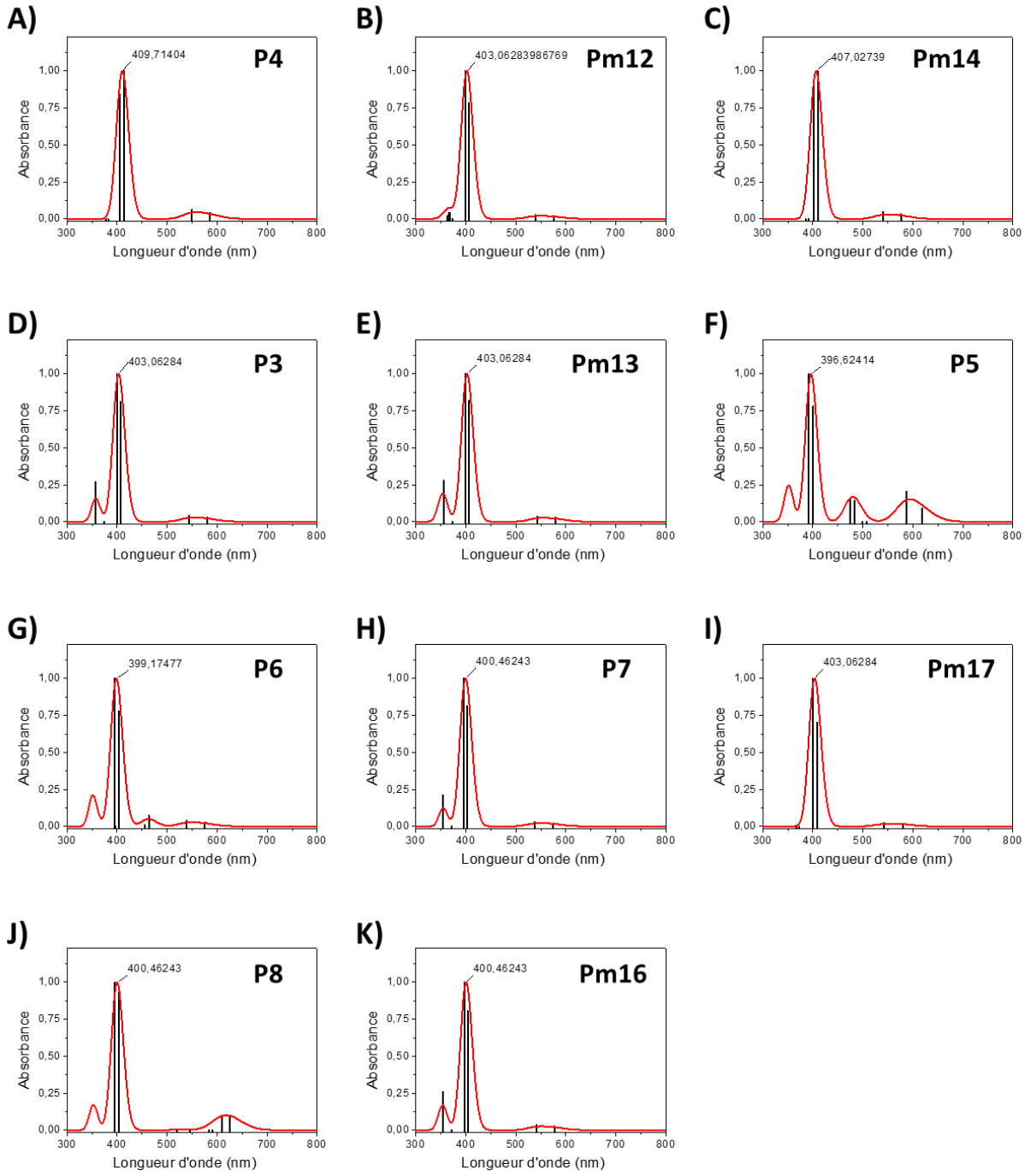

Figure S5*: Theoretical spectrum shifted to match absorption maxima (in color) with corresponding vertical transition energies (in black, corresponding to the one reported* ***Table 2Erreur ! Source du renvoi introuvable.****) for porphyrins* ***A****)* ***P4****,* ***B****) Pm12,* ***C****), Pm14,* ***D****)* ***P3****,* ***E****) Pm13,* ***F****)* ***P5****,* ***G****)* ***P6****,* ***H****)* ***P7****,* ***I****) Pm17,* ***J****)* ***P8*** *and* ***K****) Pm16.*

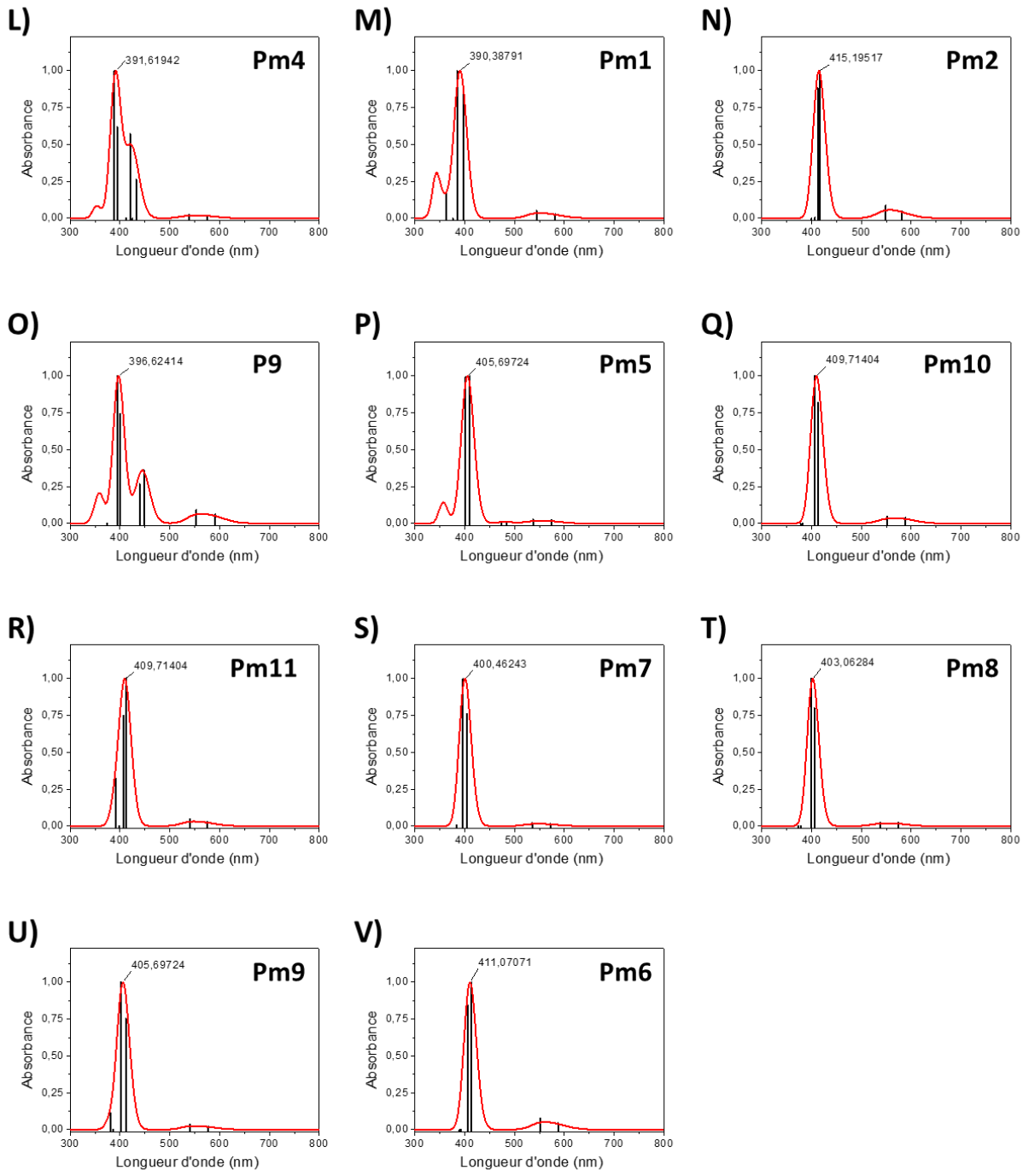

***Figure S6**: Theoretical spectrum shifted to match absorption maxima (in color) with corresponding vertical transition energies (in black, corresponding to the one reported **Table 2Erreur ! Source du renvoi introuvable.**) for porphyrins **L**) Pm4, **M**) Pm1, **N**) Pm2, **O**) **P9**, **P**) Pm5, **Q**) Pm10, **R**) Pm11, **S**) Pm7, **T**) Pm8, **U**) Pm9 and **V**) Pm6.*

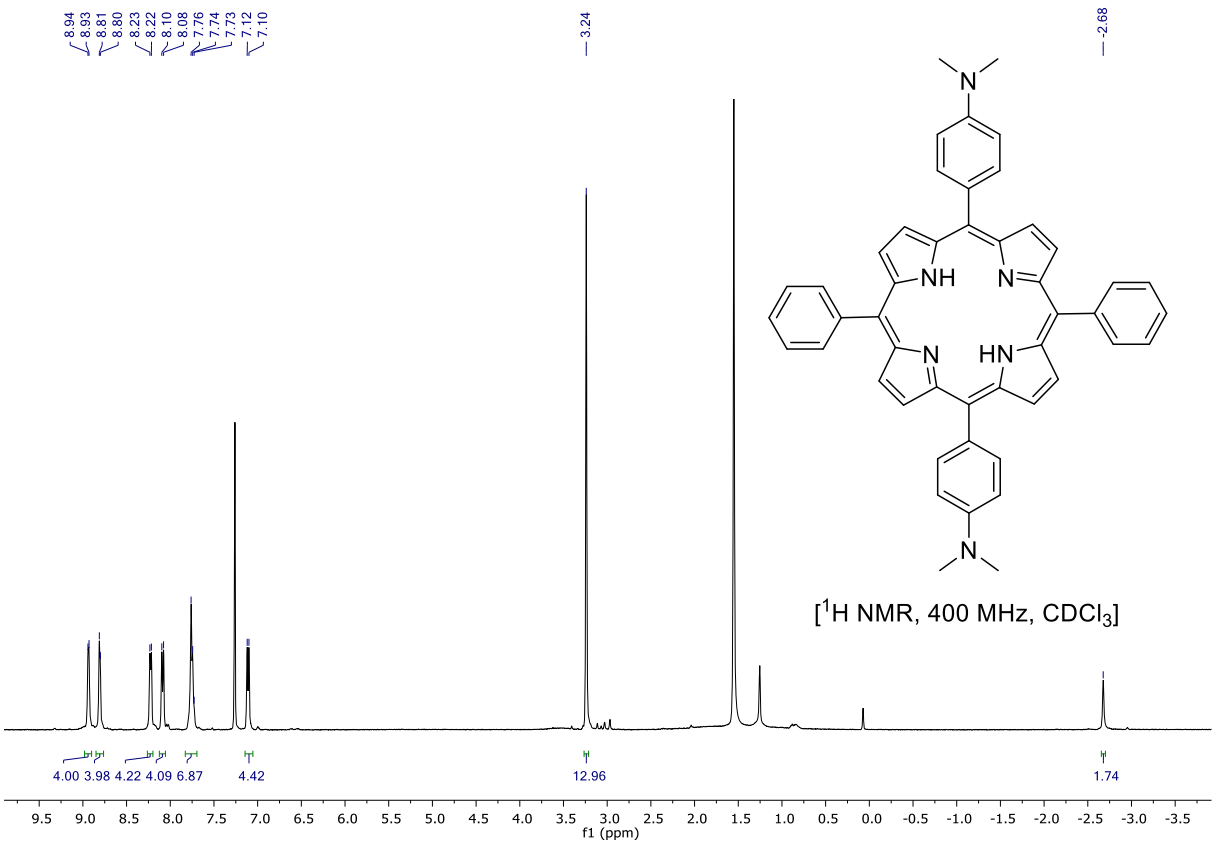

***Figure S7**: ^{1}H NMR spectrum of **P5** in $CDCl_3$.*

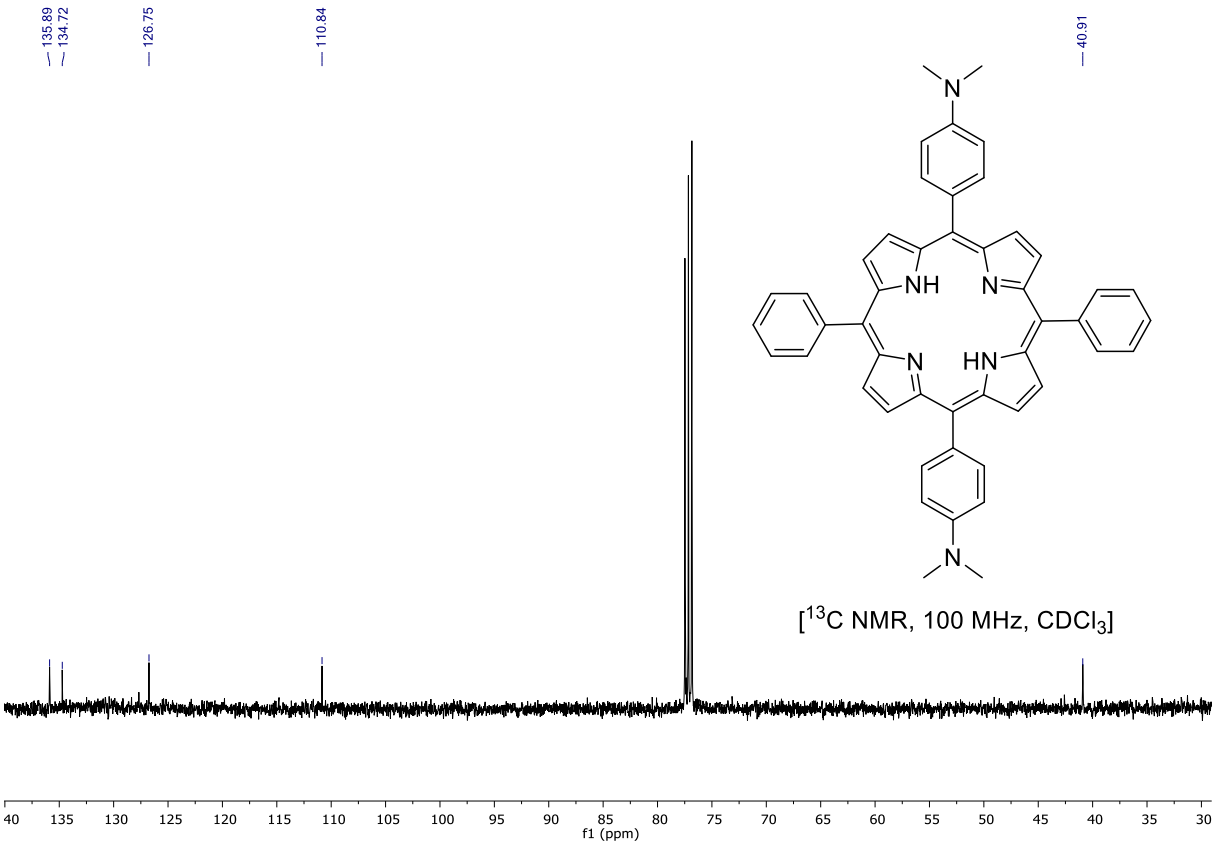

***Figure S8**: ^{13}C NMR spectrum of **P5** in $CDCl_3$.*

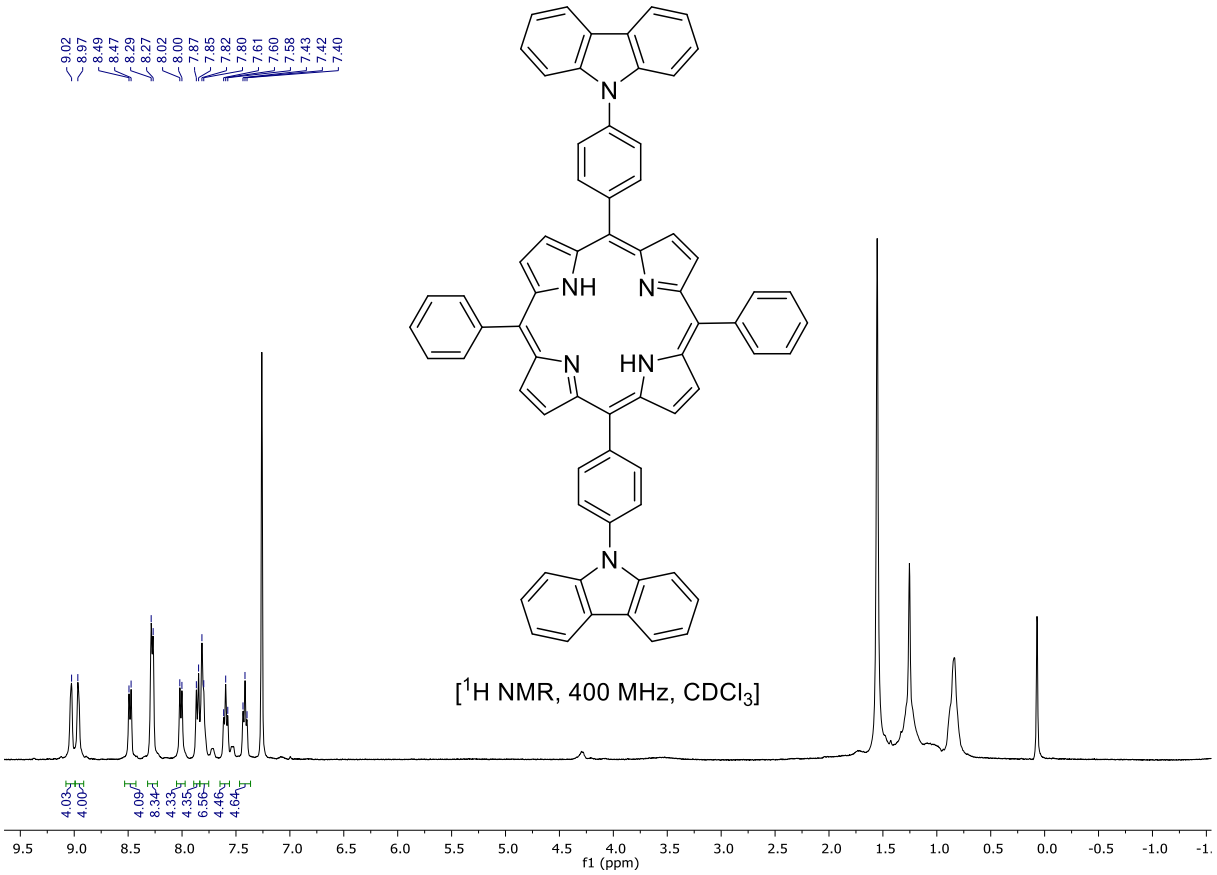

***Figure S9**: ^{1}H NMR spectrum of **P6** in $CDCl_3$.*

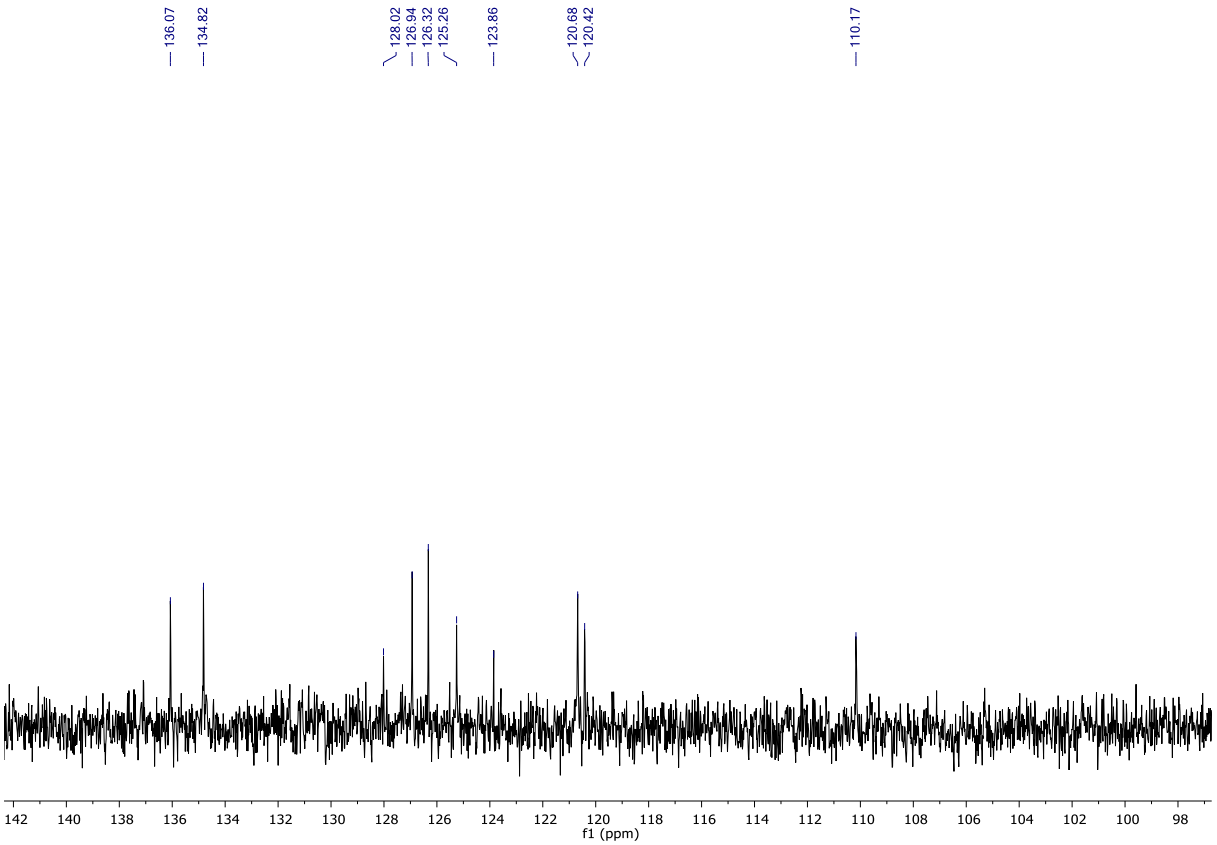

***Figure S10:** ^{13}C NMR spectrum of **P6** in $CDCl_3$*

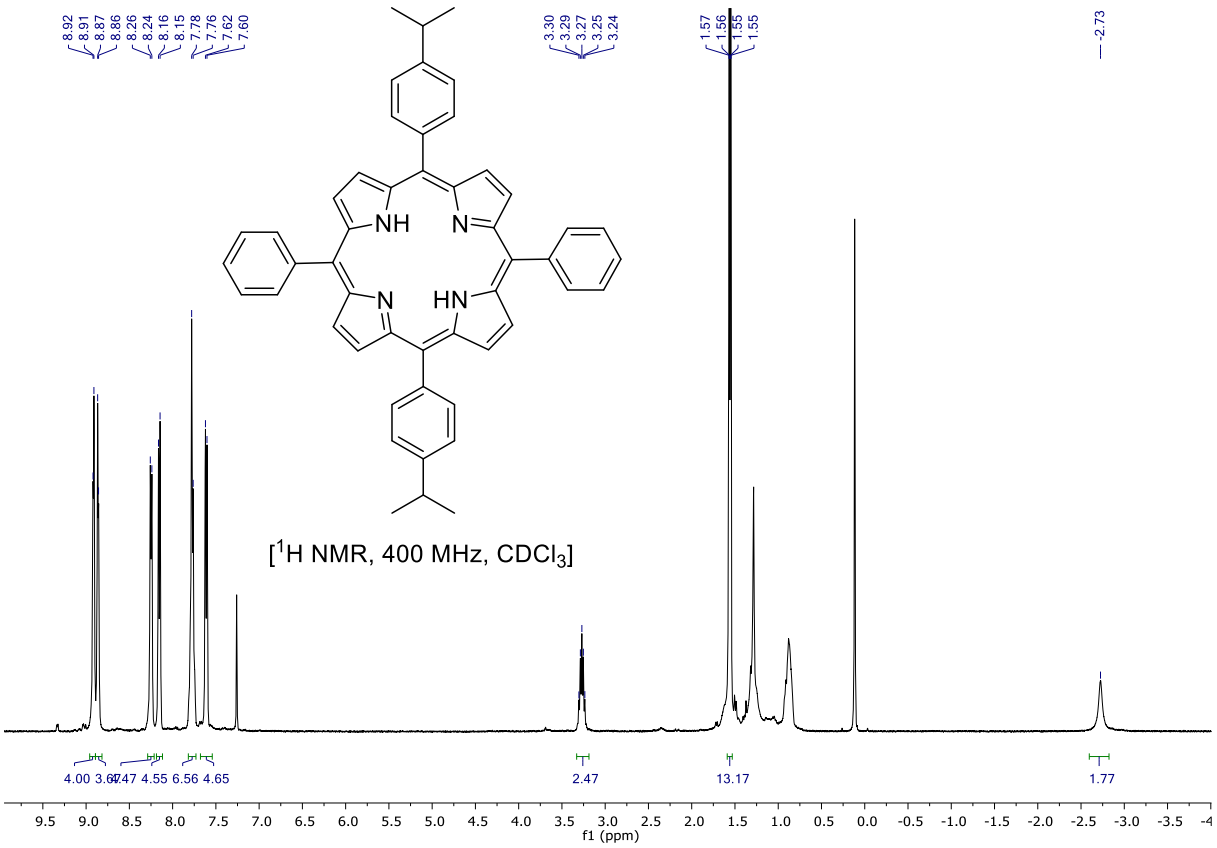

***Figure S11**: ^{1}H NMR spectrum of **P7** in $CDCl_3$.*

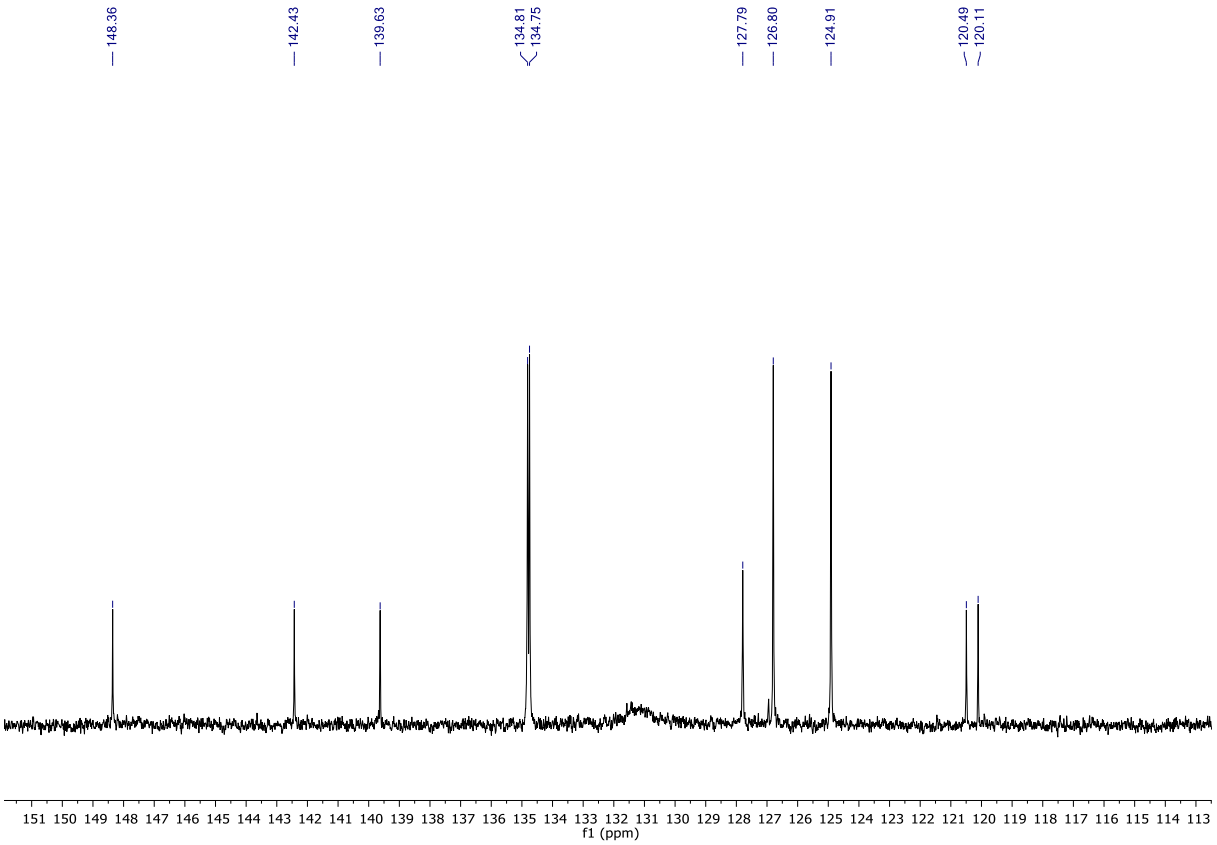

***Figure S12**: ^{13}C NMR spectrum of **P7** in $CDCl_3$*

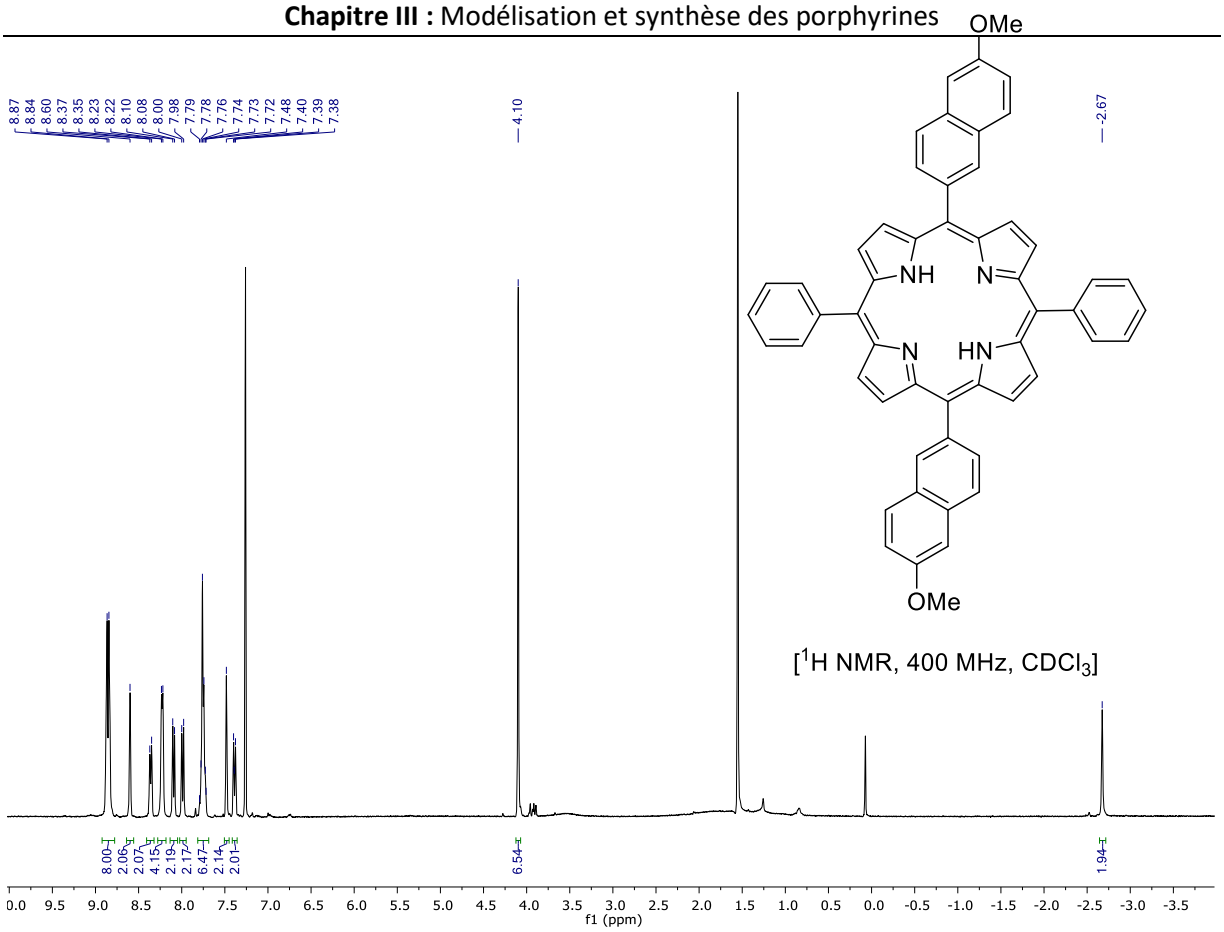

***Figure S13**: ^{1}H NMR spectrum of **P9** in $CDCl_3$.*

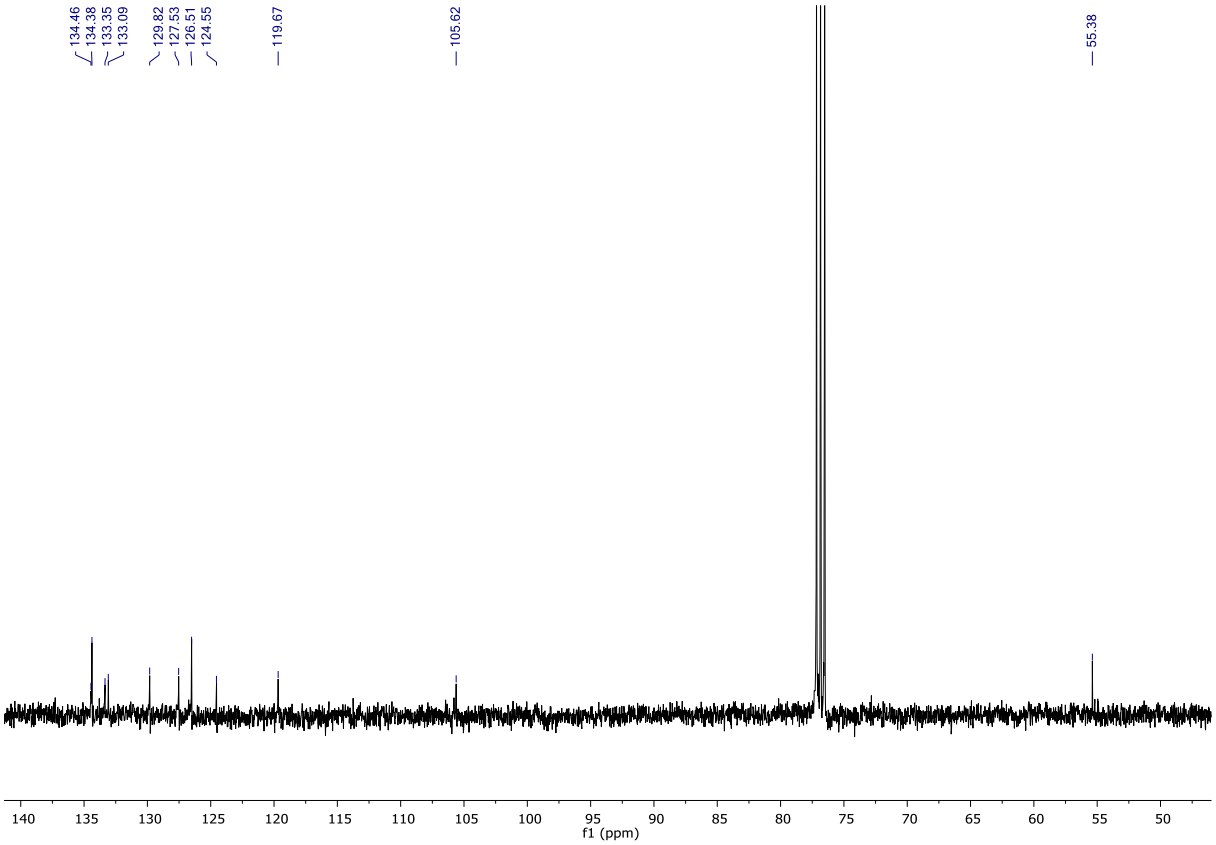

***Figure S14**: 13C NMR spectrum of P9 in CDCl3*

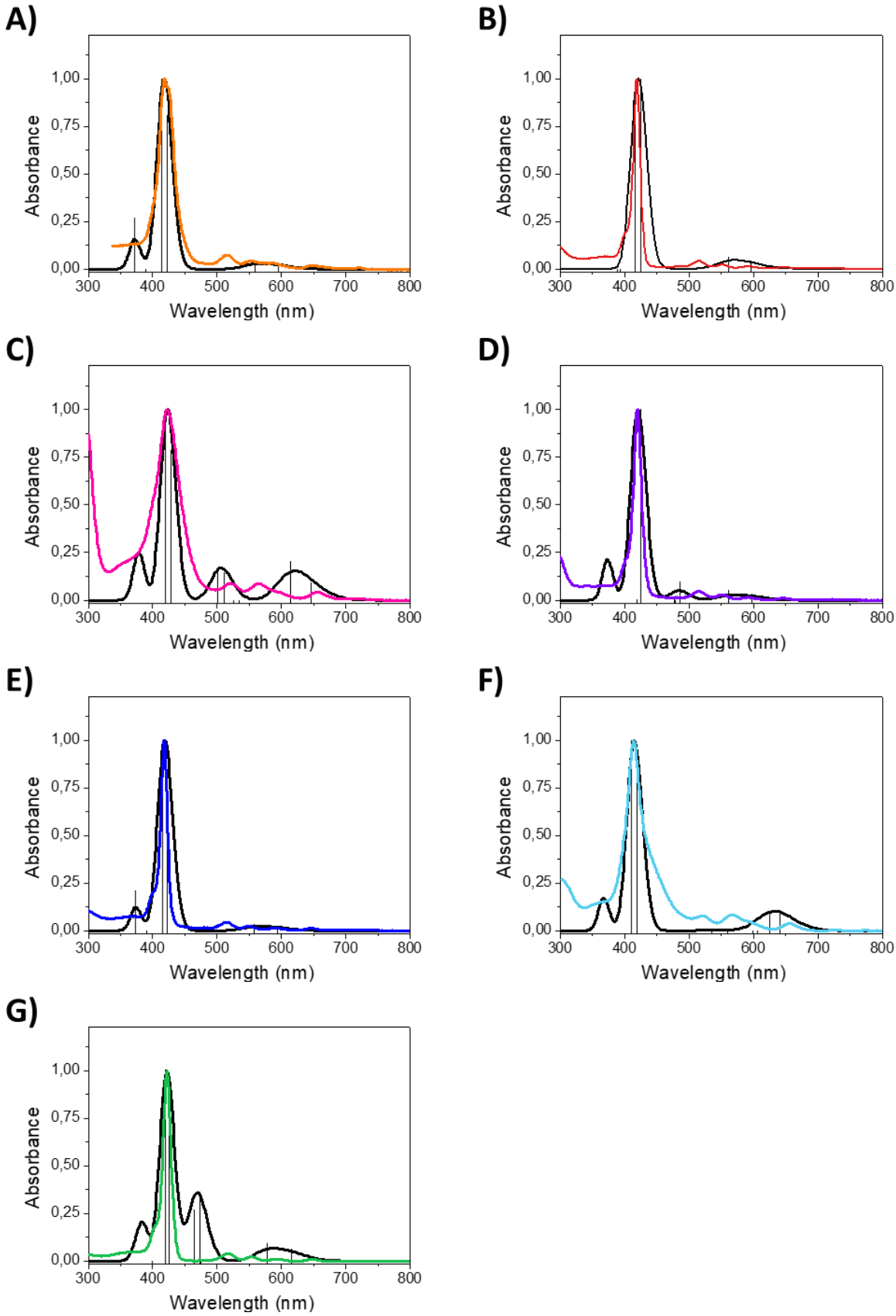

***Figure S15**: Experiment absorption spectra (in color) and theoretical spectrum shifted to match absorption maxima (in black) with corresponding vertical transition energies (corresponding to the one reported **Table 2**) for porphyrins **A**) P3, **B**) P4, **C**) P5, **D**) P6, **E**) P7, **F**) P8 and **G**) P9.*

Partie B : Généralisation à d'autres structures

I. Push Pull

I. 1. Introduction

To enhance the absorption capacity of porphyrins in the visible range and therefore enable polymerization at higher wavelengths, one strategy is to design structures with a push-pull effect, *i.e.* with an aromatic system enabling electronic communication from an electron donor to an acceptor. This type of dye enables intramolecular charge transfer (ICT) between the moieties and broader absorption of the Q and Soret bands [1]. Indeed, the ICT enable the formation of a new molecular orbital at low energy, leading to additional excited states in visible range.[2]

This type of structure have been widely studies for light-absorbing materials, like organic solar cells (OSC), or organic light-emitting diodes (OLED) [3–5], but it also have an growing interest for the development of new photoinitiating systems for in photopolymerization [6].

In this section, a series of push-pull porphyrin-based photoinitiators were studied. As shown in **Figure IIIB-1**, the donor groups 6-methoxy-2-naphthalene, 4-methoxyphenyl, and 4-dimethylaminophenyl were combined with the acceptor groups 4-nitrophenyl, 4-formylphenyl and 4-benzoate methyl to give five porphyrins. The choice of donor and acceptor groups was made *i*) on the basis of donor groups already tested in photopolymerization, *ii*) on the basis of knowledge of isomeric and mesomeric effects and *iii*) by comparison of computed results (not shown).

The selected porphyrins were studied using density functional theory (DFT) and time-dependent density theory (TD-DFT) to determine the effects of donor and attractor groups on molecular orbital energy, energy gap, electronic localisation and absorption properties. The method developed in the previous chapter have been used, and is in adequation with literature concerning computing push pull porphyrin.[7,8]

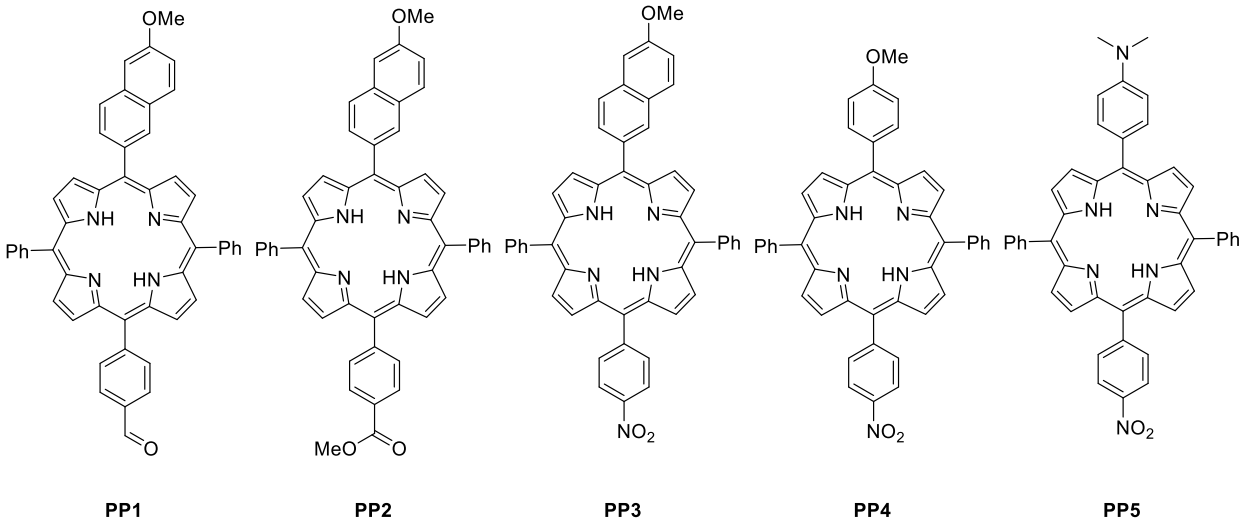

***Figure IIIB-1** : Push-pull porphyrin structure.*

I. 2. Synthesis

In order to prepare porphyrins bearing a push-pull system, we envisioned the use of two sequential Suzuki-Miyaura cross-coupling reactions (**Figure IIIB-2**). After an initial functionalization of the 10-position of 5,15-diphenylsubstituted porphyrin **1** by a bromination and cross-coupling reaction sequence, a second bromination and coupling sequence on the 20-position would deliver the expected compound **2**.

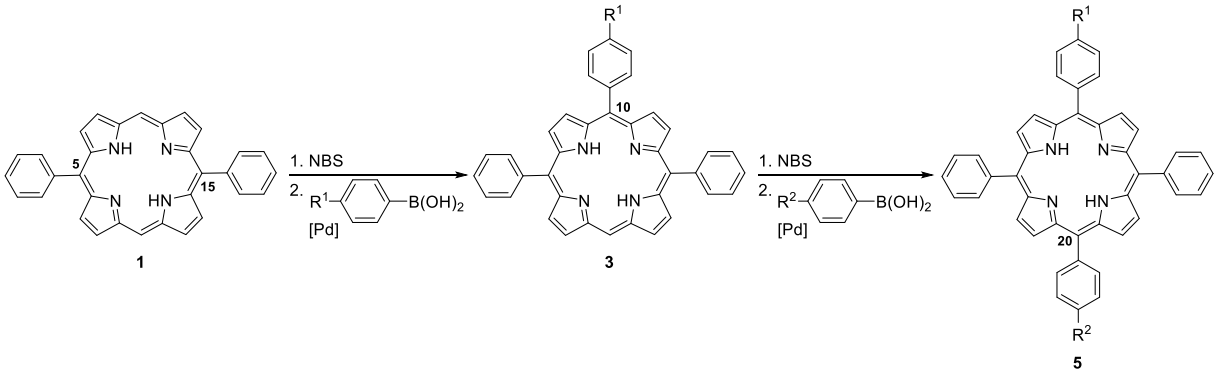

***Figure IIIB-2**: Envisioned strategy for the synthesis of push-pull porphyrins.*

The key starting material **2** of this synthesis could be easily prepared. Selective mono-bromination of 5,15-diphenyl porphyrin **1** could be achieved by treatment with a stoichiometric amount of NBS in the presence of pyridine in chloroform, leading to product **2** in 64% yield (**Figure IIIB-3**).

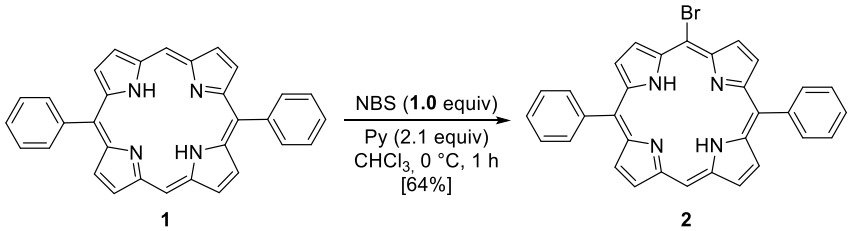

***Figure IIIB-3**: Mono-bromination of 5,15-diphenylporhyrin **1**.*

We next turn our attention to the application of our strategy for the preparation of push-pull porphyrins (**Table IIIB-1**). Based on our previous work, we selected the following conditions for both cross-coupling reactions: 1.2 equiv of arylboronic acid, 10 mol% of $PdCl_2$(dppf) and 3.0 equiv of K_2CO_3 in THF/H_2O 10:1 at reflux. As higher yield was obtained for double Suzuki-Miyaura cross-coupling reactions with electron-rich arylboronic acids, we envisioned that the electron-rich group would first be introduced. Therefore, reaction of 10-bromo-5,15-diphenyl porphyrin **2** with 6-methoxy-2-naphthaleneboronic acid **6** was achieved in a good 93% yield and subsequent bromination delivered intermediate **4a** in 84% yield. The second Suzuki-Miyaura reaction appeared to be strongly influenced by the nature of the electron withdrawing group beared by the arylboronic acid. Whereas a high 95% yield was obtained with an ester-substituted reagent (entry 1), the efficiency of the reaction decreased to 51% in the case of an aldehyde derivative (entry 2) and even to 13% with 4-nitrophenylboronic acid **8** (entry 3). It thus appeared that the stronger the electron withdrawing group, the less efficient is the reaction. Nevertheless, this lack of reactivity could be circumvented by introducing a stronger electron-donating group in the first step. Thus, after reaction with 4-methoxyphenylboronic acid **7** and bromination (50% and 99% yield, respectively), the Suzuki-Miyaura reaction with 4-nitrophenylboronic acid **8** delivered a much higher 94% yield (entry 4). Finally, the strategy needed to be changed in the case of a strongly donor dimethylamino group. Indeed, even if boronic acid **11** could be first introduced

in a correct 47% yield under our classical conditions, treatment of the resulting trisubstituted porphyrin with NBS led to a mixture of polybrominated products. We thus decided to first introduce the aryl group bearing the nitro function (57% yield) as the resulting product could be cleanly brominated in 90% yield. Pleasingly, the second Suzuki-Miyaura reaction with 4-dimethylaminoboronic acid **11** proved to be very efficient as a good 90% of the expected porphyrin has been obtained. Based on these observations, the following observations could be highlighted: a) the efficiency of the first Suzuki-Miyaura reaction decreased as the strength of the electron-donating group of the arylboronic acid increased; b) introduction of strong electron-donating group in the first step could lead to complications in the second bromination step (polybromination); c) the second Suzuki-Miyaura reaction is more efficient with weak electron-withdrawing groups and the use of a strong electron-withdrawing group required the prior introduction of a strong electron-donating group.

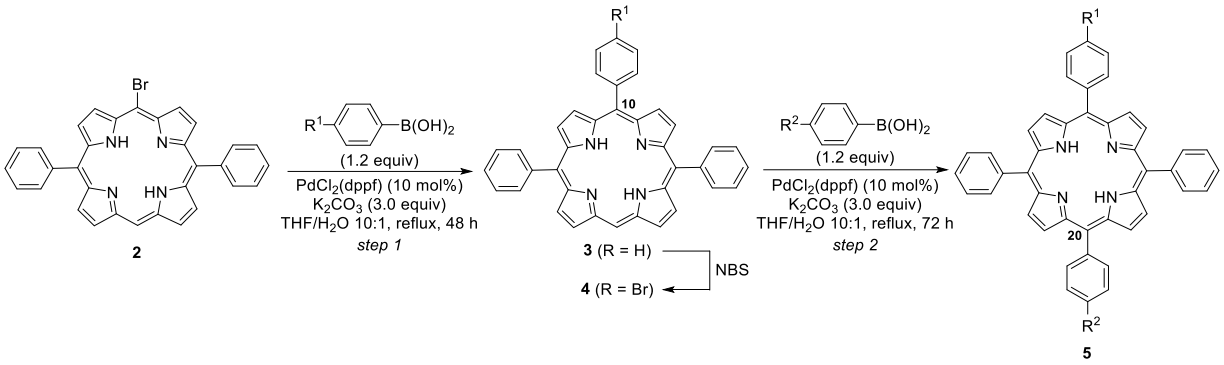

entry	$R^1–C_6H_4–B(OH)_2$	yield 1 (%)	yield bromation (%)	$R^2–C_6H_4–B(OH)_2$	yield 2 (%)
1	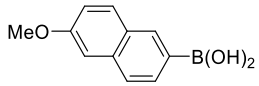 **6**	93 **3a**	84 **4a**	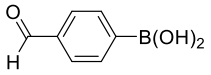 **9**	51 **PP1**
2				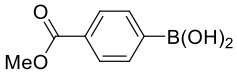 **10**	95 **PP2**
3				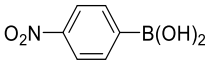 **8**	13 **PP3**
4	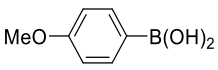 **7**	50 **3b**	99 **4b**		94 **PP4**
5	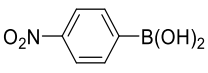 **8**	57 **3c**	90 **4c**	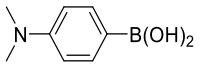 **11**	90 **PP5**

Table IIIB-1*: Scope of arylboronic acid used for the synthesis of Push Pull porphyrins.*

I. 3. Computational details

The ground state geometries and energies of the high occupied molecular orbital (HOMO) and the low unoccupied molecular orbital (LUMO) were determined by DFT using the B3LYP functional with the 6-31G(d) basis set. Vibrational frequency analyses were carried out at the same level of theory to confirm that the structures are in their true minima, without imaginary frequencies.

Frontier Molecular Orbitals. The calculated HOMO and LUMO energies are given in **Table IIIB-2**, and the molecular orbital energy levels graphic is given in **Figure IIIB-4**. The HOMO and LUMO energies of TPP are -5.16 eV and -2.46 eV respectively. Push-pull porphyrins have a lower LUMO energy than TPP. It can be noted that for TPP, the gap between the energy energies is larger ($\Delta_{HOMO-LUMO}$ = 2.70 eV) compared to the push-pull porphyrins ($\Delta_{HOMO-LUMO}$ = [2.64-2.13] eV). The porphyrins can be classified according to the value of the HOMO LUMO gap as follows: PP5 (2.13 eV) < PP3 (2.34 eV) < PP4 (2.35 eV) < PP2 (2.55 eV) < PP1 (2.64 eV). It can be expected that the smallest gaps lead to better reactivity.

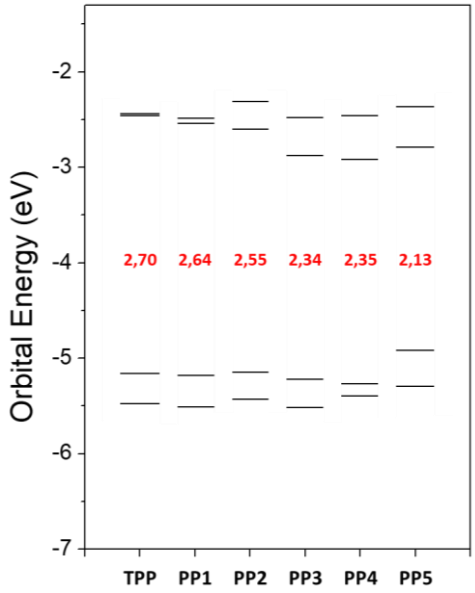

***Figure IIIB-4** : Molecular orbital energy levels of selected porphyrins and TPP.*

***Table IIIB-2**: Molecular orbital energy levels (eV) for the selected porphyrins calculated at B3LYP/6-31G(d)*

System	HOMO-1	HOMO	LUMO	LUMO+1	$\Delta_{HOMO-LUMO}$
TPP	-5,48	-5,16	-2,46	-2,44	2,7
PP1	-5,51	-5,18	-2,54	-2,49	2,64
PP2	-5,43	-5,15	-2,6	-2,31	2,55
PP3	-5,52	-5,22	-2,88	-2,48	2,34
PP4	-5,4	-5,27	-2,92	-2,46	2,35
PP5	-5,3	-4,92	-2,79	-2,37	2,13

The electronic distribution on the molecular orbitals (MO) shows the probability of electrons being found in the HOMO and LUMO orbitals of the different porphyrins (**Figure IIIB-5**). It can be noted that on TPP, the electrons are mainly located on the porphyrin core in both of the two frontier orbitals. For push-pull porphyrins, however, the electrons are located on the porphyrin core and the donor group for HOMO and on the porphyrin core and the attractor group for LUMO. This allows to obtain an efficient charge-transfer transition.

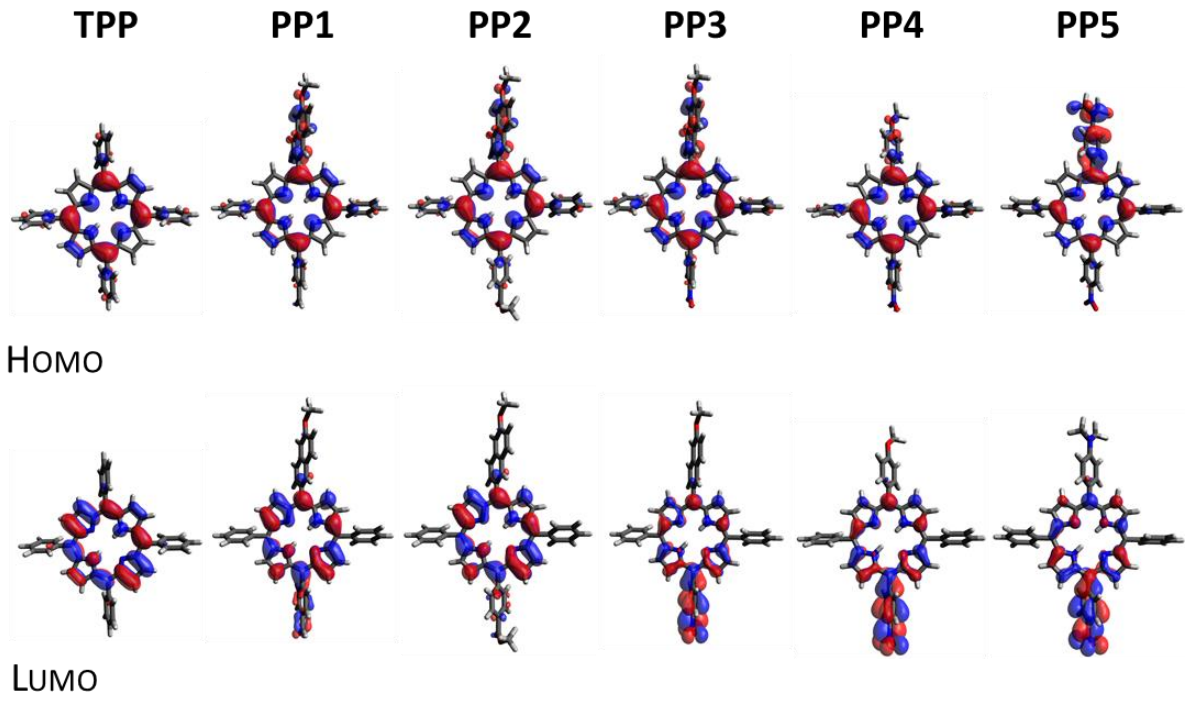

***Figure IIIB-5**: Electron distribution on the frontier orbitals.*

Absorption spectra. According to Gouterman's four orbital theory [9], porphyrins absorption spectra are composed of four vertical transition in the visible range. The lowest energetic transition Q_x and Q_y (forming the Q^I and Q^{III} bands) correspond to $S_0 \rightarrow S_1$ and $S_0 \rightarrow S_2$ transition. They can be split in free base porphyrin by vibrational mechanisms, forming the Q^{II} and Q^{IV} bands [10]. Similarly, B_x and B_y constitute the Soret band and include the $S_0 \rightarrow S_3$ and $S_0 \rightarrow S_4$.

The first ten electronic transitions were computed by TDDFT using same level of theory from the optimised geometry of the ground state. The associated wavelengths and oscillation strengths are shown in **Table IIIB-3**. It can be seen that unlike TPP, push pull porphyrins have a wider range of transitions.

The study of natural transition orbitals (NTOs) was used to highlight the electronic shift involved in the various transitions, by visualising the hole-particle pair, enabling to determine the nature of the transitions involved. The NTOs of the different porphyrin transitions are shown **Figure S1** to **Figure S9**.

It can be noted for TPP that the Q bands (in yellow in **Table IIIB-3**) correspond to the transitions $S_0 \rightarrow S_1$ and $S_0 \rightarrow S_2$. The comparison of the geometry of NTO of the other porphyrins shows that this is also the case for push pull porphyrins. Similarly, the Soret bands (in blue in **Table IIIB-3**) can be determined as the contributions of transitions with high oscillator strengths. Corresponding NTOs geometry can be compared with the ones of the TPP. Thus, Soret band pairs can then be identified as transitions $S_0 \rightarrow S_3$ & $S_0 \rightarrow S_4$ for TPP, $S_0 \rightarrow S_6$ & $S_0 \rightarrow S_7$ for **PP1** and **PP4**, $S_0 \rightarrow S_5$ & $S_0 \rightarrow S_6$ for **PP2**, $S_0 \rightarrow S_8$ & $S_0 \rightarrow S_9$ for **PP3** and **PP5**. For TPP, the Soret band corresponds to two π–π transitions located on the central ring. This is mostly the case for all here studied porphyrin with the contribution of less delocalized transition for the Soret band. In contrast, the contribution to the Q-band shows for the push-pull porphyrin a contribution to the substituents with a charge transfer from the R^1 to R^2 group.

Other transitions are also present between 530 and 420 nm, allowing a wider absorption range over all visible wavelengths and can be attributed to the internal charge-transfer.[2]

It can be seen that porphyrins with NO_2 function as acceptor part, allow total charge-transfer transition, from donor to acceptor moieties, unlike porphyrins **PP2**, which only allows transfer from acceptor to porphyrin core, and **PP1**, which allows "half" charge-transfer, by allowing the transfer from donor to porphyrin core or from porphyrin core to acceptor. Porphyrins **PP3**, **PP4** and **PP5** therefore have full charge-transfer transitions with important contribution of the MO (in green in **Table IIIB-3**), which allow the Soret band to be broadened.

Table IIIB-3*: The calculated absorption energies (λ) and oscillator strengths (f) of the first ten $S_0 \rightarrow S_i$ transitions of selected porphyrins. The Q bands are highlighted in yellow, the Soret band in blue and the total charge-transfer transition with important contribution of the MO in green.*

	S1	S2	S3	S4	S5	S6	S7	S8	S9	S10
TPP	576.08	539.69	403.59	396.08						
	0.0404	0.0544	1.3400	1.7259						
PP1	582.57	547.54	458.87	446.42	425.8	406.32	392.84	376.57	374.19	358.88
	0.0669	0.0997	0.1945	0.165	0.339	1.0294	1.2552	0.2813	0.0049	0.3539
PP2	586.19	549.82	455.42	444.47	404.92	398.86	374.73	361.57	359.42	353.85
	0.0721	0.1071	0.2356	0.1757	1.2421	1.6340	0.0047	0.0299	0.3739	0.0349
PP3	592.67	564.51	527.31	484.93	465.16	446.78	420.78	399.12	393.66	377.31
	0.1419	0.1004	0.0026	0.0663	0.1116	0.0817	0.3860	0.9963	1.5579	0.0030
PP4	586.82	558.37	522.07	483.36	415.69	403.66	395.92	383.78	376.35	366.69
	0.1109	0.0835	0.0084	0.0570	0.6323	0.8360	0.6508	0.7641	0.0006	0.0367
PP5	627.66	593.48	547.45	521.34	506.73	481.83	464.73	400.04	391.82	378.02
	0.2876	0.0600	0.0172	0.0257	0.0164	0.0377	0.2223	1.1204	1.5851	0.0022

Comparison with experimental spectra. The transitions were then used to determine the absorption spectrum by calculating Gaussian functions with half-widths of $\sigma = 0.2$ cm^{-1}, shown in **Figure S10** with the experimental absorption spectra in DCM. The effects of the solvent were included in the calculations in order to respect as closely as possible the interactions with the solute's true environment. It can be seen that, as expected, TPP has the thinnest experimental spectrum (σ = 11.4 nm) and **PP2** (σ = 14.02 nm) < **PP1** (σ = 14.27 nm) < **PP4** (σ = 16.24 nm) < **PP3** (σ = 17.85 nm) < **PP5** (σ = 33.86 nm) which has the widest Soret band thanks to transitions at higher wavelengths (**Figure IIIB-6A**). In addition, it can be observed that the Q band intensity of experimental spectra follow the same trend as theoretical results. Indeed, the oscillation strength of Q bands can be ordered as follows: TPP (0.0404) < **PP1** (0.0669) < **PP2** (0.0721) < **PP4** (0.1109) < **PP3** (0.1419) << **PP5** (0.2876) which is nearly the same order as experimentally TPP < **PP2** < **PP1** < **PP4** < **PP3** << **PP5.** However, in terms of wavelength values, it can be seen that the experimental spectra do not show as great a redshift as expected, particularly for the Q bands that occur in the same position as TPP (**Figure IIIB-6B**).

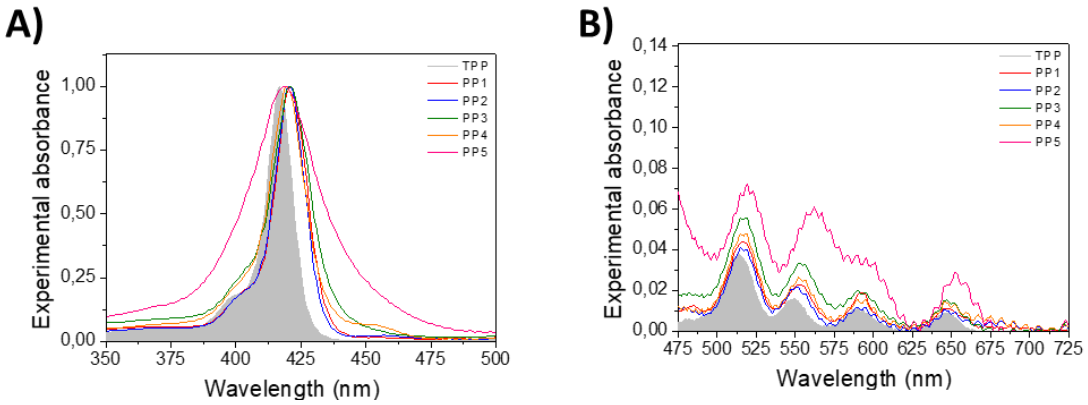

***Figure IIIB-6**: Normalized experimental absorption spectra of selected porphyrin centered on **A**) Soret band and **B**) Q bands.*

I. 4. Photopolymerization

The porphyrins computed and synthesised were used as photoinitiators in combination with MDEA to initiate the photopolymerization of acrylate functions in acrylated soya oil (SOA). Kinetic profiles showing the conversion of acrylate functions as a function of irradiation time are shown in **Figure IIIB-7** under irradiation at LED@450 nm and 625 nm under laminate. Final porphyrin monomer conversions at different irradiation wavelengths (LED@385 nm, 405 nm, 455 nm and 625 nm) under laminate and air are listed in **Table 10**. It can be seen that the PP2 porphyrin shows particularly high final monomer conversions. Indeed, this porphyrin reaches conversion rates of 99% under irradiation at 405 nm under laminate and in air, and reaches 61% and 52% conversion at 625 nm under laminate and in air respectively. In addition, all the push-pull porphyrins showed better photopolymerization initiation results, allowing better monomer conversions than TPP. These new porphyrins have also demonstrated their ability to initiate at longer wavelengths, enabling thicker systems to be polymerised.

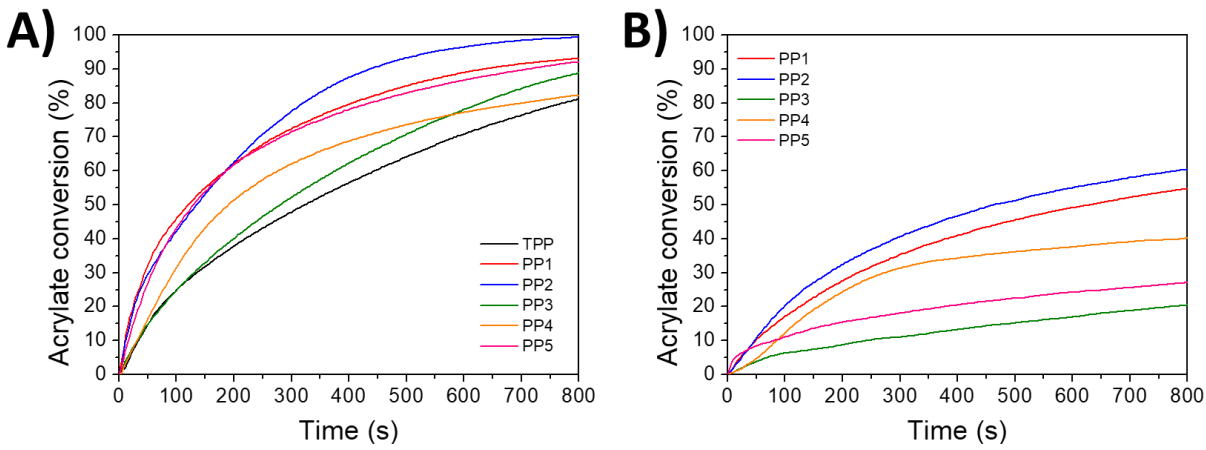

***Figure IIIB-7**: Kinetics profiles of the studies porphyrins under laminate under **A**) 405 nm or **B**) 625 nm irradiation.*

***Table IIIB-4**: Final monomer conversion.*

	Under laminate				Under air			
	385	405	455	625	385	405	455	625
PP1 MDEA SOA	68	**88**	56	**55**	45	93	49	31
PP2 MDEA SOA	64	**99**	57	**61**	57	99	66	52
PP3 MDEA SOA	72	**92**	63	**36**	50	94	46	np
PP4 MDEA SOA	60	**82**	53	**27**	23	72	30	np
PP5 MDEA SOA	77	**91**	66	**27**	50	98	70	19
TPP MDEA SOA	34	**81**	29	**np**	35	85	np	np

I. 5. Conclusion

Five new push-pull porphyrins were synthesised, and their properties were computed using the method presented in the previous section. Good correlations were obtained with the experimental spectra. In addition, the ability to initiate photopolymerization was determined, enabling quantitative monomer conversions to be obtained using the PP2 system. However, further analysis is required to determine the reason for the difference in reactivity between the porphyrins.

I. 6. Materials and methods

Synthesis of 5,10-diphenyl-10-bromoporphyrin (2). A 100 mL rounded-bottom flask equipped with a stirring bar is charged with 5,15-diphenylporphyrin (100 mg, 0.22 mmol, 1.0 equiv), chloroform (75 mL) and pyridine (0.1 mL). The mixture is treated with NBS (38 mg, 0.22 mmol, 1.0 equiv) at 0 °C for 1 h and monitored by TLC. The reaction is quenched with acetone (5 mL), and the solvent are removed under reduced pressure and the residue is triturated in methanol and filtered several times to afford the desired product (0.11 g, 64%) as a purple solid.

^{1}H NMR (400 MHz, CDCl3): δ 10.16 (s, 1H), 9.74 (d, *J* = 4.4 Hz, 2H), 9.28 (d, *J* = 3.8 Hz, 2H), 9.03 – 8.84 (m, 4H), 8.22 (d, *J* = 6.5 Hz, 4H), 7.89 – 7.61 (m, 6H), -3.01 (s, 2H). **HRMS (ESI/Q-TOF):** *m/z* [M + H$^+$] calcd for $C_{32}H_{22}N_4Br$ 541.1022; found 541.1018

General procedure of first mono Suzuki-Miyaura coupling (3).

A 50 mL rounded-bottom flask equipped with a stirring bar is charged with **5,10-diphenyl-10-bromoporphyrin** (100 mg, 0.19 mmol, 1 equiv), boronic acid (0.22 mmol, 1.2 equiv), K_2CO_3 (77 mg, 0.55 mmol, 3 equiv), THF (17 mL) and water (1.8 mL). The reaction mixture is flushed with argon, and $PdCl_2$dppf (13 mg, 0.02 mmol, 0.1 equiv) is added. The reaction is heated to reflux for 16 h. The reaction is washed with water (2 x 20 mL) and brine (20 mL), and the solvent are removed under reduced pressure. The crude product is purified by flash chromatography (silica, cyclohexane/DCM: 7/3) to afford the purified product as a purple solid.

Synthesis of 3a. Boronic acid **6** (45 mg) was used to afford porphyrin **3a** (106 mg, 93%).

^{1}H NMR (400 MHz, CDCl3): δ 10.20 (s, 1H), 9.33 (d, *J* = 4.2 Hz, 2H), 9.05 (d, *J* = 4.3 Hz, 2H), 9.01 – 8.85 (m, 4H), 8.61 (s, 1H), 8.38 (s, 1H), 8.38 – 8.23 (m, 4H), 8.07 (d, *J* = 8.3 Hz, 1H), 7.97 (d, *J* = 8.7 Hz, 1H), 7.86 – 7.75 (m, 6H), 7.47 (s, 1H), 7.39 (d, *J* = 8.9 Hz, 1H), 4.15 – 4.03 (m, 3H), -2.90 (s, 2H). **^{13}C NMR** (100 MHz, CDCl3): δ 158.41 ($2C_q$), 141.90 ($4C_q$), 137.96 ($2C_q$), 134.83 (4CH), 134.11 ($2C_q$), 133.56 (1CH), 133.36 (1CH), 131.75 (2CH), 131.55 (2CH), 130.86 (2CH), 130.11 (2CH), 127.85 (2CH), 127.69 ($2C_q$), 126.96 (4CH), 124.69 (1CH), 120.78 ($2C_q$), 119.99 (1CH), 119.80 ($4C_q$), 105.92 (1CH), 104.92 (1CH), 55.67 ($1CH_3$).

Synthesis of 3b. Boronic acid **7** (34 mg) was used to afford porphyrin **3b** (53 mg, 50%).

^{1}H NMR (400 MHz, CDCl3): δ. 10.18 (s, 1H), 9.32 (d, J = 4.3 Hz, 2H), 9.05 (d, J = 4.3 Hz, 2H), 8.99 – 8.92 (m, 4H), 8.29 (d, J = 6.8 Hz, 4H), 8.14 (d, J = 7.7 Hz, 2H), 7.89 – 7.70 (m, 6H), 7.28 (d, J = 8.0 Hz, 2H), 4.07 (s, 3H), -2.93 (s, 2H). **^{13}C NMR** (100 MHz, CDCl3): δ 159.51, 147.25 – 145.93, 141.95, 135.66, 135.06, 134.84, 131.68, 131.57, 131.36, 130.78, 127.83, 126.95, 120.63, 119.71, 112.18, 104.77, 55.67.

Synthesis of 3c. Boronic acid **8** (37 mg) was used to afford porphyrin **3c** (62 mg, 57%).

^{1}H NMR (400 MHz, CDCl3): δ 10.25 (s, 1H), 9.34 (d, 2H), 9.04 (d, 2H), 8.96 (d, 2H), 8.76 (d, 2H), 8.62 (d, J = 6.0 Hz, 2H), 8.37 (d, J = 6.4 Hz, 2H), 8.24 (d, J = 3.9 Hz, 4H), 7.84 – 7.67 (m, 6H), -3.02 (s, 2H). **^{13}C NMR** (100 MHz, CDCl3): δ 149.63, 147.74, 141.50, 135.07, 134.71, 131.74, 131.69, 131.44, 130.51, 127.93, 126.95, 121.75, 120.18, 105.65.

General procedure of mono bromation (4).

A 100 mL rounded-bottom flask equipped with a stirring bar is charged with mono-coupled porphyrin **3** (1 equiv), chloroform (0.035 M) and pyridine (0.5 equiv). The mixture is treated with NBS (1.1 equiv) at 0 °C for 1 h and monitored by TLC. The reaction is quenched with acetone (3 mL), and the solvent are removed under reduced pressure and the residue is triturated in methanol and filtered several times to afford the desired product as a purple solid.

Synthesis of 4a. Porphyrin **3a** (76 mg, 0.12 mmol), pyridine (0.07 mL, 0.06 mmol), NBS (24 mg, 0.13 equiv) were used to afford porphyrin **4a** (73 mg, 84%). **^{1}H NMR (400 MHz, CDCl3):** δ 9.68 (d, J = 3.5 Hz, 2H), 8.93 (d, 2H), 8.85 (d, 2H), 8.82 (d, 2H), 8.57 (s, 1H), 8.31 (d, J = 8.2 Hz, 1H), 8.22 (d, J = 6.2 Hz, 4H), 8.06 (d, J = 8.3 Hz, 1H), 7.96 (d, J = 9.1 Hz, 1H), 7.85 – 7.68 (m, 6H), 7.45 (s, 1H), 7.37 (d, J = 8.9 Hz, 1H),4.08 (s, 3H), -2.66 (s, 2H).

Synthesis of 4b. Porphyrin 3b (53 mg, 0.09 mmol), pyridine (0.05 mL, 0.05 mmol), NBS (18 mg, 0.10 mmol) were used to afford porphyrin **4b** (60 mg, 99%). **^{1}H NMR (400 MHz, CDCl3):** δ 9.67 (d, J = 4.9 Hz, 2H), 8.98 – 8.87 (m, 2H), 8.86 (d, J = 5.0 Hz, 2H), 8.81 (d, J = 5.0 Hz, 2H), 8.21 (d, J = 6.9 Hz, 4H), 8.09 (d, J = 8.0 Hz, 2H), 7.78 (q, J = 7.8, 7.0 Hz, 6H), 7.27 (d, J = 8.4 Hz, 2H), 4.07 (s, 3H), -2.72 (s, 2H). **^{13}C NMR** (100 MHz, CDCl3): δ 159.63, 141.95, 135.65, 134.68, 134.34, 128.01, 126.89, 121.08, 120.87, 112.42, 102.83, 55.70.

Synthesis of 4c. Porphyrin **3c** (62 mg, 0.11 mmol), pyridine (0.05 mL, 0.06 mmol), NBS (37 mg, 0.12 mmol) were used to afford porphyrin **4c** (63 mg, 90%). **^{1}H NMR (400 MHz, CDCl3):** δ 9.67 (d, J = 2.8 Hz, 2H), 8.91 (d, J = 4.8 Hz, 2H), 8.85 (d, J = 4.8 Hz, 2H), 8.69 (d, J = 4.8 Hz, 2H), 8.61 (d, J = 6.6 Hz, 2H), 8.34 (d, J = 6.9 Hz, 2H), 8.23 – 8.12 (m, 4H), 7.90 – 7.67 (m, 6H), -2.76 (s, 2H). **^{13}C NMR** (100 MHz, CDCl3): δ 148.98, 147.89, 141.61, 135.13, 134.66, 128.20, 126.99, 122.06, 121.43, 117.55, 104.02.

General procedure of second mono Suzuki-Miyaura coupling (5).

A 25 mL rounded-bottom flask equipped with a stirring bar is charged with **monobromo-monocoupled porphyrin 4** (0.10 mmol, 1 equiv), boronic acid (0.12 mmol, 1.2 equiv), K_2CO_3 (42 mg, 0.30 mmol, 3 equiv), THF (9 mL, 0.01 M) and water (1 mL, 0.001 M). The reaction mixture is flushed with argon, and $PdCl_2$dppf (7 mg, 0.01 mmol, 0.1 equiv) is added. The reaction is heated to reflux for 48 h. The reaction is washed with water (2 x 10 mL) and brine (10 mL), and the solvent are removed under reduced pressure. The crude product with triturated in methyl acetate to afford the purified product as a purple solid.

Synthesis of PP1. Porphyrin **4a** (70 mg) and boronic acid **9** (18 mg) were used to afford porphyrin **PP1** (37 mg, 51%). **^{1}H NMR (400 MHz, CDCl3):** δ 10.37 (s, 1H), 8.91 (d, J = 4.0 Hz, 4H), 8.88 (d, J = 4.0 Hz, 2H), 8.80 (d, J = 4.5 Hz, 2H), 8.61 (s, 1H), 8.41 (d, J = 7.4 Hz, 2H), 8.36 (d, J = 8.2 Hz, 1H), 8.27 (d, J = 9.7

Hz, 2H), 8.24 (d, J = 7.0 Hz, 4H), 8.08 (d, J = 8.0 Hz, 1H), 7.97 (d, J = 9.1 Hz, 1H), 7.87 – 7.67 (m, 6H), 7.47 (s, 1H), 7.38 (d, J = 9.0 Hz, 1H), 4.09 (s, 3H), -2.68 (s, 2H). **^{13}C NMR** (100 MHz, CDCl3): δ 192.59, 158.48, 148.86, 142.12, 137.39, 135.70, 135.33, 134.68, 134.15, 133.71, 133.34, 130.11, 128.17, 127.96, 127.79, 126.88, 124.91, 120.65, 120.05, 105.92, 55.69. **HRMS (ESI/Q-TOF)**: *m/z* [M + H$^+$] calcd for $C_{50}H_{35}N_4O_2$ 723.2755; found 723.2751. ν_{max} (ATR)/cm^{-1}: 3315, 2899, 2710, 2343, 1690, 1578, 1472, 1339, 1208, 966, 796, 717.

Synthesis of PP2. Porphyrin **4a** (70 mg) and boronic acid **10** (22 mg) were used to afford porphyrin **PP2** (76 mg, 95%). **^{1}H NMR (400 MHz, CDCl3):** δ 9.08 – 8.78 (m, 8H), 8.64 (s, 1H), 8.49 (d, J = 7.6 Hz, 2H), 8.42 – 8.33 (m, 3H), 8.31 – 8.22 (m, 4H), 8.06 (d, J = 8.2 Hz, 1H), 7.98 (d, J = 9.0 Hz, 1H), 7.87 – 7.66 (m, 6H), 7.46 (s, 1H), 7.38 (d, J = 8.5 Hz, 1H), 4.15 (s, 3H), 4.08 (s, 3H), -2.62 (s, 2H). **^{13}C NMR** (100 MHz, CDCl3): δ 167.51, 164.24, 158.48, 149.45, 147.21, 142.18, 137.46, 134.73, 134.68, 134.15, 133.70, 133.36, 130.12, 130.12, 129.68, 128.06, 127.92, 126.87, 124.89, 120.54, 120.04, 118.63, 105.93, 55.70, 52.60. **HRMS (ESI/Q-TOF)**: *m/z* [M + H$^+$] calcd for $C_{51}H_{37}N_4O_3$ 753.2860; found 753.2869. ν_{max} (ATR)/cm^{-1}: 3312, 2914, 2343, 1715, 1591, 1670, 1263, 1086, 1016, 795, 712.

Synthesis of PP3. Porphyrin **4a** (73 mg) and boronic acid **8** (21 mg) were used to afford porphyrin **PP3** (10 mg, 13%, contaminated by ca. 12% of boronic acid dimer). **^{1}H NMR (400 MHz, CDCl3):** δ 8.96 – 8.83 (m, 6H), 8.75 (d, J = 4.8 Hz, 2H), 8.64 (s, 1H), 8.61 (d, J = 10.0 Hz, 2H), 8.40 (d, J = 8.1 Hz, 2H), 8.29 (d, J = 8.6 Hz, 1H), 8.26 – 8.18 (m, 4H), 8.08 (d, J = 8.2 Hz, 1H), 7.98 (d, J = 9.5 Hz, 1H), 7.77 (d, J = 7.6 Hz, 6H), 7.47 (s, 1H), 7.38 (d, J = 8.9 Hz, 1H), 4.09 (d, J = 2.1 Hz, 3H), -2.71 (s, 2H). **^{13}C NMR** (100 MHz, CDCl3): δ 158.52, 149.38, 147.82, 142.03, 137.30, 135.27, 134.67, 134.18, 133.74, 133.31, 130.11, 128.37, 128.03, 127.80, 126.92, 124.94, 124.46, 122.00, 121.31, 120.84, 120.08, 116.73, 105.94, 55.70. **HRMS (ESI/Q-TOF)**: *m/z* [M + H$^+$] calcd for $C_{49}H_{34}N_5O_3$ 740.2656; found 740.2655. ν_{max} (ATR)/cm^{-1}: 3315, 2912, 2347, 1593, 1502, 1333, 1209, 966, 796, 716.

Synthesis of PP4. Porphyrin **4b** (63 mg) and boronic acid **8** (20 mg) were used to afford porphyrin **PP4** (63 mg, 94%). **^{1}H NMR (400 MHz, CDCl3):** δ 8.93 – 8.83 (m, 6H), 8.73 (d, J = 3.4 Hz, 2H), 8.63 (d, J = 8.3 Hz, 2H), 8.40 (d, J = 8.5 Hz, 2H), 8.21 (d, J = 6.8 Hz, 4H), 8.13 (d, J = 7.0 Hz, 2H), 7.77 (q, J = 8.2, 7.5 Hz, 6H), 7.30 (d, J = 8.4 Hz, 2H), 4.10 (d, J = 2.0 Hz, 3H), -2.77 (s, 2H). **^{13}C NMR** (100 MHz, CDCl3): δ 141.95, 135.65, 135.16, 134.56, 127.90, 126.79, 121.88, 112.30, 53.46. **HRMS (ESI/Q-TOF)**: *m/z* [M + H$^+$] calcd for $C_{45}H_{32}N_5O_3$ 690.2500; found 690.2509. ν_{max} (ATR)/cm^{-1}: 3315, 2980, 2895, 2347, 1581, 1502, 1331, 1232, 1169, 972, 793, 709.

Synthesis of PP5. Porphyrin **4c** (63 mg) and boronic acid **11** (19 mg) were used to afford porphyrin **PP5** (61 mg, 90%). **^{1}H NMR (400 MHz, CDCl3):** δ 8.98 (d, J = 4.4 Hz, 2H), 8.88 (d, J = 4.4 Hz, 2H), 8.84 (d, J = 4.0 Hz, 2H), 8.72 (d, J = 3.8 Hz, 2H), 8.62 (d, J = 6.7 Hz, 2H), 8.39 (d, J = 6.7 Hz, 2H), 8.22 (d, J = 7.2 Hz, 4H), 8.08 (d, J = 7.1 Hz, 2H), 7.77 (q, J = 6.6 Hz, 6H), 7.10 (d, J = 6.8 Hz, 2H), 3.23 (d, J = 2.1 Hz, 6H), -2.70 (s, 2H). **^{13}C NMR** (100 MHz, CDCl3): δ 142.19, 136.01, 135.29, 134.68, 127.95, 126.87, 121.99, 110.84, 40.86. **HRMS (ESI/Q-TOF)**: *m/z* [M + H$^+$] calcd for $C_{46}H_{35}N_6O_2$ 703.2816; found 703.2817. ν_{max} (ATR)/cm^{-1}: 3317, 2968, 2889, 2343, 1591, 1504, 1329, 1180, 966, 793, 714.

Computational details. All the calculations have been performed using Gaussian 16 package [11]. Structure optimization and frequencies calculation have been computed by density functional theory (DFT) using B3LYP functional and 6-31G(d) basis set. The lack of imaginary frequencies has been controlled to determine to true minima state. Time-dependant density functional theory (TD-DFT) have been used to compute vertical excitation energies using the same level of theory. The polarizable continuum (PCM) model have been used to consider the effect of the DCM solvent.

Polymerization. Photosensitive formulation (porphyrin/MDEA/SOA 0.5%/5% w./w.) were deposit on a BaF_2 pellet under air or under laminate. The irradiation sources was placed at 10 cm and are composed of four light emitting diodes (LEDs): LED@385 nm (35.3 $mW.cm^2$), LED@405 nm (118 $mW.cm^2$), LED@455 nm (23.8 $mW.cm^2$) and LED@625 nm (51 $mW.cm^2$). The photopolymerization kinetics are monitored by Real-Time Fourier Transformation Infrared Spectroscopy (RT-FTIR), following the decrease of acrylate function of the monomer at 1636 cm^{-1}.

I. 7. References

1 Z. Parsa, S. S. Naghavi and N. Safari, J. Phys. Chem. A, 2018, 122, 5870–5877.
2 F. Bureš, RSC Adv., 2014, 4, 58826–58851.
3 Y. Ooyama, Y. Shimada, S. Inoue, T. Nagano, Y. Fujikawa, K. Komaguchi, I. Imae and Y. Harima, New J. Chem., 2011, 35, 111–118.
4 W. Li, L. Ye, S. Li, H. Yao, H. Ade and J. Hou, Adv. Mater., 2018, 30, 1707170.
5 G. Chen, Z. Qiu, J.-H. Tan, W.-C. Chen, P. Zhou, L. Xing, S. Ji, Y. Qin, Z. Zhao and Y. Huo, Dyes Pigm., 2021, 184, 108754.
6 C. Pigot, G. Noirbent, D. Brunel and F. Dumur, Eur. Polym. J., 2020, 133, 109797.
7 X. Gu and Q. Sun, Phys. Chem. Chem. Phys., 2013, 15, 15434–15440.
8 S. J. Lind, K. C. Gordon, S. Gambhir and D. L. Officer, Phys. Chem. Chem. Phys., 2009, 11, 5598–5607.
9 M. Gouterman, G. H. Wagnière and L. C. Snyder, J. Mol. Spectrosc., 1963, 11, 108–127.
10 B. Minaev, Y.-H. Wang, C.-K. Wang, Y. Luo and H. Ågren, Spectroc. Acta A, 2006, 65, 308–323.
11 M. J. Frisch, G. W. Trucks, H. B. Schlegel, G. E. Scuseria, M. A. Robb, J. R. Cheeseman, G. Scalmani, V. Barone, G. A. Petersson, H. Nakatsuji, X. Li, M. Caricato, A. V. Marenich, J. Bloino, B. G. Janesko, R. Gomperts, B. Mennucci, H. P. Hratchian, J. V. Ortiz, A. F. Izmaylov, J. L. Sonnenberg, D. Williams-Young, F. Ding, F. Lipparini, F. Egidi, J. Goings, B. Peng, A. Petrone, T. Henderson, D. Ranasinghe, V. G. Zakrzewski, J. Gao, N. Rega, G. Zheng, W. Liang, M. Hada, M. Ehara, K. Toyota, R. Fukuda, J. Hasegawa, M. Ishida, T. Nakajima, Y. Honda, O. Kitao, H. Nakai, T. Vreven, K. Throssell, J. A. Montgomery Jr., J. E. Peralta, F. Ogliaro, M. J. Bearpark, J. J. Heyd, E. N. Brothers, K. N. Kudin, V. N. Staroverov, T. A. Keith, R. Kobayashi, J. Normand, K. Raghavachari, A. P. Rendell, J. C. Burant, S. S. Iyengar, J. Tomasi, M. Cossi, J. M. Millam, M. Klene, C. Adamo, R. Cammi, J. W. Ochterski, R. L. Martin, K. Morokuma, O. Farkas, J. B. Foresman and D. J. Fox, 2016.

I. 8. Supporting Information

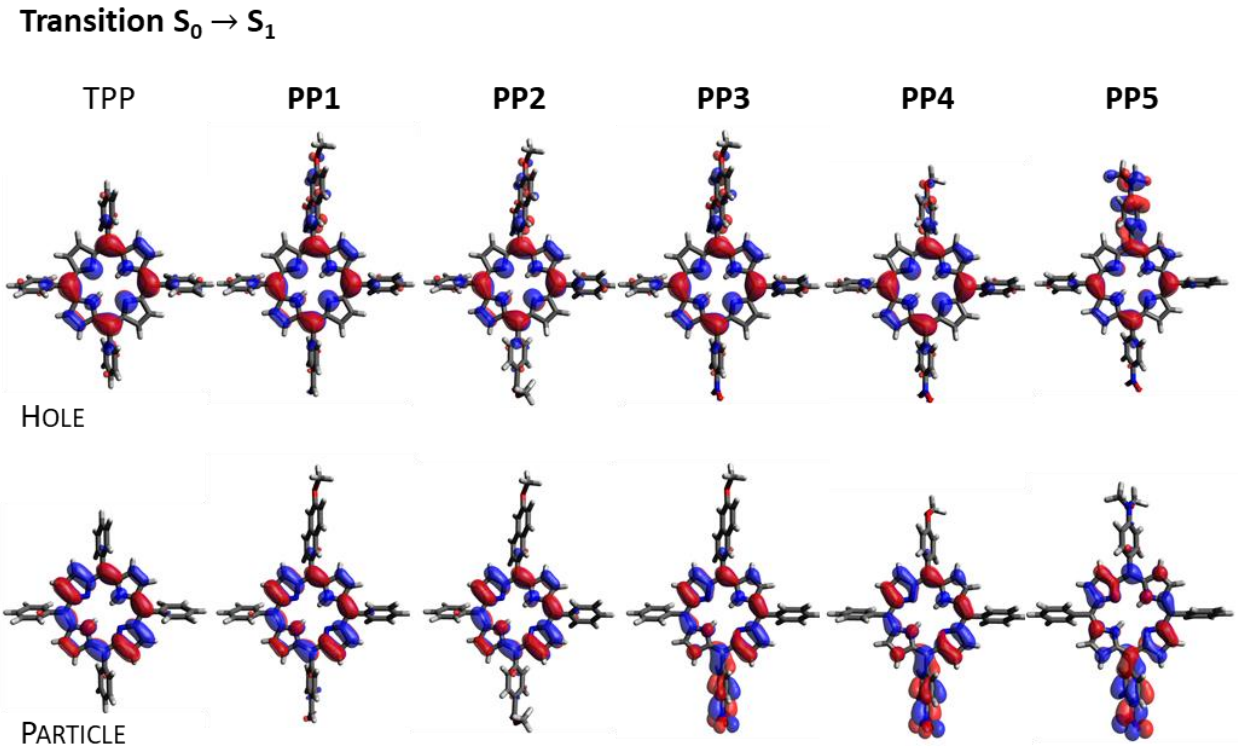

***Figure S1**: Electron densities of "hole" and "particles" NTO pairs for $S_0 \rightarrow S_1$ transition.*

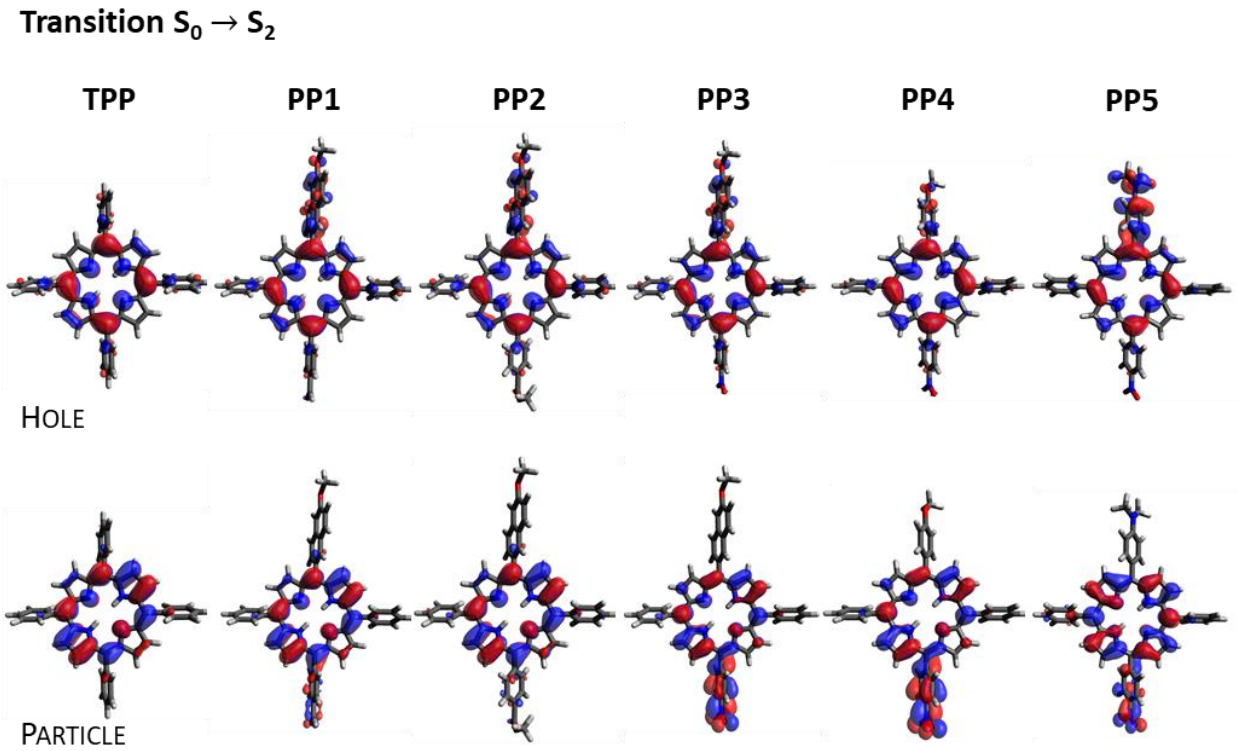

***Figure S2**: Electron densities of "hole" and "particles" NTO pairs for $S_0 \rightarrow S_2$ transition.*

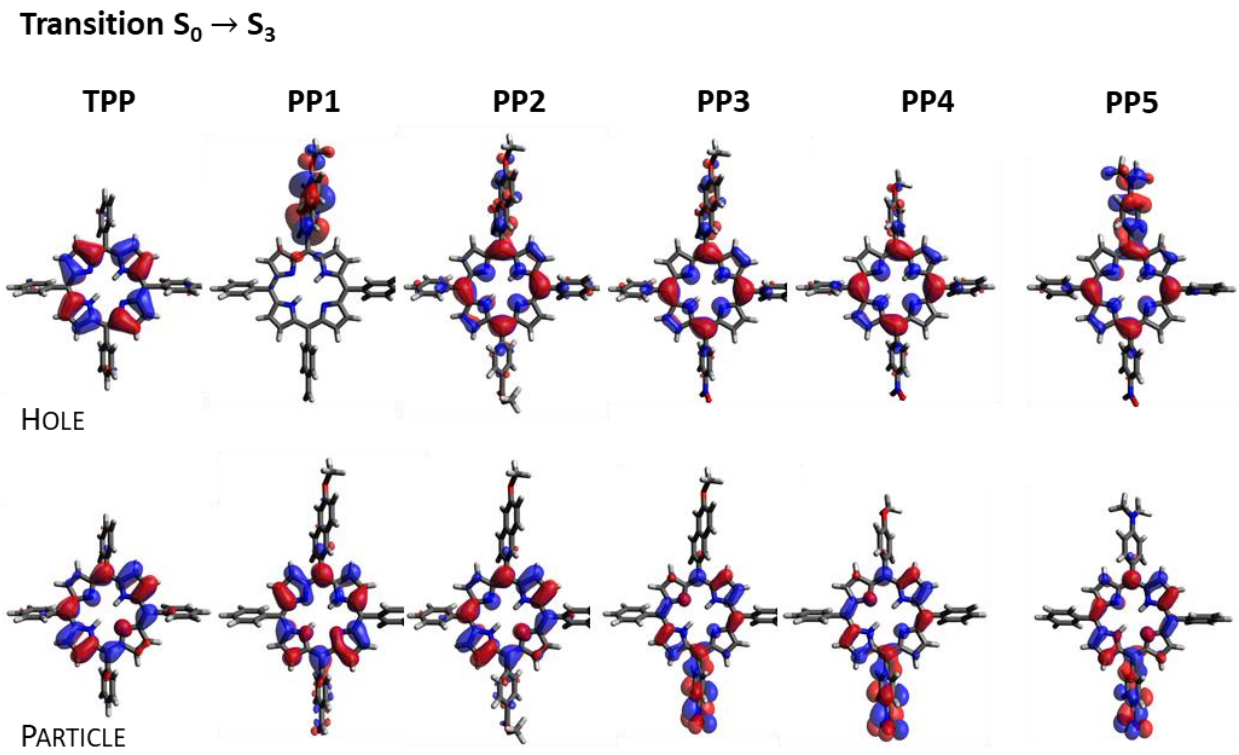

***Figure S3**: Electron densities of "hole" and "particles" NTO pairs for $S_0 \rightarrow S_3$ transition.*

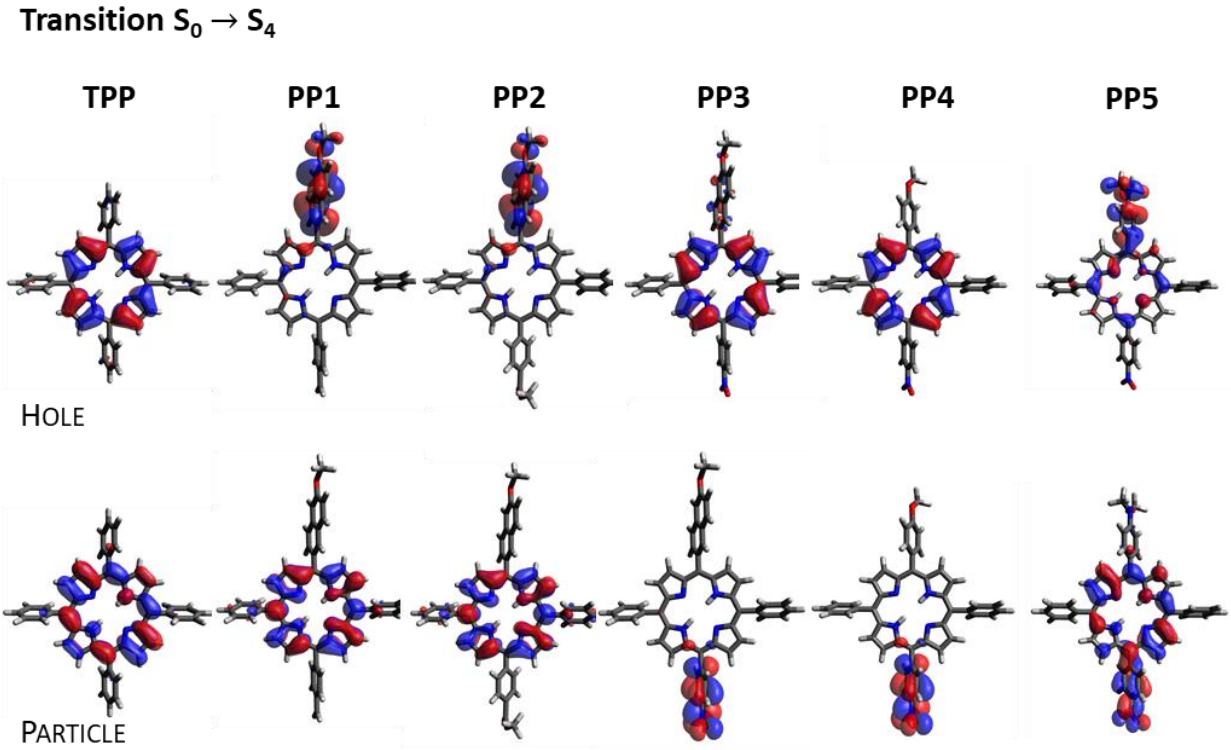

***Figure S4:** Electron densities of "hole" and "particles" NTO pairs for $S_0 \rightarrow S_4$ transition.*

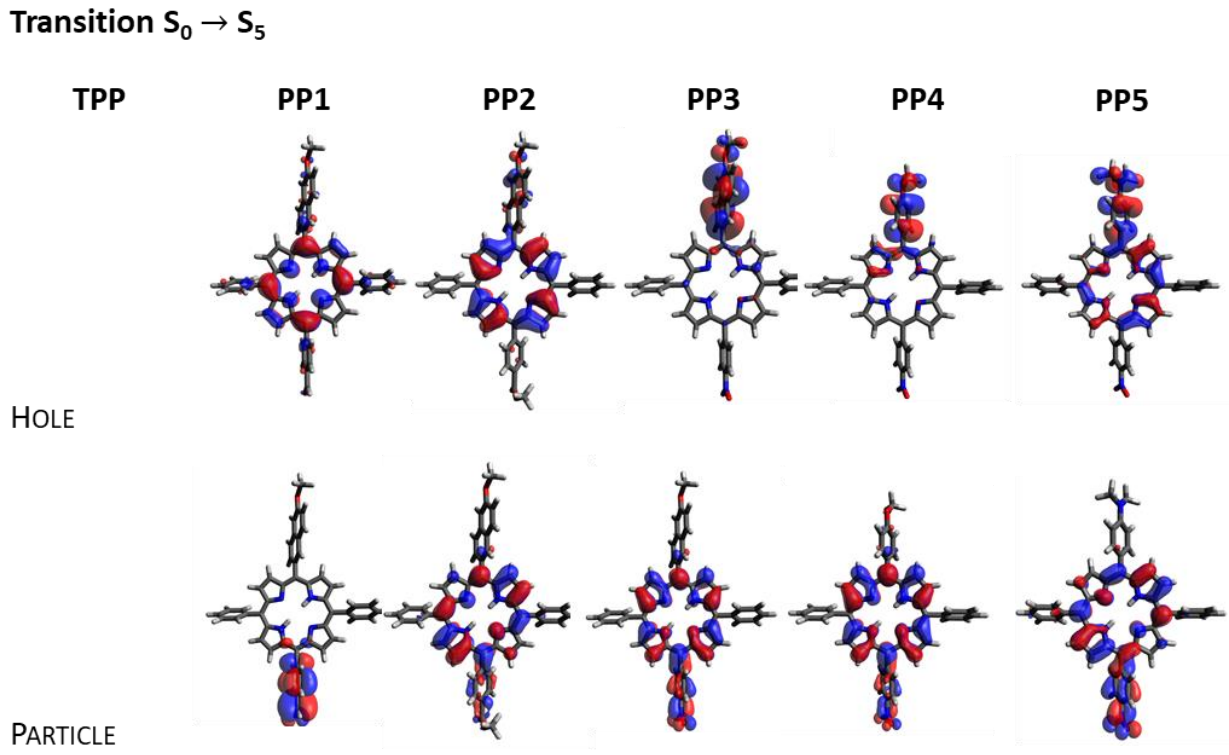

Figure S5: *Electron densities of "hole" and "particles" NTO pairs for $S_0 \rightarrow S_5$ transition. The spaces left blank correspond to transitions in the near UV, ignored in this study.*

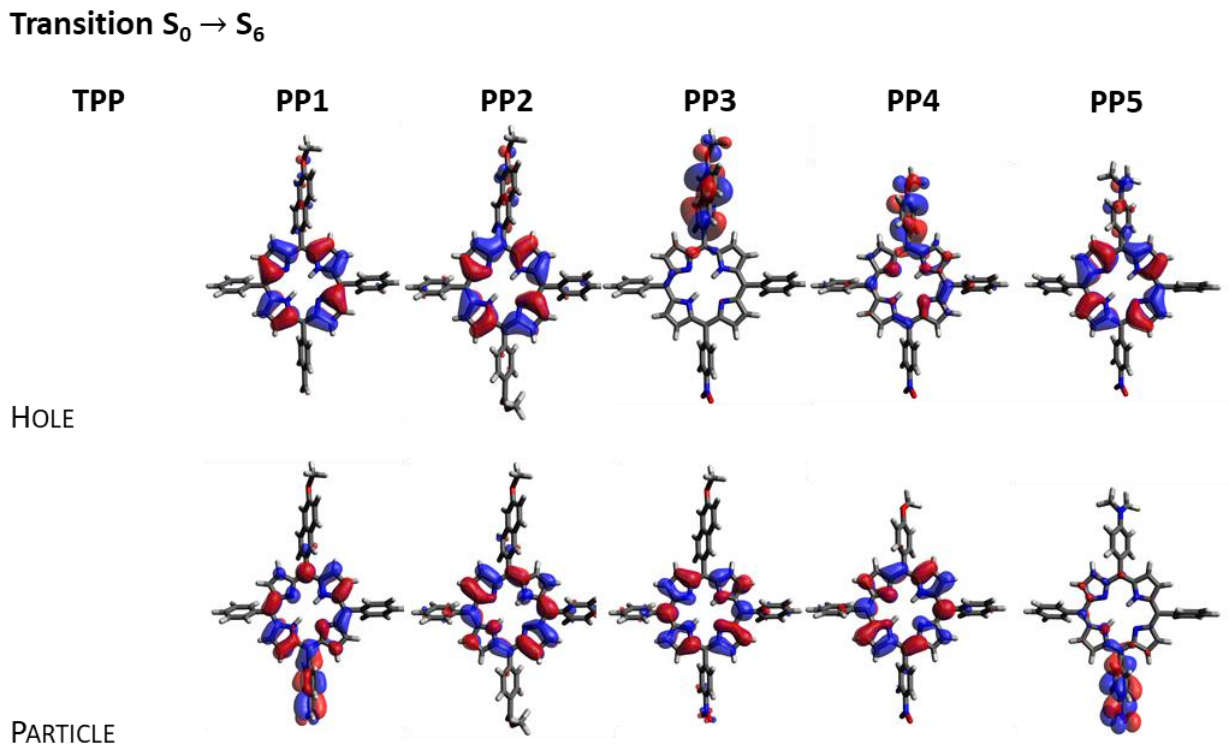

Figure S6: *Electron densities of "hole" and "particles" NTO pairs for $S_0 \rightarrow S_6$ transition. The spaces left blank correspond to transitions in the near UV, ignored in this study.*

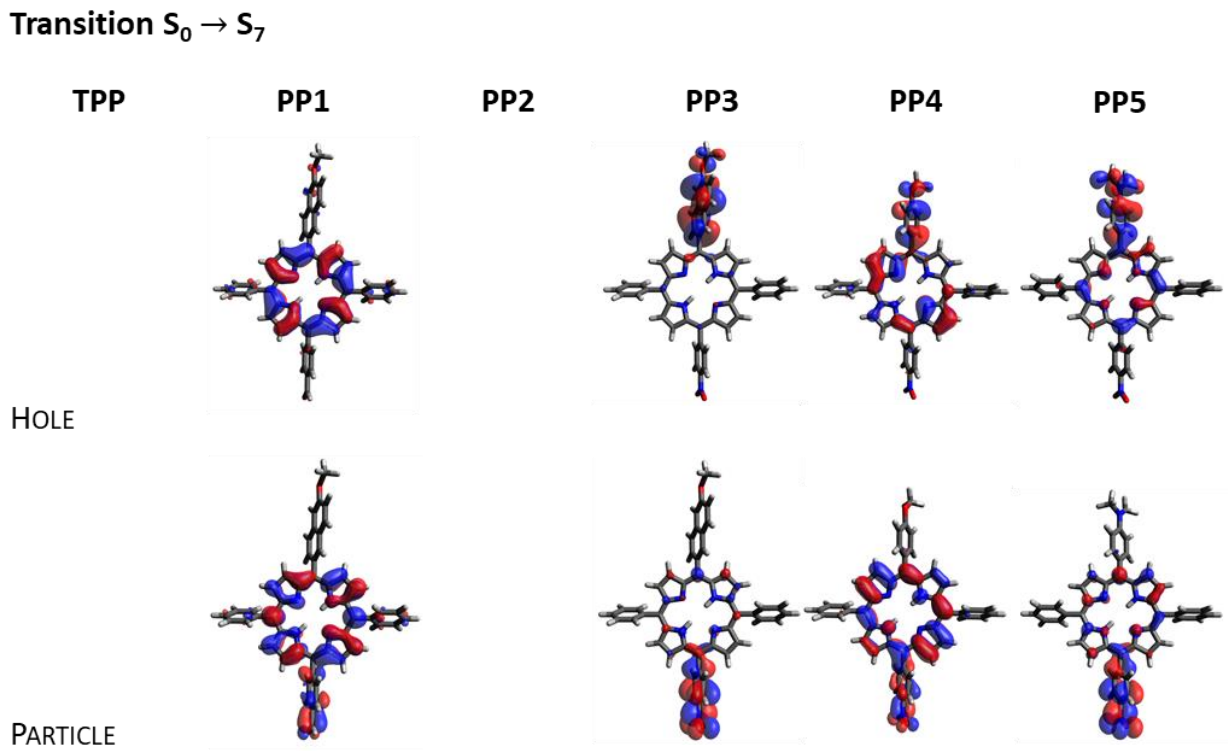

Figure S7: *Electron densities of "hole" and "particles" NTO pairs for $S_0 \rightarrow S_7$ transition. The spaces left blank correspond to transitions in the near UV, ignored in this study.*

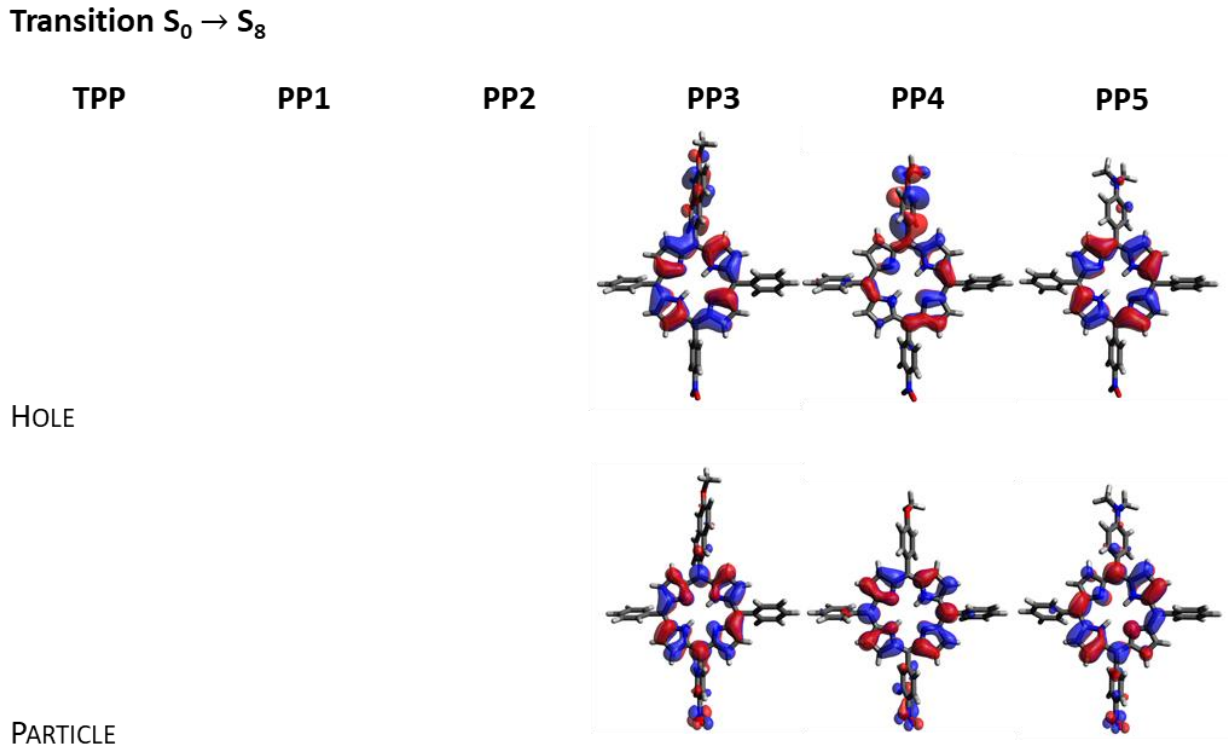

Figure S8: *Electron densities of "hole" and "particles" NTO pairs for $S_0 \rightarrow S_8$ transition. The spaces left blank correspond to transitions in the near UV, ignored in this study.*

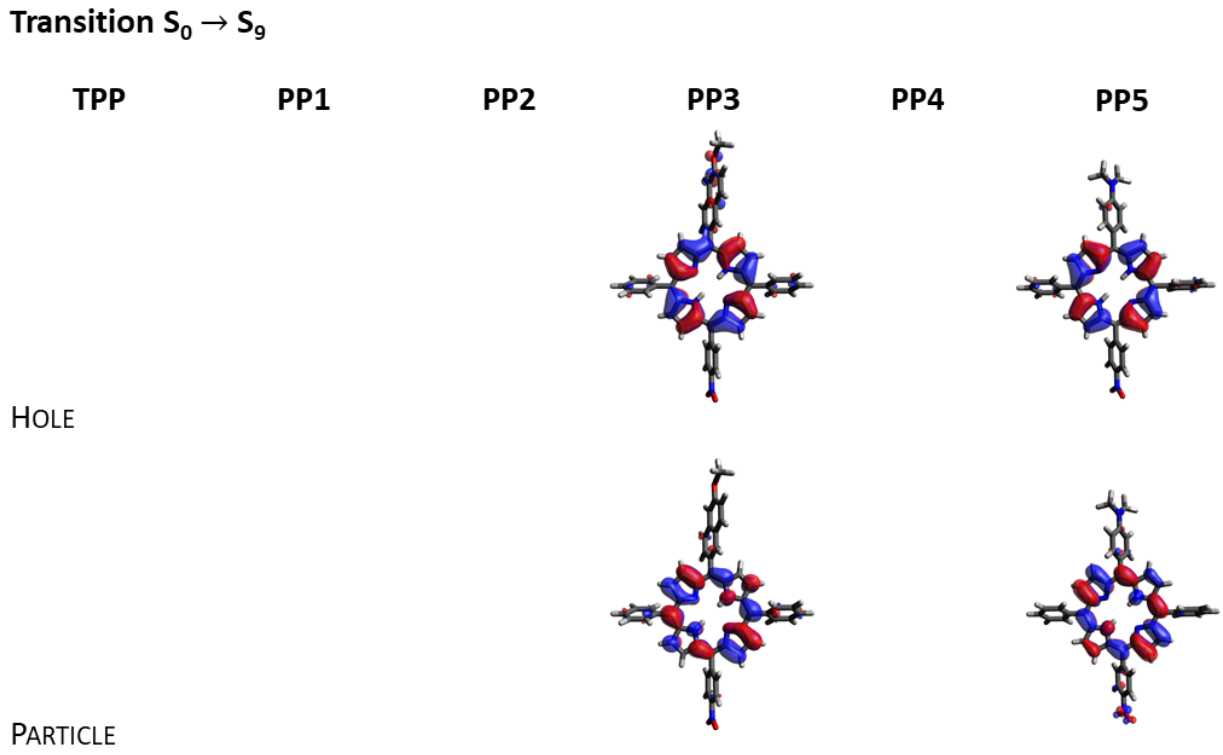

Figure S9: *Electron densities of "hole" and "particles" NTO pairs for $S_0 \rightarrow S_9$ transition. The spaces left blank correspond to transitions in the near UV, ignored in this study.*

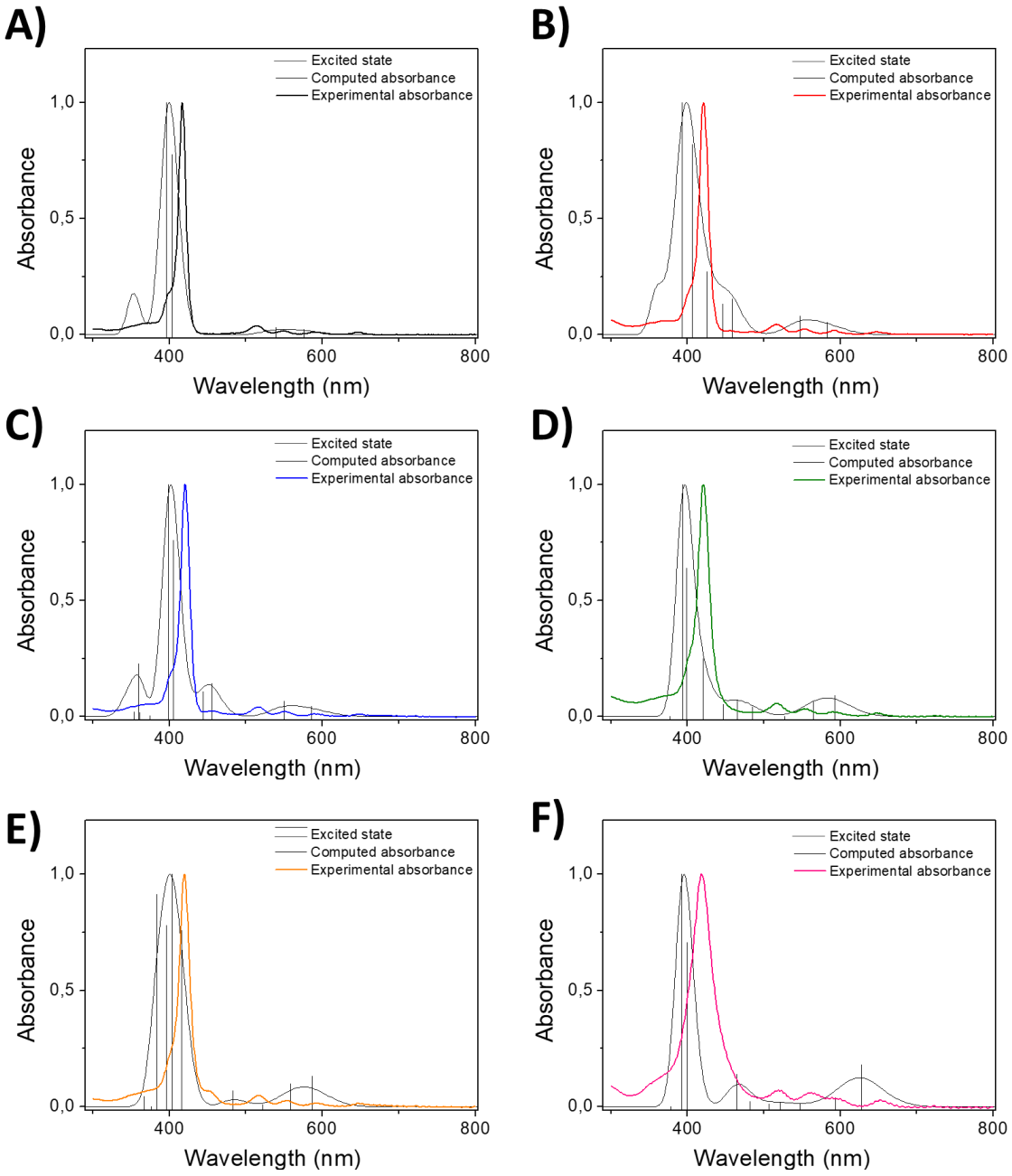

Figure S10: *Computed and experimental absorbance of the five porphyrins: A) TPP, B)* ***PP1****, C)* ***PP2****, D)* ***PP3****, E)* ***PP4*** *and F)* ***PP5.***

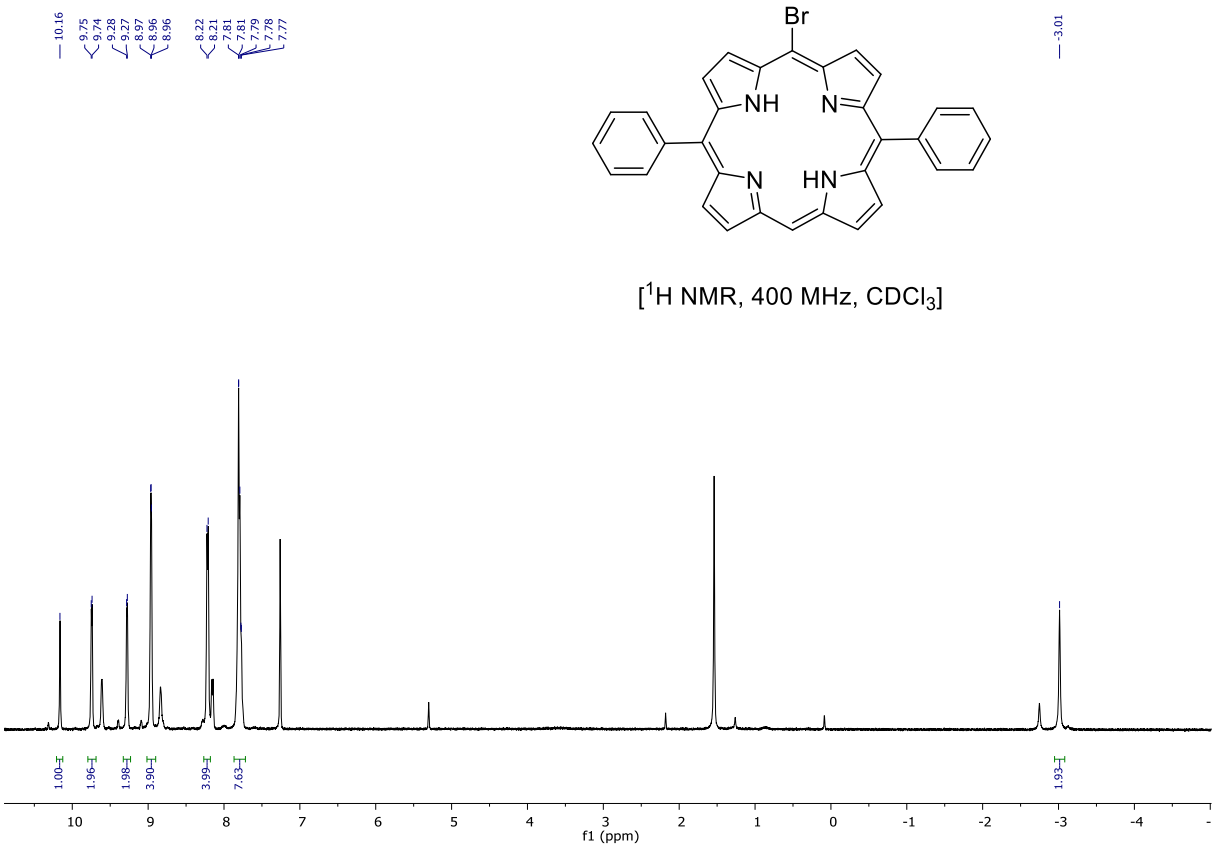

Figure S11: *^{1}H NMR spectrum of **2** in $CDCl_3$.*

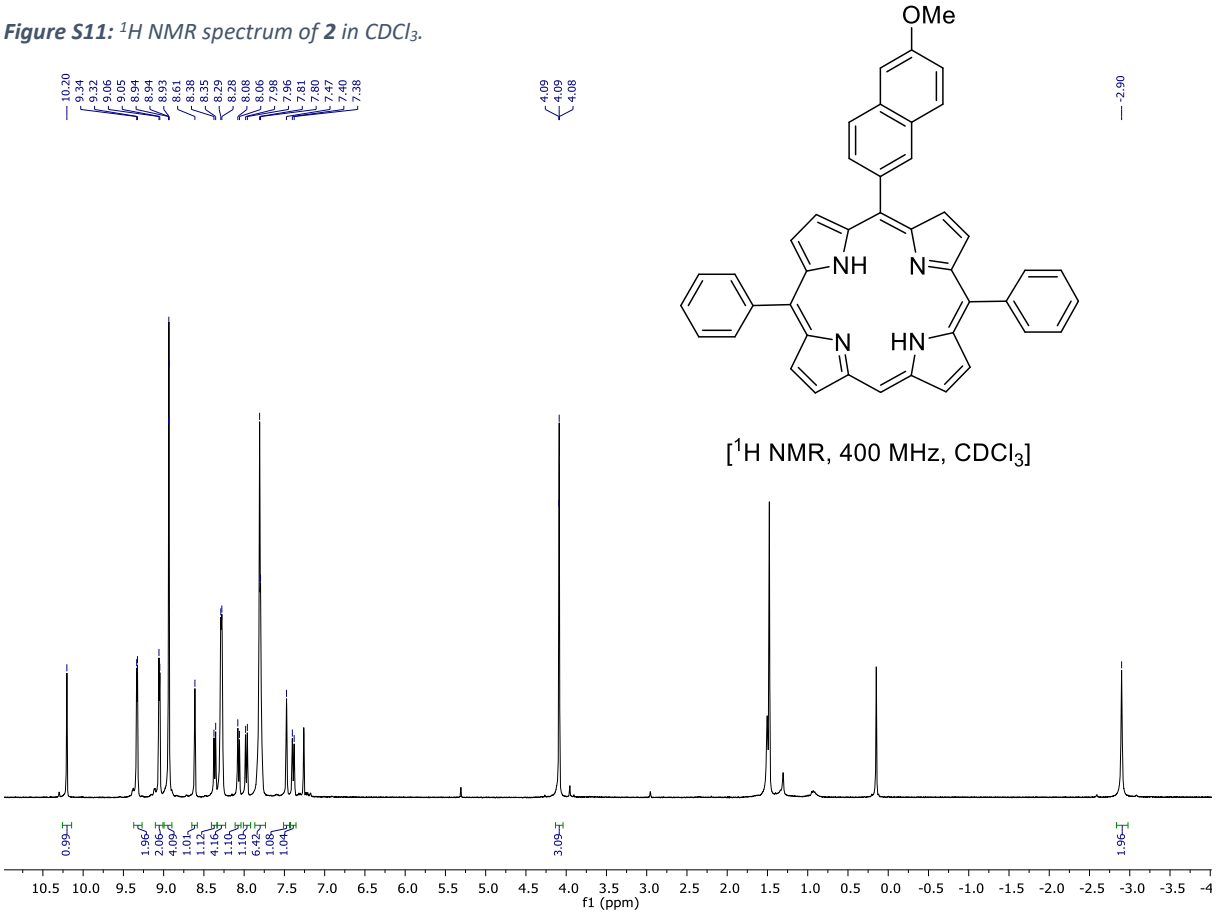

Figure S12: *^{1}H NMR spectrum of **3a** in $CDCl_3$.*

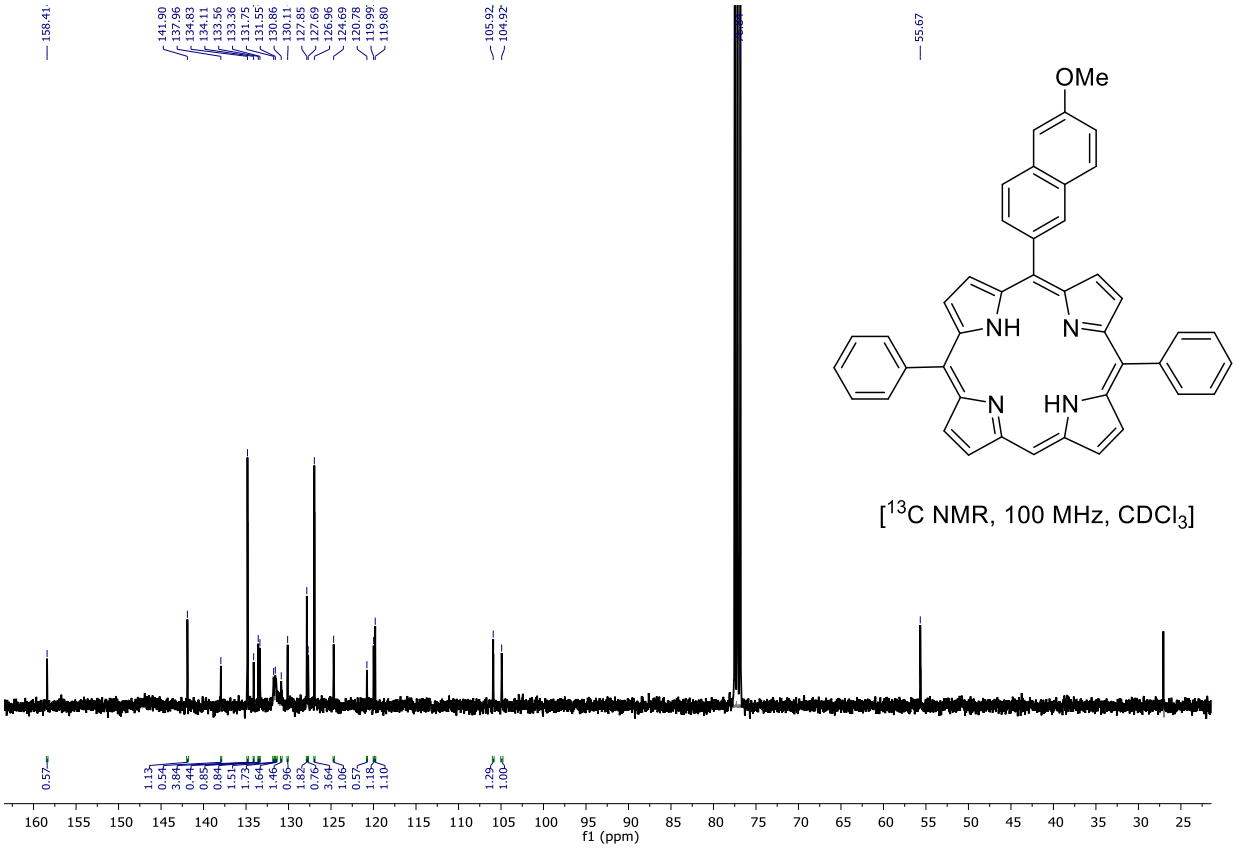

***Figure S13**: ^{13}C NMR spectrum of **3a** in $CDCl_3$.*

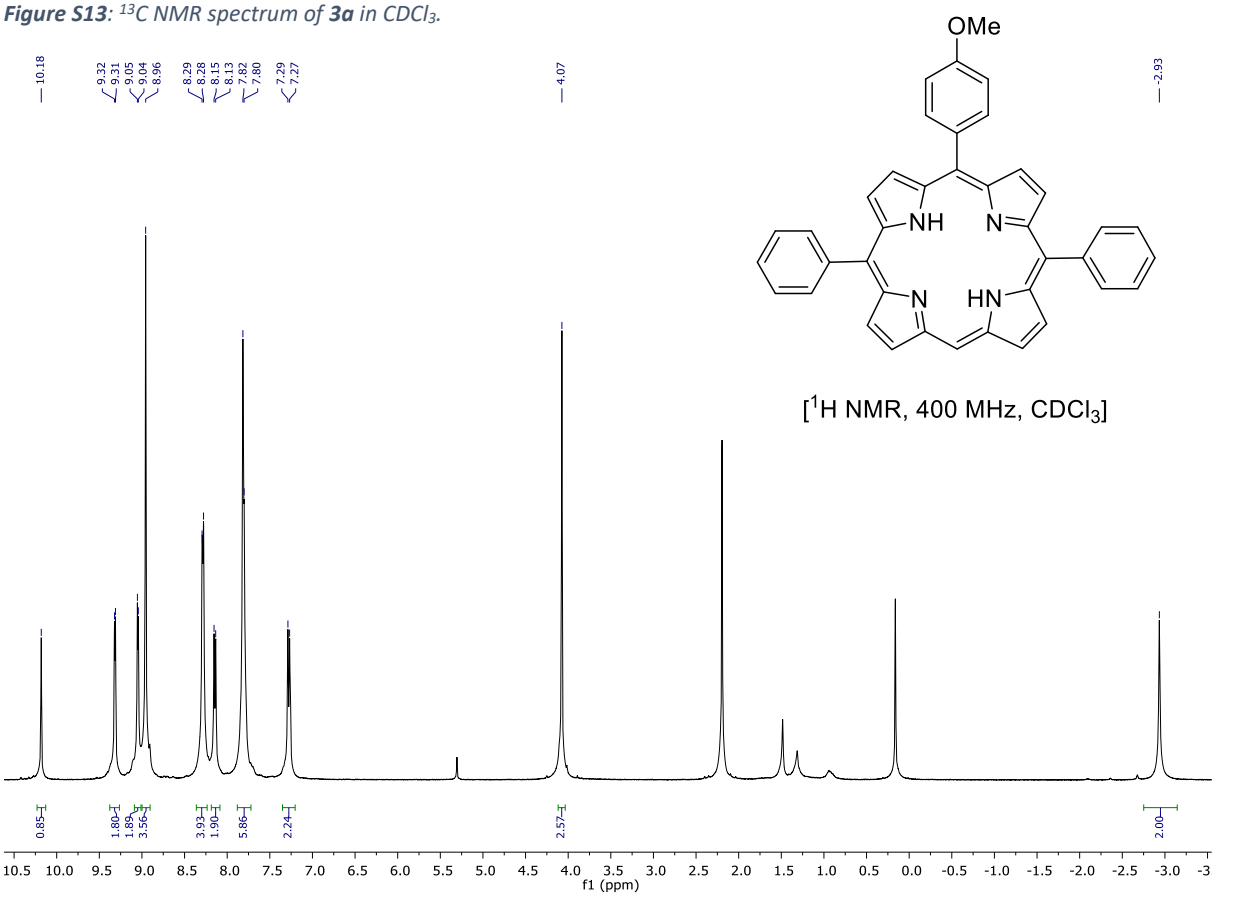

***Figure S14:** ^{1}H NMR spectrum of **3b** in $CDCl_3$.*

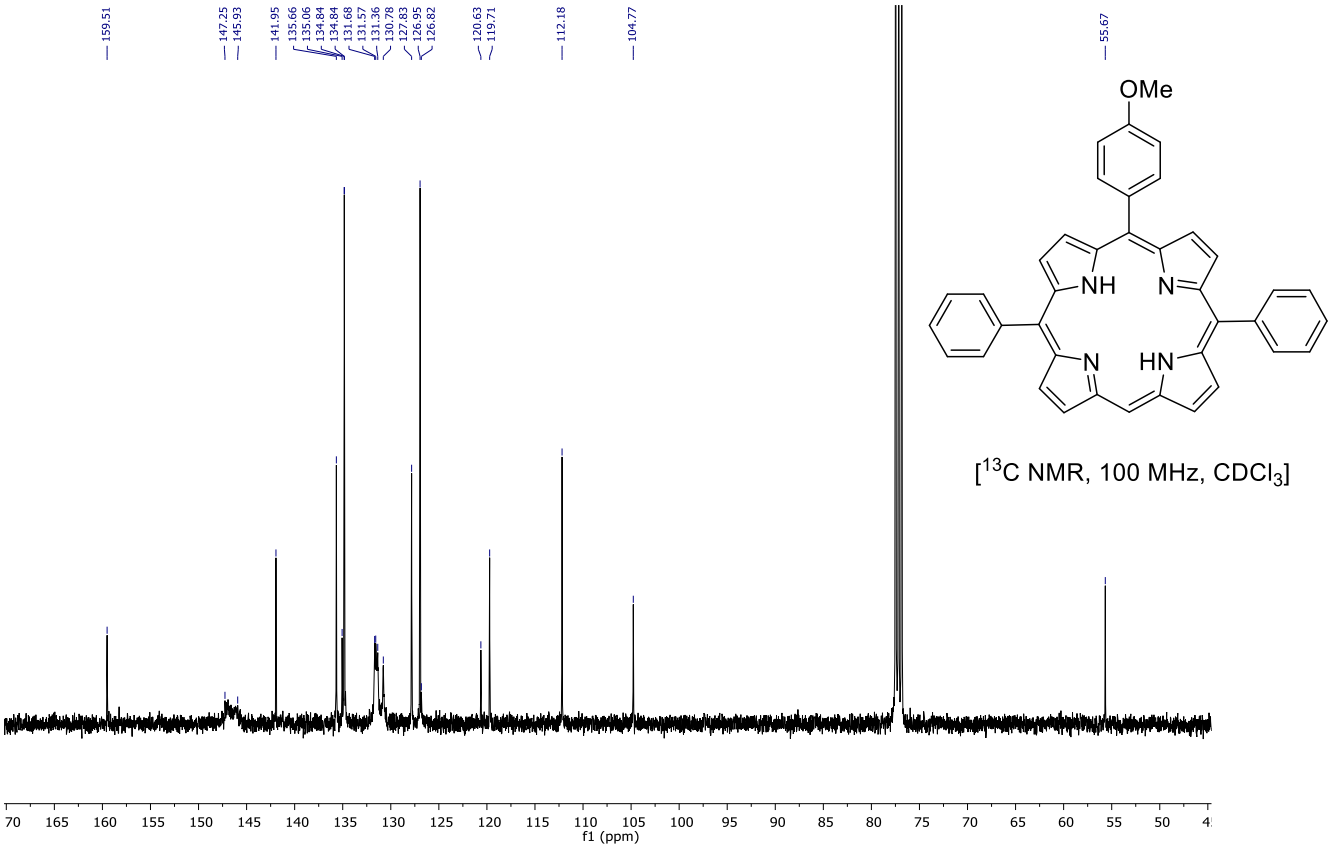

Figure S15: *^{13}C NMR spectrum of **3b** in $CDCl_3$.*

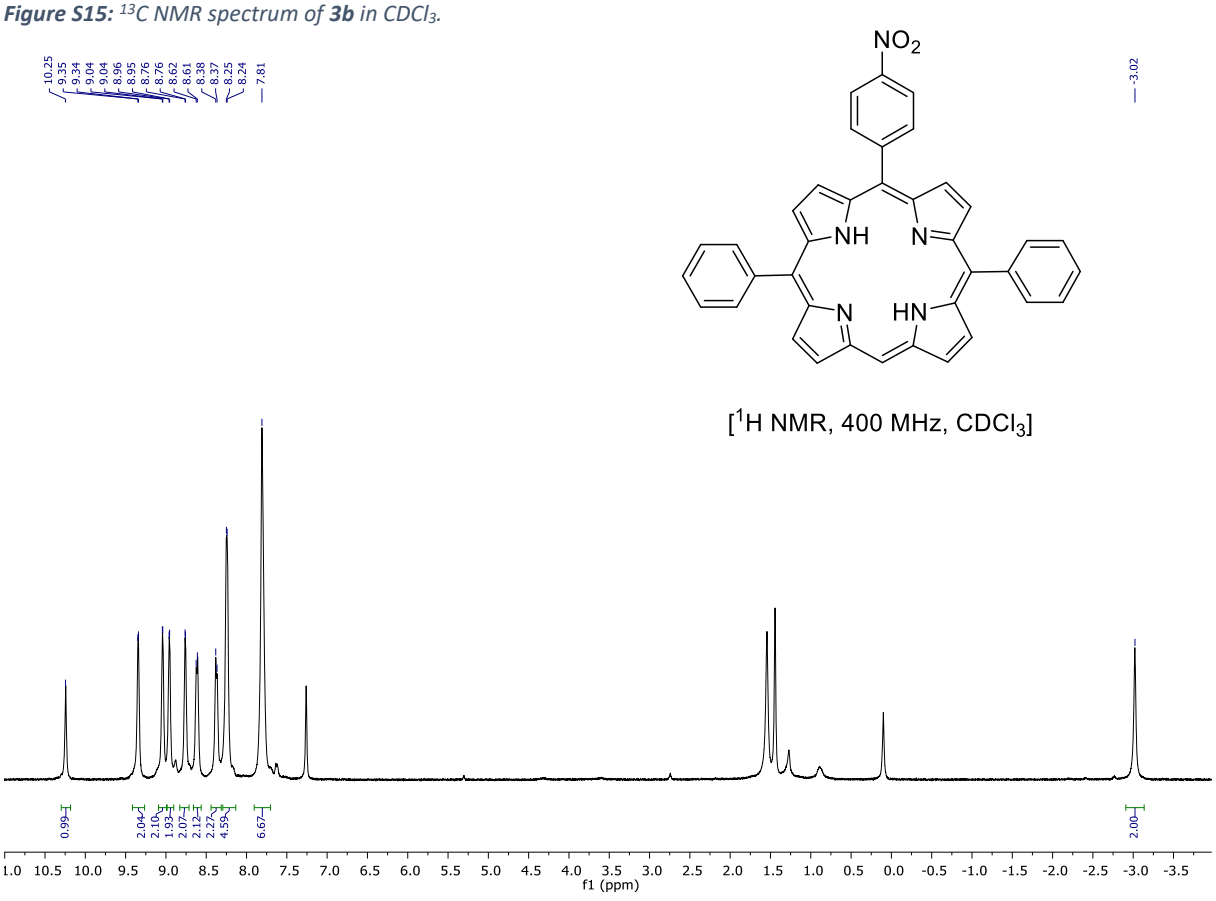

Figure S16: *^{1}H NMR spectrum of **3c** in $CDCl_3$.*

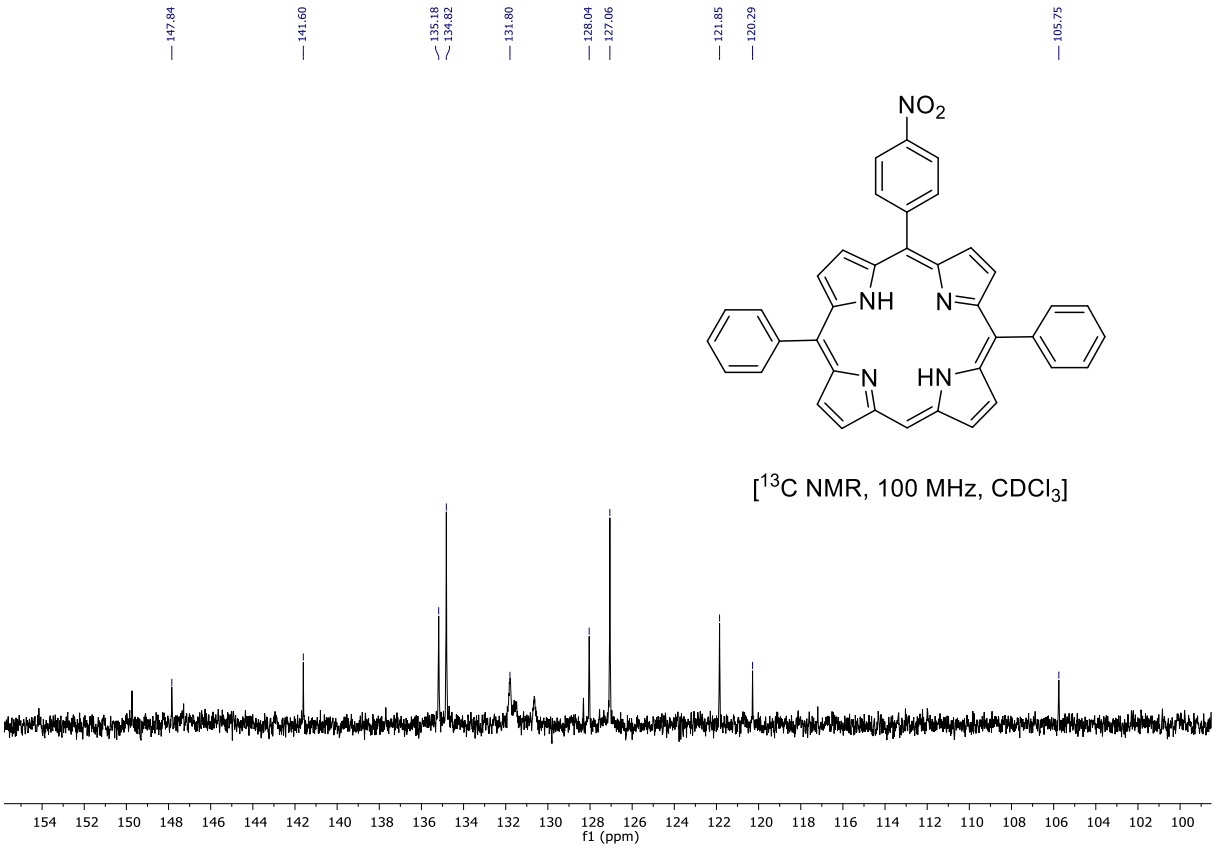

Figure S17: *^{13}C NMR spectrum of **3c** in $CDCl_3$.*

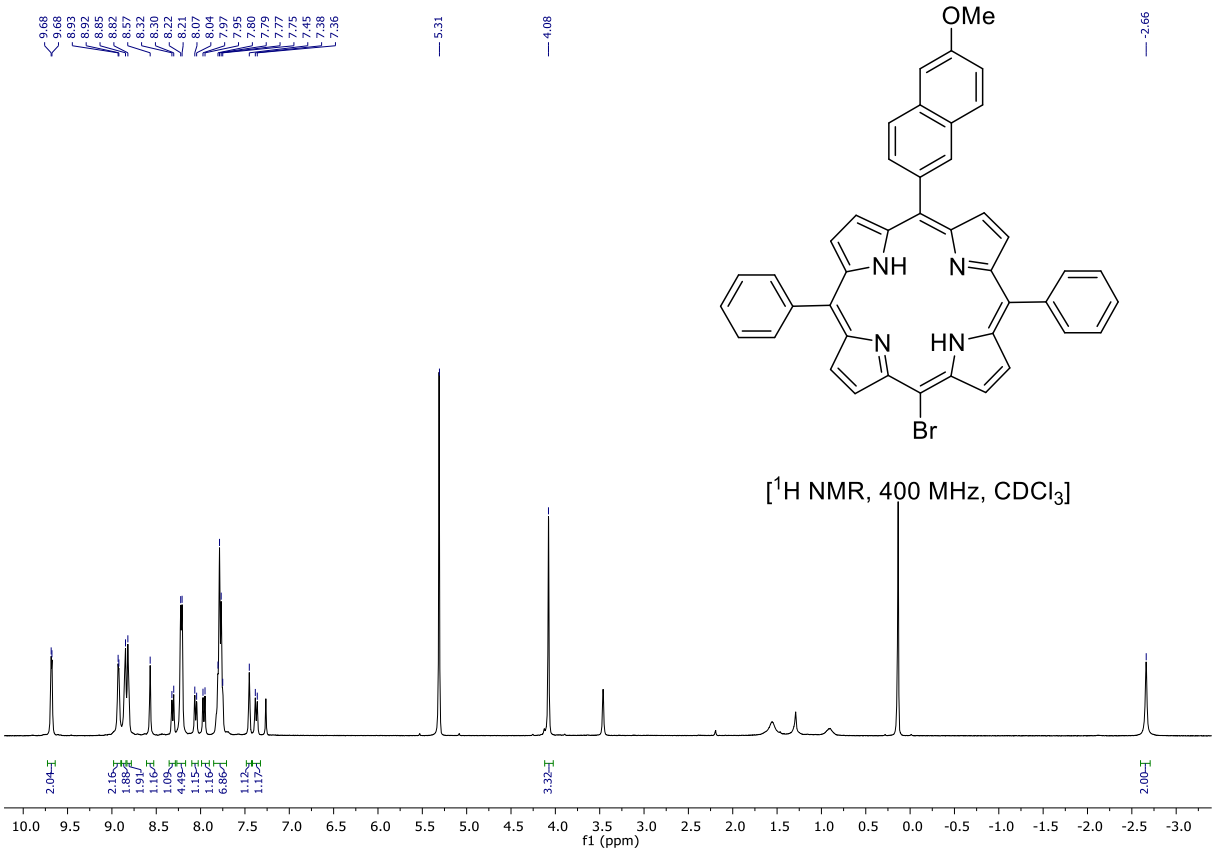

Figure S18 : *^{1}H NMR spectrum of **4a** in $CDCl_3$.*

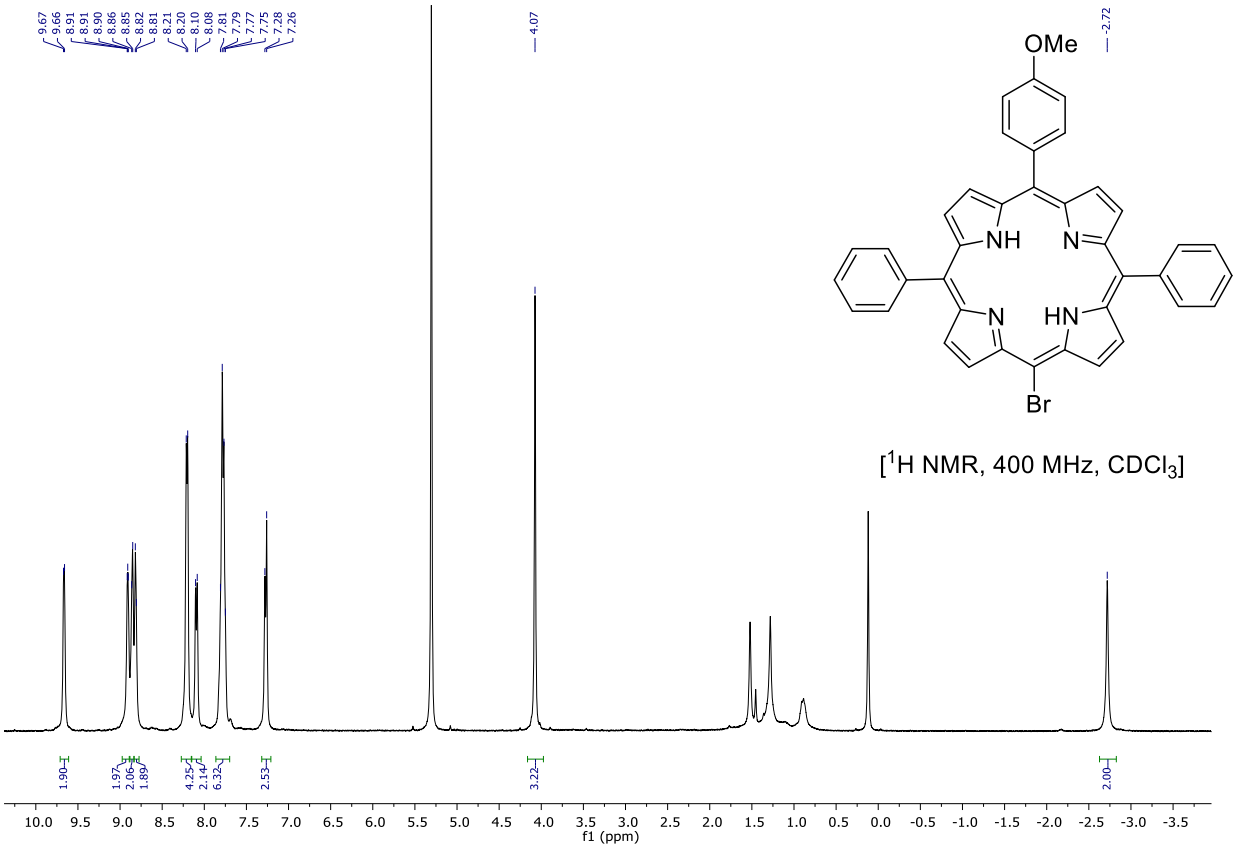

Figure S19: *^{1}H NMR spectrum of **4b** in $CDCl_3$.*

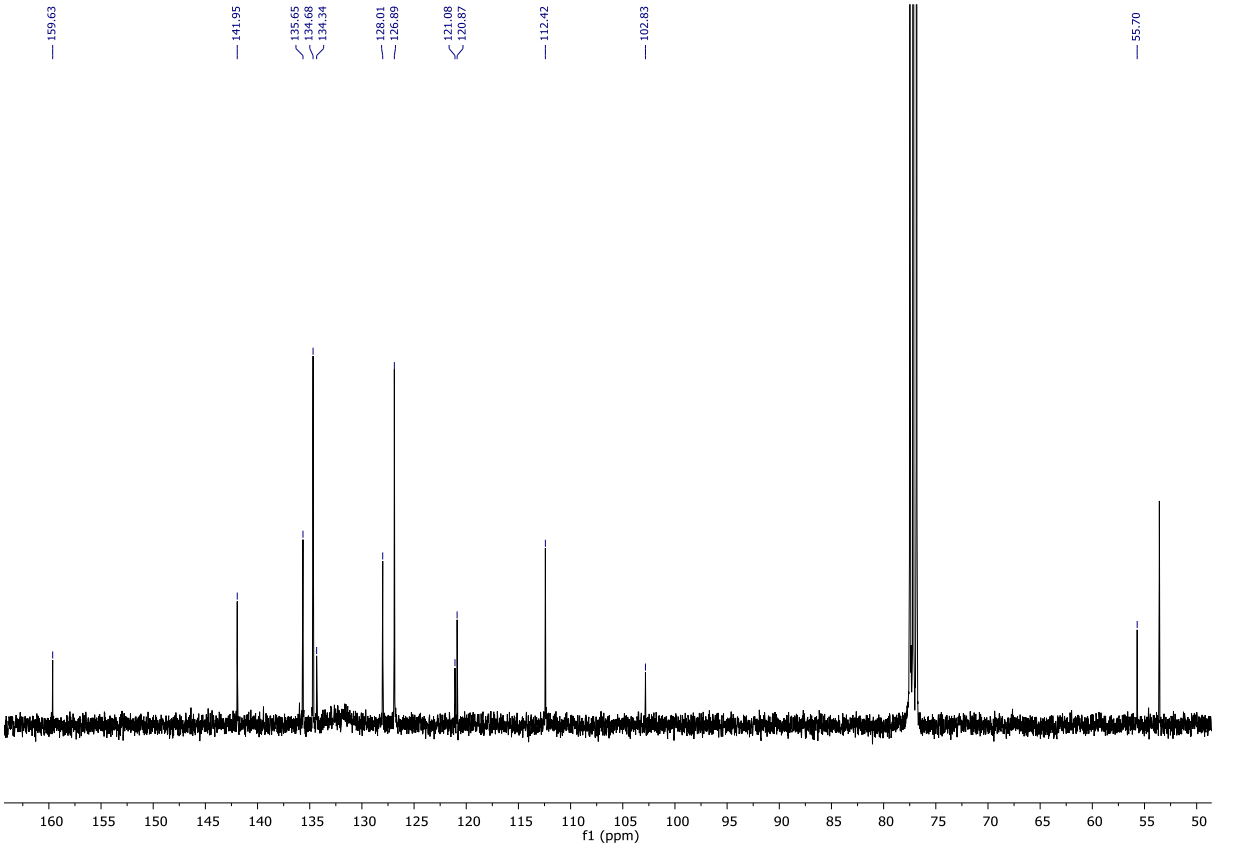

Figure S20: *^{13}C NMR spectrum of **4b** in $CDCl_3$.*

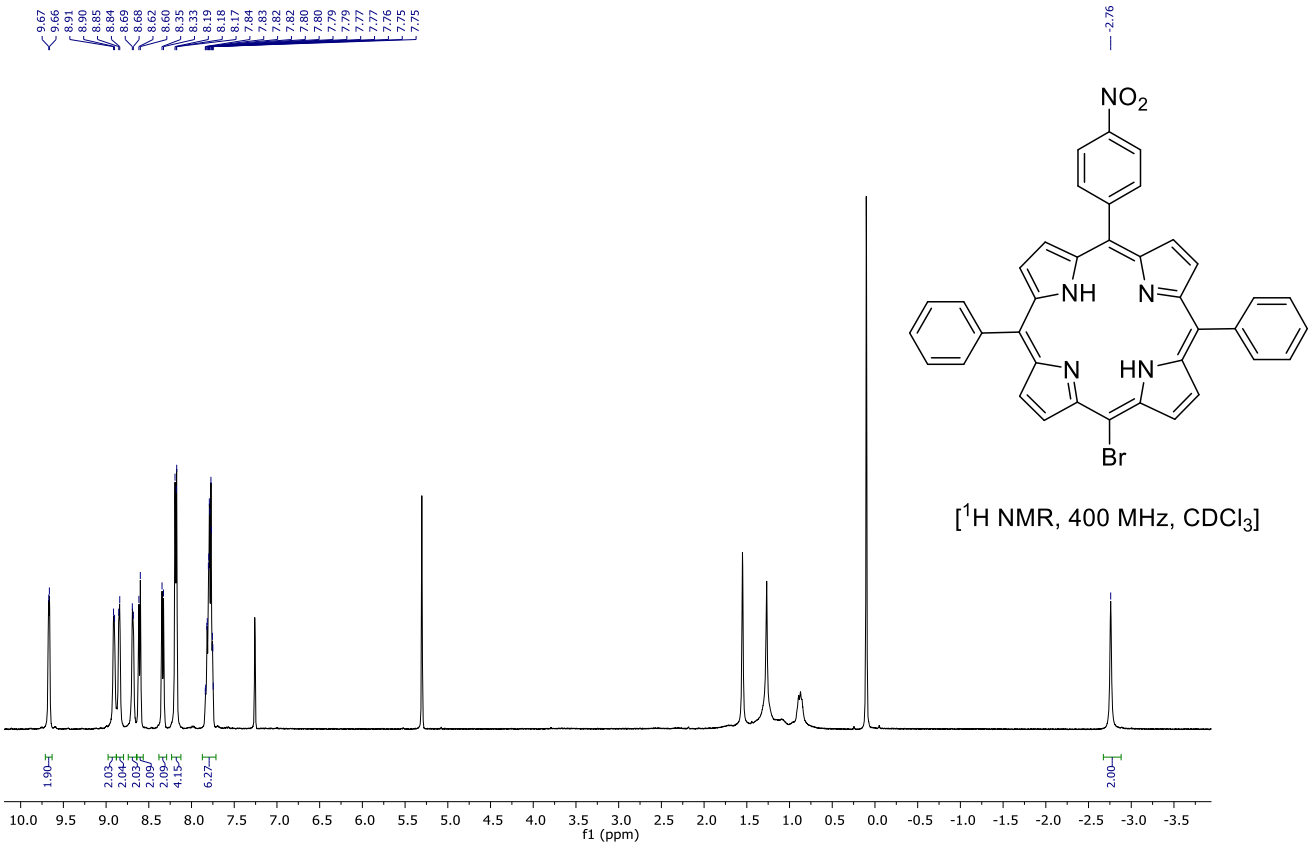

Figure S21: *^{1}H NMR spectrum of **4c** in $CDCl_3$.*

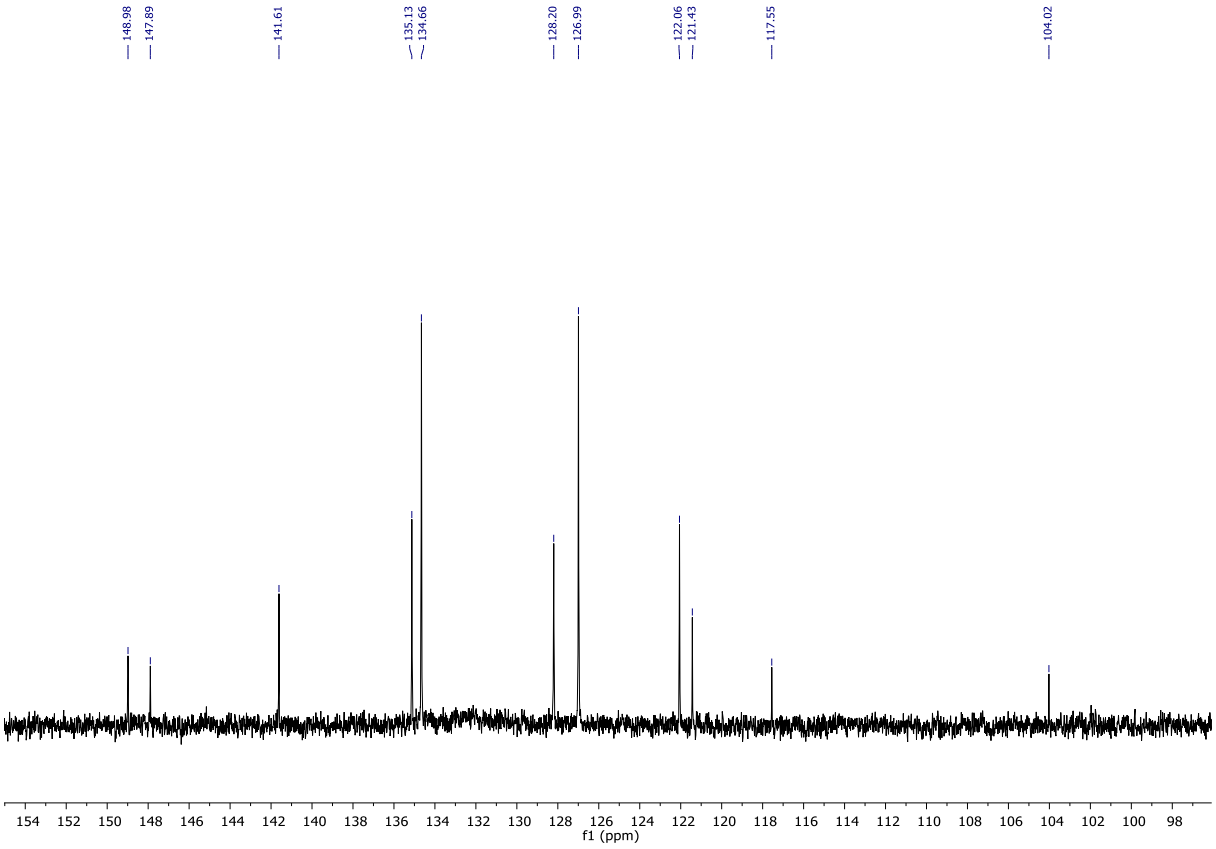

Figure S22: *^{13}C NMR spectrum of **4c** in $CDCl_3$.*

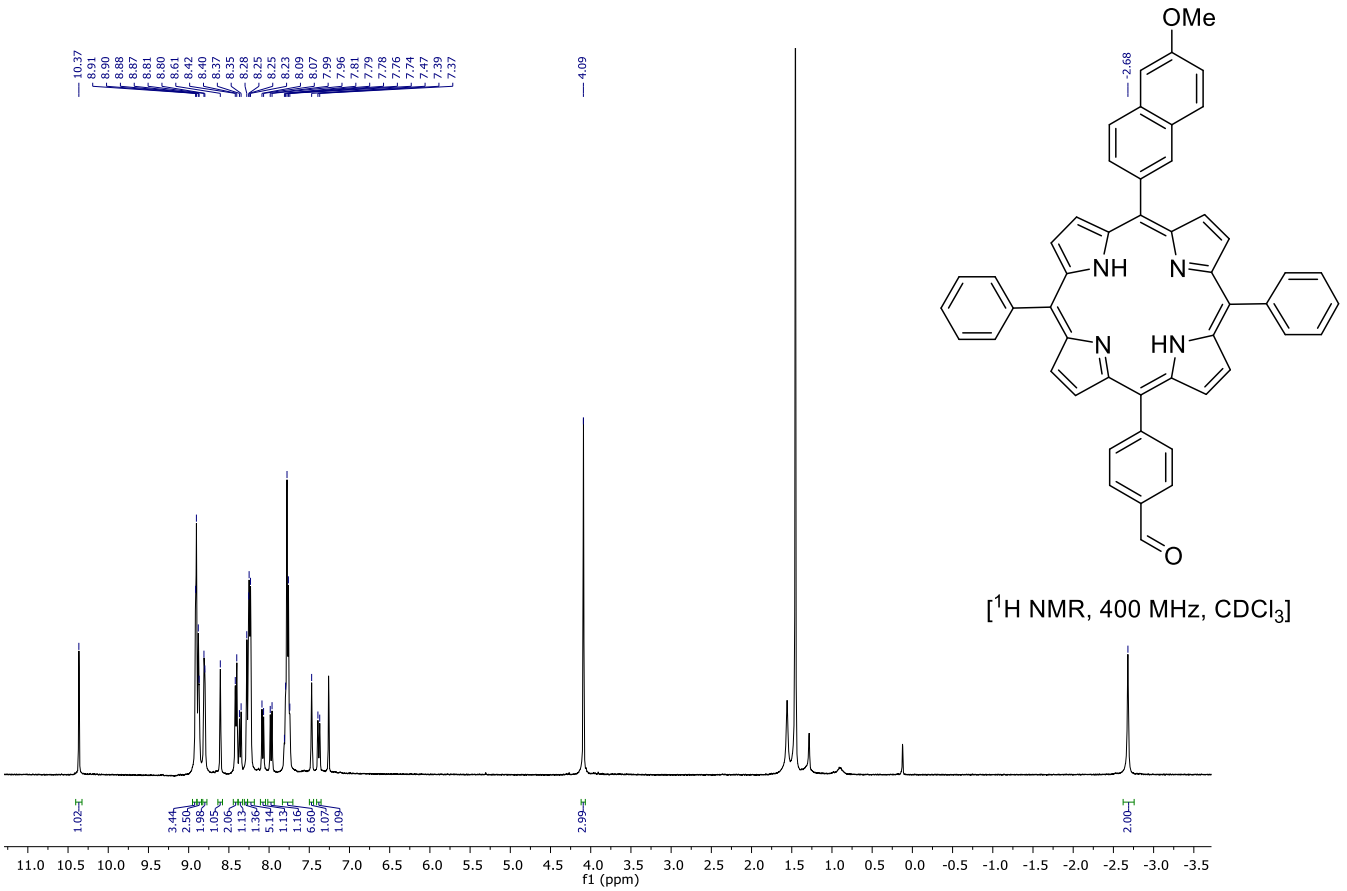

Figure S23: *^{1}H NMR spectrum of **PP1** in $CDCl_3$.*

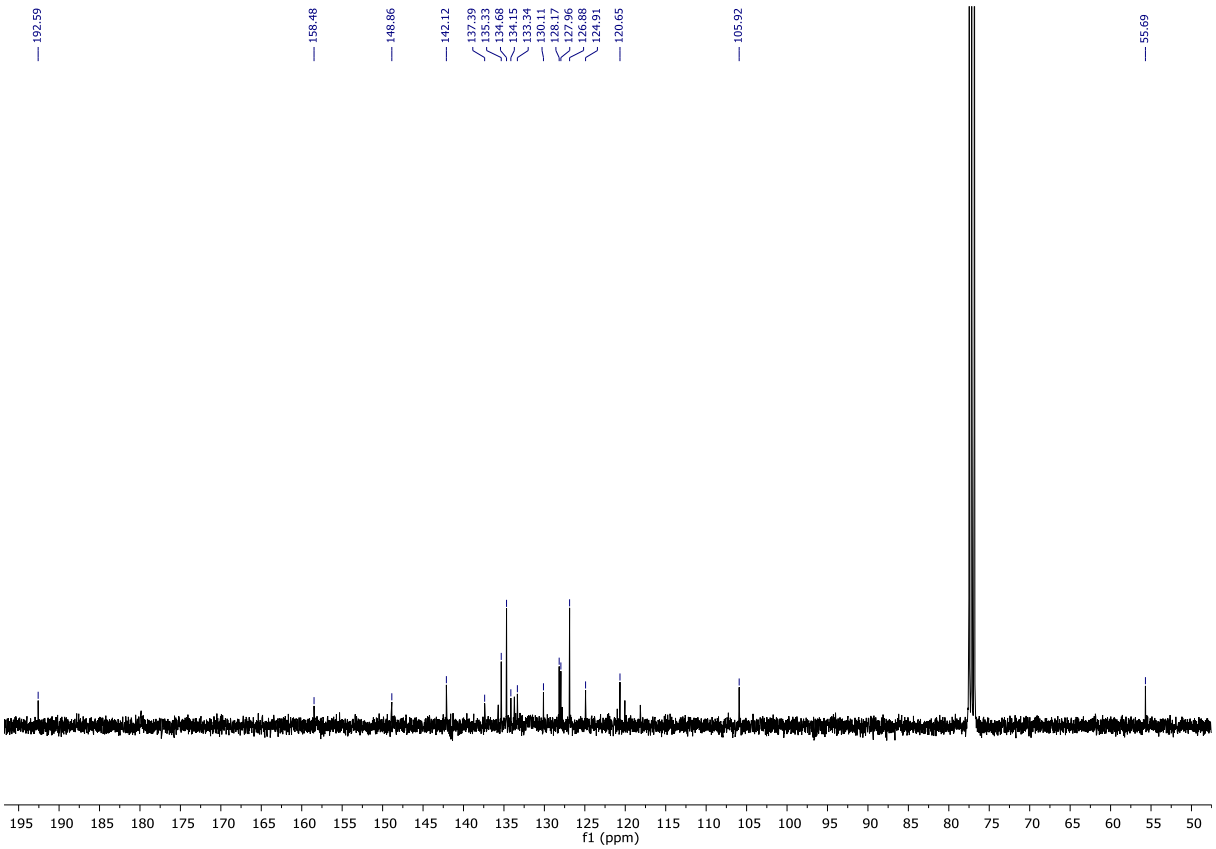

Figure S24: *^{13}C NMR spectrum of **PP1** in $CDCl_3$.*

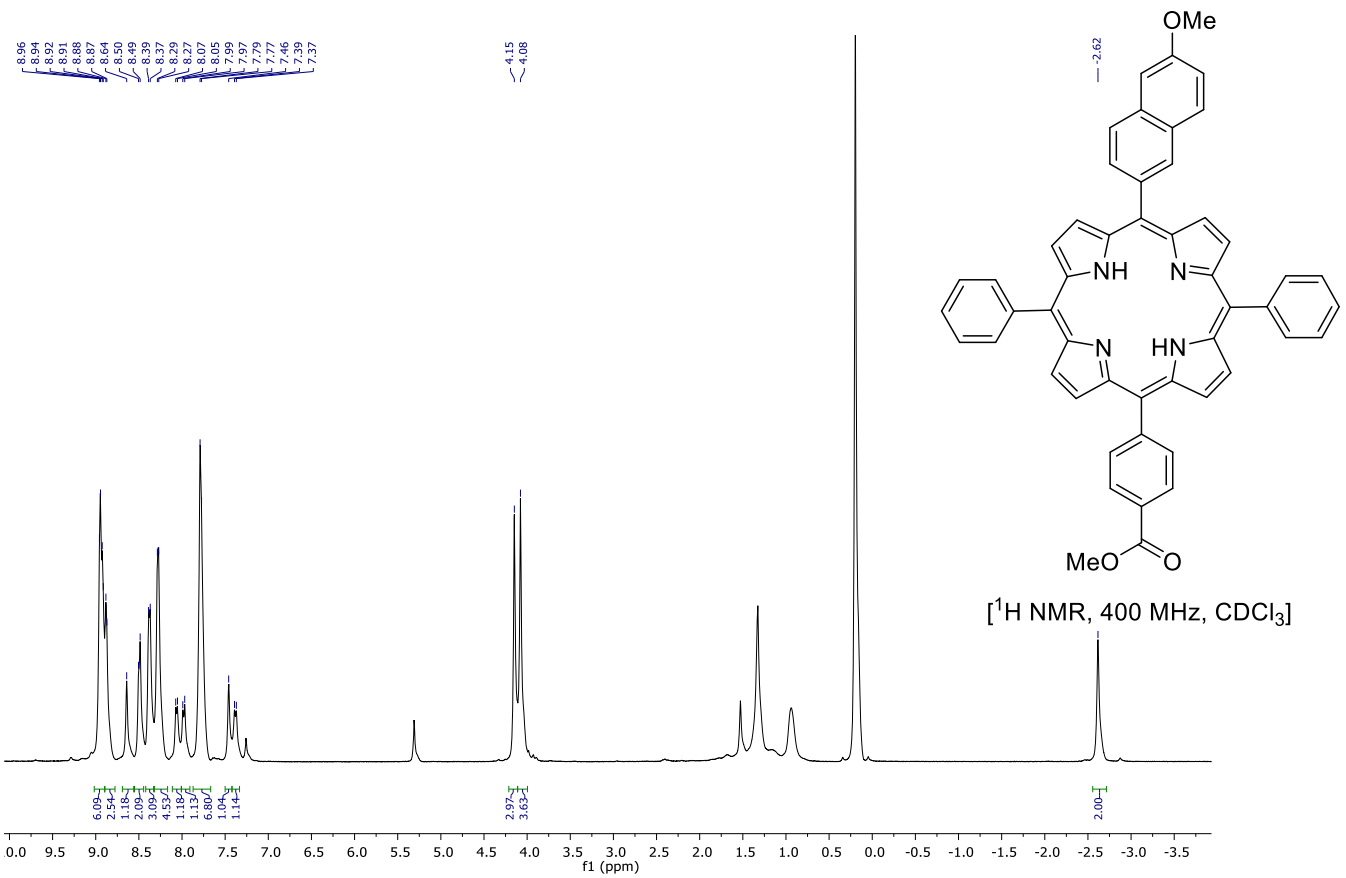

Figure S25: *^{1}H NMR spectrum of **PP2** in $CDCl_3$.*

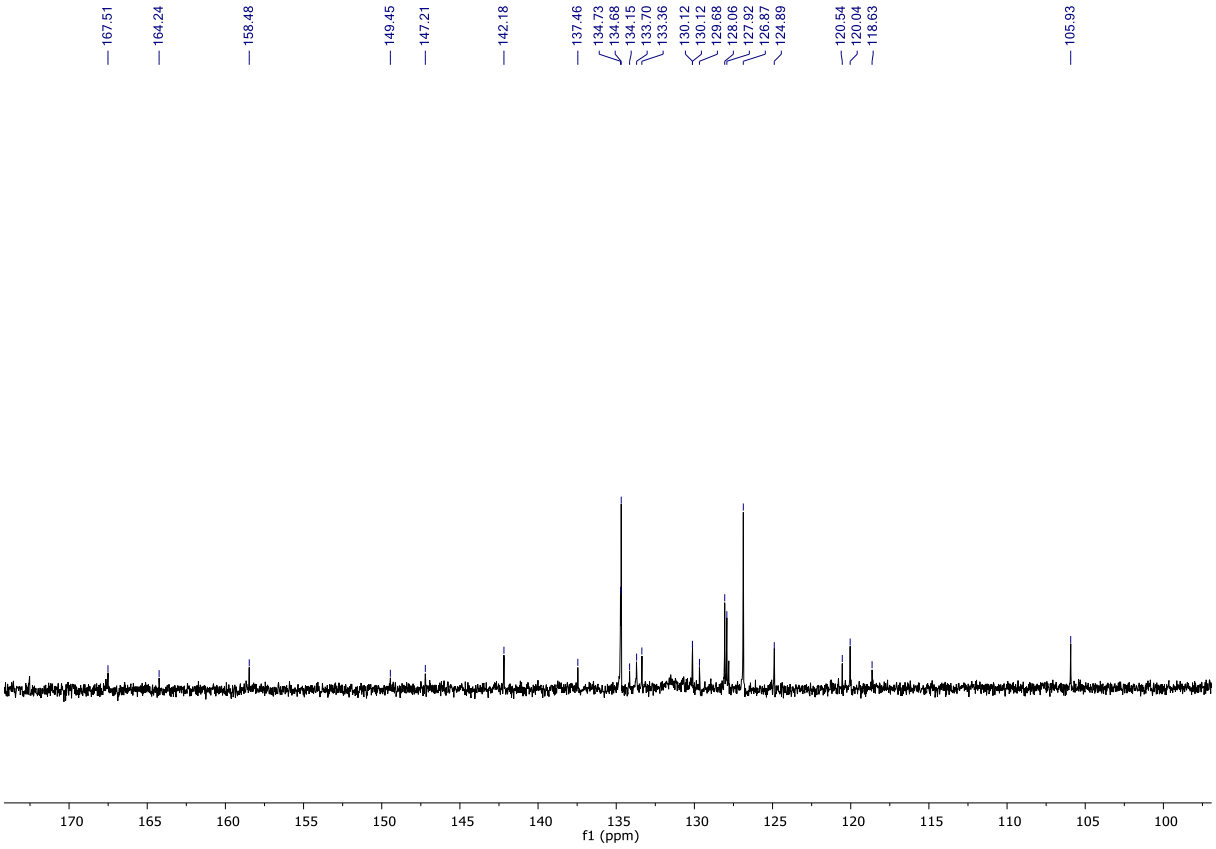

Figure S26: *^{13}C NMR spectrum of **PP2** in $CDCl_3$.*

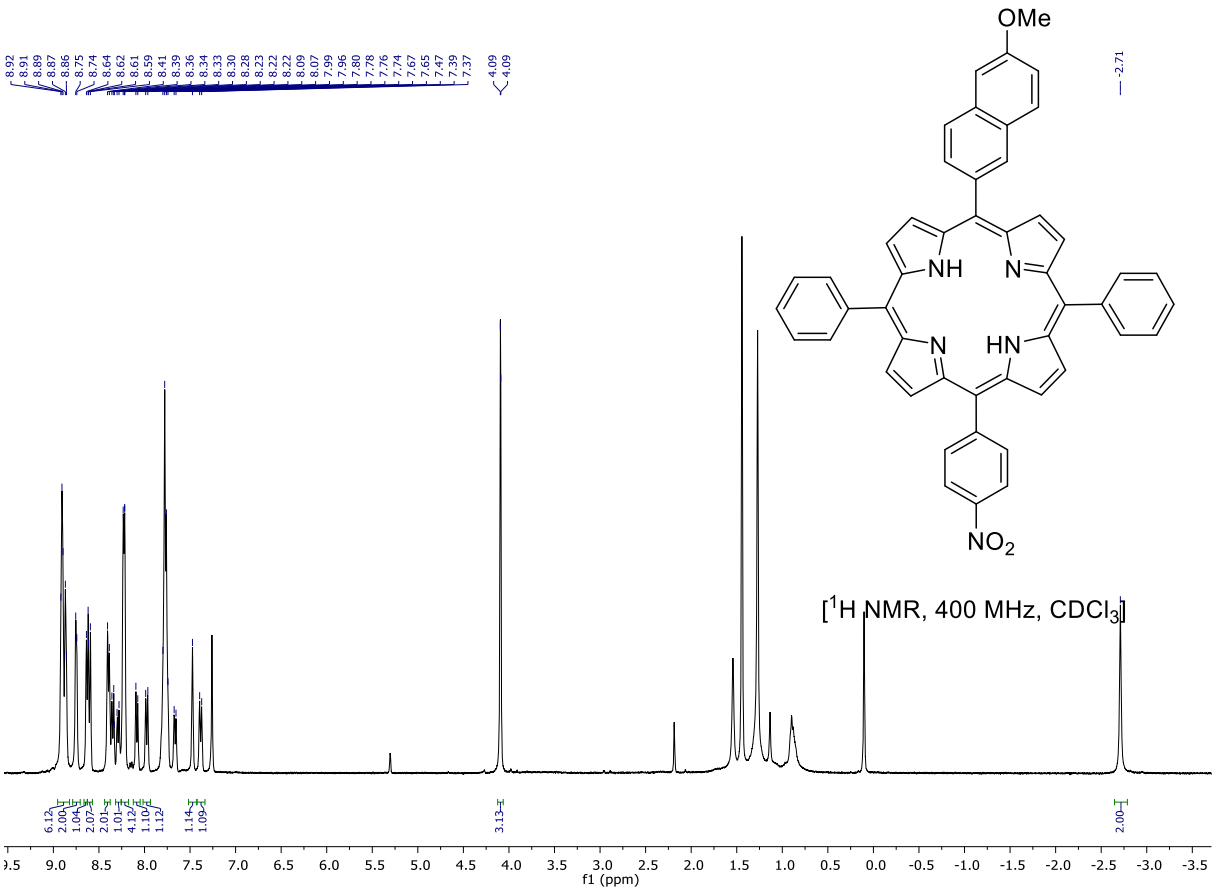

Figure S27: *^{1}H NMR spectrum of **PP3** in $CDCl_3$.*

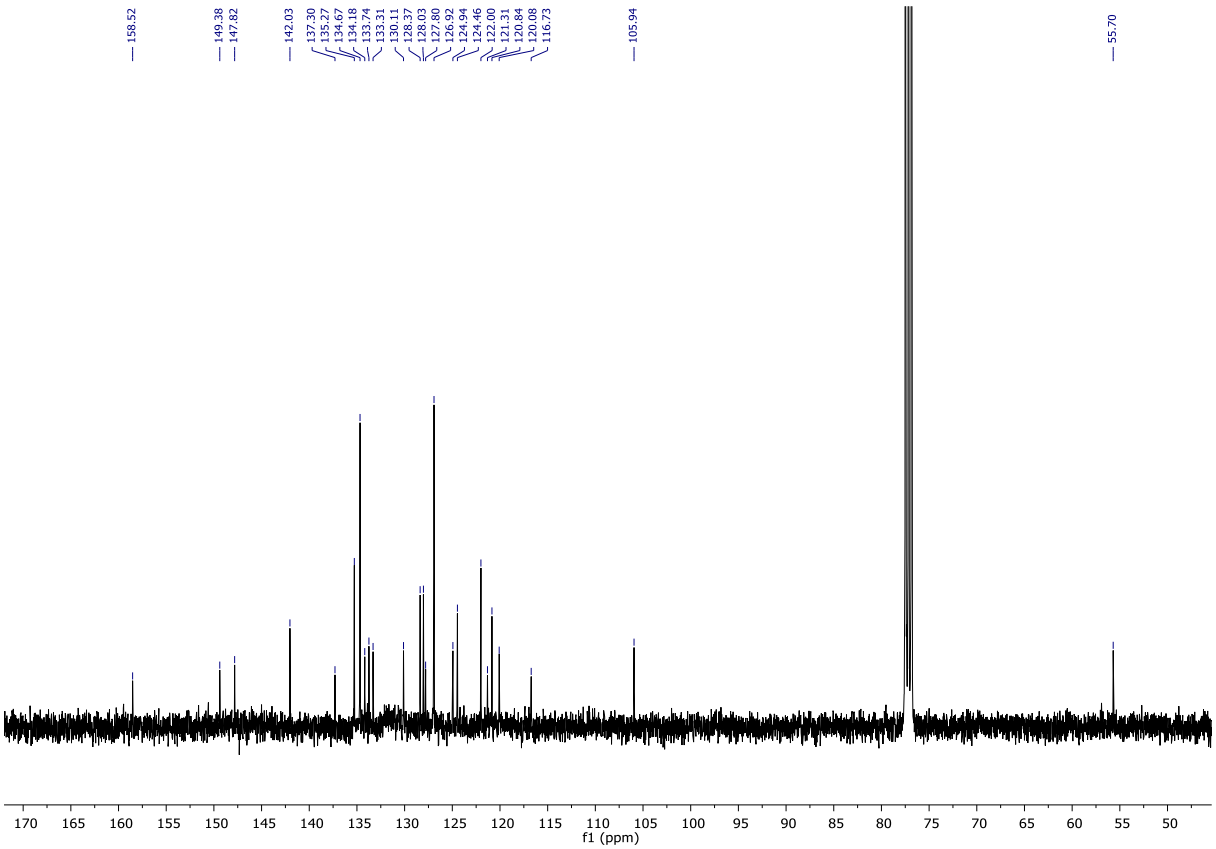

Figure S28: *^{13}C NMR spectrum of **PP3** in $CDCl_3$.*

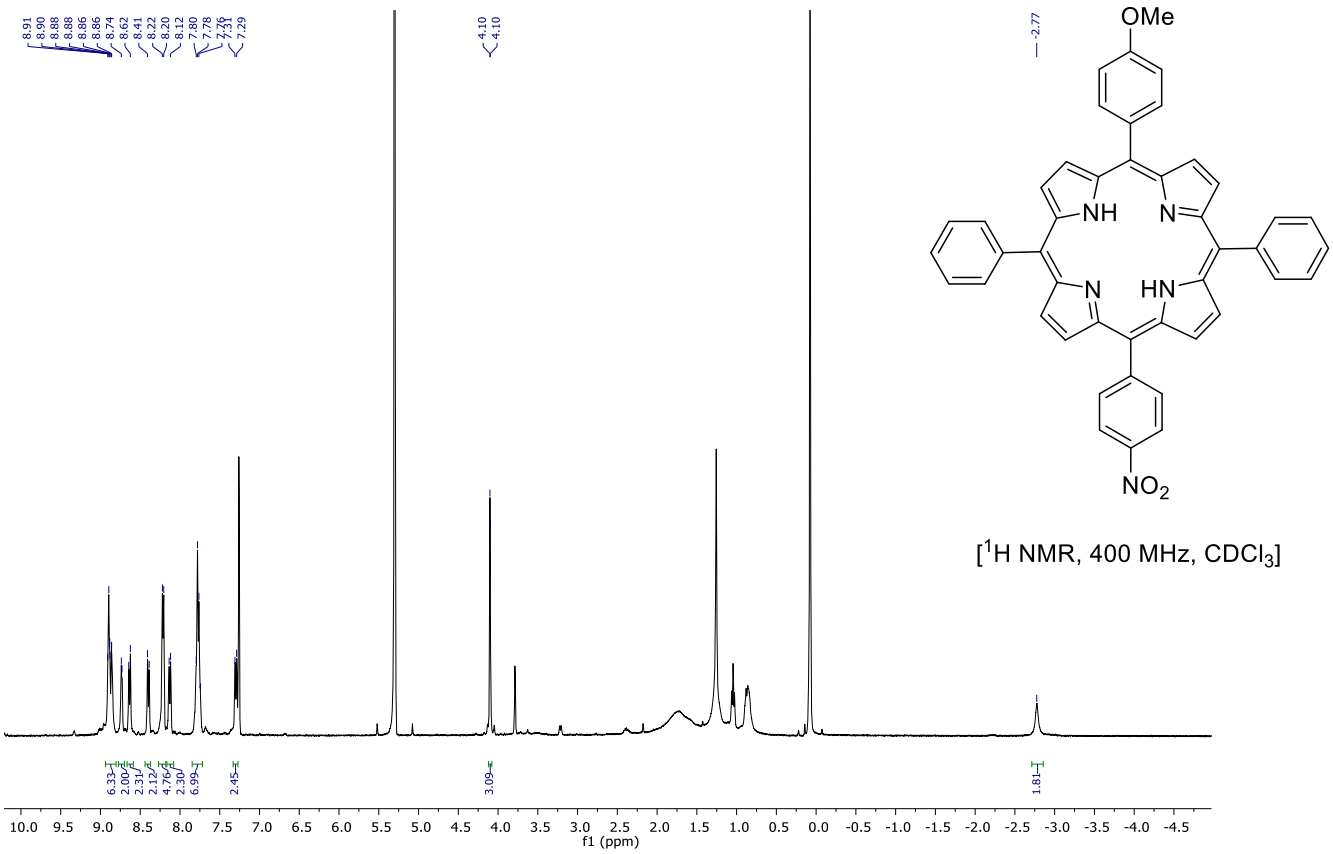

Figure S29: *^{1}H NMR spectrum of **PP4** in $CDCl_3$.*

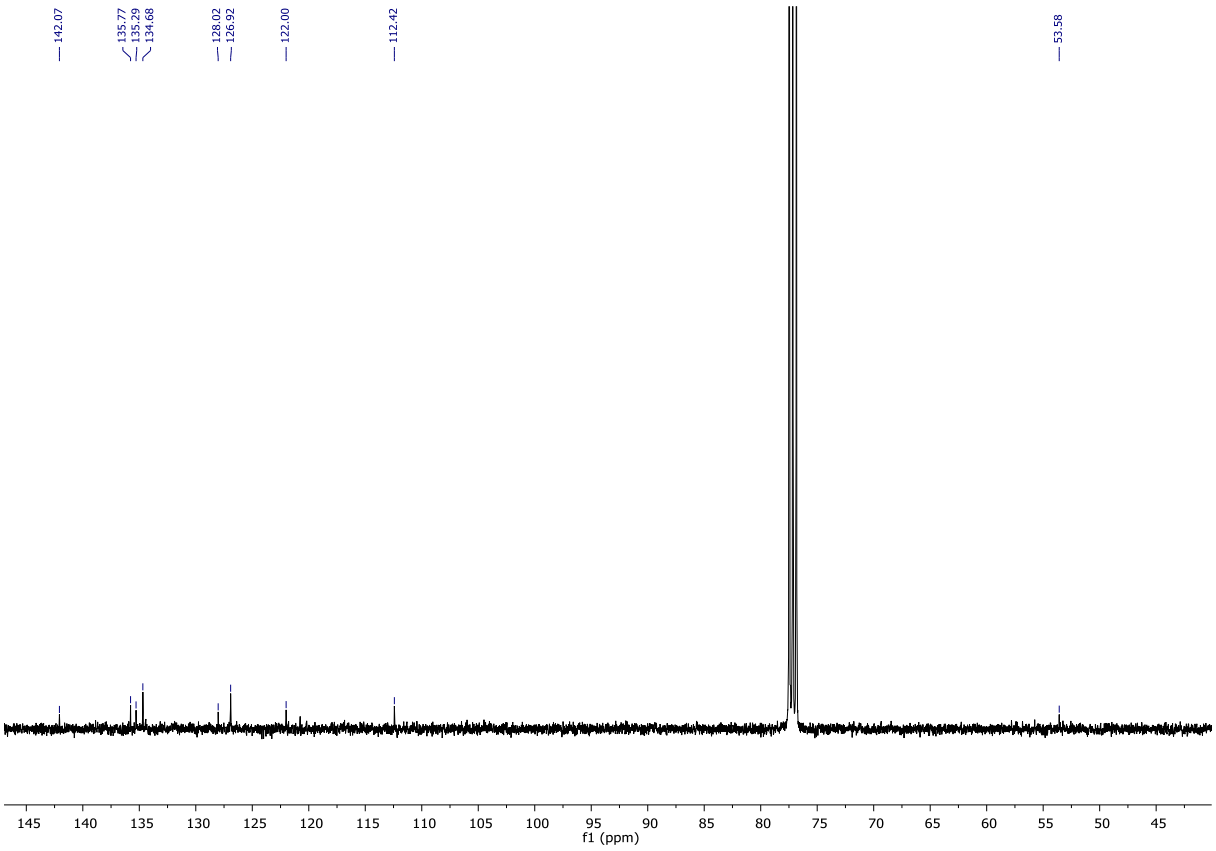

Figure S30: *^{13}C NMR spectrum of **PP4** in $CDCl_3$.*

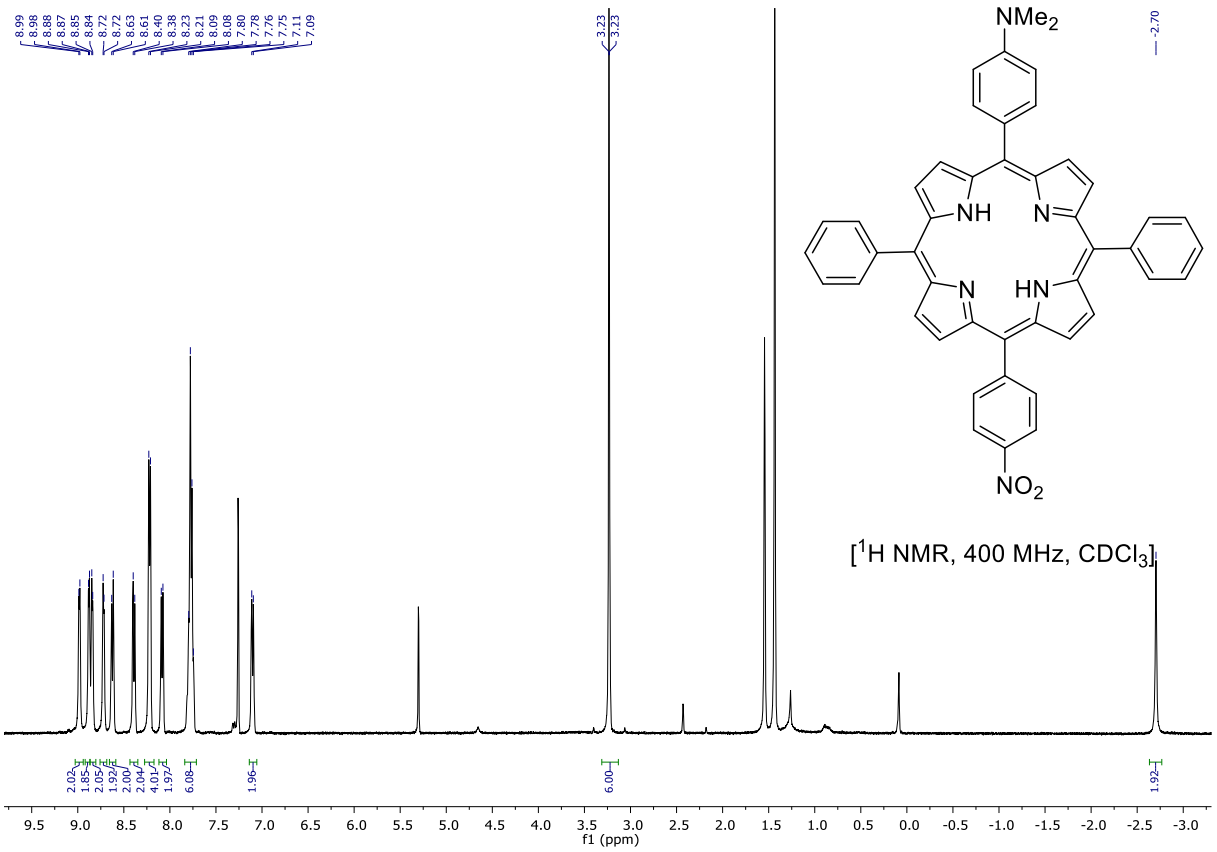

Figure S31: *^{1}H NMR spectrum of **PP5** in $CDCl_3$.*

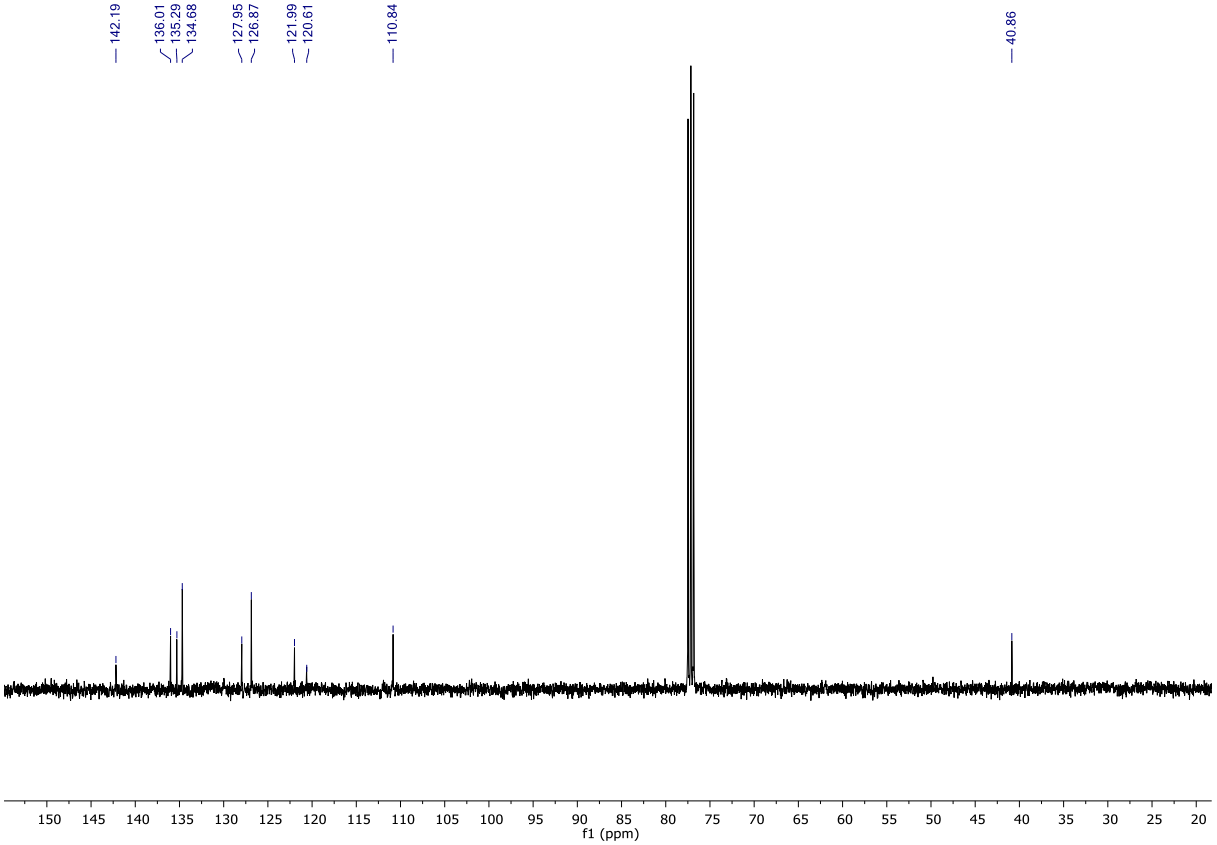

Figure S32: *^{13}C NMR spectrum of **PP5** in $CDCl_3$.*

II. Reduced porphyrins

II. 1. Introduction

To increase the absorption capacity in the visible wavelengths, and especially towards longer wavelengths, it is possible, to modify the porphyrin core to allow greater absorption. In this case, we will no longer speak of porphyrin, but of porphyrin derivatives.

Different derivate can be designed. By reduction of one or two π-bond of the porphyrin core, chlorin and bacteriochlorin can be obtained. The absorption wavelength of the Soret band is not strongly modified, but the absorption of the Q-bands is widely changed. In addition of being redshifted, they have a greatly increased molar absorption coefficient [1–3]. In the porphyrin, the two LUMOs have the same energy. In chlorin and bacteriochlorin however, as the macrocycle is less symmetrical, the two LUMOs are no longer degenerate. For HOMOs, the energies are higher for chlorin and even higher for bacteriochlorin, resulting in lower energy gaps, and thus absorption at higher wavelengths.

Chlorin and bacteriochlorin have already been used for PET-RAFT polymerization, [4,5] but not in FRP. In addition, chlorin presents greater superoxide generation properties, suggesting an improved application in water purification. [6]

II. 2. Computation

Vertical transition energies of tetraphenylchlorin (TPC) and tetraphenylbacteriochlorin (TPB) have been computed by DFT and TDDFT using B3LYP/6-31+G(d). The resulting absorption spectra are presented **Figure IIIB-8**. The high absorption at 500-700 nm of the porphyrin derivate can be observed.

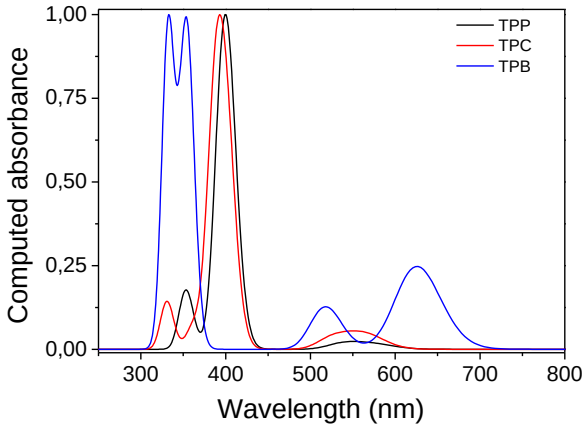

***Figure IIIB-8**: Computed absorbance of TPP, TPC and TPB.*

II. 3. Synthesis

It is possible to reduce the double bonds of porphyrin in successive ways to obtain a mixture of chlorine and bacteriochlorin (**Figure 2**) [4]. The reduction was carried out by successive addition of TsNHNH2 to porphyrin in basic medium (K_2CO_3). A mixture of the expected compounds is obtained with a yield of 41% and a chlorine/bacteriochlorin ratio of approximately 3 to 1, identified by ^{1}H NMR.

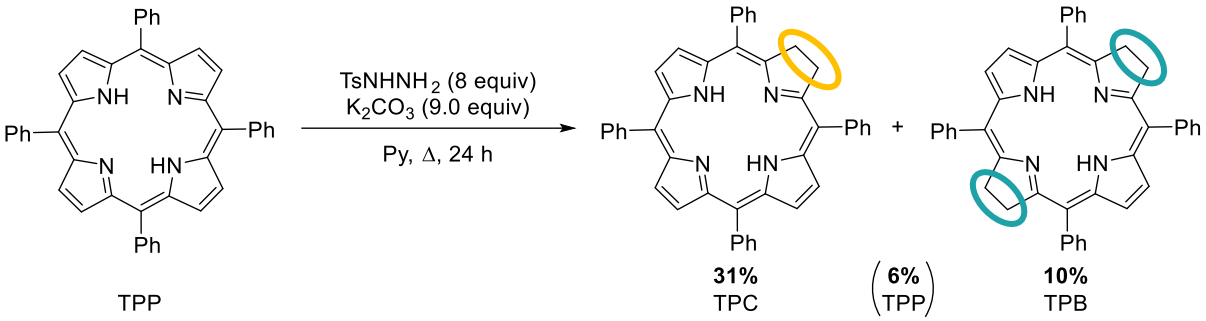

***Figure IIIB-9**: Reduction of TPP into chlorin and bacteriochlorin derivate.*

However, the separation of the compounds is impossible, and the reoxidation of bacteriochlorin into chlorin did not give the expected results. A mixture of compounds was therefore obtained, having a UV-visible absorption spectrum including the different absorption peaks of the compounds (**Figure 3**). Indeed, the peak at 650 nm corresponds to the absorption of chlorin, and the peak at 740 nm to bacteriochlorin.

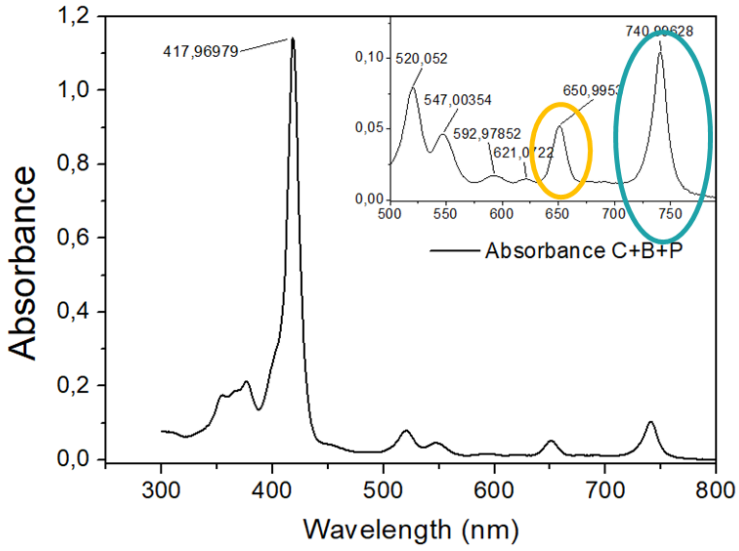

***Figure IIIB-10**: Absorption spectra of CBP mixture, containing absorption peak at 650 nm corresponding to chlorin compound and absorption peak at 740 nm corresponding to bacteriochlorin compound.*

II. 4. Polymerization

Preliminary photopolymerization tests on this mixture were carried out, in order to know its potential efficiency. The polymerization of a system containing 0.5% CBP and 55% MDEA in SOA was monitored by RT-FTIR, following the decrease in the signal corresponding to the acrylate functions. The final conversions to monomers are reported in **Table IIIB-5**, and compared to a system based on TPP. It can be noted that under near-infrared wavelengths (660 nm and 780 nm), the system based on porphyrin derivative manages to obtain monomer conversions of 27 and 36%, where the systems based on TPP do not allow any polymerization.

***Table IIIB-5** : Final acrylate conversion of SOA with different photoinitiator (0.5% wt.) in presence of MDEA (5% wt.), upon different LED (nm)*

System	405 nm/lam	405 nm/air	660 nm/lam	780 nm/lam

TPP/MDEA/SOA	84%	85%	np	np
CBP/MDEA/SOA	80%	95%	27%	36%

II. 5. References

1 W. Zhu, Y.-H. Gao, P.-Y. Liao, D.-Y. Chen, N.-N. Sun, P. A. Nguyen Thi, Y.-J. Yan, X.-F. Wu and Z.-L. Chen, European Journal of Medicinal Chemistry, 2018, 160, 146–156.

2 R. C. e Silva, L. O. da Silva, A. de A. Bartolomeu, T. J. Brocksom and K. T. de Oliveira, Beilstein J. Org. Chem., 2020, 16, 917–955.

3 M. Pineiro, A. L. Carvalho, M. M. Pereira, A. M. d'A. R. Gonsalves, L. G. Arnaut and S. J. Formosinho, Chemistry – A European Journal, 1998, 4, 2299–2307.

4 H. Cao, G. Wang, Y. Xue, G. Yang, J. Tian, F. Liu and W. Zhang, ACS Macro Lett., 2019, 8, 616–622.

5 Q. Ma, W. Wang, L. Zhang and H. Cao, Macromolecular Rapid Communications, 2022, 43, 2200122.

6 E. F. F. Silva, C. Serpa, J. M. Dąbrowski, C. J. P. Monteiro, S. J. Formosinho, G. Stochel, K. Urbanska, S. Simões, M. M. Pereira and L. G. Arnaut, Chem. Eur. J., 2010, 16, 9273–9286.

Conclusions et perspectives du Chapitre III

Dans ce chapitre, la modélisation de plusieurs types de porphyrines a été réalisée, permettant la sélection de diverses porphyrines qui ont ensuite été synthétisées.

La première partie du chapitre a permis de mettre au point une méthode qui a été appliquée pour la modélisation de nombreuses porphyrines. Même si des manquements sont toujours observés, comme l'absence des bandes de vibrations de bandes Q, la méthodologie a permis une bonne vision des propriétés d'absorption des différentes porphyrines.

De plus, deux nouveaux types de structures prometteuses ont été développés pour la photopolymérisation : les porphyrines push pull, contenant un groupement donneur et accepteur, et qui permettent jusqu'à 99% de conversion en monomère, ainsi qu'un mélange de porphyrines réduites, qui permettent des conversions à des longueurs d'onde élevées. Ce dernier type doit encore être plus largement étudié pour déterminer ses réelles propriétés.

Chapitre IV

Utilisation des porphyrines pour la réalisation de matériaux antibactériens

Contexte

Comme il a été décrit dans la partie bibliographique, de nouveaux matériaux antibactériens sont nécessaires. Il a été envisagé deux types de matériaux. Tout d'abord des polymères photosynthétisés grâce à la porphyrine, contenant ces molécules pour produire des ROS et procurer l'effet antibactérien. Ensuite, des polymères photosynthétisés grâce à des porphyrines, mais ne permettant pas leur introduction dans le matériau, et procurant ses effets antibactériens par la présence de monomères antibactériens dans la structure.

Dans la première partie de ce chapitre, la porphyrine **PBP** et son complexe de zinc (II) **PBPZn** (**Figure IV-1**) seront utilisés pour la réalisation de matériaux photosynthétisés photoactifs. Ces porphyrines possèdent des fonctions benzophénone très utilisées dans la photopolymérisation sous irradiation UV. Des systèmes photoamorceurs seront développés pour la polymérisation radicalaire de l'huile de soja acrylatée, mais également la polymérisation cationique d'un monomère contenant des fonctions époxyde. Les matériaux obtenus seront ensuite exploités pour des applications en surfaces antibactériennes.

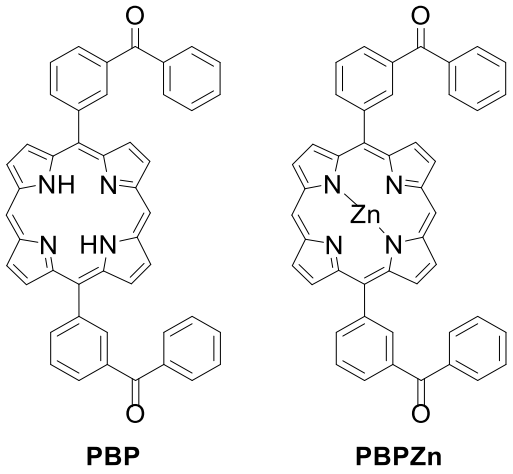

***Figure IV-1**: Structures des porphyrines PBP et PBPZn utilisées dans la partie A du chapitre.*

Enfin, les porphyrines peuvent également amorcer un autre type de polymérisation, la polymérisation PET-RAFT, permettant de développer des polymères de structure contrôlée. Le contrôle de l'addition des monomères permet d'obtenir des structures complexes, intégrant des monomères antibactériens, qui confèrent une activité antibactérienne aux polymères ainsi obtenus. Afin de pouvoir réaliser ces matériaux, il est d'abord nécessaire de déterminer les porphyrines les plus prometteuse pour ce type de polymérisation. C'est pour cela que les porphyrines étudiées au cours du manuscrit ont été étudiées pour la polymérisation PET-RAFT, en utilisant en premier lieu un monomère qui n'est pas antibactérien, pour développer une nouvelle méthode. C'est ce principe qui est présenté dans la **partie B** de ce chapitre. Une fois la méthode mise au point, des applications avec des monomères biosourcés pourront alors être envisagées

Partie A : Article 4 – Porphyrin-based photosensitizers for visible-light polymerization and antibacterial applications

Fanny Schnetz, [a] Iryna Knysh, [b] Denis Jacquemin, [b,c] Samir Abbad Andaloussi, [d] Marc Presset, [a] Sonia Lajnef, [e] Fabienne Peyrot, [e,f] Davy-Louis Versace *[a]

Abstract.

This study highlights the outstanding photo-initiating properties of two new visible-light absorbing benzophenone porphyrin-based photosensitizers (PBP and PBPZn) for the free-radical (FRP), cationic (CP) photopolymerization and thiol-ene reactions under visible LEDs exposure (405, 505 and 530 nm) under air or in laminate, and at low intensities. As confirmed by electronic paramagnetic resonance spin trapping (EPR ST) and Laser Flash Photolysis studies, both porphyrins play a dual role as electron donor molecule when combined with iodonium salt (Iod) and participate in a H-abstraction reaction in association with N-methyldiethanol amine (MDEA) or thiol derivatives (cysteamine or N-acetylcysteine). For the first time, interesting kinetic profiles for the polymerization of a bio-based monomer (SOA) are observed under blue and green-light irradiation. Notably, the 4-methylphenyl-, aminoalkyl- and thiyl radicals which are generated from the photolysis of porphyrin/Iod, porphyrin/MDEA and porphyrin/cysteamine (or N-acetylcysteine) respectively, can initiate the radical polymerization of SOA and very high FCs are observed; up to 90% under LED@405 nm and > 60% under LED@530 nm exposure. Finally, PBPZn-based materials demonstrated photoactivable properties for antibacterial applications. Under visible-light irradiation, these materials can produce biocide reactive oxygen species (ROS) leading to a tremendous inhibition of S. aureus proliferation.

Graphical abstract.

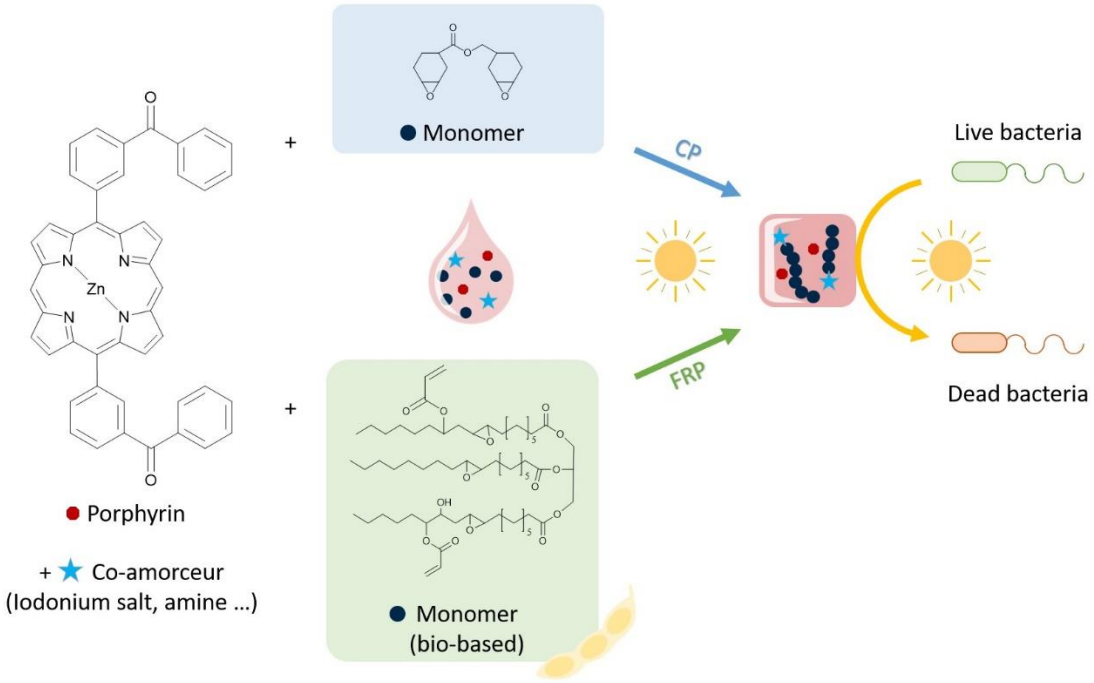

Introduction

Photochemistry gained an attracting growing interest over the last decade [1] and offers a wide range of applications [2–9] in, e.g., adhesives, microelectronics, coatings, 3D-printing processes, and (bio)medical applications. Photochemistry allows the synthesis of new materials in a reduced time without the use of harmful solvents. Extensive studies related to photopolymerization process used UV-light irradiation, however, and due to UV-handling safety issues in dentistry or in other medical fields,[10,11] its use was prohibited. This prompted researchers to focus on designing new visible-light absorbing photo-initiators or photo-initiating systems. Many examples of type I or type II, and blue-light photosensitive systems for free-radical (FRP) and cationic (CP) photopolymerization can therefore be found in literature.[12–17] Many relevant reviews have notably described such advances.[18–23] However, examples of photo-initiation under both blue and green light irradiations remain scarce highlighting the related challenges. In this context, porphyrin derivatives appear as valuable alternatives to the existing systems since their broad absorption range in the visible spectrum, and their high molar absorption coefficients between 10^3 and 10^6 $L.mol^{-1}.cm^{-1}$ are promising.

Although porphyrin derivatives have been used in a wide range of applications from photodynamic therapy to photocatalysis,[24–26] and also found an impressive enlightenment in PET-RAFT for the synthesis of well-defined polymers with controlled molecular weights,[27,28] only few examples concern their uses in free-radical (FRP), cationic (CP) photopolymerizations or thiol-ene reactions. For instance, 5,10,15,20-tetraphenyl-porphyrin Zinc (ZnTPP) was used for sensitizing diphenyliodonium chloride (DPI) in the presence of *N*-methyldiethanol amine (MDEA) for FRP and CP [29] under UV-light irradiation. Recently, Lalevée et al. highlighted the high initiating performance of ZnTPP when combined with *bis*(4-*tert*-butylphenyl) iodonium hexafluorophosphate (Iod) using visible emitting diodes.[30] Remarkably, 3D epoxy films from the photosensitive formulation *i.e.* ZnTPP/Iod/(3,4-Epoxycyclohexane)methyl 3,4-epoxycyclohexylcarboxylate), were synthesized using LED@405 nm projector. In light of these results, a series of metalloporphyrin based on palladium, copper, zinc, and iron ions complexation have been tested with iodonium salt to initiate the FRP of a mixed methacrylate resins (Mix-MA) in oxygen conditions at 405 nm and 785 nm.[31,32] Despite the high absorption properties of these porphyrin derivatives, the final methacrylate conversion under air remains smaller than 30% with a LED@405 nm irradiation. However, they demonstrated that the addition of a phosphine derivative (*i.e.*, 4-(diphenylphosphino)benzoic acid) and the thermal initiator BlocBuilder®MA to the bicomponent photo-initiating system (ZnTPP/Iod) could enhance the final methacrylate conversions of Mix-MA under LED@785 nm. More recently, pyropheophorbide *a* (Pyro), and its corresponding zinc (II) complex (Zn-Pyro) were used to perform FRP under visible and NIR irradiation when combined with Iod and thiol-amine cysteamine (Cys).[33] Approximatively, 80% of the acrylate of PEG-diacrylate were consumed with this three-component photo-initiating system, *i.e.*, Zn-Pyro/Iod/Cys, under LEDs@405nm irradiation.

In this context, two benzophenone-based porphyrins (5,15-di(3-benzophenone)porphyrin **PBP** and its zinc complex **PBPZn**) have been designed herein and used as visible-light photosensitizer. Low-intensity blue LED (405 nm) and green LEDs (505 and 530 nm) were used to evaluate the initiating properties of such porphyrins when combined with either electron acceptor molecule (*i.e.*, iodonium salt), electron donor co-initiator (*i.e.* MDEA) or H-donor molecules (*i.e.* cysteamine and *N*-acetyl cysteine). The kinetic performances on the FRP of a bio-based acrylate monomer (SOA) with different bi-component photo-initiating systems, *i.e.*, porphyrin/MDEA and porphyrin/Iod, were evaluated and compared with popular photosensitizers (benzophenone and camphorquinone). The thiol-acrylate reactions with SOA using porphyrin/cysteamine (or *N*-acetyl cysteine) were also investigated and the CP of 3,4-Epoxycyclohexylmethyl 3,4-epoxycyclohexanecarboxylate (EPOX) with porphyrin/Iod was kinetically followed by Real-Time Fourier-Transformed Infrared spectroscopy (RT-FTIR). The originality of the study lies in the use of new porphyrin derivatives not only as photosensitizers of Iod for blue and green-light initiated FRP and CP, but also as a H-abstractor agent to perform thiol-acrylate polymerization when combined with cysteamine (derived from the degradation of coenzyme A [34]) or *N*-acetyl cysteine (which is obtained after acetylation of L-cysteine produced by fermentation).[35 36] This is indeed, to the best of our knowledge, the first reported study describing the use of porphyrins in a bi-component photo-initiating systems with fully bio-based and performing co-initiators (cysteamine and *N*-acetyl cysteine). The electronic transition properties of **PBP** and **PBPZn** were studied by molecular modelling and their photo-reactivity were investigated at both singlet and triplet states by steady-state photolysis, fluorescence, laser flash photolysis, and electronic paramagnetic resonance spin-trapping (EPR ST). The photo-initiating properties of the different photosensitive systems were also described by RT-FTIR by following the decrease of the acrylate or epoxy functions of the corresponding monomers under light irradiation under air and in laminate. Finally, the final photo-induced materials generated from the photopolymerization of SOA using **PBPZn**/MDEA and incorporating **PBPZn** were evaluated as a possible photoactive antibacterial material.

Experimental

Chemical

Ethyl acetate, dichloromethane (DCM), carbon tetrachloride, chloroform, petroleum ether, diethyl ether, acid acetic, ethanol and methanol were used as received. For the Suzuki coupling, THF was distilled under argon using sodium and benzophenone. Reactant, *i.e.* trifluoroacetic acid (TFA), *m*-tolualdehyde, tetra-*n*-butylammonium bromide, azobisisobutyronitrile (AIBN), $AgNO_3$, trimethylamine, zinc acetate were provided by Merck, Bromobenzene, *N*-bromosuccinimide (NBS), pyrrole, paraformaldehyde and 2,3-dichloro-5,6-dicyano-1,4-benzoquinone (DDQ) were received from TCI. The acrylate and epoxy based-monomers, *i.e.* soybean oil acrylate (SOA) and 3,4-epoxycyclohexylmethyl-3,4-epoxycyclohexanecarboxylate (EPOX), the co-initiators, *i.e. N*-methyldiethanol (MDEA), 4-(2-methylpropyl)phenyliodonium hexafluorophosphate (Iod), cysteamine and *N*-acetyl-cysteine, 2,3,4,5-tetraphenylcyclopentadienone (TPCPD), 5,5-dimethylpyrroline-*N*-oxide (DMPO) and 1,3-diphenylisobenzofuran (DPBF) were all provided from Merck and used as received. The chemical structures of the molecules from the photo-initiating systems and monomers used in this study are described on **Table 1**.

Material characterization

Analytical thin layer chromatography (TLC) was performed on fluorescent indicator (Merck 60F254) precoated on TLC silica gel plates (0.25 mm). Visualization was effected using ultraviolet light (λ = 254 nm) or with an aqueous solution of $KMnO_4$. Flash chromatography was performed on 40–63 µm silica gel. Gas chromatography was recorded on a Shimadzu 2025 chromatograph (T_{inj} = T_{det} = 250 °C) with a ZB-5MSi capillary column (l = 5.5 m), using nitrogen as carrier gas and a flame ionization detector. UV-Visible absorption spectra were recorded using a PerkinElmer Lambda 2 UV-vis spectrophotometer. Infrared spectra were recording using a Brucker Tensor 27 spectrometer in ATR mode.

High-resolution mass spectroscopy

High-Resolution Mass Spectra were obtained at the ICOA of the Université de Orléans by electrospray ionization using a Q-TOF analyzer.

NMR spectroscopy

NMR spectra were recorded on a Bruker Avance II 400 MHz spectrometer. ^{1}H NMR chemical shifts were referenced to the residual solvent signal; ^{13}C NMR chemical shifts were referenced to the deuterated solvent signal. Results are presented as the following: chemical shift δ (ppm), multiplicity (s = singlet, d = doublet, t = triplet, q = quartet, quint = quintet, hept = heptuplet, m = multiplet, br = broad), coupling constant J (Hz), integration.

Table 1 *Chemical structures of the photo-initiating systems and monomers*

Name	Chemical structure
5,15-di(3-benzophenone)porphyrin (PBP)	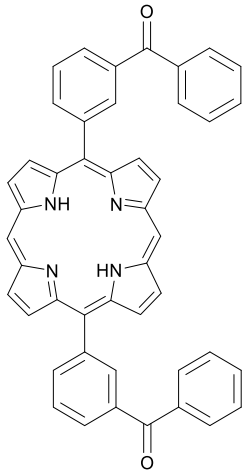
Zinc (II) 5,15-di(3-benzophenone)porphyrin (PBPZn)	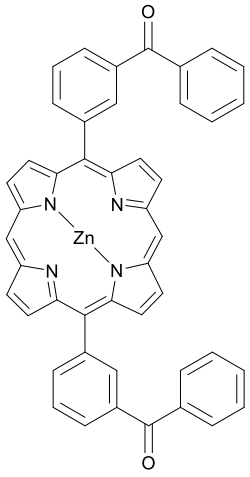
Bis(4-methylphenyl) iodonium hexafluorophosphate (Iod)	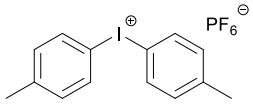
N-methyldiethanol amine (MDEA)	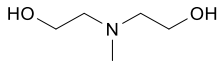
Cysteamine	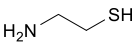
N-acetylcysteine	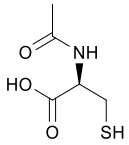

3,4-Epoxycyclohexylmethyl 3,4-epoxycyclohexanecarboxylate (EPOX)

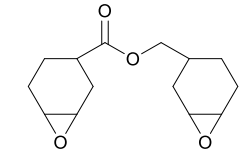

soybean oil acrylate (SOA)

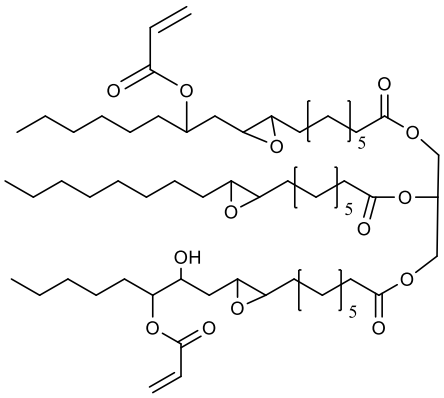

Synthesis of 3-methylbenzhydrol

A two-necked 100 mL rounded-bottomed flask equipped with a condenser, an addition funnel and a stirring bar is charged with magnesium shavings (1.55 g, 0.06 mol, 1.5 equiv) and placed under an argon atmosphere. Dry diethyl ether (ca. 5 mL, to cover Mg shavings) and TFA (0.05 mL) are successively added, and the mixture is heated to reflux with a heat gun. After cooling to room temperature, bromobenzene (0.5 mL) is added and the mixture is stood at room temperature until the reaction starts. Upon stirring, a solution of bromobenzene (6.7 mL, 0.06 mol, 1.5 equiv) in diethyl ether (42 mL) is added dropwise to maintain a gentle reflux, and the mixture is stirred 15 min. Then, the resulting solution is cooled down to 0 °C and *m*-tolualdehyde (5 mL, 0.04 mol, 1.0 equiv) solubilized in diethyl ether (40 mL) is added dropwise and the reaction is stirred at room temperature for 2 h. Then, the resulting mixture is poured into 1 M aq HCl (100 mL) and this solution is extracted with ethyl acetate (2 x 50 mL). The combined organic layers are washed with brine (50 mL), dried over Na_2SO_4 and evaporated under reduced pressure. The crude product (10.3 g, contaminated by ca. 20% of biphenyl) is obtained as a yellow oil and used without any further purification.

GC (50+10/250–5): tr = 18.0 min; **^{1}H NMR** (400 MHz, $CDCl_3$): δ 7.45 – 7.14 (m, 9 H), 5.83 (s, 1 H), 2.69 (s, 1 H), 2.40 (s, 3 H); **^{13}C NMR** (100 MHz, $CDCl_3$): δ 144.0 (C), 143.9 (C), 138.2 (C), 128.5 (2 C), 128.5 (CH), 128.4 (CH), 127.5 (CH), 127.3 (CH), 126.6 (2 CH), 123.7 (CH), 76.07 (CH), 21.5 (CH3).

Synthesis of 3-methylbenzophenone

In air, a 500 mL rounded-bottomed flask equipped with a stirring bar is charged with the previously obtained **3-methylbenzhydrol** (10.3 g, 80% purity, 42 mmol, 1.0 equiv), tetra-*n*-butylammonium bromide (1.35 g, 4.2 mmol, 0.1 equiv), ethyl acetate (140 mL) and commercial bleach (120 mL, 4.8% active chlorine). The reaction is stirred at room temperature for 18 h. The layers are separated, and the aqueous layer is extracted with ethyl acetate (2 x 50 mL). The combined organic layers are washed with water (2 x 50 mL), brine (2 x 50 mL), dried over Na_2SO_4 and evaporated under reduced pressure. The crude product (9.92 g, contaminated by ca. 16% of biphenyl) is obtained as a yellow oil and used without any further purification.

GC (50+10/250–5): t_r = 18.1 min. **^{1}H NMR** (400 MHz, $CDCl_3$): δ 7.85 – 7.80 (m, 2 H), 7.65 (s, 1 H), 7.63 – 7.57 (m, 2 H), 7.54 – 7.46 (m, 2 H), 7.42 – 7.35 (m, 2 H), 2.43 (s, 3 H). **^{13}C NMR** (100 MHz, $CDCl_3$): δ 192.6 (C), 144.0 (C), 143.9 (C), 138.2 (C), 133.2 (CH), 132.4 (CH), 130.5 (C), 130.1 (2 CH), 128.3 (2 CH), 128.1 (CH), 127.4 (CH), 21.4 (CH_3).

Synthesis of 3-(dibromomethyl)benzophenone

In air, a 250 mL rounded-bottomed flask equipped with a stirring bar is charged with the previously obtained **3-methylbenzophenone** (8.32 g, 84% purity, 42.4 mmol, 1 equiv), NBS (22.6 g, 127 mmol, 3.0 equiv), AIBN (70 mg, 0.4 mmol, 0.1 equiv) and CCl_4 (85 mL). The reaction mixture is heated to reflux for 6 h and monitored by GC analysis [until full conversion is reached, AIBN (70 mg, 0.4 mmol, 0.1 equiv) is added every 2 h]. The reaction mixture is then diluted with DCM (60 mL) and washed with $Na_2S_2O_3$ (2 x 30 mL), water (2 x 30 mL) and brine (30 mL), dried over Na_2SO_4 and evaporated under reduced pressure. The crude product (15.0 g) is obtained as an orange oil and used without any further purification.

GC (50+10/250–5): t_r = 23.9 min. **^{1}H NMR** (400 MHz, $CDCl_3$): δ 8.00 (dd, *J* = 1.8, 1.8 Hz, 1 H), 7.88 – 7.82 (m, 3 H), 7.78 (dt, *J* = 7.7, 1.4 Hz, 1 H), 7.67 – 7.61 (m, 1 H), 7.56 – 7.62 (m, 3 H), 6.72 (s, 1 H). **^{13}C NMR** (100 MHz, $CDCl_3$): δ 195.4 (C), 142.3 (C), 137.9 (C), 137.1 (C), 132.7 (CH), 131.2 (CH), 130.5 (CH), 130.0 (2 CH), 128.8 (CH), 128.4 (2 CH), 127.6 (CH), 39.8 (CH).

Synthesis of 3-formylbenzophenone

In air, a 250 mL rounded-bottomed flask equipped with a stirring bar, is charged with the previously obtained **3-(dibromomethyl)benzophenone** (15.0 g, 42.4 mmol, 1.0 equiv) and ethanol (40 mL). A solution of $AgNO_3$ (14.4 g, 84.8 mmol, 2.0 equiv) in water (170 mL) is added in one portion, and the reaction is refluxed for 4 h. Then, the reaction mixture is poured into brine (100 mL) and the mixture is stirred for 5 min. The

resulting solution is then filtered over Celite, and the aqueous and organic layers are separated. The aqueous layer is extracted with ethyl acetate (2 x 50 mL) and the combined organic layers are washed with water (2x 50 mL), brine (50 mL), dried over Na_2SO_4 and evaporated under reduced pressure. The desired product is obtained after purification by flash chromatography (silica, petroleum ether/ethyl acetate: 9/1) as a yellow oil (4.06 g, 46% over 4 steps).

GC (50+10/250–5): t_r = 20.1 min. **^{1}H NMR** (400 MHz, $CDCl_3$): δ 10.05 (s, 1 H), 8.24 (t, *J* = 1.4 Hz, 1 H), 8.06 (ddt, *J* = 16.7, 7.7, 1.4 Hz, 2 H), 7.81 – 7.73 (m, 2 H), 7.69 – 7.56 (m, 2 H), 7.52 – 7.44 (m, 2 H). **^{13}C NMR** (100 MHz, $CDCl_3$): δ 195.4 (C), 191.4 (CH), 138.5 (C), 136.8 (C), 136.3 (C), 135.4 (CH), 133.0 (CH), 132.7 (CH), 131.3 (CH), 130.0 (2 CH), 129.3 (CH), 128.6 (2 CH).

Synthesis of Dipyrromethane

In air, a 500 mL rounded-bottomed flask equipped with a stirring bar is charged with pyrrole (130 mL, 1.87 mol, 4.0 equiv), paraformaldehyde (1.41 g, 0.47 mol, 1.0 equiv), acetic acid (200 mL) and methanol (65 mL). The flask is closed with a septum and the reaction is stirred at room temperature for 16 h. Then, the reaction mixture is diluted with DCM (400 mL), and the resulting solution is washed with water (2 x 200 mL) and 1.0 M aq NaOH (2 x 200 mL). The organic layer is dried over Na_2SO_4 and the solvent and the excess of pyrrole are successively removed by evaporation under reduced pressure. The residue is purified by flash chromatography (silica, DCM/EP: 5/5) to afford the expected product (1.923 g, 7%) as a white solid, which turn black under air.

GC (50+10/250–5): t_r = 23.9 min.

^{1}H NMR (400 MHz, $CDCl_3$): δ 7.63 (s, 2 H), 6.61 (dd, *J* = 4.2, 2.6 Hz, 2 H), 6.21 (dd, *J* = 5.7, 2.8 Hz, 2 H), 6.09 (d, *J* = 0.6 Hz, 2 H), 3.94 (s, 2 H). **^{13}C NMR** (100 MHz, $CDCl_3$): δ 129.2 (2 C), 117.4 (2 CH), 108.4 (2 CH), 106.6 (2 CH), 26.4 (CH_2).

Synthesis of Porphyrin Benzophenone (PBP)

A 1 L rounded-bottomed flask purged with argon and protected from light by an aluminium foil is charged with **dipyrromethane** (400 mg, 2.7 mmol, 1.0 equiv), **3-formylbenzophenone** (604 mg, 2.9 mmol, 1.05 equiv) and DCM (700 mL). The solution is degassed by argon bubbling for 15 min, and TFA (0.17 mL, 2.2 mmol, 0.8 equiv) is added. The reaction is stirred at room temperature for 18 h. DDQ (0.87 g, 3.8 mmol, 1.4 equiv) is then added and the mixture is stirred at room temperature for 30 min. After addition of triethylamine (2 mL), the solvent is removed under reduced pressure and the residue was purified by flash chromatography (silica, DCM/EP: 7/3) to afford the desired product as a purple solid (0.92 g, 16%).

^{1}H NMR (400 MHz, $CDCl_3$): δ 10.35 (s, 2 H), 9.44 (d, *J* = 4.6 Hz, 4 H), 9.09 (d, *J* = 4.6 Hz, 4 H), 8.71 (s, 2 H), 8.51 (d, *J* = 7.5 Hz, 2 H), 8.30 (d, *J* = 7.8 Hz, 2 H), 8.10 – 8.03 (m, 4 H), 7.96 (t, *J* = 7.7 Hz, 2 H), 7.57 – 7.46 (m, 6 H), –3.16 (s, 2 H). **^{13}C NMR** (100 MHz, $CDCl_3$): δ 196.8 (2 C), 146.9 (4 C), 145.3 (4 C), 141.5 (2 C), 138.3 (2 CH), 137.6 (2 C), 136.3 (2 C), 135.7 (2 CH), 132.7 (2 CH), 132.1 (4 CH), 130.9 (4 CH), 130.1 (4 CH), 129.4 (2 CH), 128.4 (4 CH), 127.2 (2 CH), 117.8 (2 C), 105.74 (2 CH) (**Figure S1** and **S2**). **λ_{max} (CH_2Cl_2) / nm:** 406 nm (Soret band), 501, 535, 573 et 630 nm (Q bands). **ν_{max} (ATR) / cm^{-1}:** 3250, 3055, 2922, 2857, 1726, 1649, 1582, 1402, 1254, 966, 83, 779, 702. **HRMS (ESI/Q-TOF):** *m/z* [M + H$^+$] calcd for $C_{46}H_{31}N_4O_2$ 671.2442; found 671.2433.

Synthesis of Zinc (II) complex of Porphyrin Benzophenone (PBPZn)

In air, a 25 mL rounded-bottomed flask equipped with a stirring bar is charged with **PBP** (44.7 mg, 0.067 mmol, 1.0 equiv), $Zn(OAc)_2$ (29 mg, 0.13 mmol, 2.0 equiv), chloroform (10 mL) and methanol (3.5 mL). The reaction is stirred under reflux for 1.5 h. Solvents are removed under reduced pressure and the residue is triturated in methanol and filtered several times to afford the desired product (37.9 mg, 77%) as a purple solid.

^{1}H NMR (400 MHz, $CDCl_3$): δ 10.30 (s, 2 H), 9.44 (d, *J* = 4.4 Hz, 4 H), 9.10 (d, *J* = 4.3 Hz, 4 H), 8.64 (s, 2 H), 8.47 (d, *J* = 7.4 Hz, 2 H), 8.26 (d, *J* = 7.8 Hz, 2 H), 8.03 (d, *J* = 7.4 Hz, 4 H), 7.93 (t, *J* = 7.7 Hz, 2 H), 7.56 – 7.45 (m, 6 H). **^{13}C NMR** (100 MHz, $CDCl_3$): δ 197.1 (2 C), 150.5 (4 C), 150.1 (4 C), 143.3 (2 C), 138.6 (2 CH), 138.3 (2 C), 136.6 (2 C), 136.1 (2 CH), 133.0 (2 CH), 132.6 (4 CH), 132.6 (4 CH), 130.6 (4 CH), 129.6 (2 CH), 128.9 (4 CH), 127.3 (2 CH), 119.3 (2 C), 106.7 (2 CH) (**Figure S3** and **S4**). **λ_{max} (CH_2Cl_2) / nm:** 411 nm (Soret band), 539 nm (Q band). **ν_{max} (ATR) / cm^{-1}:** 2963, 2903, 1653, 1580, 1402, 1256, 1080, 1009, 864, 787, 698. **HRMS (ESI/Q-TOF):** *m/z* [M + H$^+$] calcd for $C_{46}H_{29}N_4O_2Zn$ 733.1576; found 733.1568.

Theoretical calculations

The DFT and TD-DFT calculations were performed with the Gaussian 16 code [37] on the two compounds. Default Gaussian16 thresholds and algorithms were used but for an improved geometry optimization threshold (10^{-5} au on average residual forces), a stricter self-consistent field convergence criterion (10^{-10} a.u.) and the systematic use of the *ultrafine* DFT integration grid. Firstly, the S_0 geometries have been optimized with DFT and the vibrational frequencies have been analytically determined, using the CAM-B3LYP range-separated hybrid exchange-correlation functional [38]. These calculations were performed with the 6-31G(d,p) atomic basis set. Secondly, we determined the vertical transition energies on these geometries using TD-DFT, combined with the same functional and basis set. This allowed determining the excited-state density of the four lowest states, and therefore to determine density difference plots. These plots use a contour threshold of 5 x 10^{-4} au. Thirdly, starting from the optimal ground-state geometries, we have used TD-DFT with the same functional and basis set to optimize the S_1 geometry and compute the vibrational frequencies. All optimized structures correspond to true minima of the potential energy surface. Vibrationally-resolved spectrum were determined with FC classes [39,40] using the FC-HT approach (for the Q bands) and the FC approach (for the Soret bands) and applying the "vertical Hessian" (VH) vibronic potential energy surface model,[41] the time-dependent formalism and a broadening Gaussian of 200 cm^{-1} to convolute the "stick spectrum".

Irradiation sources

Five light emitting diodes (LEDs) from THORLABS were used to initiate the polymerization *i.e.* LED@385 nm (35.3 mW.cm^{-2}), LED@405 nm (118 mW.cm^{-2}), LED@455 nm (23.8 mW.cm^{-2}),

LED@505 nm (42.5 mW.cm^{-2}) and LED@530 nm (14.6 mW.cm^{-2}).

Steady state photolysis

PBP and **PBPZn** were first dissolved in DCM, and the solutions were irradiated under air with a LED@405 nm with and without co-initiators, *i.e.* MDEA, Iod, cysteamine or *N*-acetylcysteine. [**PBP**] = 2 x 10^{-6} mol.L^{-1}, [**PBPZn**] = 6 x 10^{-6} mol.L^{-1}, [MDEA] = 2.8 x 10^{-2} mol.L^{-1}, [Iod] = 2.9 x 10^{-5} mol.L^{-1}, [cysteamine] = 1.7 x 10^{-4} mol.L^{-1} and [*N*-acetyl cysteine] = 1.1 x 10^{-4} mol.L^{-1} in DCM.

Fluorescence measurements

Fluorescence experiments were performed on a FluoroMax+ spectrofluorometer from Horiba. Emission spectra were obtained by excitation of the maximum absorption peak wavelength of **PBP** (and **PBPZn**) according to a previously described method. [42]

Laser Flash Photolysis.

The nanosecond flash photolysis experiments were performed on a nanosecond Nd:TAG laser (Powerlite 9010, Continuum) with $\lambda_{excitation}$ at 385 nm as previously described.[43] Measurements were done at RT in DCM and under saturated argon solutions of **PBP** (and **PBPZn**).

Electronic Paramagnetic Resonance (EPR)

The X-band cw-EPR spectra (modulation frequency of 100 kHz) were monitored using the EMX*plus* spectrometer (Bruker) equipped with the High Sensitivity Probe-head (Bruker) in a small quartz flat cell (Wilmad-LabGlass, WG 808-Q). The solutions prepared in chloroform (for spectroscopy Uvasol®, Merck) and carefully saturated with argon were irradiated at 295 K directly in the EPR resonator using a LED@400 nm source (λ_{max} = 400 nm; Bluepoint LED, Hönle UV Technology). The EPR spectra were recorded *in situ* upon/after a defined exposure as described previously.[43] The 5,5-dimethyl-1-pyrroline *N*-oxide (DMPO was distilled and stored at –20°C before the application) was used as the spin trapping agent. The *g*-factors were determined with an uncertainty of ±0.0001 exploiting a nuclear magnetic resonance teslameter (ER 036TM, Bruker) and integrated frequency counter. The experimental EPR spectra were analyzed by the WinEPR software (Bruker) and the calculations of spin-Hamiltonian parameters and relative concentrations of individual DMPO-adducts were performed with the EasySpin toolbox working on MatLab® platform.[44] The standard EPR spectrometer settings: microwave frequency, ~ 9.43 GHz; microwave power, 10.80 mW; center field, ~336.0 mT; sweep width, 4–10 mT; gain, 2.00×10^5; modulation amplitude,0.025–0.1 mT; sweep time, 45 s; time constant, 10.24 ms; number of scans, 5–10.

In the experiments corresponding to **Figures S24** and **S31**, the samples were prepared by mixing indicated reagents in freshly distilled chloroform in a 4 mm quartz EPR tube. Oxygen was removed by argon bubbling through the solution for one minute, and the tube was sealed with a septum cap. 5,5-Dimethyl-1-pyrroline *N*-oxide (DMPO, Sigma-Aldrich, used as received) was used as a spin trapping agent. The solutions were analysed by EPR during in-situ or post 120-s irradiation using a LED@405 nm source (THORLABS) as stated in the figure legend. EPR measurements were performed using an Elexsys E500 EPR spectrometer (Bruker, Wissembourg, France), operating at X-band (9.8 GHz) and equipped with an SHQ high-sensitivity cavity. Typical settings used were: microwave power, 10 mW; modulation frequency, 100 kHz; modulation amplitude, 0.05 mT; receiver gain, 60 dB; time constant, 10.24 ms; conversion time, 40.96 ms; datapoints, 1024; sweep width, 7 mT; sweep time, 41.94 s. 5 EPR spectra were recorded sequentially at 21°C. Figures present the sum of five experimental spectra. The magnetic field at the sample position was corrected using a Bruker weak pitch standard sample for which the g-value is accurately known. The g-values were determined from the corrected magnetic field at the center of the EPR spectrum and the microwave frequency read from the integrated frequency meter. Data acquisition and processing were performed using Bruker Xepr software. The simulated spectra were calculated with the EasySpin toolbox working on MatLab platform.[44]

Cyclic voltammetry

The evaluation of the oxidation and the reduction potentials of **PBP** and **PBPZn** were done by cyclic voltammetry according to literature [45] in DMF and under argon atmosphere. The glassy carbon, the saturated calomel and the gold wire electrodes were respectively used as the working, the reference, and the counter electrodes.

Kinetic photopolymerization studies.

The photosensitive formulations were put on a BaF_2 chip and irradiated under air or in laminate using the different LED sources. 12 µm is the thickness of the coatings. The final acrylate and epoxy conversions were determined by monitoring the decrease of acrylate and epoxy functions by Real-Time Fourier Transform InfraRed spectroscopy (RT-FTIR) at 1636 and 790 cm^{-1}, respectively according to a previously described method.[46]

Coating preparation for antibacterial applications.

Photosensitive formulations (**PBP**/MDEA/SOA or **PBPZn**/MDEA/SOA) were layed on a glass substrate which were intensively cleaned with acetone and ethanol prior to the irradiation. The substrates were then irradiated at room temperature under LED@405 nm for 10 minutes in laminate to avoid oxygen diffusion through the coatings.

Detection of the reactive oxygen species.

The capability of the porphyrin to generate singlet oxygen and superoxide ion was demonstrated by monitoring the absorbance of TPCPD or NBT respectively under LED@405 nm irradiation.

A 3 mL quartz cuvette was filled with a solution of **PBPZn** (4.0 x 10^{-7} mol.L^{-1}) containing TPCPD or NBT ([TPCPD] = 6.9 x 10^{-5} mol.L^{-1} and [NBT] = 3.1 x 10^{-6} mol.L^{-1}) and irradiated. The absorbance of TPCPD at 510 nm and those of formazan at 530 nm were then followed by UV-vis spectroscopy.

Antibacterial assays.

The ability of the porphyrin-based coatings to inhibit bacterial growth were determined using *S. aureus* ATCC6538 with and without visible-light irradiation. Experiments were performed according to literature.[45]

Results and discussion

Synthesis of PBP and PBPZn

The preparation of 5,15-di(3-benzoylphenyl)porphyrin **PBP** could be envisioned through two complementary strategies (**Fig. 1**). Indeed, the porphyrin core could be assembled either by condensation of dipyrromethane (**DPM**) with 3-benzoylbenzaldehyde **1** (path a) [47,48] or by condensation of *meso*-(3-benzoylphenyl)dipyrromethane **2** with trimethyl orthoformate (path b) [49].

Both pathways require the preparation of 3-benzoylbenzaldehyde **1**, which has been achieved as outlined in **Fig. 2**. Addition of an excess of phenylmagnesium bromide to *m*-tolualdehyde delivered an intermediate benzhydrol which was oxidized by bleach using phase transfer catalysis. The methyl group was next converted to an aldehyde group by a radical dibromation and a subsequent hydrolysis mediated by silver nitrate. By using this strategy, the expect product **1** was obtained with a global yield of 46% over 4 steps by chromatography on silica gel after one single purification.

The synthesis of **PBP** was next investigated using the two mentioned strategies (**Fig. 3**). Condensation of paraformaldehyde with an excess of pyrrole in an acetic acid/methanol mixture led to formation of dipyrromethane (DPM) in 20% yield. The reaction of this latter with aldehyde **1** in the presence of TFA led, after oxidation with DDQ, to the expected porphyrin **PBP** in 16% yield (path a). Alternatively (path b), aldehyde **1** could first react with pyrrole leading to *meso*-substituted dipyrromethane **2** in 64% yield, which was next condensed with an excess of trimethyl-orthoformate in the presence of TFA. After neutralisation with pyridine and aromatization by oxygen, the desired product **PBP** has been obtained in a similar 5% yield (path b). These two strategies revealed to be complementary but required a larger amount of aldehyde **1** to obtain the same mass of **PBP**.

The metalation of **PBP** could be efficiently achieved by treatment with zinc acetate in a chloroform/methanol mixture, leading to **PBPZn** in 77% yield (**Fig. 4**), as confirmed by ^{1}H NMR monitoring with the disappearance of the signal at –2 ppm corresponding to the proton linked to the nitrogen atom of the porphyrin ring of **PBP**.

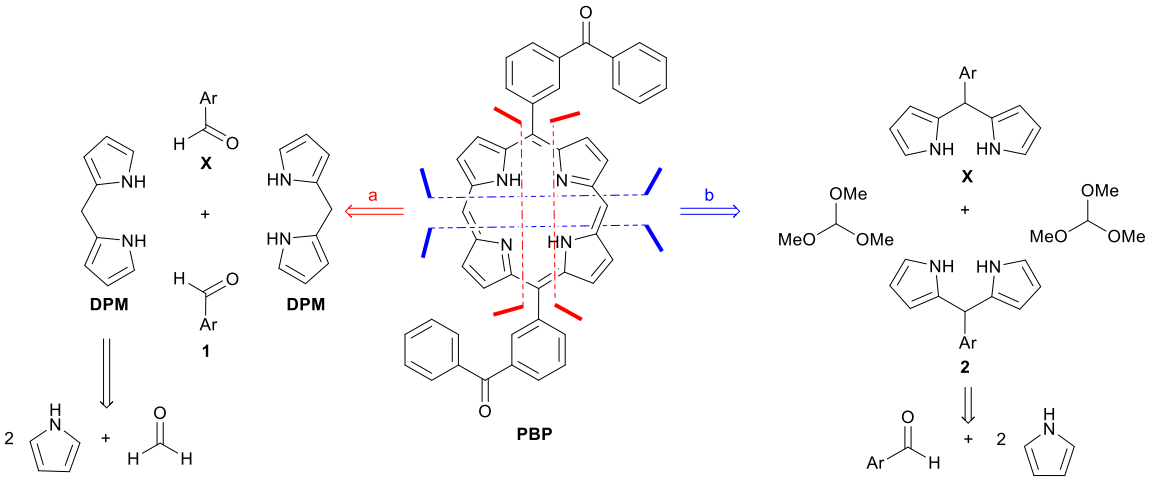

Fig. 1 Retrosynthetic routes for the synthesis of PBP. (Ar = 3-benzoylphenyl).

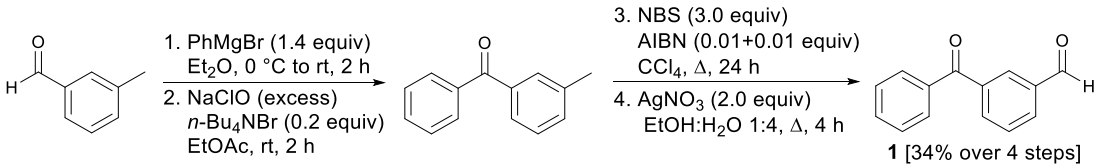

*Fig. 2 Preparation of 3-benzoylbenzaldehyde **1***

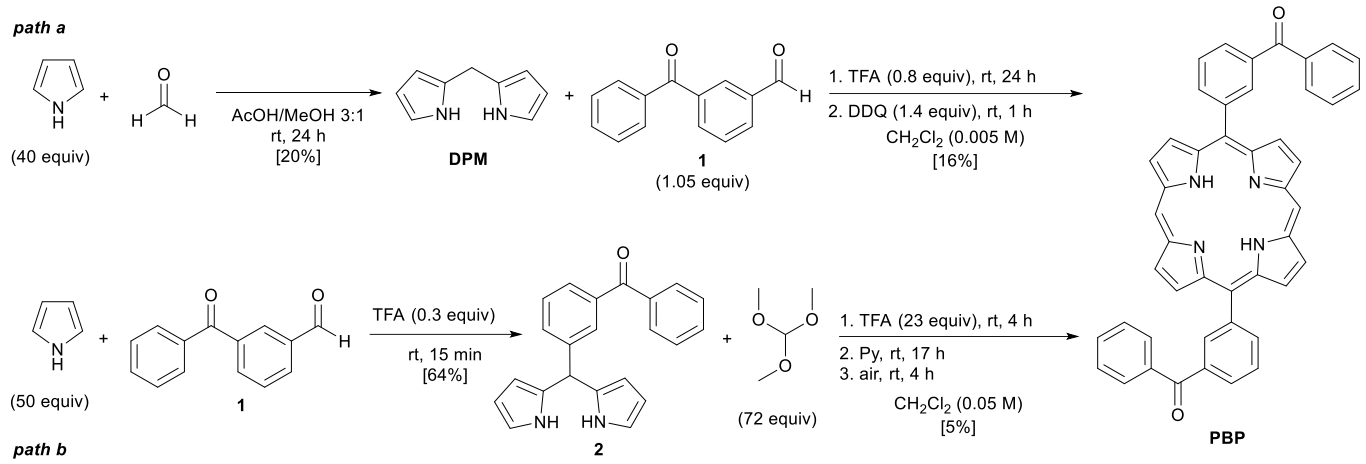

***Fig. 3** Synthesis pathways of **PBP**.*

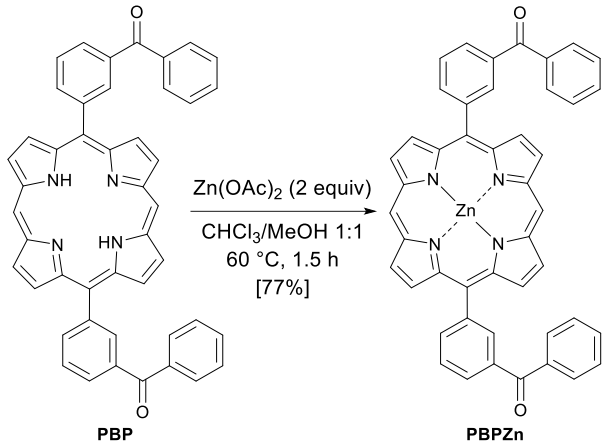

***Fig. 4** Synthesis of **PBPZn**.*

Photophysical properties of PBP and PBPZn.

The UV-vis and the fluorescence spectra of **PBP** and **PBPZn** are displayed in **Fig. 5**, and their photophysical properties are summarized in **Table 2**. The absorption spectra of the porphyrin derivatives show a very intense band at 406 nm for **PBP** and 411 nm for **PBPZn** due to the Soret absorption. Weaker visible bands between 450 and 650 nm correspond to the Q transitions following the well-known four-orbital-model of Gouterman.[50] The complexation of **PBP** with Zn metal ions yields a slight redshift of the Q bands in comparison with those of **PBP** as the closed shell metal increase the electron density of porphyrin, lowering thus the energy gap.[51,52] Notably, the number of distinguishable Q-bands in the **PBPZn** spectrum is divided by 2 compared to **PBP** as the coordination of porphyrin with metal ions increases the near-degenerate character of the excited states involved in the Q-bands.[53] Both porphyrins possess high extinction molar coefficients between 400 and 630 nm as described in **Table 2**. It can be noted that the absorption spectra of the two new synthesised porphyrins match quite well with the emission spectra of the different LEDs used for the free-radical (FRP) and cationic (CP) photopolymerizations (**Figure S5**). **PBP** and **PBPZn** can be potentially used as photosensitizers for FRP and CP.

We have used theoretical chemistry (see Methods above) to model the visible spectra of both **PBP** and **PBPZn**. The vibrationally-resolved spectrum can be found in the SI (**Figure S6-9**), and the two lowest singlet excited states, S_1 and S_2, yield the Q-bands, with pronounced vibronic couplings yielding several maxima in both compounds, whereas the two next singlet excited states, S_3 and S_4, are almost degenerated and correspond to the much more intense Soret bands, with a less clear vibronic resolution. As explained above, this is the expected behavior for porphyrin derivatives. All these states are represented in **Figure S10** (**PBP**) and **Figure S11** (**PBPZn**) in the form of electron density difference plots. One notices a full delocalization on the macrocyclic ring, with no significant contributions of the side benzophenone for any of the four states (states localized on the side moiety are higher in energy), with a clearly more symmetric pattern for **PBPZn** than **PBP**. In short, the excited states of **PBP** and **PBPZn**, are highly similar to the ones of the corresponding unsubstituted porphyrins, the addition of side groups inducing almost no significant change.

The excited singlet and triplet state properties of **PBP** and **PBPZn** are described by Laser Flash photolysis and fluorescence, respectively. To investigate the reactivity at triplet state, transient absorption measurement using nano-second laser flash photolysis were performed. The transient absorption spectra of both porphyrins between 410 and 800 nm highlight a maximum absorption band at 420 nm for **PBP** and 440 nm for **PBPZn**. Under argon atmosphere, their lifetime has been evaluated at 34 µs for **PBP** and at 17 µs for **PBPZn** but it strongly decreases under oxygen to 0.67 µs and 0.55 µs for **PBP** and **PBPZn** respectively. These results are in total accordance with the formation of triplet excited states. (**Figure S13**).

The fluorescence spectra of **PBP** and **PBPZn** are both composed of two bands, separated of 63 and 50 nm respectively. When **PBP** is complexed by Zn^{2+} ion, the emission band of **PBPZn** is blue-shifted and a significant decrease of the fluorescence intensity is observed by a factor of 1.7. Indeed, the addition of the metal central

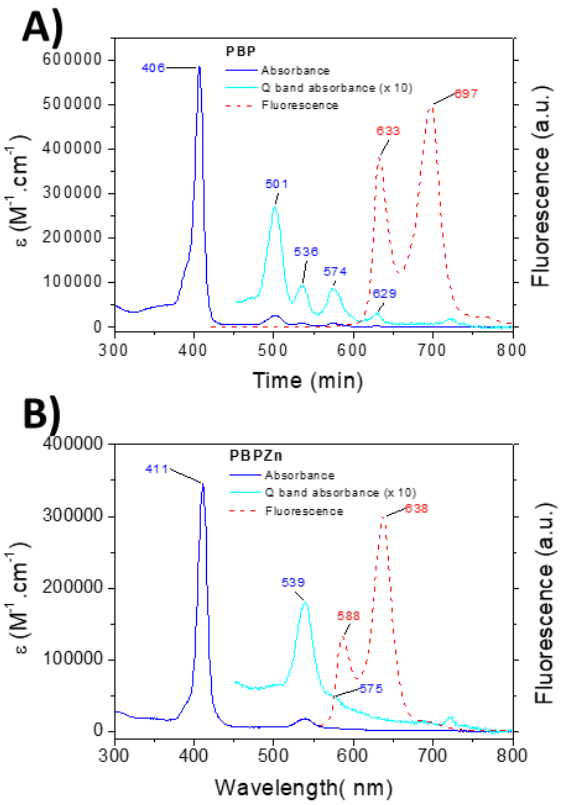

ion leads to a fluorescence quenching effect by enhancing the spin-orbit coupling.

*Fig. 5 Absorbance and fluorescence spectra of **A) PBP** and **B) PBPZn**.*

Photoreactivity of the porphyrin derivatives with and without the use of co-initiators.

The photochemical properties of some porphyrin derivatives under light irradiation have been already investigated but, to date, few photo-initiating systems including porphyrins have been proposed in the literature.[30–32]

The photochemical pathways involving **PBP** (and **PBPZn**) when associated with co-initiators (Iod, MDEA, cysteamine and *N*-acetyl cysteine) are described in detail through steady-state photolysis, EPR and LFP experiments, cyclic voltammetry and fluorescence studies. The photochemical properties of both porphyrins and co-initiators are given in **Table S1**. Oxidation and reduction potentials (E_{ox} and E_{red}) of **PBP** and **PBPZn** have been determined by cyclic voltammetry, whereas the singlet state energy (E_S) and triplet state energy (E_T) of porphyrin derivatives have been evaluated by fluorescence and nanosecond laser spectroscopy respectively. The probability of an electron transfer reaction between the singlet (or the triplet excited states) of porphyrins and the ground state of the co-initiator is evaluated by the calculation of the free energy change ΔG_S (at the singlet excited state) and ΔG_T (at the triplet excited state) respectively, using the Rehm-Weller equation: $\Delta G_{(S \text{ or } T)} = F(E_{ox} - E_{red}) - E_{(S \text{ or } T)}$. ΔG_S and ΔG_T for both porphyrins are summarized in **Table 3** with the different co-initiators.

Under LED@405 nm irradiation, no decrease of the absorbance of **PBP** is observed after 10 min, while that of **PBPZn** decreases by a half after only 3 min (**Figure S14**). While the photoactivation of **PBP** in chloroform using LED@400 nm resulted in the generation of a broad EPR signal of very low intensity (data not shown), irradiation of PBPZn under the same conditions led to the generation of a broad singlet signal (g = 2.0032) with unresolved hyperfine structure which is well compatible with the photoinduced generation of the radical cation **PBPZn**$^{\bullet+}$ [30,42,54] (**Figure S15A**). Photoexcited PBPZn* likely interacts with solvent molecules via electron transfer. This hypothesis was supported by the EPR spectra measured upon photoexcitation of **PBPZn** in chloroform in the presence of DMPO spin trap (**Figure S15C**), showing the superposition of individual signals of DMPO-adducts generated *via* the reaction of DMPO with the non-persistent free radicals derived from chloroform.[55–57] The spin-Hamiltonian parameters of the corresponding DMPO-adducts elucidated from the simulations are as follows: i) •DMPO-$CHCl_2$ (a_N = 1.401 mT, $a_{H\beta}$ = 1.997 mT; g = 2.0061), ii) •DMPO-CCl_3 (a_N = 1.363 mT, a_H^β = 1.585 mT; g = 2.0062) and iii) •DMPO-CR (a_N = 1.483 mT, a_H^β = 2.157 mT; g = 2.0059), assigned to a DMPO-adduct of a carbon-centered radical produced from **PBPZn**. In **Figure S15C** the presence of a broad signal which is attributed to **PBPZn**$^{\bullet+}$ (*) is also detectable. The same EPR signals (except for the **PBPZn**$^{\bullet+}$ signal) are observed when **PBP** is irradiated in the presence of DMPO (**Figure S15B**).

***Table 2** Photophysical properties of **PBP** and **PBPZn**.*

	λ_{Soret} (nm)	ε_{Soret} ($M^{-1}.cm^{-1}$)	$\lambda_{Q\ bands}$ (nm)	$\varepsilon_{Q\ bands}$ ($M^{-1}.cm^{-1}$)	$\lambda_{emission}$ (nm)	$\lambda_{LED\ excitation}$ (nm) / ε ($M^{-1}.cm^{-1}$)
PBP	406	585 000	501	27 000	633	385 / 10 000
			536	9 300	697	405 / 552 000
			574	8 500		505 /25 000
			629	3 100		530 / 8 000
PBPZn	411	345 000	539	9 400	588	385 / 30 000
			575	5 000	638	405 / 216 000
						505 / 7 000
						530 / 14 000

Table 3 *Thermodynamic parameters of the porphyrin-based photo-initiating systems. Calculation of the free energy changes ΔG_S and ΔG_T (kJ.mol^{-1}).*

	MDEA		Iod		cysteamine		*N*-acetylcysteine	
	ΔG_S	ΔG_T	ΔG_S	ΔG_T	ΔG_S	ΔG_T	ΔG_S	ΔG_T
PBP	-12.54	-101.31	-34.73	-123.50	6.75	-82.01	-5.79	-94.56
PBPZn	5.79	-59.82	-82.01	-147.62	25.09	-40.52	12.54	-53.07
BP		-44.65		-194.61		-25.38		-37.92
CQ		-21.20		-180.91		-1.93		-14.47

a) Effect of the addition of MDEA. Interestingly, the addition of MDEA to **PBP** (or **PBPZn**) accelerates the decrease of their absorbance under light irradiation, demonstrating thus a possible electron transfer reaction between porphyrin derivatives and MDEA (**Figure S16**). According to fluorescence experiments, the singlet excited states of both porphyrins are quenched by MDEA, and the corresponding fluorescence quenching rate (K_{SV}) for **PBP** and **PBPZn** are K_{SV}^{MDEA} (**PBP**) = 1.2 M^{-1} and K_{SV}^{MDEA} (**PBPZn**) = 0.7 M^{-1}, respectively (**Figure S17**). The lower dynamic Stern-Volmer constants with MDEA are in full agreement with the lower calculated free energies (ΔG_S = -13 kJ.mol^{-1} for **PBP** and 6 kJ.mol^{-1} for **PBPZn**). On the contrary, the free energy changes (ΔG_T) which evaluate the possible electron transfer reactions between the excited triplet state of both porphyrins and the MDEA ground state, according to the Rehm-Weller equation, appear more favourable than that observed at the singlet excited state as ΔG_T^{MDEA}(**PBP**) = -101.3 kJ.mol^{-1} and ΔG_T^{MDEA} (**PBPZn**) = -59.8 kJ.mol^{-1}. The bimolecular rate constant for the quenching of the triplet excited state of **PBP** (at 420 nm) by MDEA was evaluated to be k_q^{MDEA} (**PBP**) = 3 x 10^{-4} s^{-1}. M^{-1} (**Figure S18**).

The transient absorption spectrum of the triplet excited state of **PBPZn** highlights the formation of new radical species as the triplet lifetime highly increases from 17 μs to 55 μs. Upon the LED photoexcitation of porphyrin derivatives in the presence of MDEA in deoxygenated chloroform, the formation of broad lines (g ~ 2.0033) with unresolved hyperfine couplings was observed, as illustrated in **Figure S19**. Considering the photoinduced electron transfer between photoexcited porphyrin molecules and amine, the signals were attributed to the corresponding radical anion of porphyrins.[58] Unfortunately, the lack of hyperfine structure limits the information accessible from experimental EPR spectra. The rapid transformation of intermediate MDEA$^{\bullet+}$ resulted in the formation of reactive radicals detected by means of DMPO spin trap.[3,42] **Figure S20** shows the normalized experimental EPR spectra measured upon photoexcitation of **PBP**/MDEA/DMPO and **PBPZn**/MDEA/DMPO in chloroform under argon along with their simulations, evidencing the presence of superimposed spectral components attributed to the individual DMPO-adducts: *i*) dominant signal of $^{\bullet}$DMPO-C(*N*-aminoalkyl) characterized by the spin-Hamiltonian parameters a_N = 1.509 mT, a_H^{β} = 1.730 mT, a_H^{γ} = 0.183 mT, a_H^{γ} = 0.0730 mT; g = 2.0057,[59] *ii*) less-abundant signal of DMPO-adduct with a carbon-centered radical (a_N = 1.500 mT, a_H^{β} = 2.164 mT; g = 2.0059) and *iii*) $^{\bullet}$DMPO-$CHCl_2$ reflecting interaction of photo-initiating system with solvent.

b) Effect of the addition of Iod. The steady-state photolysis studies of the photo-initiating systems **PBP** (or **PBPZn**)/Iod have been performed by UV-Visible spectroscopy. The addition of Iod to **PBP** and **PBPZn** solutions leads to a faster diminution of the absorbance of the porphyrin derivatives than porphyrins used alone, highlighting an efficient interaction between porphyrins and Iod (**Figure S21**). Interestingly, the photolysis of **PBP** (or **PBPZn**)/Iod photo-initiating systems leads to the formation of new species which absorb over 410 nm with the appearance of an isobestic point at around 420 nm.

Quenching of fluorescence was achieved to understand the reactivity of the singlet state of both porphyrins towards the addition of Iod. The addition of an increasing quantity of Iod to **PBP** and **PBPZn** solutions leads to a slight decrease of the fluorescence emission of both porphyrins (**Figure S22**). Indeed, the corresponding fluorescence quenching rate (K_{SV}) of **PBP** and **PBPZn** by Iod are K_{SV}^{Iod} (**PBP**) = 11 M^{-1} and K_{SV}^{Iod} (**PBPZn**) = 13 M^{-1}.

To investigate the reactivity at their triplet excited state, transient absorption measurements using LFP were performed. When the concentration of Iod gradually increases, the triplet excited lifetimes of **PBP** and **PBPZn** strongly decrease (**Figure S23**): the quenching rate constants k_q^{Iod} (**PBP**) and k_q^{Iod} (**PBPZn**) were evaluated respectively to be 10^8 s^{-1}.M^{-1} and 10^9 s^{-1}.M^{-1}. These results are in accordance with an electron transfer reaction between the triplet excited states of both porphyrins and the ground state of Iod. Interestingly, and according to the values of ΔG_S^{Iod}(**PBP**) = +6.75 kJ.mol^{-1}, ΔG_S^{Iod} (**PBPZn**) = -40.52 kJ.mol^{-1}, ΔG_T^{Iod}(**PBP**) = -82.01 kJ.mol^{-1} and ΔG_T^{Iod} (**PBPZn**) = -106.13 kJ.mol^{-1}, the electron transfer reaction between both porphyrins and Iod would preferentially occur from the triplet excited states.

According to EPR ST, the addition of Iod to **PBP**/DMPO or **PBPZn**/DMPO solution leads, under irradiation, to the presence of superimposed EPR spectra composed of individual signals (**Figure S24**): DMPO-MePh adduct characterized by the spin-Hamiltonian parameters a_N = 1.36 mT, a_H = 1.59 mT; g = 2.0063 for both porphyrins (**Figures S24A** & **S24B**) and DMPO-CR adduct derivated from **PBP** (a_N = 1.45 mT, a_H = 2.10 mT; g = 2.0062, **Figure S24A**) and a broad singlet signal with unresolved hyperfine structure (g = 2.0034, Figure S24B) corresponding to the generation of **PBPZn**$^{\bullet+}$.

PBP (or **PBPZn**)/Iod photo-initiating systems can be therefore used either as radical promoters for free-radical photopolymerization or act as photoacid generators for cationic photopolymerization. The ability of **PBP** (or **PBPZn**) / Iod photo-initiating systems to produce photoacids is illustrated in **Figure S25** with rhodamine B (RhB), used as an acid indicator. In this

investigation, the photolysis of **PBP** (or **PBP**)/Iod systems in the presence of a solution of RhB leads to an increase of the absorbance at 550 nm, corresponding to the lowest energy band of the acid form of RhB. This results completely fits with the capability of porphyrins/Iod systems to produce photoacids, for promoting the cationic photopolymerization of epoxy monomers (see cationic photopolymerization section).

c) Effect of the addition of cysteamine. Although the free energy changes ΔG_S (**PBP**/cyst) and ΔG_S (**PBPZn**/cyst) are > 0, demonstrating an unfavorable electron transfer reaction between both porphyrins at their singlet excited state and cysteamine, thiyl radicals have been observed in EPR spin trapping experiments. EPR spectra measured upon photoactivation of **PBP** and **PBPZn** in the presence of cysteamine and DMPO in $CHCl_3$ under argon, confirmed the occurrence of EPR signal of •DMPO-SR spin-adduct (a_N = 1.369 mT, a_H^β = 1.247 mT, a_H^γ = 0.094 mT, a_H^γ = 0.082 mT; g = 2.0059 (**Figure S26**). [42,55] This experiment clearly evidences a H-abstraction reaction between porphyrins and cysteamine for the formation of thiyl radicals. The associated dynamic Stern-Volmer constants for the fluorescence quenching of **PBP** and **PBPZn** by cysteamine, *i.e.* K_{SV} (**PBP**/cysteamine) and K_{SV} (**PBPZn**/cysteamine), reach 1.2 M^{-1} and 6.2 M^{-1}, respectively (**Figure S27**). The bimolecular rate constant for the quenching of the triplet excited states of **PBP** and **PBPZn** by cysteamine could not be estimated as new species with a long lifetime (τ = 53 µs) were observed in laser flash photolysis experiments (**Figure S28**). To conclude, a H-abstraction reaction between the singlet (or the triplet) excited states of **PBPZn** and the ground state of cysteamine is possible. Similar reaction could be observed with **PBP** from its singlet excited states.

d) Effect of the addition of *N*-acetyl cysteine. In the presence of *N*-acetyl cysteine, the absorbance of both porphyrins remains unchanged under irradiation in comparison with porphyrins used alone (**Figure S29**). An increase of the absorbance can however be observed in the UV-range of **PBPZn** spectrum with the addition of ***N*-acetyl cysteine** under irradiation, suggesting the appearance of new radical species. The nano-second laser flash photolysis experiments highlight the presence of an interaction between **PBP** and *N*-acetylcysteine which is consistent with the steady-state photolysis results (**Figure S30**). The LED@405 nm irradiation of **PBP** (or **PBPZn**)/ *N*-acetyl cysteine/DMPO solution evidences the formation of thiyl radicals which are characterized by the following hyperfine coupling constants *i.e.* a_N = 1.421 mT, a_H^β = 1.392 mT, a_H^γ = 0.089 mT, a_H^γ = 0.104 mT; g = 2.0062 (**Figure S31**). A minor second signal can also be detected with **PBPZn**, corresponding to a DMPO-$(SR)_2$ adduct (a_N = 1.417 mT, g = 2.0058), originated from the dismutation of two DMPO-SR adducts (**Figure S32**). Note that *N*-acetyl cysteine alone in solution leads to an EPR signal associated to a DMPO-SR adduct, corresponding to a Forrester-Hepburn mechanism (**Figure S33**).[60] This signal is amplified when porphyrin/ *N*-acetyl cysteine/DMPO solution is irradiated which is relevant to the formation of thiyl radicals.

Cationic polymerization of EPOX with PBP/Iod and PBPZn/Iod.

The cationic photopolymerization were conducted under air with a 12-µm thickness formulation layer to maximize the reoxygenation within the polymer film. The two-component **PBPZn**/Iod photo-initiating system highlighted performing initiating properties under air and under LEDs@405 and 530 nm irradiation for the cationic photopolymerization of EPOX (**Table 4** and **Fig. 6**).The final epoxy conversions (FC) of EPOX reach at least 50% after 800 s of light exposure with **PBPZn**/Iod photo-initiating system. Particularly, FC reaches 65% without any inhibition time at 405 nm, which corresponds to the maximum absorbance of **PBPZn**. These results are in accordance with the rapid formation and release of photoacid (H^+) upon the irradiation of **PBPZn**/Iod photo-initiating system (experience with RhB). Remarkably, **PBPZn**/Iod system shows higher initiating properties than that of common and well-known systems *i.e.* CQ/Iod and BP/Iod. Surprisingly, **PBP**/Iod is unable to promote CP of EPOX. This is mainly due to the long-time dependent release of H^+ upon the photolysis of **PBP**/Iod system.

Table 4 *Final EPOX conversions obtained with RT-FTIR, after 800 s of irradiation with different LEDs in the presence of different photo-initiating systems under air. Photosensitizer / Iod = 0.5% / 2%, w/w.*

Photoinitiating systems	Final conversion (%)			
	385 nm	405 nm	505 nm	530 nm
PBP/Iod/EPOX	np	np	np	np
PBPZn/Iod/EPOX	50	63	30	50
CQ/Iod/EPOX	np	np	np	np
BP/Iod/EPOX	np	np	np	np
Iod/EPOX	np	np	-	-

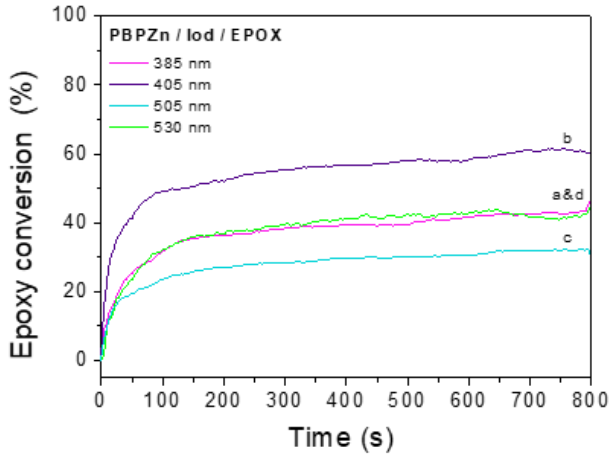

Fig. 6 *Kinetic profiles for the CP of EPOX with **PBPZn**/Iod (0.5/2%, w/w) under air and upon LEDs irradiation at a) 385 nm, b) 405 nm, c) 505 nm and d) 530 nm irradiation*

Free-radical polymerization of SOA under light irradiation.

The kinetic profiles for the FRP of SOA (acrylate function conversion *vs* irradiation time) under LED@405 nm irradiation in laminate with different photo-initiating systems based on **PBP** and **PBPZn** with MDEA, Iod, cysteamine or *N*-acetylcysteine are displayed in **Fig. 7**, and in **Figure S34-S37** for the other irradiation wavelengths. The FC of SOA after 800 s of irradiation are summarized in **Table 5**. Note that the mass percentage of cysteamine used in the photo-initiating systems has been decreased due to solubility issues.

Remarkably, the photo-initiating systems based on **PBPZn** highlight very high acrylate FCs (up to 90%) under the irradiation with different visible light emitting diodes at 405, 505 and 530 nm in laminate conditions. For instance, the acrylate FCs with **PBPZn**/Iod reach respectively 86, 52 and 75 % at 405, 505 and 530 nm. In the same experimental conditions, the final acrylate conversions of SOA with **PBPZn**/MDEA reach 91, 51 and 62 %. The high FCs at 405 and 530 nm are in part due to the high visible-light absorbance of **PBPZn** at these wavelengths. These interesting results are in accordance with the formation of highly reactive initiating species (according to EPR results) *i.e.* 4-methylphenyl and α-aminoalkyl radicals which are generated from the photolysis of **PBPZn**/Iod and **PBPZn**/MDEA photo-initiating systems, respectively. The formation of these radicals are also supported by the low free energy changes ΔG_{Tlod} (**PBPZn**) (evaluated to be -106.13 kJ.mol^{-1} for **PBPZn**/Iod) and ΔG_{TMDEA} (**PBPZn**) (evaluated to be -59.8 kJ.mol^{-1} for **PBPZn**/MDEA), confirming thus the efficient electron transfer reaction from the triplet excited states of both porphyrins to the ground state of the co-initiators (Iod or MDEA). The FCs of SOA with **PBPZn**/thiol-based systems are also relatively high but lower than that observed with the presence of MDEA or Iod. Indeed, it is known that the rate of addition of thiyl radicals to double bonds is much lower than that for methylphenyl and aminoalkyl radicals.[61]

Also, the lower delta G values with thiol-based systems confirm their lower reactivity compared with MDEA (or Iod)-based systems. Interestingly, the PBP-based photo-initiating systems (**PBP**/MDEA and **PBP**/Iod) show lower initiating properties than that observed with **PBPZn**/MDEA and **PBPZn**/Iod. Indeed, the radical cation centered on **PBPZn** (PBPZn$^{\bullet+}$) which was observed in EPR experiments, is reactive towards the acrylate functions and can initiate the free-radical photopolymerization of SOA. Despite the oxygen inhibition, the FCs of SOA with **PBPZn** (or **PBP**) /MDEA (or Iod) remain very high (up to 82% with **PBPZn**/MDEA) upon LED@405 nm irradiation. For instance, α-aminoalkyl radicals can react with oxygen to form inert initiating species *i.e.* peroxyl radicals, which can be involved in a H-abstraction reaction to re-generate α-aminoalkyl radicals. Considering the thiol-based photo-initiating systems upon LED@405 nm irradiation under air, the FCs of SOA are not surprisingly very high. The thiyl radicals generated from the photolysis of **PBP** (or **PBPZn**)/cysteamine (or *N*-acetylcysteine), according to EPR experiments, are consumed by oxygen to form peroxyl radicals (RSOO•).

The later may abstract hydrogen from cysteamine (or *N*-acetylcysteine) to form again thiyl radicals (RS•), allowing the thiol-ene reaction to occur.[62,63] We can also notice that the porphyrin-based photo-initiating systems show higher initiating properties than that observed for common CQ and BP-based systems under visible-light irradiation (> 405 nm).

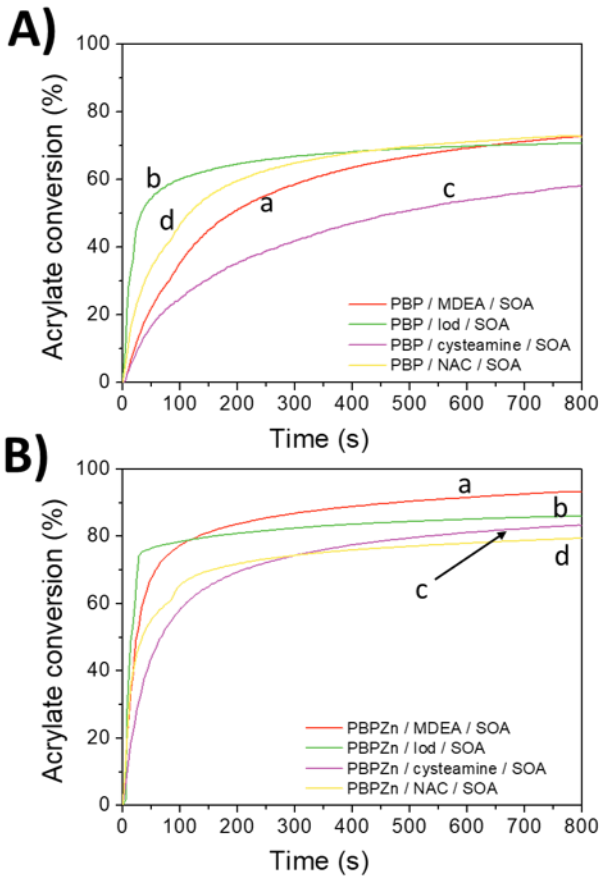

Fig. 7 *Kinetic profiles (acrylate function conversion vs. irradiation time) for the FRP of SOA in the presence of* ***A) PBP*** *and* ***B) PBPZn****-based photo-initiating systems in laminate upon LED@405 nm irradiation using (a) MDEA (2 wt %), (b) Iod (2 wt %), (c) cysteamine (1 wt %) and (d) NAC = N-acetyl cysteine (2 wt %). Porphyrin derivative = 0.5 wt%*

Table 5 *Acrylate final conversions of SOA obtained by RT-FTIR using different photo-initiating systems under air and in laminate, upon different LEDs irradiation (LEDs@385, 405, 505 and 530 nm). Time of irradiation = 800 s. N-acetylcysteine = NAC. Porphyrin derivative / co-initiator = 0.5% / 2%, w/w.*

Photo-initiating systems	**Final conversion (%)**							
	385 nm		405 nm		505 nm		530 nm	
PBP/MDEA/SOA	48 [a]	20 [b]	**72** [a]	**57** [b]	np [a]	np [b]	29 [a]	np [b]
PBPZn/MDEA/SOA	83 [a]	61 [b]	**91** [a]	**82** [b]	51 [a]	12 [b]	62 [a]	39 [b]
CQ/MDEA/SOA	43 [a]	np [b]	**80** [a]	**34** [b]	51 [a]	np [b]	41 [a]	np [b]
BP/MDEA (2%)/SOA	95 [a]	46 [b]	**97** [a]	**20** [b]	np [a]	np [b]	np [a]	np [b]
PBP/Iod/SOA	72 [a]	32 [b]	**70** [a]	**53** [b]	45 [a]	np [b]	52 [a]	7 [b]
PBPZn/Iod/SOA	76 [a]	63 [b]	**86** [a]	**77** [b]	52 [a]	np [b]	75 [a]	48 [b]
CQ/Iod/SOA	79 [a]	13 [b]	**84** [a]	**51** [b]	78 [a]	42 [b]	73 [a]	np [b]
BP/Iod/SOA	86 [a]	35 [b]	**73** [a]	**13** [b]	np [a]	18 [b]	18 [a]	np [b]

PBP/cysteamine/SOA	39 [a]	16 [b]	**57** [a]	**43** [b]	16 [a]	np [b]	23 [a]	np [b]
PBPZn/cysteamine/SOA	74 [a]	48 [b]	**83** [a]	**74** [b]	42 [a]	9 [b]	40 [a]	16 [b]
CQ/cysteamine/SOA	Polymerization at room temperature							
BP/cysteamine/SOA	92 [a]	40 [b]	**75** [a]	**20** [b]	np [a]	np [b]	np	np [b]
PBP/NAC/SOA	67 [a]	18 [b]	**72** [a]	**53** [b]	np [a]	np [b]	np [a]	np [b]
PBPZn/NAC/SOA	62 [a]	46 [b]	**80** [a]	**73** [b]	40 [a]	22 [b]	60 [a]	25 [b]
CQ/ NAC/SOA	56 [a]	np [b]	**89** [a]	**np** [b]	70 [a]	np [b]	35 [a]	np [b]
BP/NAC/SOA	94 [a]	17 [b]	**95** [a]	**10** [b]	np [a]	np [b]	np [a]	np [b]

[a] under laminate, [b] under air

Photodynamic inactivation of bacteria.

New photoinduced materials were synthesized with the most efficient photo-initiating system *i.e.* **PBPZn**/MDEA. The optical image of the resulting material is displayed in **Figure S38**. Prior to the antibacterial experiments, the capability of the porphyrin to produce reactive oxygen species (ROS) under visible-light irradiation was tested by UV-vis spectroscopy. The formation of singlet oxygen was demonstrated by the oxidation of a specific singlet oxygen trap, TPCPD, by following the decrease of its absorbance at 510 nm under light exposure (**Fig. 8A**). In light of these results, it is likely that porphyrin-based materials can be used as photoactive molecule for inducing bacterial death under visible-light irradiation.

Materials were then incubated one night into a solution of *S. aureus*, to allow their adhesion on the surface of the porphyrin-based materials. Then, half of the samples have been put in the dark at room temperature, while the other ones have been irradiated under visible light for 1 hour per side. The antibacterial properties of the materials were then evaluated according to the counting method by evaluating the number of colonies forming units (CFUs). Not surprisingly, the proliferation of *S. aureus* was observed on the "dark" samples (300000 CFUs) whereas few CFUs (6000) were evidenced at the surface of the irradiated samples, demonstrating thus their photoactive antibacterial properties of the porphyrin (**PBPZn**)-based material (**Fig. 8B**).

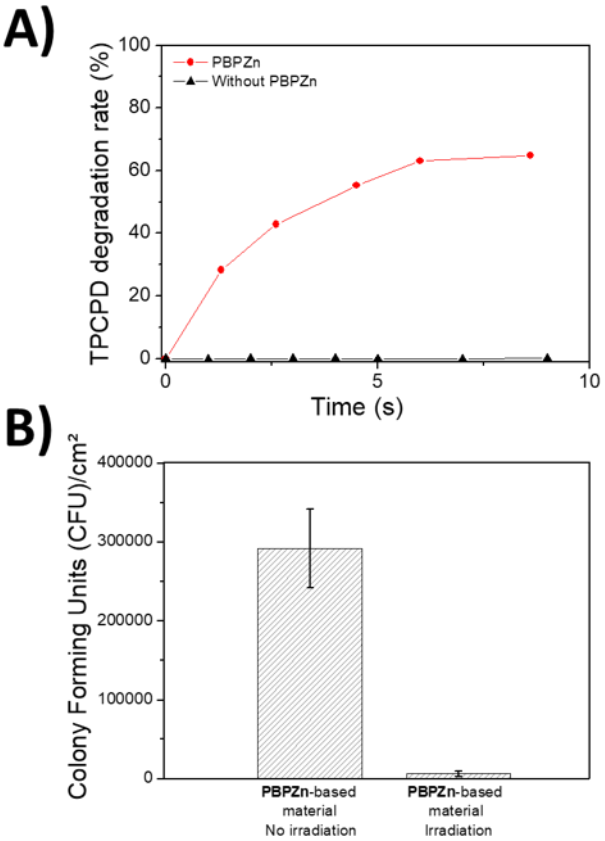

*Fig. 8 A) Degradation of TPCPD under irradiation and B) influence of the visible-light irradiation on the proliferation of S. aureus on the surface of the **PBPZn**-based material.*

Conclusions

Two new porphyrin based on benzophenone moiety *i.e.* **PBP** and **PBPZn**, have been designed and synthesized for photopolymerization applications. **PBP** and **PBPZn** are used as new visible-light absorbing photosensitizers, and their combination with suitable co-initiators leads to high final acrylate conversions (FCs) under LEDs@405, 505 and 530 nm exposure, even under air. Interestingly, both porphyrins can be used as an electron donor molecule when combined with iodonium salt, generating thus highly efficient initiating phenyl radicals and Bronsted acid (H^+) to promote free-radical and cationic photopolymerization, respectively. The metal complexation of **PBP** (**PBPZn**) demonstrates a great photopolymerization efficiency over **PBP** due to the formation of Zn-based cation radical according to EPR results. For instance, the FCs of SOA using **PBPZn**/Iod as photoinitiating system lead in laminate to 86%, 52% and 75% under LEDs@405, 505 and 530 nm, respectively. FCs obtained with **PBPZn**/Iod are higher than those observed with commonly used photosensitizers (CQ or BP) in the visible range and for λ > 405 nm. **PBP** and **PBPZn** can be also involved in a H-abstraction reaction when associated with MDEA, cysteamine and *N*-acetylcysteine. For the first time, interesting kinetic profiles for the polymerization of a bio-based monomer (SOA) were observed under blue and green-light irradiation. Notably, the aminoalkyl and thiyl radicals which are generated from the photolysis of porphyrins/MDEA and porphyrin/cysteamine (or *N*-acetylcysteine) respectively, can initiate the radical polymerization of SOA and very high FCs were observed; up to 90% under LED@405 nm and > 60% under LED@530 nm with **PBPZn**/MDEA and **PBPZn**/*N*-acetylcysteine. Finally, **PBPZn**-based materials demonstrated photoactivable properties for antibacterial applications. Under visible-light irradiation, these materials are able to produce biocide reactive

oxygen species leading to a tremendous inhibition of *S. aureus* proliferation.

Conflicts of interest

There are no conflicts to declare.

Acknowledgements

I.K. and D.J. are indebted to the French Agence Nationale de la Recherche (ANR) under contract ANR-20-CE29-0005 (BSE-Forces) for financial support. I. K. is thankful to the EUR LUMOMAT program and the Investments for the Future program (contract ANR-18-EURE-0012) for their support. The Nantes team is thankful for the generous allocations of time by the CCIPL/GliCID computational center installed in Nantes. DLV would like to thank LaBex MMCD for financial support of the PhD thesis. DLV also thank Prof. Vlasta Brezova and Arnaud Brosseau for their help in EPR and laser flash photolysis experiments.

References

1 Y. Yagci, S. Jockusch and N. J. Turro, Macromolecules, 2010, 43, 6245.
2 B. P. Chan, Tissue Engineering Part B: Reviews, 2010, 16, 509.
3 J.-H. Back, Y. Kwon, H. Cho, H. Lee, D. Ahn, H.-J. Kim, Y. Yu, Y. Kim, W. Lee and M. S. Kwon, Advanced Materials, 2023, 35, 2204776.
4 D. Kim, H. Kim, W. Jeon, H.-J. Kim, J. Choi, Y. Kim and M. S. Kwon, Advanced Materials, 2023, 2309891.
5 A. Al Mousawi, D. M. Lara, G. Noirbent, F. Dumur, J. Toufaily, T. Hamieh, T.-T. Bui, F. Goubard, B. Graff, D. Gigmes, J. P. Fouassier and J. Lalevée, Macromolecules, 2017, 50, 4913.
6 D. Ahn, L. M. Stevens, K. Zhou and Z. A. Page, ACS Cent. Sci., 2020, 6, 1555.
7 S. Shin, Y. Kwon, C. Hwang, W. Jeon, Y. Yu, H.-J. Paik, W. Lee, M. S. Kwon and D. Ahn, Advanced Materials, 2024, 2311917.
8 P. Lu, D. Ahn, R. Yunis, L. Delafresnaye, N. Corrigan, C. Boyer, C. Barner-Kowollik and Z. A. Page, Matter, 2021, 4, 2172.
9 K. Lee, N. Corrigan and C. Boyer, Angewandte Chemie International Edition, 2021, 60, 8839.
10 H. Claus, Photochemistry and Photobiology, 2021, 97, 471–476.
11 K. J. Gromkowska-Kępka, A. Puścion-Jakubik, R. Markiewicz-Żukowska and K. Socha, J of Cosmetic Dermatology, 2021, 20, 3427.
12 D. K. Balta, G. Temel, G. Goksu, N. Ocal and N. Arsu, Macromolecules, 2012, 45, 119.
13 L. Breloy, V. Brezová, A. Blacha-Grzechnik, M. Presset, M. S. Yildirim, I. Yilmaz, Y. Yagci and D.-L. Versace, Macromolecules, 2020, 53, 112.
14 Z. El Hajj, L. Pierau, J.-P. Malval, J. Marrot, P.-E. Mazeran, D. Naoufal, M.-H. Ha-Thi, K. Steenkeste, A. Dolbecq, S. Floquet, O. Oms, D.-L. Versace and P. Mialane, Macromolecules, 2023, 56, 6105.
15 C. Elian, B. Quienne, S. Lajnef, F. Peyrot, R. Moilleron, S. Abbad Andaloussi, S. Caillol and D.-L. Versace, European Polymer Journal, 2023, 112369.
16 M. Tozuka, T. Igarashi and T. Sakurai, Polym J, 2009, 41, 709.
17 K. Wang, S. Jiang, J. Liu, J. Nie and Q. Yu, Progress in Organic Coatings, 2011, 72, 517.
18 P. Xiao, J. Zhang, F. Dumur, M. A. Tehfe, F. Morlet-Savary, B. Graff, D. Gigmes, J. P. Fouassier and J. Lalevée, Progress in Polymer Science, 2015, 41, 32.
19 L. Pierau, C. Elian, J. Akimoto, Y. Ito, S. Caillol and D.-L. Versace, Progress in Polymer Science, 2022, 127, 101517.
20 M. Sangermano, I. Roppolo and A. Chiappone, Polymers, 2018, 10, 136.
21 J.-P. Fouassier and J. Lalevée, Photoinitiators for Polymer Synthesis: Scope, Reactivity, and Efficiency, John Wiley & Sons, 2012.
22 S. M. Müller, S. Schlögl, T. Wiesner, M. Haas and T. Griesser, ChemPhotoChem, 2022, 6, e202200091.
23 C. Dietlin, S. Schweizer, P. Xiao, J. Zhang, F. Morlet-Savary, B. Graff, J.-P. Fouassier and J. Lalevée, Polym. Chem., 2015, 6, 3895.
24 M. Athar, H. Mukhtar and D. R. Bickers, Journal of Investigative Dermatology, 1988, 90, 652.
25 X. Ding, Q. Xu, F. Liu, P. Zhou, Y. Gu, J. Zeng, J. An, W. Dai and X. Li, Cancer Letters, 2004, 216, 43.
26 R.-M. Ion, in Phthalocyanines and Some Current Applications, IntechOpen, 2017.
27 G. Ng, K. Jung, J. Li, C. Wu, L. Zhang and C. Boyer, Polym. Chem., 2021, 12, 6548.
28 S. Shanmugam, J. Xu and C. Boyer, J. Am. Chem. Soc., 2015, 137, 9174.
29 D. Kim and J. W. Stansbury, J. Polym. Sci. A Polym. Chem., 2009, 47, 3131.
30 A. Al Mousawi, C. Poriel, F. Dumur, J. Toufaily, T. Hamieh, J. P. Fouassier and J. Lalevée, Macromolecules, 2017, 50, 746.
31 A. Bonardi, F. Bonardi, G. Noirbent, F. Dumur, C. Dietlin, D. Gigmes, J.-P. Fouassier and J. Lalevée, Polym. Chem., 2019, 10, 6505.
32 G. Noirbent, Y. Xu, A.-H. Bonardi, D. Gigmes, J. Lalevée and F. Dumur, European Polymer Journal, 2020, 139, 110019.
33 L. Breloy, V. Brezová, S. Richeter, S. Clément, J.-P. Malval, S. A. Andaloussi and D.-L. Versace, Polym. Chem., 2022, 13, 1658.
34 M. Besouw, R. Masereeuw, L. van den Heuvel and E. Levtchenko, Drug Discovery Today, 2013, 18, 785.
35 United States, US8802399B2, 2014.
36 V. Mokhtari, P. Afsharian, M. Shahhoseini, S. M. Kalantar and A. Moini, Cell J, 2017, 19, 11.
37 M. J. Frisch, G. W. Trucks, H. B. Schlegel, G. E. Scuseria, M. A. Robb, J. R. Cheeseman, G. Scalmani, V. Barone, G. A. Petersson, H. Nakatsuji, X. Li, M. Caricato, A. V. Marenich, J. Bloino, B. G. Janesko, R. Gomperts, B. Mennucci, H. P. Hratchian, J. V. Ortiz, A. F. Izmaylov, J. L. Sonnenberg, D. Williams-Young, F. Ding, F. Lipparini, F. Egidi, J. Goings, B. Peng, A. Petrone, T. Henderson, D. Ranasinghe, V. G. Zakrzewski, J. Gao, N. Rega, G. Zheng, W. Liang, M. Hada, M. Ehara, K. Toyota, R. Fukuda, J. Hasegawa, M. Ishida, T. Nakajima, Y. Honda, O. Kitao, H. Nakai, T. Vreven, K. Throssell, J. A. Montgomery Jr., J. E. Peralta, F. Ogliaro, M. J. Bearpark, J. J. Heyd, E. N. Brothers, K. N. Kudin, V. N. Staroverov, T. A. Keith, R. Kobayashi, J. Normand, K. Raghavachari, A. P. Rendell, J. C. Burant, S. S. Iyengar, J. Tomasi, M. Cossi, J. M. Millam, M. Klene, C. Adamo, R. Cammi, J. W. Ochterski, R. L. Martin, K. Morokuma, O. Farkas, J. B. Foresman and D. J. Fox, 2016.
38 T. Yanai, D. P. Tew and N. C. Handy, Chemical Physics Letters, 2004, 393, 51.
39 F. Santoro, R. Improta, A. Lami, J. Bloino and V. Barone, The Journal of Chemical Physics, 2007, 126, 084509.

40 J. Cerezo and F. Santoro, Journal of Computational Chemistry, 2023, 44, 626.
41 F. Santoro and D. Jacquemin, WIREs Computational Molecular Science, 2016, 6, 460.
42 L. Breloy, R. Losantos, D. Sampedro, M. Marazzi, J.-P. Malval, Y. Heo, J. Akimoto, Y. Ito, V. Brezová and D.-L. Versace, Polym. Chem., 2020, 11, 4297.
43 L. Breloy, V. Brezová, J.-P. Malval, A. Rios de Anda, J. Bourgon, T. Kurogi, D. J. Mindiola and D.-L. Versace, Macromolecules, 2019, 52, 3716.
44 S. Stoll and A. Schweiger, Journal of Magnetic Resonance, 2006, 178, 42.
45 P. Sautrot-Ba, J.-P. Malval, M. Weiss-Maurin, J. Paul, A. Blacha-Grzechnik, S. Tomane, P.-E. Mazeran, J. Lalevée, V. Langlois and D.-L. Versace, ACS Sustainable Chem. Eng., 2018, 6, 104.
46 P. Sautrot-Ba, A. Contreras, S. A. Andaloussi, T. Coradin, C. Hélary, N. Razza, M. Sangermano, P.-E. Mazeran, J.-P. Malval and D.-L. Versace, J. Mater. Chem. B, 2017, 5, 7572.
47 A. Treibs and N. Häberle, Justus Liebigs Annalen der Chemie, 1968, 718, 183.
48 J. S. Manka and D. S. Lawrence, Tetrahedron Letters, 1989, 30, 6989.
49 R. W. Boyle, C. Bruckner, J. Posakony, B. R. James and D. Dolphin, in Organic Syntheses, John Wiley & Sons, Ltd, 2003, pp. 287.
50 M. Gouterman, The Porphyrins V3: Physical Chemistry, Part A, Elsevier, 2012.
51 T. Sun, Z. Zhang, J. Xu, L. Liang, C.-L. Mai, L. Ren, Q. Zhou, Y. Yu, B. Zhang and P. Gao, Dyes and Pigments, 2021, 193, 109469.
52 W. Zheng, N. Shan, L. Yu and X. Wang, Dyes and Pigments, 2008, 77, 153.
53 R. Pudi, C. Rodríguez-Seco, A. Vidal-Ferran, P. Ballester and E. Palomares, European Journal of Organic Chemistry, 2018, 2018, 2064.
54 K. Ichimori, H. Ohya-Nishiguchi and N. Hirota, BCSJ, 1988, 61, 2753.
55 M. Conte, K. Wilson and V. Chechik, Org. Biomol. Chem., 2009, 7, 1361.
56 P. Ionita, M. Conte, B. C. Gilbert and V. Chechik, Org. Biomol. Chem., 2007, 5, 3504.
57 F. Rezaei, Y. Gorbanev, M. Chys, A. Nikiforov, S. W. H. Van Hulle, P. Cos, A. Bogaerts and N. De Geyter, Plasma Processes and Polymers, 2018, 15, 1700226.
58 J. Seth and D. F. Bocian, Journal of the American Chemical Society, 1994, 116, 143.
59 A. Boulmier, M. Haouas, S. Tomane, L. Michely, A. Dolbecq, A. Vallée, V. Brezová, D.-L. Versace, P. Mialane and O. Oms, Chemistry – A European Journal, 2019, 25, 14349.
60 F. Peyrot, S. Lajnef and D.-L. Versace, Catalysts, 2022, 12, 772.
61 J. Lalevée, X. Allonas and J.-P. Fouassier, J. Org. Chem., 2005, 70, 814.
62 C. E. Hoyle and C. N. Bowman, Angewandte Chemie International Edition, 2010, 49, 1540.
63 D. Ahn, L. M. Stevens, K. Zhou and Z. A. Page, Advanced Materials, 2021, 33, 2104906.

Supporting info

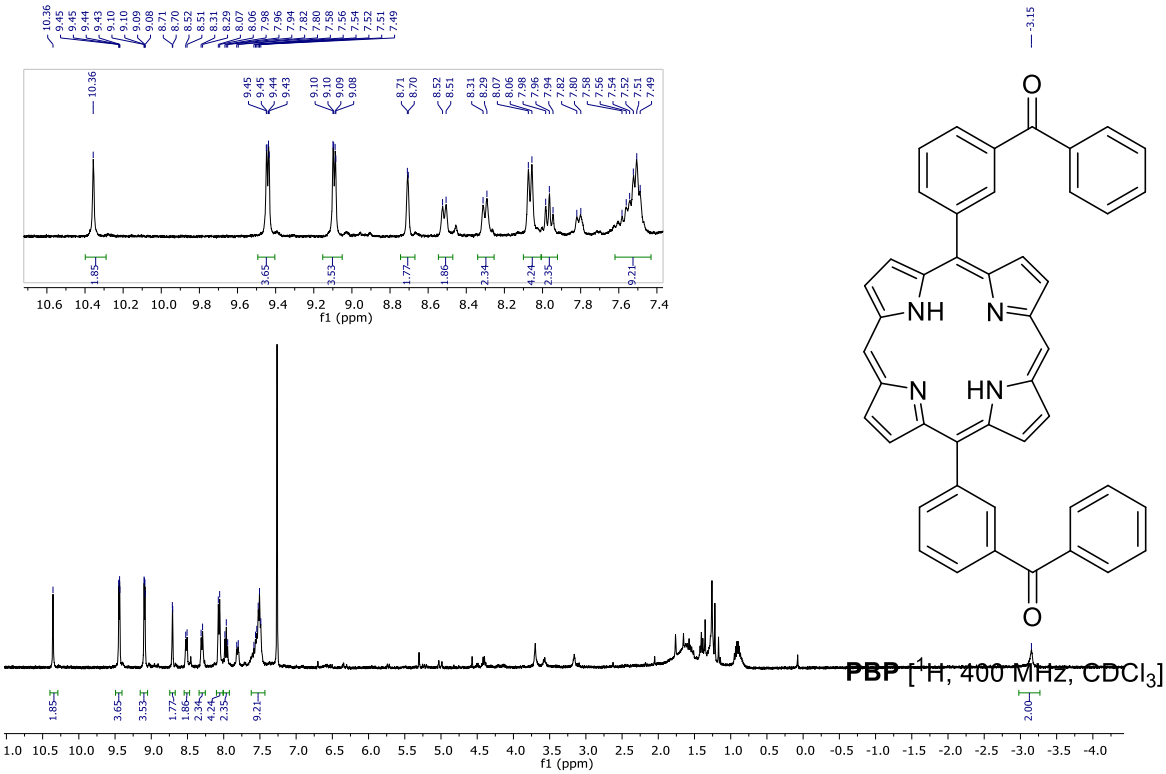

***Figure S1**: ^{1}H NMR spectrum of **PBP** in $CDCl_3$.*

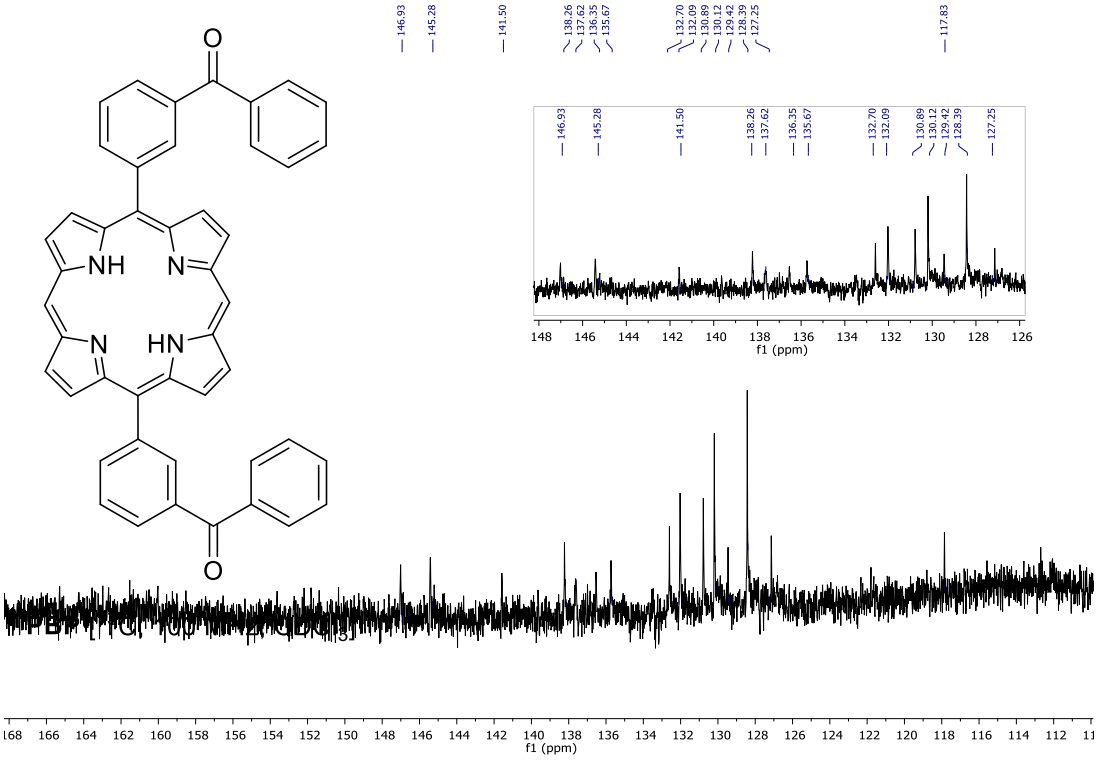

***Figure S2**: ^{13}C NMR spectrum of **PBP** in $CDCl_3$.*

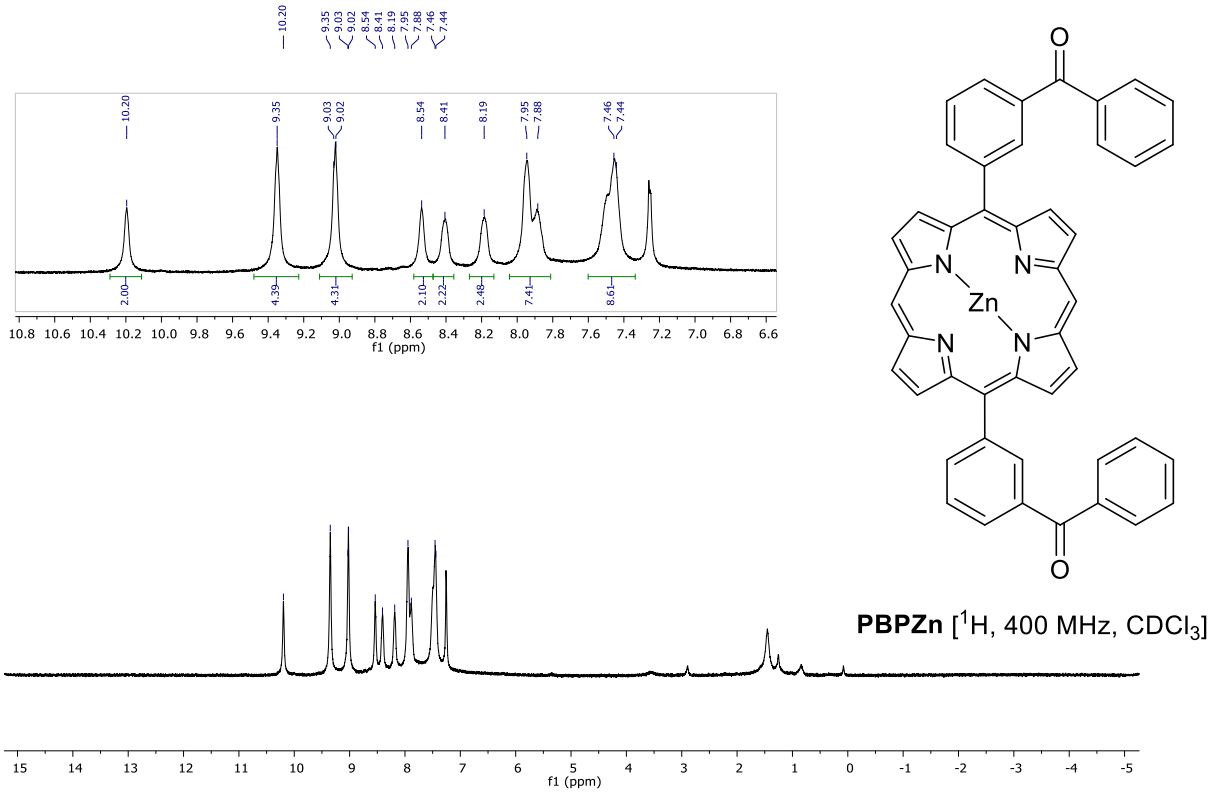

***Figure S3**: ^{1}H NMR spectrum of **PBPZn** in $CDCl_3$.*

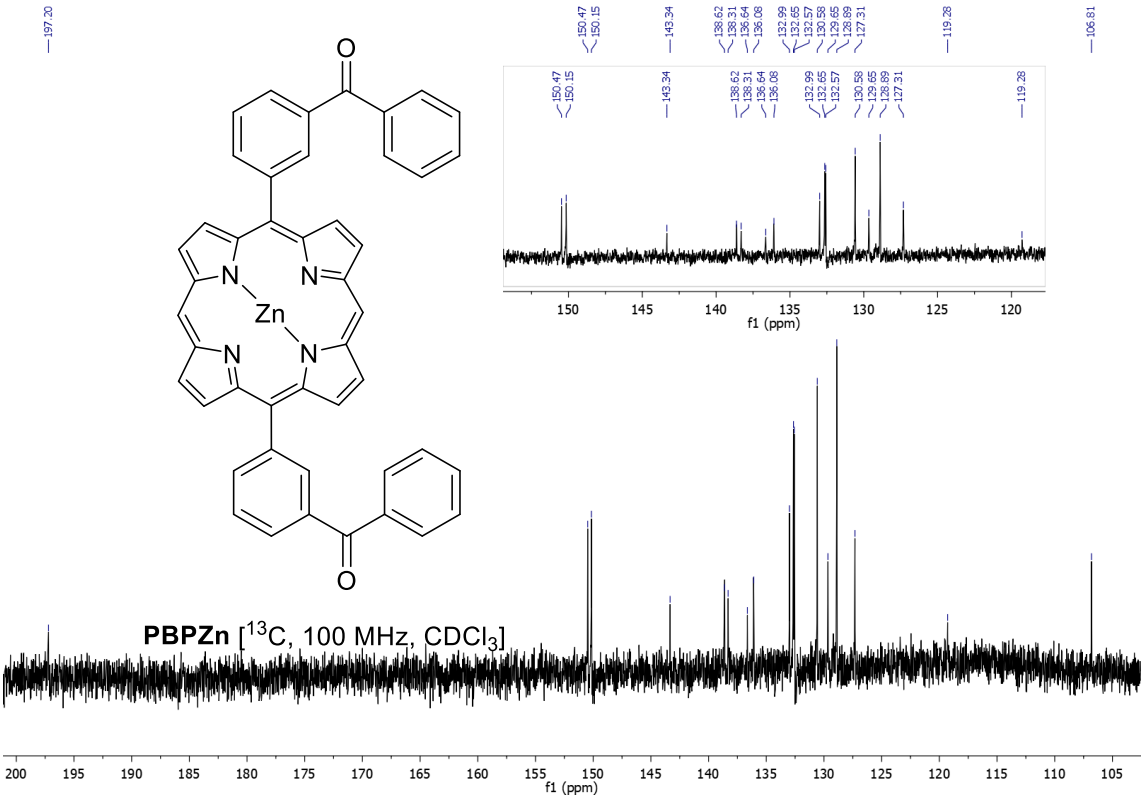

***Figure S4**: ^{13}C NMR spectrum of **PBPZn** in $CDCl_3$.*

Absorption

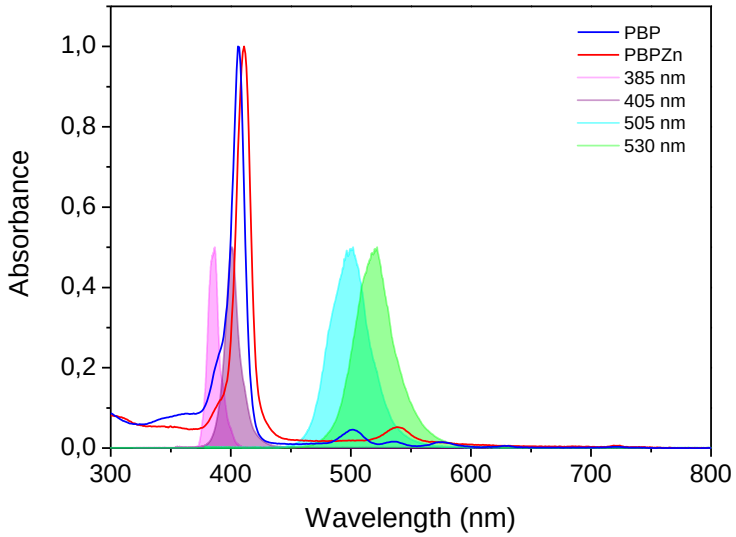

***Figure S5**: Absorption spectra of PBP and PBPZn associated with the emission spectra of the LEDs used in this study (LEDs@385, 405, 455 and 530 nm).*

TD-DFT calculations



***Figure S6**: Optimal ground-state structures of PBP (left) and PBPZn (right).*

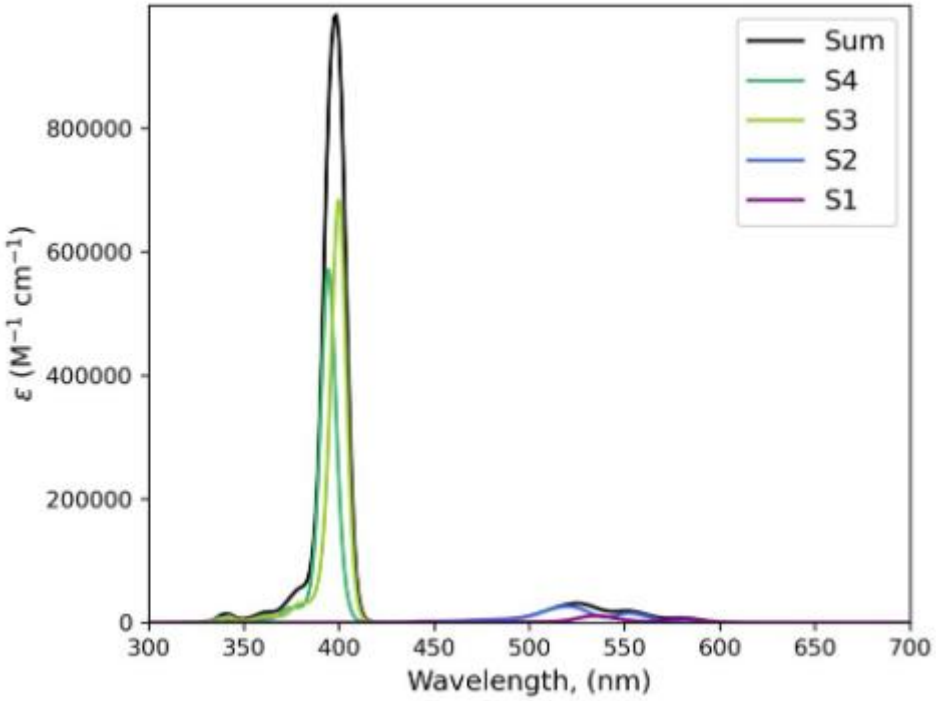

***Figure S7**: Vibrationally-resolved spectrum of PBP simulated using the Vertical Hessian model and internal coordinates.*

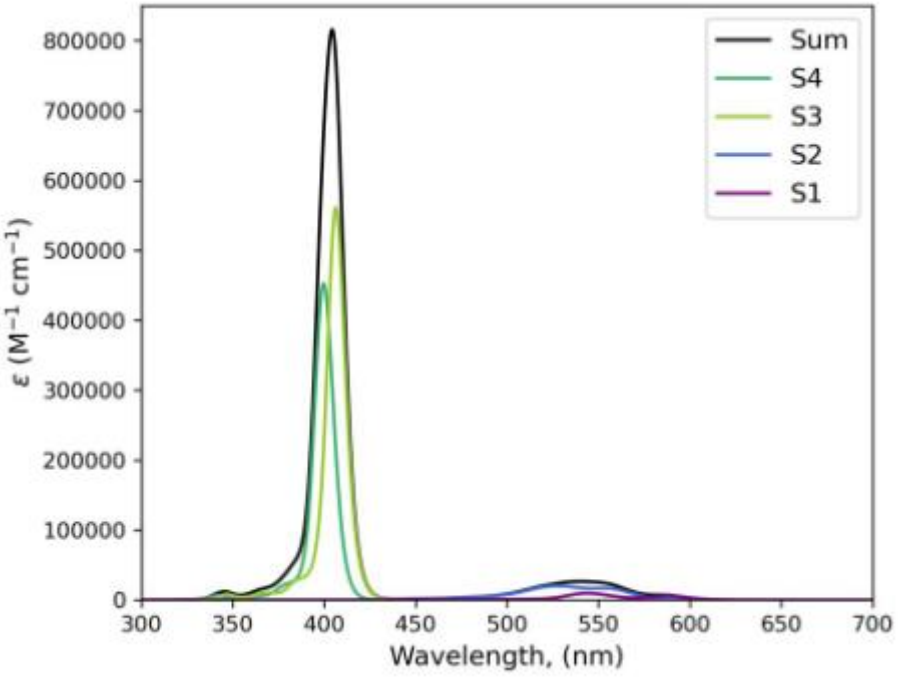

***Figure S8**: Vibrationally-resolved spectrum of PBP simulated using the Vertical Hessian model and Cartesian coordinates. The imaginary frequency for the excited states were turned real (one such frequency for S1, S2, and S4).*

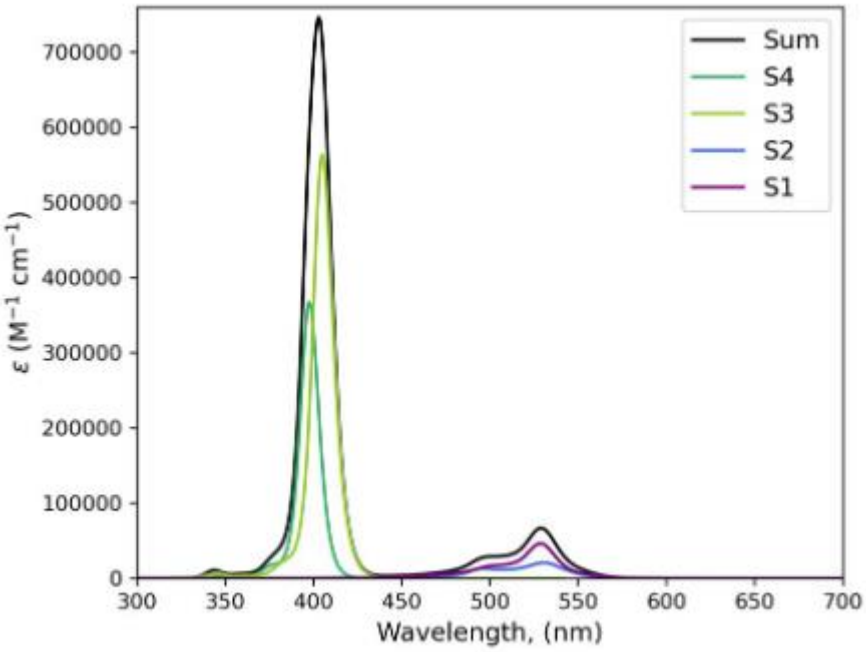

***Figure S9**: Vibrationally-resolved spectrum of PBPZn simulated using the Vertical Hessian model and Cartesian coordinates. Note that for both S1 and S4, imaginary frequencies exist in the excited-state (vertical) Hessian, and they have been turned positive.*

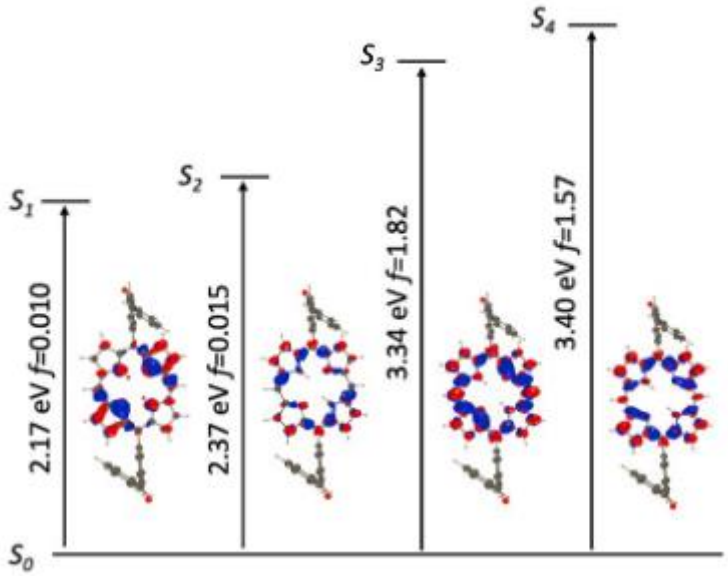

***Figure S10**: Vertical transition energies, associated oscillator strengths and electron density difference plots for PBP. In the latter representations, the blue and red lobes correspond to decrease and increase of density upon absorption (threshold 0.005 au).*

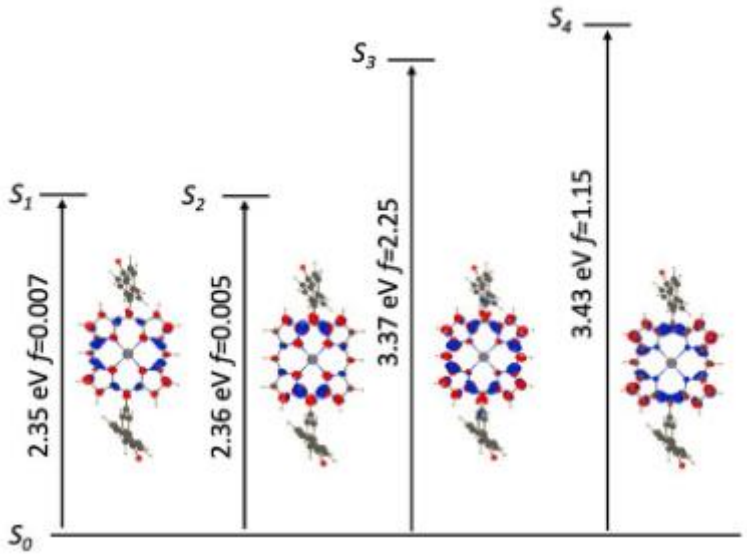

***Figure S11**: Vertical transition energies, associated oscillator strengths and electron density difference plots for PBPZn. See previous caption for more details.*

Absorption & emission

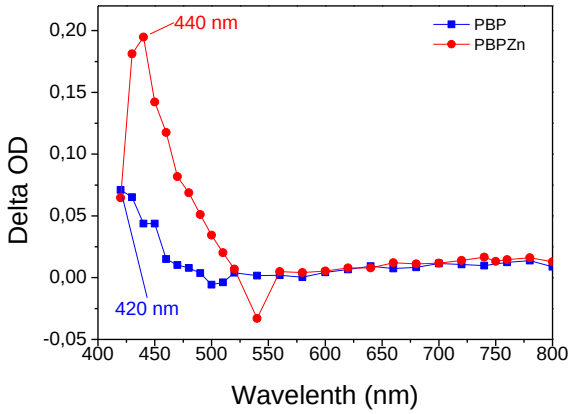

***Figure S12**: Transition absorption spectrum of PBP and PBPZn under argon in DCM (λ_{exc} = 385 nm)*

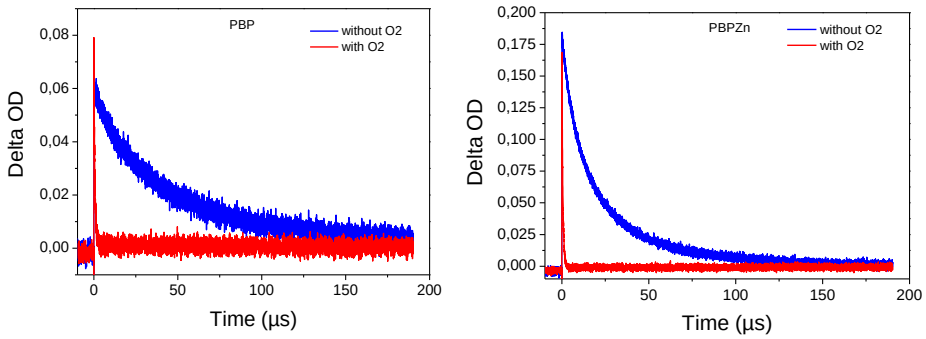

***Figure S13**: Decay traces of A) PBP and B) PBPZn triplet state after a laser pulse (λex = 385 nm) with and without oxygen.*

Cyclic voltammetry

Table S6: *Redox values and photophysical properties of the photoinitiating compounds*

Molecules	E_{ox} (eV)	E_{red} (eV)	E_S (eV)	E_T (eV)
PBP	1.47	-1.18	2.03	2.95
PBPZn	1.09	-1.48	2.14	2.82
BP	0.16 [6]	-1.20 [6]		2.38 [6]
CQ	0.12 [6]	-1.25 [6]		2.21 [6]
MDEA	0.72 [6]		-	-
Iod	-	-0.2 [6]	-	-
cysteamine	0.92 [6]		-	-
N-acetylcysteine	0.79 [6]		-	-

Photostability of the porphyrin derivatives

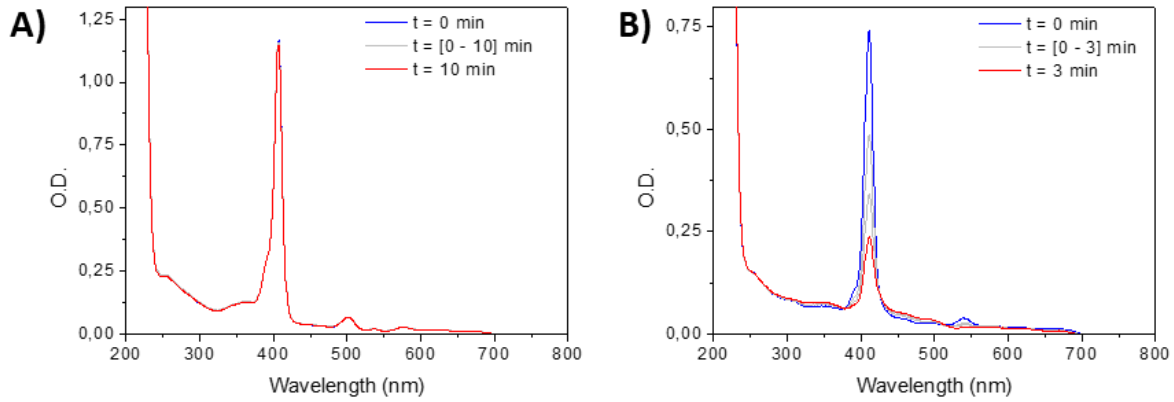

Figure S14*: Photolysis of* ***A) PBP*** *and* ***B) PBPZn*** *under irradiation with a LED@405 nm.*

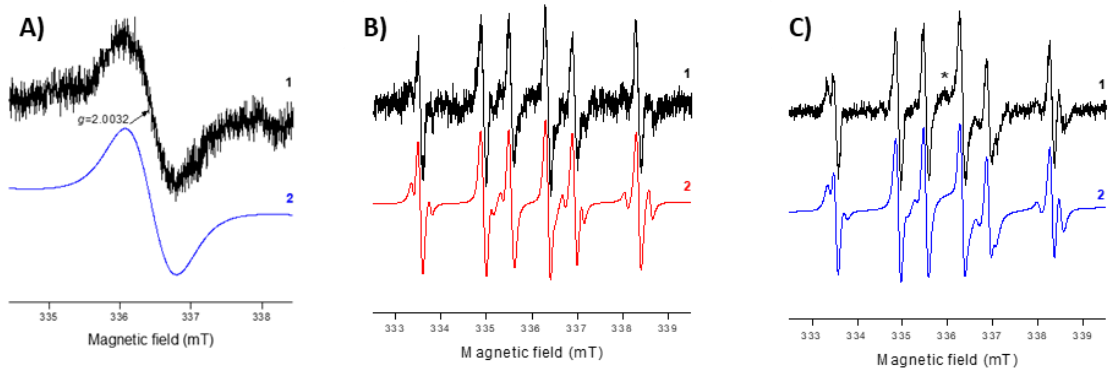

Figure S15*: The normalized experimental (1) and simulated (2) EPR spectra obtained upon continuous* in situ *LED@400 nm exposure in chloroform under irradiation for (A) PBPZn, (B) PBP with DMPO and (C) PBPZn with DMPO.*

Effect of the addition of MDEA

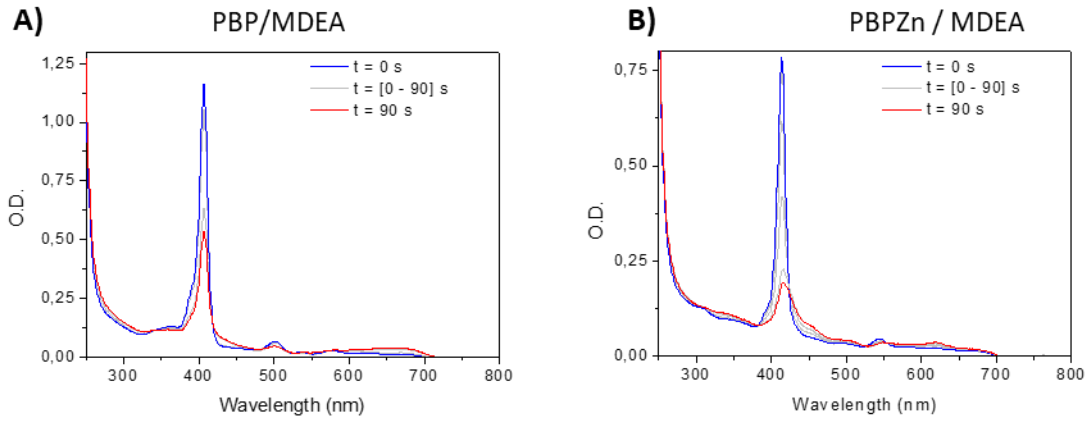

Figure S16 *: Steady state photolysis of A) PBP/MDEA and B) PBPZn/MDEA systems under air after LED @405 nm exposure.* ***[PBP]*** *= 2 x 10^{-6} mol/L,* ***[PBPZn]*** *= 6 x 10^{-6} mol/L, [MDEA] = 2.8 x 10^{-2} mol/L. Solvent = DCM.*

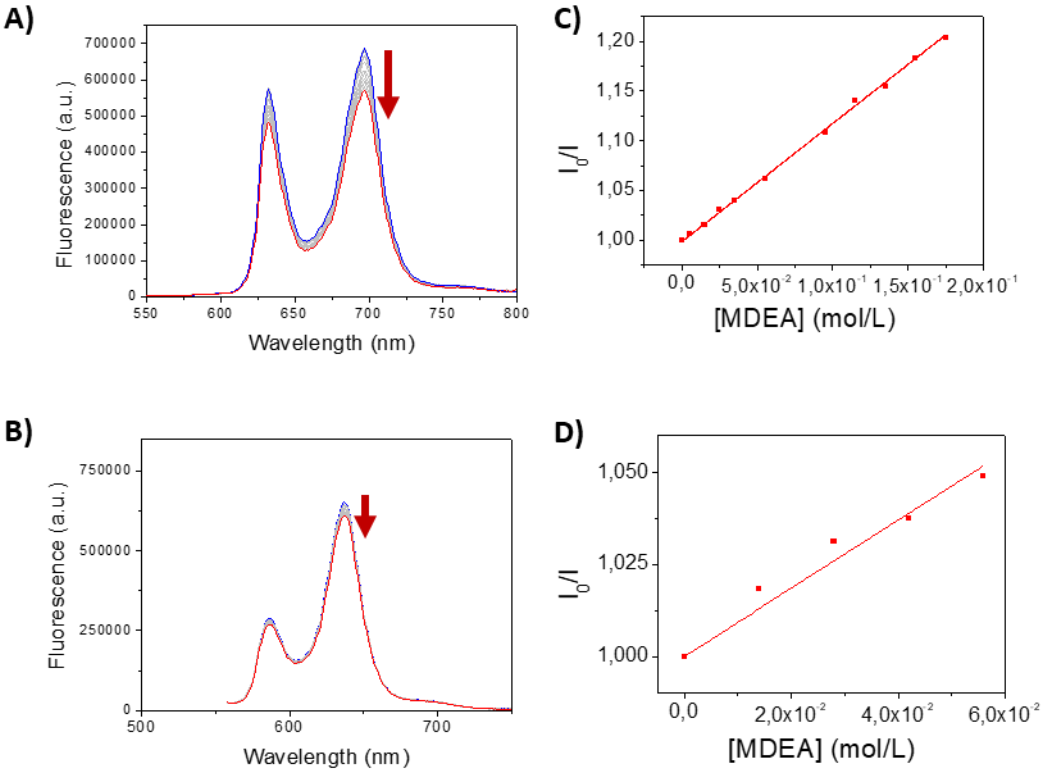

Figure S17 *: Quenching of* ***A) PBP*** *and* ***B) PBPZn*** *fluorescence after a gradual addition of MDEA.* ***[PBP]*** *=1,2x 10^{-7} mol.L^{-1},* ***[PBPZn]*** *= 5.2 x 10^{-6} mol.L^{-1} (solvent: THF). Corresponding Stern-Volmer plot for* ***C) PBP*** *($K_{SV}^{PBP/MDEA}$ = 1.2 M^{-1}) and* ***D) PBPZn*** *($K_{SV}^{PBPZn/MDEA}$ = 0.7 M^{-1}).*

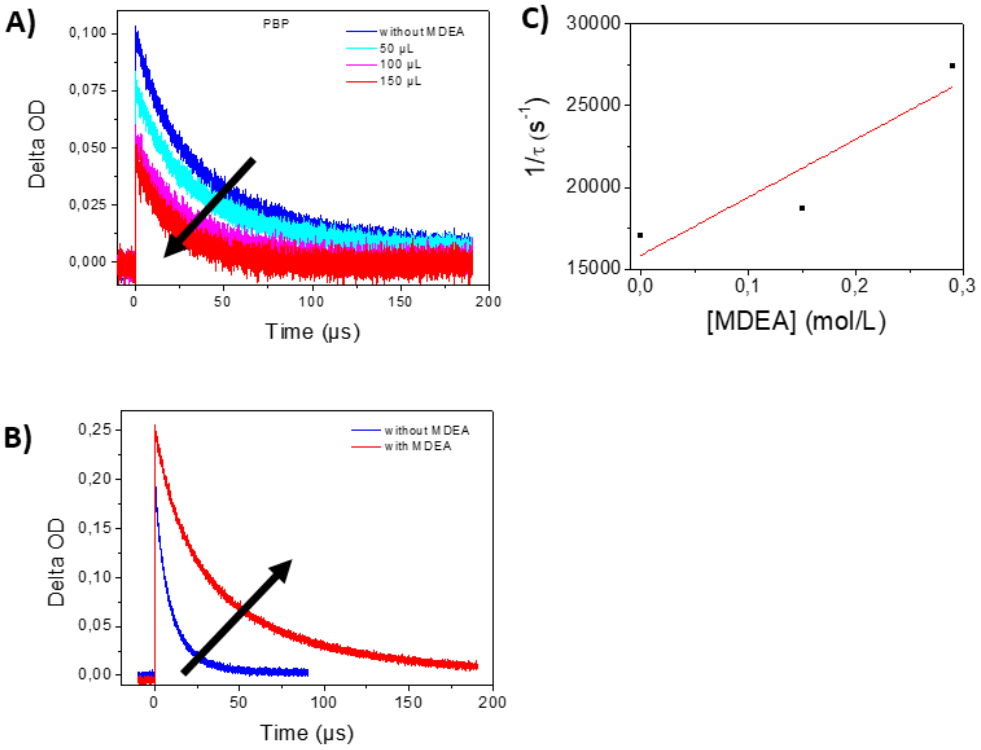

Figure S18 *: Decay traces of* ***A) PBP*** *and* ***B) PBPZn*** *triplet state after a laser pulse (λ_{ex} = 385 nm) with a gradual addition of MDEA.* ***C)*** *Corresponding Stern-Volmer plot for* ***PBP****. [****PBP****] = 1,1 x 10^{-5} mol.L^{-1} , [PBPZn] = 1,7 x 10^{-4} mol.L^{-1} , [MDEA] = 8,7 mol.L^{-1} in DCM.*

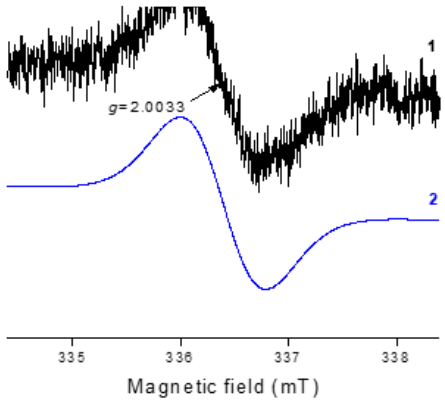

Figure S19: *The normalized experimental (1) and simulated (2) EPR spectra obtained upon continuous in situ LED@400 nm exposure of PBPZn/MDEA in chloroform and under argon.*

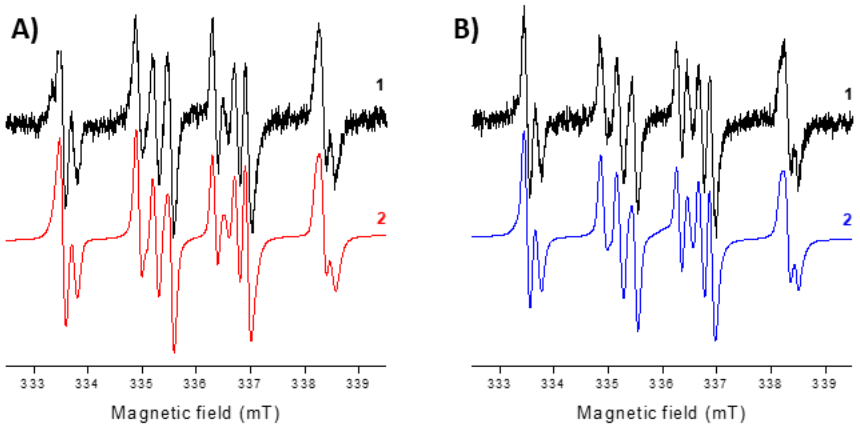

Figure S20 *: The normalized experimental (1) and simulated (2) EPR spectra obtained upon continuous in situ LED@400 nm exposure of porphyrin derivatives in chloroform under argon in the presence DMPO spin trapping agent and MDEA for* ***A)*** ***PBP*** *and* ***B)*** ***PBPZn****.*

Effect of the addition of Iod

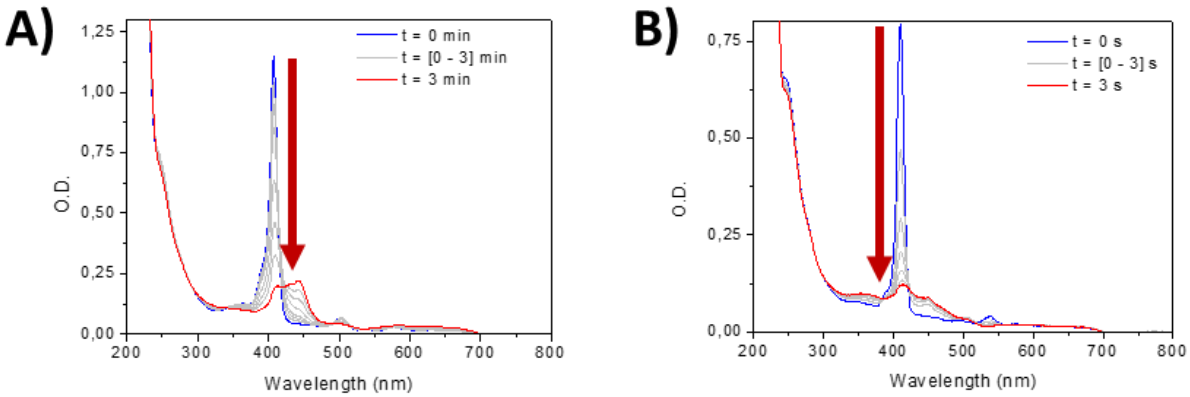

Figure S21*: Steady state photolysis of A) PBP/Iod and B) PBPZn/Iod systems under air after LED @405 nm exposure. [****PBP****] = 2 x 10*$^{-6}$ *mol/L, [****PBPZn****] = 6 x 10*$^{-6}$ *mol/L, [Iod] = 2.9 x 10*$^{-5}$ *mol/L. Solvent = DCM/*

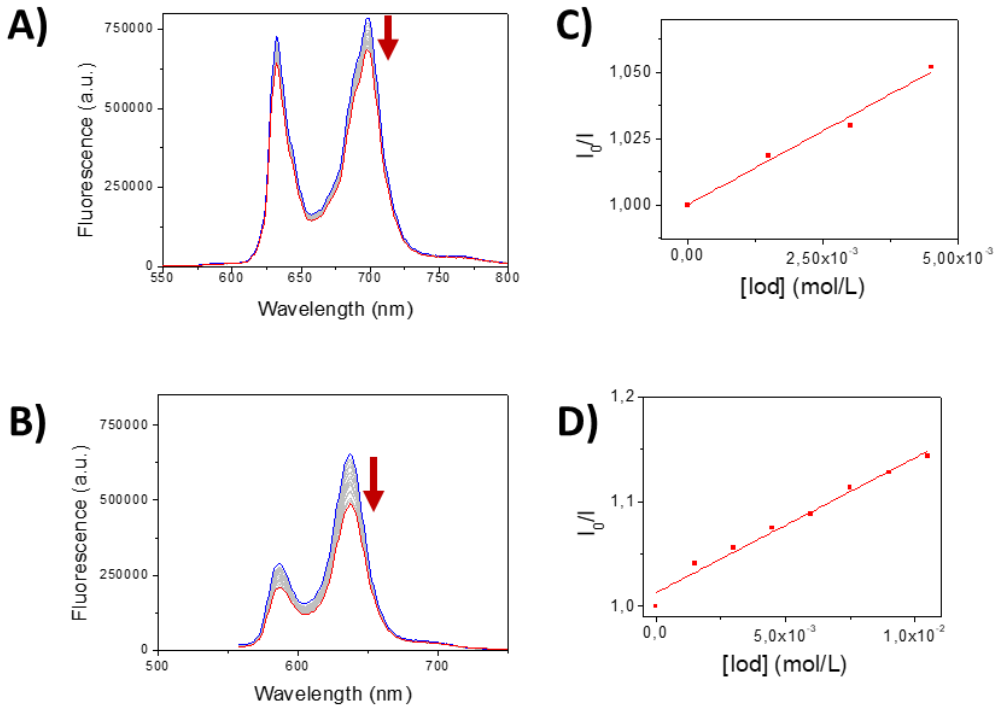

Figure S22: *Quenching of A)* ***PBP*** *and B)* ***PBPZn*** *fluorescence after a gradual addition of Iod. [**PBP**] =1,2x 10^{-7} mol.L^{-1}, [**PBPZn**] = 5.2 x 10^{-6} mol.L^{-1} (solvent: THF). Corresponding Stern-Volmer plot for* ***C) PBP*** *($K_{SV}^{PBP/Iod}$ = 11 M^{-1}) and* ***D) PBPZn*** *($K_{SV}^{PBPZn/Iod}$ = 13 M^{-1}).*

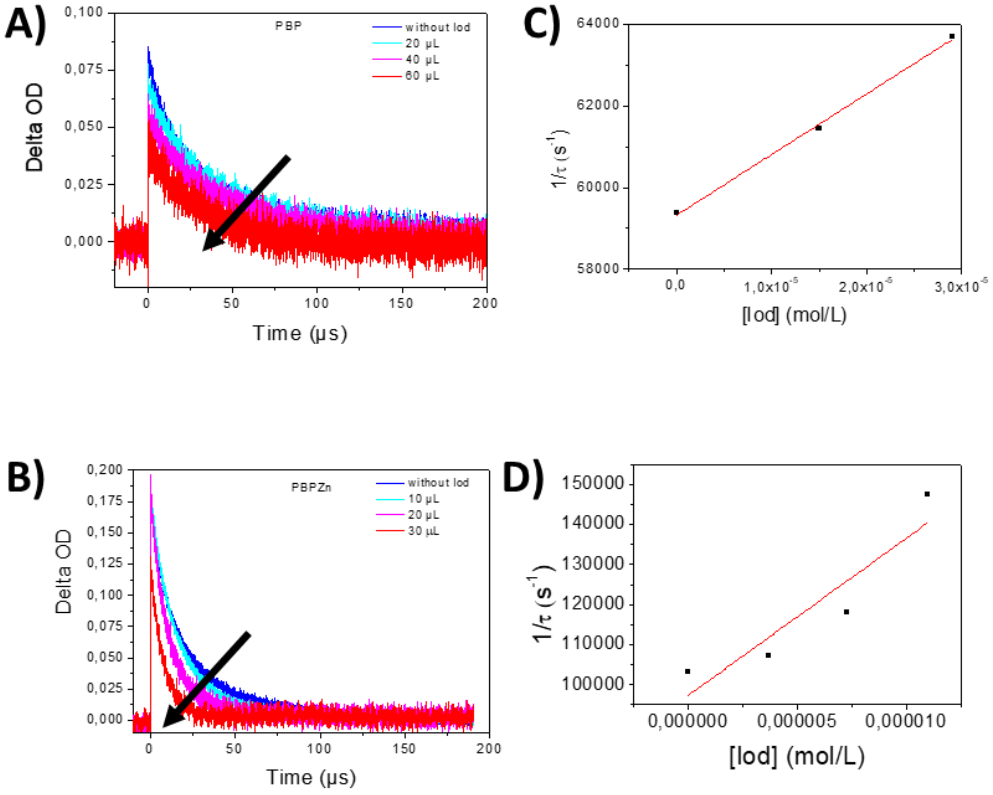

Figure S23*: Decay traces of A)* ***PBP*** *and B)* ***PBPZn*** *triplet state after a laser pulse (λ_{ex} = 385 nm) with a gradual addition of Iod. Corresponding Stern-Volmer plot for* ***C) PBP*** *and* ***D) PBPZn****. [**PBP**] = 1,1 x 10^{-5} mol.L^{-1} , [PBPZn] = 1,7 x 10^{-4} mol.L^{-1} , [Iod] = 2,2 x 10^{-3} mol.L^{-1} in DCM.*

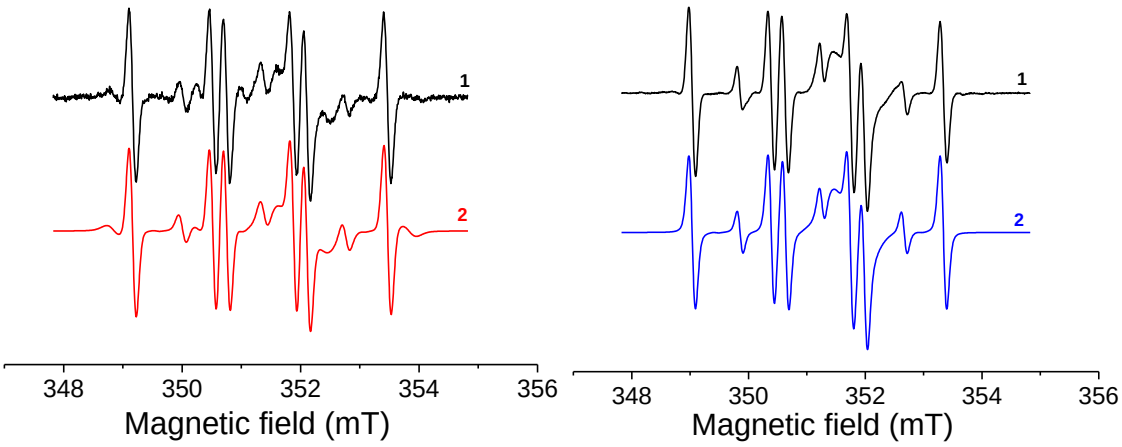

***Figure S24**: The normalized experimental (1) and simulated (2) EPR spectra obtained upon continuous in situ LED@405 nm exposure of (A) **PBP** and (B) **PBPZn**. in chloroform under argon in the presence DMPO spin trapping agent and Iod.*

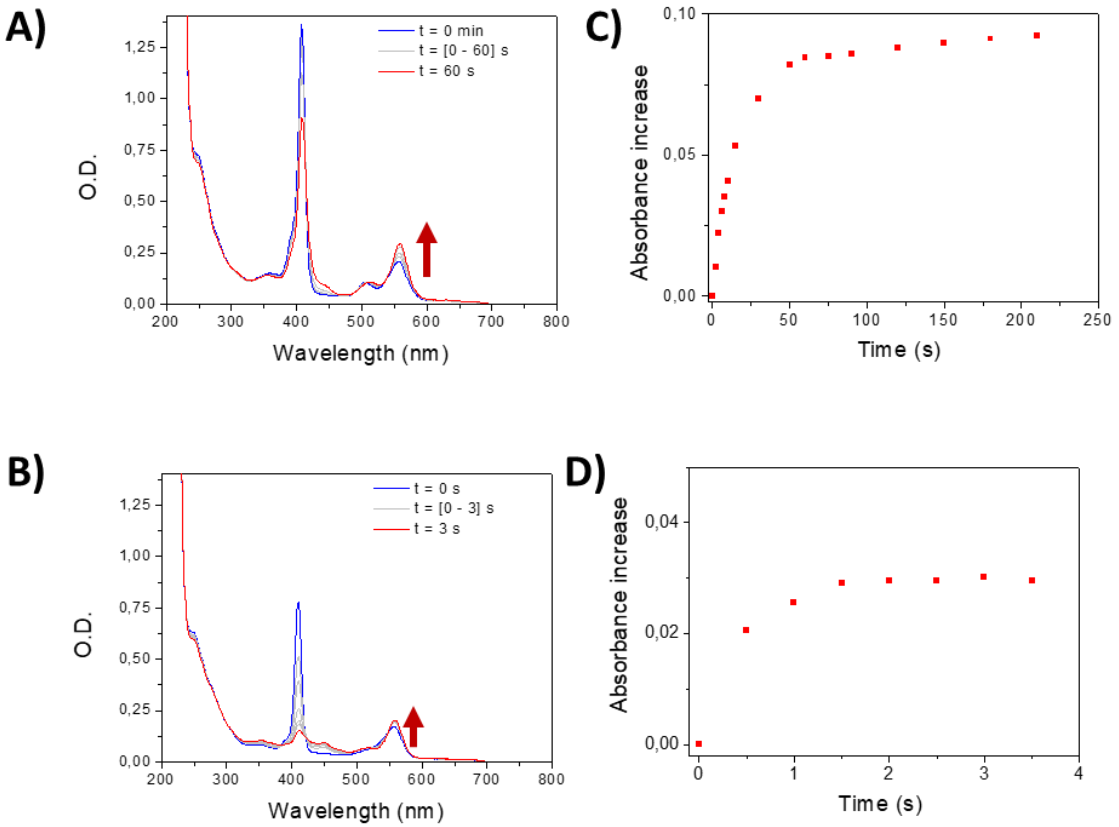

***Figure S25**: Steady-state photolysis of **A) PBP**/Iod/rhodamine B and **B) PBPZn**/Iod/rhodamine B after irradiation by LED@405 nm under air conditions. Absorbance increase at 570 nm along time for **C) PBP** and **D) PBPZn**. **[PBP]** = 2 x 10^{-6} mol/L **[PBPZn]** = 6 x 10^{-6} mol/L, [Iod] = 2,9 x 10^{-5} mol/L [RhB] = 2,4 x 10^{-5} mol/L. .*

Effect of the addition of cysteamine

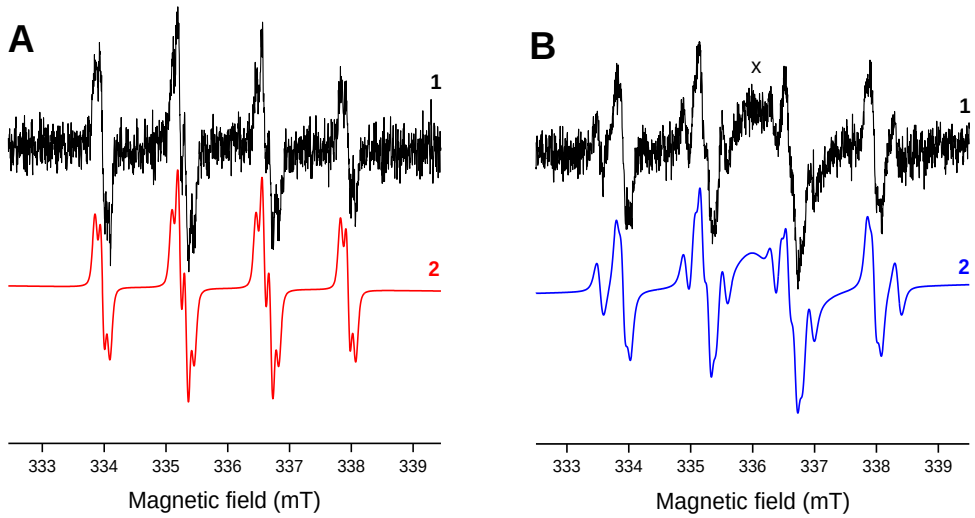

***Figure S26**: The normalized experimental (1) and simulated (2) EPR spectra obtained upon continuous in situ LED@400 nm exposure of (A) **PBP** and (B) **PBPZn** in chloroform and under argon in the presence DMPO spin trapping agent and cysteamine:. X denotes the broad signal assigned to PBPZn•–.*

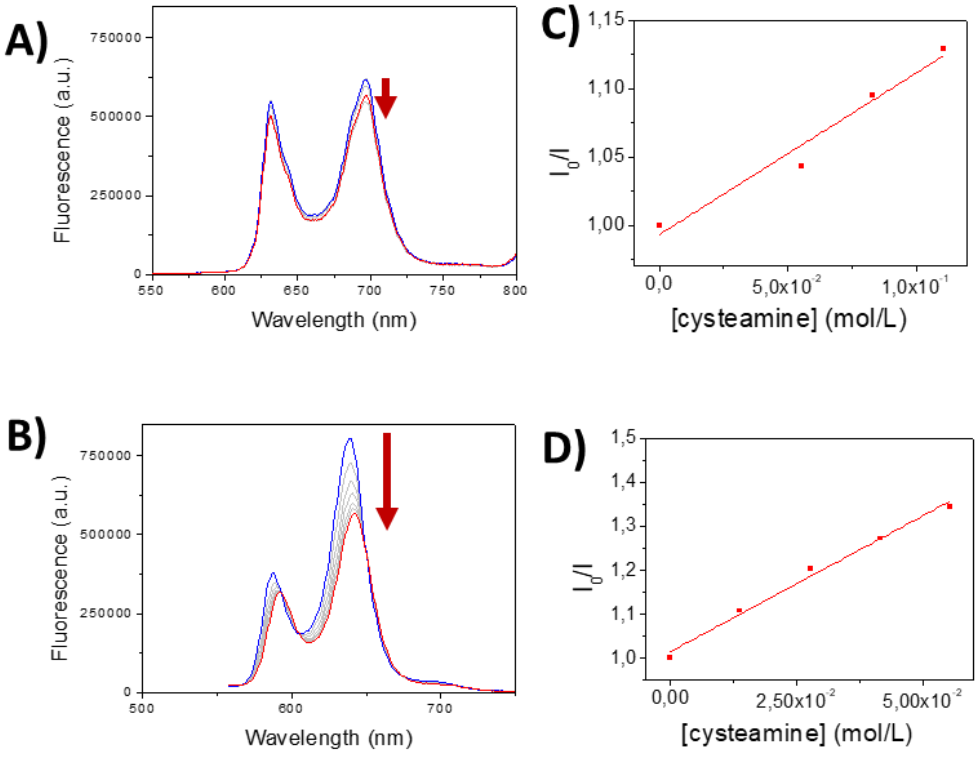

*Figure **S27**: Quenching of A) **PBP** and B) **PBPZn** fluorescence after a gradual addition of cysteamine. [**PBP**] =1,2x 10^{-7} mol.L^{-1}, [**PBPZn**] = 5.2 x 10^{-6} mol.L^{-1} (solvent: THF). Corresponding Stern-Volmer plot for **C) PBP** ($K_{SV}^{PBP/cysteamine}$ = 1.2 M^{-1}) and **D) PBPZn** ($K_{SV}^{PBPZn/cysteamine}$ = 6.2 M^{-1}).*

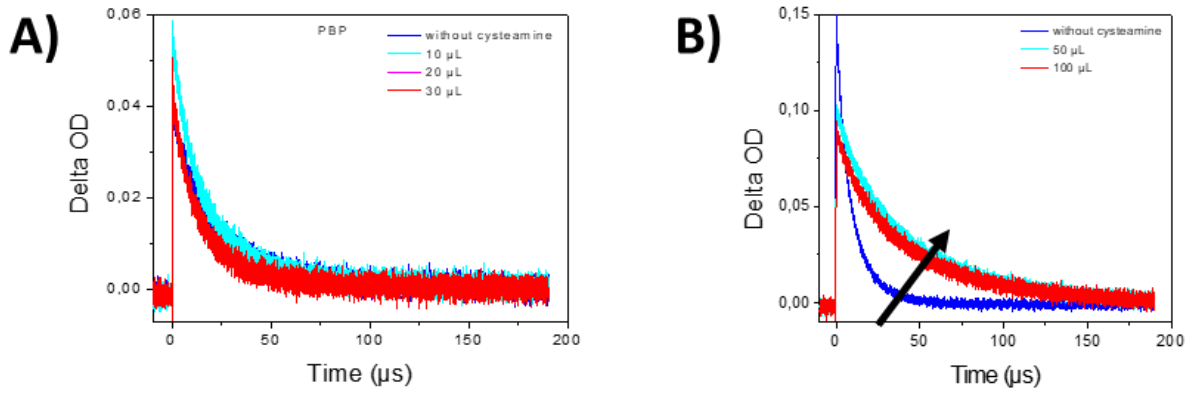

***Figure S28**: Decay traces of A) **PBP** and B) **PBPZn** triplet state after a laser pulse (λ_{ex} = 385 nm) with a gradual increase of the cysteamine concentration. [**PBP**] = 1,1 x 10^{-5} mol.L^{-1} , [PBPZn] = 1,7 x 10^{-4} mol.L^{-1} in DCM, [cysteamine] = 6,5 x 10^{-2} mol.L^{-1}.*

Effect of the addition of N-acetylcysteine

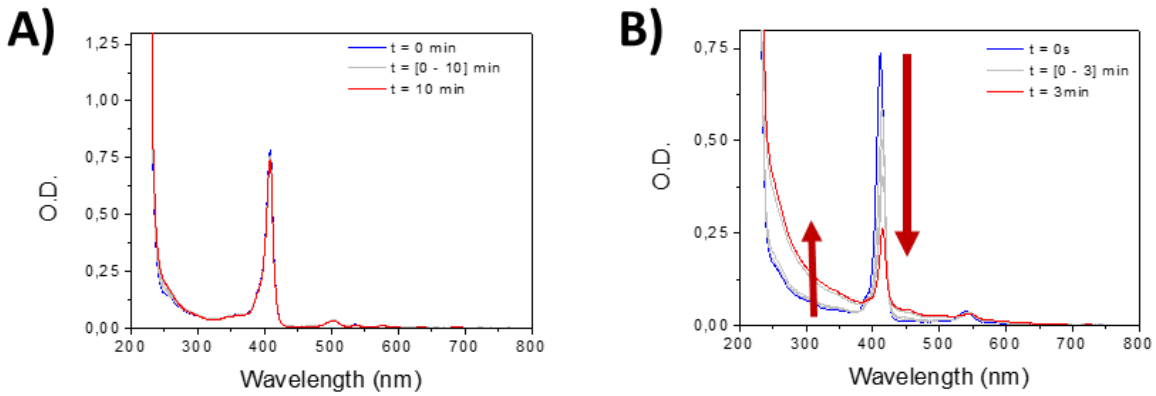

***Figure S29**: Steady state photolysis of A) PBP/cysteine and B) PBPZn/cysteine systems under air after LED @405 nm exposure. [**PBP**] = 2 x 10^{-6} mol/L, [**PBPZn**] = 6 x 10^{-6} mol/L, [cysteine] = 1.1 x 10^{-4} mol/L. Solvent = DCM.*

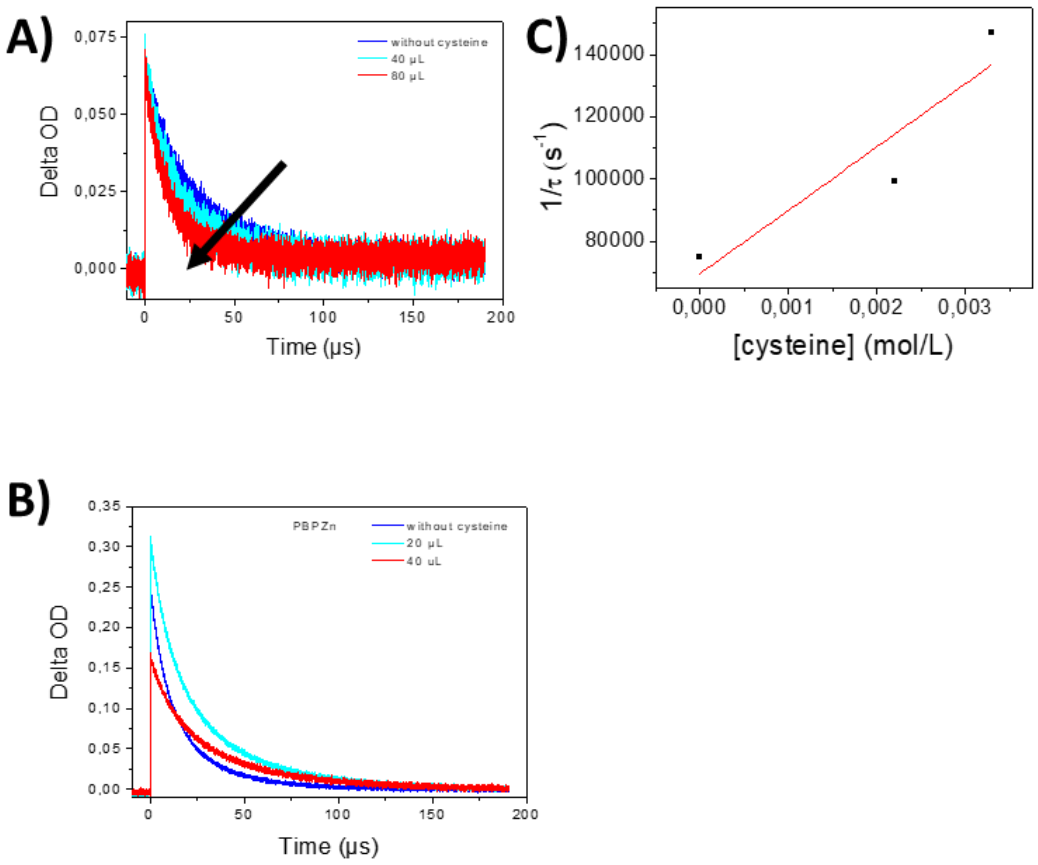

***Figure S30**: Decay traces of A) **PBP** and B) **PBPZn** triplet state after a laser pulse (λ_{ex} = 385 nm) with a gradual addition of cysteine. Corresponding Stern-Volmer plot for **C) PBP** and **D) PBPZn**. [**PBP**] = 1,1 x 10^{-5} mol.L^{-1} , [PBPZn] = 1,7 x 10^{-4} mol.L^{-1} in DCM, [cysteine] = 1,7 x 10^{-1} mol.L^{-1} in EtOH.*

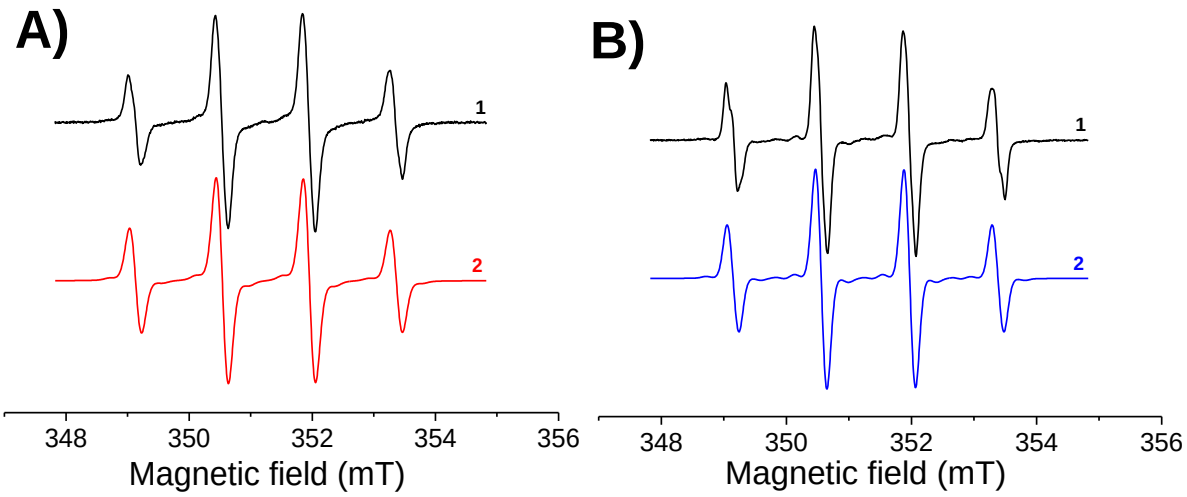

***Figure S31**: The normalized experimental (1) and simulated (2) EPR spectra obtained upon continuous in situ LED@405 nm exposure of (A) **PBP** and (B) **PBPZn** in chloroform and under argon in the presence of DMPO spin trapping agent and N-acetylcysteine. .*

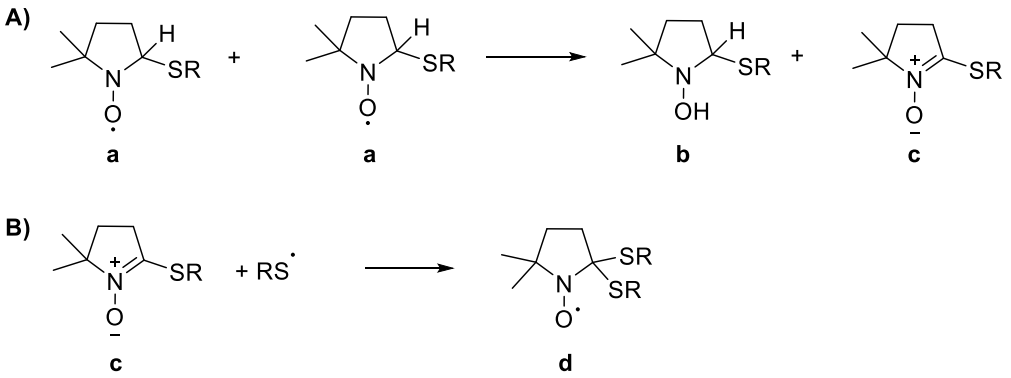

***Figure S32**: **A**) Dismutation reaction between two DMPO-SR adduct **a** leading to the formation of hydroxylamine **b** and nitrone **c** by redox reaction. **B**) Reaction between nitrone **c** and thiyl radical leading to nitroxide **d**.*

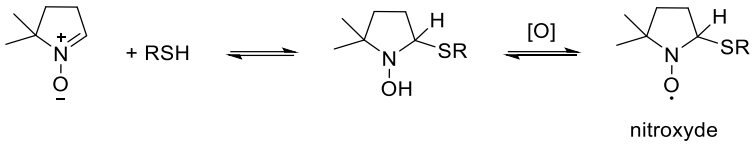

***Figure S33**: Forrester-Hepburn mechanism*



***Figure S34**: Optical image of the PBPZn-based pellet*

Partie B : Screening of porphyrins as PET-RAFT polymerization photocatalysts

I. Introduction

Radical polymerization is a widely used and effective process for producing polymers. However, many methods do not allow the distribution of polymer to be controlled. Based on this principle, controlled (or 'living') polymerization have been developed, like atom transfer radical polymerization (ATRP), nitroxide-mediated polymerization (NMP) or reversible addition-fragmentation chain transfer (RAFT) [1]. The development of photoinduced controlled polymerization have led to various methods, including photoinduced photo-RAFT [2], photo-RAFT by photolysis of the RAFT agent [3], and photoinduced eletron/energy transfer RAFT (PET-RAFT). The latter method has been extensively studied by Boyer *et al*. to develop systems for controlling polymer structure using visible light.

PET-RAFT polymerization is based on a two-part mechanism (**Figure IVB-1**): the first part is based on photoinduced electron/energy transfer (PET) to form the first oligoradical, which then participates in a reversible addition-fragmentation transfer (RAFT) mechanism.

Various photocatalysts have been developed, including porphyrins, which present good results. ZnTPP is the main one used [4,5], but other porphyrins have proved effective in aqueous media [6], and the difference in porphyrin reactivity depending on the RAFT agent and light used has been exploited to develop one-pot bipolymerisable systems [7]. New studies have been carried out to optimise the results obtained by changing the structure of the porphyrin [8].

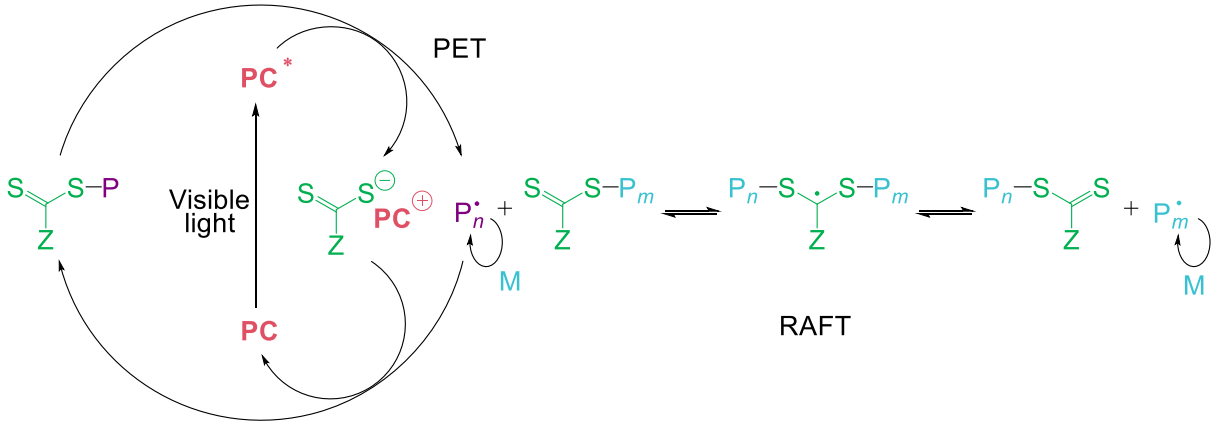

***Figure IVB-1**: Proposed mechanism of PET-RAFT polymerization.*

This study present the photopolymerization initiating properties of various porphyrins. After presenting the results for free base porphyrins under nitrogen, we will look at the influence of oxygen. We will then look at the increase in efficiency using metalled porphyrins under nitrogen and oxygen. The influence of the irradiation wavelength will also be studied. We will then show the control of polymer size, and finally the use in di-block polymerization.

II. Results and discussion

II. 1. Screening free base porphyrin

A number of free base porphyrins were used in this study (**Figure IVB-2**). These porphyrins have shown promising results for the initiation of FRP, as reported in the literature (ref **P3**/**P4** and **P8**/**P8Zn** and

theo/synthesis comparison) or in previous chapters (PushPull). However, their ability to initiate controlled radical polymerization has not been tested.

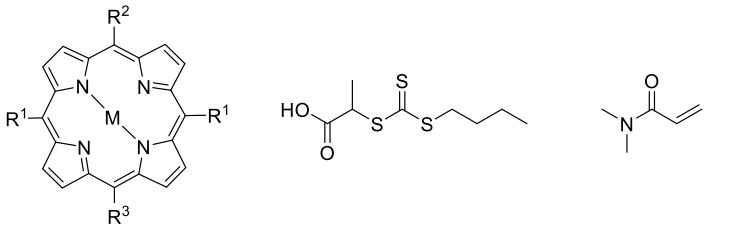

Photocatalyst RAGT agent (**BTPA**) Monomer (**DMA**)

Porphyrin	R^1	R^2	R^3	Metal
P3		Br	Br	H_2 or Zn(II)
P4				H_2 or Zn(II)
P5		N	N	H_2 or Zn(II)
P6		N	N	H_2 or Zn(II)
P7				H_2 or Zn(II)
P8		MeO N MeO	MeO N MeO	H_2, Zn(II) or Fe(III)
P9		MeO	MeO	H_2 or Zn(II)
P3H		Br	Br	H_2 or Zn(II)
TThP	S	S	S	H_2 or Zn(II)
PP3		MeO	O_2N	H_2
PP4		MeO	O_2N	H_2 or Zn(II)
TPP				Zn(II)

***Figure IVB-2**: Structure of the porphyrin, RAFT agent and monomer employed in this study.*

As porphyrins absorb over a very wide wavelength range, measurements were started at 530 nm, which corresponds to the absorption of the porphyrin Q-bands. This wavelength was chosen to avoid potential direct activation of the RAFT agent by a photoiniferter mechanism.

Screening was carried out using a [monomer]:[RAFT]:[photocatalyst] ratio of 200:1:0.0001 with a monomer concentration of 1 M in DMSO. The RAFT agent selected and the monomer used were determined by screening the best components for a variety of porphyrin[8]. DMSO was chosen to allow good solubility with porphyrins and to impart oxygen tolerance to the system by reacting with singlet

oxygen for quenching. The reagents were solubilised in DMSO, introduced into a 1 mL x 2 mm quartz cuvette and irradiated with a lamp for 6 h. Polymerization was monitored by infrared spectroscopy following the decrease in the signal corresponding to the vinyl function at 6155 cm^{-1} to determine the apparent propagation rate constant k_p^{app} and the final monomer conversion α, and by taking samples for molecular weight distribution analysis by Gel permeation chromatography (GPC).

In the first study, free base porphyrins were tested, as few free base porphyrin systems have been developed, by degassing the cuvette for 10 minutes prior to irradiation (**Table IVB-1**). Correct results were obtained, with monomer conversions above 55% obtained after 6 h of irradiation for porphyrins **P4**, **PP3** and **PP4**. The other porphyrins were able to produce polymers, but with final conversions between 21 and 47%. Only **P8** showed a very limited polymerization of 4%.

***Table IVB-1**: PET-RAFT polymerization of DMA with BTPA as RAFT agent, mediated with various porphyrins as photocatalyst. Polymerization were conducted under green LED light (λ = 530 nm, 5.5 mW/cm²) targeted at ([Monomer]:[RAFT]:[catalyst] = 200:1:0.0001 and $[Monomer]_0$ = 1.0 M). Monomer conversion (α), apparent propagation rate (K_p^{app}) were determined by FTIR spectroscopy and experimental molecular weights (M_n) and polymer dispersties (M_w/M_n) were determined by GPC using PMMA standards for calibration.*

Porphyrin	Metalled	Atmosphere	Exp	α (%) 360 min	K_p^{app} (min^{-1})	M_n ($g.mol^{-1}$)	M_w/M_n
P3	H_2	N_2	51	31	0.0023	1.2×10^4	1.09
P4	H_2	N_2	61	55	0.0042	1.1×10^4	1.07
P5	H_2	N_2	52	21	0.0006	1.9×10^4	1.02
P6	H_2	N_2	53	46	0.0017	1.6×10^4	1.06
P7	H_2	N_2	57	30	0.0010	1.3×10^4	1.14
P8	H_2	N_2	58	4	0.0002	-	-
P9	H_2	N_2	59	38	0.0013	1.6×10^4	1.04
P3H	H_2	N_2	56	47	0.0018	1.9×10^4	1.05
TThP	H_2	N_2	64	43	0.0024	0.9×10^4	1.07
PP3	H_2	N_2	62	57	0.0025	1.2×10^4	1.05
PP4	H_2	N_2	63	66	0.0030	1.3×10^4	1.04

II. 2. Influence of oxygen

One of the limitation of controlled polymerization is its sensibility to oxygen, leading to a decrease of size distribution control. Indeed, the molecular ground state oxygen can react with radical produced during polymerization process, leading to oxidation of compounds [9,10]. One of the solution is to remove oxygen from the system, by degassing the solution with inert gas, but cannot be used in industrial scale. A possible alternative is the use of a tolerant oxygen system, by using a specific photocatalyst, like transition metal photoredox [11,12], organic redox photocatalyst [13] or metalloporphyrins [4]. Indeed, the photocatalyst is able to react through a triplet-triplet annihilation with molecular oxygen to form singlet oxygen, quenched by DMSO to form $DMSO_2$ [5].

A second study have thus been performed and revealed the effect of oxygen on the systems, without any preliminary degassing of the solution (**Table IVB-2**). This mainly resulted in the observation of a period without polymerization at the start of the reaction, corresponding to the oxygen inhibition period, when oxygen is first consumed by the reaction. Maximum final conversions are maintained, with porphyrins **P4**, **PP3** and **PP4** showing conversion rates higher than 60%. In addition, porphyrins **P3**, **P7** and **P9** also showed better final conversions, with conversions around 60%. Lower conversions were obtained for **P5**, **P6**, **P8**, **P3H** and **TThP** with final conversion between 11 and 44%. **P4** gave very good results, but the acrylate functions on the porphyrin prevented the structures obtained from being determined.

***Table IVB-2**: PET-RAFT polymerization of DMA with BTPA as RAFT agent, mediated with various porphyrins as photocatalyst. Polymerization were conducted under green LED light (λ = 530 nm, 5.5 mW/cm^2) targeted at ([Monomer]:[RAFT]:[catalyst] = 200:1:0.0001 and [Monomer]$_0$ = 1.0 M). Monomer conversion (α), apparent propagation rate (K_p^{app}) were determined by FTIR spectroscopy and experimental molecular weights (M_n) and polymer dispersties (M_w/M_n) were determined by GPC using PMMA standards for calibration.*

Porphyrin	Metalled	Atmosphere	Exp	α (%) 360 min	K_p^{app} (min^{-1})	M_n (g.mol^{-1})	M_w/M_n
P3	H_2	O_2	50[b]	56	0.0023	1.9 x 10^4	1.06
P4	H_2	O_2	37	91	0.0079	1.8 x 10^4	1.05
P5	H_2	O_2	34	32[a]	0.0005	0.6 x 10^4	1.31
P6	H_2	O_2	35	37	0.0015	1.2 x 10^4	1.15
P7	H_2	O_2	30	63	0.0039	1.3 x 10^4	1.04
P8	H_2	O_2	47	11	0.0005	1.6 x 10^4	1.04
P9	H_2	O_2	23	56	0.0027	1.2 x 10^4	1.07
P3H	H_2	O_2	48	30	0.0011	1.0 x 10^4	1.10
TThP	H_2	O_2	49	44	0.0022	1.5 x 10^4	1.10
PP3	H_2	O_2	27	60	0.0029	1.1 x 10^4	1.06
PP4	H_2	O_2	28	62	0.0026	1.2 x 10^4	1.04

II. 3. Metalled porphyrin

Studies have shown that polymerization is more efficient with metalled porphyrins. Shanmugam *et al.* [4] showed that TPP porphyrin had a final monomer conversion of 13%, compared to 80% for ZnTPP porphyrin complexed with zinc. Porphyrins complexed with metals such as cobalt, nickel or iron did not give such good polymerization results (around 5% for each). Similarly, Ng *et al.* [8] showed a significant difference between two free base porphyrins and those complexed with zinc, going from 15% (and 28%) to 63% (and 62%) monomer conversion. Similar results were obtained for uncontrolled radical polymerization [14–16] (ref PBP/PBPZn). Zinc appears to be an excellent candidate for photoinitiation of radical polymerization, given its tendency to increase intersystem conversion and favour triplet states, which are more stable than singlet states and therefore more likely to react with the RAFT agent. Porphyrin metalation was therefore carried out in the presence of zinc acetate following the procedure already established [15].

As expected, the zinc-complexed porphyrins improved the final conversions, except in the case of **PP4**, which went from a conversion of 66% to 46% for metal complex. The systems achieved final DMA conversions of 97%, 87% and 86% for **P9Zn**, **P7Zn** and **P3Zn** respectively. The other porphyrins (**P4Zn**, **P5Zn**, **P6Zn**, **P3HZn** and **TThPZn**) achieved conversions greater than 77%. Only porphyrins **P8** complexed with zinc or iron were unable to achieve high conversion rates.

***Table IVB-3**: PET-RAFT polymerization of DMA with BTPA as RAFT agent, mediated with various porphyrins as photocatalyst. Polymerization were conducted under green LED light (λ = 530 nm, 5.5 mW/cm²) targeted at ([Monomer]:[RAFT]:[catalyst] = 200:1:0.0001 and [Monomer]$_0$ = 1.0 M). Monomer conversion (α), apparent propagation rate (K_p^{app}) were determined by FTIR spectroscopy and experimental molecular weights (M_n) and polymer dispersties (M_w/M_n) were determined by GPC using PMMA standards for calibration.*

Porphyrin	Metalled	Atmosphere	Exp	α (%) 360 min	K_p^{app} (min^{-1})	M_n ($g.mol^{-1}$)	M_w/M_n
P3	Zn	N_2	90	86	0.0075	1.8×10^4	1.06
P4	Zn	N_2	98	80	0.0042	2.5×10^4	1.03
P5	Zn	N_2	79	79	0.0045	1.7×10^4	1.03
P6	Zn	N_2	74	81	0.0045	1.6×10^4	1.04
P7	Zn	N_2	86	87	0.0063	1.9×10^4	1.04
P8	Zn	N_2	70	43	0.0016	1.0×10^4	1.07
P8	Fe	N_2	69	0	-	-	-
P9	Zn	N_2	82	97	0.0072	2.0×10^4	1.03
P3H	Zn	N_2	84	83	0.0048	1.6×10^4	1.04
TThP	Zn	N_2	92	77	0.0042	1.7×10^4	1.04
PP4	Zn	N_2	88	46	0.0017	1.0×10^4	1.06
TPP	Zn	N_2	71	>99	0.0113	2.1×10^4	1.03

II. 4. Metalled porphyrin under oxygen

In the same way as with free base porphyrins, porphyrins in air show comparable results to polymerization in nitrogen. Although **PP4Zn** decreased again, reaching only 4% of monomer conversion, the systems containing **P9Zn**, **P7**Z and **P3Zn** achieved very good conversions of 82%, 83% and 95% respectively. **P6Zn** also reached 90%, and the other porphyrins (**P4Zn**, **P6Zn**, **P3HZn** and **TThPZn**) achieved conversions higher than 71%. Only **P5Zn** was slightly less effective, reaching 58%. **P8Zn** and **P8Fe** continue to offer limited polymerization, with final conversions of 34% and 0% respectively.

***Table IVB-4**: PET-RAFT polymerization of DMA with BTPA as RAFT agent, mediated with various porphyrins as photocatalyst. Polymerization were conducted under green LED light (λ = 530 nm, 5.5 mW/cm²) targeted at ([Monomer]:[RAFT]:[catalyst] = 200:1:0.0001 and [Monomer]$_0$ = 1.0 M). Monomer conversion (α), apparent propagation rate (K_p^{app}) were determined by FTIR spectroscopy and experimental molecular weights (M_n) and polymer dispersties (M_w/M_n) were determined by GPC using PMMA standards for calibration.*

Porphyrin	Metalled	Atmosphere	Exp	α (%) 360 min	K_p^{app} (min^{-1})	M_n ($g.mol^{-1}$)	M_w/M_n
P3	Zn	O_2	93	95	0,0053	3.3×10^4	1.05
P4	Zn	O_2	97	71	0.0036	2.4×10^4	1.04
P5	Zn	O_2	78	58	0.0028	1.4×10^4	1.05
P6	Zn	O_2	73	90	0.0072	1.9×10^4	1.04
P7	Zn	O_2	85	83	0.0056	1.7×10^4	1.05
P8	Zn	O_2	47	34[a]	0.0018	1.6×10^4	1.04
P8	Fe	O_2	68	0	-	-	-
P9	Zn	O_2	81	82	0.0045	1.8×10^4	1.03
P3H	Zn	O_2	83	78	0.0041	1.8×10^4	1.03
TThP	Zn	O_2	91	88	0.0064	1.9×10^4	1.05
PP4	Zn	O_2	87	2	0.0001	-	-
TPP	Zn	O_2	72	>99	0.0113	1.9×10^4	1.04

II. 5. Different wavelength

Porphyrins exhibit several absorption peaks, and different conditions were used to determine the influence of irradiation wavelength on polymerization (**Table IVB-5**). The **P3**, **P4**, **P7** and **PP4** systems were selected for their efficiency, and the polymerization of DMA in the presence of BTPA was studied at two additional wavelengths, 505 and 650 nm. The evolution of $\ln([M]_0/[M]_t)$ as a function of time (**Figure IVB-3**) shows that polymerization is not significantly dependent to the wavelength employed, as porphyrins absorb well at these values.

In addition, a study of the molecular weight distribution (**Table IVB-5**) did not show any obvious influence on the polydispersity indices, which were found between 1.07 and 1.03.

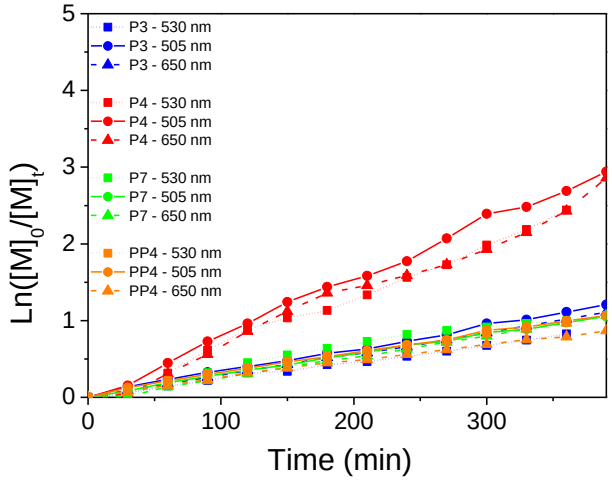

***Figure IVB-3**: Plot of $\ln([M]_0/[M]_t)$ vs exposure time for PET RAFT polymerization of DMA in presence of BTPA and various porphyrin as photocatalyst at different irradiation wavelength in presence of oxygen using [Monomer]:[RAFT]:[catalyst] ratio of 200:1:0.0001 and $[Monomer]_0$ = 1.0 M.*

***Table IVB-5**: PET-RAFT polymerization of DMA with BTPA as RAFT agent, mediated with various porphyrins as photocatalyst. Polymerization were conducted under three different wavelength (λ = 505, 530 and 650 nm), targeted at ([Monomer]:[RAFT]:[catalyst] = 200:1:0.0001 and $[Monomer]_0$ = 1.0 M). Monomer conversion (α), apparent propagation rate (K_p^{app}) were determined by FTIR spectroscopy and experimental molecular weights (M_n) and polymer dispersties (M_w/M_n) were determined by GPC using PMMA standards for calibration.*

Porphyrin	λ	Exp	α (%) 360 min	K_p^{app} (min^{-1})	M_n ($g.mol^{-1}$)	M_w/M_n
P3	505	42	67	0.0031	2.1×10^4	1.05
	530	50[b]	56	0.0023	1.9×10^4	1.03
	650	38	64	0.0029	2.0×10^4	1.05
P4	505	43	93	0.0084	3.0×10^4	1.04
	530	26	91	0.0079	1.8×10^4	1.05
	650	39	91	0.0080	3.0×10^4	1.04
P7	505	44	62	0.0028	2.1×10^4	1.07
	530	30	63	0.0039	1.3×10^4	1.04
	650	40	62	0.0028	2.0×10^4	1.06
PP4	505	45	63	0.0028	2.1×10^4	1.04
	530	28	62	0.0026	1.2×10^4	1.04
	650	41	55	0.0025	1.8×10^4	1.06

II. 6. Size controlled

The systems based on **P3** are the most promising for polymerization under oxygen, whether with or without metal complexation. The polymerization kinetics of these two systems were therefore studied in detail, using GPC to obtain molecular weight monitoring. The system using **P3Zn** as the photocatalyst showed better conversion and propagation rate constant than the **P3**-based system (α (**P3**) = 56% and α (**P3Zn**) = 95% and k_p^{app} (**P3**) = 0.0023 and k_p^{app} (**P3Zn**) = 0.005) (**Figure IVB-4A**). The molecular weight distribution (**Figure IVB-4B** and **Figure IVB-4C**) also showed good linearity (**Figure IVB-4D**). Similarly, the polydispersity of the synthesised polymers showed good agreement between the two systems (**Figure IVB-4E**), although the molecular weight distribution was more narrow for **P3Zn**, which is consistent with the higher final conversion.

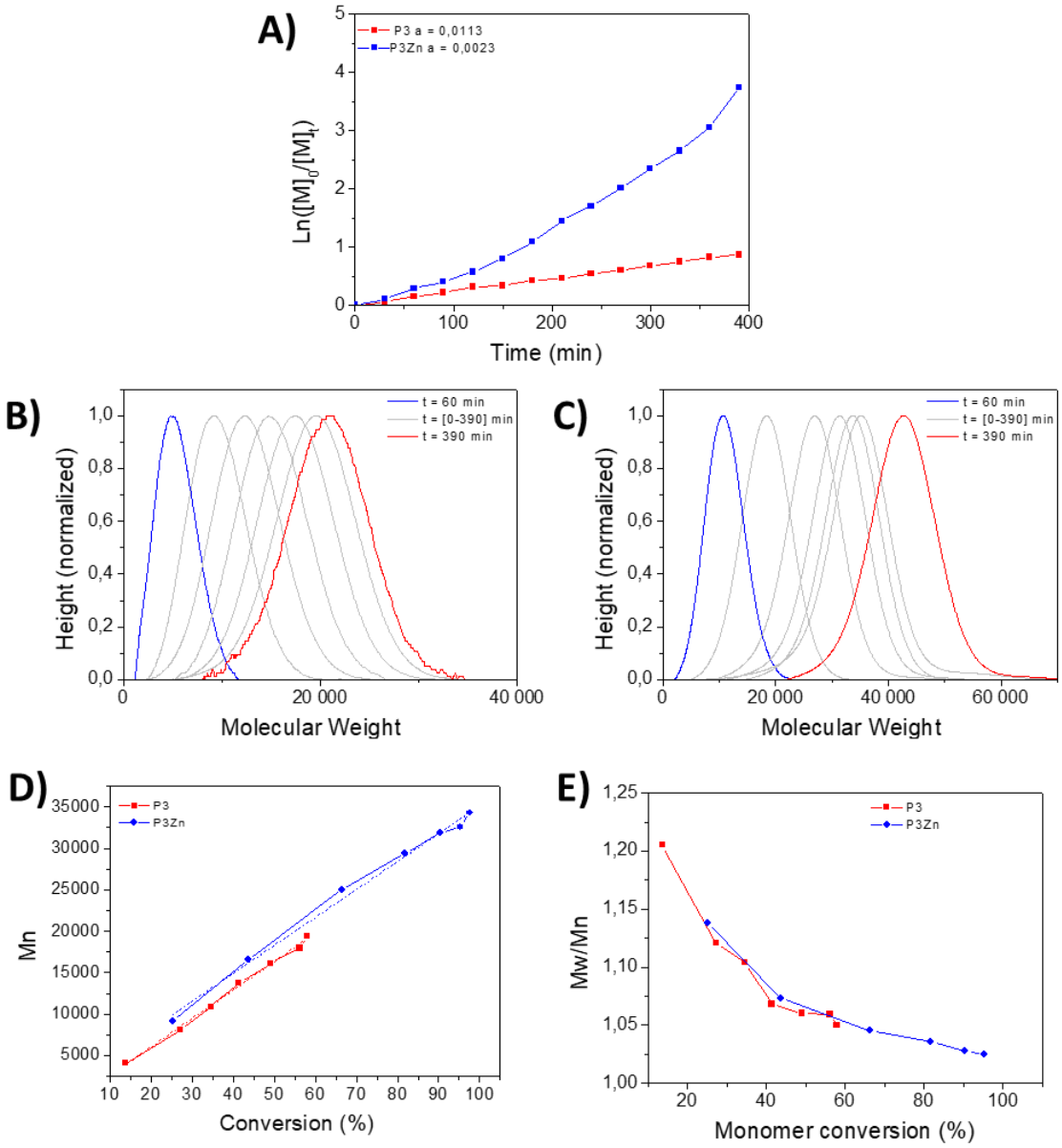

***Figure IVB-4**: **A)** Plot of $ln([M]_0/[M]_t)$ vs exposure time, Molecular weight distributions for **B) P3** and **C) P3Zn**, **D)** M_n vs conversion and **E)** M_w/Mn vs conversion, for PET RAFT polymerization of DMA in presence of BTPA and **P3** or **P3Zn** as photocatalyst under 530 nm irradiation in presence of oxygen using [Monomer]:[RAFT]:[catalyst] ratio of 200:1:0.0001 and $[Monomer]_0$ = 1.0 M.*

II. 7. Chain extension via PET-RAFT living polymerization

In order to determine the "living" character of the synthesised polymer, a chain extension was conducted. Its purpose is to confirm that the polymer formed still contains the end-group from the RAFT agent and is therefore able to undergo polymerization again after purification. In fact, two radical polymer chains can self-associate to form 'dead' polymer chains. It may also be possible to create diblock polymers, with different monomers, in order to obtain different properties, such as antibacterial properties [17].

A first DMA polymer was synthesized ($M_{n,\ GPC}$ = 19026 g/mol, M_w/M_n = 1,06 and 56% monomer conversion) in the presence of BTPA and **P3** at 1 ppm as catalyst in DMSO. The polymer was then purified to remove traces of unpolymerized monomers and catalyst. Then a second polymerization is carried out by adding DMA and **P3** catalyst at 1 ppm, but without adding BTPA. The system is placed under irradiation and the conversion of the monomer is followed by IR and GPC spectroscopy. The results of the two successive polymerizations are presented in **Table IVB-6**. It can be noted in **Figure IVB-5A** that the polymerization in maintained, despite a lower polymerization rate (k_p = 0.0019 min^{-1} for the second polymerization compared to k_p = 0.0023 min^{-1} for the first polymerization). Logically, the conversion rate after 360 min of irradiation is slightly lower, reaching 49% (compared to 56% during the first polymerization). From a molecular weight point of view, it is noticed that the molar mass also increases linearly during the second polymerization reaching 32906 g/mol. Finally, the study of polydispersity presents a constant decrease to obtain more homogeneous polymers, with a final polydispersity of M_w/M_n = 1.03.

***Table IVB-6**: Chain extension PET-RAFT polymerization of DMA with BTPA as RAFT agent, mediated with **P3** as photocatalyst. Polymerization were conducted under green LED light (λ = 530 nm, 5.5 mW/cm²) targeted at ([Monomer]:[RAFT]:[catalyst] = 200:1:0.0001 and $[Monomer]_0$ = 1.0 M). Monomer conversion (α), apparent propagation rate (K_p^{app}) were determined by FTIR spectroscopy and experimental molecular weights (M_n) and polymer dispersties (M_w/M_n) were determined by GPC using PMMA standards for calibration.*

Porphyrin	Exp	α (%) 360 min	K_p^{app} (min^{-1})	M_n ($g.mol^{-1}$)	M_w/M_n
P3 – 1st polymerization	50	56	0.0023	1.9×10^4	1.06
P3 – 2nd polymerization	100	49	0.0019	3.3×10^4	1.03

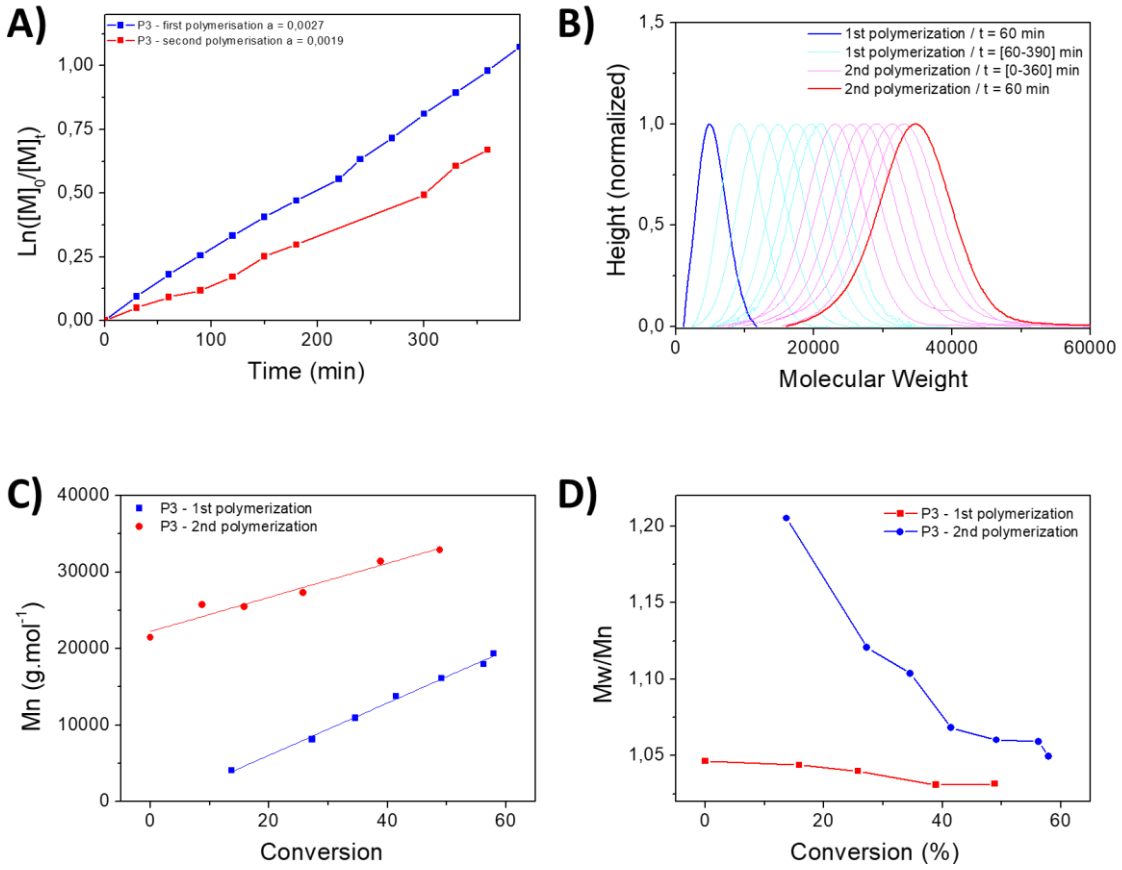

***Figure IVB-5**: **A**) Plot of ln([M]$_0$/[M]$_t$) vs exposure time, **B**) Molecular weight distributions, **C**) M_n vs conversion and **D**) M_w/Mn vs conversion, for chain extension PET RAFT polymerization of DMA in presence of BTPA and **P3** as photocatalyst under 530 nm irradiation in presence of oxygen using [Monomer]:[RAFT]:[catalyst] ratio of 200:1:0.0001 and [Monomer]$_0$ = 1.0 M.*

III. Conclusion

In conclusion, the initiating PET-RAFT polymerization properties of a series of 22 new porphyrins (free base and metalled) have been demonstrated under inert gas or ambient air. They demonstrate variable final monomer conversion, reaching 97% for **P9Zn** under nitrogen. Polymerization has also been reported under oxygen, with conversion superior to 90% for **P3Zn** and **P6Zn** (95 and 90% respectively). The synthesized polymers have presented excellent polydispersity inferior of 1.05. The conservation of end-groups was confirmed by successful chain extension.

IV. Experimental part

Materials. The monomer used, *i.e.* N,N-dimethylacrylamide (DMA, 99%) purchased from Sigma-Aldrich, was deinhibited by basic alumina chromatography column before usage. RAFT agent, 2-(n-Butyltrithiocarbonate)propionic acid (BTPA) has been synthesised according to a literature procedure [18]. Dimethyl sulfoxide (DMSO) from Ajax Chemical was used as solvent and used as received.

Photopolymerization. Photosensible systems are composed of 900 µL of a DMSO solution containing [DMA]:[BTPA]:[porphyrin] ratio of 200:1:0.0001 and [Monomer]$_0$ = 1.0 M and placed in a 1 mL quartz cuvettes with a 2 mm path length. The reaction mixture was irradiated at 6 cm by RS Component Pack Lamp Led light (5 W) at different wavelength.

Photopolymerization monitoring. The monomer conversion was monitored by following the decrease of vinylic C-H stretching overtone of the monomer at 6155 cm^{-1} by One-line Fourier Transform Near-Infrared (FTNIR) spectroscopy (**Figure IVB-6A**). The sample was removed from irradiation and placed every 15 or 30 minutes into the holder to perform the monitoring. Each spectrum is composed of 16 scans with a resolution of 4 cm^{-1}.

Molecular weight and dispersity determination. The polymer synthesized were characterized by Gel Permeation Chromatography (GPC) (**Figure IVB-6B**) using dimethylacetamide (DMAc) eluent (flow rate of 1 $mL.min^{-1}$). The instrument is composed of a Shimadzu modular system equipped with an autoinjector, a 5.0 µM bead sizeguard column (50 x 7.5 mm) and four 5.0 µM bead size column of 10^5, 10^4, 10^3 and 10^2 Å from Phenomenex and differential refractive-index and UV (λ = 305 nm) detectors.

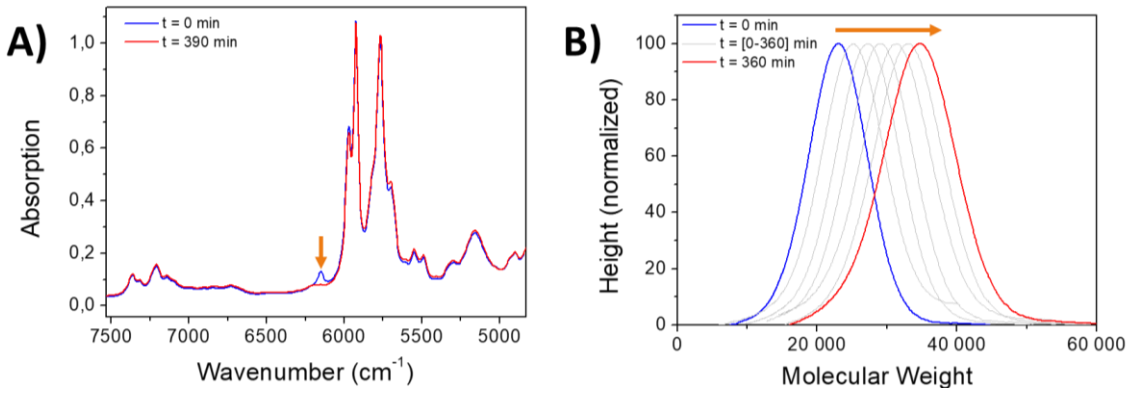

***Figure IVB-6**: Monitoring of the polymerization by **A**) following the decrease of acrylamide function at 6155 cm^{-1} by IR spectroscopy and **B**) following the molecular weight of polymer by GPC.*

V. References

1 W. A. Braunecker and K. Matyjaszewski, Progress in Polymer Science, 2007, 32, 93–146.
2 G. Moad, Polymer Chemistry, 2017, 8, 177–219.
3 J. Yeow, O. R. Sugita and C. Boyer, ACS Macro Lett., 2016, 5, 558–564.
4 S. Shanmugam, J. Xu and C. Boyer, J. Am. Chem. Soc., 2015, 137, 9174–9185.
5 N. Corrigan, D. Rosli, J. W. J. Jones, J. Xu and C. Boyer, Macromolecules, 2016, 49, 6779–6789.
6 S. Shanmugam, J. Xu and C. Boyer, Macromolecules, 2016, 49, 9345–9357.
7 J. Xu, S. Shanmugam, C. Fu, K.-F. Aguey-Zinsou and C. Boyer, J. Am. Chem. Soc., 2016, 138, 3094–3106.
8 G. Ng, K. Jung, J. Li, C. Wu, L. Zhang and C. Boyer, Polym. Chem., 2021, 12, 6548–6560.
9 A. K. O'Brien and C. N. Bowman, Macromolecules, 2006, 39, 2501–2506.
10 C. Decker and A. D. Jenkins, Macromolecules, 1985, 18, 1241–1244.
11 J. Xu, K. Jung and C. Boyer, Macromolecules, 2014, 47, 4217–4229.
12 S. Shanmugam, J. Xu and C. Boyer, Macromolecules, 2014, 47, 4930–4942.
13 J. Xu, S. Shanmugam, H. T. Duong and C. Boyer, Polym. Chem., 2015, 6, 5615–5624.
14 G. Noirbent, Y. Xu, A.-H. Bonardi, D. Gigmes, J. Lalevée and F. Dumur, European Polymer Journal, 2020, 139, 110019.
15 H. Marcille, J.-P. Malval, M. Presset, N. Bogliotti, A. Blacha-Grzechnik, V. Brezová, Y. Yagci and D.-L. Versace, Polym. Chem., 2020, 11, 4237–4249.
16 A. Bonardi, F. Bonardi, G. Noirbent, F. Dumur, C. Dietlin, D. Gigmes, J.-P. Fouassier and J. Lalevée, Polym. Chem., 2019, 10, 6505–6514.
17 P. R. Judzewitsch, T.-K. Nguyen, S. Shanmugam, E. H. H. Wong and C. Boyer, Angewandte Chemie International Edition, 2018, 57, 4559–4564.
18 S. Shanmugam, J. Xu and C. Boyer, Chem. Sci., 2015, 6, 1341–1349.

Conclusions du Chapitre IV

Dans ce chapitre, le potentiel des porphyrines pour amorcer différentes polymérisations a été déterminé. Les porphyrines **PBP** et **PBPZn** ont démontré de bonnes propriétés de photoamorçage de la polymérisation radicalaire classique, en permettant des conversions allant jusqu'à 90% sous irradiation à 405 nm. De plus, **PBPZn** a également permis d'amorcer la polymérisation cationique, en permettant la polymérisation de fonctions époxyde. Enfin, une série de porphyrines a également montré son efficacité pour l'amorçage de la polymérisation radicalaire contrôlée, la polymérisation PET-RAFT.

Enfin, les matériaux obtenus avec **PBP** et **PBPZn** ont démontré de bonnes capacités d'inhibition de la croissance de *S. aureus* sous irradiation, permettant son utilisation en surface antibactérienne. Cependant, aucun polymère antibactérien n'a pu être développé pour la série de porphyrine en polymérisation PET-RAFT. En effet, la méthodologie développée pour la polymérisation n'a pas donné de résultats suffisamment prometteurs pour prétendre à des applications plus poussées.

Conclusion générale et perspectives

Ce travail de recherche a consisté à développer des nouveaux matériaux photoactivables pour des applications en dépollution de l'eau ou comme surfaces antibactériennes. Un autre enjeu principal était le développement de ces matériaux par photopolymérisation, permettant une chimie plus respectueuse de l'environnement et plus sûre. Ces deux aspects ont été abordés par l'utilisation d'une seule molécule photoactive, qui permet sous irradiation de former d'abord des espèces réactives soit avec un co-amorceur pour la photopolymérisation, soit en agissant en tant que photoamorceur, puis de former des espèces réactives de l'oxygène pour les applications photoactivées, en agissant comme photosensibilisateur. Notre attention s'est tournée vers les porphyrines, qui sont des macrocycles facilement fonctionnalisables, relativement stables sous irradiation, et potentiellement peu toxiques sans irradiation pour permettre de créer des matériaux sûrs.

La modélisation et la synthèse de nombreux composés ont été réalisées. Nous avons ainsi pu développer de nombreux systèmes photoamorceurs, et les plus prometteurs ont été étudiés spécifiquement, et valorisés pour des applications antibactériennes et de dépollution de l'eau.

Dans le premier chapitre, deux projets complémentaires ont été présentés. Le premier projet (**chapitre II-A**), considérant les porphyrines **P3** et **P4**, a permis de poser les bases du projet. En effet, ces deux porphyrines ont été modélisées puis synthétisées, et leurs interactions avec de nombreux co-amorceurs ont été étudiées. Les capacités de photoinitiation de ces systèmes ont ensuite été exploités en utilisant un monomère biosourcé. Ces systèmes ont montré d'excellentes capacités de photopolymérisation, allant jusqu'à 90% de conversion finale des fonctions acrylates en association avec de la MDEA. Ces systèmes ont ensuite été utilisés pour la réalisation de revêtements pour la dépollution de l'eau sous irradiation UV. Les mécanismes sous irradiation ont été déterminés, permettant de mettre en lumière les étapes importantes.

Dans le deuxième projet, concernant les molécules **P8** et **P8Zn** (**chapitre II-B**), les conditions optimales pour la synthèse des matériaux déterminés par le projet précédant ont été directement utilisées. Cela a permis d'obtenir des systèmes avec des conversions finales jusqu'à 89 et 83% pour les deux porphyrines. Les matériaux obtenus ont ensuite été utilisés pour la dégradation de polluants sous irradiation UV puis visible. Si la photodégradation s'est montrée efficace sous irradiation UV, elle a présenté des résultats plus mitigés sous la gamme du visible. En effet, aucune photodégradation n'a été observée, un écart avec la photolyse ayant pu être obtenu avec l'ajout de peroxyde d'hydrogène. De plus, des mécanismes d'adsorption ont pu être obtenus avec l'ajout d'acide dans le milieu, permettant tout de même une élimination des polluants de l'eau.

Dans le deuxième chapitre, plusieurs structures de porphyrines ont été conçues afin de les modéliser pour prévoir leurs propriétés. Le troisième projet (**chapitre III-A**), présente les propriétés d'une série de porphyrines de type A_2B_2. Une méthode est définie, permettant de prévoir et sélectionner les porphyrines les plus intéressantes pour la photopolymérisation. Cela a ensuite permis de comprendre les propriétés spectroscopiques expérimentales.

Le quatrième projet, présentant les porphyrines de structure push pull (**chapitre III-B**), a permis de modéliser les porphyrines de type A_2BC. Ces structures ont réussi à démontrer des capacités élevées de photoamorçage de la polymérisation, puisqu'il est possible d'atteindre 99% de conversion dans les conditions classiques. Malheureusement pour ces deux projets, aucune corrélation entre les

propriétés théoriques et les résultats de photoamorçage expérimentaux n'a pu être trouvée. Il faudrait trouver les paramètres influençant la polymérisation afin de pouvoir prédire de manière plus juste quelles structures possèdent les meilleures capacités de photoamorçage. Cependant, un dernier type de structure, les porphyrines réduites, a pu permettre de développer des systèmes ayant de bonnes capacités de photoamorçage dans les hautes longueurs d'onde du visible ($\lambda > 600$ nm). Ce type de structure devrait permettre également de pallier au manque d'efficacité pour la dépollution de l'eau pour les polymères à base de porphyrine grâce à une bonne production d'ion superoxyde.

Enfin, dans le dernier chapitre, l'exploitation des porphyrines pour le développement de matériaux antibactériens a été mise à profit. Le cinquième projet a permis de développer deux porphyrines portant des benzophénones (**chapitre IV-A**) pour permettre un photoamorçage plus efficace, allant jusqu'à 97% de conversion. Ces matériaux ont ensuite été utilisés pour le développement de matériaux antibactériens, prouvant l'inhibition de la croissance de *S. aureus* après irradiation.

Enfin, le dernier projet a permis d'exploiter l'ensemble des porphyrines développées pour la réalisation de polymères par photopolymérisation PET-RAFT (**chapitre IV-B**). Celle-ci pourrait en effet permettre la synthèse de polymères antibactériens par introduction de monomères antibactériens dans la structure par polymérisation di-bloc. L'étape d'optimisation a permis d'obtenir un grand nombre de systèmes prometteurs pour la synthèse de polymères de tailles contrôlées sous air, avec une possibilité en polymérisation di-bloc. Cependant, les systèmes développés n'étaient pas suffisamment efficaces pour envisager la réalisation de polymères contenant des fonctions antibactériennes. Il pourrait être intéressant de déterminer les propriétés impliquées dans le mécanisme, afin de développer de nouvelles structures pour la polymérisation PET-RAFT.

Résumé

Le développement de nouveaux matériaux possédant des propriétés antibactériennes et dépolluantes par activation à la lumière est une stratégie prometteuse permettant de répondre aux enjeux de santé publique et d'environnement. Ces matériaux sont produits par photopolymérisation de monomères issus de bioressources, selon un procédé plus sûr et économique. Bien que de nombreux types de photoamorceurs aient été précédemment développés pour permettre d'amorcer la photopolymérisation radicalaire, un intérêt croissant est porté sur les structures absorbant à des longueurs d'onde dans les domaines du visible ou du proche infrarouge, afin de réduire l'énergie nécessaire à la réaction de photopolymérisation. Dans ce but, les porphyrines constituent une nouvelle famille de photoamorceurs de choix, leurs propriétés photochimiques étant facilement modulables par modification de leur substitution.

Les travaux développés au cours de cette thèse ont été consacrés à la modélisation et à la synthèse de nouveaux dérivés de porphyrines. Ces structures ont été utilisées en tant que photoamorceurs en combinaison avec un co-amorceur permettant d'amorcer la photopolymérisation dans le domaine du visible. Les propriétés photophysiques et photochimiques de ces nouveaux systèmes ont été étudiées afin de déterminer les mécanismes mis en jeu. Ces systèmes ont ensuite été utilisés pour l'amorçage de la photopolymérisation radicalaire (FRP) de l'huile de soja acrylatée, un monomère biosourcé.

Les matériaux ainsi développés contiennent les photoamorceurs à base de porphyrines qui se retrouvent piégés dans la matrice polymérique. Sous irradiation lumineuse, les porphyrines peuvent interagir avec l'oxygène de l'air pour produire des espèces oxydantes, telles que des espèces réactives de l'oxygène (ROS). Ces propriétés ont été exploitées pour développer des matériaux possédant des propriétés antibactériennes ou dépolluantes de l'eau en permettent une élimination autonome des contaminants de surface.

Mots clés : Antibactérien – Photochimie – Porphyrines – Bioressources – Modélisation – Dépollution

Abstract

The development of new materials, which have antibacterial and depolluting properties through light activation, is a promising strategy offering a solution to the public health and environmental issues. These materials are produced by photopolymerization of monomers obtained from bioressources, using a safer and more economical process. Although many types of photoinitiators have previously been developed to initiate radical photopolymerization, there has been growing interest in structures that absorb at wavelengths in the visible or near-infrared range, in order to reduce the energy required for the photopolymerization reaction. Porphyrins are a new family of photoinitiators of choice for this purpose, as their photochemical properties can easily be modulated by modifying their substitution.

The work developed during this thesis was focused on the computing and synthesis of new porphyrin derivatives. These structures were used as photoinitiators in combination with a co-initiator to initiate photopolymerization in the visible range. The photophysical and photochemical properties of these new systems were studied to determine the mechanisms involved. These systems were then used to initiate the radical photopolymerization (FRP) of acrylated soya oil, a bio-sourced monomer.

The materials thus developed contain porphyrin-based photoinitiators that are trapped in the polymer matrix. Under irradiation, porphyrins interact with atmospheric oxygen to produce oxidative species, such as reactive oxygen species (ROS). These properties have been exploited to develop materials with antibacterial or depolluting properties, allowing surface contaminants to be autonomously eliminate.

Keywords: Antibacterial – Photochemistry – Porphyrin – Bioressources – Simulation – Depollution